BUBBLE IMPINGEMENT AND THE MECHANISMS OF HEAT TRANSFER ENHANCEMENT

DAVID B. DONOGHUE

Department of Mechanical & Manufacturing Engineering

Parsons Building

University of Dublin, Trinity College

Dublin 2

Ireland

April 2014

A thesis submitted to the University of Dublin in partial fulfillment of the requirements for the degree of Ph.D.

Declaration

I declare that I am the author of this thesis and that all work described herein is my own, unless otherwise referenced. Furthermore, this work has not been submitted, in whole or part, to any other university or college for any degree or qualification.

I authorize the library of Trinity College, Dublin to lend or copy this thesis.

David B. Donoghue, April 2014

Strive not to be a success, but rather to be of value.

Albert Einstein

Abstract

Fluid agitation and mixing ensuing from two phase flow has an important role to play within two phase flow heat exchangers, which are at the forefront of energy conversion. Within these environments, vapour bubbles may impinge against the heat exchange surfaces of the device, with this behaviour thought to directly affect convective heat flow. Investigations into this complex fluid structure interaction have begun in recent years, however, the mechanisms involved in bubble movement are dynamic and complex and, in some cases, poorly understood. Although numerous studies exist for free rising bubbles, research into their effects on heat transfer is limited; even fewer studies have been performed in relation to bouncing bubbles. This study evaluates the convective heat transfer from a horizontal, heated downward facing surface due to the effect of a single air bubble rising through distilled water and impacting and bouncing on the surface. In order to evaluate the current state of the art, a comprehensive review of the relevant literature has been performed.

The present study utilises high speed, high spatial resolution, infrared thermography to measure the two dimensional transient convective heat transfer. The three dimensional bubble position and planar shape are simultaneously recorded with two high speed digital cameras, which are synchronised with the high speed infrared thermography. The local fluid direction and velocity are also evaluated by means of PIV, in a second set-up. The equipment is mounted on a purpose built frame, surrounding the test tank, so that correct alignment is achieved. Purpose specific code has been developed to analyse both the high speed visual and high speed thermal images; this allows for alignment and investigation into various surface effects. Three interchangeable orifices of internal diameter 0.5, 1 and 2 *mm* are utilized to produce bubbles of equivalent diameter 2.8, 3.3 and 4.1 *mm*. Orifice to surface release heights of 10, 20, 25, 30 and 35 *mm* are investigated, while a single release height of

30 *mm* is investigated for the PIV set-up.

A comprehensive investigation has been carried, with aspects such as the bubble's aspect ratio, velocity, shape oscillation frequency and forces associated with bubble motion being presented. The bubble's rise velocity was found to be significantly higher than that reported in literature, which was linked to the oscillations of the bubble's aspect ratio. In addition, these oscillations were found to affect the bubble bouncing sequence, resulting in large variations in the bubble's shape. Similarly, during the bubble's rise, the rise path was found to be a significant factor which affected the bouncing sequence.

In terms of convective enhancement, this was found to be affected by the impact angle of the bubble, with the bubble size and release height also being significant factors. During the direct impact and subsequent bouncing of the bubble on the surface, regions of transient negative heat flux were found to occur where previously high convective cooling occurred. The bubble's wake was found to spread significantly, in the opposite direction to the bubble's direction of motion, with a smaller portion of the wake being dragged in the direction of the bubble. The wake itself caused the highest levels of convective heat flux encountered. However, if the wake spread too far from the centre of the test section, regions of negative heat flux would again occur. Even after the bubble was fully attached to the surface, localised regions of convective cooling was found to occur lasting for 10 *s*.

Acknowledgements

This work would not have been possible without the support and guidance of my supervisor, Professor Darina Murray, without her attention to detail and knowledge of heat and fluid flow, completion of this project would not have been possible. I'd like to thank Dr. Tony Robinson in particular, foremost for his guidance and extensive knowledge of everything bubble related, as well as his enthusiasm for the subject, which has helped me out of difficult situations. In addition I would like to thank Dr. Yan Delauré and Abdulaleem Albadawi, whose support and direction throughout this project was invaluable. I'd also like to thank Dr. Tim Persoons for his advice on certain topics.

My deepest gratitude goes to Gerry Byrne whose skills and above all else, solid advice was invaluable throughout this project. I would like to acknowledge the excellent work performed by the engineering workshop, who put up with my never ending questions and "minor" additions. I'd also like to especially thank Mick Reilly, who was always there, with the kettle on, ready to discuss the next idea!

To my friends in the thermo group, thank you for the advice over last number of years. In particular Brian, Seamus, Alan, Rayhaan, Karl, Cian, Eoin, Maurice, Aimee, Kate, Rudi, Stephen, Michael and Diarmuid.

To my family and close friends who provided me with the encouragement and continual support throughout my studies, thank you.

I would most of all like to thank Cáit, as without her support and encouragement I would have not been able to complete this thesis.

Finally, I would like to acknowledge SFI and the School of Engineering for the continued funding of this project.

Contents

List of Figures

List of Tables

Nomenclature

Symbol	Description	Units
A	Acceleration	$[m/s^2]$
A	Added mass tensor	$[kg]$
A_{cs}	Cross section area	$[m^2]$
A_{aff}	Affected area	$[m]$
a, b, c	Bubble axes	$[m]$
b	Distance from plate	$[m]$
C_D	Drag coefficient	[-]
C_M	Added mass	[-]
C_p	Specific heat	$[J/kgK]$
D	Diameter of containment vessel	$[m]$
D_E	Equivalent major axis	$[m]$
D_{eq}	Equivalent diameter	$[m]$
$D_{o,i}$	Diameter of affected area	$[m]$
d_i	Inner orifice diameter	$[m]$
dx	Pixel size	$[m]$
$d_{1,2}$	Bubble major axis	$[m]$
E	Energy	$[J]$
E_σ	Surface Energy	$[J]$
E_k	Kinetic Energy	$[J]$
F	Force	$[N]$
f	Frequency	$[Hz]$
f_{V_z}	Rise velocity frequency	$[Hz]$

g	Gravitational acceleration	$[m/s^2]$
h	Heat transfer coefficient	$[W/m^2K]$
$h_{1,2}$	Bubble minor axis	$[m]$
I	Linear impulse	$[m/s^2]$
Im	Image	[-]
k	Thermal conductivity	$[W/mK]$
n	nth mode	[-]
q	Heat transfer rate	$[W]$
q''	Heat flux	$[W/m^2]$
R	Ratio of bubble axes	[-]
R	Rotation matrix	[-]
R	Bubble radius	$[m]$
r_{eq}	Equivalent radius	$[m]$
$S_{x,y,z,sl}$	Distance	$[m]$
S_x	Standard deviation	[-]
$S_{\bar{x}}$	Standard error	[-]
T	Time duration	$[s]$
T_s	Surface temperature	[°C]
T_m	Dimensionless surface temperature	[-]
Th	Threshold	[-]
T,N,B	Frenet frame	[-]
t	Time	$[s]$
t_c	Contact time	$[s]$
t^*	Dimensionless time	[-]
U_T	Terminal velocity	$[m/s]$
U_R	Rebound velocity	$[m/s]$
V	Velocity	$[m/s]$
V_{max}	Max velocity	$[m/s]$
$V_{z,max}$	Max rise velocity	$[m/s]$
$V_{x,y,z}$	Velocity components	$[m/s]$

$\|V\|$	Velocity magnitude	$[m/s]$
X	Laboratory frame of reference	[-]
x'	Ellipsoid frame of reference	[-]
x, w	Velocity	$[m/s]$
x, y, z	Geometric planes	[-]
$\bar{x}$	Mean value	[-]

Greek Symbols

Symbol	**Description**	**Units**
α	Thermal diffusivity	$[m^2/s]$
α	Rotation angle	$[^\circ]$
β	Rotation angle	$[^\circ]$
β	Bouncing constant	[-]
ΔT	Temperature difference	$[K]$
Δt	Time difference	$[s]$
δ	Surface thickness	$[m]$
ε	Ellipticity	[-]
ε_r	Coefficient of restitution	[-]
ε_{dry}	Dry coefficient of restitution	[-]
θ	Inclination angle	$[^\circ]$
$\theta_{1,2}$	Major axis angles	$[^\circ]$
θ_{max}	Max Inclination angle	$[^\circ]$
λ	Confinement parameter	[-]
λ	Wavelength	$[nm]$
μ	Dynamic fluid viscosity	$[kg/ms]$
ν	Kinematic fluid viscosity	$[m^2/s]$
ρ	Fluid density	$[kg/m^3]$
ρ_{elec}	Electrical resistivity	$[\Omega m]$
σ	Surface tension	$[N/m]$
τ	Characteristic time constant	[-]
χ	Aspect ratio	[-]

χ_m	Inverse aspect ratio	[-]
$\chi_{m,0}$	Far inverse aspect ratio	[-]
$\chi_{m,max}$	Max inverse aspect ratio	[-]

Subscripts

Symbol	**Description**
air	Air
$back$	Background image
cap	Storage
$cond$	Conducted
$conv$	Convected
cs	Cross section
D	Drag
D_{max}	Maximum drag
$diff$	Image difference
$elec$	Electrical
end	Final image
f	Foil
fc	Liquid convection
g	Gas
gen	Generated
L,B	Lift bi-normal
L,N	Lift normal
l	Liquid
lc	Lateral conduction
$lift,off$	Take off image
$Impact$	Impact image
nb	Nucleate boiling
p	Paint
p	Particle
RTD	Resistance Temperature Detector

rad	Radiation
rel	Relaxation time
sat	Saturation temperature
sb	Bubble induced convection
sphere	Spherical particle
sub	Sub-cooled
start	Start image
t	Top
w	Wall
water	Water
∞	Bulk or infinity

Dimansionless Numbers

Symbol	**Description**
Bi	Biot number, $Bi = h\delta/2k$
Ca	Capillary number, $Ca = \mu U/\sigma$
Eo	Eötvös number, $Eo = \Delta\rho g D_{eq}^2/\sigma$
Gr	Grashof number, $Gr = g\beta(T_s - T_\infty)L^3/\nu^2$
Mo	Morton number, $Mo = g\mu^4/\rho\sigma^3$
Nu	Nusselt number, $Nu = hL/k$
Pr	Prandtl number, $Pr = \nu/\alpha$
Ra	Rayleigh number, $Ra = GrPr$
Re	Reynolds number, $Re = \rho U_T d_e/\mu$
Ri	Richardson number, $Ri = Gr/Re^2$
Sr	Strouhal number, $Sr = fD_{eq}/U_T$
St	Stokes number, $St = \tau_{rel}U_0/d_c$
St^*	Modified Stokes number, $St^* = (\rho_p + C_M\rho)D_{eq}U_0/9\mu$
We	Weber number, $We = \rho U_T^2 D_{eq}/\sigma$

Chapter 1

Introduction

In this chapter, the motivation behind the research, which concern the anticipated demand for ever more efficient modes of two phase heat transfer will be discussed. This is followed by a review of literature that is relevant to the area of two phase flow. The objectives are outlined with the aim of addressing certain shortcomings relating to thermal management using two phase cooling methods.

1.1 Research Motivation

As the global demand for energy rises, the days of energy overutilisation and engineering design based on exhaustible energy sources are coming to a close, with a need for more efficient high performance technologies underpinning our future energy requirements. Advancements in thermodynamic and fluid sciences must accelerate the integration of renewable energy systems into existing infrastructures, in turn helping to develop the next generation of more flexible and robust energy systems [1].

Two phase flows occur widely in both nature and industrial applications, including energy production (oil transportation, steam generators, cooling systems) and chemical engineering (bubbly columns, mixing in reactors, aeration systems). Two phase flows produce extremely high heat transfer coefficients, an order of magnitude higher than their single phase counterparts. As a result, their practical significance has motivated numerous investigations during the past fifty years. Nevertheless, despite this continuous effort, two phase technologies are not wide spread in thermal systems and important questions remain open.

This is in part due to the inherently complex nature of two phase flows; from a heat and mass transfer perspective. From an engineering standpoint, due to gaps in the literature with respect to two phase flow, progress is impeded by the risk and uncertainty with regards to new, two phase flow technologies.

As outlined above, two phase flow is known for its ability to significantly enhance heat transfer from a variety of geometries; this has been experimentally shown by a few authors [2–10]. Current research on two phase flow is focused on the effect of a single bubble or multiple bubbles and their motion against vertical or inclined surfaces which may be heated [3, 4, 7–10]. Bubble impingement against adiabatic surfaces has received some attention [11–13]. One of the earliest examples of the notable enhancement effects of two phase flow is the work of Cornwell [5], on heat transfer within tube bundles. It was deduced that vapour bubbles generated on lower tubes impacted and slid along upper tubes and could in fact suppress nucleation, by reducing the surface temperature of the upper tubes.

Two phase flow and heat transfer is very sensitive to many, often inter-related, parameters. This is where advancements in computational and numerical analysis can provide the crucial link to bridge gaps in experimental literature. However, the computational models must first be validated against reliable experimental measurements. With a large number of parameters being influential in two phase flow, it is advantageous to focus on key fundamental aspects of the flow. Once these basic aspects are validated, then it is possible to investigate more subtle and complex features of the flow. One key aspect of two phase flow is the growth and initial departure of a single bubble, which has been modelled via a variety of multiphase flow modelling codes and validated against accurate repeatable state of the art experimental procedures [14, 15].

A two phase flow problem which has received a lot of attention is that of phase change in tube bundles, whereby bubbles are generated on one tube, and then rise through the surrounding fluid before impacting and sliding around the upper tubes; this formed the basis of an investigation by Cornwell [5]. This simple natural process can be defined by three regimes, of which the first is the bubble rise, followed by the impact and bouncing against the upper tube and finally the sliding of the bubble around the upper tube. With regard to the bubble's rise, this field has been studied for over 50 years, with some comprehensive reviews being conducted [16–19].

While sliding bubble heat transfer enhancement has received some attention in the open literature [3, 7, 20–22], only a small amount of knowledge exists for bubbles impacting and sliding around heated tubes. Yan *et al.* [23] investigated bubbles impacting a horizontal curved surface. They found that the bubbles tended to stick to the surface and cause a hot spot through local dry-out, inducing elevated temperatures, before growing and sliding away from the bottom of the cylinder. This was the first reported study into the effect of a bubble impacting a surface. A similar study was performed by Atmane & Murray [2] who measured local heat flux variation due to the motion of both vapour and air bubbles around a cylinder. Atmane & Murray [2] noted that the bubble impact mechanism significantly increased heat transfer on the lower section of the heated cylinder, while the sliding motion around the cylinder and nucleate boiling were responsible for the high levels of heat transfer on the upper section of the cylinder.

With this type of bubble motion over a curved surface it is difficult to disentangle the relationship between the bouncing motion and the sliding motion on the lower section of a tube. As the bouncing of the bubble is a precursor to sliding motion, the initial focus should be on this process. In order to isolate the bouncing process, a flat rather than curved heated horizontal surface would be advantageous; similarly this simpler surface shape and orientation would aid Computational Fluid Dynamics (CFD) analysis. The availability of literature on the bouncing of individual bubbles against a downward facing solid adiabatic surface is limited to small, stable ellipsoidal bubbles [12, 13, 21, 24–26]. To the author's knowledge, limited or no research has been conducted on the effect of a single bubble impinging and rebounding from a flat horizontal surface, with the objective of exploring the impact and rebound phases and their associated surface heat transfer. Secondary to this motion would be the effect of the wake generated by a rising bubble as reported by literature [3, 4, 16–19, 27–29].

The objective of this fundamental study will be to experimentally investigate coupled convective heat transfer and bubble motion due to the effect of a single air bubble rising through water and impacting and bouncing on a heated surface. Simultaneous measurement of heat transfer, fluid motion and bubble motion must be performed in order to further understand the complex interactions of a bubble and a heated surface.

The work presented here has been performed in conjunction with a numerical study

carried out by Dr. Yan Delauré and Mr. Abdulaleem Albadawi in Dublin City University (DCU).

Chapter 2

Literature Review

This chapter will briefly review the literature around the motion of air bubbles in a liquid. The beginning of the chapter will explore the path and shape a rising bubble takes and how the method of bubble formation affects its shape. The wake generated by the bubble will be reviewed next, followed by an introduction to how a bubble interacts with a surface. The final section will explore heat transfer enhancement due to bubbles on varied surface geometries.

The complexities of bubble shape, motion and path are ubiquitous. To fully understand their complex nature and their importance in our society, numerous studies have been performed, dating from as early as 1907 [30]. Studies have been performed for situations such as bubble growth, free rising/falling bubbles and drops, bubble to bubble interactions and bubble interaction with surfaces. Within these areas researchers have investigated the effect of fluid properties, fluid confinement and the bubble rise velocity and trajectory. The bubble wake characteristics and the interaction with surfaces of various orientations have also been studied. Research into a bubble impacting upon and/or sliding along a surface has been limited thus far, with only a few investigations being performed. The following review considers the behaviour associated with a bubble's free rise and final impact upon a horizontal surface and the associated heat transfer enhancement from bubble motion.

2.1 Bubble Shape Categorisation

Bubbles in free rise in an infinite medium under the influence of gravity can be grouped under the following headings: Spherical, Ellipsoidal and Spherical-Cap shape regimes [16].

(a) Spherical: Generally, bubbles and drops are closely approximated by spheres if interfacial tension and/or viscous forces are much more important than inertial forces. Fluid particles can be termed "spherical" if the minor to major axis ratio lies within 10% of unity.

(b) Ellipsoidal: The term "ellipsoidal" is generally used in referring to bubbles or drops which are oblate in shape.

(c) Spherical-cap: Large bubbles tend to adopt flat or indented bases and lack fore and aft symmetry. A "spherical-cap" bubble's upper surface appears similar to that of an oblate spheroid of low eccentricity. They may also develop thin trailing "skirts".

Most bubbles rise in an infinite medium, making it is possible to define a shape regime map in terms of the Eötvös[1], Morton[2] and Reynolds dimensionless numbers. The resulting plot is presented in Figure 2.1 (a), Bhaga & Weber [16]. As Re is included in the plot, the terminal velocity can be determined. Figure 2.1 (a) may be used to estimate terminal velocity as well as the bubble shape regime.

The shape of a bubble depends upon the relative magnitudes of the relevant forces acting on the bubble, such as surface tension and inertial forces; also, as bubbles have a low density when compared to that of the liquid, the inertia in the system is almost entirely due to accelerated or decelerated liquid surrounding the bubble. Figure 2.1 (b) shows sketches of the bubble's shapes, corresponding to the shape regime map in Figure 2.1 (a). In liquids of low viscosity and Morton number, such as water, the shape of intermediate-size bubbles is very irregular and oscillates unsteadily. Moreover, in liquids of high viscosity under quiescent conditions, the formation of "skirts" has been observed. "Skirts" are thin annular films of

[1] A high Eötvös number indicates that the system is relatively unaffected by surface tension effects ($Eo \gg 1$), while a low number Eötvös number ($Eo < 1$) indicates that surface tension dominates.

[2] Low viscosity fluids generally have a low Morton number ($Mo < 10^{-6}$), such as water, while high viscosity fluids, generally have high Morton number ($Mo > 10^{-2}$).

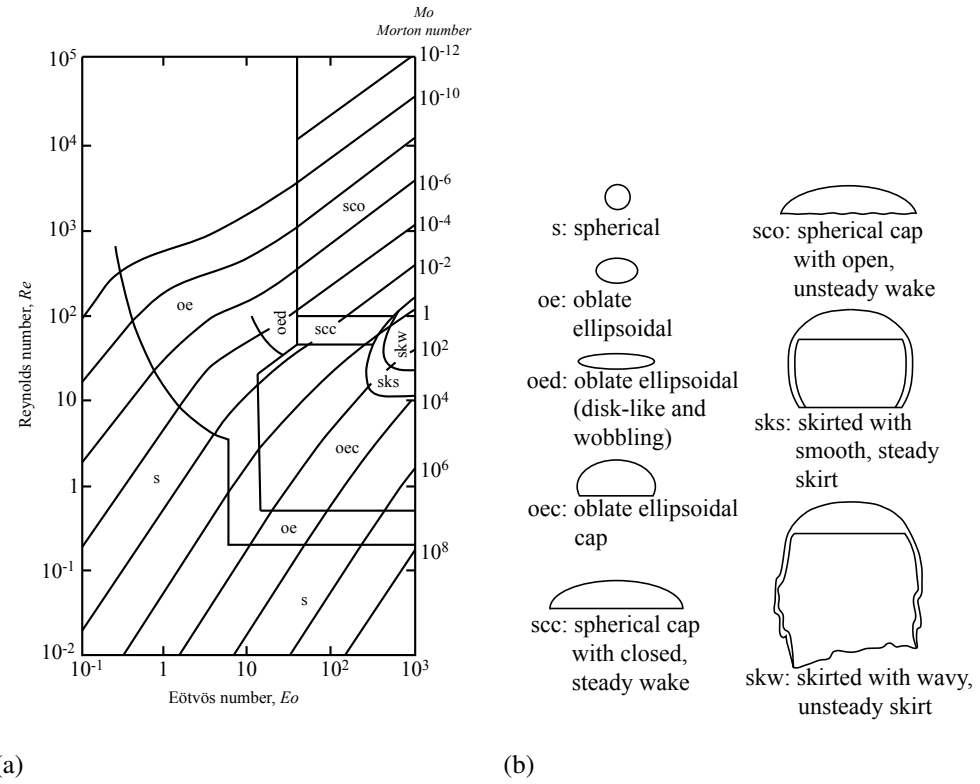

Figure 2.1: (a) Shape regime for bubbles and drops in unhindered gravitational motion through liquids, Bhaga & Weber [16], (b) Sketches of various bubble shapes observed in infinite Newtonian liquid, Fan & Tsuchiya [18].

gas trailing behind the rim of large spherical-cap bubbles. A bubble's shape cannot be completely predicted, unless all the pertinent physical variables are accounted for. Haberman & Morton [31] proposed a dimensional analysis based on eight variables: the acceleration due to gravity (g), the terminal velocity (U_T), the diameter of a sphere of equivalent volume (D_{eq}), the fluid density (ρ_l) and viscosity (μ_l), the interfacial surface tension (σ_f), and the density and viscosity of the gas inside the bubble, (ρ_g) and (μ_g). From these variables five independent dimensionless groups can be derived.

For a typical bubble in water with an equivalent diameter of $d_{eq} = 3\ mm$, a Reynolds number of 1000 is expected once terminal velocity has been achieved. Similarly, water is a low Morton number fluid and a $Mo \approx 1.1 \times 10^{-11}$ is expected, with a corresponding Eötvös number of 1.2.

2.2 Rising Bubbles

After a single bubble's departure from an orifice, it will begin its free rise through the liquid. It is of importance to fully understand the behaviour of a free rising bubble, as it is this behaviour which is responsible for heat transfer enhancement from a surface irrespective of the surface orientation. The bubble's wake has been demonstrated to be of most importance when heat transfer enhancement is concerned, most recently by Manickam & Dhir [9]. There are numerous aspects which influence the bubble's wake; these include terminal rise velocity, shape characteristics and oscillation and wake formation (both near and far). The following sections will examine the bubble's characteristic features.

2.2.1 Bubble Trajectory

As a bubble rises through a continuous medium, work is done on the medium by the bubble at a rate equal to the bubble rise velocity times the net buoyancy force acting on the bubble. In a viscous fluid, the energy associated with this work can be completely dissipated within the fluid, i.e. by viscous dissipation, resulting in a purely rectilinear motion of the bubble. In a low viscosity fluid, the energy generated by the rising bubble is not consumed by viscous dissipation alone; some energy is released through wake shedding (turbulent dissipation) which induces bubble oscillations. Bubble oscillations are known to start with the onset of vortex shedding from the wake. Saffman [17] performed a study of free rising air bubbles in filtered water with bubble equivalent diameters (D_{eq}) in the range of 1 – 8 *mm*. Bubble shape was approximated as oblate spheroid, as depicted in Figure 2.1 (b). Three bubble paths were identified:

- Rectilinear
- Zig-zagging
- Spiral

When the bubble diameter, D_{eq}, was less then 1.4 *mm*, the bubble would rise with a rectilinear path i.e. a straight line. With an intermediate D_{eq} of 1.4 – 2 *mm*, the bubble was found to zig-zag within a fixed plane, throughout its rise, although the orientation of the

plane was random. Bubbles with D_{eq} in the range of 2 – 4.6 *mm* had more complex paths, with either zig-zag or spiral motion. At about 4.6 *mm* the spiral or zig-zag motion begins to reduce in magnitude and is dissipated for diameters above 6 *mm*. For the size range in which both spiralling and zig-zag motion can occur, bubbles would usually zig-zag if they left the injecting tube in one piece, but the presence of an obstruction immediately after the injector was found to make the bubble spiral. When bubbles were released in rapid succession, one after another, the bubbles followed the preceding bubble's path; the exception to this was for bubbles of equivalent diameter less than 2 *mm* in which case it was observed that zig-zagging bubbles continued to zig-zag, even when released in the wake of a spiralling bubble. Bubbles of about 1.4 *mm* were sometimes observed to rise steadily, then zig-zag, then go straight again, zig-zag again, and so on. Similar experiments were carried out using unfiltered tap water. The results were the same except that the zig-zag motion first occurred at a D_{eq} of 1.6 *mm*, and that it was not possible to produce the spiralling motion with a bubble less than 2.2 *mm*. The experiments of Saffman [17] give us an insight into the behaviour of bubbles with D_{eq} of 1 – 8 *mm*. De Vries *et al.* [32] noted that for a bubble diameter of 1.62 *mm*, the bubble would no longer rise rectilinearly; the path becomes either zig-zag or spiral. A similar behaviour is observed for solid spheres, but at lower Reynolds numbers than for bubbles. This is due to the difference in boundary conditions at the surface of solid spheres and gas bubbles in pure waters: no-slip and non-deformable for the solid sphere, zero-tangential-stress and deformable for the gas bubble. Table 2.1 summarises the bubble size and shape and the path which the bubble will take.

In order to understand the complex motion of bubbles, numerous investigators have attempted to correlate the terminal velocity (U_T) of a bubble to important parameters such as the equivalent diameter and fluid properties [17–19, 35–43]. However, for the present investigation it is thought that the limited bubble rise height under consideration ($<$40 *mm*) would prevent the bubble achieving terminal velocity. Thus, further discussion of terminal velocity is not included here.

Table 2.1: Overview of bubble motion, Veldhuid [28], Lindt [33], Rosenberg [34]

D_{eq} [mm]	Re	description
$D_{eq} < 0.8$	$Re < 70$	Sphere, rectilinear path, C_D as for solid spheres
$0.8 < D_{eq} < 1.2$	$70 < Re < 400$	Sphere, rectilinear path, C_D less than solid spheres
$1.2 < D_{eq} < 1.5$	$400 < Re < 500$	Oblate spheroid, rectilinear motion
$1.5 < D_{eq} < 4.8$	$500 < Re < 1100$	Oblate spheroid, helical motion
$4.8 < D_{eq} < 7.0$	$1100 < Re < 1600$	Irregular oblate spheroid, almost rectilinear motion
$7.0 < D_{eq} < 16.6$	$1600 < Re < 5000$	Transition from oblate spheroid to spherical cap, almost rectilinear motion
$D_{eq} > 16.6$	$Re > 5000$	Spherical cap, rectilinear motion

2.2.1.1 Influence of Bubble Release Process

An important influence on a bubble's initial velocity and, more importantly on the direction which the bubble will take, is how the bubble is introduced into the system. The following section will explore the consequence of small and large initial deformations as the bubble is introduced into the fluid.

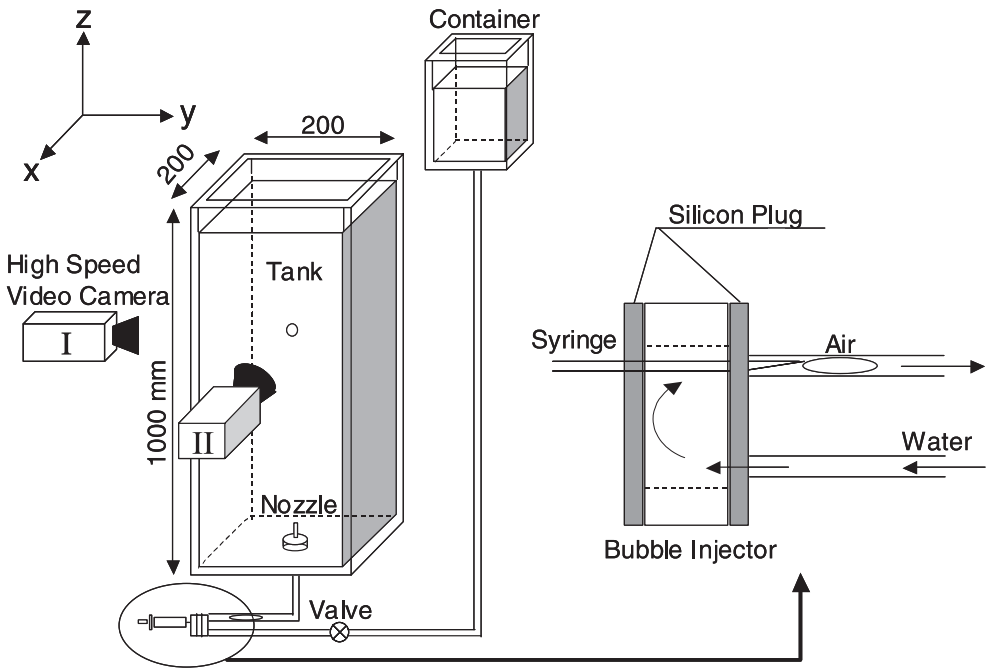

Figure 2.2: Experimental set-up and bubble injection device utilized by Tomiyama *et al.* [41].

Ellingsen & Risso [44] studied an isolated air bubble rising in still water. Both the bubble and liquid motions were investigated and the influence of surfactants was shown to be negligible. The bubble equivalent diameter was fixed at 2.5 *mm*. They observed that after the initial acceleration stage, the bubble starts oscillating on an almost planar zig-zag. This in plane motion then progressively transforms into a helix, which is the final stable trajectory.

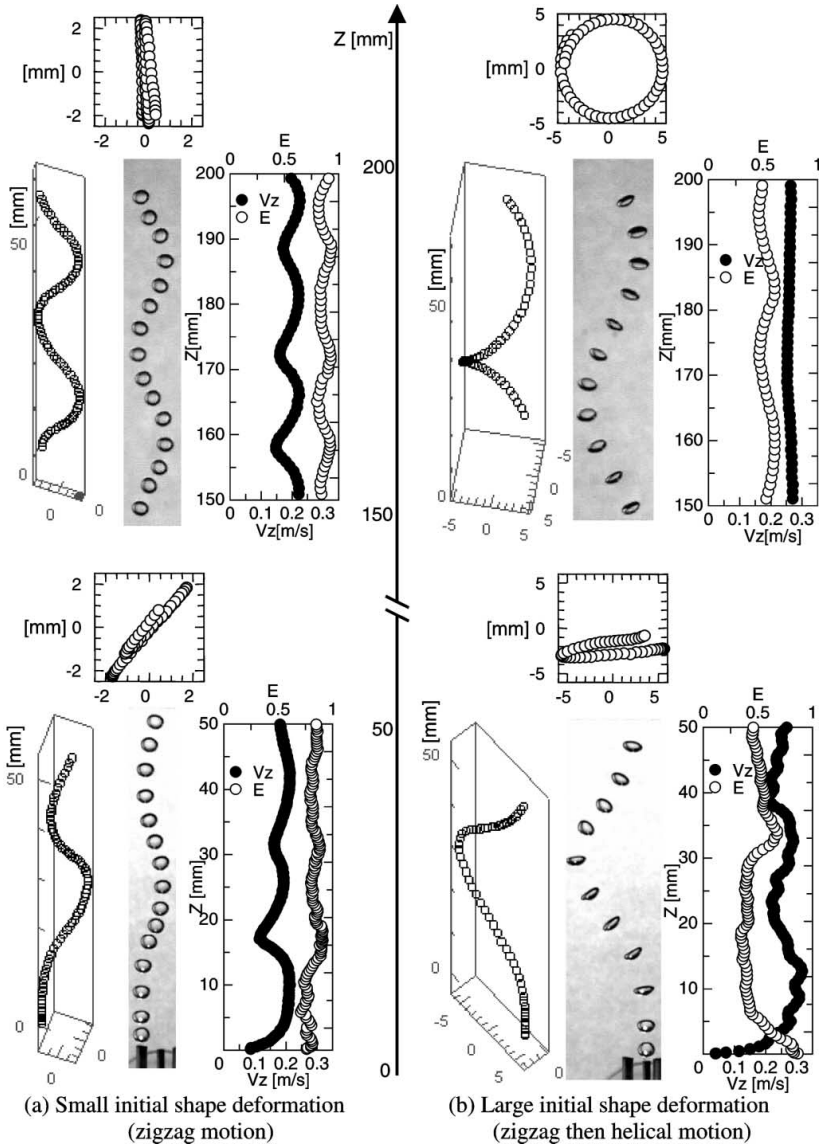

Figure 2.3: Consecutive images, elevation and plan views of trajectory, instantaneous aspect ratio and instantaneous rising velocity of a single air bubble (D_{eq} = 3 *mm*) in distilled water: (a) illustrates a small initial shape deformation (zigzag motion) and (b) a large initial shape deformation (zigzag then helical motion). Bottom images show bubble injection and top images steady state behaviour. Tomiyama *et al.* [41].

Tomiyama *et al.* [41] performed a numerical and experimental study of the terminal velocity of air bubbles rising in water and reported that bubble motion, shape and velocity were markedly sensitive to the initial condition, i.e. the method of bubble release. Four different nozzles were used to produce bubbles of various sizes. The static pressure difference was controlled by the elevation of the small container shown in Figure 2.2. This bubble release method is based on the static pressure difference, with large initial shape deformation being created by releasing a bubble either with a high static pressure difference or with a nozzle diameter which is smaller than the bubble equivalent diameter.

This view that terminal velocity is sensitive to release conditions is contrary to the previously reported view, that the bubble's terminal velocity is a function of the Eötvös and Morton numbers only, and that the large scatter in terminal velocity in the surface tension force dominant regime[3] was due to surfactant contaminants. It was noted that a bubble's motion, shape and velocity were sensitive to the initial shape deformations caused during the release from the orifice. This bubble rise motion is more inclined to be zig-zag when the initial shape deformation is small, whereas the transition from zig-zag to helical motion is enhanced when initial shape deformations are large. Figure 2.3 illustrates their findings in relation to shape deformations.

These results of Tomiyama *et al.* [41] therefore support the conclusion of Ellingsen & Risso [44] that the primary unstable mode causing zig-zag motion develops first and the secondary unstable mode causing helical motion then follows. In other words, large initial shape deformation augments the growth rate of the secondary unstable mode, whereas small initial shape deformation delays the transition from the primary to secondary unstable mode. Therefore it is impossible to predict a motion type with the only information available being D_{eq} and the fluid properties; the bubble release mechanism is also relevant.

Several examples of consecutive images of single bubbles in the distilled and contaminated waters are shown in Figure 2.4. The time interval of two consecutive bubble images is 0.02 *s*. The 3 *mm* bubble in the contaminated system was released with large initial shape deformation. However soon after detachment from the nozzle, its motion became very similar to the motion of a 3 *mm* uncontaminated bubble with small initial shape deformation. In

[3] In this case of an air-water system, bubbles with equivalent diameters ranging from 1.3 *mm* to roughly 6 *mm* correspond to a surface tension force dominant regime, in which U_T decreases with increasing D_{eq}.

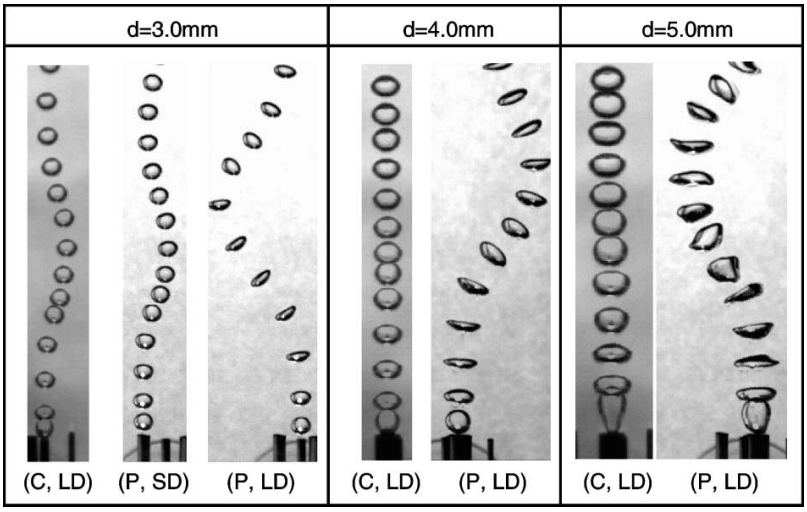

Figure 2.4: Shapes and trajectories of single bubbles in pure (P) and contaminated (C) systems: LD–large initial shape deformation; SD–small initial shape deformation. Tomiyama *et al.* [41].

the cases of D_{eq} = 4 and 5 *mm*, contaminated bubbles did not exhibit large shape oscillation due to the strong damping effect caused by a surfactant, which was liquid soap in this case.

Ellingsen & Risso [44] noted that when the bubble detaches from the injector, its shape is essentially spherical and it rapidly accelerates in the vertical direction. This first stage is followed by a period of reduced acceleration that leads to a flattening of the bubble's shape and the commencement of horizontal path oscillations. Beyond a height of 150 *mm* the initial acceleration stage is completed, the vertical velocity is approximately constant and the path-oscillation frequency is regular.

Wu & Gharib [45] conducted experiments on the shape and path of air bubbles, with a diameter range of 1 – 2 *mm*, rising in pure water. The bubble generation method used in this experiment was similar to that of Saffman [17] and Duineveld [46]. A syringe pump was operated at a slow rate to ensure that bubbles were released quasi-statically. The authors found that the inner orifice diameter, d_i, played an important role in the shape and, more importantly, the bubble's path. Bubbles that detached from a small orifice rose nearly twice as fast as those from a larger orifice. In the case of a small orifice, the curvature at the bubble detachment point exhibits a local maximum; such a deformation gives rise to substantial axisymmetric surface waves, which in turn propels the bubble to a high initial velocity. For larger orifices only weak perturbations are formed.

2.2.1.2 Bubble Rise with Side Wall Confinement

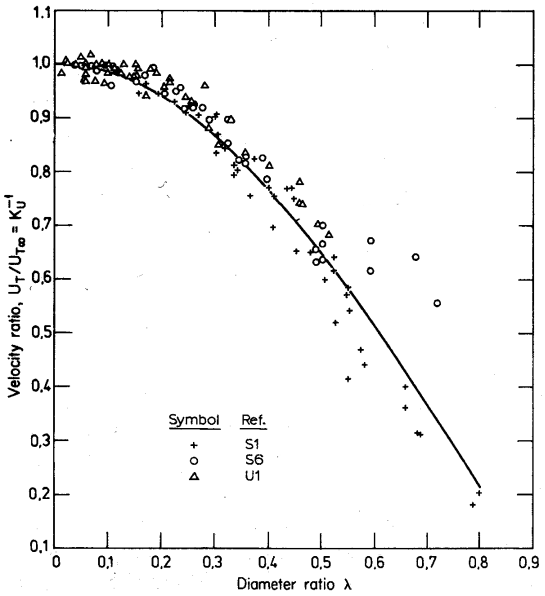

Figure 2.5: Retarding effect of column walls on the terminal velocity of bubbles of intermediate size, Clift *et al.* [19].

Although bubble rise in a confined space is an important topic, few researchers have quantified wall effects directly, by using a series of different columns of varying diameter. The aim here is to determine the influence on terminal velocity of a confinement parameter, $\lambda = D_{eq}/D$, where D in this case is the diameter of the containment vessel. It is expected that containing walls will cause elongation of bubbles in the vertical direction, suppress secondary motion (zig-zagging), and alter the wake structure [19]. An early investigation by Haberman & Morton [31] proved inconclusive, as the tank size employed was approximately $254 \times 406\ mm^2$, with an approximate maximum λ of ≈ 0.04, corresponding to the smallest tank dimension and largest D_{eq}. Clift *et al.* [19] noted that for a Reynolds number greater than 200, the confinement effect on terminal velocity was independent of Re. Therefore they represent their results by a unique relationship between $U_T/U_{T\infty}$ and λ, as shown in Figure 2.5 together with the correlation presented in Equation 2.1.

$$\frac{U_T}{U_{T\infty}} = \left[1-\lambda^2\right]^{\frac{3}{2}} \tag{2.1}$$

For the conditions of the present study, with a planned D_{eq} of 4 mm and a minimum D of 50 mm ($\lambda = 0.08$), the effect of the containing wall is unlikely to play any significant part

in influencing the bubble motion.

2.2.2 Bubble Shape Oscillations

It is anticipated that a bubble will undergo initial shape oscillations, as shown by Tomiyama *et al.* [41], as well as shape oscillations further in its rise, which results in different secondary motion. This section will explore these oscillations and their related frequencies.

Lunde & Perkins [47] observed the shape oscillations of rising air bubbles in unfiltered tap water. The apparatus was a transparent tank 700 *mm* tall with a 100 $\times$ 100 mm^2 base. No effort was made to purify the apparatus or water so some contaminants were assumed to be present; neither was surface tension directly measured. Bubbles were allowed to rise through the first 150 *mm* of the tank before being recorded at a frame rate of 400 – 500 frames per second; this corresponded to four times faster than the highest shape oscillation frequencies investigated, according to the authors. Five different bubble sizes were observed, with equivalent diameters of 2.4, 3.02, 3.52, 4.32 and 5.16 *mm* (a broadly similar range to the present study).

Table 2.2: Results of experiments by Lunde & Perkins [47] on the frequency of bubble shape and path oscillations

Bubble size, d_{eq} (*mm*)	2.4	3.02	3.52	4.32	5.16
Equivalent major axis, D_E (*mm*),	3.04	3.9	4.53	5.8	6.95
Ellipticity, ε	2.03	2.16	2.13	2.4	2.45
Terminal velocity, U_T (*m/s*)	0.326	0.299	0.284	0.264	0.252
Reynolds number, *Re*	991	1166	1286	1531	1751
Frequencies					
D_E: Mode (2,0), shape (*Hz*)	–	60.6	49.1	35.3	25.8
A: Mode (2,0), motion (*Hz*)	90.2	60.7	48.9	33.1	24.9
R: Mode (2,2), shape (*Hz*)	62.7	40.4	33.1	22.3	17.3
Vortex shedding (*Hz*)	13.1	13.5	13.7	10.7	10.8

The equivalent major axis of the ellipse is defined as

$$D_E = \left(d_{major} d_{minor}\right)^{\frac{1}{2}} \tag{2.2}$$

where d_{major} and d_{minor} are the major and minor axes as measured from the direct and mirrored image of the bubble. Averaged over numerous tests, all bubbles were within 5%

of the nominal size. The ellipticity, ε, is calculated from the mean equivalent major axis and the bubble equivalent radius. Thus

$$\varepsilon = \frac{D_E^3}{8r_{eq}^3} \tag{2.3}$$

In Table 2.2, D_E is the oscillation frequency for the equivalent major axis, A is the oscillation in the acceleration of the bubble and R is the oscillation in the ratio of the two major axes. The vortex shedding frequency is also presented in Table 2.2. Their results indicate that the low frequency lateral motion associated with the vortex shedding had superimposed on it a high frequency oscillation associated with the shape oscillations of the bubble. For all five bubble diameters, the vortex shedding frequency remained relatively stable at about 12 *Hz*, with a slight decrease with increasing bubble size; however, the shape oscillation frequency decreased significantly with increasing bubble size. The vortex shedding refers to the large regions of vorticity generated at each "turn" during the bubble's zig-zag, which is twice in one zig-zag period.

$$f_{2,0} = \frac{1}{2\pi}\sqrt{\frac{12\sqrt{2}\varepsilon^2}{(\varepsilon^2+1)^{3/2}}}\sqrt{\frac{\sigma}{\rho_l r_{eq}^3}} \quad \text{and} \quad f_{2,2} = \frac{1}{2\pi}\sqrt{\frac{8}{\varepsilon}}\sqrt{\frac{\sigma}{\rho_l r_{eq}^3}} \tag{2.4}$$

Lunde & Perkins [47] give approximate expressions for mode (2,0) and (2,2) oscillations, derived from an analytical expression by Lamb [48], as indicated in Equation 2.4; these are D_E and R oscillations, respectively. Lunde & Perkins [47] assumed mode (2,0) oscillations to be waves moving around the bubble from the front to the rear stagnation points (from pole to pole), while mode (2,2) oscillations are assumed to be waves travelling around the equator of the bubbles.

Brücker [29] presented results for bubble shape oscillations observed for a 6 *mm* zig-zagging bubble with a mean aspect ratio, χ, of 0.66. The bubble rise velocity, w, was approximately 200 *mm/s*. The lateral oscillation for a complete zig-zag cycle was measured to be 4.2 *Hz* with a maximum lateral velocity of 100 *mm/s*.

Figure 2.6 displays the evolution of the bubble contour over the first complete zig-zag cycle. The diagram at the bottom of the figure demonstrates the time variation of the breadth of the bubble b, which is measured as the width of the bubble along the x axis. The time

is made dimensionless with the duration, T, of one zig-zag. This figure demonstrates the obvious phase coupling of this asymmetric shape deformation with the bubble motion and allowed Brücker [29] to conclude that the deformation is due to an uneven pressure distribution in the equatorial plane of the bubble at the inversion points, caused by the shedding of vortices from the bubble base. There is a strong correlation between the breadth oscillations and the motion of the bubble. The oscillations of the breadth have a maximum amplitude of about 10%. The phases of large bubble breadth in Figure 2.6 represent a lower aspect ratio, i.e., a more oblate shape of the spheroid. Most importantly, the peaks repeat at each point where the bubble reverses its motion. The frequency is therefore twice that of the zig-zag motion. This motion associated with vortex shedding is referred to as "VS type" oscillation.

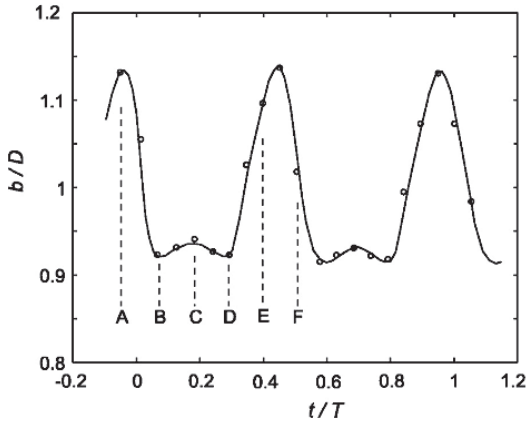

Figure 2.6: Bubble contours at characteristic moments in one zig-zag cycle and variation of the bubble breadth (b), time is normalised by the time it takes to complete one oscillation, T, Brücker [29].

In addition to this obvious oscillation of the aspect ratio linked to the vortex shedding, one can recognise in Figure 2.6 a weak secondary oscillation (compare the local maxima at $t^* = 0.2$ and $t^* = 0.7$) which has roughly half the wavelength. Lunde & Perkins [47] also recognised a second peak in the frequency spectrum of the oscillation of bubble aspect ratio. Their results for a bubble of D_{eq} = 5.8 *mm* showed a secondary peak at a frequency of 35 *Hz*. This compares with the first peak, which corresponded to a vortex shedding frequency of 10.7 *Hz*.

Lunde & Perkins [47] postulated that this additional oscillation of the aspect ratio of the bubble is associated with capillary waves travelling from the front stagnation point to the rear stagnation point (from pole to pole). Brücker [29] observed this secondary frequency

to be 17 *Hz*, and provided an alternate explanation of this secondary oscillation as linked to the spacing between the legs of hairpin vortices observed behind the bubble.

Veldhuis [28] noted that the smaller the bubble the greater the coupling between the frequency of the tangential velocity[4] and the axisymmetric shape oscillation, which is the mode (2,0) oscillation. The larger the bubble size, greater than 4 *mm*, the more frequencies appeared, and the more random the bubble path became, although the coupling remained. Table 2.3 demonstrates the wake appearance[5] frequency for several bubble diameters; for bubble diameters greater than 3.5 *mm*, distinct regions of circulation could not be determined.

Table 2.3: Results of experiments by Veldhuis [28] on the frequency of wake appearance versus bubble size.

Bubble size, D_{eq} (*mm*)	2.8	2.9	3.1	3.1	3.3	3.4	3.5
Vortex shedding wake (*Hz*)	74	65	65	54	48	45	46

Figure 2.7 demonstrates the relationship between the wake, velocity and mode (2,0) frequency. The mode (2,2) frequency is more closely related to path oscillations. Veldhuis [28] noted that shape oscillation must first trigger velocity oscillations before there is a wake effect.

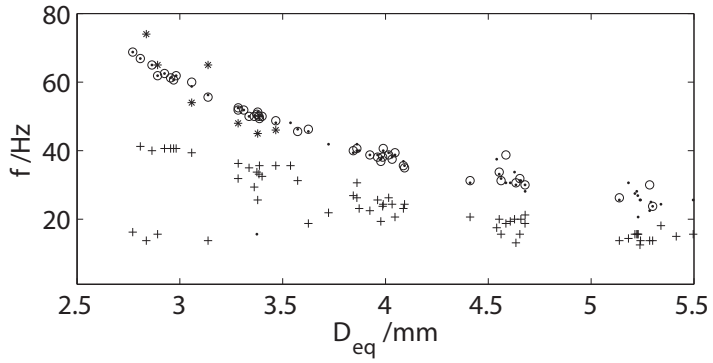

Figure 2.7: Measured frequencies versus bubble diameter, where * is the wake, ○ is the velocity, · is the shape oscillations mode (2,0) and + is the mode (2,2) oscillations. Veldhuis [28]

[4]The tangential velocity is the velocity calculated along the bubble's direction of motion.

[5]The wake appearance is when a region of separate vorticity is formed at the rear of the bubble, separate from a zig-zag wake.

2.2.3 Bubble Wake Structure

This section presents studies focused on the wake behind free rising bubbles. This is relevant for the present study on bouncing bubbles, as the bouncing phase is preceded by a rising bubble stage.

When the relative speed between a body and the surrounding medium is very low, the external fluid flow just outside the body will closely follow the body's surface. At sufficiently low Reynolds numbers, the whole contour of the body forms part of a streamline[6], known as the dividing streamline. As the Reynolds number of the flow exceeds a critical value, the flow will begin to separate[7] from the body surface. This critical value depends upon multiple criteria such as surface shape and nature, as well as turbulence intensity in the surrounding stream. The separated streamlines will rejoin some distance behind the bubble, forming a closed region described as the wake. A wake has been described as the region of non-zero vorticity downstream of a body, contained within a uniform flow. The whole wake has traditionally been divided into two regions: near (primary) and far (secondary) wake. The near wake is the zone near the base of the bubble; this region is where vortex formation, growth and shedding occurs. For low Reynolds numbers (<100), the wake region consists of a symmetric pair of stationary vortices and is often referred to as the (re)circulation region. The existence of a large-curvature surface assures the generation of vorticity at a large rate on that surface, which means that if a bubble has sharp edges, i.e. the rim of a spherical-cap bubble, the surface vorticity is generated such that all the vorticity cannot be removed efficiently by convection downstream and some will accumulate behind the bubble [18].

The far wake consists of the remainder of the wake; it has an open structure and represents a much less defined region, which is not related to the original body type. Included in the secondary wake can be free shear layers and vortices shed from the main primary wake (as in Figure 2.8 from Fan & Tsuchiya [18]). At low Reynolds numbers, the wake can be a streaming tail extending along the bubble rise path below the primary wake, whereas at higher Reynolds numbers, a vortex sheet extends far behind the rising bubble.

Wake shedding phenomena have been observed for a wide range of Reynolds numbers.

[6] A streamline has its tangent parallel to the velocity vector at every point along it. For unsteady flows it is practical to define only instantaneous streamlines

[7] Flow separation refers to the detachment of the boundary layer from the bubble surface

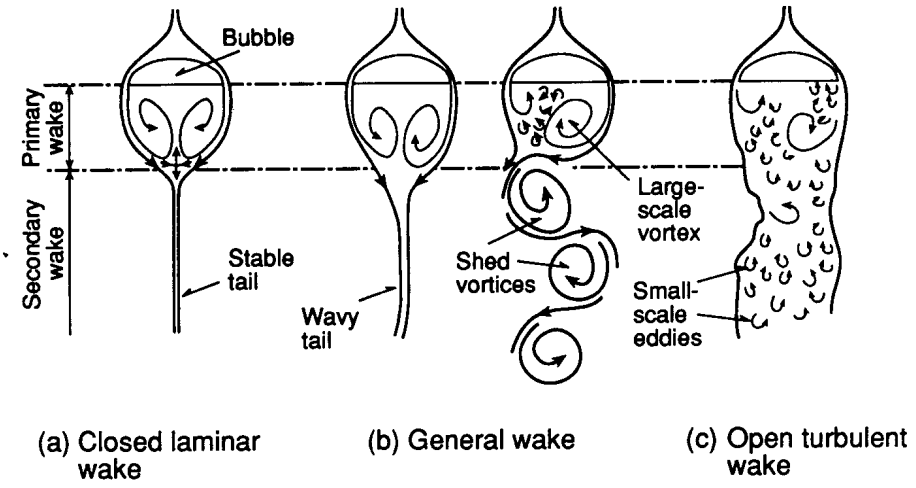

Figure 2.8: Schematic representation of general wake structure behind a spherical-cap bubble, with identifications of the primary and secondary wake structure, Fan & Tsuchiya [18].

Any bubble which experiences secondary motion (zig-zagging, etc.) will most likely shed vorticity in its wake. The onset of flow separation is related to two factors. First, the pressure downstream of a rising bubble cannot be recovered completely; this pressure drop behind the bubble induces a flow towards the base of the bubble. Secondly, as the bubble goes through shape deformation; vorticity is generated. Vortex shedding can be either symmetric or asymmetric with respect to the wake central axis.

Brücker [29] used Particle Image Velocimetry (PIV) combined with high-speed photography to study bubble rise and associated wake. The experiment was mainly focused on ellipsoidal bubbles of diameter 4 - 8 *mm*, which show spiralling, zig-zagging and rocking motion during their rise in water. De-mineralized water was used as the test liquid; small tracer particles were added to the fluid upstream in the water basin and were homogeneously distributed. From measurements of the rise velocity of the bubbles and comparison with the values from the literature (Clift *et al.* [19]) for the same size of ellipsoidal bubble, Brücker [29] concluded that the tracer particles caused the bubbles to behave as in a contaminated system. Experiments were performed either with single bubbles or with the simultaneous release of a few bubbles, in order to study their interaction in relation to wake dynamics. The bubbles were released from the bottom plate of the tank, initially into quiescent fluid.

Fluid flow velocity was measured in planes both parallel and perpendicular to the bubble

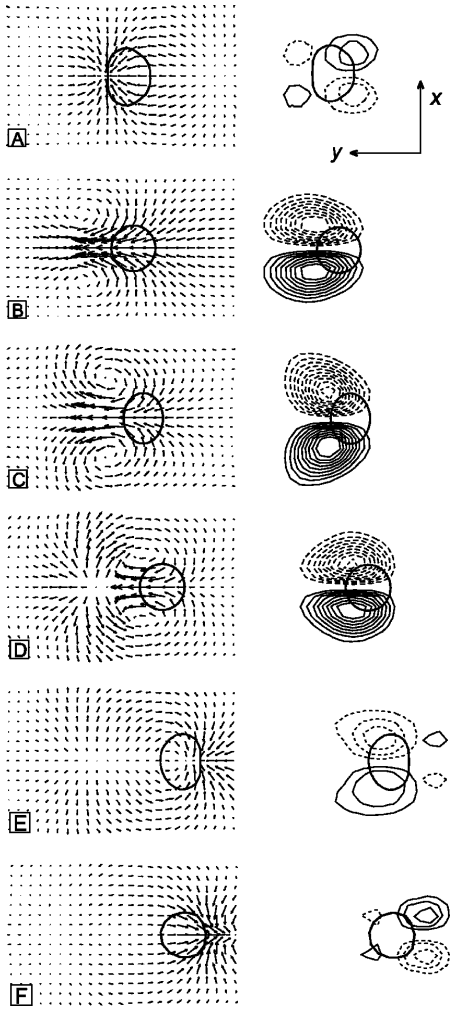

Figure 2.9: Evolution of the velocity field and streamwise vorticity distribution in a horizontal plane 10 *mm* downstream of a zig-zagging bubble. The zig-zag motion of the bubble in the horizontal plane is along the y axis. Left column: velocity field ($V_{max} = 70$ *mm/s*)); right column: regions of concentrated streamwise vorticity ω_z (contour lines start from $\pm 1/s$ in steps of 1/s; solid line: positive value, dashed lines: negative value), Brücker [29].

flow direction. PIV measurements perpendicular to the flow were taken 10 *mm* downstream of the bubble, as the bubble is stationary due to a counter flow. The flow field in this cross section showed the alternate generation of a pair of counter-rotating vortices close to the bubble base, as illustrated in Figure 2.9. Figure 2.10 shows an interpretation of the measured vortex pattern in the cross section downstream of the bubble as it cuts through the legs and the head of a hairpin vortex.

Experiments were also performed by Brücker [29], to investigate the evolution of the bubble wake in the vertical cross section. Measurements of the vertical flow field are necessary for a more complete description of the three-dimensional flow field and vorticity

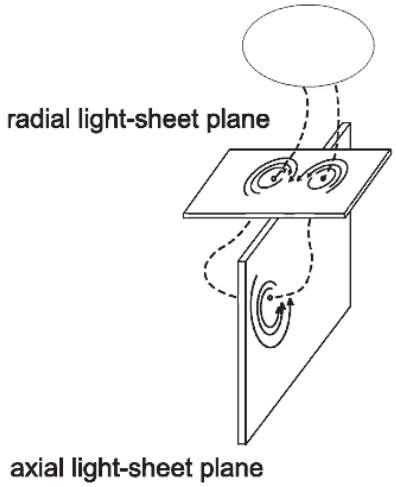

Figure 2.10: Interpretation of the measured vortex pattern in the cross section downstream of the bubble as it cuts through the legs and the head of a hairpin vortex, Brücker [29].

distribution. It was found that the structures exhibited by the bubble's movement do not represent closed vortex rings; instead the part closer to the vertical centreline is of a lower maximum vorticity and constitutes the tip of the tongue-like extended region shown in Figure 2.11. In summary, the results obtained by Brücker [29] confirm that the wake of bubbles within this range of Reynolds numbers consists of a chain of vortex loops with alternate circulation and orientation.

Results of flow measurements in the wake of spiralling bubbles demonstrate that the wake consists of a pair of attached streamwise vortices exhibiting only weak oscillations. The attached vortices remain nearly in the same position relative to the bubble while moving with the bubble and rotating around the centre of the spiral in the same way as the bubble does. The spiralling bubble, unlike the zig-zagging bubble, was found not to undergo shape oscillations [29] .

The experimental methods used by the authors mentioned above, which require adding dye or seeding with small particles, are likely to contaminate the water. Since this affects the free surface of the bubble the similarity with the behaviour of solid spheres may be a consequence of the contamination. As previously discussed, above a certain volume bubbles no longer rise rectilinearly: the path becomes a zig-zag or a spiral. A similar behaviour is observed for solid spheres, but at lower Reynolds numbers.

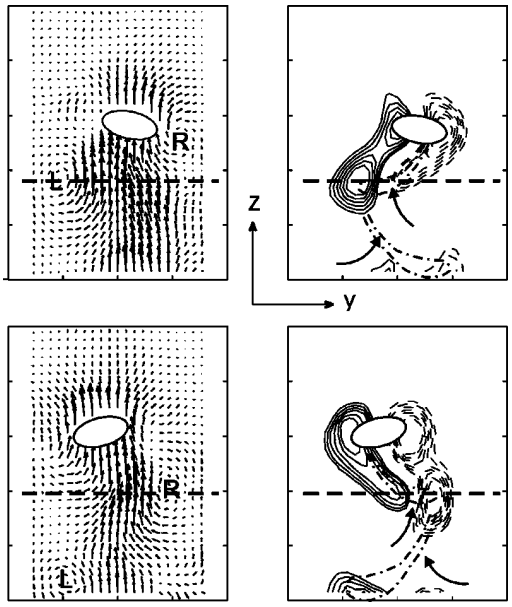

Figure 2.11: Flow field in a vertical plane through the wake of a rocking bubble at two characteristic moments within the cycle (the vertical velocity component of the imposed counterflow has been subtracted; the thick dashed lines display the reference location for the spatio-temporal reconstruction of the vortex tongue like regions), Brücker [29].

De Vries *et al.* [32] employed the use of the schlieren optical technique[8] to visualise the wake behind bubbles of high Reynolds number in highly purified water. This technique was used because it does not contaminate the water. The difference in the bubble's boundary conditions influences the vorticity production at the surface and therefore the final structure of the wake. De Vries *et al.* [32] considered that the addition of contaminants such as PIV seeding by Lunde & Perkins [47], Ellingson & Risso [44] and Brücker [29] to visualise the bubble's wake in fact hinders their understanding of the wake structure, as the surfactants change the boundary condition on the bubble's surface from no-shear to no-slip which results in an increase in the drag.

Their rig consisted of a $150 \times 150 \times 500\ mm^3$ glass tank filled with ultra purified water (less than 10 parts per billion organic particles). A density variation is generated by heating the upper part of the tank, and as the bubble rises through the lower, cooler layers, it entrains cold water in its wake and drags it into the heated water above. Most importantly the temperature gradient was shown to have negligible effects on the bubble motion (De Vries [27]).

[8]Schlieren photography is an optical technique that is used to photograph the flow of fluids of varying density

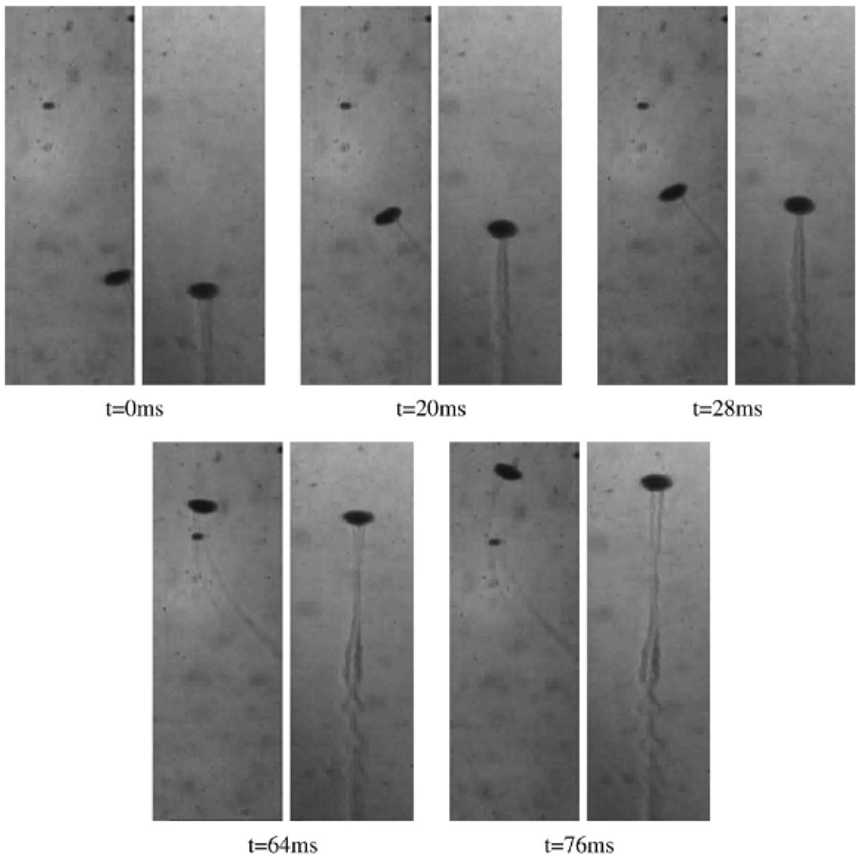

Figure 2.12: Successive images of a zig-zagging 2 *mm* bubble at t = 0, 20, 28, 64 and 76 *ms*. The left image is recorded perpendicular to the right simultaneously. The double threaded wake exists until t = 20 *ms*, where the curvature of the path is zero. Following this, it then forms a single thread and sheds a horseshoe (tongue-like) shaped vortex. Farther downstream the double-threaded wake becomes unstable, De Vries *et al.* [32].

Figure 2.12 illustrates a sequence of images obtained for a case in which the plane of the zig-zag coincides with a camera projection plane. The right hand image of the bubble path shows a straight path, whereas the left images depict the zig-zag motion of the bubble. In the right view immediately behind the bubble a double-threaded wake is visible (t = 0 *ms*); in the left view only a single thread vortex is visible due to one thread blocking the view of the other. Further behind the bubble the two threads change into a single thread, which subsequently splits and the double-threaded wake reappears. The double-thread was found to be present whenever the curvature of the bubble's path is non-zero. A double-threaded wake consists of a pair of counter-rotating vortex filaments. The wake immediately behind the bubble consists of hairpin-type loops, which were formed and closed each time the bubble passes through the axis of symmetry of the zig-zag.

As the bubble proceeds forward, new components of the wake are added, and the corresponding change in the momentum carried by the wake implies that a lift force is exerted on the bubble in the opposite direction. This force, which is normal to the direction of motion, causes the bubble to follow a curved path. De Vries *et al.* [32] estimated the lift force by using self-induced motion of a double-threaded wake, to calculate the velocity of the vortex. The lift force when the wake is a double-threaded wake was found to be approximately 2.5×10^{-5} *N*.

Fan & Tsuchiya [18] describe the wake for bubbles of intermediate size. Firstly, separation of the boundary layer formed along the bubble frontal surface takes place at a specific point along the bubble rim. The vorticity generated at this separation point is discharged downstream in the form of a vortex filament, as observed by the previous authors. This vortex filament tends to move towards the wake central axis due to the pressure defect in the wake region. At the same time, the filament tends to form a spiral due to the rotation of the separation point along the bubble's rim. The resulting wake structure is a continuous discharge of a vortex filament, as shown in Figure 2.12.

Veldhuis [28] utilized a stereoscopic Schlieren technique, to follow on from the work of De Vries *et al.* [32]. Figure 2.13 illustrates the wake structure behind six bubbles of increasing equivalent diameter: (a) 1.3, (b) 1.5, (c) 2.0, (d) 2.2, (e) 2.5, and (f) 2.8 *mm*. Notably, due to the temperature gradient the visibility of the bubble's wake is strongly dependent on the amount of fluid motion at the rear of the bubble, therefore the wake's visibility is higher for the larger bubbles. Figure 2.13 illustrates the varied paths which a bubble may take, from rectilinear to spiral. The bubbles were found to rise with their minor axis aligned with the direction of the bubble's path. In most cases the wake is quite stable; the exception to this is seen in Figure 2.13 (f), where bubble shape oscillations occur, creating almost separated zones of high vorticity. Veldhuis [28] utilized the experimental data to calculate the lift and drag forces at the rear of the bubble, with links being made to vorticity structure behind the bubble.

Veldhuis [28] noted that a bubble rising rectilinearly produces an axisymmetric wake, which becomes a double-threaded wake when the path instability sets in. Bubble shape oscillations were found to be present for a bubble diameter greater than 2.8 *mm*, although for a 2.5 *mm* bubble its wake became unstable at its outer positions during a mild spiral path.

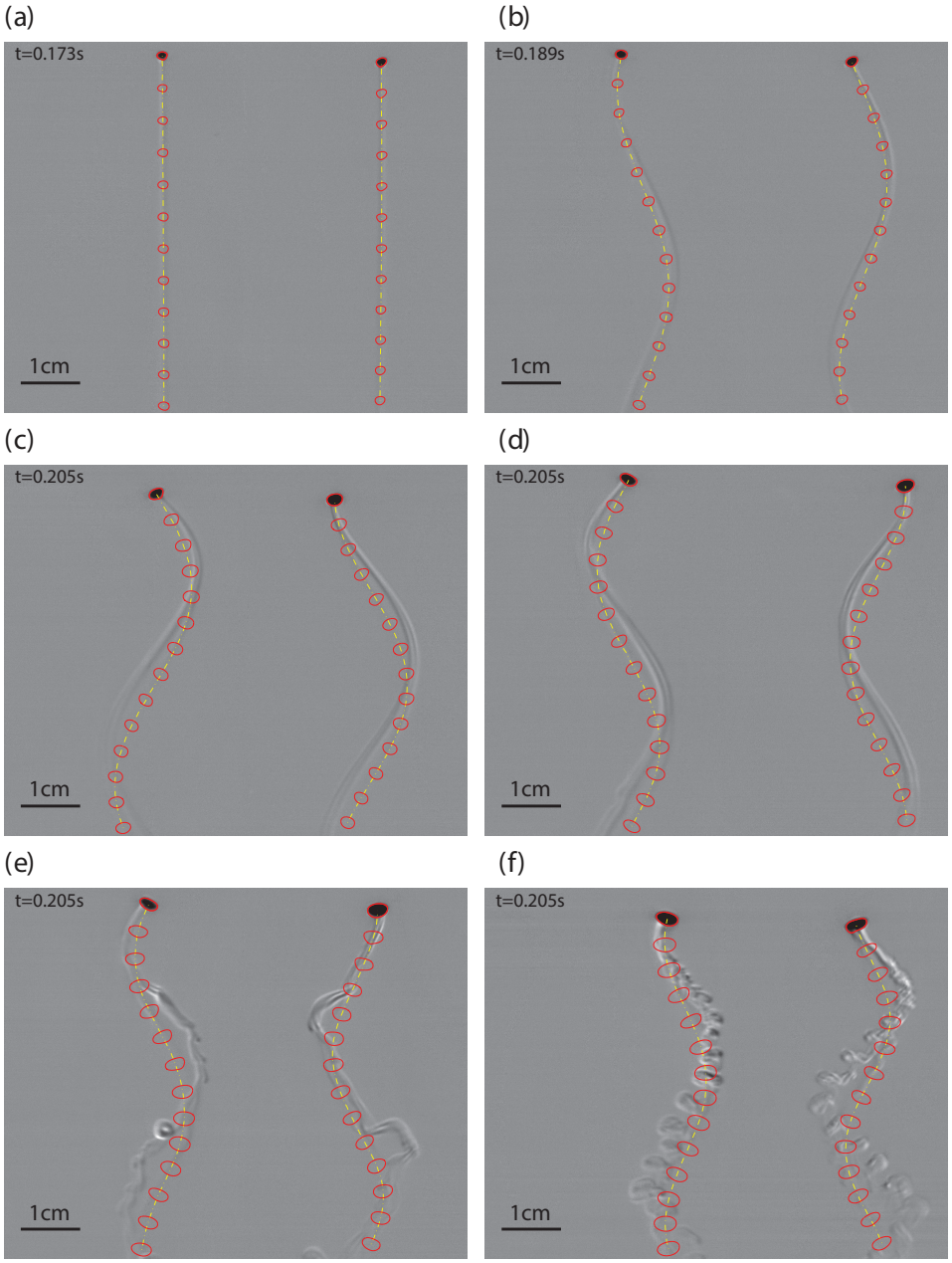

Figure 2.13: Stereoscopic Schlieren images of bubbles with their paths: dash-dotted line and bubble shape: solid red line. Images are recorded with 640 *fps*. The bubble shapes are plotted every 10 frames, giving a time interval of 0.64 *s* between the bubble shapes. The elapsed time starting from the first bubble shape is indicated in the upper left corner. The equivalent diameters are (a) 1.3, (b) 1.5, (c) 2.0, (d) 2.2, (e) 2.5, and (f) 2.8 *mm*. Veldhuis [28].

Interestingly, the shape of the bubble was found not to be influenced by these instabilities in the wake. Veldhuis [28] postulated that the "presence of wake oscillations without shape oscillations suggests that the wake oscillations trigger shape oscillations when the bubbles are large enough, and not vice versa".

In the case where the bubble's path was a pure spiral, the lift forces in directions normal and bi-normal to the tangential vector were found to be equal, while in the case of zig-zagging bubbles the lift force in the bi-normal direction vanishes. Veldhuis [28] analysed the vorticity structure behind spiralling bubbles and noted that it consisted of two counter-rotating vortex threads, which generate the necessary lift to curve the bubble's path, the same result as reported by De Vries *et al.* [32].

In a study by Sanada *et al.* [49], photochromatic dye was used to visualise the wake behind a rising bubble. A single nitrogen gas bubble was generated from a single nozzle in a glass tank with dimensions of $150 \times 150 \times 400\ mm^3$, filled with silicone oil solution infused with photochromic dye with a concentration of 25 *ppm*. The equivalent bubble diameter D_{eq} ranged from 0.66 to 0.93 *mm* in this experiment. The authors concluded that "clean bubble" conditions hold in the solution of silicone oil and toluene with dissolved dye, as the effect of contaminants was found to be negligible.

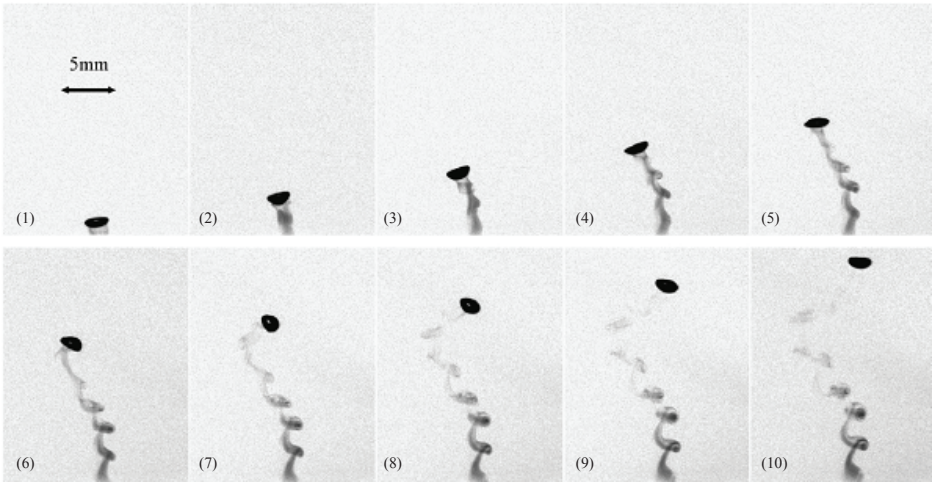

Figure 2.14: Wake of zig-zagging bubble motion, side view (Δt = 10 *ms*, *Re* = 330 , *We* = 3.0), Sanada *et al.* [49].

Firstly, the existence of a standing eddy at the rear of a bubble rising rectilinearly was experimentally confirmed. It was observed also that a pair of double-threaded vortices changed places with each other, as if they were rotating. This phenomenon was not observed by previous authors. Sanada *et al.* [49] indicates that numerical work predicted that the double-threaded vortices change places with each other twice in one period of zig-zag motion. It was observed that when a pair of streamwise vortices periodically approached each other and separated from each other, a horse-shoe like structure of vortices formed in that region.

Wake structures of a single bubble rising in a zig-zag path are shown in Figure 2.14 and 2.15, from the study of Sanada *et al.* [49].

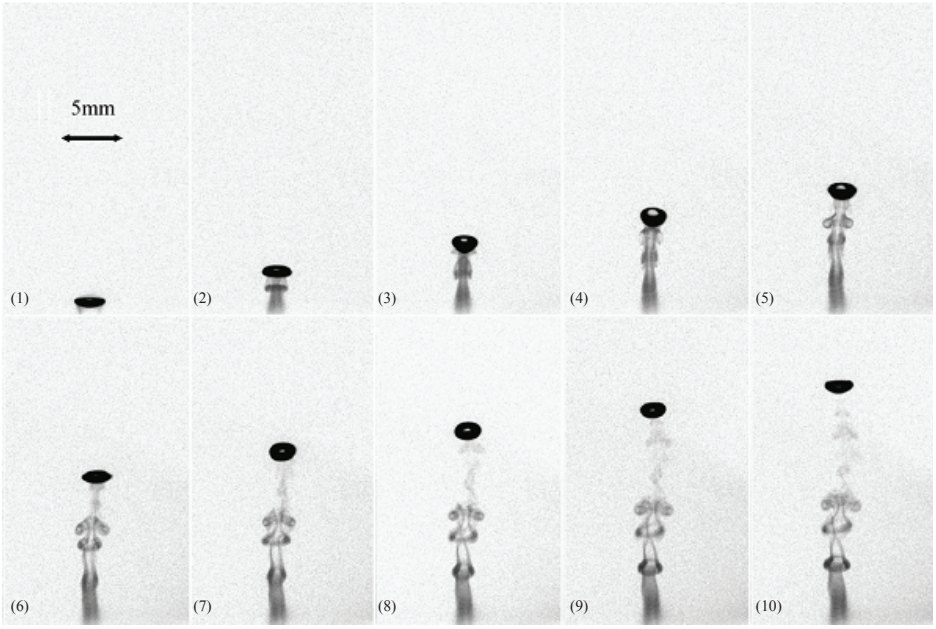

Figure 2.15: Wake of zig-zagging bubble motion, front view (Δt = 10 *ms*, *Re* = 330 , *We* = 3.0)

Figure 2.14 and 2.15 illustrates two different bubbles, both aligned in different geometric planes with a $\Delta t = 10ms$. The authors also question the statement by Brücker [29] and Lunde & Perkins [47] that a horse-shoe type vortex is formed every time the bubble changed its direction, i.e. twice in one period of a zig-zag motion. Their results, shown in Figure 2.14 and 2.15, suggest that vortices were formed not twice but multiple times in one period, which is similar to the result of Veldhuis [28]. The authors suggest that this multiple vortex formation is probably linked to shape oscillations, as also indicated by previous authors.

2.2.4 Multiple Bubbles

In most engineering examples more than one bubble is present, with some aspects of bubble to bubble interactions having interesting effects [17, 50–53]. If bubbles are separated by a significant time period, it has been found that the residue of the wake would affect the next bubble, causing its path to be purely spiral, rather than zig-zag [17, 53]. In cases where a new bubble is released promptly after the first one, the second bubble may draft the original bubble; catching up to the bubble. Once the second bubble has caught up, the

bubbles are found to tumble, exchanging places as shown by Vélez-Cordero *et al.* [52]. If individual bubbles are released along side one another, this causes either attraction or repulsion, whereby the bubbles would either push away from one another or be attached to one another later in their rise [50].

2.3 Bouncing Bubbles

The dynamics of bubbles and their direct impact against surfaces has only received a small amount of attention in recent years. Of most importance for the present study is the effect of a bubble rising through a liquid and impacting on a horizontal surface. Some studies have investigated the nature of bubble coalescence[9] with a free liquid surface, as well as bubble impact against a solid substrate. The following section will explore the impact of bubbles against free, hydrophobic and hydrophilic surfaces.

2.3.1 Free Liquid Surface Impact

Kirkpatrick & Lockett [54] investigated the coalescence of a single bubble with an air/water interface. The authors identified two basic types of coalescence, which depended on the bubble's approach velocity. At a low approach velocity bubble coalescence is rapid, but coalescence times are considerably increased at large approach velocities. For pure liquids, the authors conjecture that at low approach velocities film rupture can occur before the approaching bubbles are brought to rest. At large approach velocities a bubble is brought to rest before rupture occurs. In the latter case bubble bounce can occur and the total coalescence time is thereby considerably increased.

Krzan *et al.* [55] investigated a bubble rising in distilled water and in an aqueous pentanol-1 solution as it approached the air/liquid interface. Single bubbles were formed at a capillary orifice of inner diameter 0.07 *mm*, in a glass test tank of 40×40 mm^2 in size. As a bubble approaches a liquid surface it neither ruptures immediately nor coalesces at the surface. After having formed a "dome", the bubble starts to move backward, that is, opposite to the direction of the initial buoyancy force. Simultaneously, the bubble starts to pulsate very

[9] Once the bubble coalesces with the free surface the bubble disappears.

rapidly. These oscillations are evident in Figure 2.16, which shows the bubble's velocity, up until coalescence with the surface.

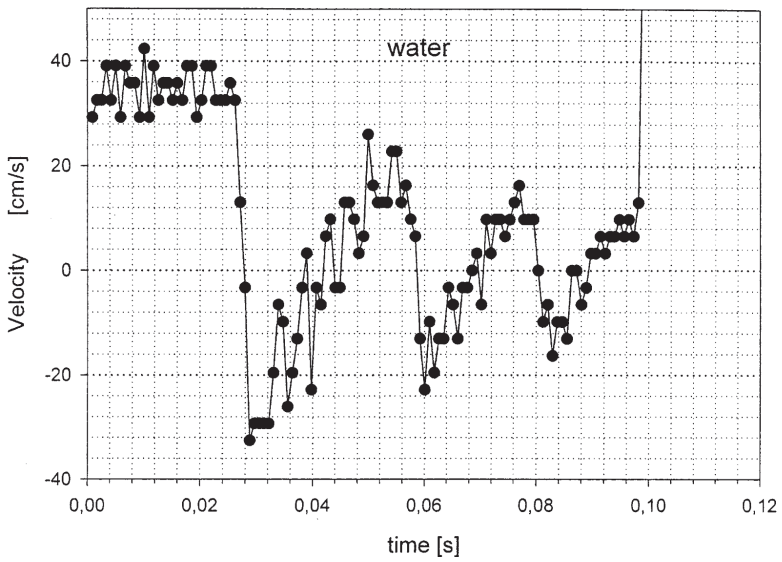

Figure 2.16: Variations in the bubble's velocity as it impact and rebounds from a free liquid surface. Coalescence occurs at the fourth approach at a time of 0.1 *s*. Krzan *et al.* [55].

After impact the bubble's shape is seen to oscillate at a high frequency, limited only by the maximum frequency of the camera. The amplitude of the bubble's shape pulsations and the velocity variations were found to decrease with each impact and rebound. It was found that with increasing pentanol-1 concentration, the amplitude of the bubble shape pulsation and its bouncing velocity decreased. The presence of a surface-active substance was reported to deliver the following effects: (i) a decrease of the bubble's rising velocity, (ii) a diminishing of the bubble's amplitude of bouncing and shape pulsations, and (iii) a prolongation of the bubble lifetime at the free surface, as a result of the increased stability of the thin liquid layer, known as the foam film, separating the bubble from the atmosphere.

Malysa *et al.* [24] examined the nature of a bubble's interaction with a liquid/gas interface and a solid interface in various fluids. This work was a continuation of the work performed by Krzan *et al.* [55]. The authors found that the presence of surfactant (surface active substance) had a profound effect on the bubble.

The variation in surface tension as a result of the bubble motion and the deformation of the thin film at the surface, according to the authors, is responsible for damping of the bubble's shape pulsations and for preventing the bubble rupture due to enhanced stability

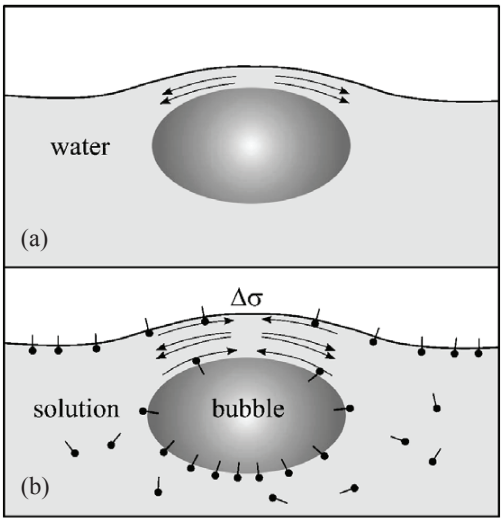

Figure 2.17: Schematic illustration of the surface tension gradient's action during the thin liquid layer thinning, Malysa *et al.* [24].

of the foam film being formed. The mechanism of the surface tension gradient's action is illustrated schematically in Figure 2.17. In a surfactant solution (Figure 2.17 (b)) the surface tension gradients induced act in the opposite direction to the liquid flow from the thin liquid layer, above the rising bubble. This liquid motion counteracts the outflow and leads to a reduction in the thinning of the liquid film. The authors hypothesised that the surface tension gradients tend to restore uniform coverage over deformed liquid/gas interface, which in turn results in the motion of the surfactant molecules to be against the flow of the outflowing liquid.

Suñol & González-Cinca [56] present experimental results on the behaviour of air bubbles rising through a liquid and coalescing with a free surface. A cubic methacrylate tank of $250 \times 250 \times 250\, mm^3$ was filled with ethanol to a height of 200 *mm*. Air bubbles with equivalent diameters between 0.1 and 2 *mm* approximately were released from a syringe placed at the bottom of the tank, and rose to the free surface under the action of buoyancy. Figure 2.18 illustrates the bouncing and coalescence of three bubbles with equivalent diameters of 1.62, 1.06 and 0.43 *mm* in ethanol.

The collision between the bubble and the free surface generates oscillations on the bubble's surface. The authors were only able to measure the frequency of oscillations of large bubbles, since smaller bubbles have higher oscillation frequencies. The first oscillation mode corresponds to a volume oscillation, but the authors were unable to measure it due to

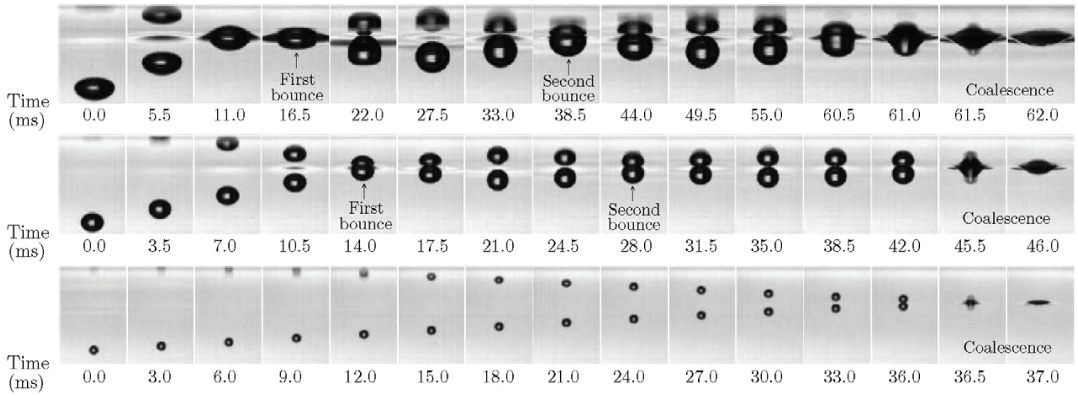

Figure 2.18: Rising bubbles and the interaction with the free surface in ethanol. From top to bottom: bubble equivalent diameters are D_{eq} = 1.62, 1.06 and 0.43 *mm*, Suñol & González-Cinca [56].

low resolution of their measurement system. Lamb [48] gives the general relation for the frequency of the *n*th mode of an oscillating bubble in an unbounded fluid as:

$$f_n = \frac{1}{\pi}\sqrt{\frac{2(n+1)(n-1)(n+2)\sigma}{\rho D_{eq}^3}} \quad \text{for} \quad n > 1 \tag{2.5}$$

Using Equation 2.5 the relation between the frequency of the second mode and the bubble equivalent diameter can be evaluated as:

$$f_2 = \frac{1}{\pi}\sqrt{\frac{24\sigma}{\rho D_{eq}^3}} = \frac{2}{\pi}\sqrt{\frac{6\sigma}{\rho D_{eq}^3}} \tag{2.6}$$

Suñol & González-Cinca [56] found good agreement between their experimental results and the theoretical predictions of Lamb [48]. They concluded also that the presence of the free surface did not affect the frequency of the second mode of bubble oscillation. The authors found that bubbles with a diameter greater than 0.47 *mm* start to deform below the free surface.

Sato *et al.* [57] studied a bubble bouncing on a free surface, and derived a model that can predict the contact time, which is the time duration of the bubble contact with a free surface, before bouncing again. Their model consists of two linear springs connected in series to account for the restoring forces of both the bubble and free surfaces. Di Marco [58] noted that the threshold for a bubble to either coalesce with a free surface or to bounce is a Weber number of approximately 0.1. As the Weber number increases a dimple is formed upon impact as previously discussed. This dimple, according to Di Marco [58], favours bubble

bouncing rather than coalescence.

2.3.2 Solid Surface Impact

Tsao & Kock [21] observed the interactions between small bubbles with high Reynolds number, which impacted a solid horizontal surface. For bubble impact experiments against a horizontal wall, a glass plate was placed at the top of a glass column containing water with a 45 $\times$ 45 mm^2 square cross section and 75 *mm* height. An air bubble with an equivalent diameter of about 1 - 2 *mm* was released from a needle at the base and rose to the surface under the action of buoyancy forces. Through their calculations, it was found that 95% of the energy contained in the initial kinetic and bubble surface energy is converted into bubble surface deformation during the bubble collision.

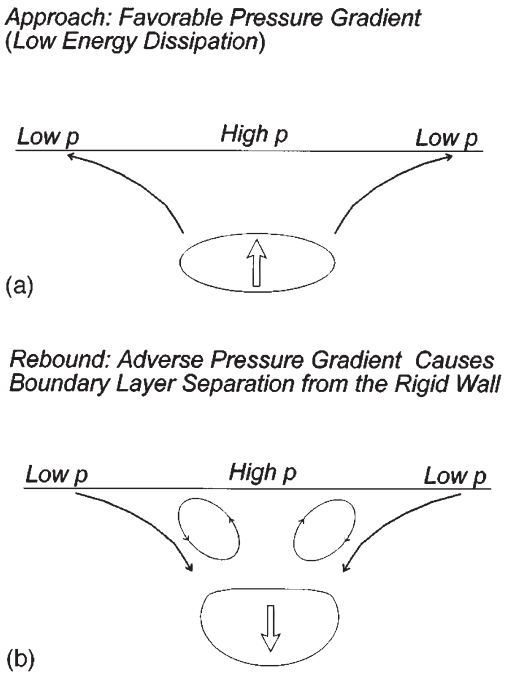

Figure 2.19: Schematic sketch of the bubble's approach to (a) and rebound from (b) a horizontal wall. The pressure is highest along the centre line. This leads to a favourable pressure gradient for the boundary layer on the solid wall during the approach and an adverse pressure gradient during the rebound, Tsao & Kock [21].

The authors hypothesize two possible mechanisms of energy loss. One possible mechanism is the acoustic radiation of energy due to shape oscillations induced by the collision. Another is the energy loss in boundary layer separation from the rigid wall, which is anal-

ysed by using potential flow. This potential flow leads to a pressure that is largest along the axis of symmetry for both the cases of an approaching and a rebounding bubble as shown in Figure 2.19. It was found that a significant fraction (59%) of the bubble's total energy was lost during a collision and that most of this loss occurred during the rebound.

Malysa *et al.* [24] investigated the phenomena occurring when a rising bubble approaches and collides with a hydrophilic glass plate in distilled water. Similarities were found with the results of the water/air surface impact. In both cases, the bubble colliding with the interface was not stopped, but started to move backward, with rapid pulsations, changing its shape during time intervals shorter than 0.845 *ms*. With every bounce the bubble approach velocity, both to the glass plate and the free water interface, decreased in a similar fashion, as shown in Figure 2.20.

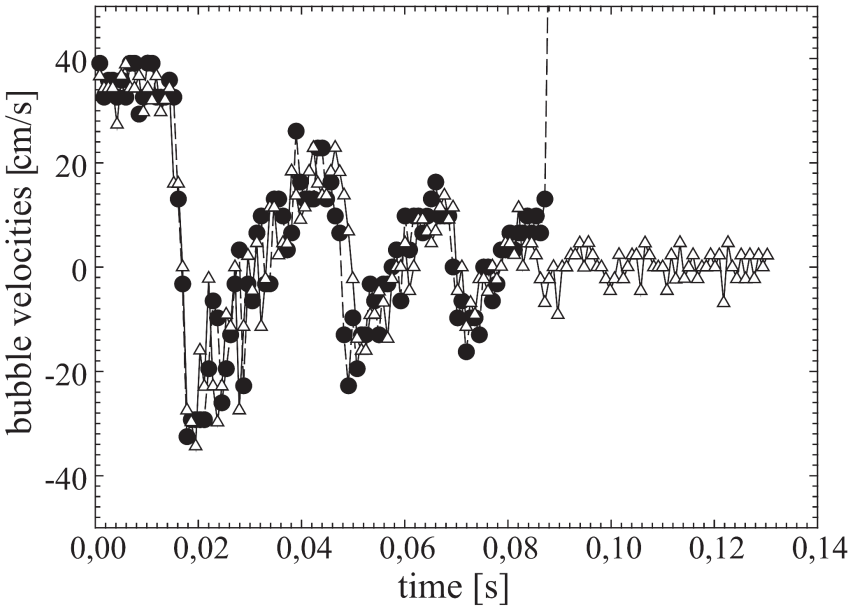

Figure 2.20: Variations of the bubble velocity during collision with water/air interface (solid circles) and water/glass interfaces (triangles), Malysa *et al.* [24].

In a further extension of the experiment by Malysa *et al.* [24], using a hydrophobic surface, Teflon, it was observed that even with a hydrophobic surface, bubble attachment did not occur at first collision and that the bubble can bounce a few times without attachment. In the experiment with Teflon of high surface roughness it was found that the presence of a micro-bubble at the Teflon surface facilitated the bubble attachment. During the approach

to the wall, the bubble starts to decelerate. Tsao & Koch [21] found that a part of the bubble kinetic energy is dissipated by the liquid viscosity (mostly in the film) and a part is transformed into bubble surface energy as the bubble impacts a surface.

Krasowska & Malysa [25] studied further the influence of surface roughness of Teflon plates on the kinetics of bubble attachment. The bubble velocity variations during collisions with the liquid/solid interface were determined by measurements of the coordinates of the bubble bottom pole (lower surface) on every consecutive frame of the camera recordings. Five pieces of Teflon were used in this investigation; the roughness of the surface of the plates was modified with the help of abrasive papers of different grid numbers and characterised with a microscope and atomic force microscopy.

Krasowska & Malysa [25] hypothesize that the lack of attachment during the first collision of the bubble with the smooth hydrophobic surface, with a surface roughness of less than 1 μm, was caused by too short an impact time to allow thinning and rupture of the intervening liquid layer. In the case of rougher Teflon surfaces the presence of a micro-bubble[10] facilitated bubble attachment.

Legendre *et al.* [13] studied 2.1 to 3.3 *mm* drops rising in water and bouncing under a horizontal plate. Toluene drops in quiescent de-mineralized water were used. Before the impact with the wall, the drops are spherical and move along a rectilinear trajectory with a constant terminal velocity corresponding to the velocity of a solid sphere of the same diameter and density. At impact, their velocity is significantly reduced due to the dissipation associated with the film formed between the drop and the wall. During the impact with the wall the drops are deformed and exhibit a close to ellipsoidal shape. The bouncing was found to be very dissipative, almost 80% of the energy being lost during the interaction with the wall. The deformation of the drop is governed by the balance between its inertia and capillary effects and evolves like a dissipative mass-spring system. The authors noted that the bubble contact time with the surface is proportional to the velocity, according to Hertz theory i.e. $t_c \propto U_T^{-1/5}$. They also define the coefficient of restitution, ε_r, which is the ratio of the velocity reached by the drop when leaving the wall, U_R, to the terminal velocity U_T of the drop before its decrease due to the interaction with the wall:

[10]The micro-bubble was created on the first rebound from the surface, with a tiny proportion of the bubble remaining attached due to the surface roughness.

$$\varepsilon_r = -\frac{U_R}{U_T} \tag{2.7}$$

Fujasová-Zedníková *et al.* [26] studied the interaction of a small bubble with an immersed horizontal solid surface. The effect of surfactant (limited to a specific non-ionic surfactant, α-terpineol, of various concentrations) and of surface materials such as cleaned glass, polypropylene, polyethylene, and Teflon was investigated. The set-up consists of a rectangular cell of $110 \times 110 \times 260\ mm^3$. An injection orifice with a inner diameter of 250 μm produces bubble sizes in the range of 0.4 to 1.9 *mm* diameter. The study focused on two particular stages of interaction: (i) the period of the first bubble bounce/collision with the wall, including the bubble approach, first contact with the wall and the possible rebound, (ii) the period of bubble attachment, with formation of the three-phase contact line. The visual observations of the bubble-wall collision reveal that the surfactant presence not only decreases the bubble rise velocity but also limits the bubble deformation and suppresses the rebound from the wall. Figure 2.21 shows a record of the collision in deionised water and in the most concentrated α-terpineol solution.

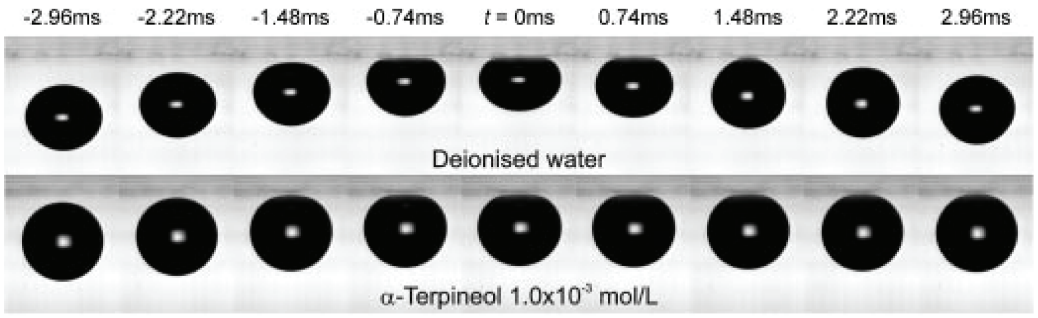

Figure 2.21: Sequence of a bubble bouncing in deionised water and in most concentrated α-terpineol solution. Bubble size is D_{eq} = 1.05 *mm*, Fujasová-Zedníková *et al.* [26].

In pure water, the bubble deforms from its initial spherical shape before impacting the wall. The deformation is caused by an increase of pressure in the thinning liquid body, which separates the bubble from the wall. The number of rebounds was observed in deionised water and was found to depend on the bubble size. A similarity between the data obtained for deionised water and α-terpineol indicates that the liquid flow around the bubble displaces the surfactant molecules to the rear of the bubble, while the interface at the bubble front remains mobile even in the α-terpineol solutions. During the bubble rebound, a portion of

surface energy is converted back to the kinetic energy and the bubble rebounds from the wall.

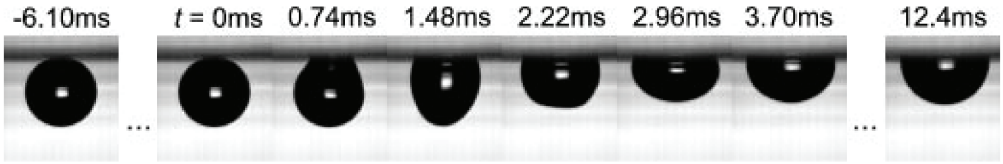

Figure 2.22: Sequence of bubble attachment process to the solid surface; polyethylene (hydrophobic) surface in deionised water, D_{eq} = 1.05 *mm*, Fujasová-Zedníková *et al.* [26].

In the case of hydrophobic surfaces, bubble attachment is sudden and a three-phase contact line is formed, as illustrated in Figure 2.22. Before attachment, the liquid in the film separating the bubble from the wall is squeezed. As the film becomes increasingly thinner, the drainage (dry-out) was found to be related to the inter-molecular forces. In the case of hydrophilic surfaces, these forces stabilise the film and the bubble never attaches to the solid. However, in the case of hydrophobic surfaces the film becomes unstable and when its thickness is below a critical value, the intermolecular force breaks it and the bubble attaches to the solid surface.

Overall, it was found by Fujasová-Zedníková *et al.* [26] that the presence of α-terpineol in water decreased the bubble velocity and also suppressed its rebound from the surface. No bubble rebound was observed in the 1×10^{-3} *mol/L* solution of α-terpineol.

Zenit & Legendre [12] studied the motion of air bubbles undergoing collisions with solid walls. One of the objectives of their study was to investigate if the universal description of the coefficient of restitution found for solid spheres is also applicable for the case of air bubbles colliding against walls. Experiments were performed in a glass cylindrical container with a height of 300 *mm* and a diameter of 100 *mm*. The bubble collided with a fully immersed horizontal glass surface.

A rebound occurs when some of the available kinetic energy of the bubble is stored as surface deformation and the dissipation of energy is not too large. Zenit & Legendre [12] give the surface energy stored in the bubble as

$$E_\sigma = \frac{8}{5}\pi\sigma D_{eq}^2 \chi_{m,0}^{-1/3}\left[1-\left(\frac{\chi_{m,0}}{\chi_{m,max}}\right)^{2/3}\right]^2 \tag{2.8}$$

where $\chi_{m,0}$ and $\chi_{m,max}$ are the aspect ratio away from the wall and at a maximum deformation. The bubble kinetic energy, away from the wall, is

$$E_k = \frac{\pi}{12}\left(\rho_g + \rho_l C_M\right) D_{eq}^3 U_0^2 \tag{2.9}$$

The ratio of these two quantities is indicative of the energy transfer during the contact process

$$\frac{E_\sigma}{E_k} = \frac{96}{5}\frac{\chi_{m,0}^{-1/3}}{We^*}\left[1 - \left(\frac{\chi_{m,0}}{\chi_{m,max}}\right)^{2/3}\right]^2 \tag{2.10}$$

where $We^* = D_{eq} 8\left(\rho_g + \rho_l C_M\right) U_0^2 \sigma$ is a modified Weber number.

Figure 2.23 shows a sequence of images of the bubble for different instants before, during, and after the collision. Zenit & Legendre [12] noted that for the same nominal conditions, sometimes either bubble rebound or bubble arrest could be observed. Surface active agents, which might be present in their testing facility, wall wettability, and surface roughness are all variables that could prevent the bubble from leaving the wall in some tests.

In summation, Zenit & Legendre [12] found that the bubble approach process is dominated by the inertia in the draining film between the bubble and the wall. When the inertia associated with the bubble motion dominates over viscous dissipation, the bubble is seen to rebound from the surface. However, when the inertia is not sufficient to overcome viscous dissipation, the bubble may oscillate or come to rest on the surface; no rebound is observed.

2.3.2.1 Added Mass Coefficient

Added mass or virtual mass is the inertia added to a system because an accelerating or decelerating body must move some volume of surrounding fluid as it moves through it, since the object and fluid cannot occupy the same physical space simultaneously.

Zenit & Legendre [12] characterized collisions in terms of a modified Stokes number, St^*, which includes a term for the added mass coefficient, C_M, which is calculated using the bubble's aspect ratio, χ_m:

$$C_M(\chi_m) = \frac{\left(\chi_m^2 - 1\right)^{1/2} - \cos^{-1}\chi_m^{-1}}{\cos^{-1}\chi_m^{-1} - \left(\chi_m^2 - 1\right)^{1/2}\chi_m^{-2}} \tag{2.11}$$

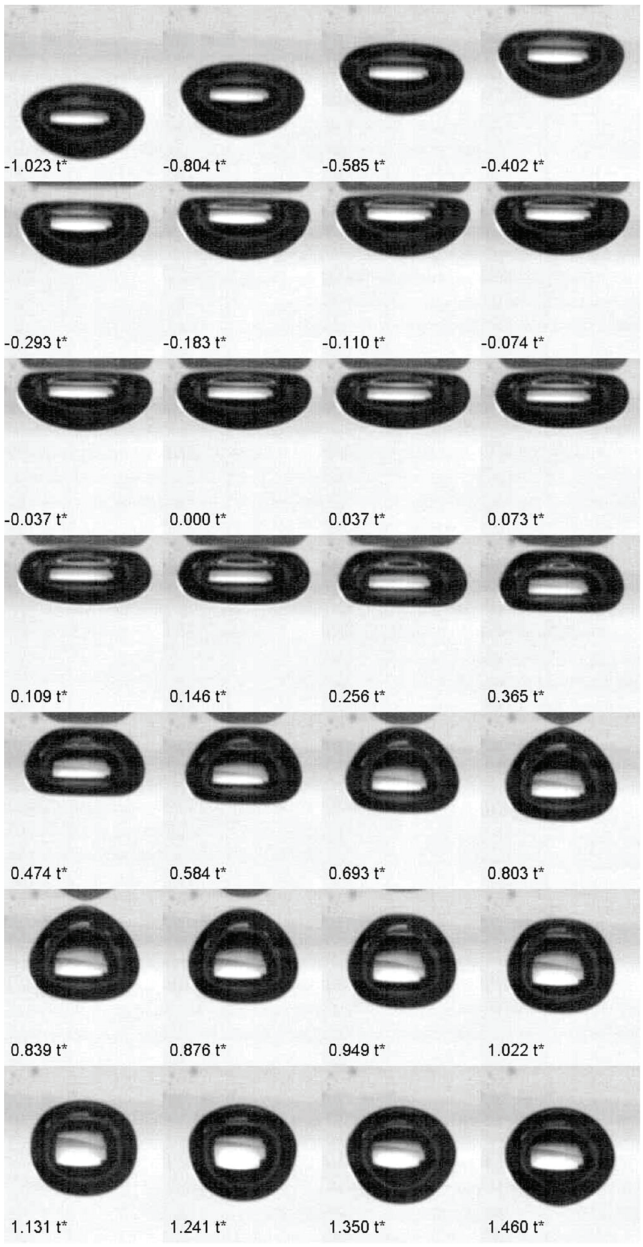

Figure 2.23: Images of typical bubble collision. For the case shown, $D_{eq} = 2.62\ mm$, $\chi_0 = 1.63$, and $U_0 = 287\ mm/s$, which corresponds to $Re = 214$ and $We = 3.37$ for a liquid with $Mo = 5.7 \times 10^{-9}$. In this case, $E_\sigma/E_k = 0.51$. The time stamp for each bubble is in terms of $t^* = tU_0/D_{eq}$, Zenit & Legendre [12].

Tsao & Kock [21] noted that the added mass coefficient is given by;

$$C_M = \frac{\alpha}{2-\alpha} \tag{2.12}$$

where

$$\alpha = \frac{2\chi_m^2}{\chi_m^2 - 1}\left[1 + \frac{1}{(\chi_m^2-1)^{1/2}}\cos^{-1}\left(\frac{(\chi_m^2-1)^{1/2}}{\chi_m} - \frac{\pi}{2}\right)\right] \tag{2.13}$$

The initial added mass coefficient for the bubble rising at its terminal velocity, is $C_M(1.79) = 0.98$, which is about twice the value, $C_M(1) = 1/2$ for a spherical bubble. The added mass coefficient term is used to determine the loss in kinetic energy when a bubble impacts and rebounds from a surface.

2.3.3 Film Thickness

Some work has been done on evaluating the film thickness between a bubble/drop and a surface [59–61]. This analysis was performed by utilising lubrication theory. Hendrix *et al.* [62] tracked a single rising and bouncing bubble and employed simultaneous laser interferometry between the glass surface and the bubble surfaces; this monitors spatial-temporal evolution of the trapped water film. An example of their finding is given in Figure 2.24, in which a small ($D_{eq} = 0.77$ *mm*) bubble impacts against a glass surface; the interference patterns are used to measure the film thickness as the bubble impacts and rebound from the surface, with a minimum film thickness of approximately 4 μm.

2.4 Bubble Motion & Heat Transfer

2.4.1 Introduction

Boiling heat transfer, in which bubbles form and move relative to a heated surface occurs in a wide variety of engineering applications including energy conversion systems, manufacturing processes, and cooling of advanced electronic systems. In some particular processes, such as in nucleate boiling on the surface of a horizontal tube or during the production of aluminium, the bubbles are nucleated on downward facing surfaces; these bubbles contribute to induced flow in the system. The above processes involve sliding bubbles, whether vapour or gas bubbles. Heat transfer enhancement due to sliding vapour bubbles is a complex mechanism found to be a combination of the effects of bubble nucleation, detachment and sliding. The following section considers heat transfer both at the location of the bubble

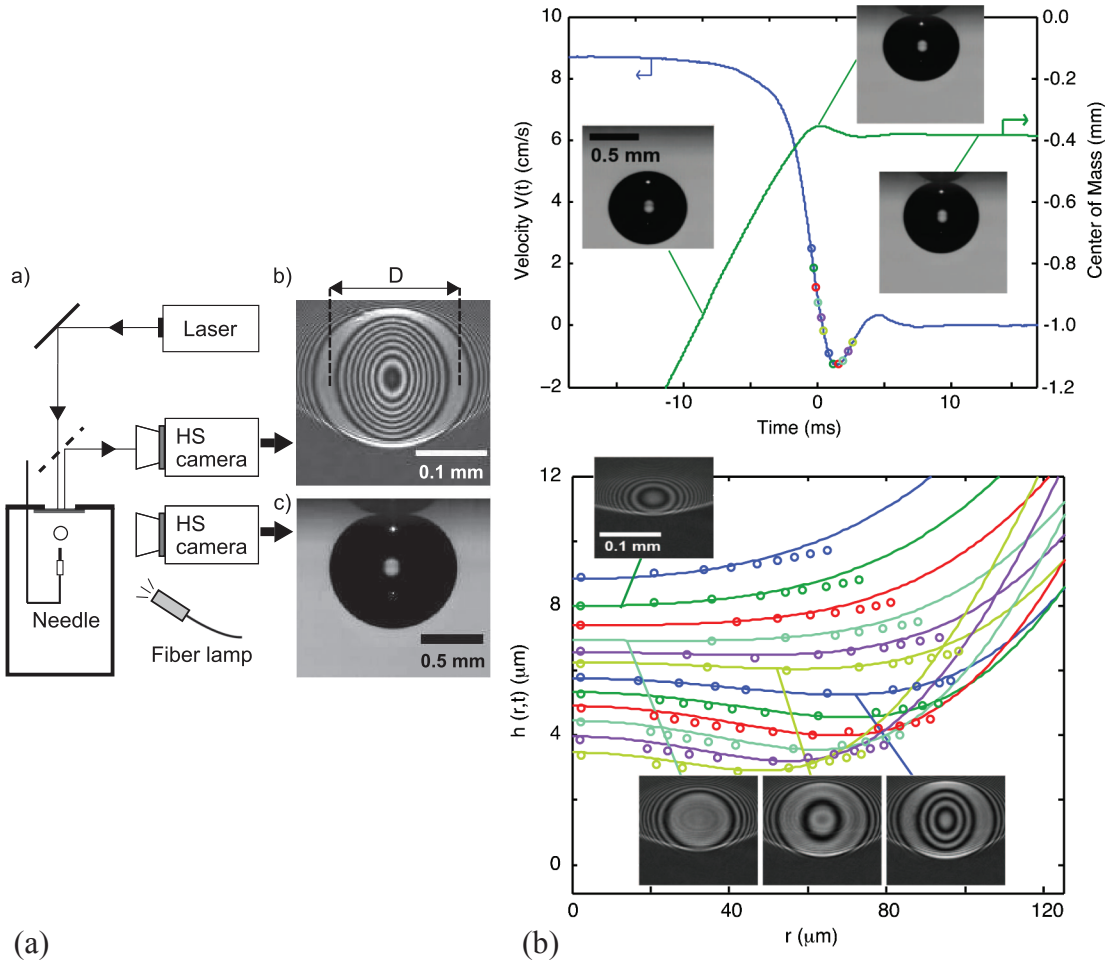

Figure 2.24: (a) experimental set-up and analysis, (b) measured time variations of the velocity and position of the centre of mass of a bubble (D_{eq}) approaching the glass surface, and profiles of the film thickness ($h(r,t)$) at times indicated by circles in upper image. Symbols denote experimental results, and solid lines represent an analytical model for a rise velocity of 87 *mm/s*. Hendrix *et al.* [62].

and in its wake. Current literature does not address the heat transfer enhancement due to bouncing bubbles, much of the current research is focused on sliding bubble heat transfer enhancement. Enhancement associated with a bubble passing by a vertical heated surface is less relevant for a bouncing bubble study and is not included here.

2.4.2 Bubble Induced Heat Transfer

An early study by Cornwell [5] investigated the influence of bubbly flow for boiling from a tube in a bundle. An attempt was made to separate the total heat transfer coefficient h into parts in order to quantify the influence of the bubbly flow on heat transfer; this is outlined in

Equation 2.14.

$$h = h_{fc} + h_{sb} + h_{nb} \tag{2.14}$$

where h_{fc} is the contribution due to liquid convection at the local fluid velocity and h_{sb} is the contribution from bubbles existing in the approaching free stream. In a tube bundle these bubbles originate from upstream tubes and slide along the downstream tubes. This term is composed of a part due to the turbulence caused in the liquid boundary layer as the bubble slides across the surface and a part due to evaporation of the thin layer under the bubble. The third component, h_{nb}, relates to bubbles which nucleate and grow on the surface as in pool boiling on a single tube. The rig comprised of thirty four 19 *mm* diameter stainless-steel tubes mounted in two in-line columns within a Perspex boiling cell. The working fluid was R113 at 1 *atm* and a constant mass flux. The instrumented test-tube was made of copper with six radially positioned thermocouples. All the tubes in the bundle were heated to give a constant mean bundle heat flux, while the test-tube heat flux was varied.

Firstly, the test tube was subject to a low level of heating, insufficient to cause nucleation on the test-tube itself. The resulting value of h was attributed to the liquid convection and to the sliding bubbles within the surrounding bubbly flow generated on upstream tubes. This initial test separated out the nucleation component of Equation 2.14, h_{nb}. Following that separate experiments under single phase liquid conditions allowed measurement of the forced convective heat transfer coefficient, h_{fc}. This value was subtracted from the previous values of h, allowing for the calculation of the heat transfer contribution due to the sliding bubbles.

Cornwell [5] found that heat transfer from a tube to the saturated liquid increased significantly when there were bubbles in the flow. This was particularly evident at low ΔT, prior to nucleation commencing, when the only other heat transfer mechanism was liquid convection. It was postulated that this mechanism was due to bubbles within the flow that slide around the tubes. It was found also that bubbles rising from a lower tube could completely suppress nucleation of new bubbles on an upper tube. A follow up study by Houston & Cornwell [6] employed the same experimental technique as previously explained but, instead of vapour bubbles, air bubbles were introduced into the system. The main outcome

of this study was the finding that bubbly-flow turbulence is a dominant mechanism in heat transfer. Barthau [63] suggested that site seeding in the wake of sliding bubbles promoted the nucleation of bubbles with small departure diameters and irregular frequencies.

Bayazit *et al.* [64] analysed the heat transfer enhancement effect caused by the passage of a sliding vapour bubble. Experiments were conducted on an electrically heated thin-foil surface. The apparatus consisted of a rectangular chamber of $400 \times 200 \times 190\ mm^3$, constructed of thin aluminium plates, and the test surface could be rotated relative to the horizontal. The test fluid was FC-87, a dielectric perfluorocarbon fluid manufactured by the 3M Corporation. A 51 μm thick $210 \times 168\ mm^2$ stainless steel foil served as the electrically heated test surface and was mounted on top of the chamber. The test fluid touched the bottom face of the test surface, and a thermochromic liquid crystal (TLC) was applied to the upper (dry) face of the heater. Two synchronised cameras recorded the images of the upper and lower surfaces of the foil. Tests were performed at a plate inclination angle of 12° to the horizontal. The bubble velocity ranged up to 200 mm/s with the bubble volume up to 2 ml. Hemispherical, ellipsoidal and cap-shaped bubbles were observed; these grew rapidly due to evaporation and created a triangular thermal wake with sharp lateral edges. Measurements of the velocity and volume of vapour bubbles agreed well with those of Maxworthy [20] for adiabatic gas bubbles.

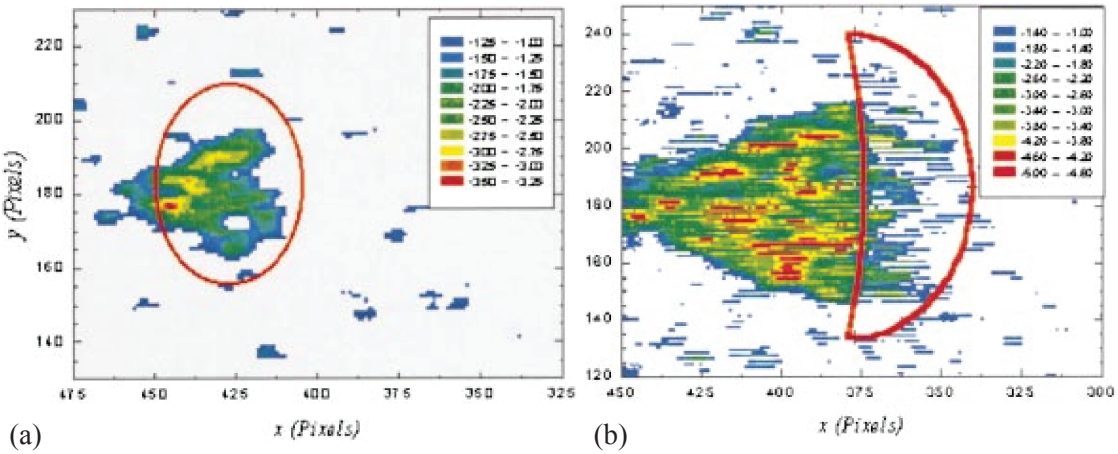

Figure 2.25: Contour plot of the change in wall temperature caused by the passage of a vapour bubble. The bubble is outlined in red. The red on the contour plot indicates a drop in wall temperature of approximately 4°C and blue represents a drop of approximately 1°C, (a) $t = 140\,ms$, (b) $t = 280\,ms$, Bayazit *et al.* [64].

Figure 2.25 shows contour plots constructed from the TLC images at 140 *ms* and 280 *ms*, where the initial wall temperature has been subtracted. The bubble is moving from left to right in these figures. After the bubble has long passed, the surface temperature was found to be still thermally depressed: this was attributed to enhancement from the bubble's wake.

Kenning & Yan [65] used liquid crystal thermography to investigate pool boiling of water on a thin, electrically heated stainless steel plate, in conjunction with high speed tracking of the moving bubble. The heated stainless steel plate measured 28.1 $\times$ 40.8 mm^2 and was 0.13 *mm* in thickness. Two dimensional dynamic temperature and wall heat flux plots of the surface are presented throughout. Their measurements confirmed the cooling of the wall during bubble growth was consistent with evaporation of a liquid micro-layer, while further cooling of the surface occurred during the bubble's departure, as the bubble's base contracted inwards.

An earlier study by Yan *et al.* [23] investigated the effect of sliding bubbles on heat transfer for inclined and curved surfaces, with the use of liquid-crystal thermography. A single camera was used along with a mirror arrangement to record both the bubble motion and liquid-crystal colour patterns simultaneously. Yan *et al.* [23] related the rate of heat flow into the bubble to its volume increase and found that the heat flux from the wall was not sufficient to explain the bubble growth. In order to explain the bubble growth, heat flow to the bubble must come also from the superheated liquid around the bubble. There was no evidence to suggest a hot spot in the temperature contours beneath the bubble; it was assumed that a continuous layer of liquid existed between the wall and bubble (referred to as the liquid micro-layer). The thickness of this layer was estimated to be in the range of 100 to 200 μm.

The main focus of this study was to validate the liquid crystal technique which was successfully achieved. A continuation study by Yan *et al.* [66] investigated the effect of injected steam bubbles sliding under an inclined plate heated to low superheats, using the same experimental techniques as Kenning & Yan [65]. For the sliding bubble experiments, the rig consisted of a 75 μm thick stainless steel plate measuring 40 $\times$ 35 mm^2. Wall angles were varied from 15° – 45° relative to horizontal. The lower surface was immersed in degassed water at atmospheric pressure and the water pool was held at a temperature of 96°C to 100°C. In order to eliminate the effects of nucleate boiling, steam was generated by

an external heater and injected into the pool, through either a single injector or an array of injectors close to the lower end of the inclined plate.

For a plate angle of 15° the bubble's velocity was calculated to be 140 *mm/s*. As the bubble grew, a cooling wake was left trailing, with an approximate width of the bubble. Immediately behind the bubble's leading edge a rapid reduction in wall temperature was noted, although there was still a region of slightly elevated temperature near its rear edge. The author noted that the bubble's wake cooling for larger inclination angles persists far behind the bubble, eventually affecting a region 50% wider than the bubble.

For the case of a curved surface, bubbles nucleating under near-horizontal surfaces or approaching from below tend to stick to the surface and cause a hot spot through local dryout, inducing elevated temperatures; these bubbles grow slowly to 4 – 8 *mm* diameter before sliding away from the bottom of the cylinder. As the bubble starts to slide, it take this dried-out spot with it. The travelling dry spot may activate unstable nucleation sites along the plate.

Atmane & Murray [2] investigated the influence of a plume of rising air and vapour bubbles on heat transfer from a horizontal cylinder. In the first case the bubbles originated in nucleate boiling on the cylinder surface and in the second case a stream of air bubbles was injected from a point below the cylinder. During the nucleate boiling study, heat transfer was found to be highest on the upper part of the cylinder; this was attributed to the detachment of vapour bubbles that slid around from the lower surface of the cylinder. In the case of the injected air bubbles, the heat transfer on the lower part of the cylinder was found to increase due to the impact and bouncing of the introduced bubbles.

Qiu & Dhir [7] conducted an experimental study on the flow patterns and heat transfer associated with a vapour bubble sliding on a downward facing heated surface. They set out to improve the understanding of the dynamics of sliding bubbles and the associated heat transfer mechanisms in a larger parameter range, along with explaining some of the contradictions present in the literature. The bubble shape and trajectory were compared between the different inclination angles of a downward facing heater surface. They utilized a polished silicon wafer, 185 *mm* in length and 49.5 *mm* in width, as the test surface to ensure no nucleation on the surface. Kapton foil heaters provided the heat to the surface and miniature thermocouples measured the surface temperature. This arrangement allowed the wall

superheat to be maintained at a near uniform level, in the sliding direction, by separately heating the elements. Fluorinert liquid PF-5060 was used as the test liquid. Holographic interferometry was used to measure the fluid temperature in a plane parallel to the bubble flow direction and perpendicular to the heater surface. Bubbles were generated by an artificial cavity machined into the heater surface. Tests were conducted for liquid subcoolings of 0.7 – 5.0°C and inclination angles θ of 5° –75°.

In experiments for the inclination angle $\theta \leq 60°$, bubbles slid along the heater face. For the same bubble size and shape, increasing angle of inclination led to a larger sliding velocity before the bubble reached the terminal velocity. During the sliding process the bubble was observed to grow in size, although for angles greater than 60 degrees only spherical sliding bubbles were observed. At high angles, the spherical bubble initially slid a few centimetres, before the bubble lifted off from the surface, then rose nearly vertically before returning to the surface again, so as to hop along the surface. The lift-off means that the forces pushing the bubble towards the wall, which include the buoyancy component normal to the surface and the expansion force, cannot balance or overcome the forces, such as shear lift force, pushing the bubble away from the surface. A recoil force results from the evaporation of the thin film on the wall while the shear lift force can be created by vorticity due to the relative velocity between the liquid and the bubble.

It was observed that smaller inclination angles to the horizontal led to the bubble being elongated in the direction of the plate width (49.5 *mm*). Larger wall superheat also leads to a larger bubble. An extreme case was observed to occur at high wall superheat and small inclination angles, θ, of both 5° and 15°, where the bubble covered the entire width of the heater. A wedge like liquid gap was observed underneath the bubbles for plate angles between 15 and 60°, this penetrated into the bubble base. The apparent liquid wedge angle was seen to decrease with an increase in the bubble size. No liquid wedge existed for plate angles of 5°, where the bubbles were generally flat in shape. The film thickness was found to vary from 160 to 64 μm from front to back. This value corresponded well to the value obtained by Kenning *et al.* [67].

The flow patterns associated with the sliding motion of the bubble can be more clearly seen from the fringe pattern. Two inclination angles were chosen, 15° and 75°, and measurements were taken 11.5 *mm* from the nucleation point where bubbles were generally

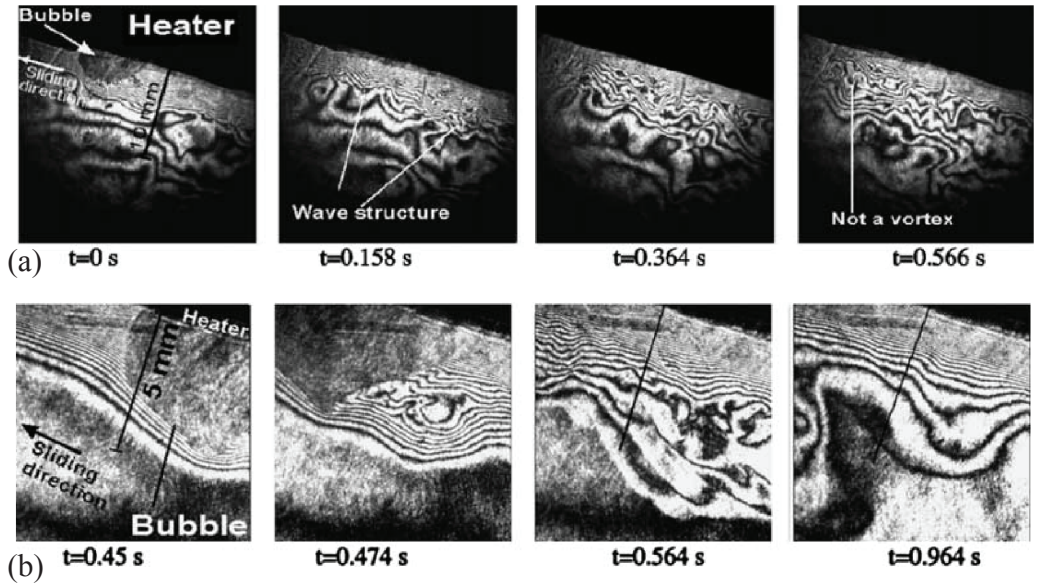

Figure 2.26: (a) Far field fringe pattern around and behind a sliding bubble for a liquid with small superheat ($\theta = 15°$, $T_w - T_{sat} = 0.8°C$, $\Delta T_{sub} = 0.4°C$, $Ra = 1.0 \times 10^9$), (b) Near field fringe pattern ($\theta = 15°$, $T_w - T_{sat} = 1.0°C$, $\Delta T_{sub} = 0.5°C$, $Ra = 1.26 \times 10^9$), Qiu & Dhir [7].

large. Figure 2.26 shows the fringe pattern for the temperature profiles around the bubble sliding on a heated surface at an inclination of 15° with two different Rayleigh numbers. In Figure 2.26 (a), it was observed that in the frontal top region of the bubble the fringes turn towards and around the bubble cap. This illustrates that the hot liquid originally in the thermal boundary layer is diverted to the bubble top due to sliding motion. Far behind the bubble, oscillatory wave type behaviour of the liquid layer continued long after the bubble had left the region; the outer fringes spread into the bulk liquid.

In Figure 2.26 (b), at $t = 0.45$ *s*, the bubble has just entered the view of the camera. In front of the bubble a thermal boundary layer of natural convection type can be seen. This boundary layer is forced away from the heater surface and around the bubble. At $t = 0.474$ *s*, the fringe pattern in the centre of the extended zone was found to be slowly rotating and then lagged behind the bubble.

It was found by Qiu & Dhir [7] that large latitudinal vortices were formed at axial distance downstream of the bubble (not shown here). These vortices appear to rotate in an anti-clockwise direction. The vortices were found to detach from the already disturbed thermal boundary layer and to move into the bulk fluid, before being dissipated. The shedding of vortices from the thermal layer had the added effect of higher heat removal from the sur-

face. Smaller vortices were found to form between the bulk liquid and the thermal boundary layer. From the video motion pictures it was found that some of these developed into large vortices while others dissipated without leaving the thermal layer.

For a small inclination angle, $\theta = 15^\circ$, and saturated liquid it was concluded that wavy motion of the liquid near the heater surface and the spreading of the wavy structures into the bulk liquid were the major flow patterns in the wake of the sliding bubble. PIV measurements at an angle of $\theta = 30^\circ$ revealed that, in the frontal portion, liquid was pushed outwards away from the wall. In the rear of the bubble, liquid was pulled inwards and a vortical structure was seen to exist behind the bubble. When the inclination angle was set as high as 75° the bubble lifted off and impacted the heater surface alternately along the surface. It was found that the heat transferred to the bubble through the liquid micro-layer contributed about 17% of the heat required for the bubbles to grow. Donnelly *et al.* [3] performed an experimental study on the flow dynamics and related heat transfer for a bubble sliding along a heated inclined surface. Donnelly *et al.* [3] noted that the majority of the heat transfer enhancement resulted from the bubble's wake effect rather from than the direct motion of the bubble.

Delauré *et al.* [4] utilised PIV to study local fluid velocities adjacent to a vertical and inclined, heated surface along with the associated heat transfer. The swirling flow resulting from the shedding of vortices and fluctuations in the external fluid temperature due to bubble agitation were found to enhance the local heat transfer. The shedding of hairpin vortices from the bubble wake increased the temperature fluctuations in the thermal boundary layer by bringing colder fluid into contact with the heated surface. Enhancement of heat transfer, as well as local reductions, was noted. Testing for a range of plate inclinations showed that the local heat transfer enhancement could be maximised by inclining the block to 45°, forcing the bubble to cut through the boundary layer.

Donnelly *et al.* [68] investigated the dynamics of a rising bubble and its influence on heat transfer from a vertical heated plate utilising the hot film sensor technique. Two methods of heat transfer enhancement were found, with the first being the bubble acting as a bluff body when its path was sufficiently close to the surface. However, when the bubble was further from the plate, the ensuing wake was found to affect heat transfer, although this was susceptible to the path orientation of the bubble. A further study by Donoghue *et al.* [53]

demonstrated the effect on heat transfer of whether the bubble's zig-zag path is normal or parallel to the heated surface, with the zig-zag path being controlled by the novel use of a hypodermic needle.

Manickam & Dhir [9] performed a further study, with the same experimental apparatus as Qiu & Dhir [7]. The heater was at an inclination of 75° to the vertical and PF-5060 was the test liquid. Measurements were made for ΔT_{sub} ranging from 0 to 1.2°C and ΔT_{wall} ranging from 0.2 to 1.0°C. Holographic interferometry was used to measure the temperature field surrounding the bubble. It was found that the bubble shapes changed from spheroids to elongated cylinders and segment of spheres in that order, as the bubble slid on the heated surface. Most importantly the area averaged heat fluxes in the presence of sliding bubbles were found to be about two orders of magnitude higher when compared to that for natural convection.

2.5 Closing Remarks

A comprehensive review of the literature has been presented for bubble departure, free rise and impacting or bouncing bubbles. It is clear from this review that numerous studies on bubble detachment and on rising bubble dynamics have been performed over the last number of years. For the present study the area of interest is bouncing bubbles and their effect on convective heat transfer. While a few studies have been performed on the dynamics of bouncing bubbles, their main focus was on resolving the energy dissipation due to the bubble's impact, utilising small, stable bubbles. These studies do not address heat transfer enhancement due to the bouncing motion of a bubble or its ensuing wake. While the wake of a rising bubble has been studied by means of PIV and Schlieren techniques, these methods have not been applied to the study of bouncing bubbles.

To the author's knowledge no investigations into the effect on heat transfer of bubbles bouncing against a solid horizontal surface have been performed. Kenning & Yan [65] investigated bubbles nucleating under a near-horizontal curved surface and approaching from below. They found that the bubbles tended to stick to the surface and cause a hot spot through local dry-out, inducing elevated temperatures, before growing and sliding away from the bottom of the cylinder. A similar study was performed by Atmane & Murray [2]

for bubbles impacting a horizontal cylinder from below, although a different experimental technique was used.

The aim of the present study is to simultaneously investigate the motion, shape and velocity of air bubbles impacting on a heated horizontal surface, along with the associated heat transfer. This investigation will be performed by varying the release height and bubble diameter. The aim is to understand the convective heat transfer mechanisms resulting for a single air bubble impacting and rebounding from a horizontal surface immersed in pure water. The final stage will be to investigate synchronised fluid motion and convective heat transfer by means of PIV, in order to fully understand important aspects of bouncing bubble motion.

Chapter 3

Test Facility and Instrumentation

This chapter describes the different experimental set-ups designed to explore the heat transfer characteristics associated with a single bouncing bubble, for various bubble diameters and release heights. Two experimental set-ups are utilised, with the first investigating the bubble's motion together with the variation in convective heat transfer. The second set-up will investigate the fluid flow during and after the bouncing event, by means of Particle Image Velocimetry (PIV).

This chapter begins with a description of the experimental set-up and equipment for the tracking of the bubble's motion and associated heat transfer; this is followed by a description of the PIV set-up.

3.1 Case 1: Bubble Motion & Infrared Imaging

In this section the main test surface will be detailed along with the instrumentation which surrounds the test surface and water tank. The tank itself is constructed of 3 *mm* thick glass bonded using water resistant silicone. The tank measures approximately $100 \times 115 \times 200$ mm^3. The surface upon which the bubble impacts sits atop the tank, with the impact surface being submerged 3 *mm* below the surface of the water.

To support the tank, Rexroth aluminium structural members are connected together to

form an adjustable support frame. The frame supports the tank, along with both high speed cameras, LED lighting, light diffusers and the high speed infrared camera, and with an adjustment, can support the laser optics for the PIV system. This means that the cameras and lighting are always in the same perpendicular position relative to the test surface and glass wall. The aluminium frame is completely adjustable, allowing for all the cameras to be aligned correctly, while also ensuring that they are level. The bubble injection system, which is discussed later, is inserted into a movable platform within the tank and is adjusted using a slider mechanism positioned above the tank, with four stainless steel rods connecting the platform to the slider mechanism. The outline of the experimental set-up is detailed in Figure 3.1.

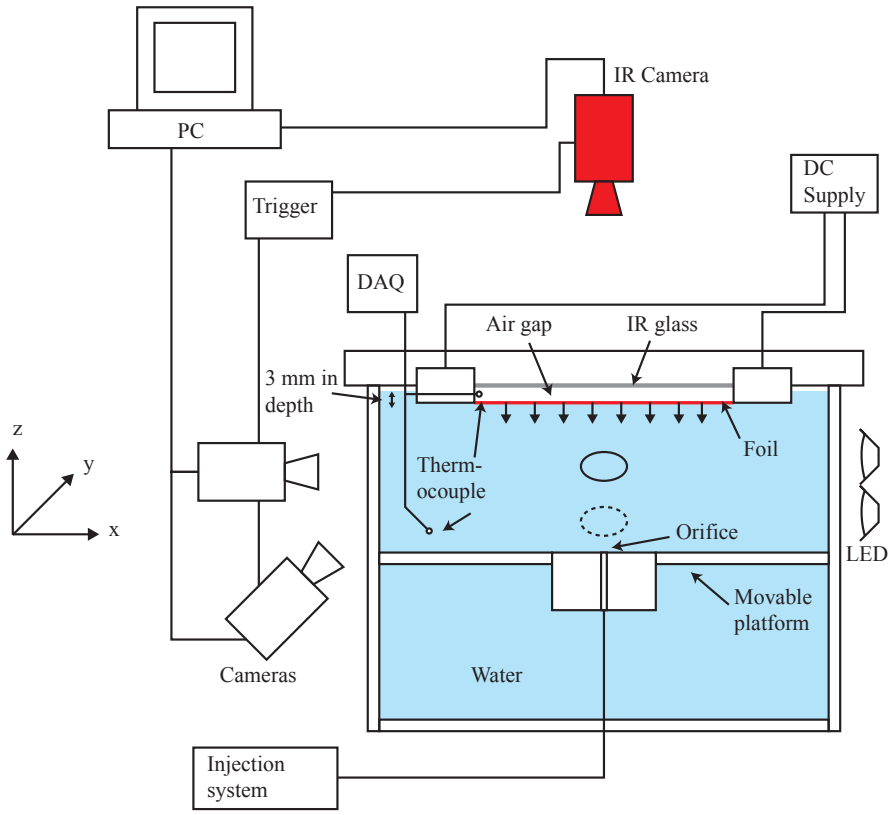

Figure 3.1: Schematic diagram of experimental set-up

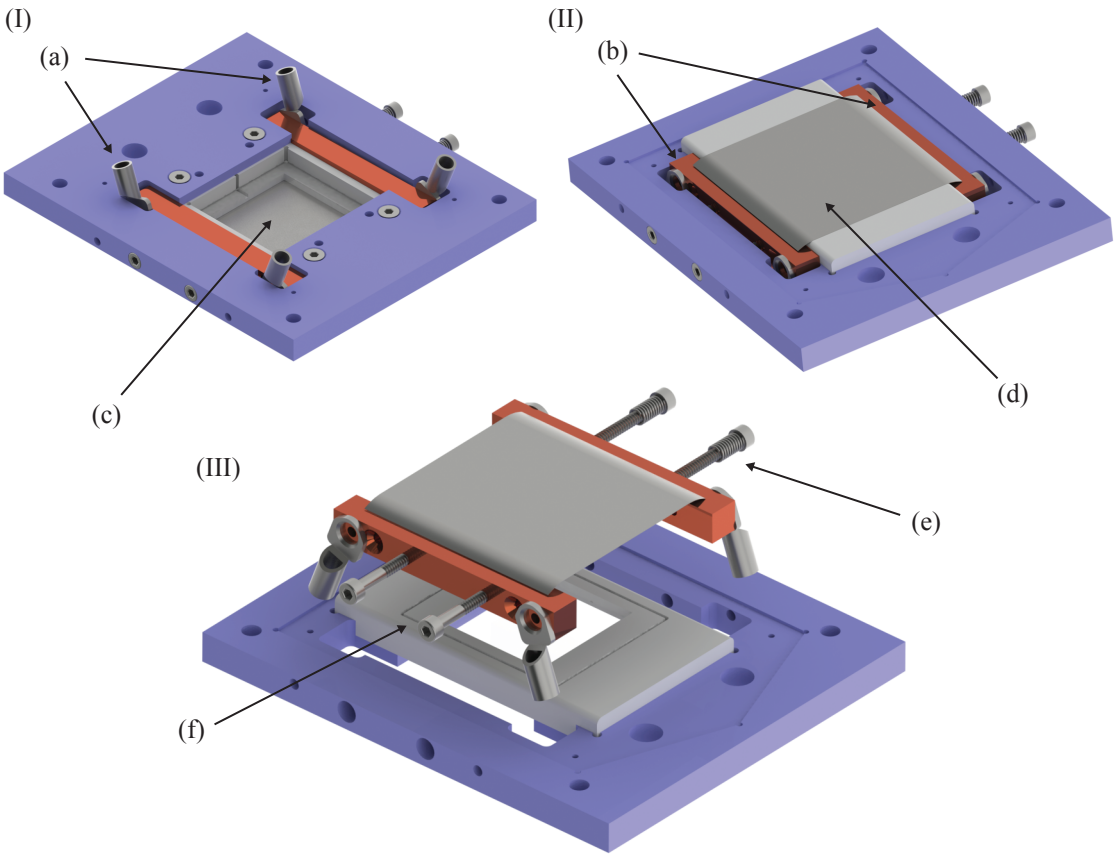

Figure 3.2: Heated surface assembly. (I) upper view, (II) inverted view and (III) exploded inverted view. (a) Power supply connections, (b) copper bars, (c) infrared transparent glass, (d) Constantan foil, (e) foil tensioning springs and (f) foil seal.

3.1.1 Heated Surface and Structure

The main test section is shown in Figure 3.2. The test surface consists of a 10 μm thick, 70 $\times$ 81.5 mm^2 Constantan® foil (Cu55/Ni45) manufactured by Goodfellow. Each side of foil is bonded between two copper bus bars measuring 5 $\times$ 10 $\times$ 84 mm^3, using silver based electrically conductive glue. The glue is applied between the two copper surfaces using a fine nylon paint brush. Two screws are then tightened, subsequently removing trapped air and evenly distributing the glue, allowing for good electrical contact and uniform heat generation. The glue is allowed 48 hours to cure, after which it is connected to a power supply and tested to ensure an even current, and hence an even temperature distribution, across the foil.

Each copper bar has two connections at either end, which receive power via 6 mm^2

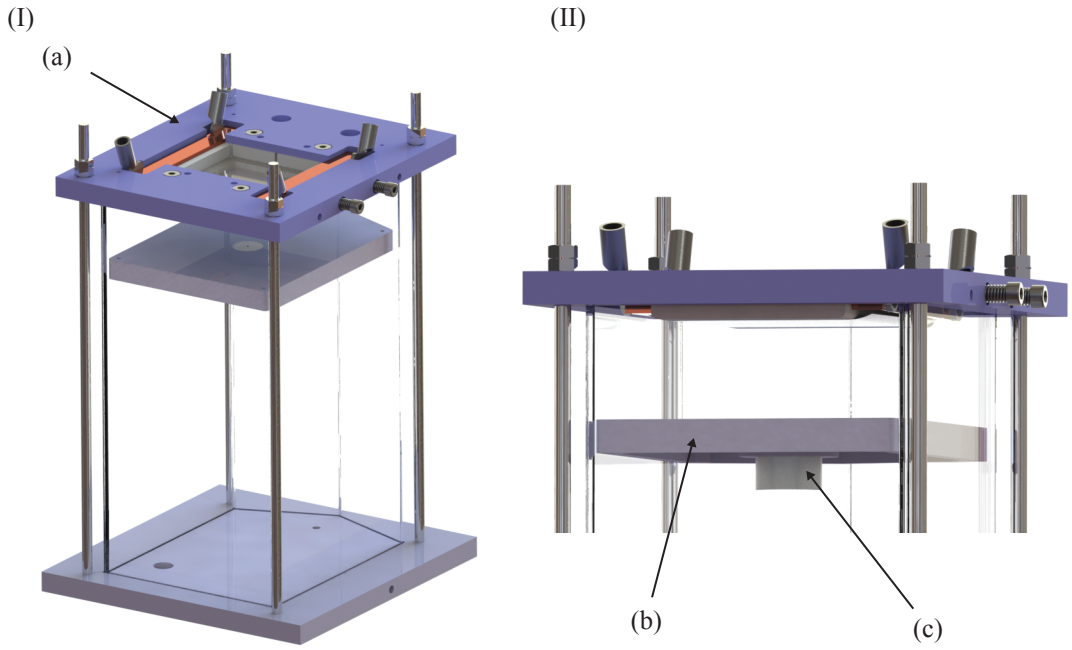

Figure 3.3: Heated surface and water tank assembly. (I) total view and (II) side view of bubble injection platform and test section. (a) Test surface, (b) adjustable floor and (c) bubble injection orifice.

copper cables, connected to a Lambda GENESYS GEN6-200 d.c. power supply. The power supply has the capability to provide 6 volts and 200 amps in either constant voltage or constant current modes. Constant current mode allows the user to apply a constant current through the foil, thereby heating it up to a desired temperature. When current is applied to the 10 μm foil, warping of the foil may occur; in order to reduce this problem, the foil must be tensioned.

To tension the foil, one copper bar clamping the foil is attached to the outer structure, with the second copper bar being capable of movement on the opposite side; the tensioning is applied using two springs. The main structure surrounding the test surface is made from TUFNOL Tufset (shown in purple in the schematics), with the components in direct contact with the foil being produced from a high temperature rigid plastic (>200°C), Peek 1000. The placement of the test surface on top of the water tank is illustrated in Figure 3.3.

Above the upper surface of the foil sits an infrared transparent Calcium Fluoride (CaF2) glass window measuring 50 $\times$ 52 $\times$ 1.1 mm^3. This is placed on top of a supportive ledge,

3 *mm* above the foil as shown in Figure 3.2. Calcium Fluoride glass was incorporated due to its high percentage transmissibility, within the spectrum of the infrared camera (wavelength of 3 – 5 μm), as detailed in Figure 3.4.

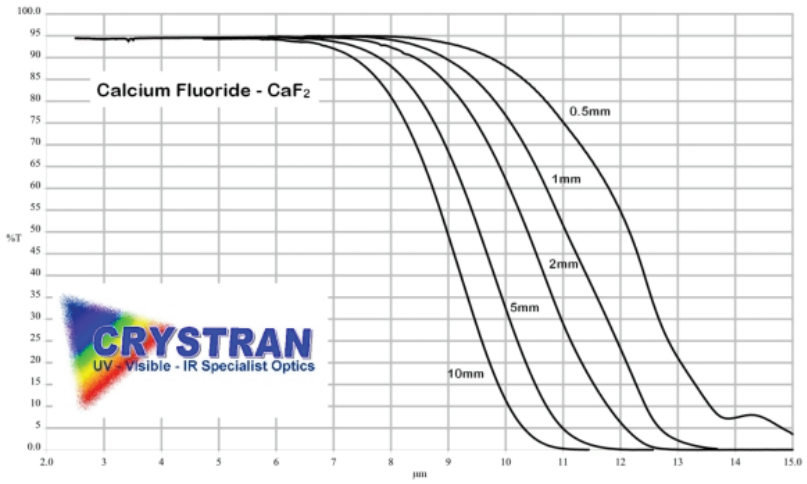

Figure 3.4: Percentage transmission of IR light for calcium fluoride (CaF2) glass, depending on thickness and wavelength, Crystran [69].

This arrangement is used to trap a small quantity of air behind the foil that heats up when the foil is heated (the air gap is shown in Figure 3.1). During the test the trapped air acts as a thermal barrier, ensuring that the majority of the heat generated in the foil is convected to the liquid below. To measure the air temperature within the 3 *mm* gap, a 0.5 *mm* diameter T-type thermocouple is used. The bottom surface of foil is immersed in the water, to a depth of 3 *mm*, as shown in Figure 3.1. The top and underside of the heat transfer test section are shown in Figure 3.2 and test section and water tank assembly is shown in Figure 3.3.

3.1.2 Bubble Injection

In order to control the size of bubbles generated, three orifice inserts were manufactured from stainless steel, just viewable in Figure 3.3. These inserts screw into the adjustable injection surface, until level with that surface. From the base of the inserts a silicone tube, with an internal diameter of 0.8 *mm*, connects the orifice to a gas tight syringe. The total length of tubing from the pump to the injection orifice is 400 *mm*. A Hamilton (GASTIGHT 1002 series) 2.5 *ml* syringe was utilised. The gas flow rate was controlled by a medical grade infusion pump manufactured by KdScientific (KDS 200 cz), which allows the selection of

the specific model of syringe employed. The growth rate of the bubble was found to be linear, with the stepper motor having no influence on the bubble growth dynamics as shown by Albadawi *et al.* [14, 15, 70]. From tables programmed into the pump, the infusion pump is capable of supplying the correct gas flow rate up to a maximum of 280 *ml/hr*. Lesage *et al.* [71] and Lesage [72] noted that the critical volumetric flow rate that will yield bubble growth within the quasi-static regime is determined by the ratio of the force due to gas momentum and capillary force, which should be less than 10^{-5} during the growth stage. This analysis would suggest that the growth stage of the smallest bubble is not in the quasi-static regime, although from the work of Lesage *et al.* [71], it is apparent that their critical flow rate is a very conservative value, with transition to dynamic growth occurring at a higher volumetric flow rate. This injection process satisfies the condition proposed by Oguz & Prosperetti, with the limit for the quasi-static regimes being 4400 *ml/hr* for the 0.5 *mm* orifice. Di Marco [73] noted that the limit for the quasi-static regime is $EoFr^{0.5} < 0.5$, with the current value being approximately 0.13. This analysis demonstrates that for the present study the bubble growth stage is within the quasi-static regime.

In order to mitigate the effects of a height differential, the infusion pump was placed at the same vertical height as the injection orifice. Once the pump is activated, at a specified injection rate, a stepper motor rotates a threaded bar which moves a ram to compress the plunger of the syringe. Once a single bubble is injected at the specified rate, the pump is stopped.

3.1.3 Visual Cameras

Two NAC Hi-Dcam II high speed digital video cameras and pci boards are used to record the bubble motion. The cameras are both controlled by a dedicated computer using the *Lynk-sis* camera software. Both cameras can be synchronised by means of a signal cable from the master camera to the slave pci board; this ensures that both cameras start recording simultaneously. Each camera is capable of frame rates up to a maximum of 20000 *fps*, depending on the resolution. The maximum resolution is 1280×1024 *pixels*, although higher frame rates are only achievable at lower resolution than this. The maximum frame rate at full resolution is 250 *fps*. For these experiments, the cameras recorded at 1000 *fps*

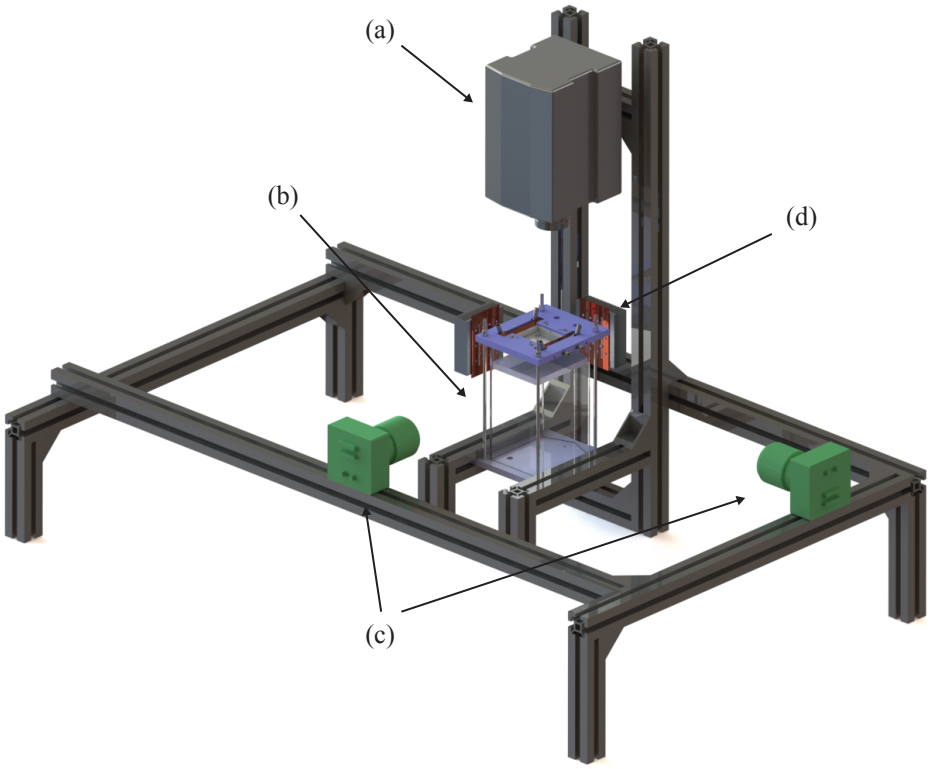

Figure 3.5: Illustration of the visual cameras and lighting system. (a) Infrared camera, (b) water tank, (c) high speed cameras and (d) LED lighting.

with an exposure time of 0.5 *ms*; this corresponds to a resolution of 1280×512 *pixels*. This set-up ensures sharp, crisp images, along with good temporal detail. Both cameras are mounted to the aluminium structure, in perpendicular orientation to each other, as shown in Figure 3.5.

The cameras are fitted with two identical Nikon 50 *mm* $f/1.4$ AF NIKKOR lenses, fitted with 12 *mm* extension tubes. These lenses were chosen as they offer very low image distortion, i.e. image barrelling. Even with the attachment of the extension tubes, which increases magnification, very little distortion was observed; this was verified by means of a reference grid. The lens aperture is set to $f/5.6$; this ensured sufficient depth of focus for the current set-up.

3.1.4 Back Lighting

Illumination of the test area is provided by an array of 3×3 Light Emitting Diode's (LED), per camera. The layout of the LED circuit is illustrated in Figure 3.6, with their mounting position being illustrated in Figure 3.5. These LEDs were positioned directly in front of the cameras. In order to diffuse the light, high quality tracing paper is placed between the LEDs and the side face of the tank. The diffusers ensure even light distribution, giving the bubble a dark outline, while providing an almost white background. The LED's are CREE X-Lamp, with each LED having a luminous flux of approximately 260 *lm*, while drawing almost 3 *W* of power. The colour of the LED's is "neutral white", which is best suited for the present study. The LEDs were overdriven, to provide an approximate luminous flux of 380 *lm*, with each set (3×3) consuming 28.8 *W*. Due to the increased luminous output a specially machined heat sink was required to dissipate the heat generated. The additional heat sink was notched so that it is in contact with the LEDs heat sink and not with the electrical junction at the rear of the LEDs.

3.1.5 Infrared Camera

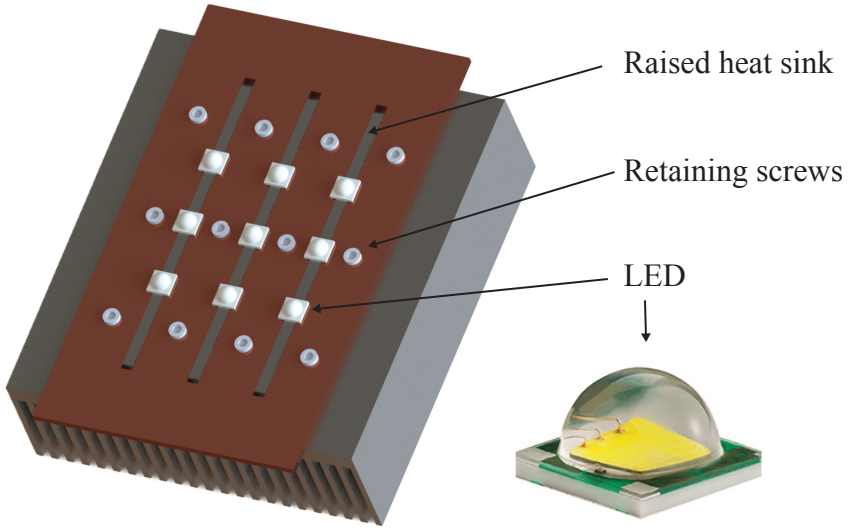

Figure 3.6: LED backlighting provided by nine CREE neutral white LEDs.

To capture high speed IR images, a FLIR SC6000 high resolution, high frame rate infrared camera was utilized for the present study. This is used in conjunction with a high

speed data recorder (HSDR) and camera controller computer. FLIR's ExaminIR integrated software was used to acquire the data.

The camera is mounted on the aluminium structure, directly above the test surface as shown in Figure 3.5. To reduce external reflections, the path between the camera lens and the test surface is surrounded by a black card enclosure.

The camera has an Indium Antimonide (InSb) 640×512 *pixel* focal plane array (FPA) sensor which is vacuum sealed in a cooler assembly. A Stirling motor cools the sensor to approximately 78 K, thereby reducing the effects of noise in the resultant images. If the surroundings were not cooled the sensor would be flooded with infrared light from its own surroundings. The FPA is sensitive in the $3 - 5$ μm range, which is known as the Mid-Wavelength InfraRed (MWIR) range. For the present study a 25 *mm* lens was utilized.

Data from the camera are transferred to the HSDR via a Camera link connection, which bypasses the dedicated computer's motherboard. A 1 Gb/s ethernet connection provides instructions and live image to and from the camera. For the present study, the frame rate is controlled via an external pulse generator, although an internal source can also be utilized.

The thermal camera is set to record an image that is 160×168 *pixels* in size, through a 25 *mm* lens, which is the maximum allowable image size for a frame rate of 1000 *fps*. As the image is no longer full frame, an offset must be selected. In order to reduce reflections, the centre of the area of interest was offset from the centre of the focal array. This is necessary because of a phenomenon known as the Narcissus effect, in which the camera sees its own sensor due to internal lens reflections. Offsets of 208 and 20 *pixels* in x and y directions were chosen, respectively. Also, it is necessary to tilt the camera at approximately a 5° angle from the horizontal, again to further reduce the Narcissus effect. The IR camera has a 14 *bit* sensor meaning that each pixel can detect between 0 and 16383 individual levels, or counts. An integration (exposure) time of 0.8 *ms* at 1000 *Hz* was chosen so that the highest temperature recorded (no more than 60°C) corresponded to a count value of approximately 15000.

For every operation of the camera, seven files are saved, with file extensions of `.sfmov`, `.pod`, `.scg`, `.sbp`, `.sco`, `.cal` and `.inc`. The `.sfmov` file contains the raw infrared measurement data, in counts, from the camera. The `.pod` file contains data on the exact time of each frame obtained from the IRIG clock in the HSDR computer. The `.scg`, `.sco` and

`.sbp` are the gain, offset and bad pixel files respectively. The `.cal` and `.inc` files relate to the calibration of the camera, as explained later.

After a recording, the raw data are contained in a file with an extension of `.sfmov`, as just stated. This file contains header data, which are then followed by every *pixel*, saved in binary, and encoded in a 16 *bit* format. Each frame is loaded individually, and the Non Uniformity Correction (NUC) data are applied; this is followed by the conversion from 14 *bit* counts to temperature.

3.1.6 Triggering System

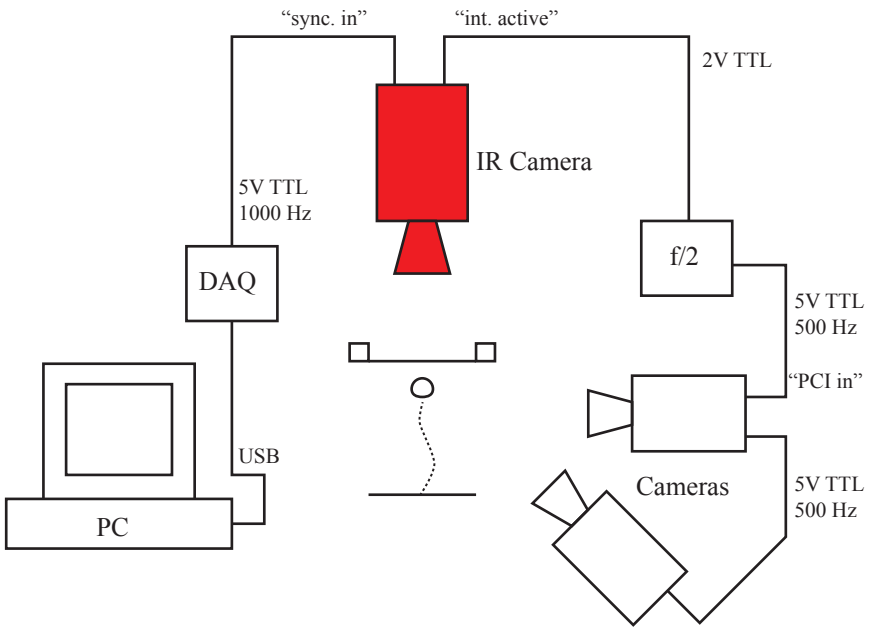

Figure 3.7: Trigger system for all three cameras.

The trigger system ensures that all the relevant systems begin recording simultaneously. To simultaneously trigger the set-up, a LabVIEW program was devised, which when enabled sends a signal to the IR camera. The *VI* creates a 5 *V* TTL signal utilising a NI-9263 DAQ, which is at 1000 *Hz*. The signal is output from the generator through a BNC connector and coaxial cable, then passed directly to "sync. in", a connector on the rear of the IR camera. The camera controller sets the camera to external trigger, so it may record one frame on the rising edge of the trigger signal. An output of the IR camera, "int. active", out-

puts a signal whenever the camera sensor is active. This output frequency, although regular, is too high a frequency to trigger the visual cameras so a frequency splitter is integrated into the coaxial cables; also, the maximum voltage is 2 *V*. The output frequency from the camera is split ($f \Rightarrow f/2$) and fed into the PCI board of the visual master camera. Both visual cameras begin recording on the rising edge of the signal. A diagram depicting the various components is shown in Figure 3.7.

The output from the IR camera is the "int. active" port, which is the integration time signal. As the integration time is 0.8 *ms*, the sensor is not active for 0.2 *ms* in every image. By means of an oscilloscope, it was found that the sensor only begins 0.188 *ms* after the frame begins. This, in turn, dictates that both high speed cameras are 0.188 *ms* slow; this is less than the *ms* time frame corresponding to the 1000 *Hz* frame rate and thus has no bearing on the results reported.

3.1.7 Calibration

To capture accurate infrared thermography information, the infrared camera requires both a temperature calibration and a non uniformity correction (NUC) for the IR sensor. Thus, infrared focal plane arrays (IR FPA) are known to show differences in the response of the individual pixels. In addition, inhomogeneities introduced by the optics (both lens and IR window) lead to non-uniform illumination of the IR detector. The main technique to correct for the non-uniformity is by performing a non uniformity correction (NUC), where a flat-field black-body is heated to two temperatures successively and the raw signals of the pixels are corrected by individual gains and offsets to the respective mean values. A secondary technique for calculating a NUC is demonstrated by Ochs *et al.* [74], involves varying the integration time of every pixel on the FPA.

The black body source needs to be heated to 70% of the maximum temperature (65°C) that will be observed by the camera, with the second setting being at room temperature (20°C). First, the high temperature source is placed directly in front of the lens, fully occupying its entire field of view; 16 images are then recorded. The same is done with the low temperature source. In each case the sixteen images are then averaged. The ExaminIR software then calculates a gain, bad pixel, and offset correction for the sensor (`.scg`, `.sbp`

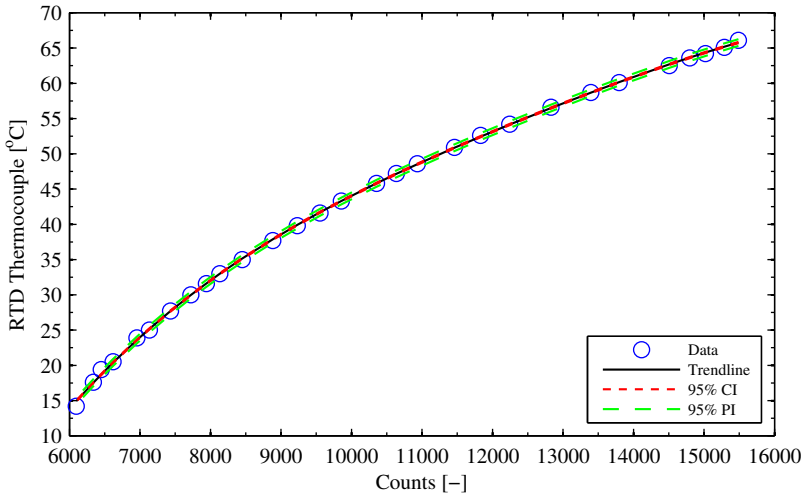

Figure 3.8: Calibration curve for infra-red camera, including 95% confidence and precision limits and a quadratic curve fit.

and `.sco`), for a particular integration time chosen. When the correction is applied, each pixel should now read the same value when a uniform temperature source is placed in front of the camera. Prior to calibration, the software asks for a value of atmospheric attenuation in the 3 – 5 μm range, which is important for correctly calculating surface radiance.

To ensure an accurate calibration the procedure is performed with the calcium fluoride glass window in place. This method of calibration is known as an *in situ* calibration, as presented by Schulz [75] and more recently by Ochs *et al.* [76]. This method ensures that the effect of the window and paint emissivity are accounted for. To ensure a uniform foil surface temperature for the calibration, a mixing system was implemented. A certified RTD master thermocouple probe is used as a temperature reference. Initially the tank is filled with water at 80°C and the temperature is stabilised by moving a platform. Once the temperature has settled to the maximum allowed by the camera, the water is left to settle for a few seconds before a data point is taken, this ensures that the any large scale movement of fluid is reduced.

The foil surface is assumed to reach the same temperature as the water. This was found to be a valid assumption due to the thickness of the foil and the insulating effect of the air gap behind it. To take a data point an interrogation window was positioned so that no reflections affected the calibration. The water bath was allowed to cool naturally, while continuing to

be agitated to ensure the temperature was uniform, and readings were performed every 5°C. It is then possible to directly convert count values to temperature values using Matlab.

$$T_s = -4.54 \times 10^{-15} c^4 + 2.324 \times 10^{-10} c^3 - 4.592 \times 10^{-6} c^2 + 0.0454c - 137.3238 \quad (3.1)$$

The calibration curve for the infra-red camera is plotted in Figure 3.8 and the curve-fit equation is presented in Equation 3.1. The uncertainty of the fit, for a count level of 7900 which is approximately 41°C, is 0.0914°C. This corresponds to around 0.22% at a confidence level of 95% (although difficult to see in Figure 3.8). The uncertainty in the measurements is addressed in the next section.

$$T_{RTD} = 0.9963\ T_{air} + 0.2516 \quad (3.2)$$

$$T_{RTD} = 0.9919\ T_{water} - 0.1186 \quad (3.3)$$

Two T-type thermocouples were used to measure the bulk water temperature and the insulating air layer temperature trapped between the foil and infra-red transparent glass. Both thermocouples were calibrated simultaneously against the master RTD probe. The thermocouples were immersed in a constant temperature water bath, with the temperature being varied from 5 to 80°C in 5 degree increments. The calibration curves are shown in Figures 3.9 and 3.10.

Equations 3.2 and 3.3 are the equations for a linear curve-fit for the air and water thermocouples respectively. The uncertainty of the regression curve for T_{air} at a temperature of $32.5°C$ is $0.075°C$, while the uncertainty of the bulk water temperature (T_{water}) at a temperature of $24.5°C$ is $0.088°C$.

3.2 Case 2: PIV & Infrared Imaging

Particle image velocimetry (PIV) is a flow tracking technique, which in certain flow conditions can provide quantitative time varying flow field data. PIV relies on minute seeding

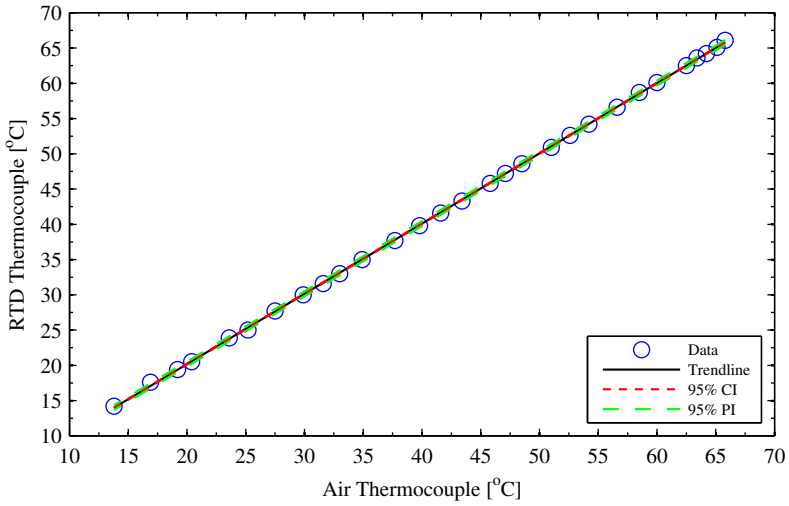

Figure 3.9: Calibration curve for air thermocouple, including 95% confidence and precision limits and a linear curve fit.

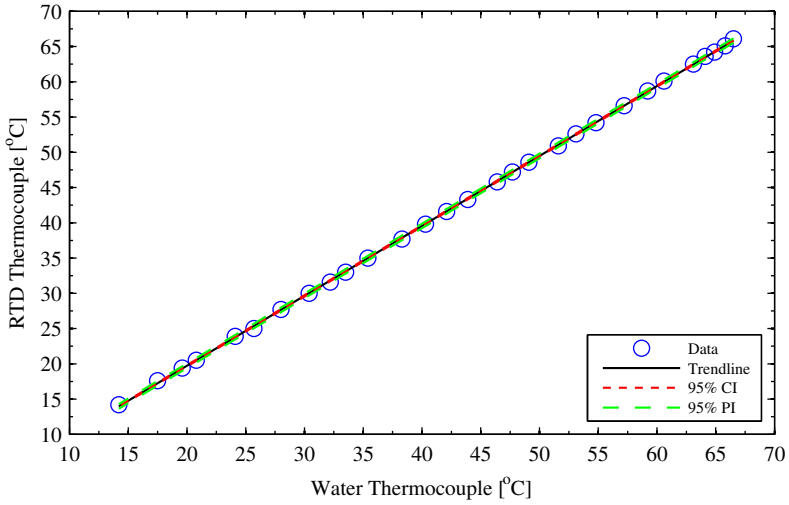

Figure 3.10: Calibration curve for water thermocouple, including 95% confidence and precision limits and a linear curve fit.

particles, which are ideally neutrally buoyant, being illuminated by a high intensity light sheet, provided by a laser. This light sheet is usually less than 1 *mm* in thickness, thereby only illuminating particles within it. Again depending on the flow conditions, the tracer particles usually follow the flow path closely. The laser light is scattered by the particles via Mie scattering, which is proportional to the square of the particles' diameter. The amount of

light from a particle due to Mie scattering is dependent on angle of view, with the optimum for PIV being a camera that is placed perpendicular to the light sheet.

The current set-up is manufactured by LaVision which supplies all components and the data processing software, DaVis 7.2. The laser system is comprised of a Quantronix Darwin Duo high repetition Nd:YLF laser (Neodymium: Yttrium Lithium Fluoride, $\lambda = 527\ nm$, 0.1–0.3 J/s at 1000 Hz). This consists of two individual Darwin lasers and a beam combination system fitted in one laser body, allowing high frequency pulses (190 ns) with time separations of 6 μs. The output of the laser is guided by an optical arm, which consists of metal tubing fitted with optics to guide the beam to the arm head where a cylindrical lens converts the beam to a thin light sheet. Within this arm head focusing optics allow for the sheet to be focused in the region of interest.

A high speed CMOS camera (Photron HighSpeedStar 6, 1024×1024 *pixels*, 12 *bit*) is used to record the illuminated seeding particles within the light sheet and is placed perpendicular to the light sheet. The camera was fitted with a Nikon 50 mm $f/1.4$ AF NIKKOR lenses, fitted with 12 mm extension tube. For these experiments, the camera recorded at 1000 *fps* with an exposure time of 0.2 ms, with the lens aperture being set low (f/2.8); which ensures that the near and far focus region is within the laser light sheet.

In order to get accurate PIV data a number of parameters must be controlled. Such parameters include the time between successive images (Δt), interrogation window size, image exposure time, camera focus, particle density etc. The Δt in this case is 1 ms. The interrogation window size was varied from a 16^2 to a 12^2 window in a multi-pass algorithm so particles within the interrogation window travel approximately $1/4$ of the width of the interrogation window [77]. An important aspect in determining the exposure time is limiting streaking of particles; this is where particles appear as streaks as their velocity is too high for the exposure time.

In order to get sub-pixel accuracy, where vectors are normally distributed and not peak locked to integer values, an optimum particle size is required. For most applications, the particle image diameter captured by the high speed camera must be approximately 2 *pixels* in diameter, below this value peak locking occurs [77]. This is achieved by defocussing the camera very slightly. The final aspect which is used to ensure high quality PIV correlation accuracy is the particle density or concentration, where 10 or more illuminated particles are

needed to ensure correct evaluation of the fluid's direction.

3.2.1 Particle Seeding

The distilled water was seeded with hollow glass spheres (Sphericel 110P8) of mean diameter in the range of 4 –16 μm, with a mean value of 11.7 μm [78]. The particle density was found to be higher than that of water, $\rho_{sphere} = 1100 \pm 50\, kg/m^3$ [78, 79]. This type of seeding is specifically designed for flows in water as the particles are close to being neutrally buoyant. However, as the particles' size and density varied, it was found that some particles would either float or sink over time. In order to remove this variation, particles were first mixed with 100 *ml* of distilled water and allowed to settle for 24 *hours*. It was found that a significant majority of the particles either sank or created a crust on top of the water. In order to get particles which were neutrally buoyant, a syringe was utilised to collect the particles within the centre of the beaker, this would ensure that only the most suitable glass spheres were used for PIV testing.

3.2.2 Laser Alignment & Camera Calibration

The camera was positioned perpendicular to the laser light sheet, which shone through the centre plane of the injection orifice. In order to calibrate the camera a custom made calibration target was made. This target, made from perspex, was covered in a printed plastic scale. This scale is made up of white dots with a diameter of 2 *mm*, with a horizontal and vertical spacing of 10 *mm*. Firstly, the laser light sheet is positioned, then the scale is positioned along the light sheet, splitting the light sheet. Once the camera is focused on the scale, DaVis detects each of the white dots and sets the scale accordingly.

3.2.3 Triggering System

The trigger system, shown in Figure 3.11, ensures that all the relevant systems begin recording simultaneously and is similar to the previous set-up. In this case the output of the frequency splitter is sent to the PIV timing unit. This, in turn, converts the input trigger (500 *Hz*) to 1000 *Hz*, which is sent to both the camera and the high speed laser. The timing unit

only requires a start trigger, which is similar to the previous case. This start trigger initiates the 1000 *Hz* TTL to both the laser head and the single high speed camera.

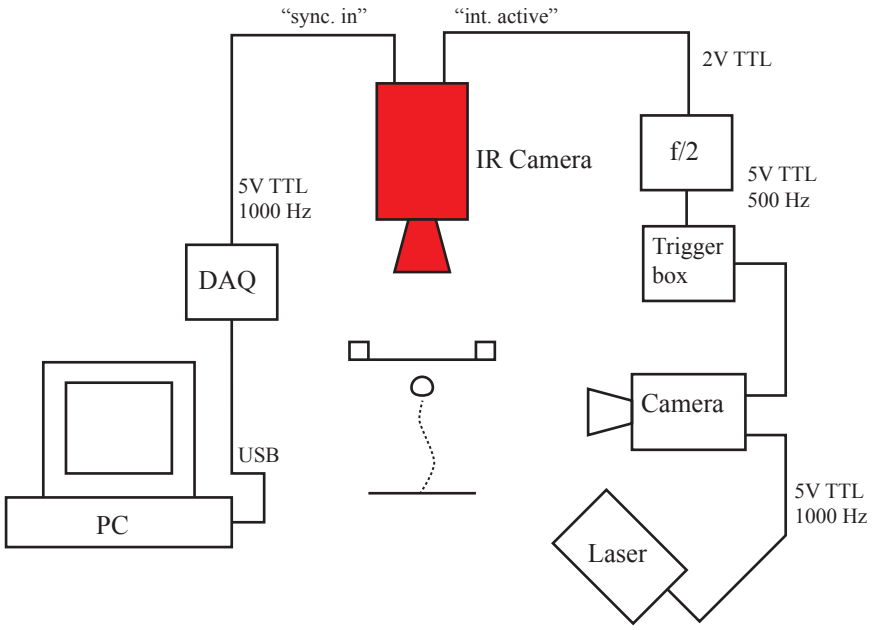

Figure 3.11: Trigger system for the IR camera, high speed camera and laser for the PIV set-up.

3.3 Experimental Procedure

The experimental procedure differs slightly, depending on whether the bubble motion or the fluid flow measurement is being investigated. Firstly, for both types of testing, the tank is filled with distilled water. The distilled water is low in impurities and dissolved oxygen.

3.3.1 Case 1: Bubble Motion & Infrared Imaging

The outline of the procedure is detailed in Figure 3.12. Firstly, the appropriate bubble injection insert (0.5, 1 or 2 *mm* in diameter) is inserted into the movable platform. The movable platform is adjusted to the appropriate release height (10, 20, 25, 30 or 35 *mm*). Once in place the test surface is levelled. In the next phase all the equipment is switched on, with the high speed IR camera being armed to record for 8 seconds. The high speed cameras are set to record for their respective maximum, which is approximately 5 seconds. The entire

system is allowed 30 seconds to settle, before the system is triggered. Once triggered a single air bubble is injected. Once the experiment is complete the power to the foil is switched off and the bubble is removed. The entire system is allowed 30 minutes to settle before the experiment is repeated; during this period, the respective camera images are moved to a hard-drive.

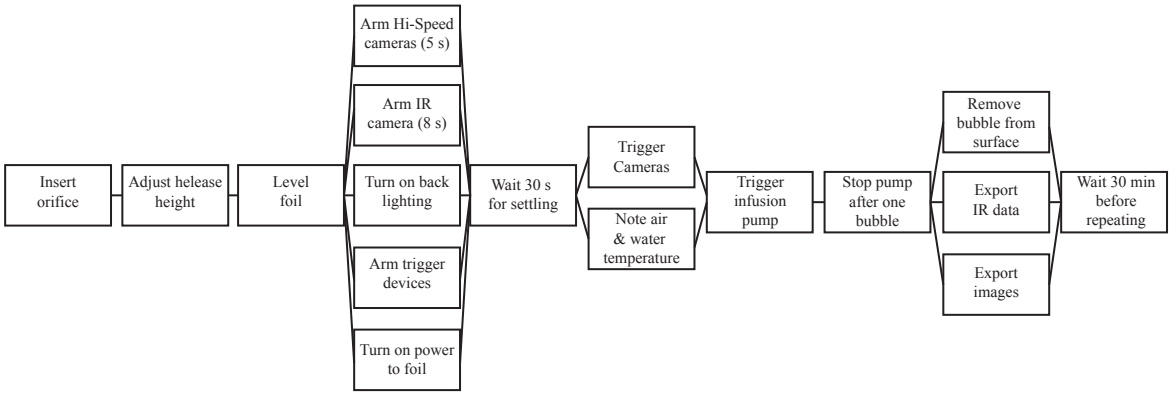

Figure 3.12: Experimental procedure for the bubble motion and heat transfer set-up.

3.3.2 Case 2: PIV & Infrared Imaging

The experimental procedure for PIV is broadly similar to that of previous case. In this case only a single camera is employed, with the laser being used in place of the back lighting. In this set-up only one release height (30 *mm*) was investigated. As the maximum speed of the bubble was less than 380 *mm/s*, only one laser of the two available within the PIV system was required, this is known as single pulse PIV. In order to reduce overexposure of the camera's sensor to reflected laser light, a black card window was designed, with only the minimum required region being visible.

3.4 Closing Remarks

Two experimental set-ups are employed in this study to evaluate the heat transfer from a single bouncing bubble. The first set-up allows the direct motion of the bubble to be evaluated, which is directly linked to the change in convective cooling. The second set-up evaluates the

fluid motion due to the bubble's motion, both during and after the bouncing event. Again this fluid motion is linked to the change in surface temperature. The following chapter will address the data processing and analysis techniques used in this study for tracking the bubble, calculating the convective heat flux and determining the local fluid velocity and direction.

Chapter 4

Experimental Analysis

In the previous chapter the experimental set-up for capturing the bubble motion, fluid motion and change in surface temperature as a function of time have been presented. In this chapter, the techniques used for the determination of the bubble's instantaneous 3D position, that have been developed and assessed in order to obtain accurate quantitative bubble motion, are described. This is followed by the calculations for local heat transfer, by way of an element-wise energy balance performed on the basis of the measured fluctuating temperature measurements. Finally, the analysis for determination of the liquid velocity field in the vicinity of the bubble is described.

The final section of this chapter will deal with characterising and determining the errors and uncertainties in the measurement techniques.

In order to interpret the measured data, a substantial amount of pre and post processing must be undertaken. The pre-processing involves extraction of all the acquired movies (for each camera) from their respective files, along with correct labelling. For the visual images, some important features of the bubble's motion must be determined: the times at which the bubble is still attached to the orifice, the time at which it impacts the surface and the times corresponding to two different types of bouncing bubble motion. This is followed by the determination of the bubble's outline, which is accomplished by applying an image thresholding method to successive bubble images, in both the x-z and y-z planes. Once the bubble

is correctly identified, both camera images are combined and important characteristics, such as the bubble's centroid and shape, centroidal velocity and aspect ratio are calculated.

The next phase is the determination of the local heat transfer. The temperature is first ascertained by means of an in-situ calibration that was previously performed (as described in Chapter 3). The calibrated data are then processed to account for conduction losses to the air, radiation from the foil, lateral conduction within the foil and the change in thermal storage due to the material's specific heat capacity. This is followed by a sensitivity analysis of the time varying heat transfer to changes in the material thermal properties. The final section will outline the basic analysis that is utilized to determine the flow vector field from two time separated PIV images.

4.1 Case 1: Bubble Motion & Infrared Imaging

The first case will detail the analysis techniques utilised for the combined bubble motion and heat transfer set-up. Firstly the image processing technique will be detailed, followed by a description of the procedures involved in locating, aligning and tracking of the bubble. This is followed by a detailed discussion on how the local heat flux was calculated.

4.1.1 Bubble Image Processing

The captured visual images are firstly exported from their respective cameras in the form of RGB bitmaps (`.bmp`). Each image has a resolution of 512 $\times$ 1280 *pixels*, respectively, with a colour depth of 24 *bit*, which is known as "true-colour". In order to correctly determine the bubble's outline in successive images, in-house code requires information about the bubble's location at specific times, which is stored in a separate spreadsheet, detailing all the experiments performed. Specific frames need to be separated out, these include: the first image when the bubble appears, Im_{start}; the final image when the bubble is no longer moving, Im_{end}; the bubble lift off from the orifice, $Im_{lift,off}$; and the image when the bubble initially impacts the surface, Im_{impact}. Once the bubble impacts the surface, two processes occur: free bouncing and repeated impact on the surface. The free bouncing utilises the same analysis technique as the rising bubble, while the impact phase was analysed in a

different fashion. The frame numbers associated with these processes must be provided in order to fully capture the bubble's movement. In order to correctly identify the bubble outline a reference background image is required, Im_{back}; this image contains no bubble.

To facilitate image processing, only a small portion of each image is actually processed at each time interval. The initial bounding box is user selected, with the bounding box encasing the entire bubble. This bounding box is coupled to the bubble's centroid, thereby following the bubble throughout the test tank.

During the bubble growth stage, the bubble creates a shadow on the Stainless Steel orifice, due to the orifice being highly polished. The location of the orifice must be first selected by the user, with the shadow being removed during processing. Similarly, as the bubble impacts the polished horizontal surface, due to lens effects, the bubble's reflection may be viewed above the actual bubble. Again, the user selects the initial point of contact which is then automatically shifted, depending on the bubble's location on the surface.

4.1.1.1 Locating and Tracking of the Bubble

Figures 4.1 and 4.2 illustrate the steps required to detect the bubble for both the departure and impact frames, with the free rise motion being less complicated.

The first stage of locating the bubble is done by loading the first image containing the bubble Im_1, and the background image, Im_{back}; this is done in `VisualImages`. The bubble in this case is attached to the growth orifice. Both images are rotated through ninety degrees, so that the bubble's rise path is correctly viewed as vertical[1] (Figure 4.1 (a)-(b)). Initially the images are loaded in their original size, but once entered into the sub-function `BubbleLocator`, the images are clipped according to the original bounding box selected by the user (Figure 4.1 (c)-(d)).

The next stage is determining the outline of the bubble via image subtraction (Equation 4.1), with the back image (Im_{back}) being subtracted from the bubble image (Im_i), resulting in a value, ($Im_{diff,i}$). This was undertaken by a predefined Matlab function, `imsubtract`, as shown in Equation 4.1. This is followed by converting the RGB clipped and subtracted image to the HSV colour space, with HSV standing for *hue*, *saturation*, and *value*

[1]The cameras are positioned on their sides during the experiment as this allows more of the bubble's rise motion to be captured. The cameras high frame rate reduces the amount of usable pixels.

(brightness). The conversion to the HSV format is computationally expensive, therefore the conversion is applied to the resultant subtracted image rather than the original images to decrease computation time; however, the final outcome is the same. The *value* element of the HSV colour space ranges from 0 – 1 and is also known as the image intensity or brightness; it is this value that is used for the rest of the image processing.

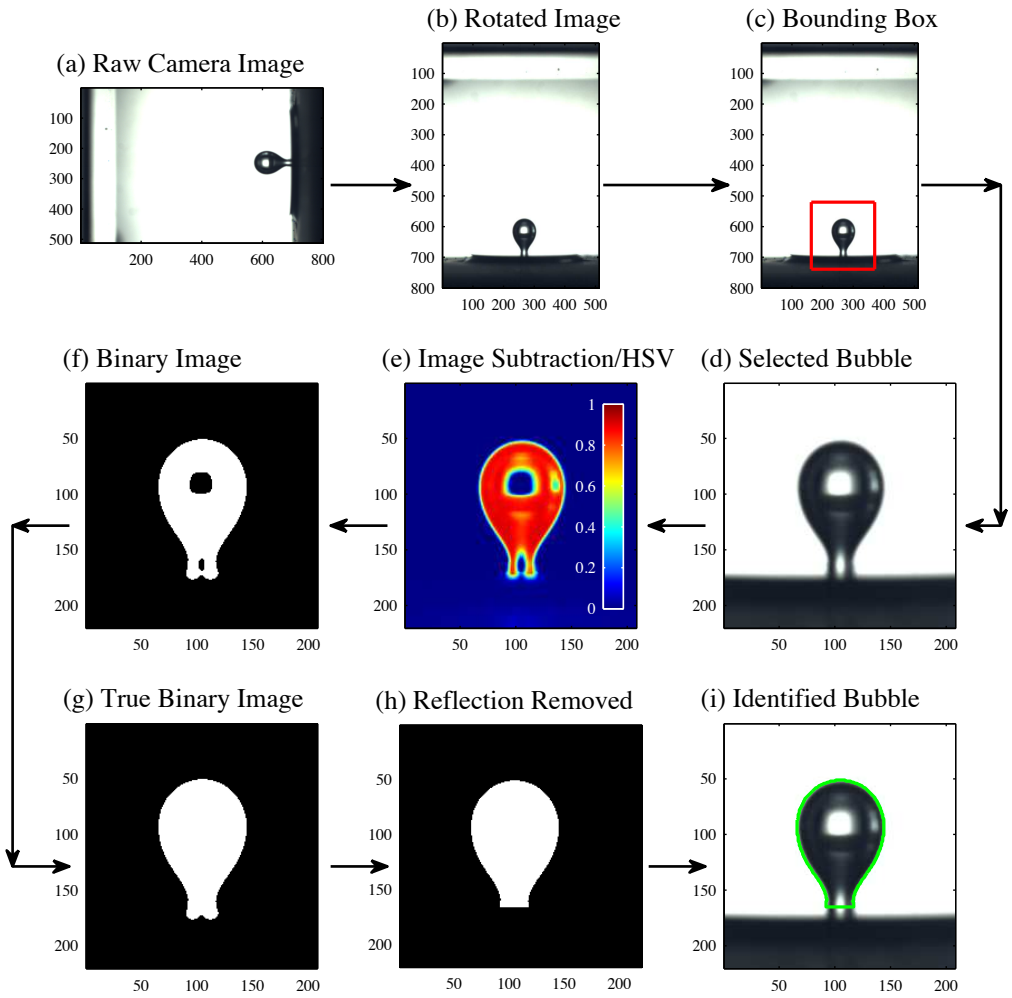

Figure 4.1: Image processing operations applied to successive bubble images which were in contact with the growth orifice. All dimensions are in pixels.

The resulting image, $Im_{diff,i}$, now varies between values of 0 – 1, as illustrated in Figure 4.1 (e). The next phase is noise reduction, as all captured images have some form of underlying noise. This noise is insignificant, however its removal aids object detection. The

removal of the noise is accomplished by means of a median filter[2]; this filtering method was found to have no effect on the final bubble shape.

$$Im_{diff,i} = Im_i - Im_{back} \tag{4.1}$$

The next stage is the conversion of $im_{diff,i}$, to a binary image containing only zeros and ones. To achieve this, a threshold must be applied to $im_{diff,i}$. This threshold, Th, is given an initial value[3] at the beginning of the code; this is just an initial reference number and all values are dynamically found and compared to the initial and previous (Th_{i-1}) threshold values. It was found that insignificant variations in the threshold value occured, in part due to the high image quality and contrast between the bubble and the background. The image thresholding algorithm is shown in Equation 4.2.

$$g(x,y) = \begin{cases} 1 & if \quad f(x,y) > Th \\ 0 & if \quad f(x,y) \leq Th \end{cases} \tag{4.2}$$

This thresholding method results in a binary image of the bubble. In some cases, the interior of the bubble has a zero binary number due to the effect of the light sheet; to "fill" this defect a Matlab function `imfill` fills the interior of the bubble (Figure 4.1 (f)-(g)). The next phase is the determination of the bubble's properties; this is accomplished by means of inbuilt Matlab functions: `regionprops` and `bwboundaries`. The boundary of the bubble was traced using `bwboundaries`, while `regionprops` identifies each individual region of a binary image and calculates various properties of each region as selected by the user. All bubble properties are computed relative to the origin at the upper left corner of the bounding box and must be converted to the full image ordinates prior to saving.

During the bubble rise only one object is detectable, whereas within the vicinity of the horizontal surface the bubble's reflection appears. In this case two apparent bubbles are detected; if the object has a lesser *pixel* area than the bubble (which is assumed to have the largest area), then the smaller object is simply removed, but a more difficult situation occurs when the bubble's reflection appears prior to impact with the surface. This reflection can be of similar size, but can be removed by noting that its position relative to the bubble's

[2]Median filtering is a non-linear operation often used in image processing to reduce 'salt and pepper' noise.
[3]This initial value is determined by a simple test image and user observation to determine the outline.

centroid from the previous frame, i.e. the distance moved in the time step is implausible.

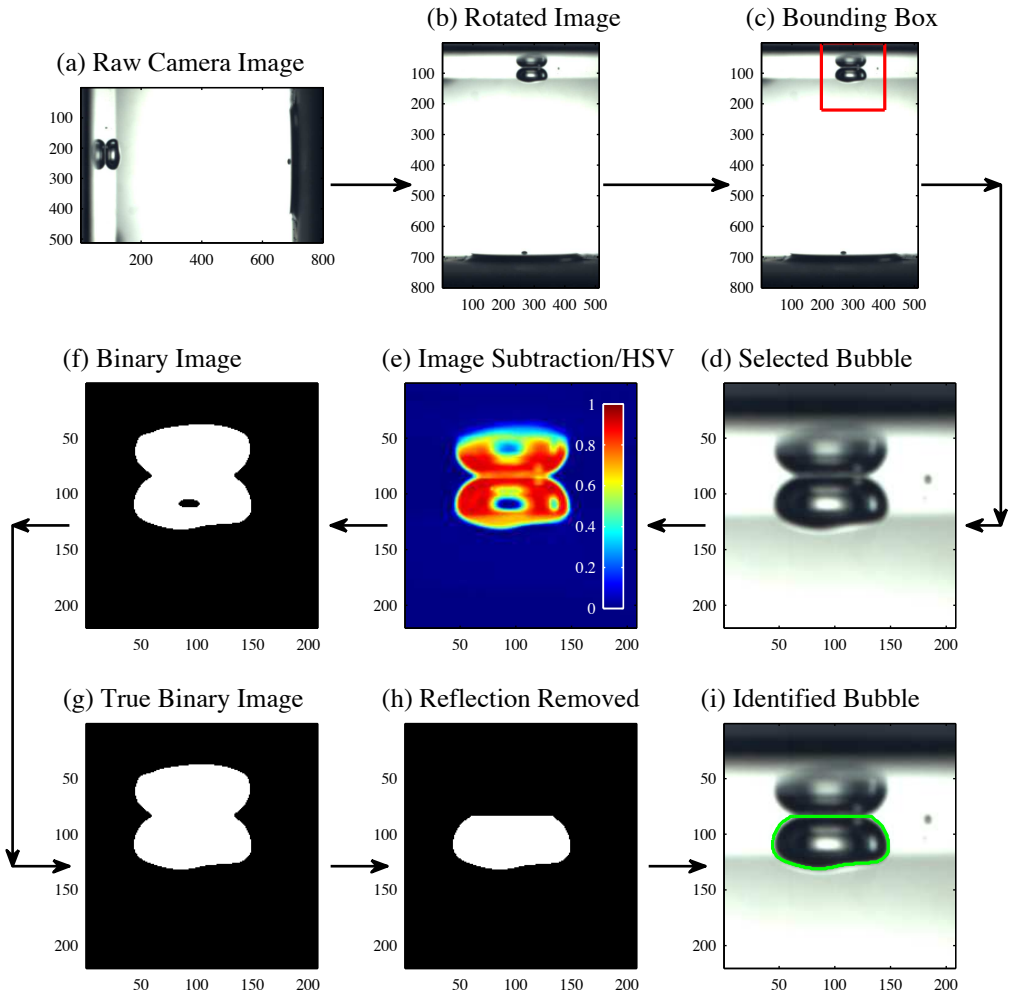

Figure 4.2: Image processing operations applied to successive bubble images which were in contact with the surface. All dimensions are in pixels.

As previously noted, in the first image the bubble is attached to the orifice, this is shown in Figure 4.1. Prior to the bubble departing the injection orifice, the shadow of the bubble on the orifice insert must be isolated and removed; this shadow is created due to the highly polished nature of the orifice, with this being depicted in Figure 4.1. The function, `BubbleLocator` uses the user's initial input, which is taken to be the lowest point in the binary image. All values of one below this line are removed from the bubble's outline, by setting them to zero. A separate technique is applied for when the bubble impacts the heated

surface, with the sequence of events being depicted in Figure 4.2. The code uses the initial contact line provided by the user to determine the contact point; subsequent frames determine the contact line by determining the smallest horizontal distance between the bubble and its reflection (i.e. the choke point, Figure 4.2 (g)). This line is then compared to the previous contact line and it is determined whether it is acceptable or not. Once the bubble breaks contact from the surface a separate function, similar in function to code used for free rising bubbles, is implemented.

The function `BubbleLocator` returns multiple values to the main program, upon completion of the processing of an image. These data are then allocated to memory. As previously discussed, a bounding box surrounds the bubble; after each frame, this box is moved a certain distance, depending on bubble centroid differences. In cases where a limited spatial array of pixels are available, due to the frame rate and/or due to the bubble leaving the visual array, the frame halts at the edge of the bitmap image.

4.1.1.2 Alignment and Scaling

To correctly align the images in their respective x, y and z-axes, the images must first be scaled correctly. An image of an object of known dimension is taken, then the user selects the extremities of the object; this information is used to scale the images correctly. Selecting the edges of this object can have an associated error but this has a very small effect on the size of the final image ($\pm$ 1 *pixel*). To remove this error, the master camera is calibrated first by measuring a known distance. This is followed by comparing the maximum width of a bubble, from both the master and slave cameras. The image chosen for this comparison is that of the bubble just prior to lift off, $Im_{take,off-1}$, as the bubble is assumed to be axisymmetric; the variation was found to be extremely small in terms of pixels.

To align the images, spatial planes x-z and y-z were chosen to be horizontal planes, while the z-axis is the vertical height direction; this dimension was selected from the master camera. Most of the alignment process takes place on the experimental apparatus, prior to testing. This mitigated the need to align the images during the post-processing.

An important parameter in bubble dynamics is the bubble's equivalent diameter, which is obtained when the volume of the bubble is equated to that of a sphere with a diameter D_{eq}.

The bubble's volume is determined by utilising the first few bubble images after departure, in which the bubble is axisymmetric and nearly spherical in both camera views. From both projection outlines the 3D bubble shape is reconstructed. Once the 3D shape is established, then the bubble's volume is calculated using two methods: finite slices[4] and Convex hull[5]. Both methods produce the same results, thereby providing some validation for each.

4.1.1.3 Aspect Ratio Correction

In order to determine the bubble's aspect ratio, firstly the actual dimensions of the bubble must be reconstructed from the bubble image projections captured by both high speed cameras. If the bubble has a vertical rise path then the bubble's major and minor axes may be easily extracted from the 2D image projections; this is because the bubble is considered as an oblate spheroid with elliptical 2D projections [27, 28, 44]. In order for a bubble to be considered an oblate spheroid its major axes a and b must be equal and the minor axis c must satisfy the following condition, ($c < a$). An oblate spheroid has three rotation angles, α, β and γ. The rotation angle, γ, around the c-axis is set to zero as there is only rotation around both major axes.

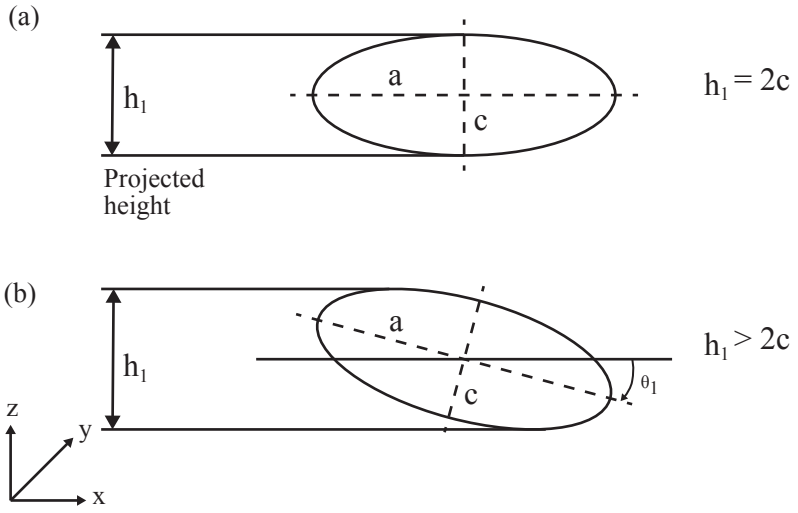

Figure 4.3: Bubble outline and projected height, (a) no major axis tilting and (b) with major axis tilting. The projected height is the height observed by the secondary camera.

[4]Finite slices implies that the bubble is sliced horizontally, with the volume of each slice being calculated and added to the total volume.

[5]A MatLAB function, `convexHull`, is utilised to cover the bubble with a tight fitting hull, with the hull points being found utilising a Delaunay triangulation function. The hull function returns the enclosed volume.

When the bubble tilts along one axis, then the minor axis viewed in that projection is larger than the minor axis projection viewed on the other plane, as illustrated in Figure 4.3. In this case the actual minor axis height can be extracted, as there is tilt in one plane only. When the bubble tilts in both planes, whether with different or similar tilt angles, then a reconstruction method must be applied to the projected minor axes to determine the smaller actual minor axis height.

The 2D bubble projections have the following basic parameters d_1, d_2, h_1, h_2, θ_1 and θ_2, which are the two major axes, minor axes and the tilt angle from both 2D projections. In order to utilise this analysis the following restrictions apply: $a = b = d_1 = d_2$; this allows the bubble to be classed as an oblate spheroid. The bubble outline and projected height is shown, both with and without tilting of the major axis, in Figure 4.3.

Firstly the rotation angles are converted from the projection angles to the actual rotation angles needed for the analysis by using the following two equations [28]:

$$\alpha = -\theta_1 \quad \text{and} \quad \beta = \tan^{-1}(\cos\theta_1 \tan\theta_2) \tag{4.3}$$

The relationship between the laboratory fixed frame of reference and the bubble frame of reference is defined by the following:

$$X = Rx' \tag{4.4}$$

where X is the laboratory frame vector, x is the ellipsoid frame and R is the rotation matrix for an oblate ellipsoid. The rotation matrix is a combination of rotation matrices for each of the axes, combined as follows:

$$R = R_x R_y R_z = \begin{bmatrix} \cos\beta & 0 & \sin\beta \\ \sin\alpha\sin\beta & \cos\alpha & -\sin\alpha\sin\beta \\ -\sin\beta\cos\alpha & \sin\alpha & \cos\alpha\cos\beta \end{bmatrix} \tag{4.5}$$

In order to determine the c-axis from the projections, the highest point aligned with the c-axis is extracted from both views (X_t, Y_t, Z_t) in the laboratory frame. As the bubble projections obey the previous restrictions, then the bubble follows the equation for an ellipsoid,

where:

$$\frac{x_t'^2}{a^2} + \frac{y_t'^2}{b^2} + \frac{z_t'^2}{c^2} = 1 \tag{4.6}$$

In this case again ($a = b$) and the coordinate vector (x_t', y_t', z_t') can be determined by inverting the rotation matrix [28] as shown by Equation 4.7.

$$x_t' = R^{-1} X_t \tag{4.7}$$

This results in the determination of the actual c-axis of the oblate spheroid. The next phase is the calculation of the bubble's aspect ratio. In literature a bubble's aspect ratio is defined in two different ways, the first being $\chi = c/a$, where χ is always less than one and the second $\chi_m = a/c$, where χ_m is greater than one. The former will be used for all proceeding figures, while the latter will be employed in the calculation of the bubble's added mass component (Equation 4.12) for the determination of the forces which act on the rising bubble.

4.1.1.4 Forces Acting on a Rising Bubble

In order to obtain a comprehensive understanding of the nature of a bubble's rise, the forces which act on the bubble need to be calculated. The equations and concepts in the following section were developed by Moore [80], De Vries *et al.* [27], and Veldhuis [28, 81] and will be utilised to explain the bubble's motion.

In order to determine the forces which act on the bubbles in the present study it is advantageous to compute the bubble's motion and associated forces in the Frenet-Serret reference frame. The Frenet-Serret frame is a moving orthogonal frame with the tangent to the curve, T, which points in the direction of motion; the other directions are the normal to the curve, N, and the binormal, B, as unit vectors.

In order to transform from the laboratory to Frenet-Serret reference frame, firstly the time dependent position vector, $r(t)$, and the distance traveled along the curve from some arbitrary initial instant, $s(t)$, are defined. Then the unit vectors are defined as follows:

$$T = \frac{dr}{ds}, \quad N = \frac{\frac{dT}{ds}}{\left|\frac{dT}{ds}\right|}, \quad B = T \times N \tag{4.8}$$

The Frenet-Serret formulae which define the curve are as follows:

$$\frac{dT}{ds} = \kappa N, \quad \frac{dN}{ds} = -\kappa T + \tau B, \quad \frac{dB}{ds} = -\tau N \tag{4.9}$$

where κ and τ are the curvature and torsion of the curve defining the bubble's path, respectively. In the Frenet-Serret reference frame the equations of motion reduce to:

$$F_{D,T} = A\frac{dU}{dt} - \rho V g_T, \quad F_{L,N} = A\kappa U^2 - \rho V g_N \quad F_{L,B} = -\rho V g_B \tag{4.10}$$

where $F_{D,T}$ is the component of the vortex force in the tangential direction, which is the drag force. The components in normal and bi-normal directions are the lift forces in either direction, defined as $F_{L,N}$ and $F_{L,B}$, respectively. The reconstruction of these forces in the Frenet-Serret frame requires that the bubble's minor axis coincides with the tangent vector and considering that the bubble path does not deviate significantly, this condition is assumed to be true. The added mass tensor A is defined as

$$A = \rho V M_z \tag{4.11}$$

with

$$M_z(\chi_m) = \frac{(\chi_m^2 - 1)^{\frac{1}{2}} - \cos^{-1}\chi_m^{-1}}{\cos^{-1}\chi_m^{-1} - (\chi_m^2 - 1)^{\frac{1}{2}}/\chi_m^2} \tag{4.12}$$

as given by Lamb [48], where, χ_m is the inverse aspect ratio. The forces acting on the bubble now are in the form of (F_T, F_N, F_B), but it is more convenient to present them in the laboratory frame of reference (F_x, F_y, F_z). Thus, the drag force on the bubble is:

$$F_D = -F_T T \tag{4.13}$$

and the lift force is given by:

$$F_L = F_N N + F_B B \tag{4.14}$$

It should be noted that if the curvature of the path (κ) is straight then there is no lift force and the drag force is always in the direction opposed to motion i.e. the opposite direction to the tangent along the path at any instant.

4.1.2 Thermal Image Processing

As discussed earlier, *ExaminIR* produces an encoded movie file after each experiment (`.sfmov`), which contains initial header data about the camera configuration, followed by every pixel of every image encoded in 16 *bit*. Each image has a size $m \times n$ which determines the length of the bit sequence. Each pixel contains 14 *bit* data, which is combined in Matlab as a two-dimensional "count" array. These values are then converted to temperature values, T_s, within Matlab; these values correspond to the temperature at the rear surface of the foil. An energy balance must be performed on this temperature map, which will result in determining the heat convected to the fluid.

Within a Matlab program, `HeatTransfer`, the various fluid, foil and paint properties are input, along with the calibration curves for the bulk water thermocouple, T_{bulk}, and air gap thermocouple, T_{air}. In order to evaluate the heat convected to the fluid, uniform heat generation is assumed within the foil, while it is also assumed that the temperature is constant through the thickness of the foil; this will be explored in the next section.

4.1.2.1 System Response

In order to accurately determine the heat convected to the fluid, both the foil and paint layer thickness must be known. To achieve this numerous measurements were taken with a digital micrometer (Mitutoyo No. 29334070 IP 65). It was found that the foil always measured 10 $\pm$ 0.1 μm, while the thickness of the paint layer was found to be 11.62 $\pm$ 0.87 μm.

In order to evaluate the second assumption a simple Lumped Thermal Capacitance analysis was applied to the system. The idea of the lumped capacitance method is that the temperature of a solid is spatially uniform at any instant during a transient process. Figure 4.4 illustrates a simple heated wall through which conduction occurs over a constant area.

An energy balance around the two vertical dashed lines in Figure 4.4, reveals a dimen-

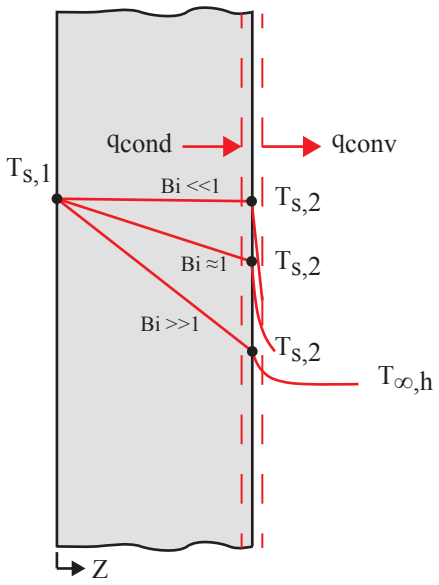

Figure 4.4: Effect of Biot number on steady state temperature distribution in a plane wall with surface convection, Incropera *et al.* [82].

sionless quantity, the Biot number, Bi, which is the ratio of the thermal resistance for conduction through the solid, to that for convection to the fluid. The Biot number provides a measure of the temperature drop in the solid relative to the temperature difference between the surface and the fluid. If the Biot number (Equation 4.15) is very much less than one, then it can be assumed that the temperature is uniform within the solid at any time during the transient process. For particle applications, the following criterion is used to determine whether the lumped capacitive approach is valid:

$$Bi = \frac{hL_c}{k} < 0.1 \tag{4.15}$$

where h is the highest heat transfer coefficient encountered, and k is the thermal conductivity of the solid. L_c is the characteristic length of the body, $L_c = Volume/Area_{surface}$. This characteristic length reduces to a half-thickness, L, for a plane wall of thickness, δ, cooled from both sides ($2L = \delta$), Incropera *et al.* [82]. For the current set-up the material properties are discussed in subsection 4.1.3, while a maximum heat transfer coefficient of around 12000 W/m^2K is experienced. Therefore the maximum Biot number observed is $Bi \approx 2.59 \times 10^{-3}$. For the paint layer, an average thickness of $\delta_p = 11.6 \times 10^{-6}\ m$ was obtained, which results in a Biot number of $Bi \approx 733.9 \times 10^{-3}$.

While the paint layer does have a Biot number larger than 0.1, it has been noted by Patel & Chen [83] that the "critical value of 0.1 is not an absolute measure and it is used as a relative "yard-stick""; this suggests that the lumped thermal capacitance analysis is still broadly applicable for the current set-up. Furthermore, this Biot number estimate is based on a thermal conductivity that was obtained from a commissioned measurement, as described in Section 4.1.3. This parameter is difficult to measure for a thin paint layer and the fact that it is substantially lower than reported values in the literature suggests that the paint Biot number may have been over-estimated.

Another way to characterise the test surface is by means of the characteristic time constant[6] for thermal diffusion across the thickness of the foil and paint. The characteristic time constant for diffusion across a wall of thickness (δ) is shown in Equation 4.16 (Maranzana *et al.* [84] and Golobic *et al.* [85, 86]).

$$\tau_\delta = \frac{\delta^2 \rho C_p}{k} = \frac{\delta^2}{\alpha} \tag{4.16}$$

where all the values relate to the properties of the wall. For quasi steady heat transfer problems, the following time constant is employed, $\tau_\infty = \rho C_p \delta / \bar{h}_\infty$, where $\bar{h}_\infty$ is the asymptotic steady state heat transfer coefficient as defined by Maranzana *et al.* [84].

For the present study, the paint layer was found to have the highest time constant, of $\tau_\delta \approx 5.15 \times 10^{-3}\ s$, whereas the time constant for the foil is $\tau_\delta \approx 1.49 \times 10^{-5}\ s$. This analysis shows that, at any location (x, y), the Constantan foil can be considered as having a uniform temperature across its thickness, for both steady state and transient regimes. This is because the camera integration time, t, is $8.5 \times 10^{-4}\ s$, which indicates that the camera would be the limiting factor for the current set-up if only the foil was present.

4.1.2.2 Element-wise Energy Balance

An element by element analysis is required in order to determine the energy flow within the system and to extract the energy convected to the fluid. This analysis is applied by means of an energy conservation method, as defined by Equation 4.17, Incropera *et al.* [82]:

[6]The time constant, τ, is the rise-time (to 63.2% of its span) characterising the response to a time-varying input of a first-order, linear time-invariant (LTI) system.

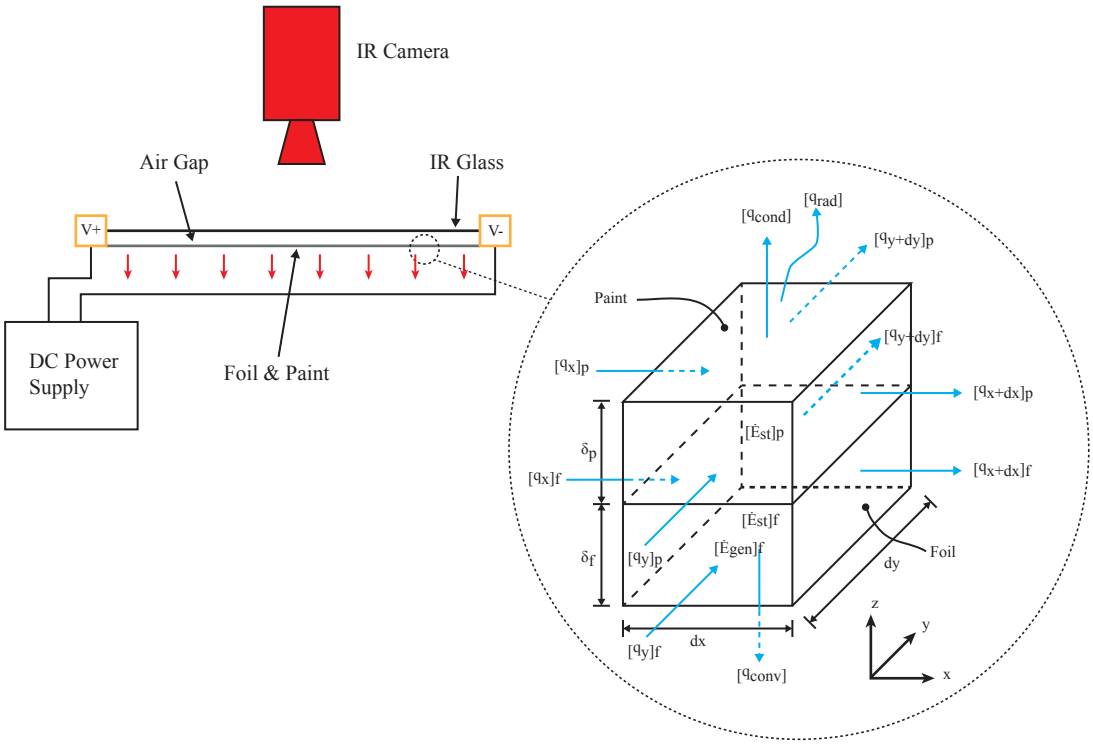

Figure 4.5: Illustration of heat transfer set-up and the thermal flow through a single element with a surface area of $dx \times dy$ and thickness of δ_f, δ_p for the foil and paint layer respectively.

$$\dot{E}_{in} + \dot{E}_{gen} - \dot{E}_{out} = \Delta \dot{E}_{st} \tag{4.17}$$

in which $\dot{E}_{in}$ and $\dot{E}_{out}$ refer to energy transport across the control surfaces in Figure 4.5, $\dot{E}_{gen}$ is the thermal energy generation within the control volume and $\dot{E}_{st}$ is the stored thermal energy.

A differential control volume for both the foil and paint layer is illustrated in Figure 4.5. The energy balance for the control volume is represented by Equation 4.18, which has units of W/m^2:

$$q''_{conv} = q''_{gen} - q''_{cond} - q''_{rad} + 4\left(k_f \delta_f^2 + k_p \delta_p^2\right)\left(\frac{\partial^2 T}{\partial x^2} + \frac{\partial^2 T}{\partial y^2}\right)\Big/ dx - \left(\rho_f C_{p,f} \delta_f + \rho_p C_{p,p} \delta_p\right)\frac{\partial T}{\partial t}\Big/ dx^2 \tag{4.18}$$

where f and p denote the foil and paint layers respectively, q''_{gen} is the heat generated, q''_{conv} is the heat convected to the fluid, q''_{cond} is the heat conducted through the 3 mm air layer, to the CaF_2 glass. The air within the gap is assumed to be stagnant, as the Rayleigh number for the cavity was estimated to be $Ra = 47$. This compares with a critical value of Ra_c =1708, as reported by Incropera *et al.* [82]. Therefore, heat transfer from the bottom to the top surface occurs by conduction and radiation. q''_{rad} is the radiation from the rear side of the foil; there is very little radiation from the front of the foil, both due to the foil's low emissivity and the fact that the adjacent water has low transmissivity in the wavelength range considered. The final two sections represent the lateral conduction and the change in internal energy within the control volume.

For the present study dx is equal to dy, shown in Figure 4.5. Equation 4.18 assumes a constant thermal conductivity, along with a constant thickness, δ. The electrical energy generation is distributed through out all the elements within the foil, thereby allowing the Joule heating to be calculated on an element by element basis.

The heat generated within each element by the Joule effect is given by Equation 4.19.

$$q''_{gen} = \frac{I^2_{elec} R_{elec}}{dx^2} \tag{4.19}$$

where I_{elec} is the current through one foil element of resistance, R_{elec}. Equation 4.19 is derived from Ohm's law, $V = IR$. To determine the resistance of an element of foil, the electrical resistivity[7] of the foil, denoted here as ρ_{elec}, must be known.

$$R_{elec} = \rho_{elec} \frac{l}{A_{cs}} \tag{4.20}$$

where ρ_{elec} is the electrical resistivity of Constantan, l is the length parallel to the current flow and A_{cs} is the cross-sectional area, i.e. $\delta_f \times w$. From these equations the power generated can be calculated. The power generated by one element of size $\delta_f \times dx^2$, is calculated by separating the total surface area of the foil into elements of size, dx^2.

The lateral conduction term is denoted as q''_{lc} and has units of W/m^2 as indicated by Equation 4.21. The surface temperature distribution and the lateral conduction within the test surface are illustrated in Figure 4.6.

[7]Electrical resistivity is a measure of how strongly a material opposes the flow of electric current.

$$q''_{lc} = -\frac{\left(k_f \delta_f^2 + k_p \delta_p^2\right)\left(\frac{\partial^2 T}{\partial x^2} + \frac{\partial^2 T}{\partial y^2}\right) \times 4dx}{dx^2} \tag{4.21}$$

where δ and k are the thickness and thermal conductivity of either the foil (f) or paint (p). The negative sign indicates that the heat flow is in the direction of decreasing temperature. The partial differential of the temperature field can also be represented by the Laplacian $\nabla^2 T$. This migration of heat occurs through an area of $4\delta dx$, which is the four sides of an element, as shown in Figure 4.5. To solve this equation a finite-difference (*central-difference*) method is applied to the temperature field.

$$q''_{lc,ij} = -\frac{\left(k_f \delta_f^2 + k_p \delta_p^2\right)\left(\frac{T_{i+1,j} + T_{i-1,j} + T_{i,j+1} + T_{i,j-1} - 4T_{i,j}}{dx^2}\right) \times 4dx}{dx^2} \tag{4.22}$$

To calculate this Laplacian of the temperature field, Matlab provides a function called, `grad`. This function implements a *central-difference* method in the main field and automatically switches to *first order differences* near the edges of the field. A second order partial derivative applied to a data set with underlying occurring experimental noise[8] acts to further amplify this noise. To reduce the effects of this noise, a median filter was applied to both the first and second derivatives of Equation 4.22.

The capacitive effects associated with the foil and paint layers are determined by Equation 4.23, while the surface temperature and energy stored within the test surface are illustrated in Figure 4.7.

$$q''_{cap} = \frac{\left(\delta_f \rho_f C_{P,f} + \delta_p \rho_p C_{P,p}\right)\frac{\partial T}{\partial t}}{dx^2} \tag{4.23}$$

where ρ and C_P represent the density and specific heat capacity of an element, with $\partial T/\partial t$ being the temperature difference with respect to time. The change in internally stored energy can be calculated by measuring the change in temperature with respect to time for each foil element. The magnitude of this term depends on the temperature change, over the specific

[8] This noise is also known as "Salt & Pepper" noise.

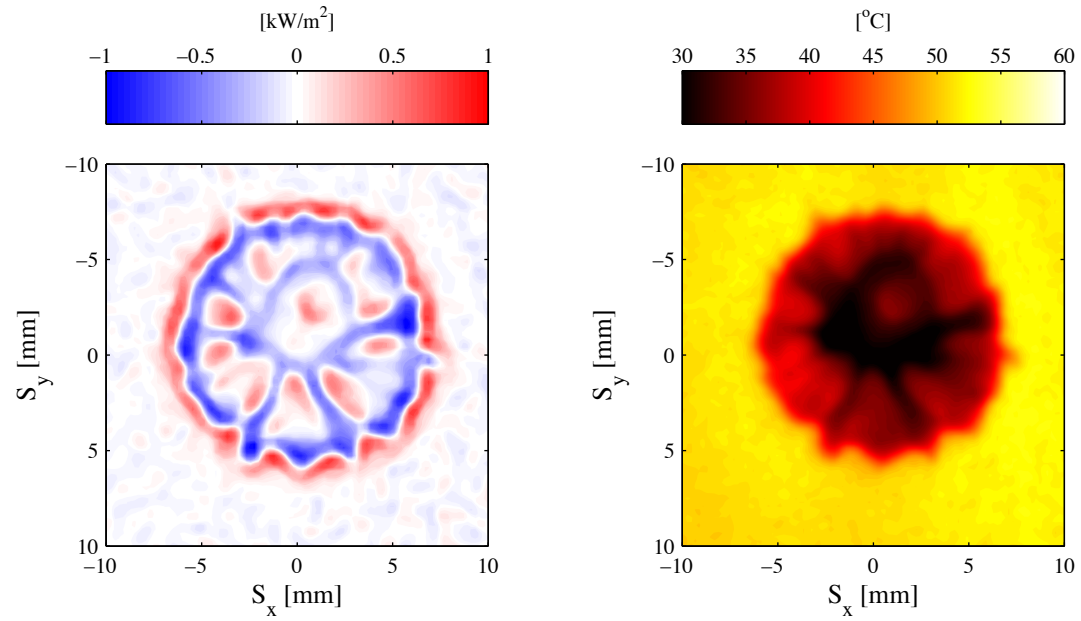

(a) (b)

Figure 4.6: (a) Typical instantaneous lateral conduction term (kW/m^2) and (b) instantaneous surface temperature for a section of the foil's surface. Positive values of heat flux indicate heat transfer into a foil element.

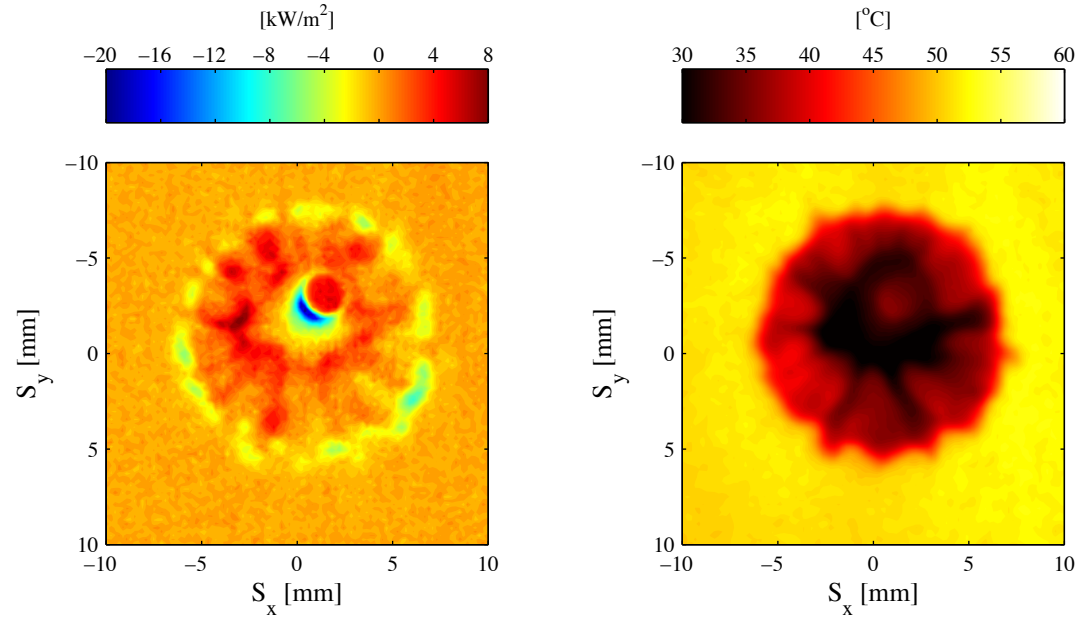

(a) (b)

Figure 4.7: (a) Energy storage term (kW/m^2) and (b) surface temperature for a section of the foil's surface at a specific instant in time.

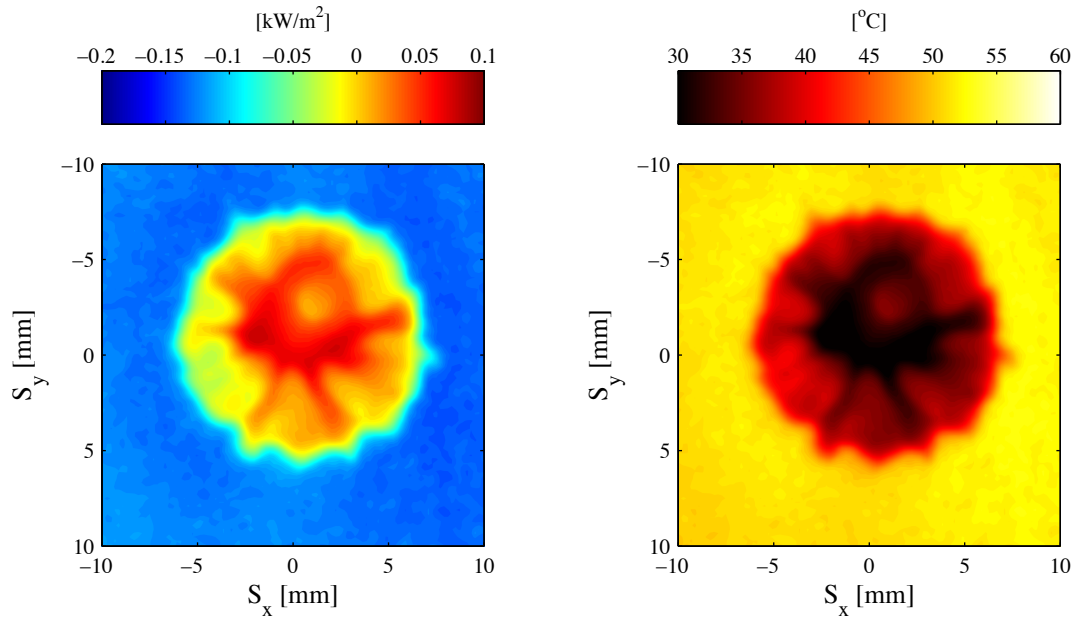

(a) (b)

Figure 4.8: (a) Conductive heat flux (kW/m^2) through the 3 *mm* air gap and (b) surface temperature from a section of the foil's surface. Positive values indicate heat transfer into a foil element at a specific instant in time.

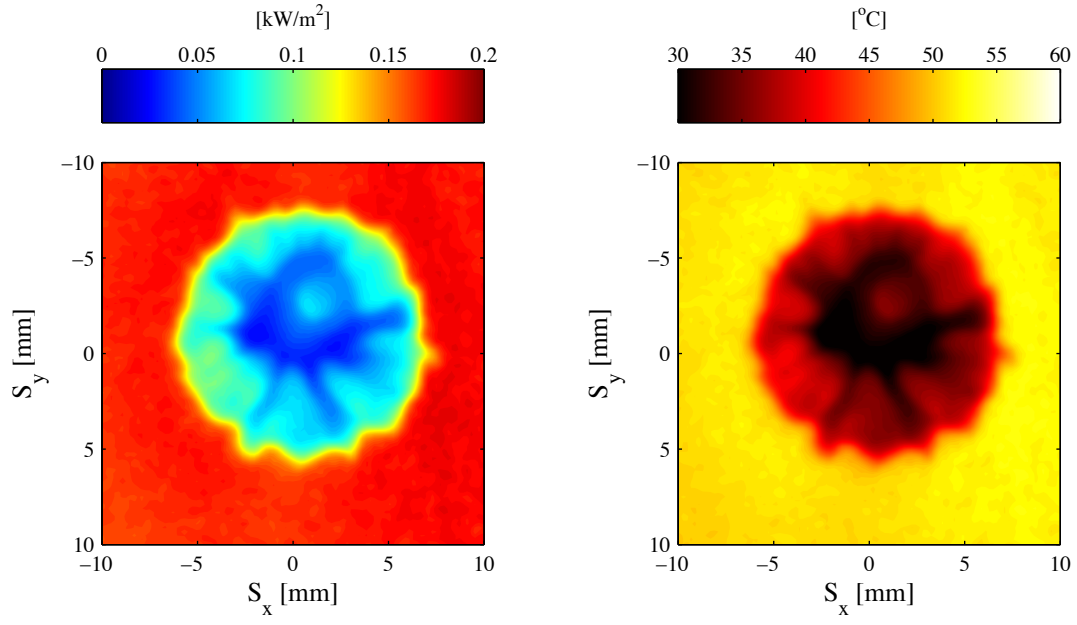

(a) (b)

Figure 4.9: (a) radiative exchange (kW/m^2) from a section of the foil's top surface and (b) foil temperature.

time period. An important parameter for internal energy storage is the thermal diffusivity, which provides a measure of the substrate's thermal inertia. In a substance which has a high thermal diffusivity, heat flows through the substance rapidly due to the influence of high conductivity and low volumetric heat capacity.

To calculate the change in internal energy storage, three successive thermal images are required, T_{t-1}, T_t and T_{t+1}. The change in temperature with time of each element is computed using a central difference approach as follows:

$$\frac{dT}{dt} = \frac{T_{t+1} - T_{t-1}}{2\Delta t} \tag{4.24}$$

where Δt is the time difference between two successive images, which is the inverse of the camera frame rate. This derivative is then combined with the density and thermal capacitance of a element, to give the general change in stored energy as follows:

$$q''_{cap} = \frac{\left(\delta_f \rho_f C_{P,f} + \delta_p \rho_p C_{P,p}\right) \frac{T_{t+1} - T_{t-1}}{2\Delta t}}{dx^2} \tag{4.25}$$

From preliminary analysis it was determined that the influence of the previously discussed noise within the temperature field has some influence on the calculated internally stored energy. Two different noise reduction methods were investigated, with the first being higher order central difference coefficients and the second being a weighted filter; this consists of a weighted averaging of each pixel in time, as presented in Equation 4.26.

$$T_{avg.} = \frac{T_{x,y,i-2} + 2T_{x,y,i-1} + 3T_{x,y,i} + 2T_{x,y,i+1} + T_{x,y,i+2}}{9} \tag{4.26}$$

The weighted filter approach was employed for all the experiments as it had the least effect on the data [87].

To account for conduction through the 3 *mm* air gap, Fourier's law is applied. The surface temperature and heat conducted through the 3 *mm* layer is illustrated in Figure 4.8.

$$q''_{conduction} = -k_{air} \frac{dT}{dz} \tag{4.27}$$

where k_{air} is the thermal conductivity of air and dT/dz is the temperature gradient across

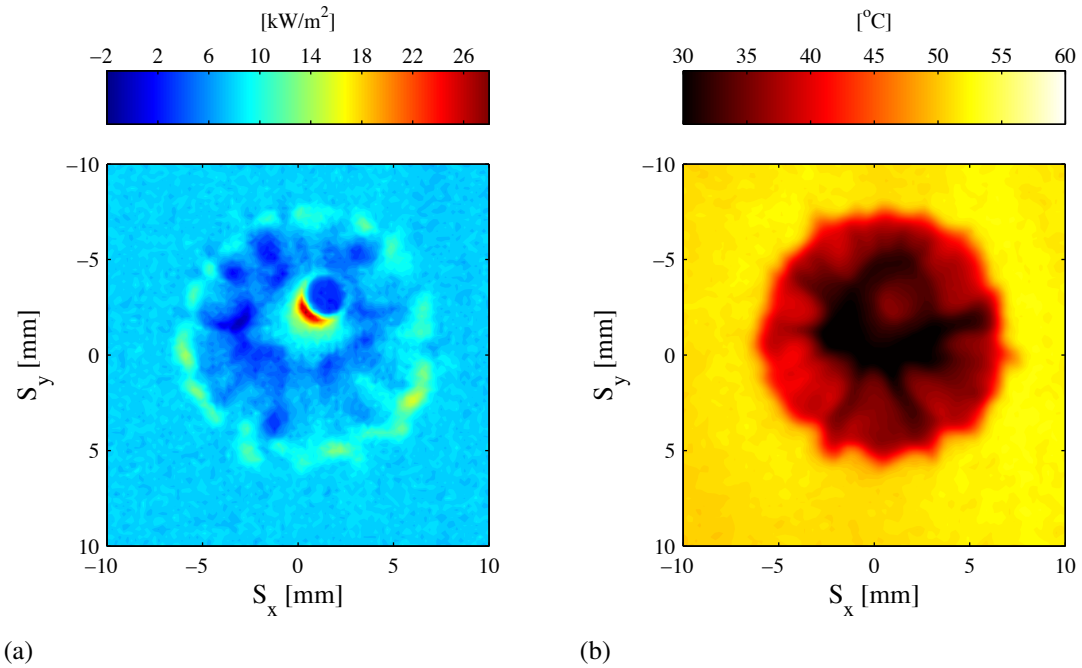

Figure 4.10: (a) Instantaneous convective heat flux (kW/m^2) to the bulk fluid and (b) surface temperature.

the air gap to the glass.

The radiative heat loss is represented by Equation 4.28:

$$q''_{rad} = \varepsilon_p \sigma \left(T_s^4 - T_\infty^4\right) \tag{4.28}$$

where ε_p is the emissivity of the painted surface, σ is the Stefan-Boltzman constant, T_s is the surface temperature and T_∞ is the measured lab air temperature. The surface temperature and the radiative heat loss are illustrated in Figure 4.9.

The instantaneous convective heat flux is illustrated in Figure 4.10 and has units of kW/m^2. The following sections will outline how the terms in Equation 4.18 that represent lateral conduction and energy stored within each element of the surface are calculated and quantified.

4.1.3 Material Properties

To implement Equation 4.25, apart from the material thickness (δ), the density (ρ) and the heat capacity (C_P) of both the foil and paint must be known. Properties for Constantan foil

are freely available, although the density was measured in-house. For the Constantan, the density (ρ), thermal conductivity (k) and heat capacity (C_P), were found to be: 8.637×10^3 kg/m^3, 23.13 W/mK and 401.54 J/kgK respectively. Both the thermal conductivity and heat capacity were determined for the average surface temperature of 37°C, utilising data by Sundqvist [88]. Over the temperature range under consideration, the variation in the thermal conductivity and heat capacity was found to be 2.1% and 0.55%, respectively. The difference between the measured density and the tabulated values is 2.95%.

Table 4.1: [1]Thermal properties of paint samples measured using the PA scanning technique (Raghu & Philip [89]). [2]A travelling photothermal technique (Philip *et al.* [90]). [3] infrared imaging (Decker & Mackin [91]). [4] Golobic *et al.* [86]. [5] Pulsed laser technique (Moksin *et al.* [92]). [6] Thermal wave interferometry (Moksin & Almond [93]).

Sample paints	Substrate test on	Density kg/m^3	Thermal diffusivity $\times 10^{-7}$ m^2/s	Heat capacity J/kgK	Thermal conductivity W/mK
I[1]	Copper	1331 ± 39	2.10 ± 0.15	5184 ± 518	1.45 ± 0.11
II[1]	Copper	1303 ± 39	2.21 ± 0.12	2557 ± 230	0.74 ± 0.04
III[1]	Copper	1251 ± 37	3.56 ± 0.11	1670 ± 100	0.74 ± 0.02
IV[1]	Copper	1251 ± 34	1.72 ± 0.11	2835 ± 283	0.57 ± 0.05
Enamel[2]	Glass	1331 ± 39	2.13 ± 0.04	-	-
Enamel[2]	Copper	1331 ± 39	2.08 ± 0.04	-	-
I[3]	Steel	-	1.85 ± 0.2	-	-
I[4]	Titanium	-	1.4	-	-
I[5]	Steel	-	2.46 ± 0.08	-	-
II[5]	Steel	-	2.04 ± 0.06	-	-
I[6]	-	-	2.2	-	-
II[6]	-	-	2.0	-	-

The precise properties of the paint used in this study were not available, so tests were commissioned to measure them. The density of the paint was measured and found to be 1.277×10^3 kg/m^3, which is similar to values reported for paint by Raghu & Philip [89]. The thermal conductivity of the paint was measured by means of Hot Disk Transient Plane Source Method [94] at room temperature and was found to be 0.095 W/mK.

The testing commissioned was unable to determine the heat capacity of the paint due to the difficulty in producing a sample with a thickness greater than 60 μm. It was therefore decided to use values from Raghu & Philip [89]. Experimental data from Raghu & Philip [89] and Philip *et al.* [90] are shown in Table 4.1, along with the thermal diffusivity as determined by other authors. The three paint samples of interest for this study are I, II and IV, as paint III is a metal based paint, with the final two paints being the same sample

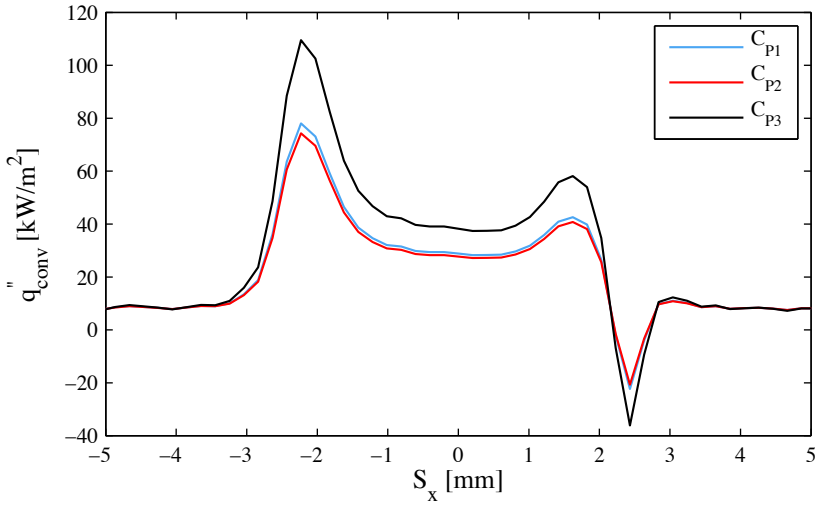

Figure 4.11: Variation in convective heat flux along a line on the surface at a particular instant, which captures both high and low levels of convective heat flux. The paint samples, C_{p1}, C_{p2} and C_{p3} correspond to paint samples, IV, II and I in Table 4.1.

as paint I, just sampled using a different experimental method.

Figure 4.11 illustrates the variation in convective heat flux, when the paint's heat capacity is varied. It is clear from Figure 4.11, that there is a significant variation in convective heat flux when comparing different paint samples. The paint samples, C_{p1}, C_{p2} and C_{p3} correspond to paint samples, IV, II and I in Table 4.1. While data for C_{p1} and C_{p2} are very similar, the calculated heat flux for C_{p3} is significantly different. In order to choose the heat capacity which best matches the current paint, both the thermal conductivity and density of the paints investigated by Raghu & Philip [89] were compared with the experimentally determined values of the paint used here. It was found that paint sample IV, had the best match, both in terms of thermal conductivity and density. Thus, a value of 2835 J/kgK (C_{p1}) was used for the paint's heat capacity. This is a conservative value, in that it gives lower variations in convective heat flux as evident from Figure 4.11, while closely matching other parameters.

The thermal diffusivity of the paint was estimated as $2.62 \times 10^{-8}\ m^2/s$, based on the commissioned measurement of the thermal conductivity together with data from the literature. This value is an order of magnitude lower than that found in the current literature as shown in Table 4.1, with the thermal conductivity of the paint being the contributing factor.

The thermal conductivity is used to determine the lateral conduction within the heated surface, while the volumetric heat capacity is used to determine the change in stored energy. Both the lateral conduction and change in stored energy have been found to be important parameters in determining the convective heat flux, but the storage term plays the bigger role. Thus, uncertainty around the paint thermal conductivity would not significantly change the convective heat flux levels observed. With regard to the paint layer, the Biot number analysis (although not definitive because of uncertainty in the thermal properties) does indicate that rapid changes in temperature on the side of the foil in contact with the bubble may be attenuated through the paint layer thickness. Thus, some transient changes in behaviour may not be detected. Variations in the thermal properties of both the paint and foil will be accounted for in Section 4.3.

4.2 Case 2: PIV & Infrared Imaging

The following section outlines the methods used to process the PIV images captured by the current set-up, with the thermal images being processed using the same method as previously discussed in Section 4.1.2.2.

4.2.1 PIV Processing

The flow velocity was processed using LaVision's purpose developed DaVis software. This software is designed to process raw image data and produce velocity vectors, which are further analysed in Matlab. Each image within the recorded sequence contains tracer particles, with their displacement being analysed between successive images to determine the fluid velocity and direction. Each image in the PIV recording is subdivided into sub-regions known as interrogation windows, with an optimum density of ten illuminated particles per window as shown in Figure 4.12. The tracer shift should be less then a quarter of the interrogation window size and out-of-plane tracer shift should be reduced. In order to get sub-pixel displacement, seeding particles need to appear as approximately two pixels in diameter on the CCD image; this will reduce a phenomenon know as peak-locking, whereby displacement vectors are locked to integer based displacements, instead of being evenly distributed.

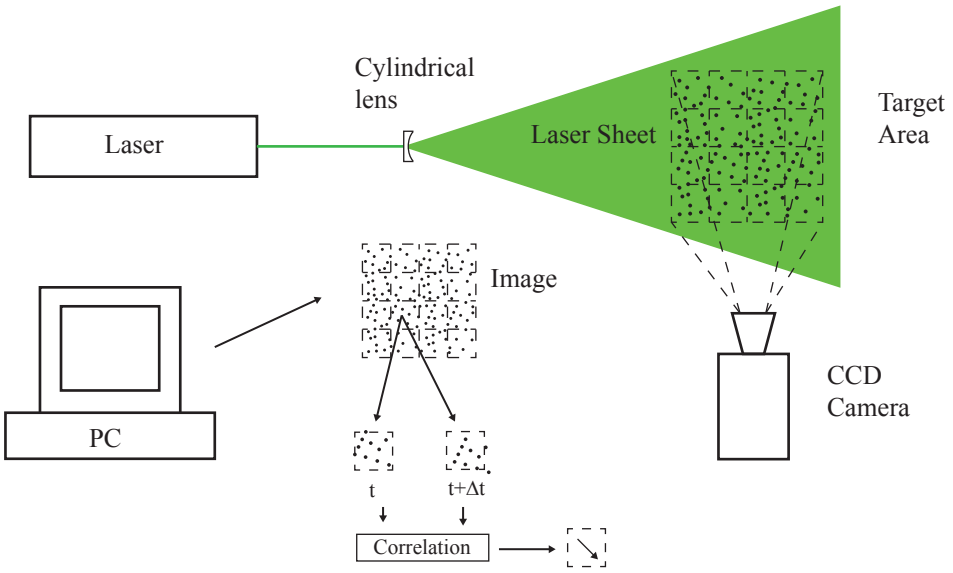

Figure 4.12: PIV set-up and basic processing technique.

The first procedure in determining the final vectors is defining a mask, whereby only displacements within the mask are calculated; masking significantly reduces computational time. The masked region was then sub-divided into interrogation windows, with the interrogation window size being related to the fluid velocity. Within each interrogation window a cross-correlation was performed between successive images; this produces one velocity vector for each window. For accurate vector field calculations a multi-pass cross-correlation function is recommended [95]. A 'decreasing window size' analysis method was chosen, as the initial pass investigates the main averaged fluid flow, with the secondary smaller interrogation windows detecting velocity variations within the larger interrogation window.

During the bubble rise and initial impact, high fluid velocity requires short image separation times (Δt) whereas after the bubble has settled lower fluid velocities occur, which require longer Δt. All recordings are performed at 1000 Hz. Depending on what was being observed, wake specific frame separation times were chosen, so that an optimum pixel shift of 5 pixels was observed. In order to capture sufficient velocity information an initial interrogation window size of 16^2 was chosen, which was followed by a 12^2 window. In order to capture slow and fast moving particles, and particles that leave interrogation windows, a window overlap of 50% for the initial pass and 75% for the final passes was utilised. During multi-pass processing a median filter is applied to the data, which removes and replaces spu-

rious vectors. Post-processing of the final vector field was applied to remove any remaining spurious vectors that were either outside the area of interest or were a result of the light sheet being blocked by the bubble, causing a shadow behind the bubble, which was again outside the area of interest. The final operation was processing of the *.vc7* files for analysis utilising Matlab, where the vorticity was calculated employing the `curl` of the vector field.

4.3 Uncertainty Analysis

The following sections will outline the analysis used in determining the accuracy of the calibration and the uncertainty in the convective heat flux calculations.

Error or uncertainty can be classified into two categories, (i) *precision* errors, and (ii) *bias* errors [96–99].

Precision Errors. Precision errors, also known as random errors, due to their nature can come from multiple sources. Most often they are associated with the "least count" of the scale on an analog instrument. Precision errors cause scatter in experimental data, although they can be statistically quantified.

Bias Errors. Bias errors, also known as systematic errors, can occur in many situations. Calibration errors may be a *zero-offset* or a scale error, in which the slope of a graph is incorrect. Once a bias error has been corrected it is no longer uncertain.

The mean of a number of samples is as follows:

$$\bar{x} = \frac{1}{N}\sum_{i=1}^{n} x_i \tag{4.29}$$

The measured values of scatter around the sample mean allow for the determination of the standard deviation S_x, i.e. a sample-based estimate of the standard deviation of the population mean.

$$S_x = \left[\frac{1}{N-1}\sum_{i=1}^{n}(x_i - \bar{x})^2\right]^{(1/2)} \tag{4.30}$$

where x_i are the measured quantities and N the number of samples. The standard error of the mean is the standard deviation of the sample-mean's estimate of a population mean, which

is as follows:

$$S_{\bar{x}} \cong \frac{S_x}{N^{1/2}} \tag{4.31}$$

The above analysis is utilised for the determination of single point measurements e.g. thickness measurement of the foil. In the case where the output of a system depends on the input a different approach must be applied to the data.

For a linear fit[9] the data set (x_i, y_i) = 1, 2, ..., N, is replaced by (x_i, Y_i) and the equation $\bar{Y} = mx + c$. In this case $\bar{Y}$ indicates that values of Y will not fall on the curve-fit. Analogous to the standard deviation of a sample in Equation 4.30, the standard deviation for a curve-fit is as follows:

$$S_Y = \left[\frac{1}{N-2}\sum D_i^2\right]^{1/2} \tag{4.32}$$

where $D_i = Y_i - \hat{Y}$ and $\hat{Y}$ is the result from the least squares fit, $\hat{Y} = mx + c$. The factor $(N-2)$ is appropriate here as there would be no error in a straight line if $N = 2$.

4.3.1 Uncertainty

The precision uncertainty in a measurement is the estimate of the probable error in a measurement. If we are $C\%$ confident that the true value X_{true} of a measurement X_i lies within the interval $X_i \pm P_X$, then P_X is called the precision uncertainty at a confidence level of $C\%$ [99]. In accordance with Kim *et al.* [98] a 95% confidence level is chosen for most experiments.

If a measurement sample is normally distributed with independent values and the sample is large ($N > 10$) then the following relationship is valid:

$$P_X \cong 2S_X \quad (C = 95\%, N > 10) \tag{4.33}$$

The probable error in a sample mean is less than in individual measurements because $S_{\bar{x}} \cong \frac{S_x}{N^{1/2}}$ for a large N. Then the precision uncertainty of the sample mean is

$$P_{\bar{X}} \cong 2S_{\bar{X}} \quad (C = 95\%, N > 10) \tag{4.34}$$

[9]For any Least-Squares curve fit of a data set (x_i, y_i) = 1, 2, ..., N, x_i and y_i are sample averages.

When considering precision errors for a curve-fit with data (x_i, Y_i), the precision uncertainty for a straight-line curve-fit is

$$P_{\hat{Y}} = t_{\nu,\%} \left\{ S_Y^2 \left[\frac{1}{N} + \frac{(x-\bar{x})^2}{S_{xx}} \right] \right\}^{1/2} \quad (C = 95\%, N > 10) \tag{4.35}$$

where S_Y is the standard deviation defined by Equation 4.32, and $t_{\nu,\%}$, is the critical value that encloses 95% of a t-student distribution with $\nu = N - 2$ degrees of freedom. Also,

$$S_{xx} = \sum x_i^2 - \left(\frac{1}{N} \right) \left(\sum x_i \right)^2 \tag{4.36}$$

Equation 4.35 gives the 95% confidence interval, which is the range where the curve fits will fall 95% of the time, for repeated measurements. Of less importance is the uncertainty associated with where a single measurement, taken in the future, will fall. This is known as the 95% prediction interval, Mills & Chang [99].

$$P_Y = t_{\nu,\%} \left\{ S_Y^2 \left[1 + \frac{1}{N} + \frac{(x-\bar{x})^2}{S_{xx}} \right] \right\}^{1/2} \quad (C = 95\%, N > 10) \tag{4.37}$$

Once the data have been curve fitted, it is the precision of the curve fit that is of interest, not the precision of individual data points used to create the curve, Mills & Chang [99]. Therefore the 95% confidence interval for the curve fit is utilised rather than the 95% prediction interval. This analysis is applied to the calibration data for both the water and air thermocouple and to the *in-situ* calibration of the IR camera as shown in Figures 3.8 to 3.10. In order to evaluate the uncertainty of the calibration and its knock on effect in terms of the uncertainty of the heat flux measurements, the confidence interval at the typical operation parameter is evaluated from Figures 3.8 to 3.10 and utilised in the following section.

4.3.2 Propagation of Precision Uncertainties

The uncertainty of an experimental set-up and/or a calculated parameter is of significance, in situations where the experimental data are to be referenced against other similar studies. To date, little detailed information from literature is available on the propagation of uncertainties. Similar experimental methods which utilise a thin metal substrate report uncertainty values, but without a detailed explanation of the analysis conducted to arrive at these values

[85, 86]. However, the need for this important analysis is used now being recognised in the literature [100–102].

Since precision uncertainties are random, their propagation in measurements can be determined through statistics, by utilising the Taylor Series Method (TSM). For a simple calculated result Y that is a function of N independent measurements X_i, if the uncertainties P_i are small, then a first order Taylor expansion of Y is used:

$$Y(X_1+P_1, X_2+P_2, ..., X_N+P_N) \tag{4.38}$$

$$\cong Y(X_1, X_2, ..., X_N) + \frac{\partial Y}{\partial X_1}P_1 + \frac{\partial Y}{\partial X_2}P_2 + \cdots + \frac{\partial Y}{\partial X_N}P_N \tag{4.39}$$

Y is now a linear function of independent variables and a theorem of mathematical statistics can be employed (Coleman [97]):

$$P_Y = \left[\sum_{i=1}^{n}\left(\frac{\partial Y}{\partial X_i}P_i\right)^2\right]^{1/2} \tag{4.40}$$

where all uncertainties in the individual X_i must be at the same confidence level i.e. 95%. The partial derivatives are known as *absolute sensitivity coefficients*.

For correlated systematic errors, which are those that are not independent of each other, these correlated systematic errors may influence the experimental results and final uncertainty. For a simple case where

$$r = r(X_1, X_2) \tag{4.41}$$

To determine the systematic uncertainties Equation 4.40 is used, along with an additional term to account for the correlated variables. Thus, by utilising the TSM method, the systematic standard uncertainty, b_r, of the calculated result is defined as:

$$b_r^2 = \left(\frac{\partial r}{\partial X_1}b_1\right)^2 + \left(\frac{\partial r}{\partial X_2}b_2\right)^2 + 2\rho_{X_1,X_2}\left(\frac{\partial r}{\partial X_1}\right)\left(\frac{\partial r}{\partial X_2}\right)b_{12} \tag{4.42}$$

where $b_{12} = (b_1)(b_2)$ is the covariance term and, b_1 and b_2 are the precision uncertainties of each variable X_1 and X_2, at the same confidence level (95%) and ρ_{X_1,X_2} is the Pearson product-moment correlation coefficient [96], which is a measure of the correlation.

For both the lateral conduction and heat storage terms an additional term is added to the standard propagation equation for a multi-variable function; this is known as the covariance term (b_{12}) as described by Equation 4.42. In order to determine how correlated a pixel is to its neighbouring pixel and similarly to the same pixel but with a time shift, both a cross-correlation and autocorrelation analysis was performed and used to determine the degree of correlation (ρ_{X_1,X_2}), which will affect the covariance term in Equation 4.42 [103]. These equations form the basis for the determination of the uncertainty in the experimental measurements.

4.3.3 Visual Images

In terms of detecting the bubble's outline, this was found to depend on the threshold value (Th), as described by Equation 4.2. This results in the uncertainty in detecting the bubble's outline being ± 1 *pixel*. This relates to a metric value of ± 0.039 *mm*, therefore the bubble's major axis has an uncertainty of ± 0.0789 *mm*, with the smallest bubble equivalent diameter being 2.8 *mm*. This low value is due to the high spatial resolution of the measurement set-up.

4.3.4 Thermal Images

The temperature resolution of a thermal imaging camera is related to the "noise" within the sensor. This "noise" is described by the Noise Equivalent Temperature Difference (*NETD*) and is a measure of the sensitivity of a detector of thermal radiation. It is calculated using the following equation:

$$NETD = \frac{\sigma}{SiTF} \tag{4.43}$$

where σ is the standard deviation of the temporal signal in Analog to Digital counts, (*AD Counts*). The Signal Transfer Function, *SiTF*, is a measure of a sensor's response to the change in the object's temperature and has units of $ADCounts/^{\circ}\mathrm{C}$. The *SiTF* is calculated using the following equation:

$$SiTF = \frac{\Delta(ADCounts)}{\Delta T} \tag{4.44}$$

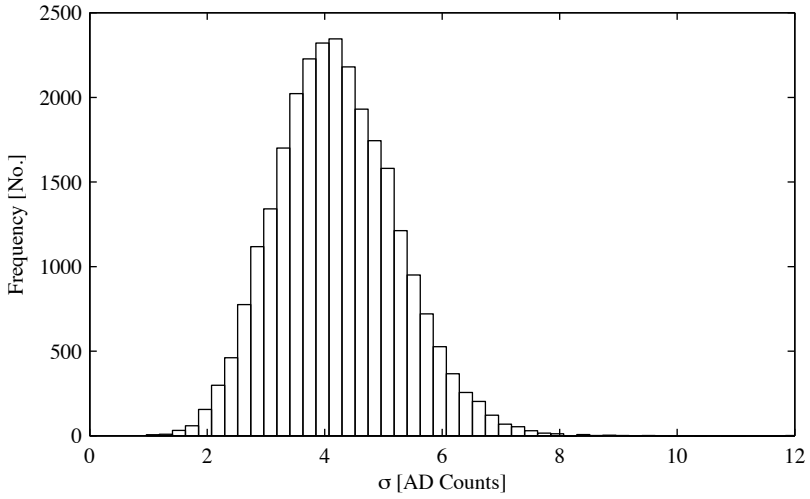

Figure 4.13: Standard deviation of the entire population of pixels for 800 images (0.8 *ms*), illustrating the variation at a mean temperature of approximately 50°C. The majority of the pixels have a standard deviation of 4 Analog–Digital Counts.

where ΔT is the temperature difference between the background with a temperature T_0 and the object with a temperature, T_{BB}, where this is a black body temperature. The *SiTF* is the slope of the plotted line, where the response of the camera is linear [104–106]. The *SiTF* for the Flir SC6000 was found to be 161.4 $ADCounts/°C$. Figure 4.13 illustrates the temporal standard deviation of 800 images taken at 1000 *Hz*, which shows that the majority of the pixels within the 160×168 area utilised for the experiment vary by 4 *ADCounts* at approximately 50°C.

Equation 4.43 is then utilized to determine the *NETD* for the Flir SC6000 camera, which is shown in Figure 4.14. Notably the majority of the pixels have a *NETD* of approximately 25 *mK* or *m*°C, which is, in fact, within the specifications of the camera. The *NETD* is usually considered as the minimum detectable temperature difference. However, it is actually just a good indicator of the minimum temperature difference and is not the exact minimum value, as temperature changes below this level can be detected [107].

At a temperature of 48.82°C, which corresponds to a *Count* value of 11000, the temperature sensitivity of the calibration is ± 4.52 *mK*. In terms of spatial resolution, each pixel corresponds to a value of 0.2027 *mm*, therefore the viewable area is 32.43×34.05 mm^2.

Figures 4.15 and 4.16 illustrate both the instantaneous convective heat flux and the cor-

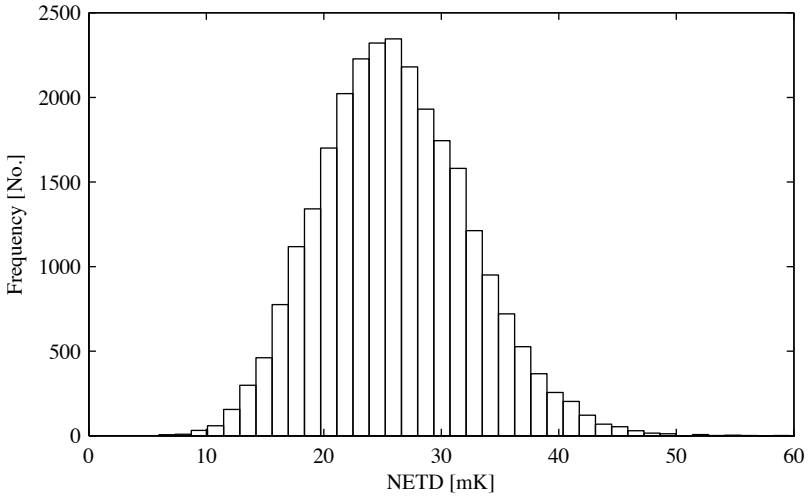

Figure 4.14: Noise Equivalent Temperature Difference (*NETD*), using the data in Figure 4.13.

responding uncertainty heat flux at times of 14 and 114 *ms* after the bubble has impacted the surface. These two instants in time were chosen to illustrate uncertainty as they capture the range of heat flux levels encountered in these experiments. Prior to the bubble's impact, the uncertainty in determining the convective heat flux due to liquid natural convection is $8.3 \pm 0.3\ kW/m^2$, which is approximately 3.5%. In Figure 4.15, where the maximum convective heat flux is approximately 180 kW/m^2 the percentage uncertainty is 16.6%. This is significantly larger due to the contribution of the various heat flux corrections that are detailed in Equation 4.18. Each of these terms in Equation 4.18 contains temperature or temperature gradients, all of which have associated and inter-related uncertainties, which have been propagated using Equation 4.40. In Figure 4.16 the maximum convective heat flux is approximately 34 kW/m^2, resulting in an uncertainty value of 13.2%.

4.4 Closing Remarks

This chapter has explained the analysis behind bubble detection and tracking as it rises through the test tank. This analysis includes the calculation of the bubble's aspect ratio and the forces which act upon it as it rises. The basis for local heat transfer calculation from the surface temperature by way of a element-wise energy balance performed on the temporal

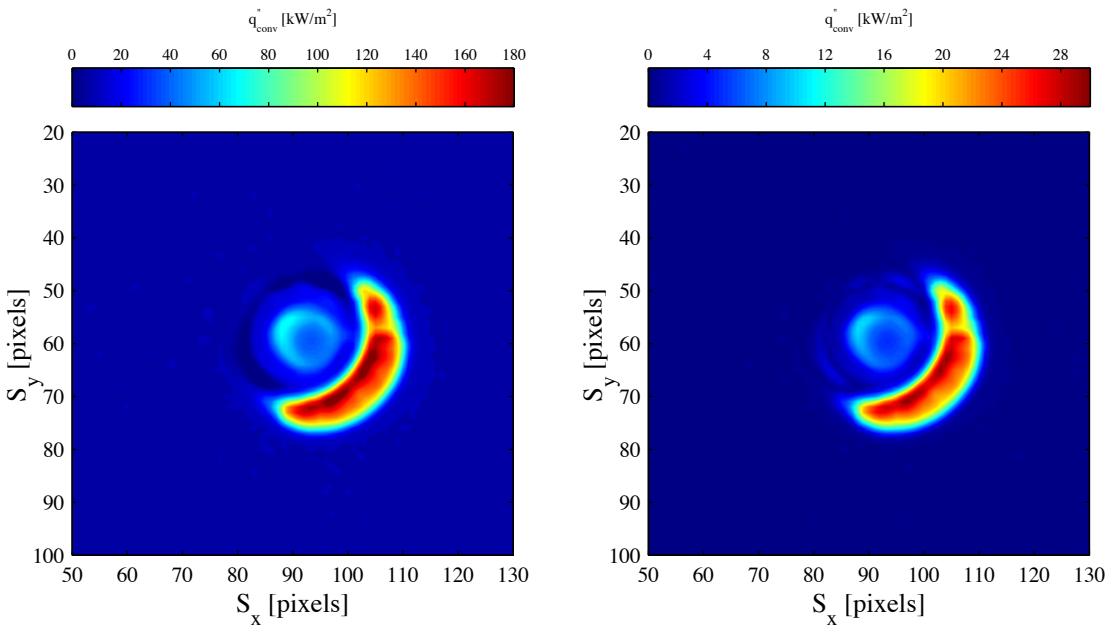

(a) (b)

Figure 4.15: (a) Instantaneous convective heat flux 14 *ms* after impact and (b) Instantaneous uncertainty convective heat flux 14 *ms* after impact .

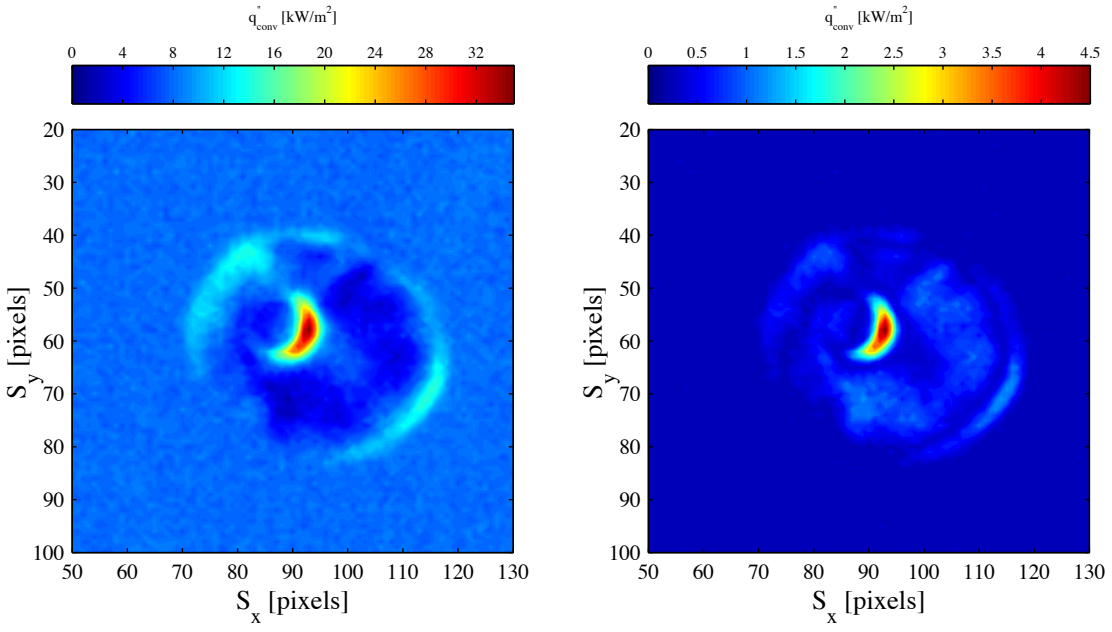

(a) (b)

Figure 4.16: (a) Instantaneous convective heat flux 114 *ms* after impact and (b) Instantaneous uncertainty convective heat flux 114 *ms* after impact .

temperature measurements was then explained. This was followed by a brief outline of the PIV measurement technique which was used to determine velocity field within the vicinity

of the bubble. The final section of this chapter dealt with characterising and determining the errors and uncertainties in the measurement techniques.

Chapter 5

Bubble Motion

This chapter presents the general features of a single air bubble (equivalent diameters of 2.8, 3.3 and 4.1 mm) rising through distilled water (rise heights of 10, 20, 25, 30 and 35 mm) before impacting and rebounding from a horizontal surface. All three bubbles may be classed as oblate spheroids. As the bubbles rise, large shape oscillations are observed, which are initiated during the departure from the injection orifice.

The bubble path, orientation, aspect ratio and shape, as determined from the experimental data, will be introduced. This is followed by the calculation of the bubble's centroidal velocity and discussion of the oscillations associated with the change in the bubble's rise velocity. Following the bubble rise section, the way in which the bubble interacts with a horizontal surface is reported. This includes a detailed account of the entire bubble bouncing event.

This chapter serves as a general introduction to rising and bouncing bubble motion. The following chapters will discuss heat transfer associated with the bubble motion.

5.1 Rising Bubble

Once the bubble has departed the growth orifice, it immediately commences its rise through the test media, as a consequence of its lower density. The vertical force causing the bubble to rise through the liquid is known as the buoyancy force. This acts in the direction opposing gravity and is equal to the weight of the medium displaced, which is water in the present study. A secondary force which acts against the buoyancy force is the drag force. A single small stable bubble, rising vertically, will have a constant drag force; if the bubble is very small this drag force will be similar to that acting on a solid sphere. Once equilibrium is achieved, the bubble will be traveling at terminal velocity. The terminal velocity achieved is dependent on the Morton, Reynolds and Eötvös numbers as shown in Figure 2.1.

Larger bubbles display more complex rise pattens; these include both zig-zag and spiral rise paths, or a combination of both patterns. As noted by previous literature, the rise path of larger bubbles is dictated by the previously mentioned dimensionless numbers. However, as noted by Tomiyama *et al.* [41] and Wu & Gharib [45] the path, shape and velocity of the bubble are extremely sensitive to initial shape deformation during the departure process. Thereby, the injection process will have a profound effect on the bubble's shape and motion.

A representative sample of results detailing the motion of three bubbles generated in orifices of diameters 0.5 *mm*, 1 *mm*, and 2 *mm*, released from five different heights (10 *mm*, 20 *mm*, 25 *mm*, 30 *mm* and 35 *mm*) will be presented in the following section. The results presented include the motion through both purified and contaminated water. The motion of the bubble will be broken into two main parts: firstly the bubble rise, followed by the bouncing process.

5.1.1 Bubble Position, Shape and Orientation

Figures 5.1 to 5.3 illustrate the centroidal path and instantaneous shape for a rise of 10 *mm* and for bubbles with equivalent diameters of 2.8 *mm*, 3.3 *mm* and 4.1 *mm*, respectively. The centroidal motion is shown in blue for both the x–z and y–z plane. The projected bubble outline for both planes is presented in red and black, with a time interval of 4 *ms* between successive bubbles. It is immediately notable that, for all cases, the bubble path was aligned vertically (S_z) without horizontal deviation.

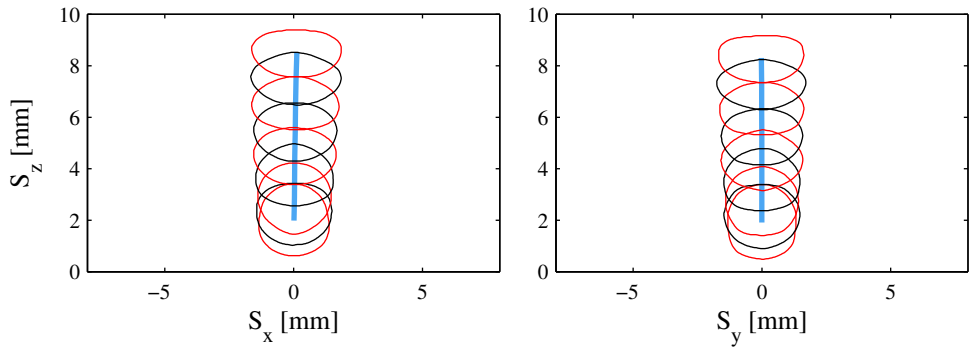

Figure 5.1: Bubble boundary and centroid path for both the x–z and y–z planes at time intervals of 4 *ms* between red and black outlines for a bubble with a D_{eq} of 2.8 *mm*. The bubble rise distance is 10 *mm*.

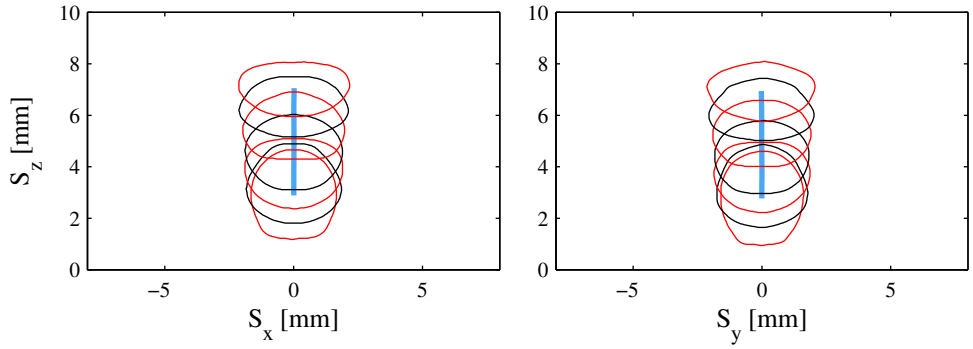

Figure 5.2: Bubble boundary and centroid path for both the x–z and y–z planes at time intervals of 4 *ms* between red and black outlines for a bubble with a D_{eq} of 3.3 *mm*. The bubble rise distance is 10 *mm*.

Immediately after departure (2 – 4 *ms*) the bubble's shape was found to be akin to that of a sphere, whereas further along its rise path, the bubble's shape shifts to that of an oblate spheroid. This spheroidal shape was found to vary significantly over the entire rise path. This shape change will be discussed in a later section, with respect to variation in the bubble's aspect ratio.

Figures 5.4 to 5.6 illustrate the centroidal path and instantaneous shape for an interme-

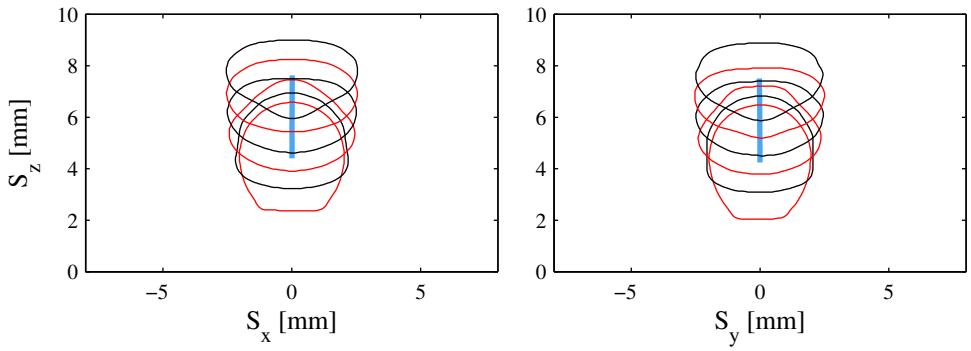

Figure 5.3: Bubble boundary and centroid path for both the x–z and y–z planes at time intervals of 4 *ms* between red and black outlines for a bubble with a D_{eq} of 4.1 *mm*. The bubble rise distance is 10 *mm*.

diate rise height of 25 *mm* and for bubbles with equivalent diameters of 2.8 *mm*, 3.3 *mm* and 4.1 *mm*, respectively. Path deviation is evident for both the 2.8 and 3.3 *mm* bubbles.

Figures 5.7 to 5.10 depict the motion of three bubbles that rise 35 *mm*, with their corresponding centroidal motion shown in blue. As before, their projected outlines have a time interval of 4 *ms*. What is notable about the increased rise height is firstly the presence of path deviation and secondly an increase in the amount of shape change observed.

Path deviation was expected for the bubble sizes encountered in the current experiment. All three bubble sizes are expected to have either a zig-zag pattern or a zig-zag with transition to a spiral rise path. A stable path was not observed due to the height restriction imposed for the present study[1]. It is notable that vertical path deviation occurs at a lower height for a bubble with a D_{eq} of 2.8 *mm*, when compared to the larger bubbles. This deviation occurs at a height above 14 *mm*, whereas for the two larger bubbles, this deviation occurs at heights of above 20 and 25 *mm*, respectively. This deviation is not obvious from the figures shown, as these numbers are lower limits, with the deviation is some cases being extremely small and difficult to detect.

As a bubble approaches a solid boundary, the bubble will begin to decelerate before impacting the surface with the drainage of the film being described using lubrication theory.

[1]For a stable zig-zag path, at least one zig-zag cycle would have to be completed.

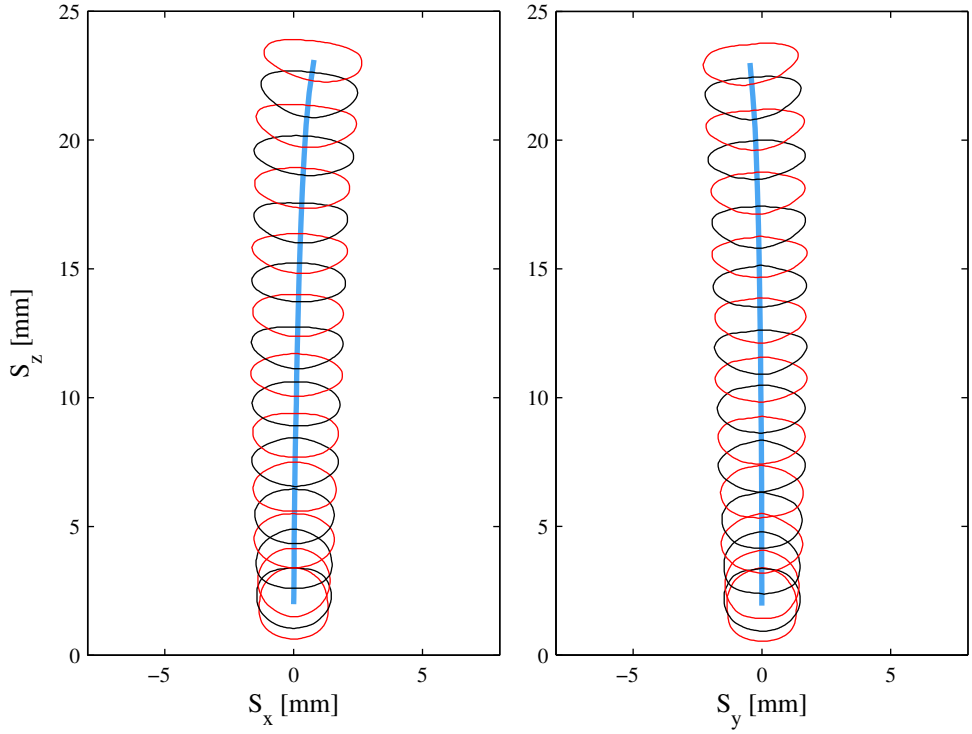

Figure 5.4: Bubble boundary and centroid path for both the x–z and y–z planes at time intervals of 4 *ms* between red and black outlines for a bubble with a D_{eq} of 2.8 *mm*. The bubble rise distance is 25 *mm*.

During this period a number of forces act to slow the advance of the bubble, which include the added mass due to the acceleration of the liquid around the bubble, the history force, which accounts for the finite time required by the surrounding flow to adjust itself to the change in slip velocity (Klaseboer *et al.* [61]), the lift force due to the vorticity in the flow and the buoyancy and drag force. When the bubble is in the vicinity of the wall, the film pressure starts to increase, the corresponding force becoming much larger in intensity than the buoyancy force, as noted by Klaseboer *et al.* [61].

As shown by Tsao & Kock [21] in Figure 2.19, regions of both high and low pressure are present in the film as the bubble approaches the solid surface.This pressure gradient allows the liquid film that is entrapped between the bubble and wall to drain along the wall and also causes a local overpressure at the bubble center, resulting in the formation of the dimple. This phenomenon was reported by Canot *et al.* [108], who noted that the size of this dimple was dictated by the Weber number, with higher Weber numbers corresponding

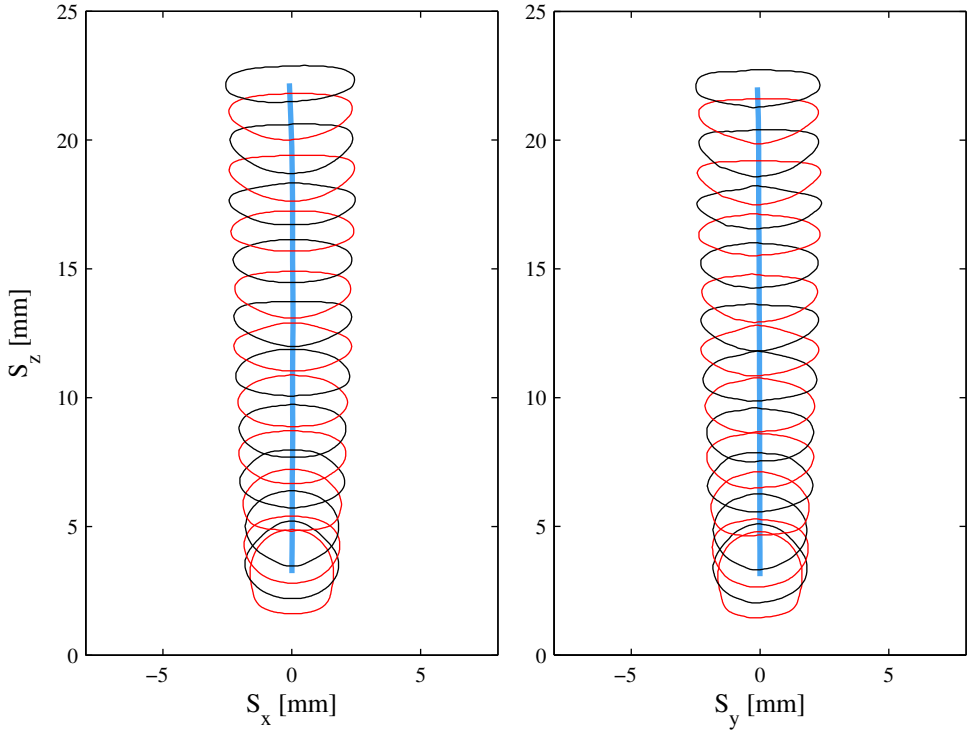

Figure 5.5: Bubble boundary and centroid path for both the x–z and y–z planes at time intervals of 4 *ms* between red and black outlines for a bubble with a D_{eq} of 3.3 *mm*. The bubble rise distance is 25 *mm*.

to larger dimples.

In Figures 5.8 and 5.10 large shape changes were found to occur at heights above 25 *mm*, with obscure shapes occurring at heights of 30 *mm*. Prior to these unusual shape changes at 30 *mm*, it can be inferred that at heights of $25 \leq S_z \leq 30$, the bubble was elongated[2] in both the x-z and y-z plane, with this elongation believed to be initiated upon release from the growth orifice. As the bubble rises its surface area increases until a point is reached where the surface area is too large, making the bubble's shape unstable; this results in the bubble reducing its velocity, while reverting its shape to that of a more stable sphere, which has the lowest surface area per unit volume. This rapid shape change only occurs within the vicinity of the solid surface. This instability is thought to result from a combination of the bubble size and the pressure increase that occurs as the bubble approaches the surface.

As the bubble approached the surface the bubble's upper surface was found to cup, cre-

[2]Elongation indicates that the bubble has a very low aspect ratio and is very flat.

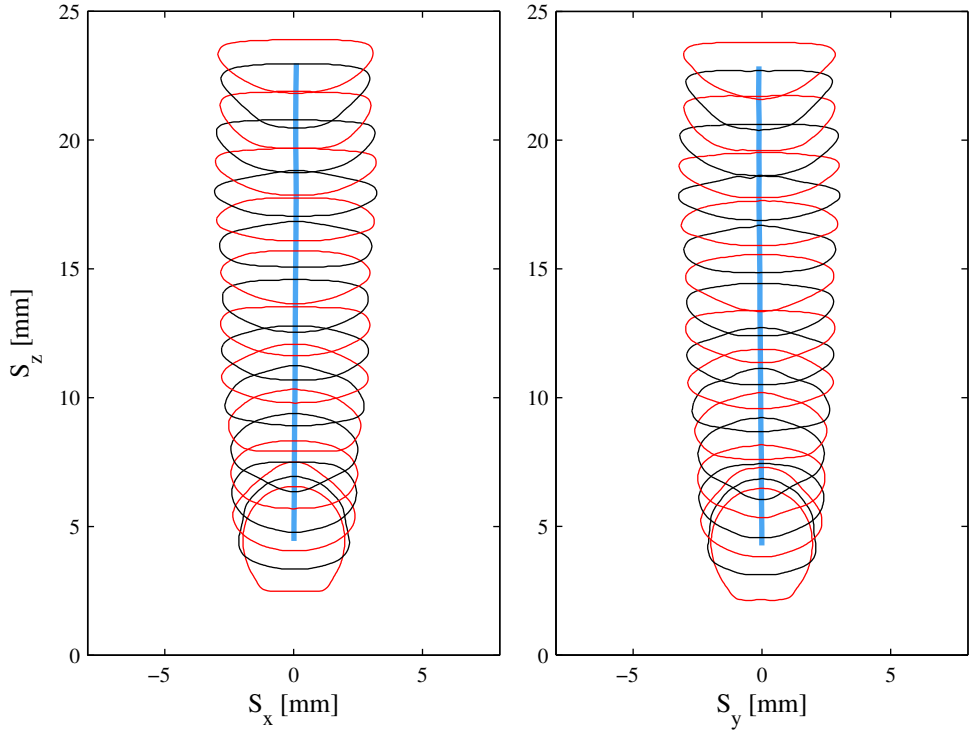

Figure 5.6: Bubble boundary and centroid path for both the x–z and y–z planes at time intervals of 4 *ms* between red and black outlines for a bubble with a D_{eq} of 4.1 *mm*. The bubble rise distance is 25 *mm*.

ating a bowl like shape; this is not visible in Figures 5.8 and 5.10, as these are projection outlines of the bubble's shape. This cupping was noticeable due to the transparent nature of the bubble, with the reflected dimple prior to impact shown in Figure 5.9. This cupping, although not measured was visually apparent at heights just beyond 25 *mm*, immediately prior to the complete flattening and inversion process. It was found that the larger the bubble, the more significant the dimpling would be.

In addition to these baseline clean water tests, experiments were performed in contaminated water[3]. It was found that there was no obvious variation in bubble rise path, with only minor differences being observed; these minor differences are discussed in later sections.

For the largest bubble in the present investigation, 4.1 *mm*, an unusual event occurs just as the bubble reverts its shape from being an elongated ellipsoid to a more spherical shape;

[3]For the present study the contamination added to the purified water was hollow glass spheres, used for PIV measurements.

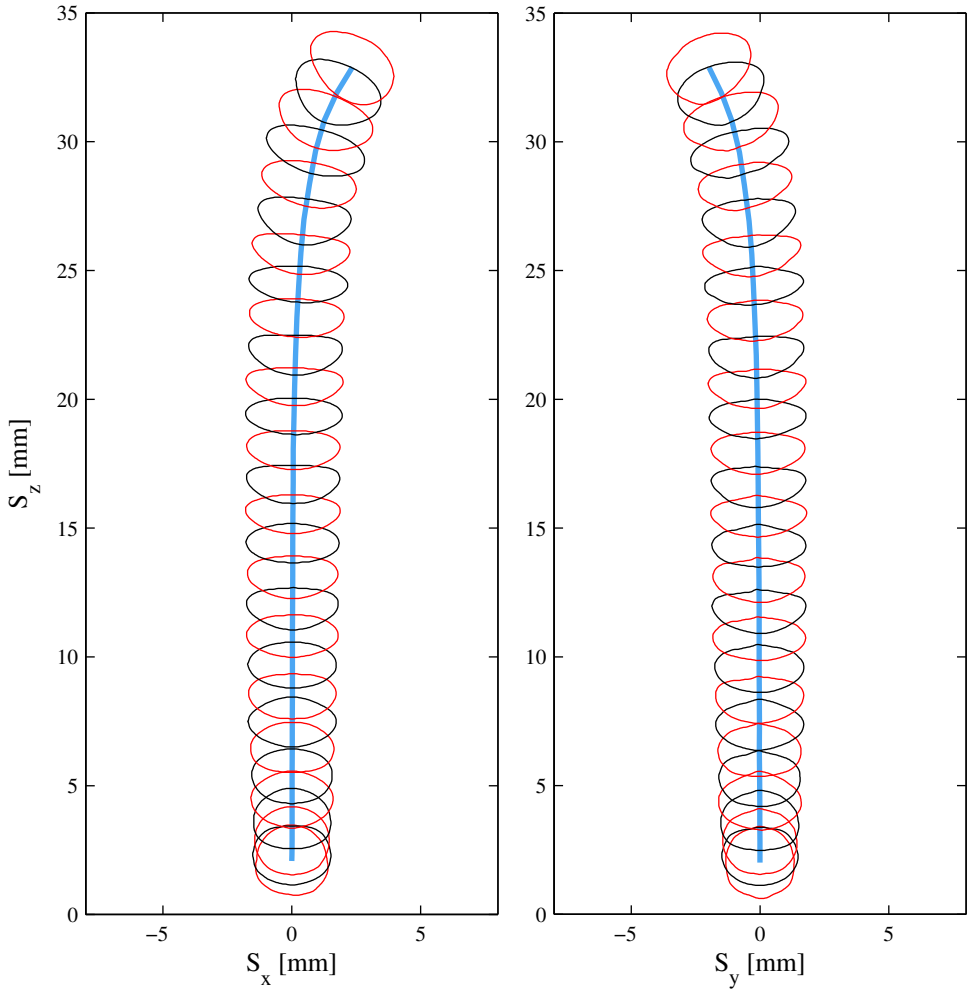

Figure 5.7: Bubble boundary and centroid path for both the x–z and y–z planes at time intervals of 4 *ms* between red and black outlines for a bubble with a D_{eq} of 2.8 *mm*. The bubble rise distance is 35 *mm*.

a micro bubble was formed. This micro bubble detached from the rear of the main bubble as shown in Figure 5.11. This event occurred due to the bubble's deceleration followed by a rapid shape change, subsequently followed by an acceleration stage as the bubble's shape transforms, resulting from an increased local pressure as the bubble neared the surface. The detachment can be observed at the rear of the bubble as seen in the final bubble outline in Figure 5.10, with the final bubble shape prior to detachment shown in Figure 5.11 (a); the detached micro bubble can be seen in Figure 5.11 (b).

This micro bubble has a diameter of less than 1 *mm*, which indicates that it has a reduced

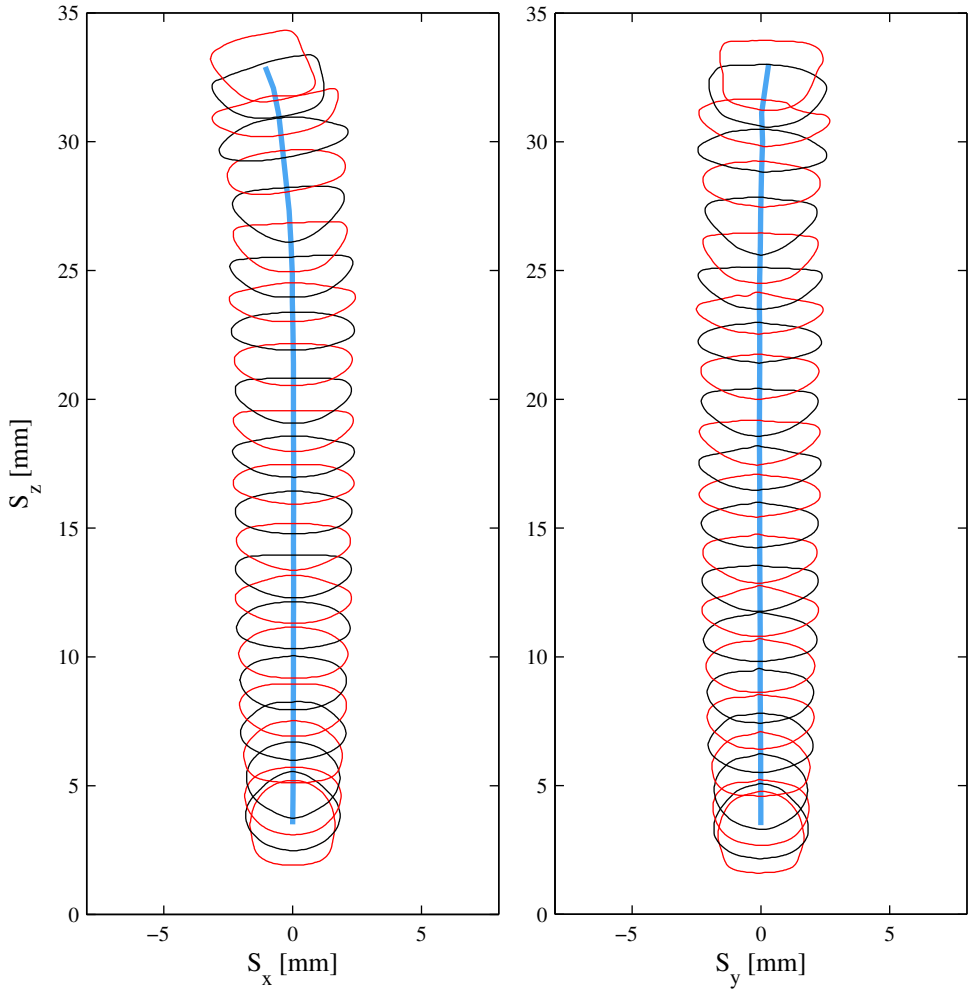

Figure 5.8: Bubble boundary and centroid path for both the x–z and y–z planes at time intervals of 4 *ms* between red and black outlines for a bubble with a D_{eq} of 3.3 *mm*. The bubble rise distance is 35 *mm*.

buoyancy force when compared to the large original bubble. This makes the small bubble susceptible to the influence of local fluid motion, often moving in a direction opposing the buoyancy force. This fluid motion was initiated by the larger main bubble.

The maximum observed horizontal displacement in both the S_x and S_y, direction was found to be dependent on bubble diameter but never exceeded ± 4 *mm*. However, for cases where the fluid was contaminated a larger horizontal displacement of 5 *mm* was observed. This is due to an increase in fluid shear at the bubble's interface, resulting in greater path deviation; once deviation, has begun due to instabilities in its rise.

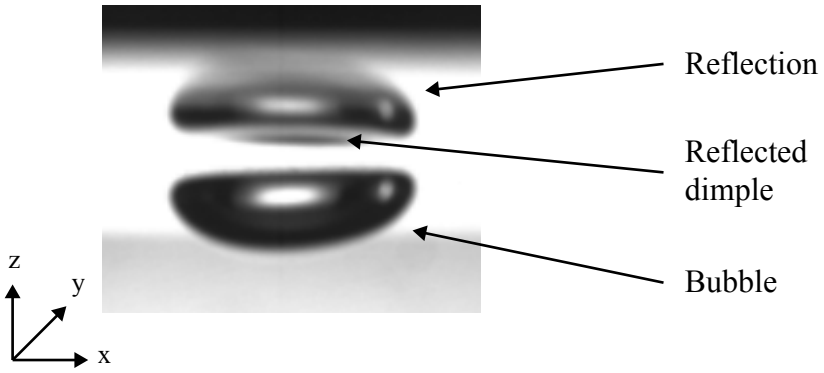

Figure 5.9: Bubble (D_{eq} = 3.3 *mm*) and its reflection, its dimple is apparent in the reflected bubble image.

5.1.2 Bubble Orientation Angle

Figures 5.12 and 5.13 illustrate the maximum absolute orientation angle relative to the horizontal of a single bubble for every experiment performed in clean water and contaminated water respectively. The figures include the five different release heights along with the variation in angles in both the *x-z* and *y-z* planes. Figures 5.12 and 5.13 represent the maximum angle encountered but also, and more importantly, show the spread in the bubble equivalent diameter data. For the largest bubble, 4.1 *mm*, large orientation angles are observed in some cases ($> 50°$); this is believed to be due to the bubble inverting and thereby changing the orientation of the major axis, relative to the horizontal. It is important to note that the course each bubble took was entirely random and was dictated by minute instabilities during the bubble's departure and rise. These instabilities in the bubble's rise are to be expected, considering the bubble sizes in question.

Figure 5.12 for the clean water shows tight grouping with respect to the bubble equivalent diameter for all three orifice sizes. A systematic reduction in the orientation angle for an increase in bubble diameter from 2.8 *mm* to 3.3 *mm* is also evident. In contrast, Figure 5.13 illustrates a far greater spread in the bubble equivalent diameters, despite the fact that the same orifice and injection systems were utilised for both tests, with the fluid being the only variable. This would indicate that the contaminated fluid has a marginal influence on the bubble growth process, although the overall trends are the same for both the clean and contaminated fluid.

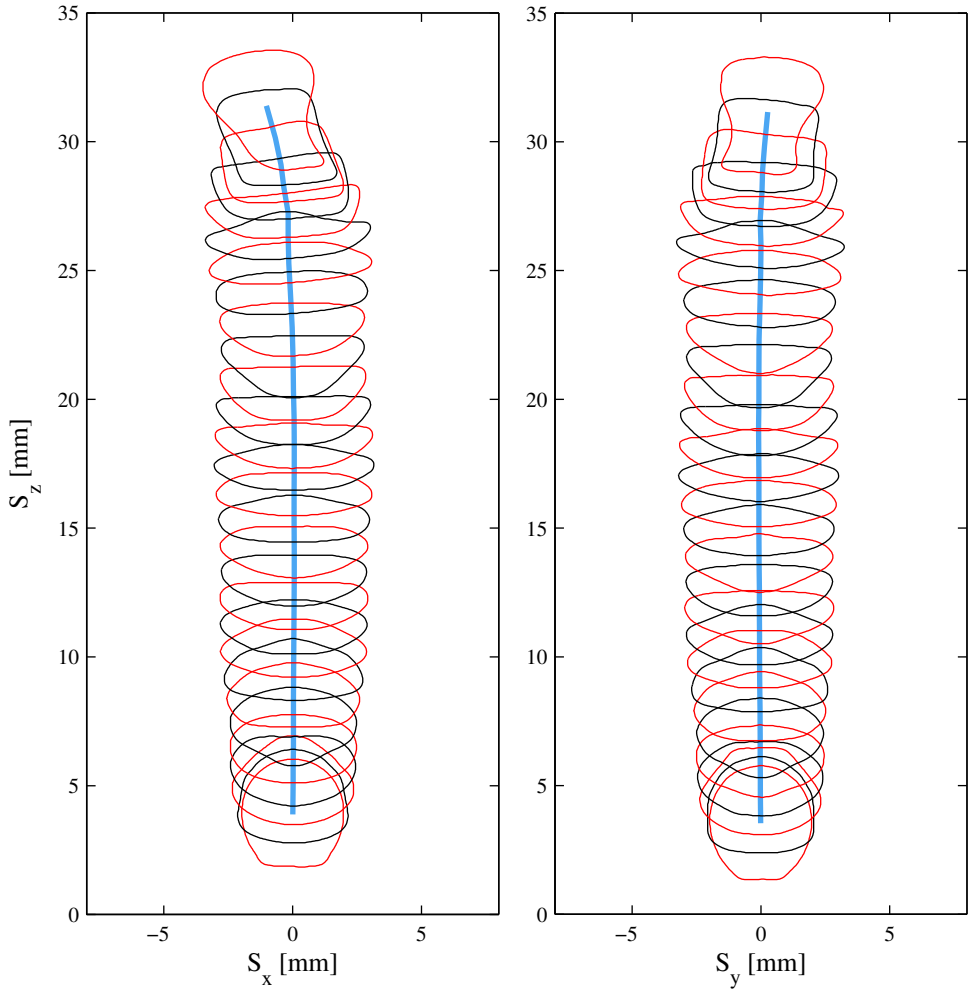

Figure 5.10: Bubble boundary and centroid path for both the x–z and y–z planes at time intervals of 4 *ms* between red and black outlines for a bubble with a D_{eq} of 4.1 *mm*. The bubble rise distance is 35 *mm*.

5.1.3 Aspect Ratio

Figures 5.14 and 5.15 illustrate the time varying aspect ratio (χ) for the three different bubble sizes and the five different heights for clean and contaminated water respectively. The time in all cases is non-dimensionalized with respect to the maximum rise time for each individual height. The bubble's aspect ratio is a measure of oblateness, also known as flattening. A value of one indicates that the bubble is a perfect sphere whereas a value less than 0.4 indicates that the bubble is elongated along the a and b ellipsoid axes.

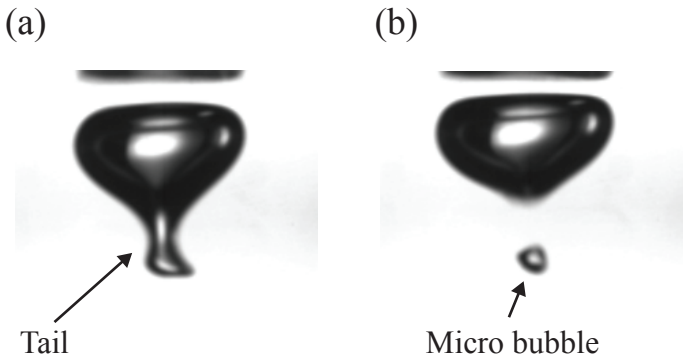

Figure 5.11: (a) Bubble with extended tail and (b) bubble and detached micro bubble.

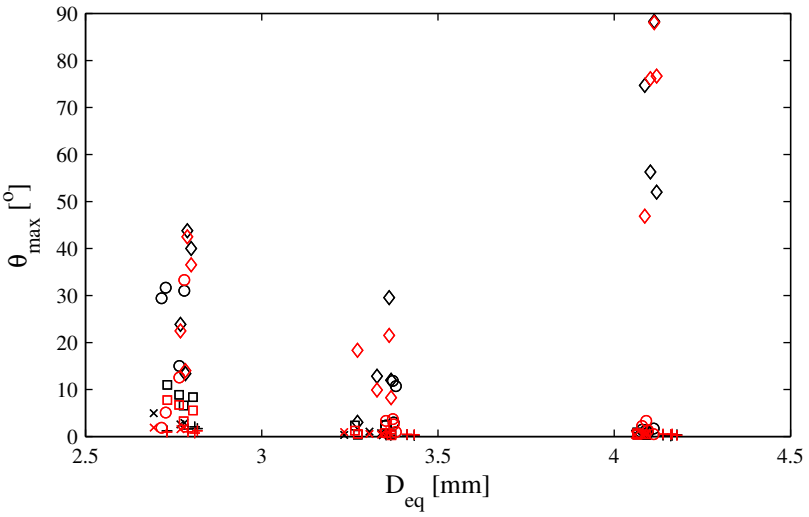

Figure 5.12: Maximum absolute orientation angle for all bubble release heights and all bubble sizes in pure water. The symbols represent the different release heights, while the black and red colours represent S_x and S_y planes, respectively. $+$ is 10 *mm*, $\times$ is 20 *mm*, $\square$ is 25 *mm*, $\bigcirc$ is 30 *mm* and $\diamond$ is 35 *mm*.

What is immediately apparent in Figure 5.14 (a)-(e) is the similarity among subfigures for the portion of the time period that is common to all. Thus, the same peaks and valleys that are obvious in Figure 5.14 (a) for the 10 *mm* rise height can be perceived at the beginning of Figure 5.14 (b)-(e) for the longer rise heights. This indicates firstly that the bubble behaves in a similar fashion as it rises and secondly, and more importantly, it indicates the repeatability of the experiment. For each bubble diameter it was established through multiple experiments that the bubble always exhibited the same trend, so it is sufficient to only illustrate one

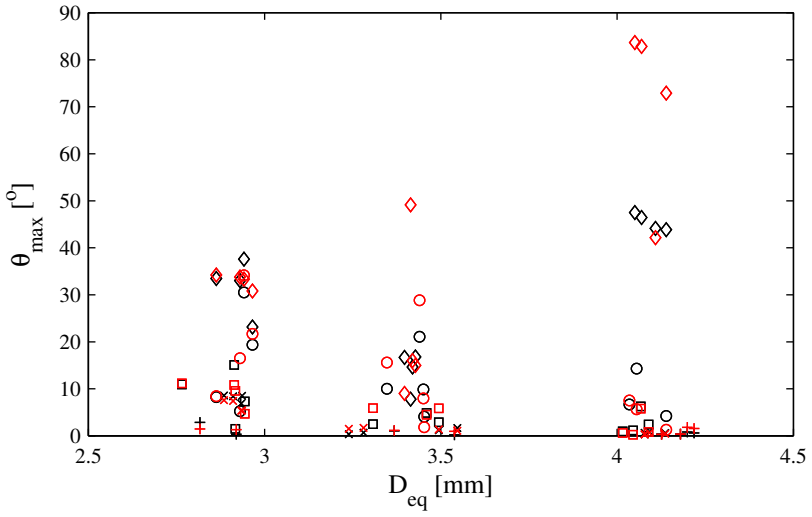

Figure 5.13: Maximum absolute orientation angle for all bubble release heights and all bubbles size in contaminated water. The symbols represent the different release heights, while the black and red colours represent S_x and S_y planes, respectively. $+$ is 10 *mm*, $\times$ is 20 *mm*, $\square$ is 25 *mm*, $\bigcirc$ is 30 *mm* and $\diamond$ is 35 *mm*.

example per height change in the discussion that follows.

Once the bubble departs the orifice it immediately reverts to a shape close to that of a sphere; this can be inferred from the aspect ratio of near unity in the early stages of Figures 5.14 and 5.15. As the bubble begins to accelerate vertically it also begins to flatten. The amount of flattening was found to be related to the bubble diameter; the larger the bubble the greater the degree of flattening i.e. the lower the aspect ratio. At a height of 35 *mm* (Figure 5.14 (e)), it can be seen that the bubble's aspect ratio rises towards the end of its rise path. An increase in local pressure between the bubble and the surface causes the bubble to flatten as it nears the surface, resulting from the no-slip condition at the surface interface. As the bubble's outline is captured as a projected image, the newly created dimple is not included in the bubble's outline, causing the aspect ratio to be slightly overestimated in the vicinity of the surface.

In the case of the 3.3 *mm* and 4.1 *mm* bubbles, this is due to the bubble rapidly changing shape; this may be due to the bubbles being too "flat" and unstable, with the surface also exerting an influence as the bubble approaches impact. For the small 2.8 *mm* bubble, a steady increase in its aspect ratio was observed. This is perhaps due to the fact that the

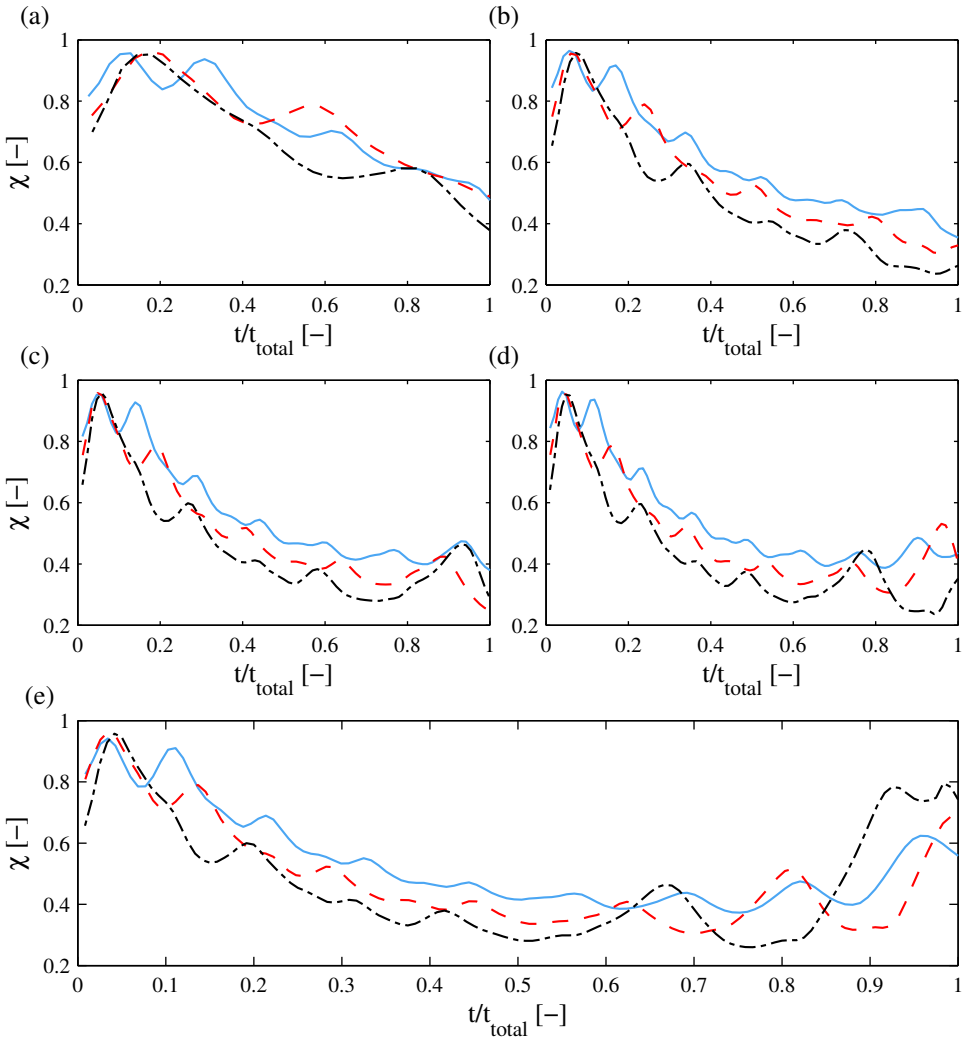

Figure 5.14: The time varying aspect ratio (χ) for three bubble sizes in clean water, with the — solid line representing D_{eq} of 2.8 *mm*, – – dashed line representing, D_{eq} of 3.3 *mm* and - – dot dash representing D_{eq} of 4.1 *mm*. The five different release heights of 10, 20, 25, 30 and 35 *mm* are shown in (a) to (e) respectively.

bubble is no longer accelerating vertically and is in a quasi-static state in terms of velocity. This allows the bubble to reduce its surface area to that of a sphere and become more stable.

Also evident from Figures 5.14 and 5.15 are considerable oscillations in the bubble's aspect ratio. Again these were found to be dependent on the bubble size, with a greater number of peaks occurring for the smallest bubble. These peaks and valleys indicate that the bubble's velocity may also be varying significantly during its rise, with this point being discussed further in the next section.

A comparison of Figures 5.14 and 5.15 for purified water and contaminated water respectively shows that, for the most part, they are visually similar. However, there is a difference to be found in the trace of the small 2.8 *mm* bubble. In subfigure (5.14 (e), 5.15 (e)) it can be seen that the bubble's aspect ratio is flatter i.e. the amplitude of the peaks are lower, for the contaminated fluid from a dimensionless time of 0.7 onward, when compared to the clean water. Likewise a slight shift in the time corresponding to the locations of the peaks in the latter stages of the rise was found, although this difference was moderate.

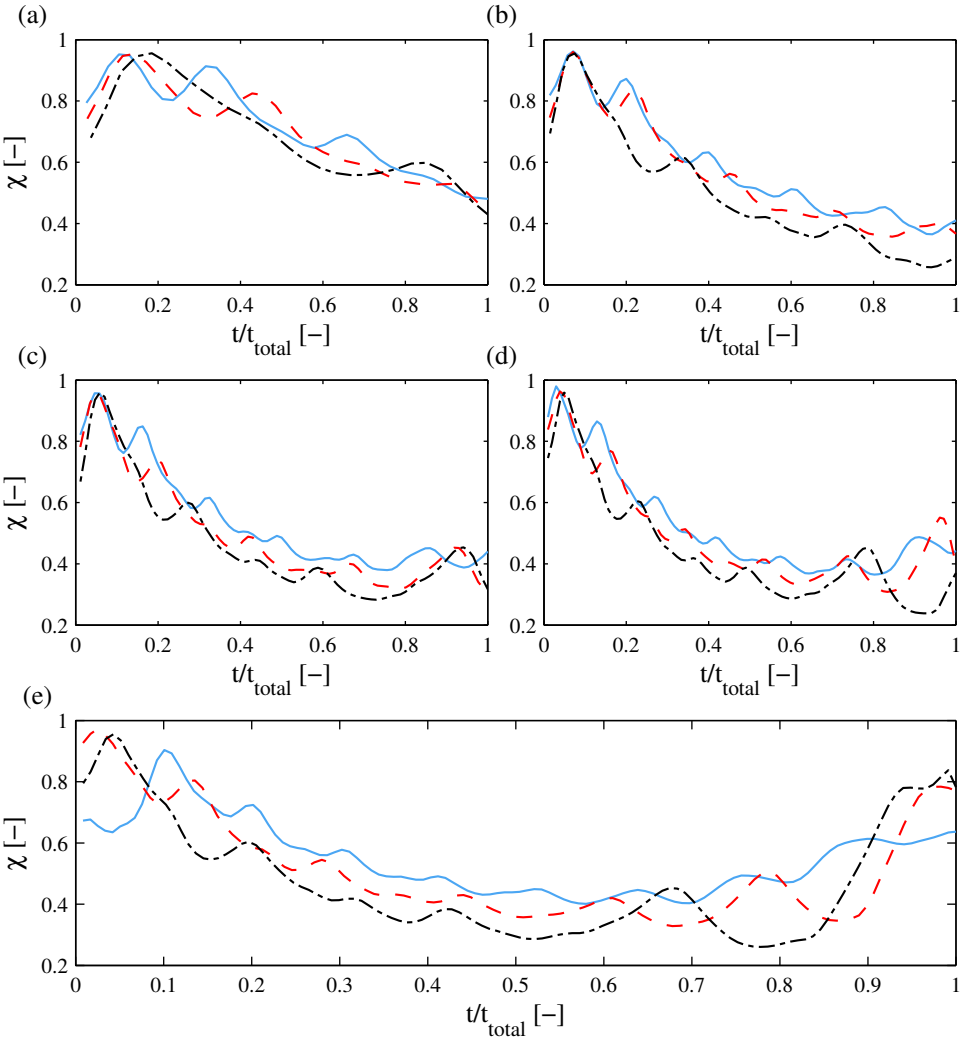

Figure 5.15: The time varying aspect ratio (χ) for three bubble diameters in contaminated water — solid line D_{eq} of 2.8 *mm*, – – dashed line D_{eq} of 3.3 *mm* and - – dot dash D_{eq} of 4.1 *mm*. The five different release heights of 10, 20, 25, 30 and 35 *mm* are shown in (a) to (e) respectively.

5.1.4 Bubble Instantaneous Velocities

The instantaneous bubble velocity component have been calculated using the following equations:

$$V_x(t) = \frac{S_x(t+\Delta t) - S_x(t)}{\Delta t} \tag{5.1}$$

$$V_y(t) = \frac{S_y(t+\Delta t) - S_y(t)}{\Delta t} \tag{5.2}$$

$$V_z(t) = \frac{S_z(t+\Delta t) - S_z(t)}{\Delta t} \tag{5.3}$$

where Δt is 1 *ms* and S_x, S_y and S_z are the centroidal positions in the x, y and z directions, respectively. The velocity magnitude is calculated using the following equation:

$$|V| = \left(V_x^2 + V_y^2 + V_z^2\right)^{1/2} \tag{5.4}$$

The effect of fluid contamination on the bubble's terminal velocity[4] has been the subject of several investigations. Work by Clift *et al.* [19] and Bhaga & Weber [16] has shown that the bubble's terminal velocity depends only on three of the main dimensionless numbers: Reynolds number, Morton number and Eötvös number. However, subsequent experiments by Tomiyama *et al.* [41] found that the large scatter in their terminal velocities was primarily due to initial release conditions, with small initial shape deformations resulting in low velocities and high aspect ratios, whereas large initial deformations resulted in higher terminal velocities and flatter bubbles of lower aspect ratio. A similar study by Wu & Gharib [45] found that the bubble detachment had a significant effect on the bubble's rise velocity. Lesage & Marois [109] determined experimentally, that even if the bubble growth was quasi-static the pinch-off process was found to be a dynamic process, which could influence the bubble rise velocity, resulting in the observations by Tomiyama *et al.* [41] and Wu & Gharib [45]. With this knowledge the next section will report on the individual velocities recorded for the three different bubble diameters in clean water.

[4]Terminal velocity is the bubble velocity reached when the drag force and buoyancy force are in equilibrium and bubble is not longer accelerating, but rising steadily.

5.1.4.1 Centroidal Velocity

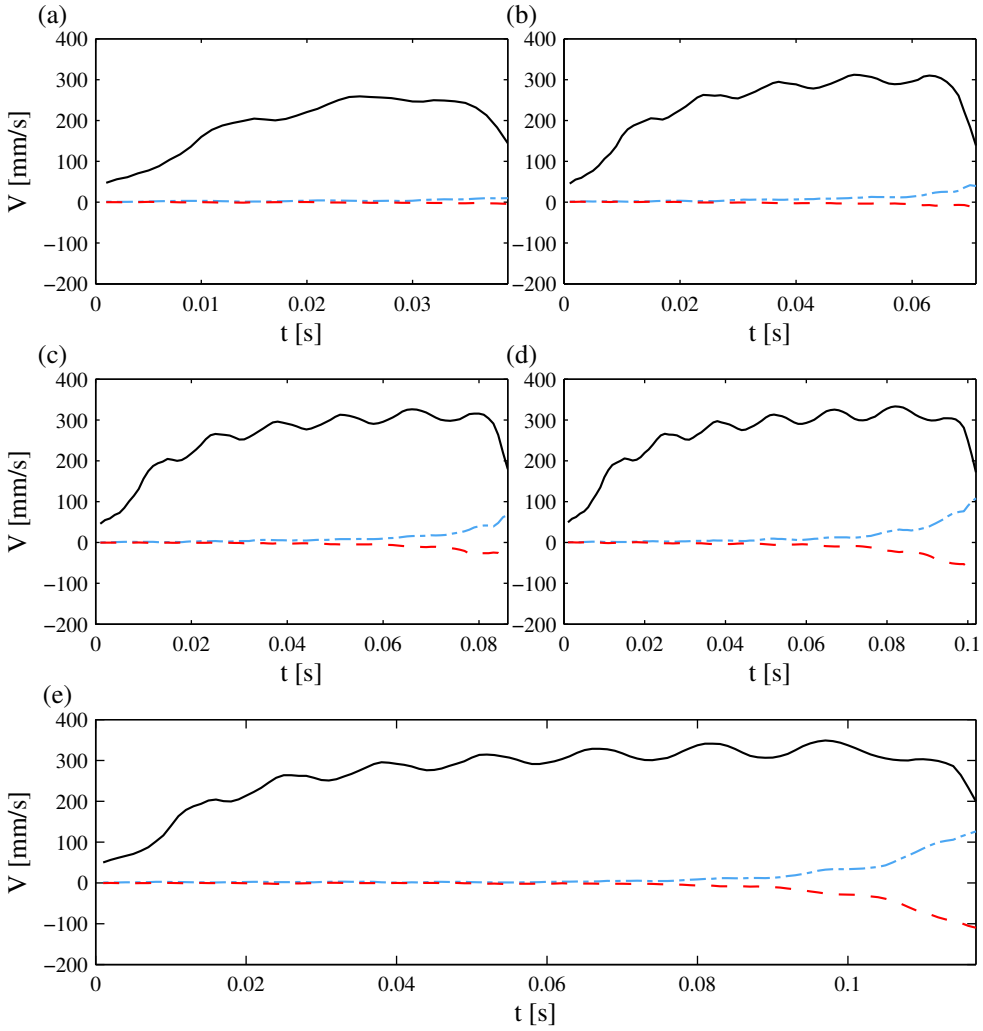

Figure 5.16: The time varying individual velocity components for a 2.8 *mm* bubble. The — solid line is the vertical velocity V_z, – – dashed line is the horizontal y velocity, V_y and - – dot dash line is the horizontal x velocity, V_x. The five different release heights of 10, 20, 25, 30 and 35 *mm*, are shown in (a) to (e) respectively.

Figures 5.16 to 5.18 illustrate the time varying individual instantaneous velocity components for the 2.8 *mm*, 3.3 *mm* and 4.1 *mm* bubble respectively, at the five different release heights. The solid line in each case relates to the vertical rise velocity, V_z, the single dashed line relates to the horizontal velocity in the y-z plane, V_y, and the double dashed line is the horizontal velocity in the x-z plane V_x, respectively. The results shown represent only a small sample of the entire data collected, however it was found that variability in the instan-

taneous velocity was very low; the same was evident for the bubble's aspect ratio. Data in Figures 5.16 to 5.18 correspond to testing in clean water.

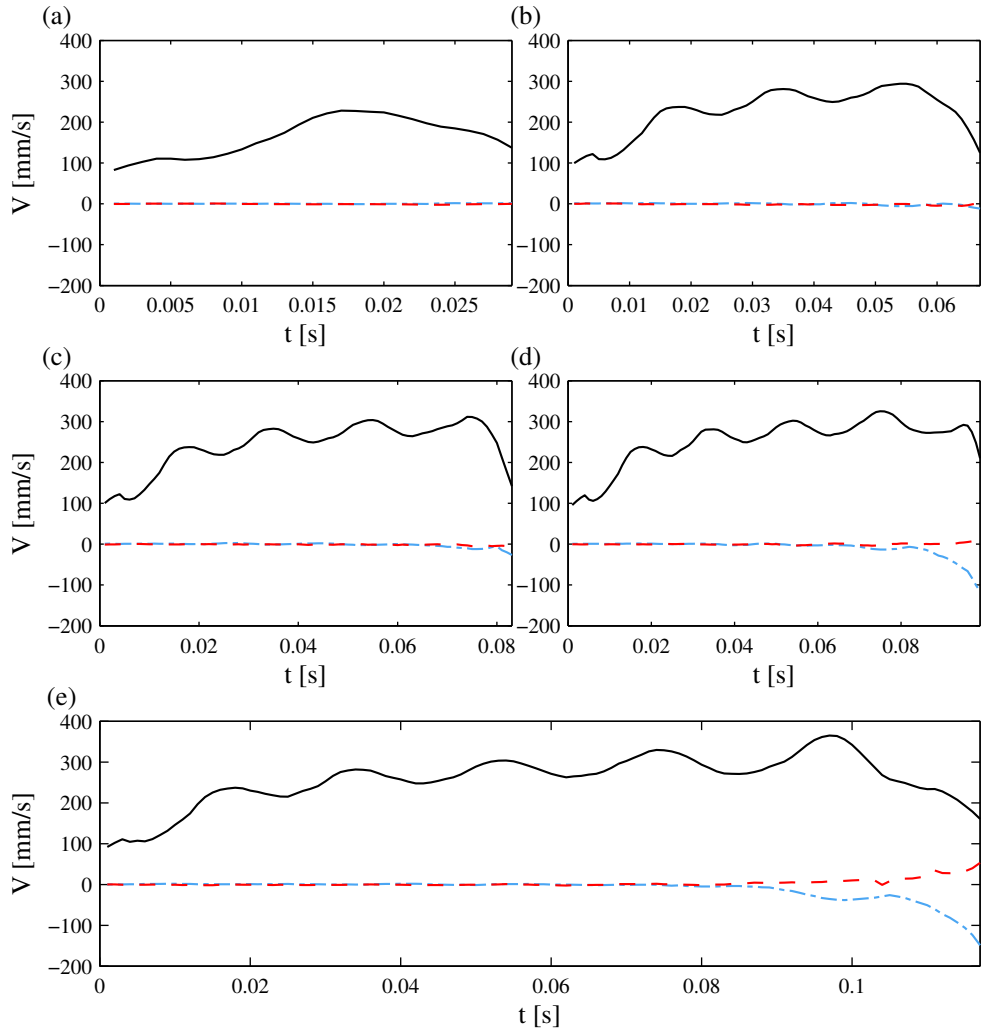

Figure 5.17: The time varying individual velocity components for a 3.3 *mm* bubble. The — solid line is the vertical velocity V_z, – – dashed line is the horizontal y velocity, V_y and - – dot dash line is the horizontal x velocity, V_x. The five different release heights of 10, 20, 25, 30 and 35 *mm*, are shown in (a) to (e) respectively.

As with the aspect ratio plots, all three data sets exhibit undulations in the vertical rise velocity V_z. These undulations are linked to the previously mentioned aspect ratio fluctuations, which will be discussed further in Section 5.1.4.3.

From Figures 5.16 to 5.18 it can be seen that the bubble very quickly gains momentum upon leaving the growth orifice, with the time to reach a "stable" rise velocity being approx-

imately 0.05 *s* for all three bubbles. A closer look at the initial stages of the bubble's rise shows a slight reduction in the instantaneous rise velocity at a time of less than 0.01 *s*. This reduction is not apparent for the small 2.8 *mm* bubble, whereas this "spike" can be observed for both the 3.3 *mm* and 4.1 *mm* bubble, being more prominent for the largest bubble. This "spike" is thought to be related to the initial shape changes that occur upon departure from the orifice, with the bubble's tail retracting into the main bubble body upon departure.

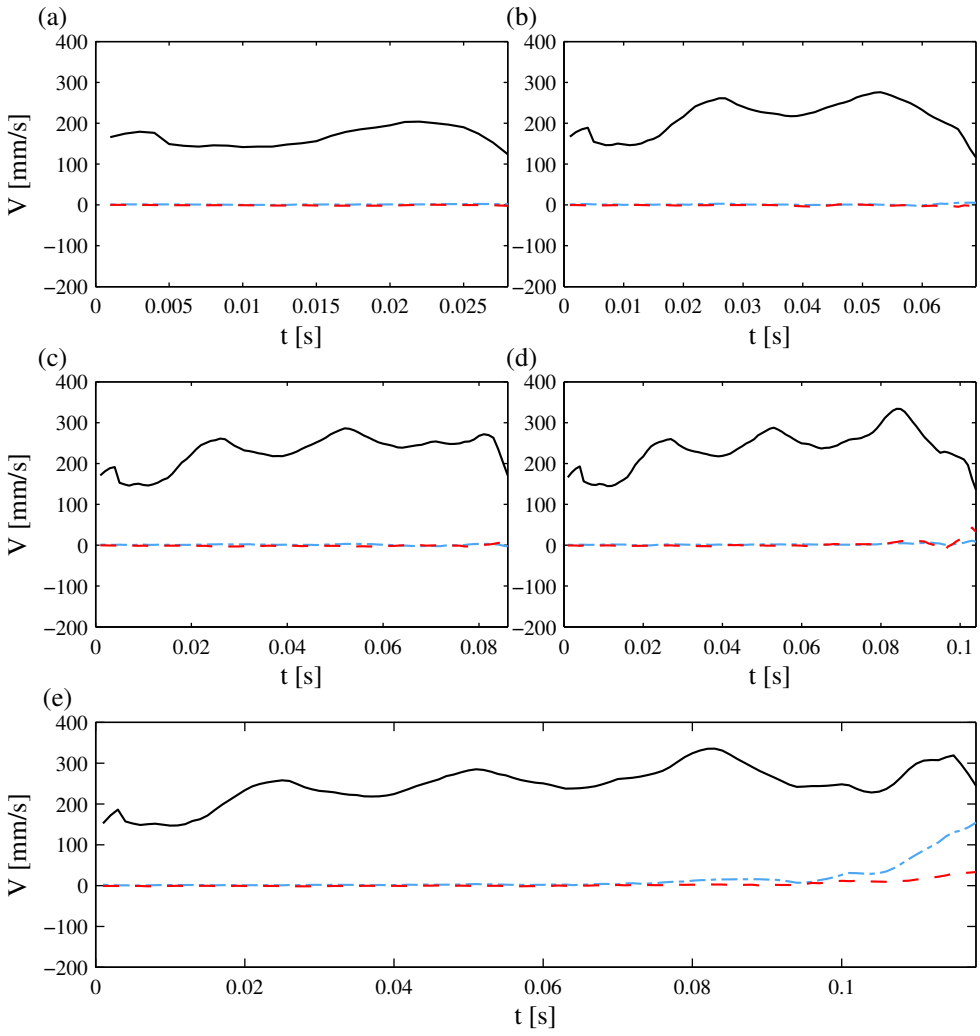

Figure 5.18: The time varying individual velocity components for a 4.1 *mm* bubble. The — solid line is the vertical velocity V_z, – – dashed line is the horizontal y velocity, V_y and - – dot dash line is the horizontal x velocity, V_x. The five different release heights of 10, 20, 25, 30 and 35 *mm*, are shown in (a) to (e) respectively.

At the beginning of the bubble's rise significant acceleration takes place as the bubble's

velocity jumps from 100 *mm/s* to 200 *mm/s* in only 0.02 *s*. Beyond this point in time a lower acceleration was observed. It can be seen from Figures 5.16 to 5.18 that a sharp drop in the bubble's vertical velocity, V_z, occurs once the bubble is near the solid surface, which may be related to an increase in local pressure due to the surface, halting the bubble's advance.

For the most part the horizontal velocity components are zero during the bubble's vertical rise, but once the bubble begins to tilt, the horizontal components of velocity increase, to an approximate maximum of $\pm$ 100 – 150 *mm/s*; this is dependent on the bubble size and random influences and instabilities. The velocity profiles shown in Figures 5.16, 5.17 and 5.18 are remarkably similar to data from Tomiyama *et al.* [41], shown in Figure 2.3 (b), where large initial deformation of a 3 *mm* bubble occurs when the bubble leaves the injection orifice. In Figure 2.3 (b) it is notable, that the bubble's aspect ratio is similar to the present study; this suggests that the bubble's velocity and shape changes are related to the injection process.

5.1.4.2 Maximum Rise Velocity

Figures 5.19 and 5.20 illustrate, for clean and contaminated water respectively, the maximum attained rise velocity ($S_{z,max}$). This is taken from Figures 5.16 to 5.18 for the clean water case, and calculated in a similar manner for the contaminated water case. Firstly it must be noted that the max rise velocity for five different heights has been included for completeness, with the different heights being indicated in the figure captions. The data are averaged for both the bubble equivalent diameter and maximum rise velocity and represented by the larger, red symbols. The two lines in Figures 5.19 and 5.20 represent data from previous authors, with the most important being the data from Clift *et al.* [19] as indicated by the – – dashed line. This information is for terminal velocity, when the bubble is in a stable rise path. The present experimental data are for the maximum rise velocity; however, the bubble's path is quite stable[5], thereby allowing a comparison to be made.

The figures also includes data from Velhuis [28], which are approximately 7% higher than the data obtained by Clift *et al.* [19], demonstrating the variability in published results. For both figures, if the lower release height data are neglected, trends and distinct grouping are visible in this data. This grouping is very tight for the small bubble 2.8 *mm*, less so for

[5]The bubble's path is stable, however the bubble itself is not, with its aspect ratio fluctuating during its rise.

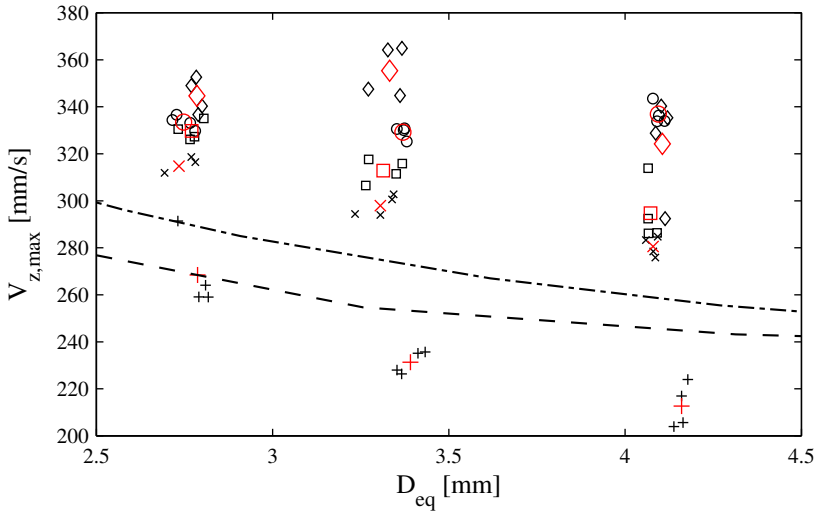

Figure 5.19: Maximum rise velocity ($V_{z,max}$) for each experiment in clean water. The five different heights are represented as follows: + is 10 *mm*, × is 20 *mm*, □ is 25 *mm*, ○ is 30 *mm* and ◇ is 35 *mm*. The larger red symbols represent the average for each individual height. The different bubble diameters can be inferred from the data. The – – dashed line corresponds to terminal velocity data from Clift *et al.* [19], while the - – dot dash line corresponds to terminal velocity data from Velhuis [28].

the 3.3 *mm* bubble, and finally the 4.1 *mm* bubble appears to have two distinct groups. This grouping in evidently related to the rise height, as a height of 20 *mm* or greater was needed for the 2.8 *mm* bubble to reach its maximum rise velocity. For the 3.3 *mm* bubble, a height of greater than 25 *mm* was necessary to reach maximum rise velocity while for the largest bubble a height of greater than 30 *mm* was necessary.

As previously mentioned there is a spread in the equivalent diameter results between the clean and contaminated water cases. It might be expected that this slight spread would influence the bubble's velocity. On the contrary, a closer inspection of Figures 5.19 and 5.20 reveals that when averaged for both D_{eq} and $V_{z,max}$, both clean and contaminated water have comparable values; this is a positive result for experimental repeatability, as it suggests that small differences in water quality between tests will not significantly affect the results.

The most striking result in Figures 5.19 and 5.20 is the fact that the velocities are significantly higher than those reported by literature, approximately 25% higher than those reported by Clift *et al.* [19]. However, the previously mentioned work by Tomiyama *et al.* [41] indicated that rise instabilities i.e. fluctuating aspect ratio, have a significant effect

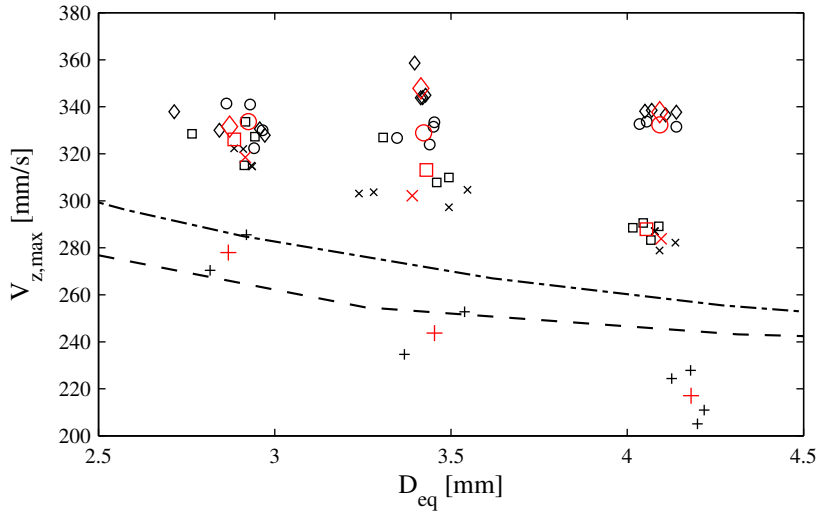

Figure 5.20: Maximum rise velocity ($V_{z,max}$) for each experiment in contaminated water. The five different heights are represented as follows: + is 10 *mm*, × is 20 *mm*, □ is 25 *mm*, ○ is 30 *mm* and ◇ is 35 *mm*. The larger red symbols represent the average for each individual height. The different bubble diameters can be inferred from the data. The continuous line data is explain in Figure 5.19.

on the bubble's velocity. It is possible that the velocities are higher due to the rapidly fluctuating aspect ratios, although to test this hypothesis further experiments would have to be performed that are outside the scope of this thesis. It must be noted however, that the maximum initial velocity in Figure 2.3 (b) (Tomiyama *et al.* [41]) is quite similar to the present values, while in the latter stages of Figure 2.3 (b), at a height greater than 150 *mm*, the bubble's velocity settled at approximately 280 *mm/s*. This is the approximate value reported by Clift *et al.* [19], which perhaps indicates that the bubbles in the present study would indeed reduce in velocity if the impact surface was not present.

Similarly, work by Wu & Gharib [45] demonstrated the effect of different bubble injection methods on the bubble rise velocity and aspect ratio. Wu & Gharib [45] noted that the curvature at the bubble detachment point affected the axisymmetric surface wave, which in turn propels the bubble to large initial velocities; with the larger orifice producing weak perturbations upon detachment when compared to the small orifice with the same bubble volume. As the three bubbles in the current set-up have the same injection rate but different injection velocities, the effect of the gas momentum force might be a contributing factor, although this has not been investigated for the current set-up.

5.1.4.3 Velocity Fluctuation Frequency

Figures 5.21 and 5.22 illustrate the oscillation frequency in the bubble rise velocity (V_z) for the three different bubbles in clean and contaminated water respectively. Only four rise heights are exhibited here, as below 20 *mm* only one relevant peak in the rise velocity was observed, therefore it is not possible to show data for the 10 *mm* release height.

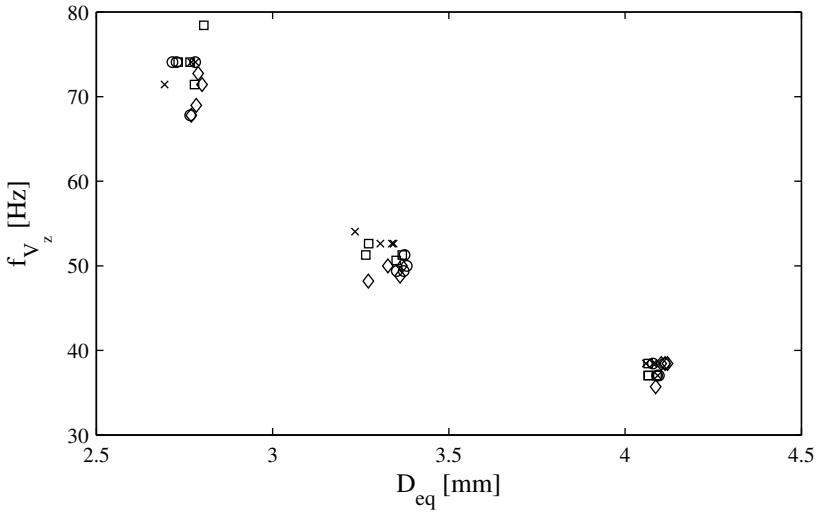

Figure 5.21: Rise velocity (V_z) oscillation frequency for the three different bubbles in clean water. The data only contains four release heights, where $\times$ is 20 *mm*, $\square$ is 25 *mm*, $\bigcirc$ is 30 *mm* and $\diamond$ is 35 *mm*.

It is immediately apparent that there is a relationship between the bubble equivalent diameter and the oscillation frequency of V_z; the larger the bubble the lower the oscillation frequency, for the range of bubbles sizes under consideration. An exponential function has been determined separately for both the clean and contaminated water, as is shown below:

$$\begin{aligned} f_{V_z} &= 269.67e^{-0.486 \cdot D_{eq}} \qquad \text{(Clean water)} \\ f_{V_z} &= 250.04e^{-0.468 \cdot D_{eq}} \qquad \text{(Contaminated water)} \\ 2.5 &\leq D_{eq} \leq 4.5 \end{aligned} \tag{5.5}$$

Again what is notably different between the clean and contaminated cases of Figures 5.21 and 5.22 respectively is the spread in the frequency data for each bubble size. However, this

spread has little effect on the averaged data, which are utilised to determine the coefficients in Eq. 5.5.

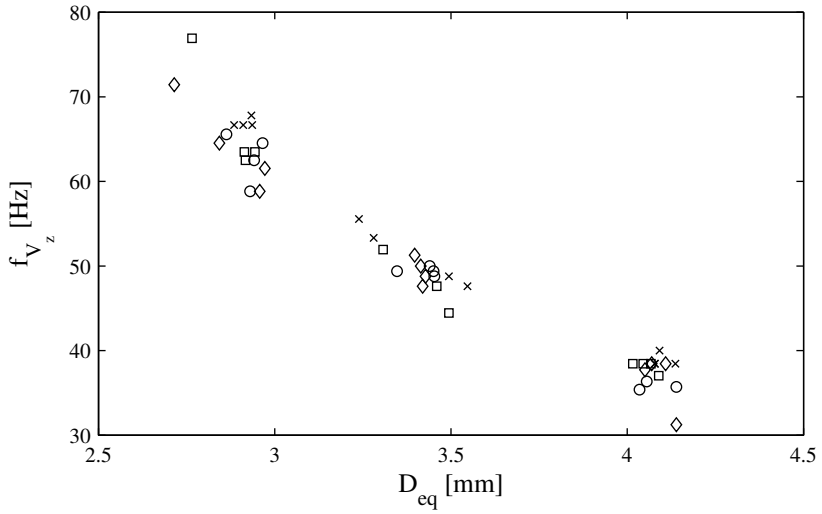

Figure 5.22: Rise velocity (V_z) oscillation frequency for the three different bubbles in contaminated water. The data only contains four release heights, where $\times$ is 20 *mm*, $\square$ is 25 *mm*, $\bigcirc$ is 30 *mm* and $\diamond$ is 35 *mm*.

In order to determine the origins of the velocity fluctuations, the frequency mode (2,0), which relates to surface oscillations from pole to pole, is quantified, utilising the following equation from Lunde & Perkins [47] and Veldhuis [28, 110]:

$$f_{2,0} = \frac{1}{2\pi}\sqrt{\frac{12\sqrt{2}\chi_m^2}{\left(\chi_m^2+1\right)^{3/2}}}\sqrt{\frac{\sigma}{\rho_l r_{eq}^3}} \tag{5.6}$$

where χ_m is equal to $1/\chi$. As illustrated in Figure 5.14, the bubble's aspect ratio, χ, changes significantly with respect to time, making it difficult to determine a realistic mean value, as utilised by other authors. To overcome this difficulty two values of χ_m are chosen; the minimum value and the mean value, which occurs in the central portion of the bubble's rise. The frequency results are presented in Table 5.1.

The calculated mode (2,0) frequencies from Equation 5.6, which are oscillations from pole to pole, match very closely to the frequency of rise velocity oscillations shown in Figures 5.21 and 5.22. Similarly, when Figures 5.21 and 5.22 are compared to Figure 2.7 from Veldhuis [28], the results again closely match. In Figure 2.7, it was noted that the

Table 5.1: Calculated mode (2,0) frequency versus bubble equivalent diameter.

D_{eq}	$\chi_{m,min}$	$\chi_{m,mean}$	$f_{2,0,min}$ Hz	$f_{2,0,mean}$ Hz
2.8 *mm*	2.63	2.38	68.7	70.8
3.3 *mm*	3.33	2.85	49.5	52.3
4.1 *mm*	3.84	2.85	33.8	37.8

velocity oscillation frequency, the wake production frequency and the mode (2,0) frequency closely match. From this match, Veldhuis [28], suggested that the velocity fluctuations are perhaps evidence that regions of separate vorticity are generated at the rear of the bubble as it rises; this is similar to Figure 2.13 (f), which is for a 2.8 *mm* bubble. Mode (2,2) frequencies are not compared to the present data, as this type of motion is usually related to lateral bubble motion i.e. stable, cyclic zig-zagging or spiralling motion, which for the most part is not present due to the reduced height in the present study.

5.1.5 Induced Forces Acting on a Rising Bubble

Figures 5.23 to 5.25 present both the drag and lift forces for bubbles of diameter 2.8 *mm*, 3.3 *mm* and 4.1 *mm* respectively versus the five different release heights. All data refers to clean water conditions. The forces are shown in the laboratory frame of reference. For the most part, as the bubbles rise vertically their lift force is zero, up until they begin to tilt. This tilting begins due to instabilities in the bubble's wake and shape. The lift force was extremely small in all cases due to lack of significant path deviation, whether the path is spiralling or zig-zagging. The maximum encountered lift force (F_L) for bubbles of diameter 2.8, 3.3 and 4.1 *mm* was approximately 0.6×10^{-4} N, 1×10^{-4} N and 1.8×10^{-4} N, respectively. These lift forces are comparable with the work of Veldhuis [28], however, they do not play a significant role in the present study, due to the reduced release height.

The most significant aspect of Figures 5.23 to 5.25 is the variation in the bubble's drag force (F_D), with large undulations being observed for all three bubbles. It is worth noting that drag force is over-estimated in the vicinity of the solid horizontal impact surface i.e. the bubble is subject to deceleration as it nears the surface. This is partially due to surface and viscous influences and not necessarily to a rapid increase in the drag force, as suggested by Figures 5.23 to 5.25.

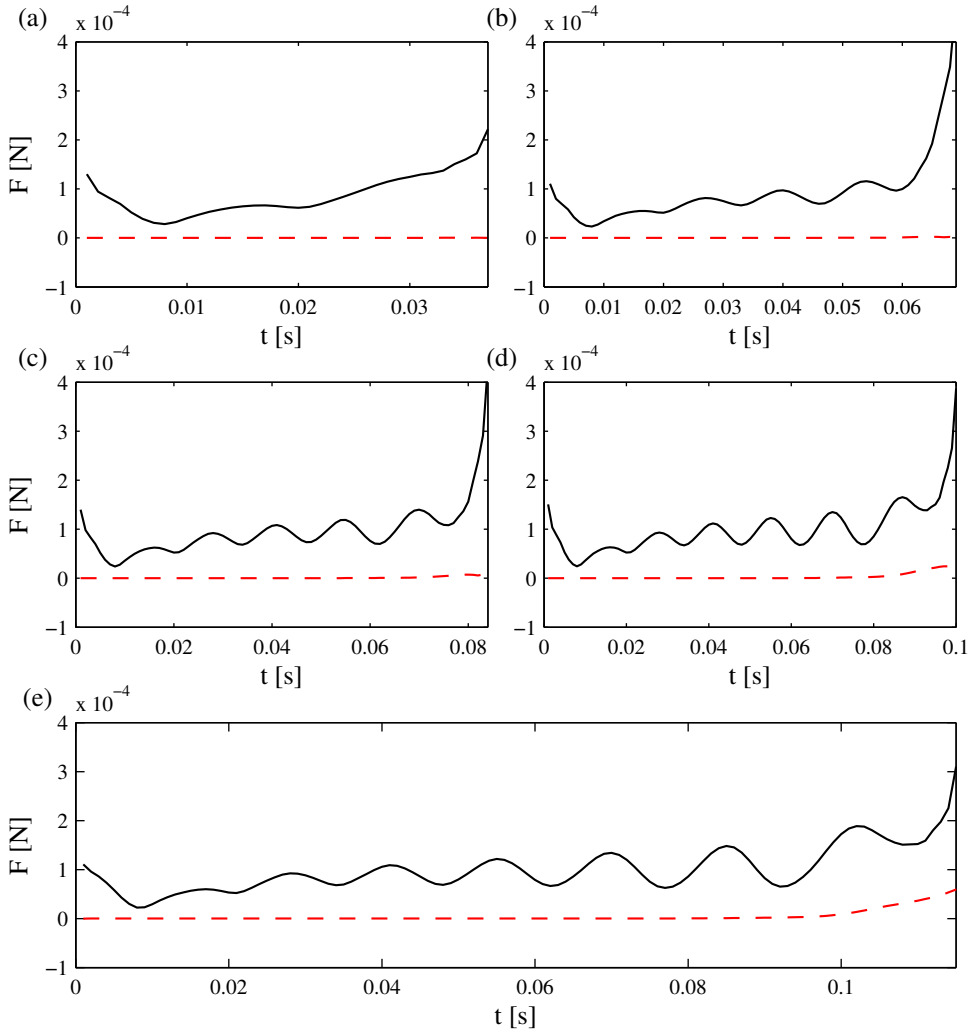

Figure 5.23: The time varying individual force components for a 2.8 *mm* bubble. The — solid line is the drag force F_D, the – – dashed line is the total lift force F_L, both in the laboratory coordinates. The five different release heights of 10, 20, 25, 30 and 35 *mm*, are shown in (a) to (e) respectively.

The frequency of undulations of the drag forces shown in Figures 5.23 to 5.25 is intrinsically linked to the frequency of rise velocity fluctuation illustrated in Figure 5.21; this link results from the change in both the bubble's aspect ratio and acceleration as indicated in Equations 4.10 through 4.14. The maximum drag forces[6] for bubbles of diameters 2.8, 3.3 and 4.1 *mm* are approximately 2×10^{-4} *N*, 6×10^{-4} *N*, and 10×10^{-4} *N*. These drag force magnitudes are difficult to compare to literature, mainly due to the absence of data for bubbles with equivalent diameters similar to those in the present experiment; also, the

[6]These values are approximate and are observed between times of 10%–90% of the maximum time.

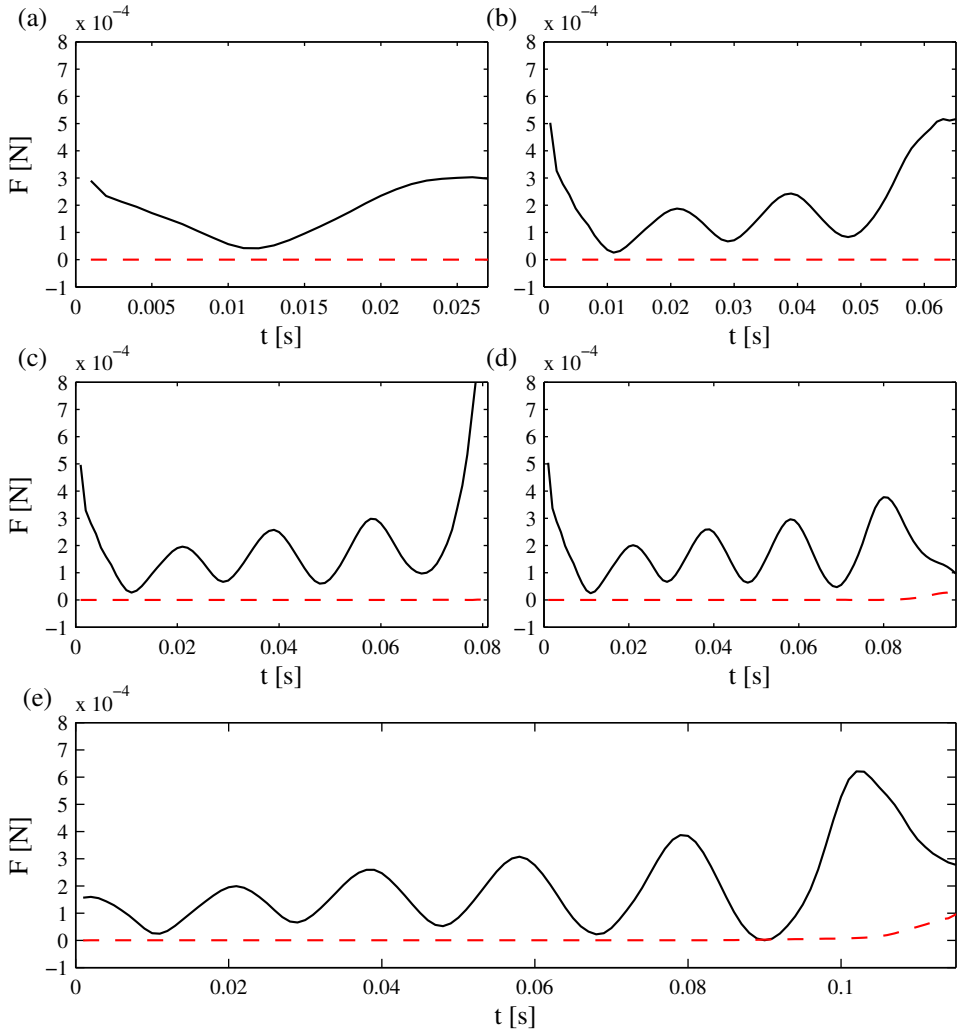

Figure 5.24: The time varying individual force components for a 3.3 *mm* bubble. The — solid line is the drag force F_D, the – – dashed line is the total lift force F_L, both in the laboratory coordinates. The five different release heights of 10, 20, 25, 30 and 35 *mm*, are shown in (a) to (e) respectively.

reduced release height hinders comparison.

Figure 5.26 illustrates the intrinsic link between the bubble's aspect ratio, acceleration and drag force for a 3.3 *mm* diameter bubble released 35 *mm* from the surface. The bubble's aspect ratio (χ) already varies between 0 – 1, as does the dimensionless drag force shown in Figure 5.26 (b). The bubble's acceleration is shown on the right axis. Figure 5.26 (a) illustrates the times when the bubble's acceleration becomes negative, indicated by grey vertical dashed lines; the bubble's shape is depicted at the relevant times. The art work depicting the bubble's shape is significantly exaggerated, for illustrative purposes. The drag

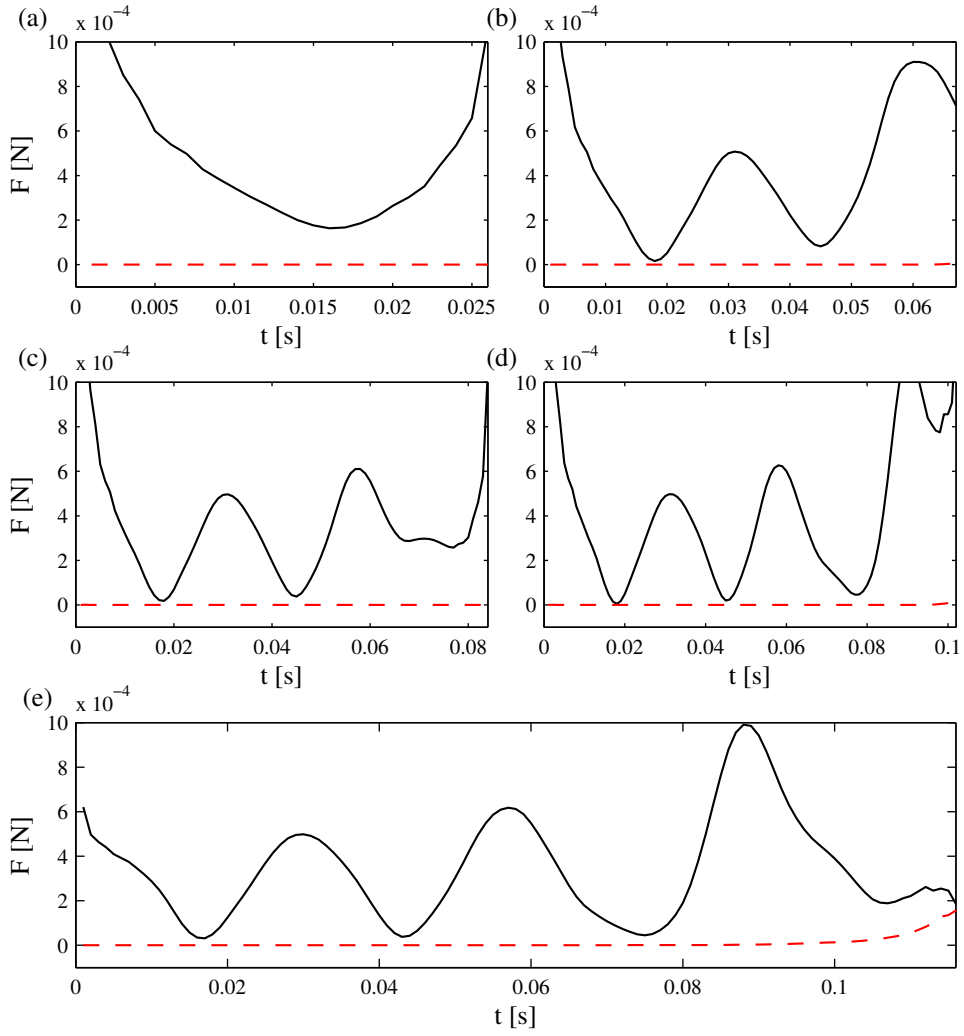

Figure 5.25: The time varying individual force components for a 4.1 *mm* bubble. The — solid line is the drag force F_D, the – – dashed line is the total lift force F_L, both in the laboratory coordinates. The five different release heights of 10, 20, 25, 30 and 35 *mm*, are shown in (a) to (e) respectively.

force, F_D, is non-dimensionalized using the following equation:

$$F_D = \frac{F_D}{F_{D_{max}}} \tag{5.7}$$

However, it must be noted that extreme values of the drag force, when the bubble is in the vicinity of the surface, are not used for non-dimensionalizing the data, just the maximum drag force within approximately 10% – 90% of the total rise period.

From Figure 5.26 (a) it is apparent that there is a strong link between the bubble's ver-

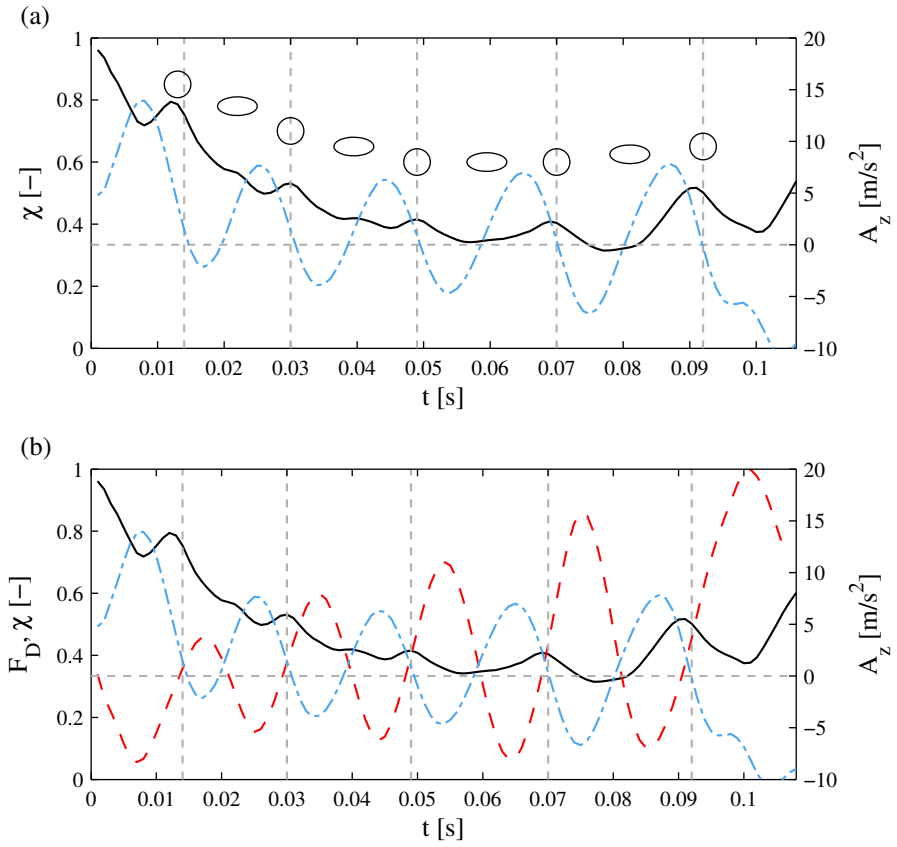

Figure 5.26: (a) time varying aspect ratio (— solid line) and acceleration (- – dot dash line) for a 3.3 *mm* bubble released from 35 *mm*. The vertical grey dashed lines indicates the times that the bubble's acceleration reverts to being negative. The horizontal grey dashed line indicates when the acceleration is zero, for clarity. The bubble's shape is depicted at each relevant stage, with this shape exaggerated for illustrative purposes. (b) is similar to (a) but the non-dimensionalized drag force (F_D, – – dashed line) is superimposed on top of the original data.

tical acceleration, A_Z, and its aspect ratio, χ. For example, at a time of around 0.03 *s*, the acceleration of the bubble is zero; this coincides with a local peak in aspect ratio. Similar observations can be made at times of 0.049 and 0.07 *s*. This zero acceleration is followed by a deceleration as the bubble flattens, sketched in Figure 5.26 (a). Once flattened, shape recovery begins, inducing a vertical acceleration of the bubble. This peaks just prior to the bubble becoming circular again; this again coincides with zero acceleration, from where the process repeats.

If the drag force experienced by the bubble is overlaid, as shown in Figure 5.26 (b), it is apparent that the bubble's acceleration is entirely dictated by the change in the aspect ratio and drag force. After a time of 0.03 *s* the bubble starts to experience a deceleration; this is

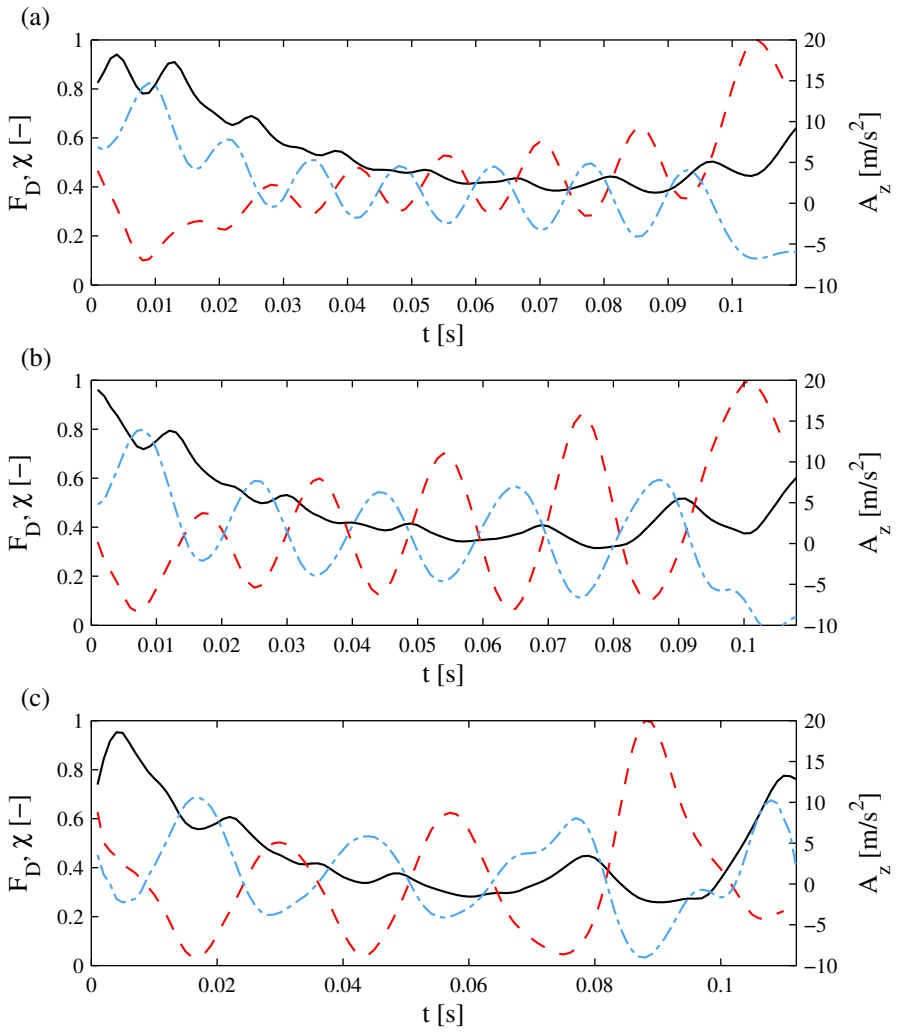

Figure 5.27: The time varying drag force, aspect ratio and acceleration for all three bubbles with release height of 35 *mm*. The — solid line is the variation in aspect ratio χ, the – – dashed line is the dimensionless drag force F_D and - - dot dash line is the vertical acceleration A_z. (a) is D_{eq} = 2.8 *mm*, (b) is D_{eq} = 3.3 *mm* and (c) is D_{eq} = 4.1 *mm*.

induced by a rising drag force, which peaks at an approximate time of 0.034 *s*. As the drag force reduces so does the deceleration. When the drag force is at a local minimum (0.044 *s*) the acceleration is at a local maximum. This phenomenon, whereby an interplay of forces and shape changes has been observed for all three bubble sizes, is more prevalent in the centre of the bubble's rise, where disturbance effects due to the injection and impact process are not noticeable. These disturbances are observed in Figure 5.26 (a), for the first and last grey vertical line, which are slightly shifted from the peak in aspect ratio at that time.

Figure 5.27 demonstrates the variation in drag force, aspect ratio and acceleration for all three bubbles with a release height of 35 *mm*. The same general trends are seen for all bubble sizes, consistent with the discussion associated with Figure 5.26. However, for the largest bubble slight discrepancies appear; these are believed to be related to the bubble rise instabilities discussed previously for this bubble size.

5.2 Bouncing Bubbles

As the bubble approaches the surface, with a velocity higher than its terminal velocity, symmetric deformation of the bubble occurs. Some initial deformation occurs, often prior to impact, which is evident on the upper surface of the bubble; this forms a bowl or cupped surface, trapping fluid between the bubble and the surface as shown in Figure 5.9 and also evident in Figure 5.11. The amount of cupping or dimpling was found to be a function of bubble diameter; the larger the bubble the more pronounced the dimpling. This dimpling effect is due to pressure differences within the regions encompassing the bubble and has been discussed by a number of authors, such as Zapryanov & Tabakova [111] and Tsao & Kock [21].

Once the bubble impacts the surface a further, significant amount of deformation occurs. This deformation depends on the bubble size, velocity and fluid properties. Upon impact, due to the bubble's high impact velocity, the bubble becomes quite flat and elongated, with a large surface area. The bubble then retracts from being an elongated unstable shape to that of a spherical bubble. This retraction causes the bubble to rebound from the surface, the maximum rebound distance depending on the bubble size, shape deformation and initial approach velocity. Once at a maximum rebound distance, its second approach occurs, followed by a further bounce. The number of bounces is variable and is influenced by the bubble size, impact velocity, fluid properties and impact surface properties. Subsequent to the bouncing event, the bubble may oscillate on the surface for some time before attaching and spreading along the surface.

In the present case, terminal velocity is not reached due to instabilities in the bubble's rise; this leads to a large fluctuation in the bubble's rise velocity. These fluctuations are influenced by the bubble's aspect ratio, which is continually varying, triggered by the re-

lease from the orifice. The next section will illustrate the influence these fluctuations in the bubble's rise velocity have on the impact process.

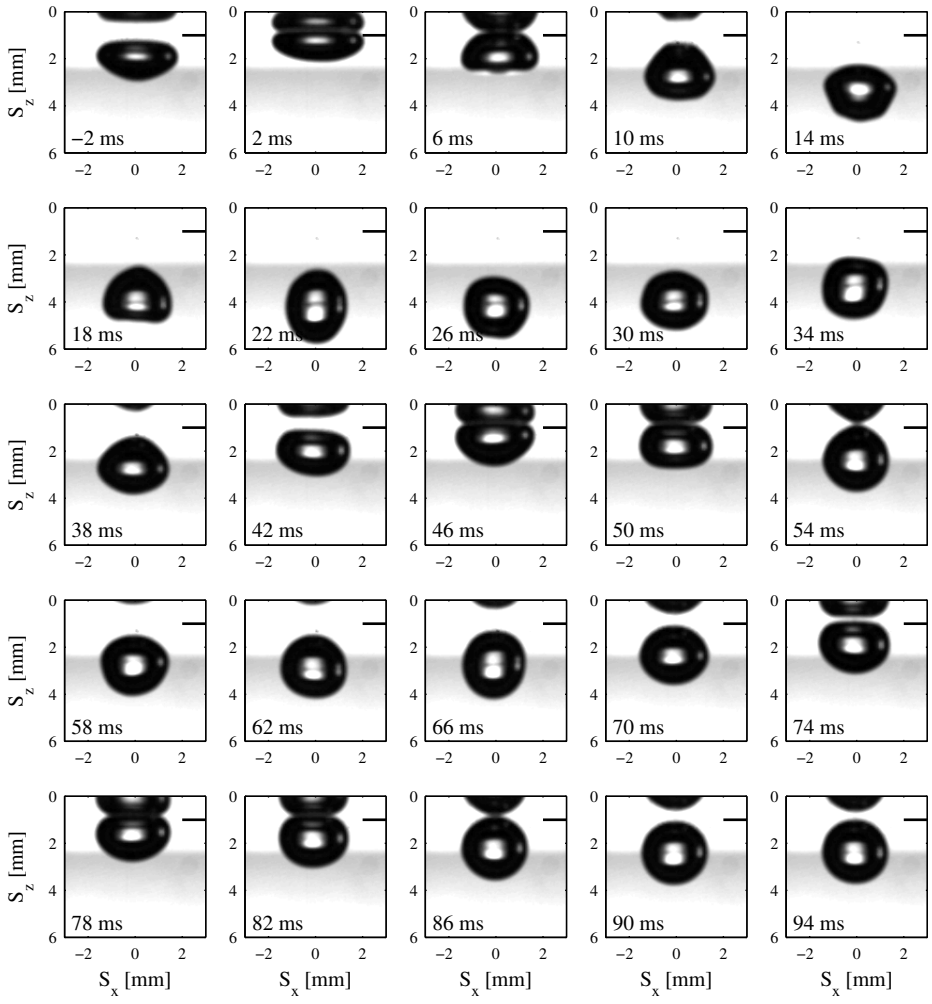

Figure 5.28: Image sequence for a 2.8 *mm* bubble with a release height of 10 *mm*. The time between images is 4 *ms*. On the right of each image a small horizontal line indicates the approximate location of the contact line.

5.2.1 Bubble Position & Shape

As the bubble approaches the surface, a thin liquid film forms between the bubble and the surface. Once the bubble impacts the horizontal surface, the bubble shape flattens considerably. The surface tension energy stored within the flattened bubble is partially converted

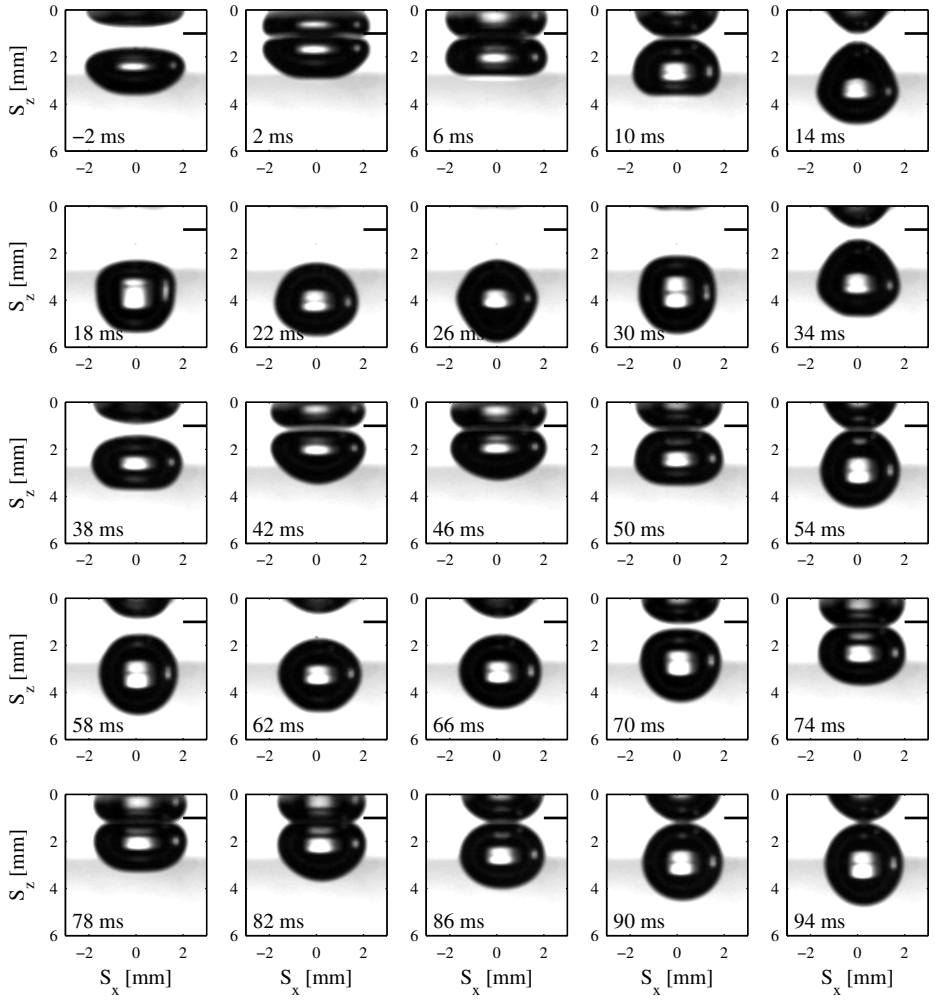

Figure 5.29: Image sequence for a 3.3 *mm* bubble with a release height of 10 *mm*. The time between images is 4 *ms*. On the right of each image a small horizontal line indicates the approximate location of the contact line.

to kinetic energy as the bubble springs back from the surface, the remainder being dissipated by acoustic, viscous and thermal means. During the rebound from the surface even more significant shape changes occur as the bubble tries to revert to a more spherical stable configuration.

As previously mentioned, upon approach the bubble's upper surface begins to dimple, once it is close to the surface[7]. As the bubble gets ever closer, the bubble begins to flatten

[7]The distance from the surface at which dimpling begins was found to be influenced by a number of factors, which include bubble size, centroidal velocity, aspect ratio, direction of tilt and release height.

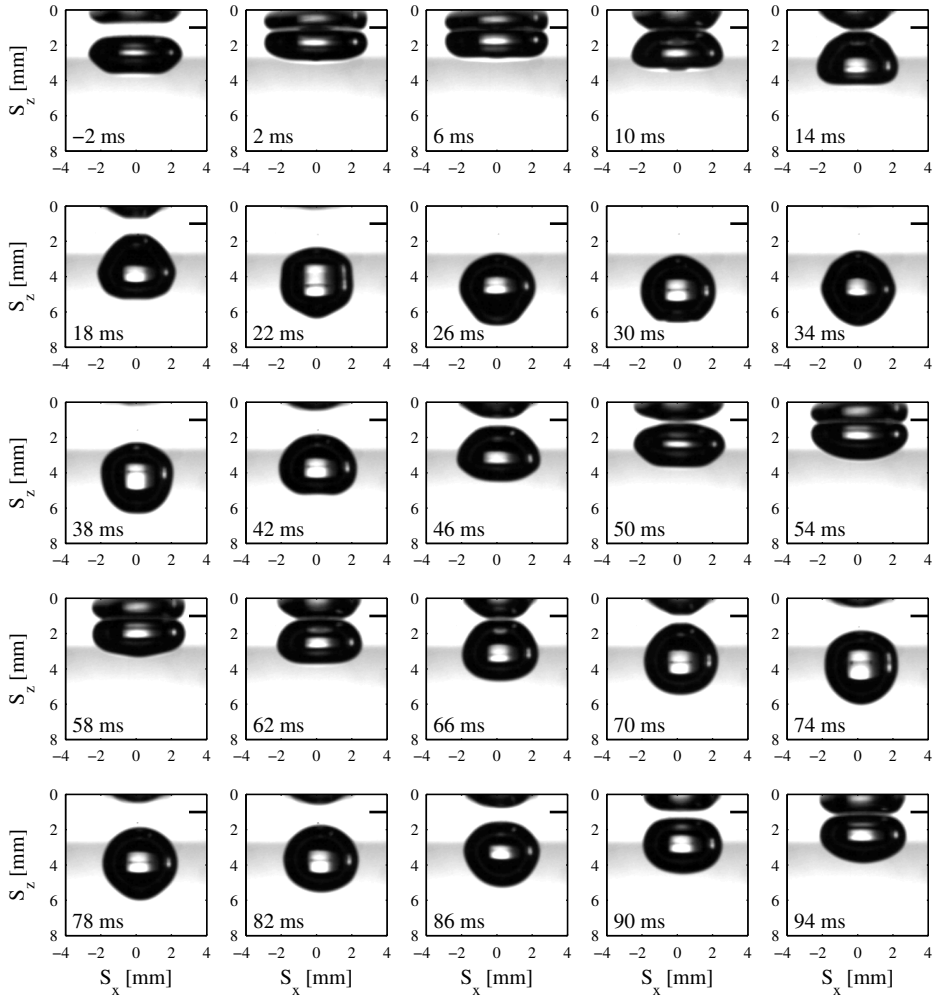

Figure 5.30: Image sequence for a 4.1 *mm* bubble with a release height of 10 *mm*. The time between images is 4 *ms*. On the right of each image a small horizontal line indicates the approximate location of the contact line.

even more, resulting from pressure variations, within the impact zone. This pressure variation is depicted in Figure 2.19 (Tsao & Kock [21]), with the pressure being the highest along the centre line of the bubble; this results in the bubble spreading to take up a large area upon impact. On impact with the surface, the bubble is not directly in contact with the surface; instead a film of liquid separates the bubble from the surface.

Manica *et al.* [112] and Hendrix *et al.* [62] experimentally established that this film can be as low as 3 – 4 μm in thickness, although this was for a bubble with a D_{eq} of approximately 0.7 *mm*; this is a very small and stable bubble, outside the scope of the present study.

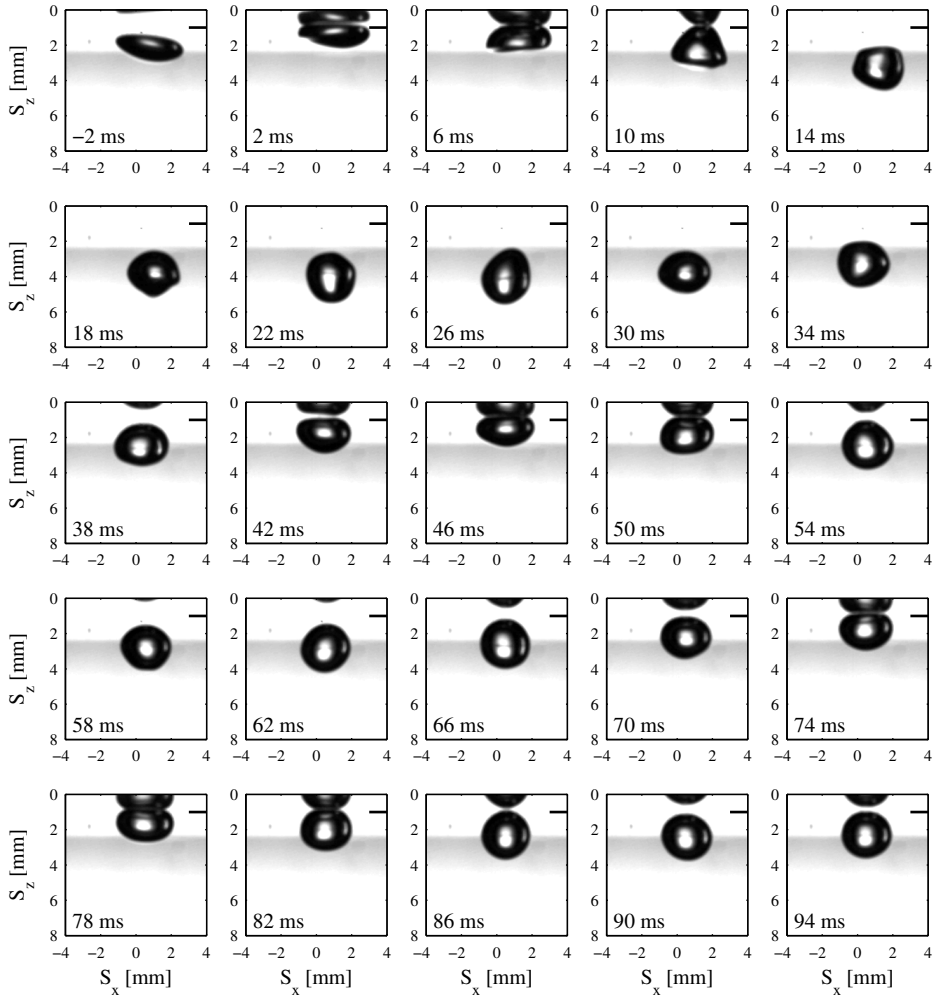

Figure 5.31: Image sequence for a 2.8 *mm* bubble with a release height of 25 *mm*. The time between images is 4 *ms*. On the right of each image a small horizontal line indicates the approximate location of the contact line.

The dimpling of the bubble's surface was visually observed for the current bubble sizes. The height of the dimple was found to be quite small for low release heights and bubble diameters, whereas the greater the release height the larger the dimple size[8].

The next stage of the bouncing process, after the initial impact, is the rebound stage. This involves the bubble recovering its shape, from that of a flat disk like bubble to a more spherical bubble. For very small bubbles, similar to those presented in literature, this is quite a stable process, however the larger the bubble, the larger the instabilities that can

[8]This is based on visual observations.

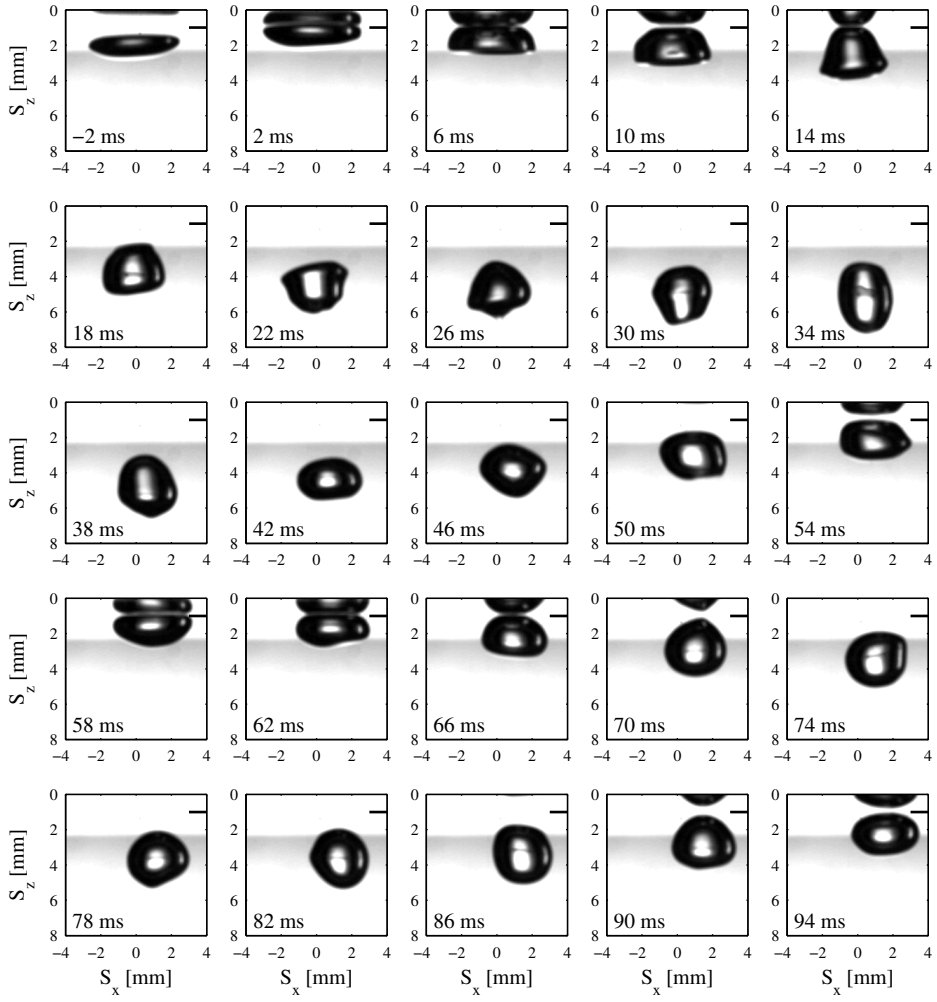

Figure 5.32: Image sequence for a 3.3 *mm* bubble with a release height of 25 *mm*. The time between images is 4 *ms*. On the right of each image a small horizontal line indicates the approximate location of the contact line.

occur; large instabilities were observed for the current experiments. Figures 5.28 to 5.30 illustrate the bouncing process for the three bubble sizes of 2.8 *mm*, 3.3 *mm* and 4.1 *mm*, for a single release height of 10 *mm*, respectively. A small black line (upper right corner of every image) indicates the approximate location of the surface in the plane, with the time after impact indicated on the lower left of each image[9].

The rebound process is quite unstable, with its stability and symmetry being related to the bubble size and the approach angle. When the bubble's major axis is aligned with the

[9]Note that the axes change dimensions between figures, so as to allow the maximum field of view.

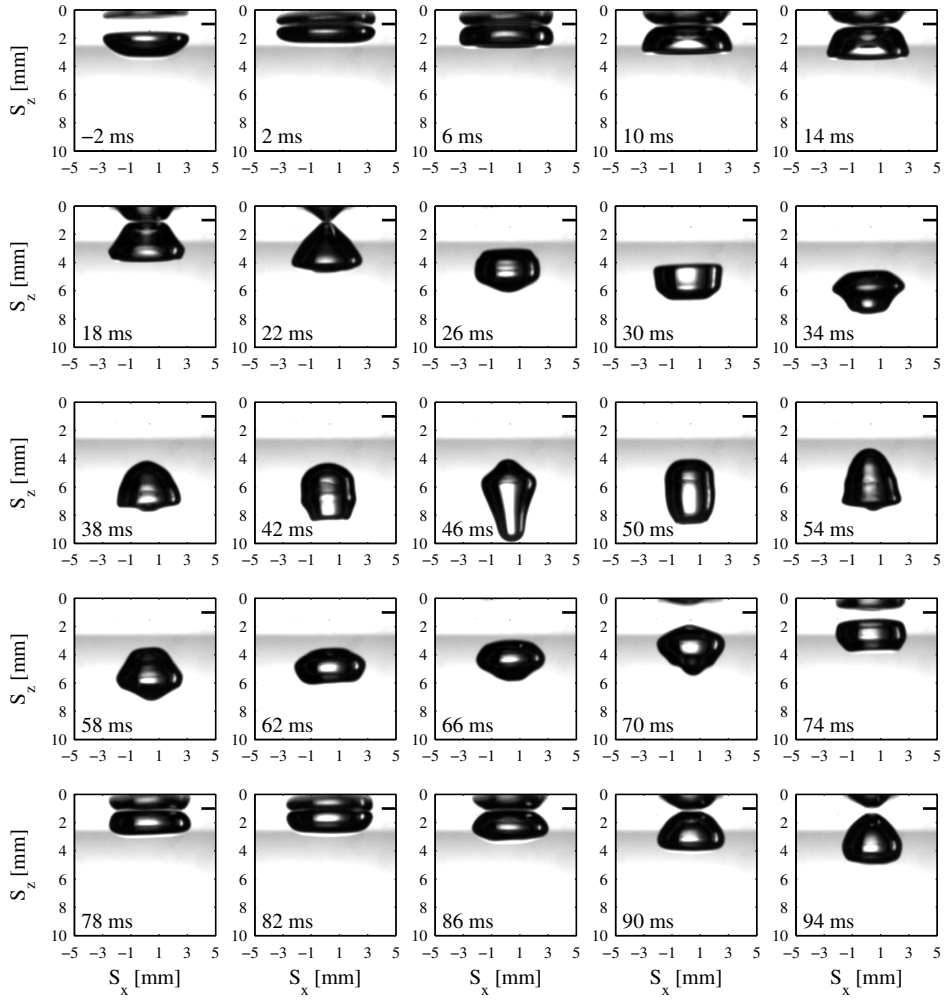

Figure 5.33: Image sequence for a 4.1 *mm* bubble with a release height of 25 *mm*. The time between images is 4 *ms*. On the right of each image a small horizontal line indicates the approximate location of the contact line.

horizontal plane, then the rise path is vertical, therefore making it likely that the bubble's rebound is symmetric[10]. This symmetrical rebound process is apparent in Figures 5.28 to 5.30, where the approach height is low, 10 *mm*, with only a small asymmetry being observed in Figure 5.28 for the smallest bubble.

As the rebound begins, a part of the surface energy is recovered back as kinetic energy. The bubble edges begin to recover first, as the center portion of the bubble incurred less

[10]Even a vertical rise path does not fully ensure that the rebound process will be symmetric, as surface impurities may affect the rebound process.

initial surface deformation during the initial impact. As the rebound develops, the central region lags slightly behind the bubble edges, which is thought to be due to an increased local pressure below the bubble. This causes the centre portion to lag, creating a cupped surface, opposite in form to the original dimple, before rapidly inverting. This inversion pulls in the edges of the bubble ahead of the central region, which can be observed in Figure 5.28 between times of 6 and 10 *ms*. This process occurs at different times depending on bubble diameter; this is at a time of 10 *ms*, 14 *ms* and 18 *ms* as depicted in Figures 5.28, 5.29 and 5.30, respectively. This process is followed by waves rippling up and down the bubble as it bounces further away from the surface, before reaching a maximum rebound distance. These waves continue, albeit less pronounced, as the bubble begins its next approach.

As the bubble begins its next approach, it again begins to flatten, although to a lesser extent than the initial impact. This is followed by the same sequence of events as the initial impact and rebound; however, variations in the bubble's aspect ratio are far less pronounced. For the first three cases illustrated (Figures 5.28 to 5.30), several bounces were observed: 4, 3 and 3 for the three different bubble sizes respectively. The final bounce was insignificant, as the bubble just left the surface.

After the initial bouncing period the bubble was found to oscillate on the surface for a period of time. This was followed by the bubble attaching to the surface, as the film of fluid separating the bubble from the surface breaks. This attachment process was difficult to observe; in some cases attachment began unevenly i.e. one side of the bubble began attachment before the other, this would cause the bubble to oscillate in the S_x or S_y direction.

Figures 5.31 to 5.33 illustrate the bouncing process for the three bubbles sizes of 2.8 *mm*, 3.3 *mm* and 4.1 *mm* respectively, for a single release height of 25 *mm*. While the bouncing process is broadly comparable to the lower height, a far less stable bouncing event occurs in all cases. As previously mentioned, with a low release height the bubble's major axis is horizontal and parallel to the surface. In contrast, bubbles released from a higher release height do not have major axes parallel to the surface; the smallest bubble has the largest tilt angle relative to horizontal, reducing with an increase in bubble diameter.

This change in major axis tilt angle and its effect on the bubble impact can be inferred from Figure 5.31, where a 2.8 *mm* bubble impacts the surface at an angle; the left hand side of the bubble contacts the surface first, followed by the right hand side. This, in turn,

dictates that the left hand side of the bubble is the first to depart from the surface, which causes asymmetric waves to propagate over the bubble's surface. What was also notable is the different degrees of flatness between the bubble images of Figures 5.28 and 5.31 at a time of -2 *ms*. The second bounce was found to be a more stable and symmetric process, again similar to that of the lower release height of 10 *mm*.

Figures 5.32 and 5.33 demonstrate the effect of increasing the release height for the larger bubbles, with some very unusual and complex bubble shapes being created as the bubble rebounds from the surface. At times of 46 *ms* and 54 *ms* in Figure 5.33, two peculiar shapes are formed; to the author's knowledge these shapes have not been reported previously in the literature. Through observation it is clear that the stability and symmetry of the bouncing process is related to the bubble size and, more importantly, the bubble's approach velocity, shape and tilt angle.

5.2.2 Aspect Ratio, Velocity & Position During Bouncing Process

In order to investigate some dynamics of the bouncing bubble process, Figures 5.34, 5.35 and 5.36 illustrate the time varying bubble vertical position (S_z), aspect ratio (χ) and the bubble's vertical velocity (V_z) for rise heights of 10 *mm*, 25 *mm* and 30 *mm* respectively. The data sets are constructed from the images presented in Figures 5.28 to 5.30 (for 10 *mm* rise height) and 5.31 to 5.33 (for 25 *mm* rise height). The time of zero refers to when the bubble makes initial contact with the surface. In order to display the bubble's vertical centroidal position, the data for both release heights are non-dimensionalized using the following equation:

$$S_z = \frac{S_z - S_{z,max} + 10}{10} \tag{5.8}$$

This allows the bubble's position to vary between 0 – 1. For instance, if the position of the bubble is shown at a height of 0.7, this would indicate that the centroidal position of the bubble is 3 *mm* away from its highest point. This highest point, $S_{z,max}$, is the maximum centroidal position of the bubble, which depends on the bubble diameter. Similarly, a height of 0.8 indicates that the bubble is 2 *mm* away from the surface.

Figure 5.34 illustrates that the maximum rebound distance for the bubbles is: 2.75 *mm*,

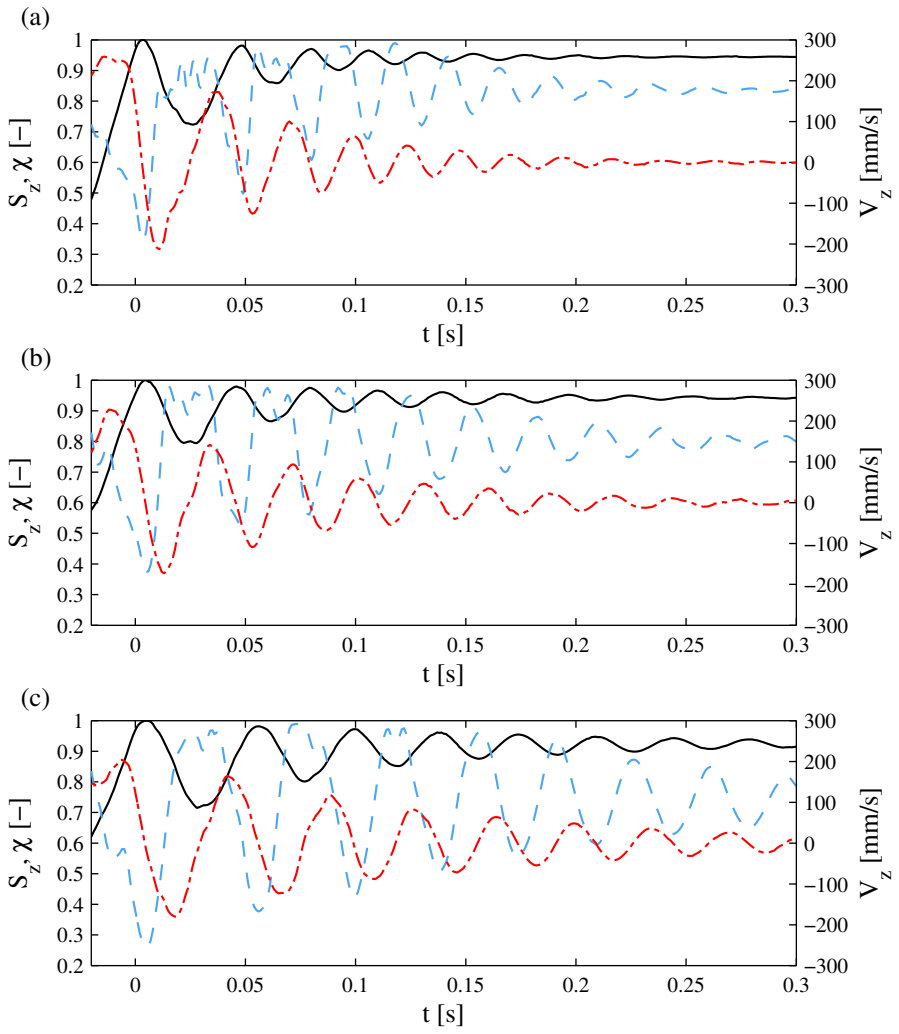

Figure 5.34: The time varying position (S_z), aspect ratio (χ) and centroidal rise velocity (V_z) for the three different bubble diameters, with a release height of 10 *mm*. The — solid line is the non-dimensionalized position, the – – dashed line is the aspect ratio and - – dot dash line is the rise velocity. A time of zero refers to the moment when the bubble first comes in contact with the surface. (a) D_{eq} = 2.8 *mm*, (b) D_{eq} = 3.3 *mm* and (c) D_{eq} = 4.1 *mm*.

2 *mm* and 2.8 *mm* for the 2.8 *mm*, 3.3 *mm* and 4.1 *mm* bubbles, respectively. Similarly the maximum rebound velocities for the three cases are 203 *mm/s*, 169 *mm/s* and 180 *mm/s*, respectively. These maximum rebound velocities were found to have significant variation, being dependent on the impact velocity, shape changes and impact angle. Another notable feature is the bubble's aspect ratio just immediately after impact ($t \approx 0$ *s*), with the largest bubble having the lowest aspect ratio. The maximum rebound distance (S_z) occurs at similar times of: 0.025 *s*, 0.025 *s* and 0.031 *s* for the bubbles of diameter 2.8 *mm*, 3.3 *mm* and 4.1

mm respectively. What is notable is the rapid fluctuations in aspect ratio, centred around the first peak in S_z, with fewer fluctuations being observed as the bubble size increases.

Both the 2.8 *mm* and 3.3 *mm* bubble, as seen from Figure 5.34 (a) and (b), respond quite similarly, with the peaks in the bubble's vertical position being closely aligned. However, for the 4.1 *mm* bubble the period between peaks is longer. This was also reflected in the settling time[11], this being approximately 0.25 *s* for the 2.8 *mm* bubble, 0.3 *s* for the 3.3 *mm* and 0.45 *s* for the 4.1 *mm* bubble.

Figure 5.35 illustrates comparable data for the three bubbles for a release height of 25 *mm*. There is a significant difference in bubble behaviour between the two release heights of 10 *mm* and 25 *mm*; this can be inferred from the variation in the bubble's dimensionless height, during the initial bounce process. In general, the bubbles bounced further away from the surface, due to the increased release height. Similarly, it was found that the bubbles took longer to settle, with settling times of 0.25 *s*, 0.42 *s* and 0.55 *s*, the 2.8 *mm*, 3.3 *mm* and 4.1 *mm* bubble, respectively. The smallest bubble was found to have the same settling time as at the lower release height. However, for the larger bubbles as the release height is increased, so too is the time for the bubble to settle. This may be related to the larger instabilities created upon impact. For both the 3.3 *mm* and 4.1 *mm* bubble, fluctuations in the bubble's velocity can be observed during the first bouncing event; the same trend is evident in both plots but to different degrees. This is perhaps related to the unusual shape changes observed in both Figures 5.32 and 5.33 at times centred around 30 *ms* and 42 *ms*.

Figure 5.36 illustrates comparable data for the three bubbles for a release height of 30 *mm*. In this case, the most noticeable difference when compared to the 25 *mm* release height is the significantly reduced rebound distance. This indicates that significantly more bubble deformation occurs upon impact, which reduces the bubble's rebound height. In Figures 5.34 to 5.36, and as shown earlier in Figures 5.16 and 5.18, the rise velocity for each bubble size is very similar just prior to impact, with an increase of between 50 – 100 *mm/s* with increasing release height. This point being discussed further in Section 6.3.

Equation 5.9 is utilized to compare the bubble velocity before and after the collision process, with $V_{depart,max}$, being the maximum rebound velocity and $V_{rise,max}$, being the max-

[11]The time at which the bubble has settled is defined as when the vertical velocity, S_z, is approximately zero and no longer oscillating.

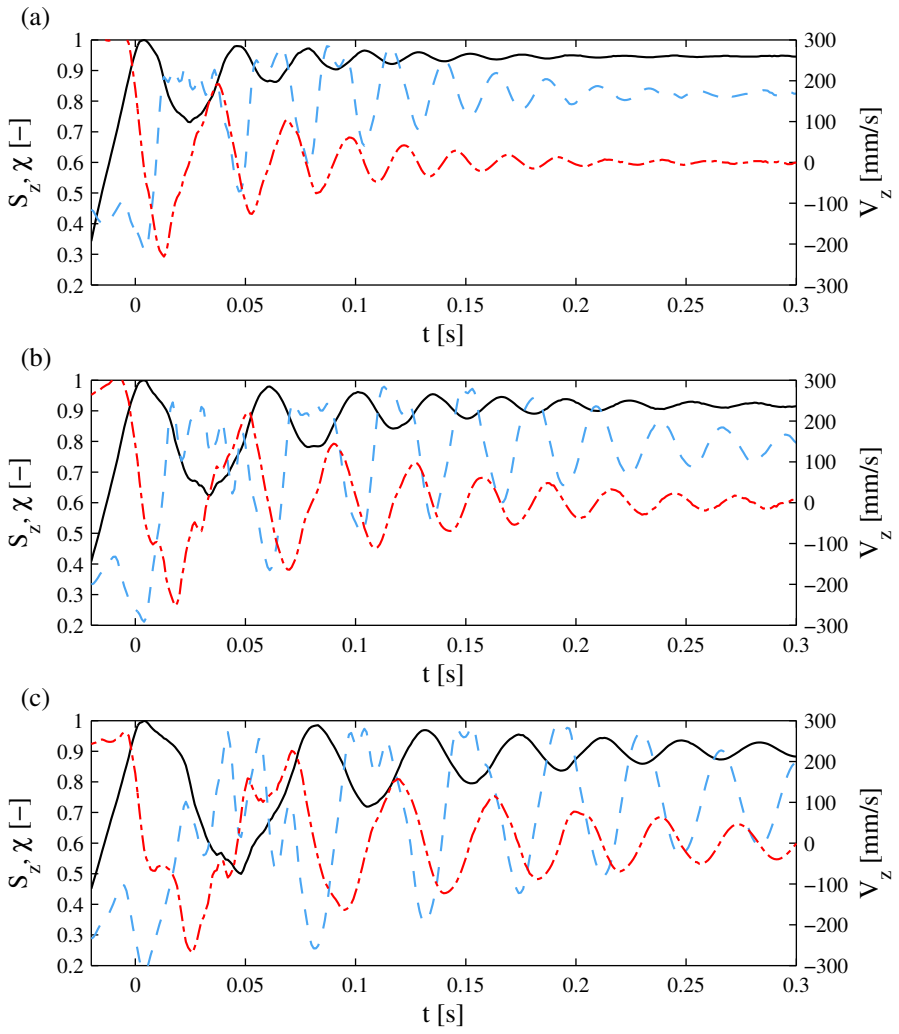

Figure 5.35: The time varying position (S_z), aspect ratio (χ) and centroidal rise velocity (V_z) for the three different bubble diameters, with a release height of 25 *mm*. The — solid line is the non-dimensionalized position, the – – dashed line is the aspect ratio and - – dot dash line is the rise velocity. A time of zero refers to the moment when the bubble first comes in contact with the surface. (a) D_{eq} = 2.8 *mm*, (b) D_{eq} = 3.3 *mm* and (c) D_{eq} = 4.1 *mm*.

imum approach or rise velocity. These values were chosen as reference values. The terminal velocity would be the more usual reference velocity but, as referred to earlier, terminal velocity is not achieved in the present study. A value of one indicates that the bubble has achieved the same departure velocity as approach velocity, i.e. the coefficient of restitution is one.

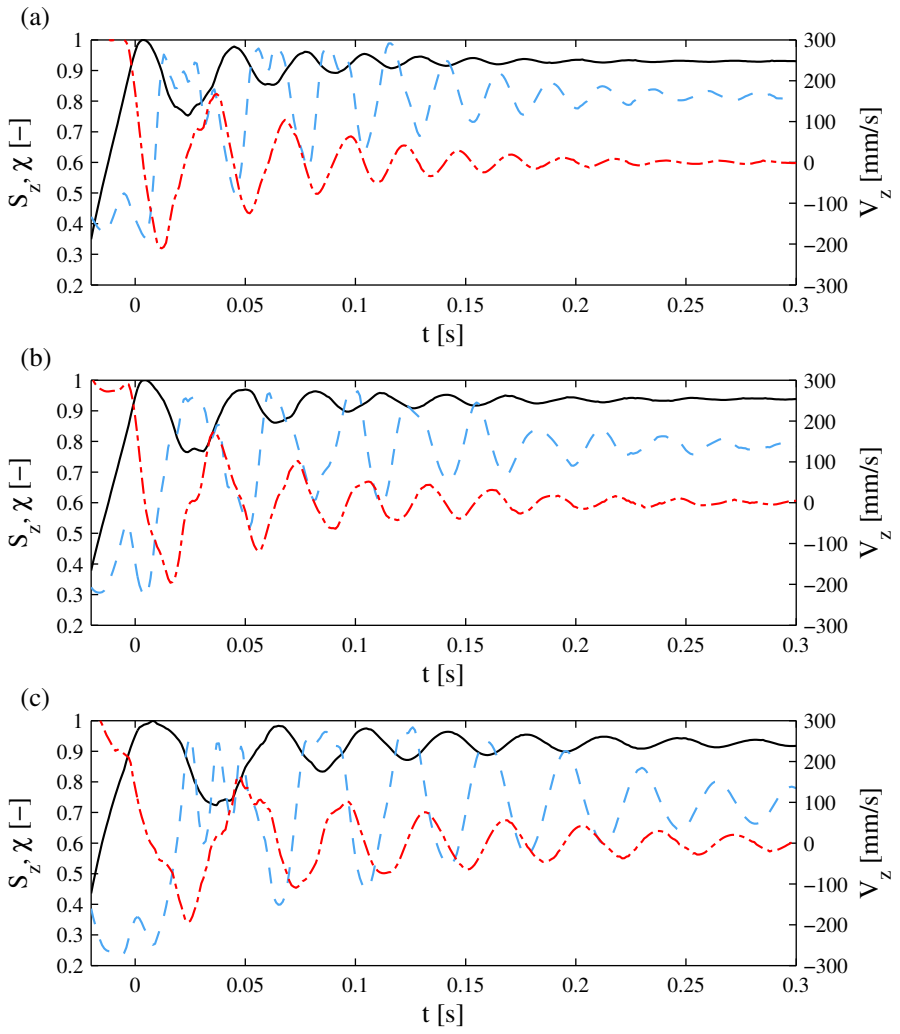

Figure 5.36: The time varying position (S_z), aspect ratio (χ) and centroidal rise velocity (V_z) for the three different bubble diameters, with a release height of 30 *mm*. The — solid line is the non-dimensionalized position, the – – dashed line is the aspect ratio and - – dot dash line is the rise velocity. A time of zero refers to the moment when the bubble first comes in contact with the surface. (a) D_{eq} = 2.8 *mm*, (b) D_{eq} = 3.3 *mm* and (c) D_{eq} = 4.1 *mm*.

$$\varepsilon = -\frac{V_{depart,max}}{V_{rise,max}} \tag{5.9}$$

Figure 5.37 illustrates the coefficient of restitution for all three bubble diameters and all five release heights. It can be seen from Figure 5.37 that for the lower release heights there is a higher coefficient of restitution, whereas the greater the release height the lower the coefficient of restitution.

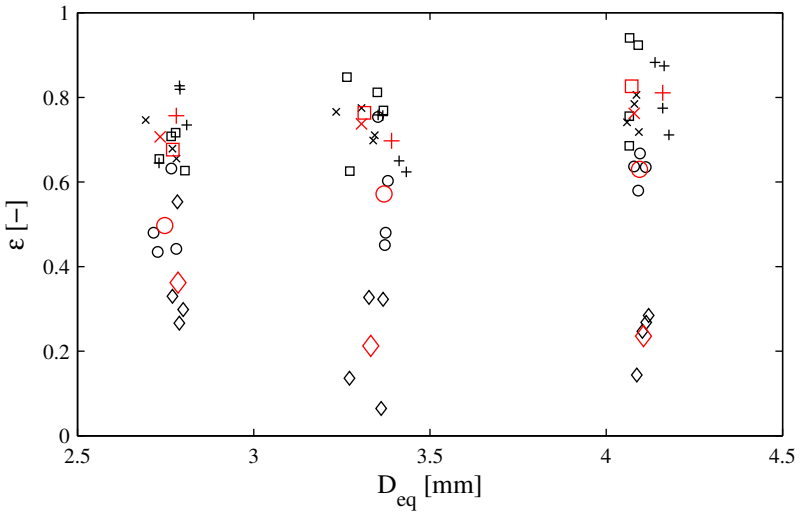

Figure 5.37: Coefficient of restitution, (ε) versus bubble equivalent diameter (D_{eq}) for each experiment in clean water. The five different heights are represented as follows: + is 10 *mm*, × is 20 *mm*, □ is 25 *mm*, ○ is 30 *mm* and ◇ is 35 *mm*. The larger red symbols represent the average for each individual height. The different bubble diameters can be inferred from the data.

Some of the lowest values of ε are, in fact, due to the bubble slowing down and inverting just prior to impacting the surface; which was mentioned earlier. However, the overall trend indicates that more of the bubble's kinetic energy is dissipated into bubble surface deformation for the larger release heights. This is consistent with the images shown in Figures 5.28 to 5.33, with the bubbles being flatter for the larger release heights.

5.3 Closing Remarks

This chapter has examined the motion of three different sized bubbles released from five different release heights, in both clean and contaminated water. Firstly, the bubble rise through the test section has been investigated, with important aspects such as the bubble's shape and rise path being identified. Secondly, the motion of each bubble as it impacts a solid horizontal surface is analysed, with important features and parameters being presented.

With regard to the rise path, this was found to be vertical up to a height which increased with increasing bubble diameter; beyond this height, the bubble would tilt, changing its direction. The angle of tilt was found to decrease with respect to increasing bubble size.

The bubble's aspect ratio was found to decrease during its rise, with regular oscillations being observed. Similarly these oscillations were present in the bubble's vertical velocity component. The frequency of these oscillations has been measured and compared for both clean and contaminated water. An exponential decrease in frequency was observed for an increase in bubble size, with very little variability between the two water conditions. The source of the oscillation was proposed to be a result of the injection process.

The relationship between the bubble's aspect ratio, acceleration and the forces which act on the bubble, was investigated next. The reference frame was converted to the Frenet-Serret frame of reference for the determination of the forces which act on the bubble. A plausible explanation was given with respect to the influence the drag force has on the rising bubble with regards to the changing aspect ratio.

The final section of this chapter described the motion of the bubble as it impacts and rebounds from a horizontal surface. The impact event was presented for all three bubble sizes and two release heights. It was shown that the bounce event was sensitive to the bubble size, the release height and also the approach angle of tilt. Similarly it was observed that the greater the release height the longer it took for the bubble to fully settle on the surface.

Chapter 6

Bouncing Bubble Local Heat Transfer

This chapter presents the local variation in surface temperature and convective heat flux associated with a single air bubble ($2.8 \leq D_{eq} \leq 4.1$ mm) rising through distilled water (for rise heights of 10, 20, 25, 30 and 35 mm) before impacting and rebounding from a horizontal heated surface.

Firstly, the liquid natural convection will be presented, with measured values compared to commonly referenced correlations. This is followed by the variation in both the maximum and minimum dimensionless surface temperature, as the bubble rises, impacts and bounces on the surface; this is presented for the full time period from when the bubble leaves the orifice up until the end of the recorded sequence of 8 s*. This is then followed by an investigation into the variation in convective heat flux as the bubble impacts the surface. In order to fully explore the complex convective heat transfer associated with the bouncing process, point locations on the surface are chosen, with the temporal variation in the convective and stored heat flux, along with the surface temperature, being presented. The final stage is the presentation of the maximum and minimum heat flux values for all the test conditions, along with their time of occurrence.*

This chapter serves as a detailed introduction to the complex bouncing bubble heat transfer enhancement. The following chapter will discuss the convective heat transfer process due to the bubble's wake.

6.1 Natural Convection

When a surface is heated, a relative movement of fluid takes place between the bulk colder fluid and the warmer fluid adjacent to the surface. A downward facing surface has the disadvantage of impeding the natural buoyancy effect, where warm rising fluid is impeded by the surface; this results in the fluid moving horizontally along the surface before ascending and or descending (if constrained) beyond the edge of the surface. As noted by Incropera *et al.* [82], this form of natural convection is somewhat ineffective in terms of transferring energy to the bulk fluid. In the present study the heated surface is submerged by 3 *mm* (depicted in Figure 3.1), thereby restricting the ascension of warm fluid. This limits the free convection flow and associated heat transfer. Circulation may occur although, due to the short test duration, this effect it is likely to be very limited; this was confirmed by PIV testing.

A number of Nusselt number correlations exist for downward facing heated surfaces, although most relate to constant surface temperature boundary conditions instead of constant heat generation. Incropera *et al.* [82] presents the following correlation:

$$\overline{Nu}_L = 0.27 Ra_L^{1/4} \qquad (10^5 \leq Ra_L \leq 10^{10}) \tag{6.1}$$

where the Rayleigh number is defined in terms of a characteristic length, L_c, which, for a horizontal plate is defined as

$$L_c = \frac{A_s}{P} \tag{6.2}$$

where, A_s is the surface area and, P is the surface perimeter.

For the present study the surface boundary condition is approximated as constant heat generation, thereby meaning that Equation 6.1 is not directly applicable. Also, Equation 6.1 assumes that there is infinite bulk fluid, whereas for the present study, the bulk fluid is restricted within the small test enclosure and by the movable injection platform. Similarly, the test surface itself is not square, which again inhibits fluid flow in one direction.

$$\overline{Nu}_L = 0.58 Ra_L^{1/5} \qquad (10^6 \leq Ra_L \leq 10^{11}) \tag{6.3}$$

Equation 6.3, experimentally established by Fujii & Imura [113], evaluates the fluid properties at a modified film temperature defined as $T_s - 0.25(T_s - T_\infty)$ and determines the volumetric thermal expansion coefficient, β, at the standard film temperature. Summation tables of available literature by Radziemska & Lewandowski [114] and Khalifa [115] demonstrate the significant variation in available correlations, with most correlations being evaluated for either circular or square downward facing, inclined and horizontal plates.

A study by Su *et al.* [116] for a downward-facing horizontal circular heated surface in water with a variable confinement gap, shows the effect of confinement. Correlations were developed, however, significant variations in experimental data were noted, demonstrating that accurate and consistent Nusselt number correlations are difficult to obtain for this configuration. From the study by Su *et al.* [116] two main correlations are recommended, which are as follows:

$$\overline{Nu}_L = 0.01037 Ra_L^{0.4264} \qquad (10^3 \leq Ra_L \leq 10^9) \tag{6.4}$$

$$\overline{Nu}_L = 0.006721 Ra_L^{0.4264} Pr^{0.4378} \qquad (10^3 \leq Ra_L \leq 10^9) \tag{6.5}$$

In the present study the foil was heated by means of a constant current power supply, which provided the surface with a constant current of $30.6\,A$. This gave a surface temperature of approximately 50°C, although this varied slightly depending on the bulk fluid temperature, which was around $23°C$. The experimentally generated heat flux is approximately 8.2 kW/m^2, when losses to the surroundings by conduction to the stagnant air layer above and by radiation, are accounted for. This gives an experimentally determined natural convection heat transfer coefficient of around 300 W/m^2K.

Table 6.1: Natural convection heat transfer for downward facing horizontal surfaces.

Equation	Ra [-]	$\overline{Nu}_L$ [-]	h_{corr} $[W/m^2K]$	$1 - \frac{h_{act}}{h_{corr}}$ [%]
Eq. 6.1	6.0×10^6	13.37	446	32.7
Eq. 6.3	6.5×10^6	13.38	451	33.5
Eq. 6.4	6.0×10^6	8.06	269	-11.5
Eq. 6.5	6.0×10^6	10.21	340	11.8

Table 6.1 compares the measured experimental heat transfer coefficient to that obtained

from correlations in the literature. Equations 6.1 and 6.3 do not account for restricted geometries as reflected in the higher heat transfer predictions. However, Equations 6.4 and 6.5 do account for confinement, while the latter includes the Prandtl number dependence on fluid temperature, to further refine the correlation. The experimentally measured heat transfer coefficients from the present study lie within $\pm 12\%$ of the values predicted by Equations 6.4 and 6.5; this is consistent with the experimental uncertainty.

6.2 Surface Temperature Variation (Spatial & Temporal)

In this section, the effect on surface temperature due to the bubble's motion will be discussed, with the later sections discussing convective heat transfer to the fluid. Firstly, the surface temperature variation for the duration of the experiment will be analysed, with both the maximum and minimum surface temperature being presented in a dimensionless format, indicated by Equation 6.6.

$$T_m = \frac{T_{s,t=n} - T_\infty}{T_{s,t=0} - T_\infty} \tag{6.6}$$

$T_{s,t=n}$ is the surface temperature at each time step, from $t = 0$ to $t = 8\ s$, $T_{s,t=0}$ is the surface temperature at the beginning of the test and T_∞ is the bulk fluid temperature. The temporal variations in the maximum and minimum surface temperature are not geometrically locked to one location on the surface, but both temperatures relate to the most extreme temperature at a particular instant in time ($t = n$). Increases in T_m are indicative of decreased heat transfer whereas decreasing T_m is indicative of increased local heat transfer. During all of the experiments the bulk water temperature was found to have an average value of $23.3^\circ C$ with a standard deviation of $2^\circ C$; this variation is due to the small volume of the tank, especially with the release height of 10 *mm*. This slight variation in bulk temperature over the duration of all the experiments in turn dictates the approximate surface temperature, which also varied slightly.

6.2.1 Case 1: 2.8 *mm* Bubble

Figures 6.1 and 6.2 plot the maximum and minimum dimensionless wall temperature histories from the time at which the bubble was released from the orifice to the end of the recording, which is 8 *s*. Figure 6.1 relates to a 2.8 *mm* diameter bubble with a 25 *mm* release height whereas Figure 6.2 shows data for a 2.8 *mm* diameter bubble released 30 *mm* below the surface. As previously mentioned, increases in T_m are indicative of decreasing heat transfer whereas decreasing T_m indicates improved local heat transfer. From Figure 6.1, three regions have been identified with regard to the coupling of the fluid mechanics and the heat transfer. The first regime corresponds to heat transfer due to natural convection to water alone (Regime *I*). This regime extends from when the bubble departs from the orifice until the bubble impacts the heated surface[1]. As mentioned, T_m is unity across the foil so that $T_{max} = T_{min} = 1$ during the bubble release rise phase. The second regime extends from when the bubble has initially impacted the surface until it becomes attached to the surface (Regime *II*). This attachment time was determined from the moment the surface temperature began to rise, indicating that the liquid film separating the bubble from the surface had broken. In some cases the attachment process may be visually observed, although this is not always clear, especially for smaller bubbles. The final regime (Regime *III*) starts once the bubble has attached to the surface and extends until the point at which the foil has again reached steady state i.e. natural convection (Regime *I*). This may not be achieved by the end of the 8 *s* test period. This chapter will focus on the effect of the bouncing bubble regime (Regime *II*), while Chapter 7 will focus on investigating the fluid motion by means of PIV. This section will focus on the temperature change for the larger release heights of 25 *mm* and 30 *mm*. Similar T_m profiles occur for the lower release heights, however, for the 10 *mm* release height, T_m, rarely dips below 0.7 during the bouncing period.

The natural convection regime lasts approximately 0.1 *s*, corresponding to the bubble rise time with marginal differences between Figures 6.1 and 6.2, which is consistent with different bubble rise times. The first major difference between Figures 6.1 and 6.2 is the bouncing time, which is the time period when bubble is bouncing and/or oscillating on the surface. The bouncing time is approximately 0.113 *s* and 0.076 *s*, for the 25 *mm* and 30

[1]Mild changes in temperature were found to occur approximately 5 *ms* prior to impact.

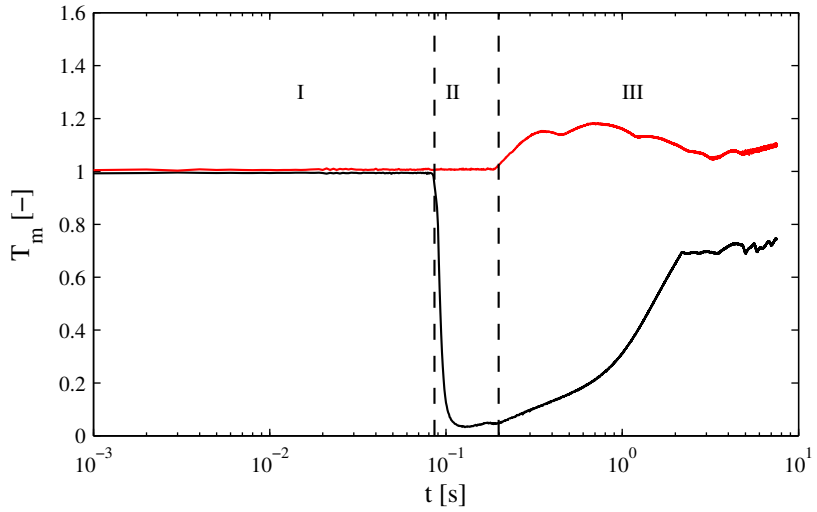

Figure 6.1: Minimum surface temperature (— black) and maximum surface temperature (— red) for a 2.8 *mm* bubble, released from a height of 25 *mm*. (*I*) is the liquid natural convection regime, (*II*) bouncing bubble regime, (*III*) bubble attachment to the surface, with this region relating to the bubble's wake interacting with the surface heated surface and to fluid motion around the stable bubble.

mm rise heights, respectively. This difference is a result of the variation in the rise path with release height, with the bubble in Figure 6.2 impacting the surface at a greater tilt angle, causing more bounce instabilities and surface deformation. This, in turn, reduces the bubble's bounce height and number of bounces observed.

In both cases the maximum temperature (T_{max}) shows similar trends, with a sharp rise upon attachment[2] with the surface at the beginning of regime *III*. This is followed by a couple of small peaks, with the only difference between Figures 6.1 and 6.2 being the more defined local peaks in Figure 6.1. This may be related to greater and more defined bubble oscillations for the lower release height, while the bubble is attached to the surface. In both cases, the time scale associated with the temperature rise in regime *III* is very similar.

The minimum temperature (T_{min}) plots again are remarkably similar in both cases, with both displaying a very slight double dip at the intersection of regime *II* and *III*. This is followed by a larger, more pronounced dip in the middle of regime *III*, mainly evident in Figure 6.2. Within regime *III*, at approximate start times of 2 *s* (for 25 *mm*) and 3.5 *s* (for

[2]Attachment is defined when the thin layer of fluid separating the bubble from the surface breaks, thereby beginning the attachment process.

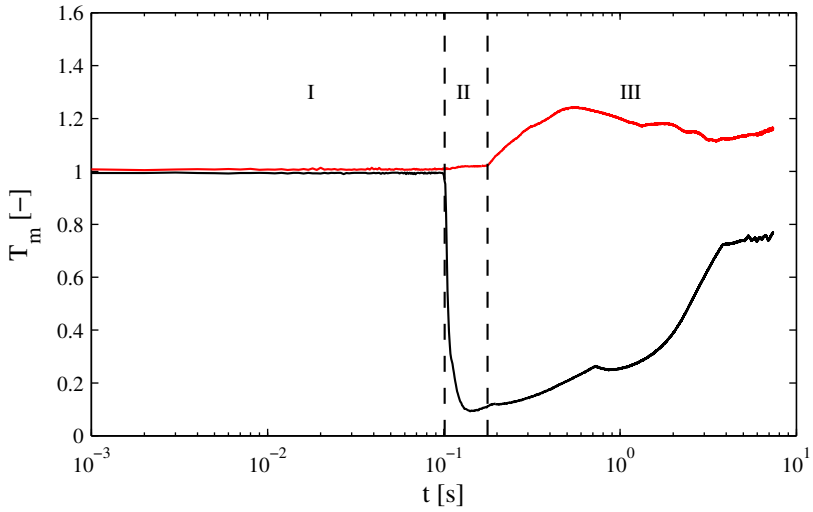

Figure 6.2: Minimum surface temperature (— black) and maximum surface temperature (— red) for a 2.8 *mm* bubble, released from a height of 30 *mm*. (*I*) is the liquid natural convection regime, (*II*) bouncing bubble regime, (*III*) bubble attachment to the surface, with this region relating to the bubble's wake interacting with the surface heated surface and to fluid motion around the stable bubble.

30 *mm*), a plateau occurs, with minute undulations; this is present for the remainder of the experiment.

6.2.2 Case 2: 3.3 *mm* Bubble

Figures 6.3 and 6.4 illustrate the maximum and minimum dimensionless surface temperature for a 3.3 *mm* bubble, again with release heights of 25 *mm* and 30 *mm*, respectively. These graphs show a notable increase in the bouncing time, when compared to the smaller bubble of Figures 6.1 and 6.2. A sharp drop in temperature is noted at approximately 7 *s* in both figures. This is due to the power supply being switched off prematurely and does not affect the observed trends as this chapter is focused primarily on the direct bouncing of the bubble (Regime *II*).

It is clear from Figures 6.3 and 6.4 that the maximum dimensionless observed temperature for the 3.3 *mm* bubble is significantly higher than that associated with the 2.8 *mm* bubble. This is perhaps due to the increased bubble size, which would inherently have a larger footprint once the bubble is attached to the surface. Once the maximum tempera-

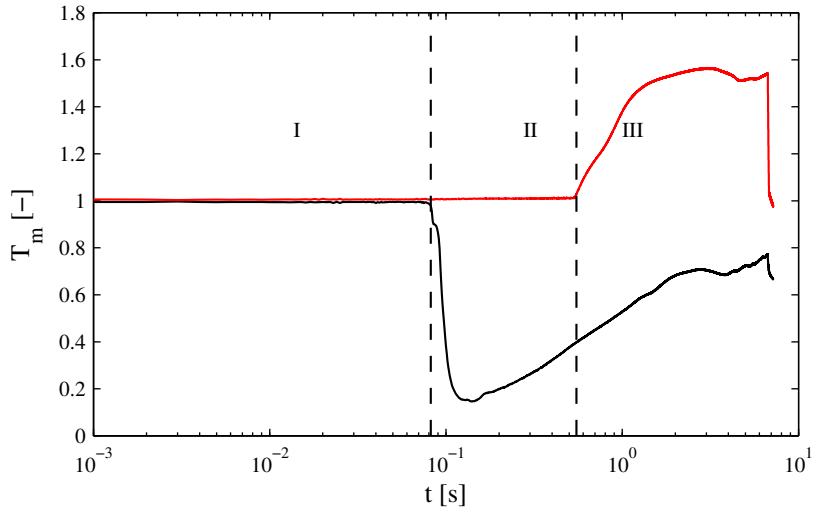

Figure 6.3: Minimum surface temperature (— black) and maximum surface temperature (— red) for a 3.3 *mm* bubble, released from a height of 25 *mm*. (*I*) is the liquid natural convection regime, (*II*) bouncing bubble regime, (*III*) bubble attachment to the surface, with this region relating to the bubble's wake interacting with the surface heated surface and to fluid motion around the stable bubble.

ture is reached, Figures 6.3 and 6.4 show that this stays relatively constant, with smaller undulations when compared to the 2.8 *mm* bubble.

The most noticeable difference between the 2.8 *mm* and 3.3 *mm* bubbles is the significant increase in time for the bubble bouncing event (Regime *II*). The bouncing duration is 0.47 *s* for the 25 *mm* height and 0.35 *s* for the 30 *mm* height, increases of 76% and 78% respectively relative to the smaller 2.8 *mm* bubble. However, when the small bubble was deemed to be attached to the surface, it was observed that it continued to move very slowly in the direction of motion that had prevailed prior to attachment; this did not occur with the larger bubbles. The variation in minimum surface temperature (T_{min}) was found to be entirely related to the rising bubble motion and whether the bubble's major axis tilted, causing the bubble's path to veer in random directions.

6.2.3 Case 3: 4.1 *mm* Bubble

Figures 6.5 and 6.6 illustrate the maximum and minimum dimensionless wall temperatures for a 4.1 *mm* bubble, with release heights of 25 *mm* and 30 *mm* respectively. For this large

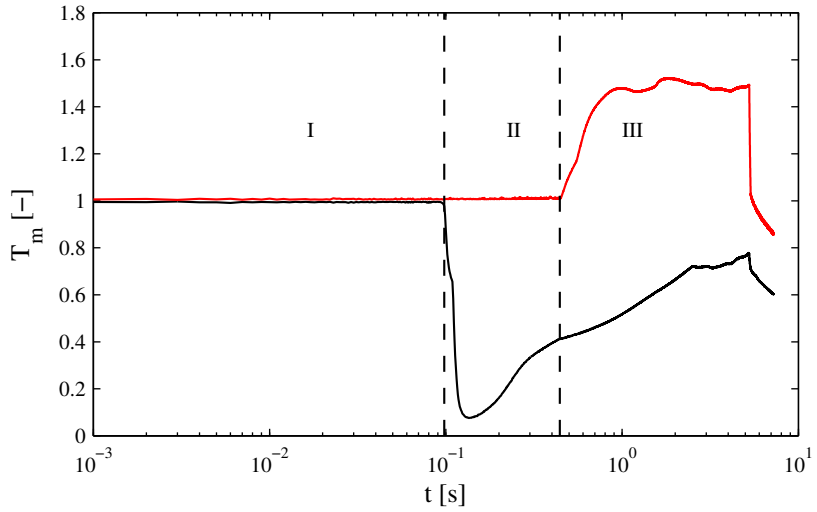

Figure 6.4: Minimum surface temperature (— black) and maximum surface temperature (— red) for a 3.3 *mm* bubble, released from a height of 30 *mm*. (*I*) is the liquid natural convection regime, (*II*) bouncing bubble regime, (*III*) bubble attachment to the surface, with this region relating to the bubble's wake interacting with the surface heated surface and to fluid motion around the stable bubble.

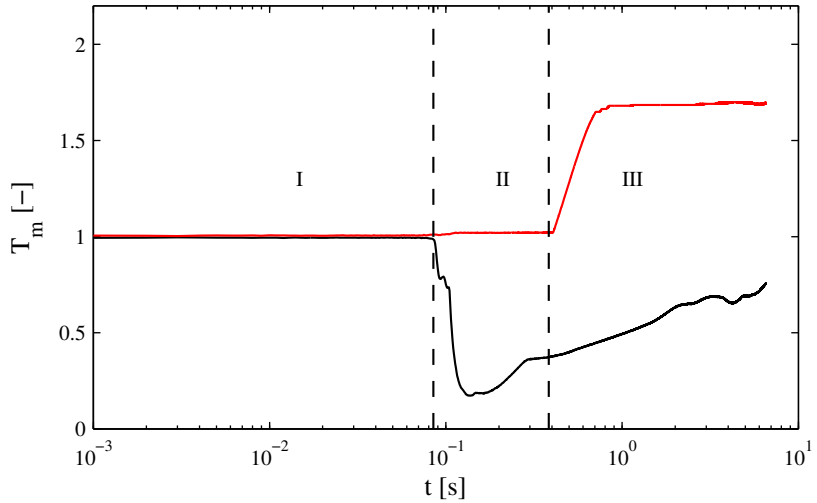

Figure 6.5: Minimum surface temperature (— black) and maximum surface temperature (— red) for a 4.1 *mm* bubble, released from a height of 25 *mm*. (*I*) is the liquid natural convection regime, (*II*) bouncing bubble regime, (*III*) bubble attachment to the surface, with this region relating to the bubble's wake interacting with the surface heated surface and to fluid motion around the stable bubble.

bubble, T_{max} was found to saturate the infrared camera; this is due to the low integration time which was set at 0.8 *ms*, which results in a maximum observable temperature of $67°C$. This explains the uniform distribution of T_{max} for much of the regime *III*. As the present focus is on regime *II*, this camera saturation was deemed acceptable; an increased integration time would reduce the sensitivity of the experiment and provide less information on the important temperature changes during the bouncing sequence.

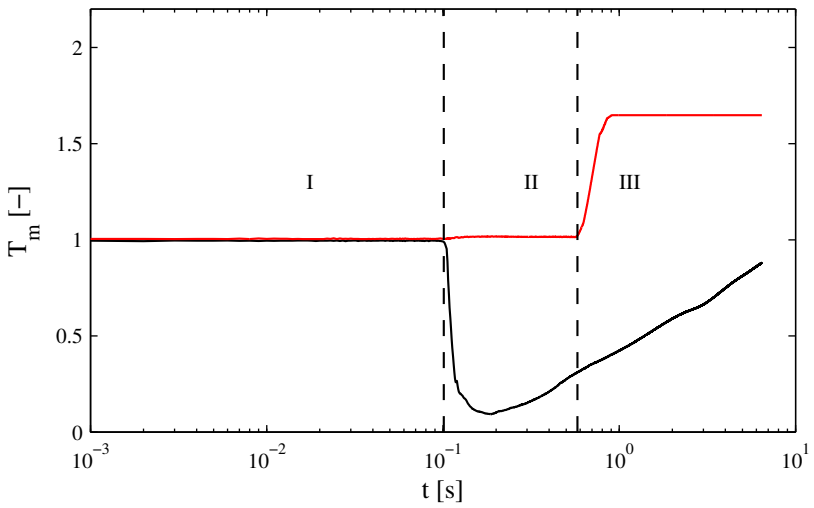

Figure 6.6: Minimum surface temperature (— black) and maximum surface temperature (— red) for a 4.1 *mm* bubble, released from a height of 30 *mm*. (*I*) is the liquid natural convection regime, (*II*) bouncing bubble regime, (*III*) bubble attachment to the surface, with this region relating to the bubble's wake interacting with the surface heated surface and to fluid motion around the stable bubble.

In Figures 6.5 and 6.6 the minimum surface temperature plots exhibit the same general trends but with a significantly larger temperature drop and settling time for the 30 *mm* release height. Overall, the 4.1 *mm* bubble showed more variability in surface temperature data over the range of tests than either of the smaller bubbles. The most significant variation is in regime *III*, which occurs after the bubble has attached to the surface. This regime was found to be a complex and unsteady process, which in a majority of the experiments could be split into two further regimes; this is discussed further in Chapter 7.

6.3 Local Heat Flux Variation (Spatial & Temporal)

In order to evaluate the complex process of heat flow associated with a bubble impacting the heated surface, the instantaneous bubble motion will be coupled with the instantaneous convective heat flux, with images shown at 4 *ms* intervals. Results are shown here for the three bubble sizes and for four release heights of 10, 20, 25 and 30 *mm*. In these images, the time at which the bubble initially impacts the surface is taken at the new reference time of 0 *ms*. Note also that the heat flux map limits vary between figures, so as to capture significant changes. The figures shown here may not reflect the maximum or minimum values encountered, which will be explored in a later section.

6.3.1 Case 1: 2.8 *mm* Bubble

Figures 6.7 to 6.10 illustrate the initial impact and subsequent rebound of a bubble with an equivalent diameter of 2.8 *mm* released from heights of 10, 20, 25 and 30 *mm*, respectively. The instantaneous convective heat flux is coupled with the location and shape of the bubble as it impacts and bounces upon the horizontally heated surface. The time separation between image pairs is 4 *ms*. The heat flux scale is displayed above each figure and varies depending on the particular data.

Figure 6.7 illustrates the impact and two subsequent bounces of a 2.8 *mm* bubble upon the surface, for a release height of 10 *mm*. The second bubble impact with the surface occurs at a time of approximately 32 *ms* (Figure 6.7 (i)), whereas in Figures 6.8 to 6.10 for the longer release heights this second impact of the small bubble occurs at approximately 36 *ms*. This process is influenced by the bubble approach velocity and the bubble's coefficient of restitution, as was illustrated in Figure 5.37. The third impact is only observable in Figure 6.10 at a time of 56 *ms*, with the tests with shorter release heights experiencing the third impact at a time later than 56 *ms*.

It is clear from the convective heat flux maps shown in Figures 6.7 to 6.10 that substantial and distinct variation in convective heat flux occurs; this is considered to be related to the bubble's shape and the deformation which occurs at impact and during the bouncing events that follow. From Figure 6.7 for the 10 *mm* release height, the bubble's shape and the resulting convective heat flux maps were found to be symmetric both vertically and horizontally;

this is a consequence of the approach shape and major axis angle of the bubble, which was parallel to the surface upon impact. In turn, the bubble's rebound was found to be symmetric but with significant surface oscillations, relatively evenly distributed over both sides of the bubble's surface. It can be inferred from Figure 6.7 that the convective heat flux has distinct regions of both high and low enhancement; in some cases a region of high enhancement at one instant in time can exhibit particularly low convective heat flux at a later instant.

The maximum convective heat flux in this case (Figure 6.7) occurs at an approximate time of between 2 – 4 *ms* and was found to be localised annularly at the extremities of the bubble upon impact; this is primarily attributed to the bubble ploughing through the thermal boundary layer. This ploughing has not been observed in the literature for bouncing bubbles, although a similar situation exists for sliding bubble motion beneath a downward facing heated surface. Qiu & Dhir [7] and Manickam & Dhir [8, 9] utilised holographic interferometric to measure the local fluid temperature, which demonstrated the fluid motion ahead of the sliding bubble as well as the unsteady wake at the bubble's rear.

The central region, which is located beneath the bubble, was found to have a substantially lower convective heat flux when compared to the edges of the bubble. This is perhaps due to the cupping of the bubble upper surface upon approach to the surface, as noted by Zapryanov & Tabakova [111] and Tsao & Kock [21] and observed in the present study. This results from a viscous effect, trapping fluid between the deformable bubble and the rigid boundary. As the bubble approaches the surface, the bubble must displace fluid in order to rise; this results in higher pressure at the leading edge of the bubble, which has the effect of pushing fluid to regions of lower pressure. This dimpling, in effect, protects the surface from the direct impact of the bubble, thereby resulting in a lower observed convective heat flux in the centre of the affected region. During the bubble rise fluid is displaced ahead of the bubble, which might be expected to increase convective heat flux prior to the bubble directly impacting the surface. In this instance a slight enhancement is shown in Section 6.2, due to the small temperature changes.

At a time of 8 *ms* in Figure 6.7 (c), after the initial impact, an annular region of negative heat flux may be observed, at the location of a region of previously high heat flux. This type of heat transfer event coincides with the beginning of the bubble's rebound from the surface. This ring of negative heat flux steadily moves towards the centre of the test section, as the

bubble continues its rebound from the surface. Similarly, a region of low heat flux may be observed at a time of 32 *ms* as the bubble re-impacts the surface; this is believed to be warm fluid re-impacting the surface, as a result of the bubble's impact. At a time of 56 *ms* the heat flux levels are quite low when compared to the high levels achieved upon impact. However, although difficult to observe from the images, the convective heat flux is still higher than that of liquid natural convection, as the bubble continues to bounce and oscillate on the heated surface.

When Figure 6.7 is compared to Figures 6.8 to 6.10 for higher release heights of 20, 25 and 30 *mm*, it is clear that in those cases the bubble's approach path is at an angle, with the tilt increasing in severity with increasing release height. This tilt was referred to in Chapter 5 and found to be related to the bubble size and release height, with its direction being random. If the bubble's major axis is not parallel with the surface this usually indicates that the bubble's rise path is not vertical, but rather deviates on its final approach, as illustrated in Figures 5.1 to 5.10. The major axis tilt angle varies in Figures 6.8 to 6.10, with Figures 5.12 and 5.13 having already demonstrated that with increasing release height there is an increase in the major axis angle; the smaller bubble is more susceptible to this variation.

This tilt angle significantly affects heat transfer, both in terms of spatial and temporal variation as well as the overall degree of enhancement. In Figure 6.8, a 2.8 *mm* bubble is released from a height of 20 *mm*; when compared to the 10 *mm* release height, substantial variations in convective heat flux levels occur. At a time of 4 *ms*, the lower release height has a maximum convective heat flux following impact of 73 kW/m^2 whereas the release height of 20 *mm* has a maximum impact heat flux of 55 kW/m^2.

Once the bubble begins to rebound from the surface, again low levels of localised negative heat flux can be observed in Figure 6.8. To the left of the impact zone a region of high heat transfer develops between the times of 8 – 28 *ms*. Heat flux levels in this region far exceed that of the initial impact and are not directly related to the impact of the bubble but to the wake which follows the bubble during its rise. This wake flow will be discussed in more detail in Chapter 7. The pattern of heat transfer enhancement in Figure 6.8 is broadly similar to that of Figure 6.7, although in this case the pattern is symmetric along the direction of bouncing motion, which is at an angle along the surface.

During the rebound process the bubble with the higher release height undergoes far

greater and more unstable shape changes, as detailed in Figures 5.28 to 5.33. This is determined by a combination of impact velocity and impact angle. On the bubble's second approach to the surface (Figure 6.8 (h), 28 *ms*), a region of low heat flux was observed for the lower release height in Figure 6.7, but in Figure 6.8 for the height of 20 *mm*, a small region of positive enhancement can be observed at a time of 36 *ms*. This region of localised positive enhancement may be due to the bubble returning to the surface and convecting cool fluid towards the surface, with its absence in the lower release height perhaps a result of the bubble only convecting warm boundary layer fluid, rather than cool bulk water. For lower release heights the vertical bubble motion dictates that bubble rebounds back in the direction it has come from, thereby halting and disturbing rising cool fluid, which is continually rising due to its momentum. In the case of path deviation, the rebound is usually away from the rise path of the bubble, thereby not significantly disturbing the rising cool fluid; this point will be further analysed in Chapter 7, when the wake will be explored. At the beginning of the second bouncing event low convective heat flux can be observed, as the bubble's motion drafts in warm boundary layer fluid. This is similar to the initial annular region of negative heat flux, during the first rebound.

Figures 6.9 and 6.10 depict the bouncing event for a 2.8 *mm* bubble released from heights of 25 and 30 *mm*, respectively. In both cases the bubble tilt has increased compared to the lower heights, which results in a slight variation in the heat transfer patterns. As the bubble approach is at an angle, it follows that the impact process varies from left to right in the case of Figure 6.9. As the bubble impacts, the convective heat flux increases from left to right, again in an annular fashion. This is followed by the bubble peeling away from the surface, again starting from the left, resulting in a ring of low negative heat flux (Figure 6.9 (c), 8 *ms*) in the region which was previously subjected to localised high heat flux. The maximum heat flux observed during the impact process was approximately 65 kW/m^2, which was followed for a very brief period by a negative heat flux of approximately -5 kW/m^2.

The enhancement due to the bouncing motion in this case is again overshadowed by the effect of the wake, which impacts on the left hand side of the bubble, with a maximum value of approximately 200 kW/m^2 at a time of 6 *ms*. This wake begins to surround the impact zone in a "c" shape, as the bubble retreats from the surface. When comparing the retreating bubble's shape in Figure 6.9 to that of Figures 6.7 and 6.8, it is noticeable that the bubble's

shape is asymmetric in the S_x plane, as a result of the uneven impact event. This in turn causes the bubble to bounce along the surface, away from the main impact zone. Notably, at the bubble re-impact time of 36 *ms*, a region of higher heat flux is again present; this is followed by a period of low heat flux as the bubble begins its second bounce, which was similarly observed for the 20 *mm* release height.

Figure 6.10 displays a far less regular heat transfer event, with the bubble impacting at a higher major axis tilt, while bouncing a more significant distance away from the initial impact zone. Despite the fact that the bubble's initial impact is unstable, at a time of 12 *ms* the rebound event is quite stable; this is perhaps due to the bubble losing significantly more kinetic energy to impact deformation. The maximum convective heat flux due to the direct impact of the bubble is approximately 70 kW/m^2, with a negative heat flux of approximately -12 kW/m^2 at 12 *ms*. This is thought be due to the faster initial rebound from the surface, which pulls warm fluid atop the previously cooled annular region; this will be discussed further in Section 6.4 and in Chapter 7. Again, the ensuing wake provides the most significant enhancement in this case, reaching a maximum value of 210 kW/m^2. At a time of 28 *ms* in Figure 6.10 (h) a second zone of high heat flux appears at a position of S_x = 2 *mm*. This separation of the rising wake has been observed for rising bubbles by Sanada *et al.* [49] shown in Figure 2.14 and Figure 2.13 by Veldhuis [28], with this being fully discussed in Section 7.2.2.

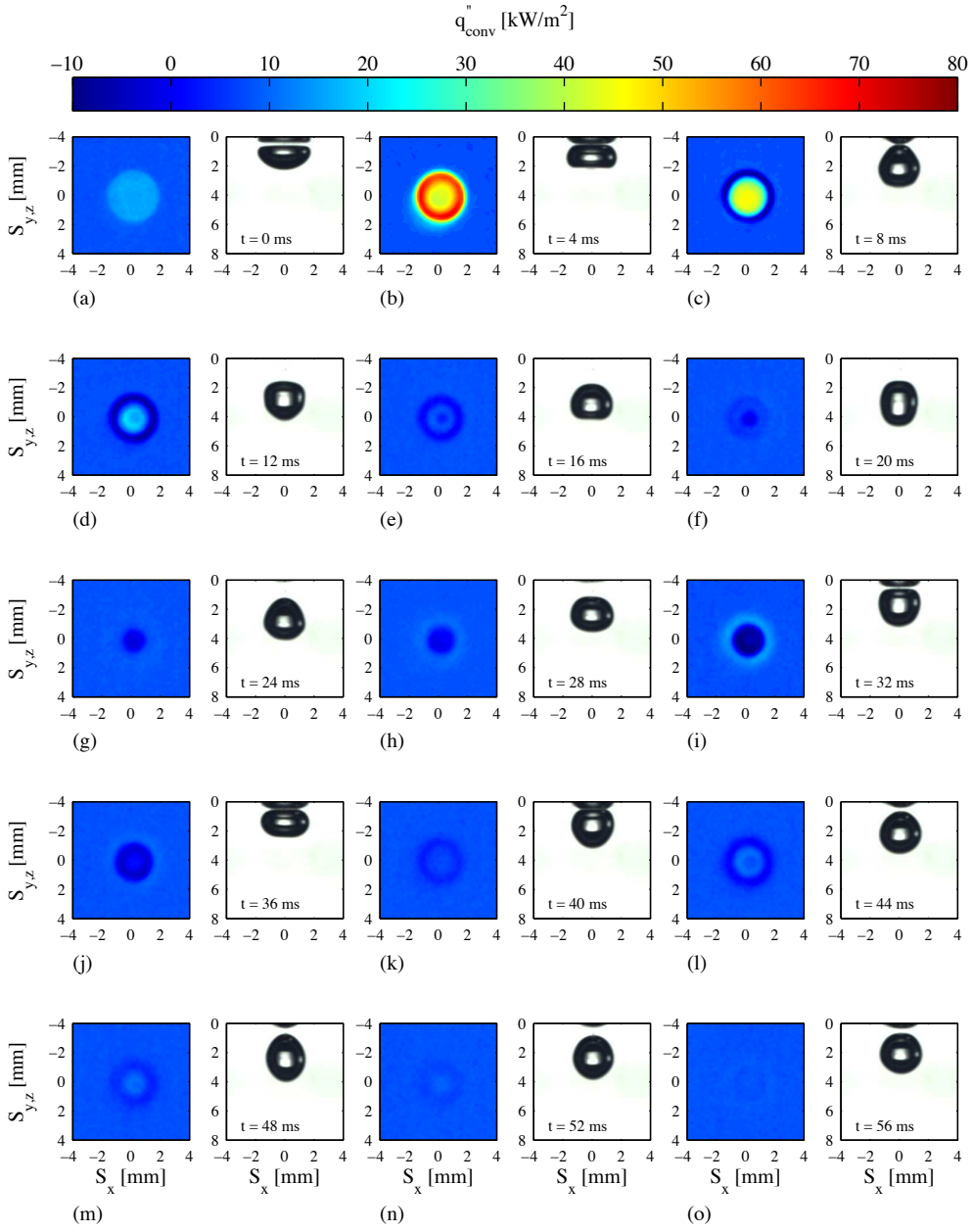

Figure 6.7: Sequence of images depicting convective heat flux and bubble location for a 2.8 *mm* bubble, released from a height of 10 *mm*, with a time separation of 4 *ms* between each image pair. Each image pair illustrates the convective heat flux and bubble's location, with the convective heat flux scale being displayed above the images.

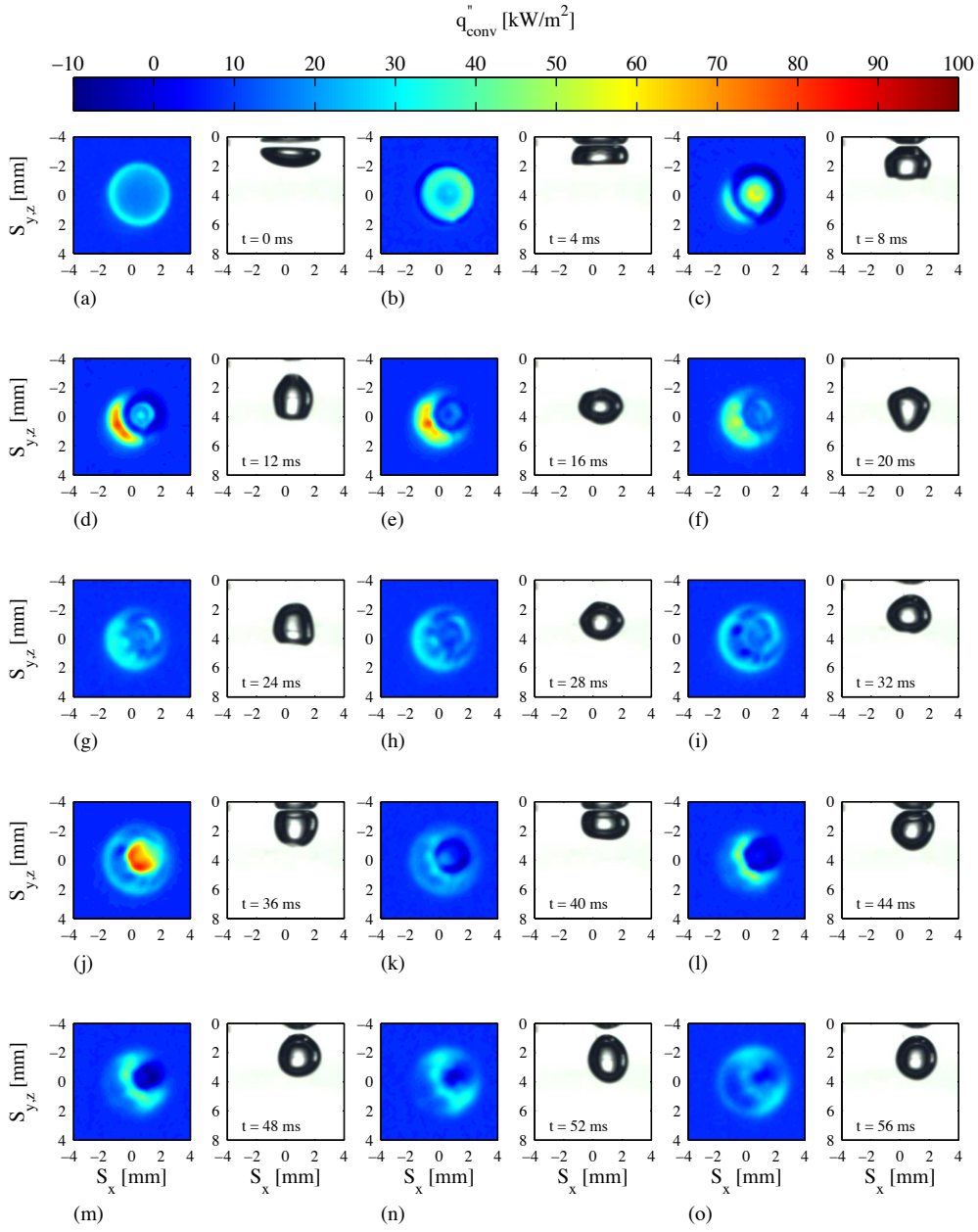

Figure 6.8: Sequence of images depicting convective heat flux and bubble location for a 2.8 *mm* bubble, released from a height of 20 *mm*, with a time separation of 4 *ms* between each image pair. Each image pair illustrates the convective heat flux and bubble's location, with the convective heat flux scale being displayed above the images.

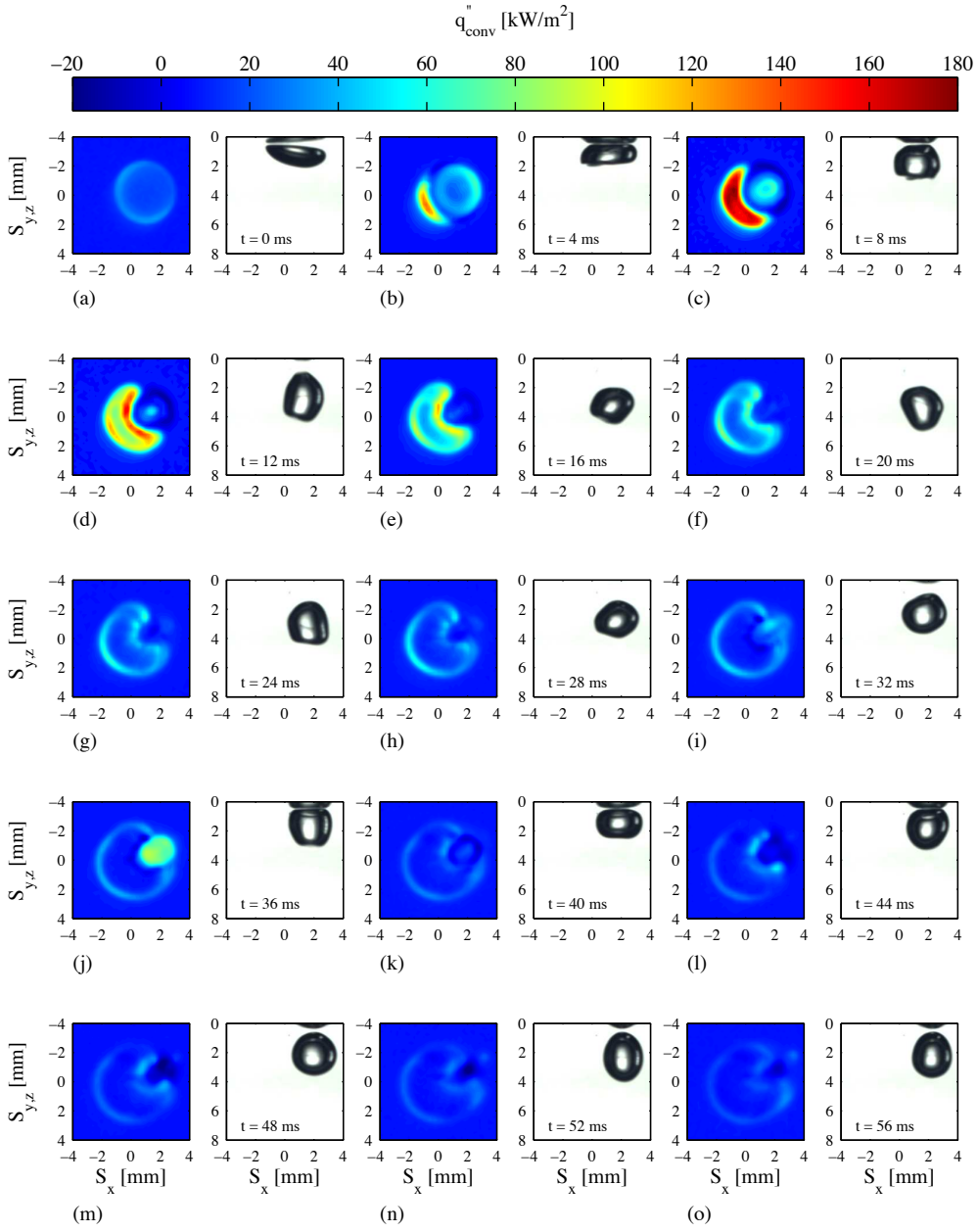

Figure 6.9: Sequence of images depicting convective heat flux and bubble location for a 2.8 *mm* bubble, released from a height of 25 *mm*, with a time separation of 4 *ms* between each image pair. Each image pair illustrates the convective heat flux and bubble's location, with the convective heat flux scale being displayed above the images.

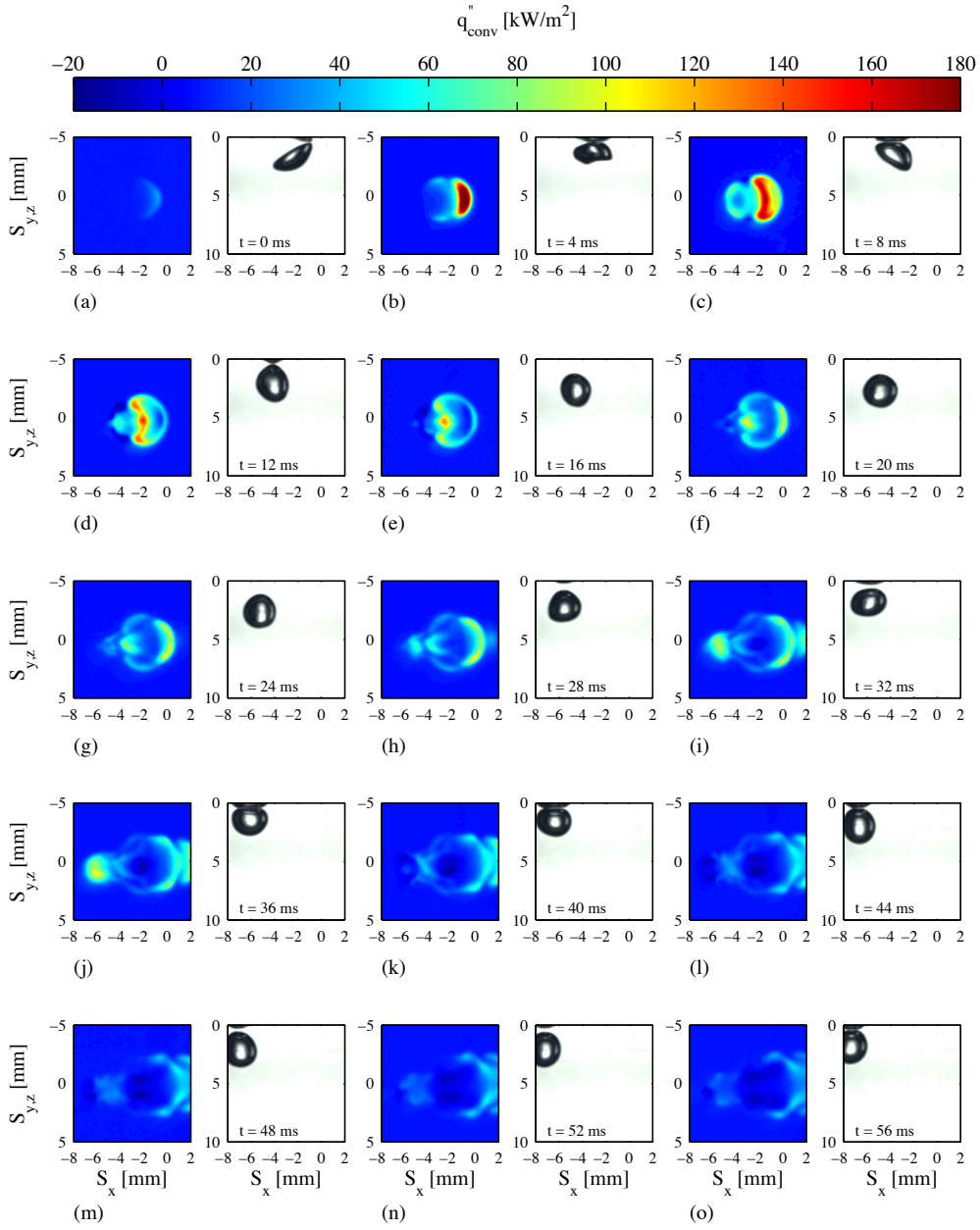

Figure 6.10: Sequence of images depicting convective heat flux and bubble location for a 2.8 *mm* bubble, released from a height of 30 *mm*, with a time separation of 4 *ms* between each image pair. Each image pair illustrates the convective heat flux and bubble's location, with the convective heat flux scale being displayed above the images.

6.3.2 Case 2: 3.3 *mm* Bubble

Figures 6.11 to 6.14 illustrate the initial impact and subsequent rebound of a bubble with an equivalent diameter of 3.3 *mm* released from heights of 10, 20, 25 and 30 *mm*, respectively. What is immediately evident is the similarities in the convective heat flux maps between the larger 3.3 *mm* bubble and that of the 2.8 *mm* bubble. In Figures 6.11 to 6.13 the bubble impacts the surface with a major axis angle which is approximately parallel to the heated surface; this dictates the type of convection and bouncing that occurs. In the first case, Figure 6.11, an annular heat transfer pattern is present. When this is compared with the corresponding patterns in Figure 6.7 for the smaller bubble, it can be seen that the convective heat flux maps have more variability now, in terms of annular variation, during the bouncing event.

The duration of the initial convective enhancement is longer in this case due to the increased duration of bubble contact with the surface, which is thought to be a result of the increased footprint of the bubble upon impact. In Figure 6.11 the bubble only begins to depart from the surface after 12 *ms*, whereas the smaller bubble begins its departure 8 *ms* after the initial impact. At 12 *ms*, a spike in heat transfer can be observed at the centre of the bubble. This is though to be a result of the bubble's shape inversion, which occurs due to the previously dimpled bubble inverting as it rebounds from the surface. This inversion process accelerates trapped fluid contained within the dimple, which was captured prior to impact, towards the surface. During this initial rebound a ring of negative heat flux, which has a value of approximately -12 kW/m^2, corresponds to a region which previously had a positive enhancement with a maximum heat flux of 75 kW/m^2. When the bubble re-impacts the surface, the local enhancement at the centre is replaced by a reduction in convective heat transfer; this occurs at around 30 *ms*. The second bouncing event has similar convective enhancement patterns, with an annular region of higher local heat flux at a time of 36 *ms*, followed by a region of low heat transfer at a time of 44 *ms*. However, the central region is still subject to low, and intermittently negative, heat flux.

Figure 6.12 has similar features to that of the lower release height, although for the identically sized bubble, the affected area is greater for the larger release height, with higher heat flux levels being encountered. The increased area affected is a result of the bubble's

impact size, which is larger and flatter, due to the higher approach velocity. In this case, the maximum convective heat flux on first impact is 42 kW/m^2, followed by a lower heat flux of -6 kW/m^2. From Figure 6.12 it is evident that the maximum convective heat flux in this case occurs between the times of 16 – 20 *ms*, with a symmetric, annular pattern. In the case of the smaller bubble at the same release height (Figure 6.8), this enhancement was usually asymmetric and to the side of the bubble as it bounced away from its impact zone. It is considered that this annular region of enhancement at 16 – 20 *ms* is due to the bubble's wake, which flows around the bubble during the bubble's rebound. This process can be inferred at a time of 16 *ms* (Figure 6.12 (e)), where the bubble is elongated in the vertical direction, with the outer boundary of the bubble corresponding to the beginning of the annular region of high heat flux. This region of high heat flux continues to expand radially during the bouncing event, with only slight movement towards the centre of the impact zone. The bubble looks to be about to re-impact the surface at a time of 36 *ms*, however instead it changes shape before actually impacting at 44 *ms*. At this time an annular region of low heat flux occurs at the extremities of the new impact zone. An increase in convective heat transfer from this second impact does not occur until a time of 52 *ms*, 12 *ms* after the impact. This is due to the bubble beginning to bounce away from the surface again, drawing in cool wake fluid.

Figure 6.13 illustrates a 3.3 *mm* bubble released from a distance of 25 *mm*. It was found to have similar features to that of the bubble released from a 20 *mm* height in Figure 6.12, with the only variation being the duration of certain key events. It is apparent that the bubble impacts at a very slight angle, due to the slight asymmetry of the bubble's shape during the bouncing event. This, in turn, results in a heat transfer pattern which is not perfectly stable and symmetric. Again the maximum convective heat flux occurs at a time of 12 *ms*, with a value of 130 kW/m^2. The remainder of the bouncing event is similar to that of the 20 *mm* release height.

Figure 6.14 illustrates the bouncing event for a 3.3 *mm* bubble released from a height of 30 *mm*. In this case the bubble's impact is at a slight angle, similar to that of the smaller bubble, with the right hand side of the bubble impacting before the left. This type of impact reduces the time in which the bubble is actually bouncing away from the surface as more kinetic energy is transferred to deformation of the bubble surface, when compared to a direct

impact. As in previous cases where the bubble has impacted at an angle, the ensuing wake takes precedence over the direct impact process, with regions of low heat flux (8 *ms*) being enveloped by the impacting wake, which is always opposed to the direction of motion of the bubble. The wake develops around the bubble in a "c" shape, with the area directly beneath the bubble being shielded due to the bubble rebounding. At a time of 16 *ms*, at the bubble's centre, a region of localised high heat flux can be observed, this again is perhaps due to the inversion of the dimple created during the initial impact process. During the bubble's second approach to the surface, a second region of high heat flux is usually observed. However, in this case the opposite occurs, with a few localised regions of negative heat flux appearing, with values approaching -15 kW/m^2 in Figure 6.14 (k). The region beneath the bubble is due to the bubble pushing warm rather than cool fluid ahead of it as it re-impacts the surface, while the symmetric[3] regions either side of the bubble are thought to be a result of circulating wake fluid, capturing warm boundary layer fluid, bringing it back towards the cooled surface.

[3]Symmetric along the direction of motion of the bubble.

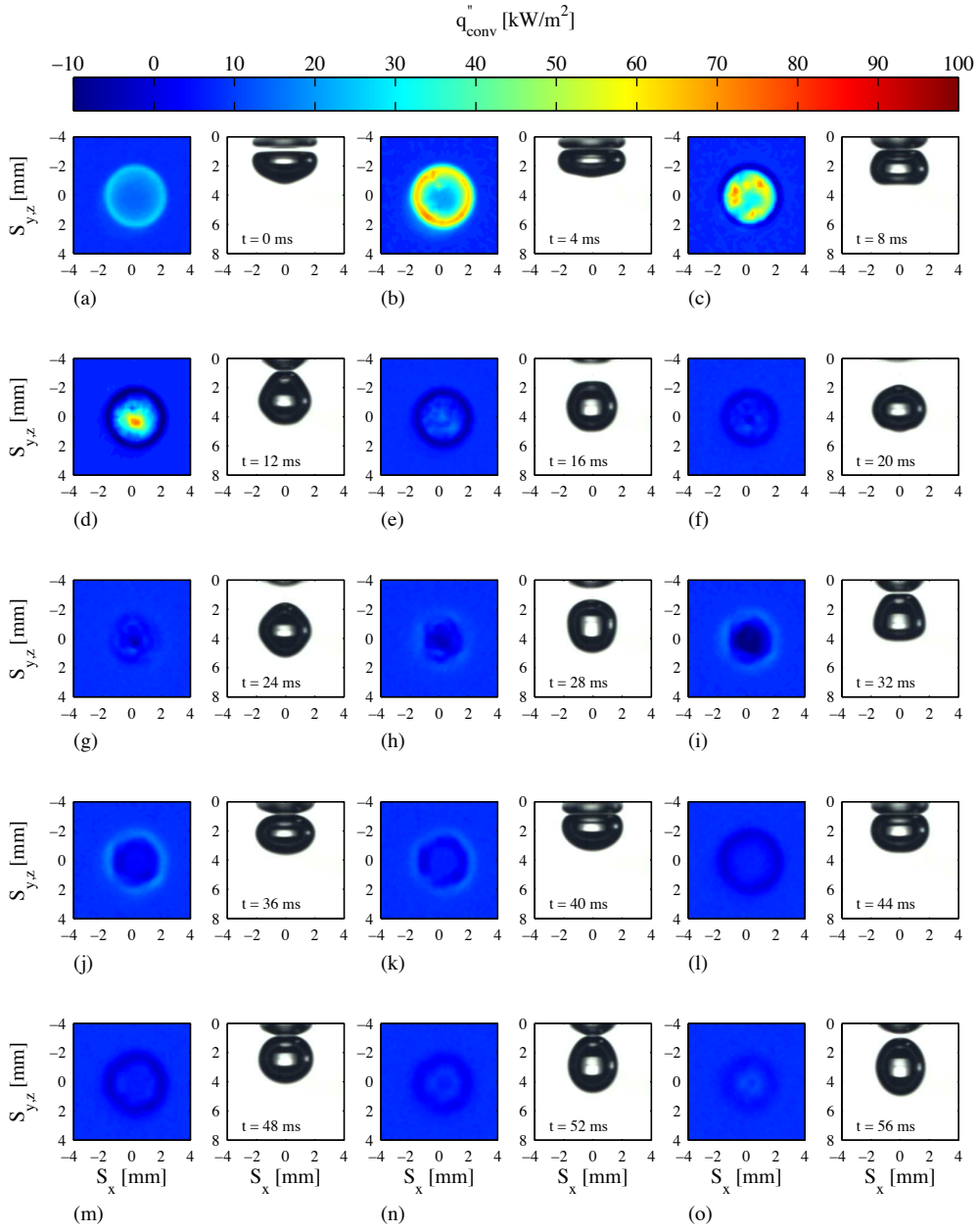

Figure 6.11: Sequence of images depicting convective heat flux and bubble location for a 3.3 *mm* bubble, released from a height of 10 *mm*, with a time separation of 4 *ms* between each image pair. Each image pair illustrates the convective heat flux and bubble's location, with the convective heat flux scale being displayed above the images.

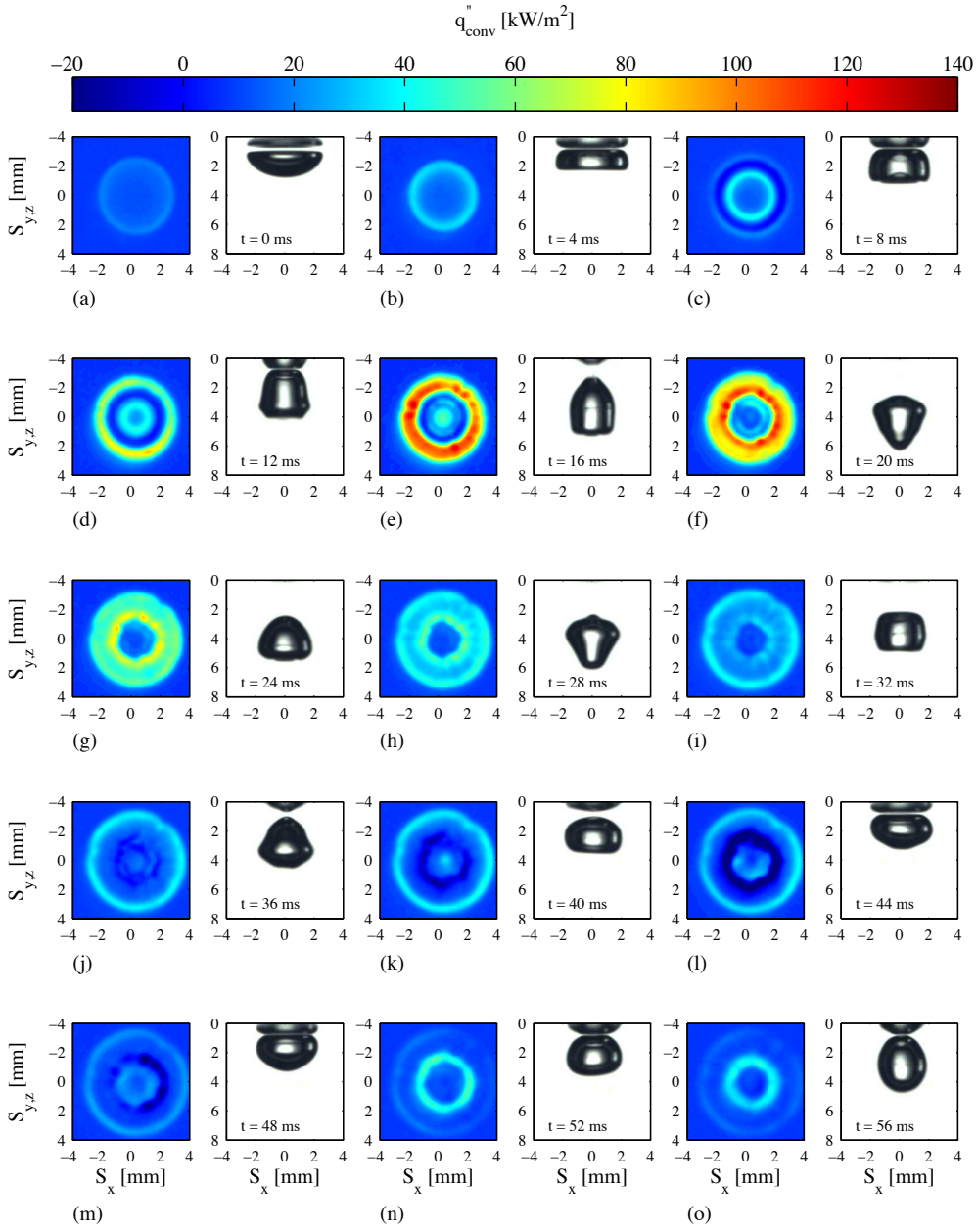

Figure 6.12: Sequence of images depicting convective heat flux and bubble location for a 3.3 *mm* bubble, released from a height of 20 *mm*, with a time separation of 4 *ms* between each image pair. Each image pair illustrates the convective heat flux and bubble's location, with the convective heat flux scale being displayed above the images.

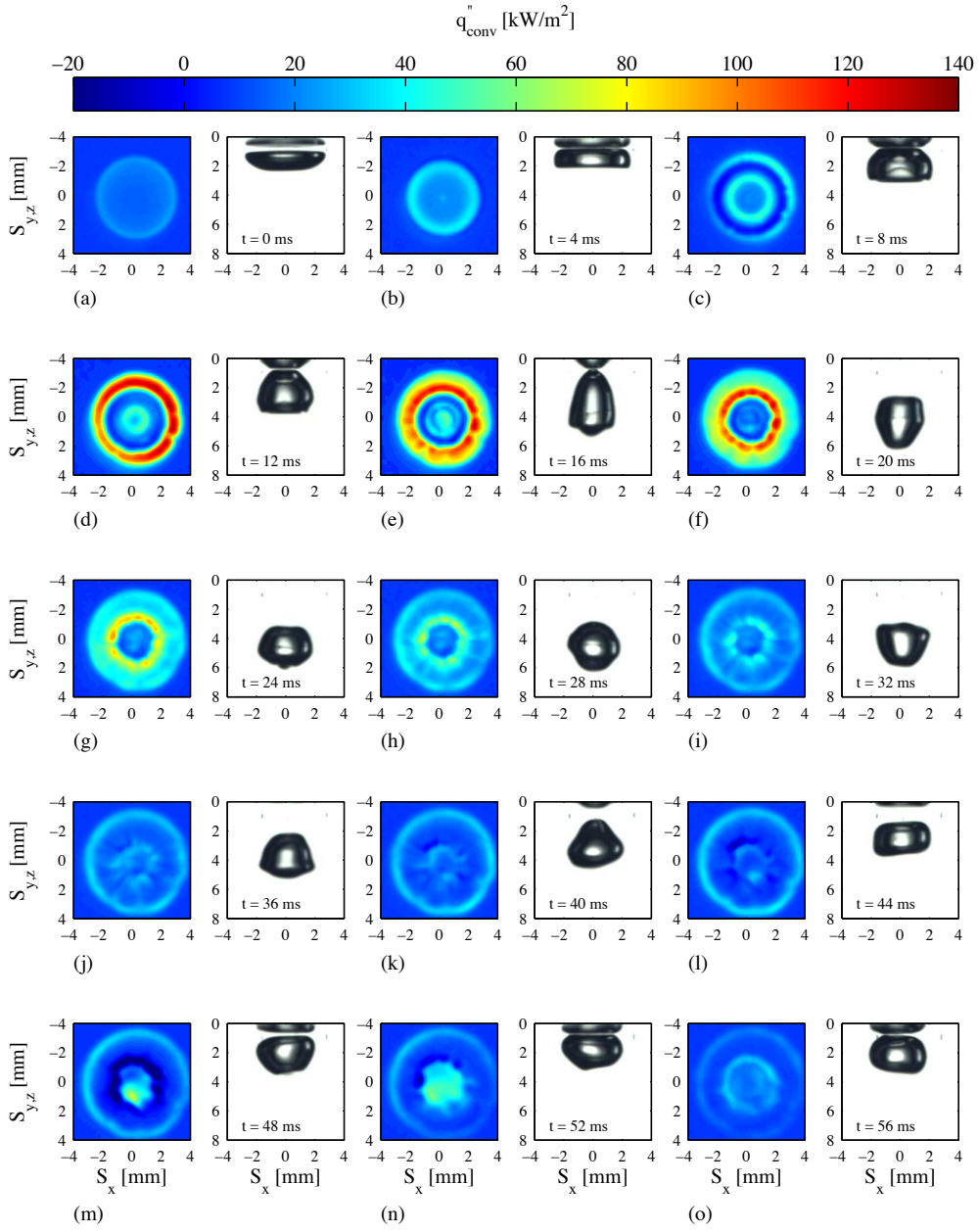

Figure 6.13: Sequence of images depicting convective heat flux and bubble location for a 3.3 *mm* bubble, released from a height of 25 *mm*, with a time separation of 4 *ms* between each image pair. Each image pair illustrates the convective heat flux and bubble's location, with the convective heat flux scale being displayed above the images.

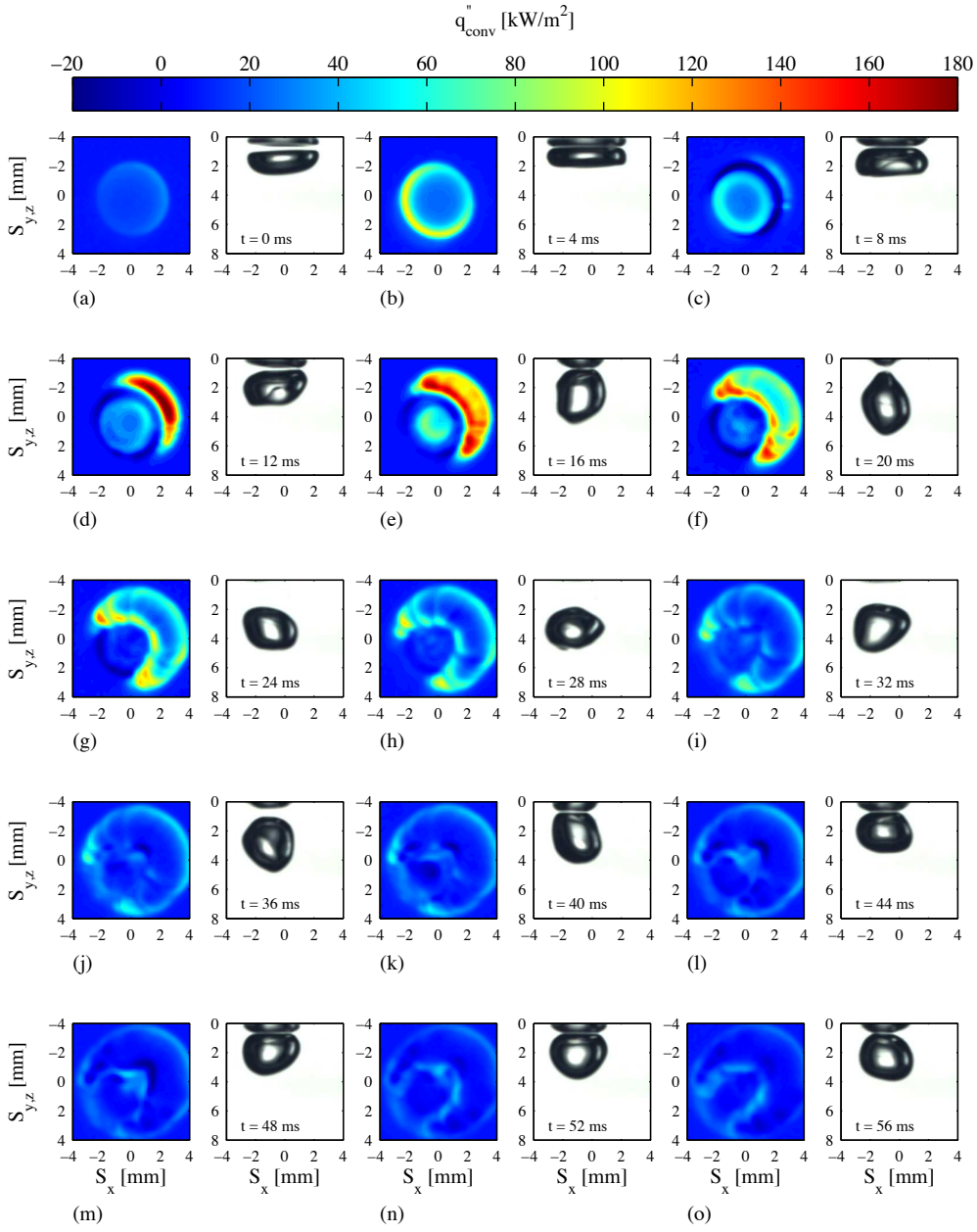

Figure 6.14: Sequence of images depicting convective heat flux and bubble location for a 3.3 *mm* bubble, released from a height of 30 *mm*, with a time separation of 4 *ms* between each image pair. Each image pair illustrates the convective heat flux and bubble's location, with the convective heat flux scale being displayed above the images.

6.3.3 Case 3: 4.1 *mm* Bubble

Figures 6.15 to 6.18 illustrate the initial impact and subsequent rebound of a bubble with an equivalent diameter of 4.1 *mm* with release heights of 10, 20, 25 and 30 *mm*, respectively. In each case, the bubble's major axis upon impact is approximately parallel with the surface; this accounts for the symmetry of the heat transfer patterns.

Figure 6.15 exhibits comparable convective heat flux structures to the smaller bubbles, with the main variation being the increase in affected area. A maximum heat flux at impact of 80 kW/m^2 occurs at a time of 5 *ms*, with a reduced heat flux of -17 kW/m^2 at a time of 13 *ms*. During the bubble's second impact, a region of low heat flux can be observed, with a minimum value of -15 kW/m^2. Figure 6.16 depicts a 4.1 *mm* bubble released from a height of 20 *mm*. The impact area is somewhat larger than that of the lower release height, similar to the finding reported for the 3.3 *mm* bubble. Notably, the maximum convective heat flux does not occur upon impact but instead as the bubble has begun its rebound from the surface; this occurs at a time of 18 *ms*. At a time of 16 – 20 *ms*, the zone of maximum enhancement extends from ± 2 *mm* to ± 4 *mm*, while the bubble extends to ± 2 *mm* during this time period. This suggests that wake fluid, which is continually rising, manoeuvres around the bubble, even though the bubble is now moving in the opposite direction, away from the surface. This cool fluid is now close to, but not in contact with, the surface. Between times of 16 – 20 *ms* the bubble shape becomes elongated in the vertical direction; this elongation causes a suction, which pulls and accelerates the cool fluid against the surface. This suction effect only influences fluid which is already above the bubble's centroidal height in the vertical direction (S_z). This fluid motion has been observed by means of the Schlieren effect, which is present during some experiments, depending on lighting conditions; this point will be examined in detail in Chapter 7. This region of high heat flux reduces over time, while steadily spreading along the surface. In this case the development of the wake region is not quite symmetrical but instead develops first on the left of the bubble, with this being due to the very slight variation in the bouncing event from left to right. At a time of between 52 – 56 *ms*, the bubble impacts the surface for the second time and an increase in convective flux is observable beneath the bubble.

For a release height of 25 *mm*, Figure 6.17 exhibits similar features to those reported

for the lower release height of 20 *mm*, although with variations in the times at which events occur. The maximum enhancement due to the direct impact of the bubble occurs at a time of 5 *ms*, with a heat flux of 95 kW/m^2. In this case extremely low convective heat flux levels were observed at a time of 11 *ms*, with a minimum heat flux of -30 kW/m^2. The maximum heat flux level due to the wake impact occurs at a time of 23 *ms*, with a value of approximately 190 kW/m^2. As the bubble is close to re-impacting the surface at 48 *ms*, zones of low heat flux are present with minimum values of -22 kW/m^2. However, at a time of 56 *ms* a small zone of negative heat flux with a value of -45 kW/m^2 appears, coinciding with the direct impact of the bubble on the surface. It is thought that this very low heat flux may be due to warm boundary layer fluid, collected during the initial rebound, being pushed towards the surface, causing a local and short term heating of the surface.

Figure 6.18 depicts the impact of a 4.1 *mm* bubble, released from a height of 30 *mm*. With bubbles of this size the major axis is usually parallel with the surface upon impact, although at a height of greater than 25 *mm* a sudden shape change occurs. This was seen in Figure 5.10, and caused a reduction in the impact area of the bubble as it impacted the surface. In this case the maximum convective heat flux occurs at a time of 11 *ms*, with a value of 210 kW/m^2; this high heat flux is a result of the combined effects of the rising wake and bubble retraction. In this case very little enhancement is observed within the centre of the bubble (8 *ms*); this maybe due to the unusual shape changes which occur prior to impact. At times of between 20 – 28 *ms*, a secondary region of high heat flux is observable within the central region of the impact zone. This is thought to be a result of the bubble pulling inwards, removing the boundary layer, as it recovers its shape. At a time of 28 *ms*, an inner ring appears, which is thought to be due to the inversion of the dimple. At a time of 56 *ms*, as the bubble re-impacts the surface, an increase in heat flux is observed. As previously noted, the final impact velocity increases slightly with increasing release height, which is thought to be a contributing factor for the increased levels of convective heat flux upon impact.

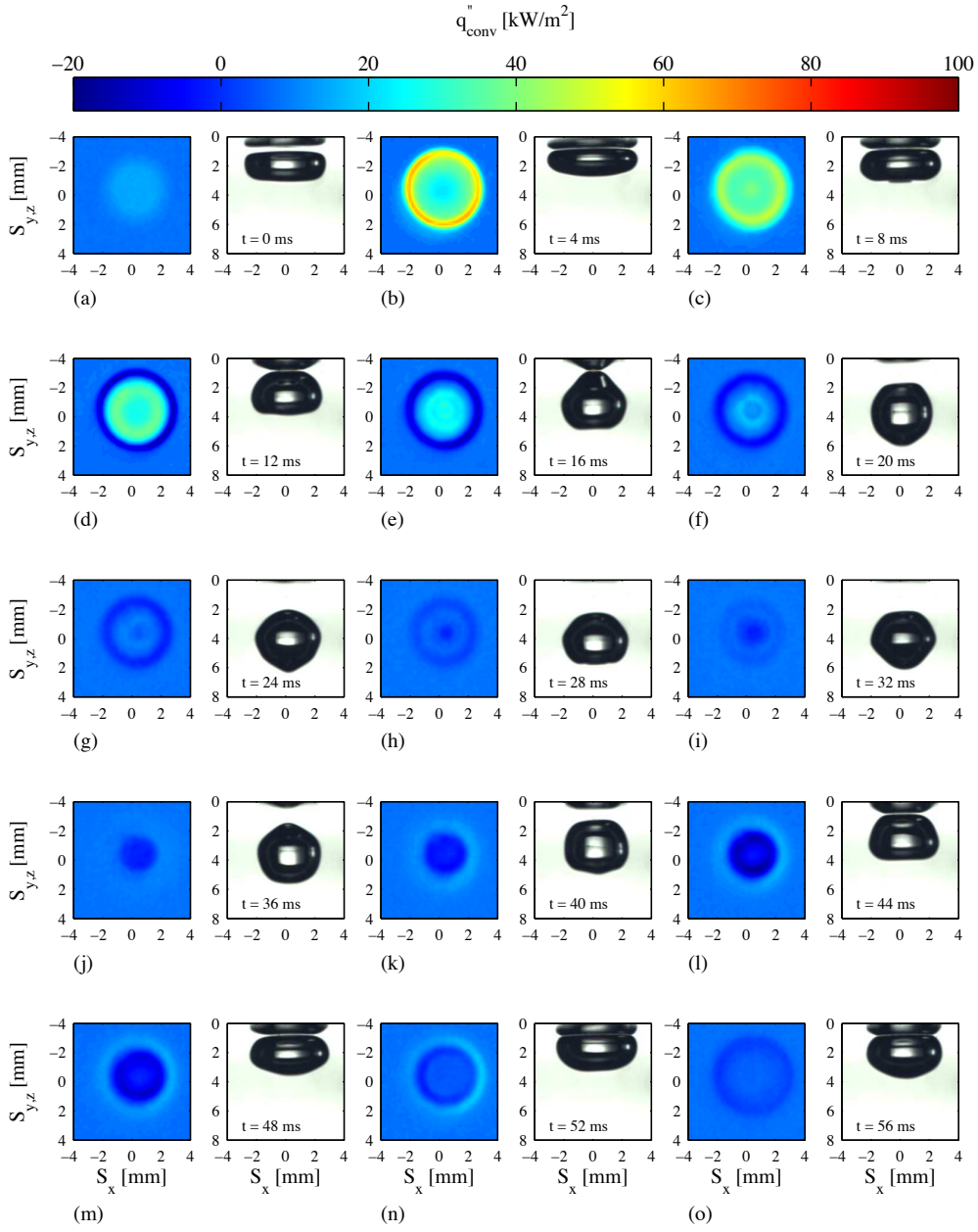

Figure 6.15: Sequence of images depicting (left to right) both bubble motion and convective heat flux of a 4.1 *mm* bubble, released from a height of 10 *mm* with a time separation of 4 *ms* between each image pair. Each image pair illustrates the convective heat flux and bubble's location, with the convective heat flux scale being displayed above the images.

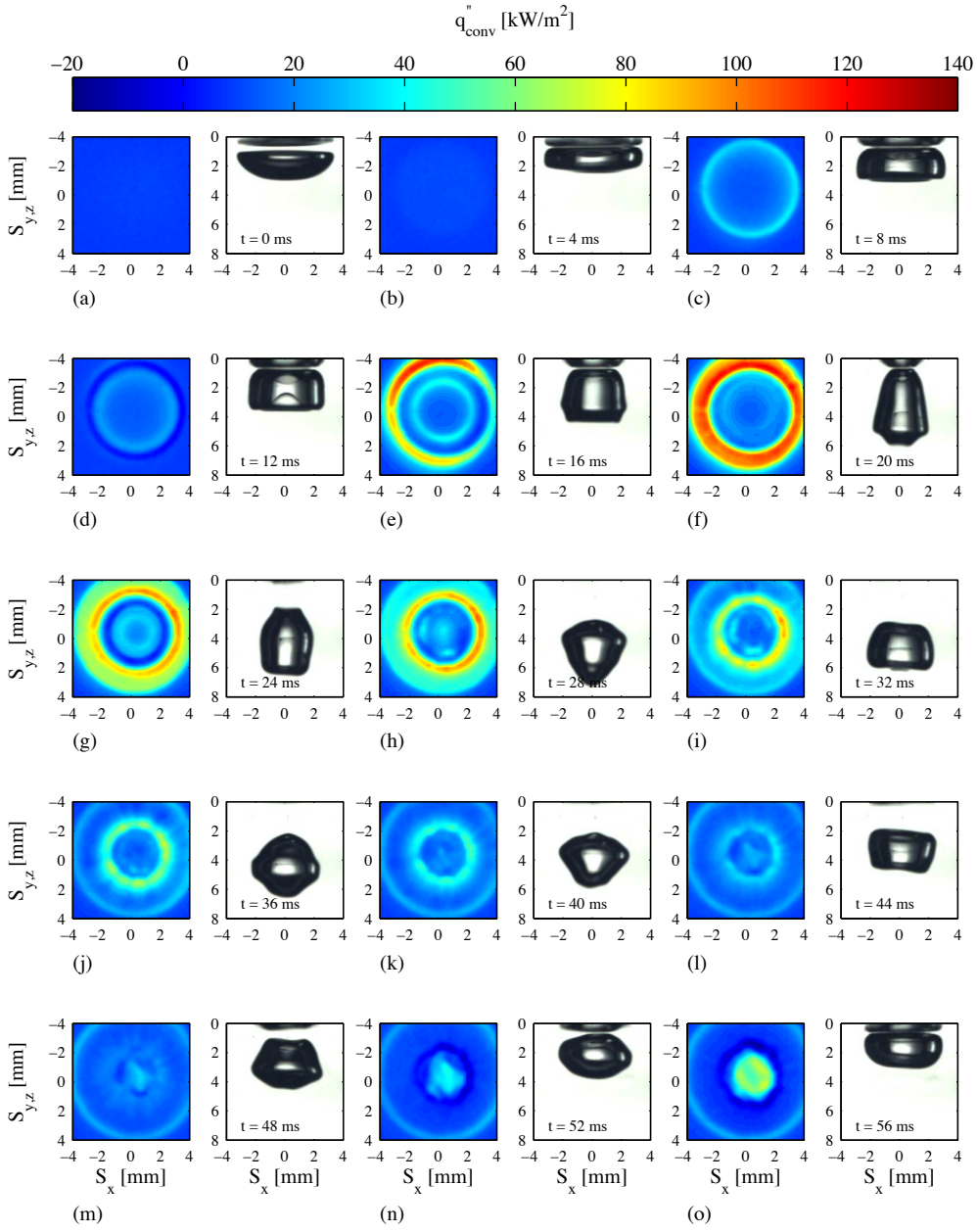

Figure 6.16: Sequence of images depicting (left to right) both bubble motion and convective heat flux of a 4.1 *mm* bubble, released from a height of 20 *mm* with a time separation of 4 *ms* between each image pair. Each image pair illustrates the convective heat flux and bubble's location, with the convective heat flux scale being displayed above the images.

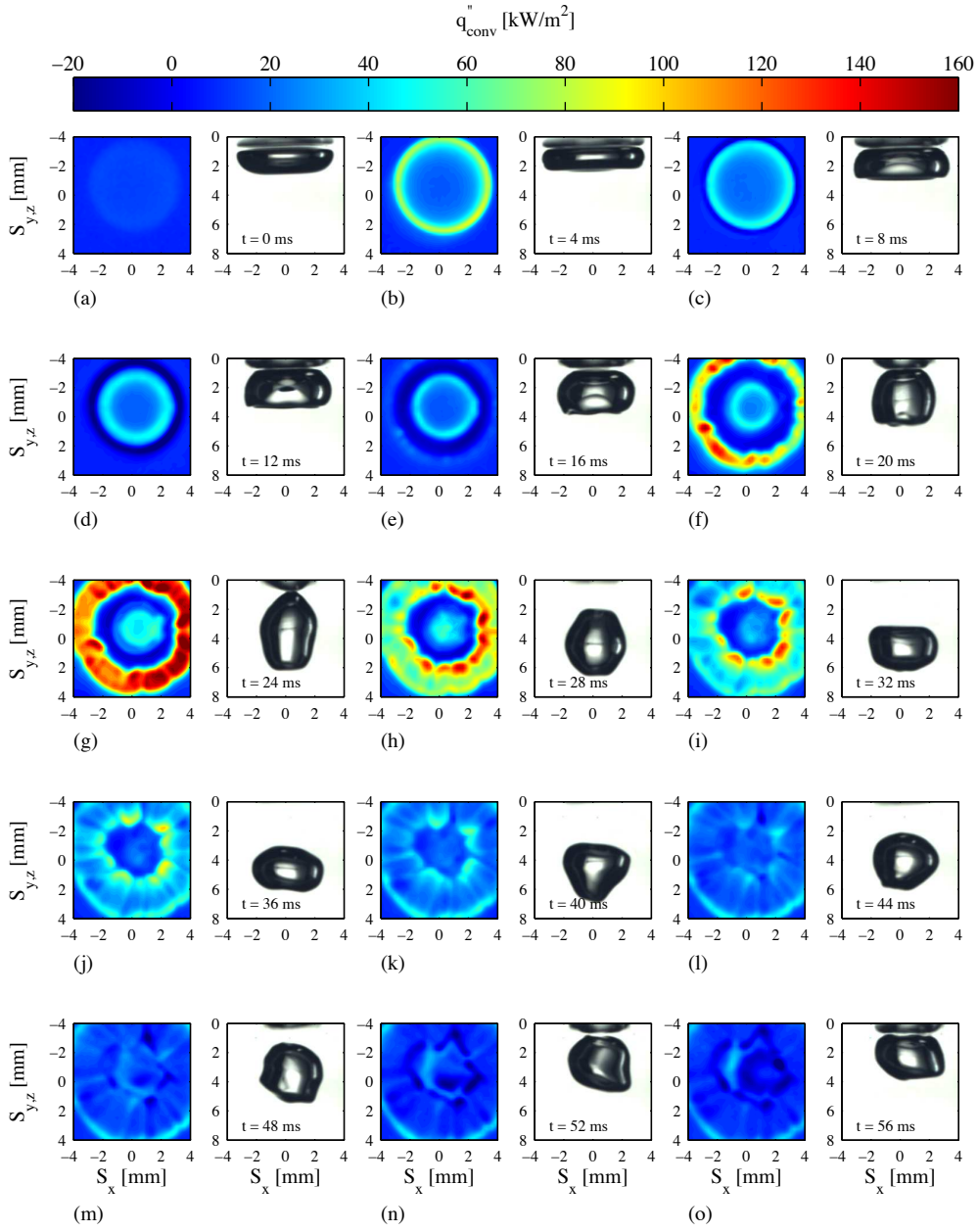

Figure 6.17: Sequence of images depicting (left to right) both bubble motion and convective heat flux of a 4.1 *mm* bubble, released from a height of 25 *mm* with a time separation of 4 *ms* between each image pair. Each image pair illustrates the convective heat flux and bubble's location, with the convective heat flux scale being displayed above the images.

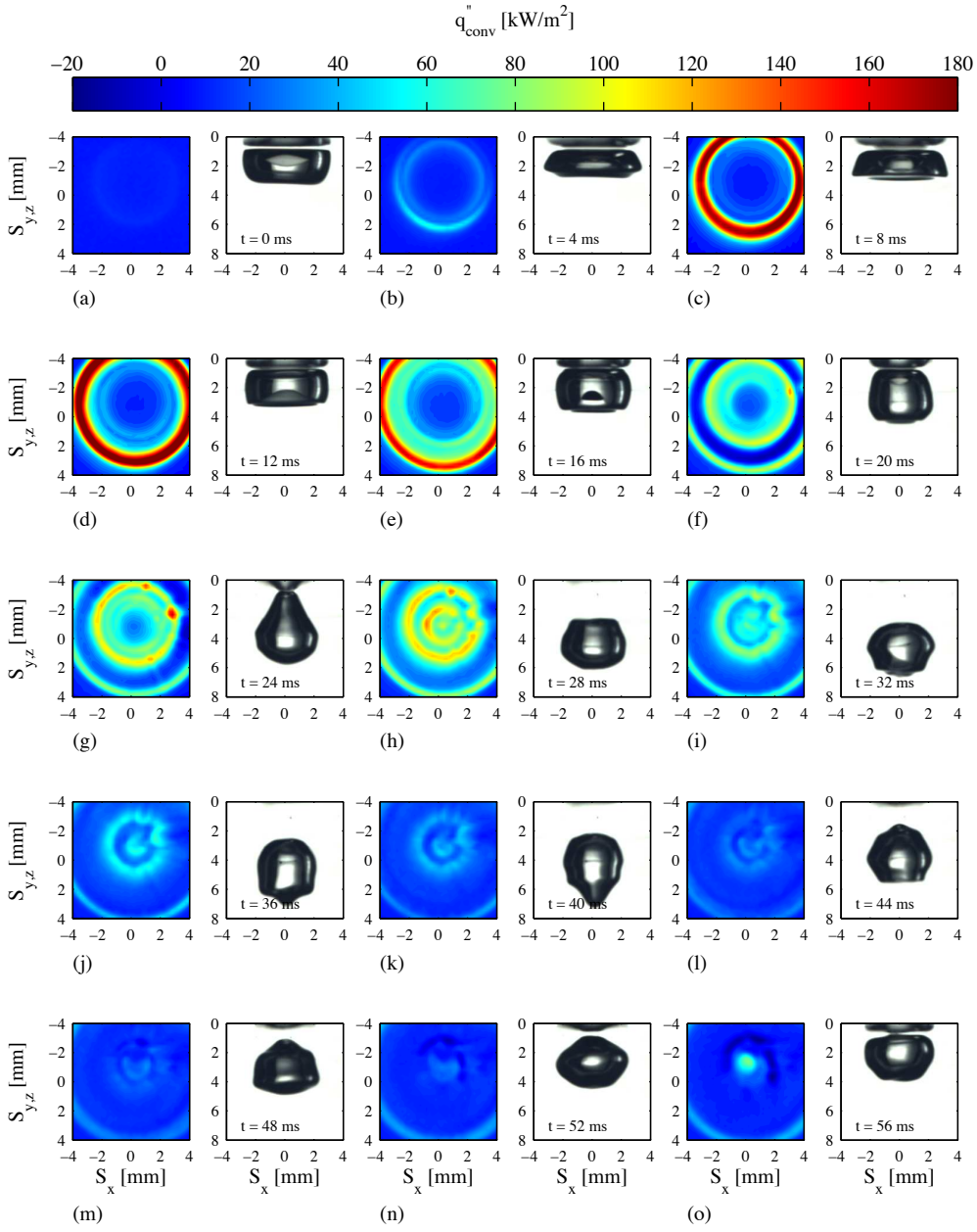

Figure 6.18: Sequence of images depicting (left to right) both bubble motion and convective heat flux of a 4.1 *mm* bubble, released from a height of 30 *mm* with a time separation of 4 *ms* between each image pair. Each image pair illustrates the convective heat flux and bubble's location, with the convective heat flux scale being displayed above the images.

6.4 Temporal Heat Flux Variation

In order to evaluate the complex process of heat flow to and from the surface, in the presence of a bubble bouncing on the surface, specific locations of interest on the surface have been chosen. A time trace of heat flux and temperature at these points will be presented in the following section. Only data for bubbles released from a height of 25 *mm* will be presented in this section. The four points chosen are those which best represent the variation in convective heat flux.

6.4.1 Case 1: 2.8 *mm* Bubble

Figure 6.19 shows the instantaneous convective heat flux at two distinct times for a 2.8 *mm* bubble, with the first being 6 *ms* after the initial impact of the bubble (Figure 6.19 (a)), and the second being the last moment that the bubble is not in contact with the surface; after this time the bubble is either resting or oscillating on the surface (Figure 6.19 (b)). The bubble in some cases was found to continually migrate along the surface, while oscillating, after the initial bouncing events. To accompany these instantaneous images, the time varying aspect of the convective heat flux will be explored, at the four points of interest marked in Figure 6.19. Referring to Figure 6.20, the time period, (*a*), represents the impact process up until the bubble initially rebounds from the surface. Period (*b*), extends up until a point in time when the bubble no longer leaves the surface, which corresponds to the instant illustrated in Figure 6.19 (b), while period (*c*), represents the remainder of the test period shown. The direction of motion of the bubble in this case is at approximately 45 degrees, with respect to S_x.

Figure 6.20 illustrates the time varying convective heat flux and surface temperature for the first point of interest, which is marked as point (1) in Figure 6.19, and is at an approximate position of (3, -1.5) *mm*. The initial impact process was found to dictate the motion of the bubble, as in this case the angular trajectory of the bubble results in the bubble moving along the surface, initially bouncing, then reducing to oscillatory motion. Point (1) was at the edge of the initial impact zone, but the bubble's travel means that point (1) is at the centre of the final bounce location. The black solid line in Figure 6.20 (i), represents the time varying convective heat flux, the red dashed line represents the change in the stored flux,

with the horizontal line representing the generated heat flux before impact. Figure 6.20 (ii) corresponds to the surface temperature at the same location. A significant variation in convective heat flux can be observed in Figure 6.20 (i), with three distinct peaks in convective heat flux being present. These peaks all have heat flux levels greater than 40 kW/m^2, but with distinct enhancement mechanisms in each case.

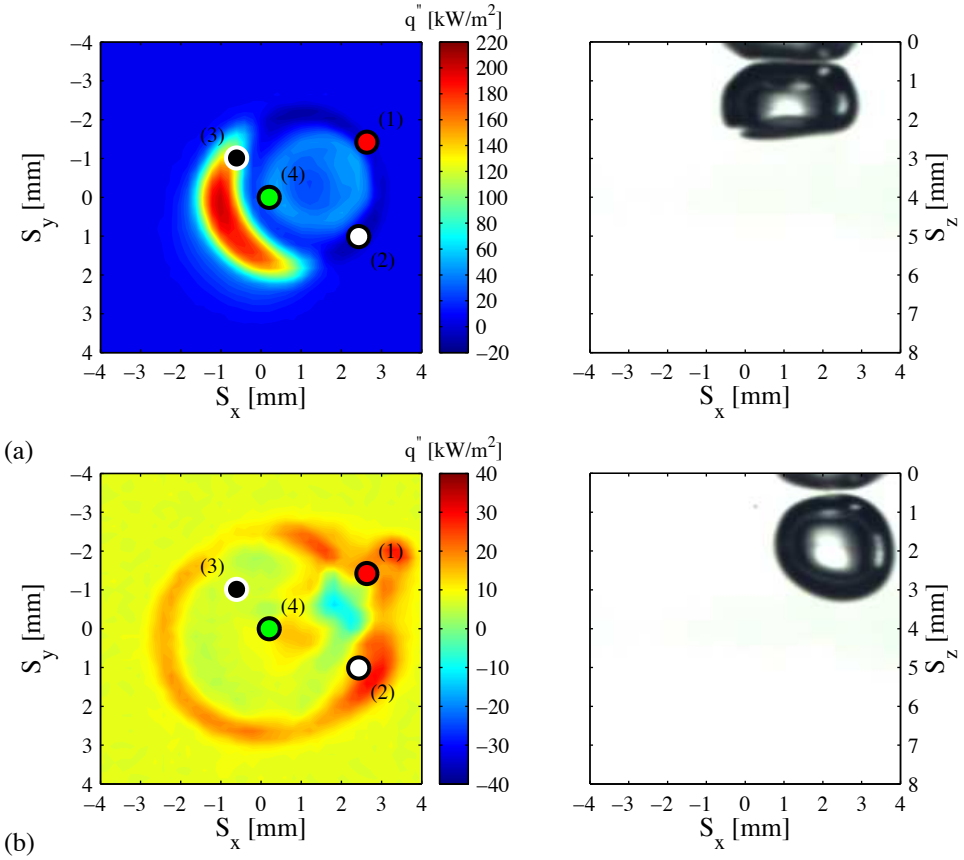

Figure 6.19: Image pair depicting both convective heat flux and bubble location on the surface and the points of interest (1, 2, 3 and 4). (a) corresponds to a time of 6 *ms* after impact and (b) corresponds to the bubble approaching the surface for the final time after completing a number of bounces, which in this case is 52 *ms*. The convective heat flux scale varies between the two cases, illustrating the enhancement reduction with time. In this case the release height is 25 *mm*, with a bubble diameter of 2.8 *mm*.

The first notable peak in Figure 6.20 is due to the direct impact of the bubble, with point (1) being at the edge of the impact zone. This peak is followed by a sharp drop in convection, as the bubble begins to peel away from the surface. The initial impact and rebound process is sketched in Figure 6.21 (a) – (b). In this case the convective heat flux drops to zero during the initial rebound period (Figure 6.21 (b)) and only begins to rise again once the bubble

has completely left the surface (Figure 6.21 (c)). From the beginning of time period *b* in Figure 6.20, the heat flux steadily rises to a maximum at an approximate time of 35 *ms* after the initial impact. This peak coincides with the bubble's second impact on the surface, with point (1) being beneath the bubble. As the bubble impacts for the second time its velocity is significantly lower, which results in less spreading upon impact, as depicted in Figure 6.21 (d). The secondary smaller spike in convective heat flux at a time of 45 *ms* is thought to be due to the centre of the new smaller dimple inverting as the bubble begins its second rebound from the surface.

At a time of between 45 – 50 *ms* a spike of negative convective heat flux can be observed. This coincides with a positive spike in the stored flux, which is greater than the generated heat flux, along with a slight increase in the surface temperature at the same time. This negative spike in convective heat flux is a result of the bubble rebounding from the surface, drawing in warm boundary layer fluid, as depicted for the initial impact in Figure 6.21 (b). The maximum convective heat flux during the re-impact was approximately 90 kW/m^2, with small annular regions of negative heat flux having a value of -12 kW/m^2. At a time of approximately 60 *ms*, a small peak in convective flux occurs, which is due to the bubble impacting the surface for the third time. Again, this peak is followed by a period of reduced convective heat flux as the bubble bounces on the surface but does not visibly separate from the surface. This further bounce allows the bubble to move along the surface, almost as if it were sliding but with oscillatory shape changes. As the bubble moves past point (1), it creates a slight wake at its rear. This wake is responsible for the third peak at 95 *ms* in Figure 6.20. The bubble moves only a few millimetres, however this is sufficient to drag in steadily rising cooler wake fluid.

Figure 6.22 illustrates the time varying convective heat flux and surface temperature for the second point of interest, which is marked as point (2) in Figure 6.19 at an approximately position of (2.5, 1) *mm*. This point is initially positioned at the right side edge of the impact zone away from the direction of motion of both the bubble and its wake. In Figure 6.22 (i), the sharp peak and dip in convective heat flux observable in time period *a*, are related respectively to the impact and initial peeling away of the bubble as it rebounds from the surface. The bubble and fluid motion during the rebound is depicted in Figure 6.21 (b), with a shift in the thermal boundary layers being observed. At point (2) the convective flux rises

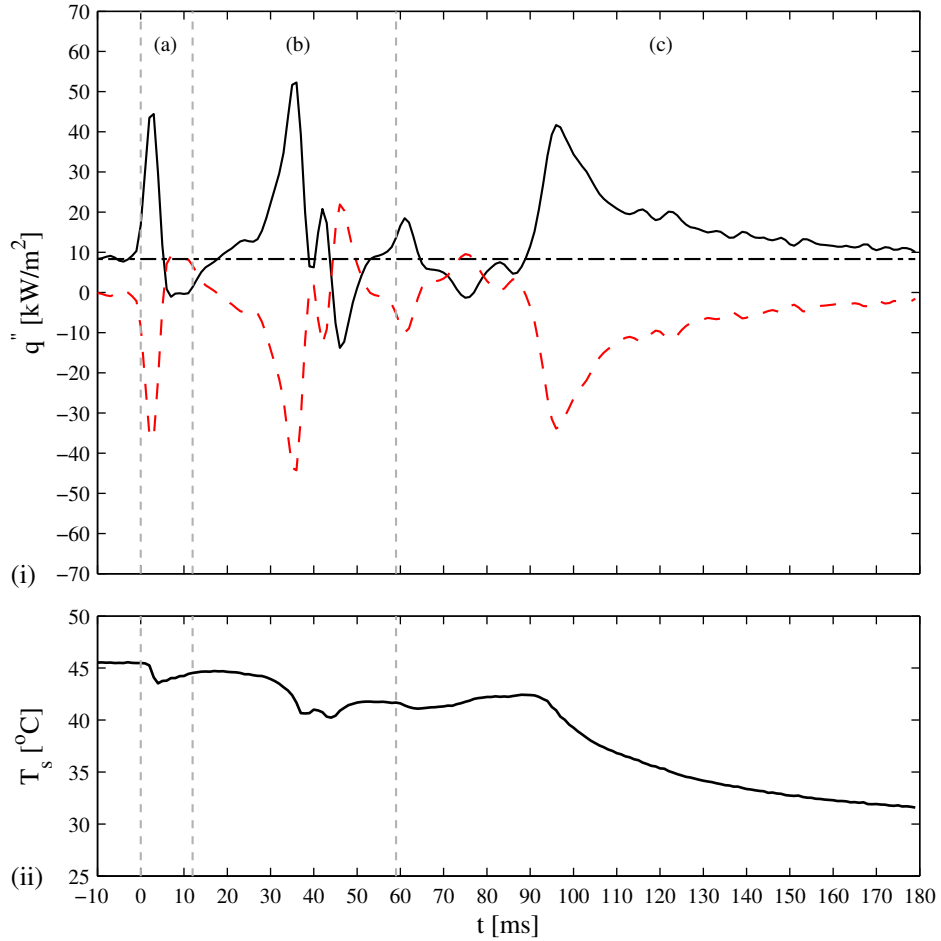

Figure 6.20: Time trace of (i) heat flux and (ii) temperature at point (1), shown in Figure 6.19. The time begins from when the bubble impacts the surface. The upper graph illustrates the change in surface heat flux, with the lower graph illustrating the change in surface temperature. The — solid line represents the convected heat flux, with the – – dashed line being the stored flux. *a*, *b* and *c* represent distinct bubble motion periods, with *a* corresponding to the impact, up until the bubble leaves the surface. Period *b*, extends from when the bubble leaves the surface up until the bubble no longer bounces away from the surface, with *c* corresponding to the time the bubble is no longer moving away from the surface, while still oscillating.

sharply as the bubble impacts the surface. The peak in stored flux towards the end of time period *a*, is due to warm fluid being drawn atop of the previously cooled surface; this heats the surface locally, which is also evident in the temperature rise shown in Figure 6.22 (ii).

At the beginning of time period *b*, the convective heat flux begins to rise again, just as the bubble departs from the surface; this is thought to be a result of the bubble's wake. This rising wake impacts initially on the left hand side of the bubble. However, as the bubble

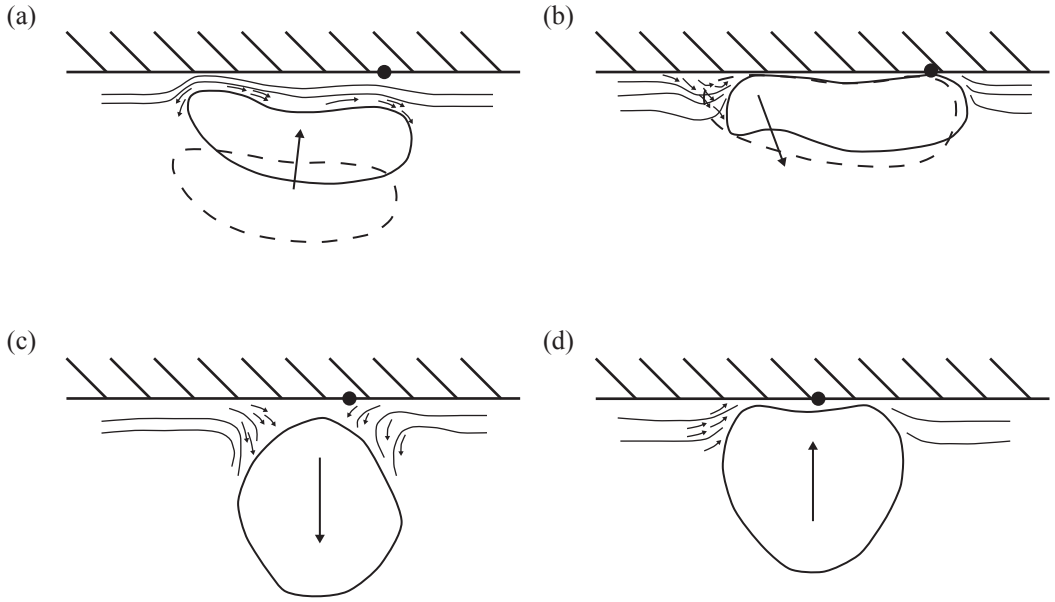

Figure 6.21: Sketches showing (a) the bubble approach (-4 – 0 *ms* prior to impact), (b) bubble initial rebound from the surface (0 – 2 *ms*), (c) complete rebound from the surface (12 –14 *ms*) and (d) fluid flow during bubble's second impact (34 *ms*). The black circle indicates the approximate location of point (1). The dashed bubble outline precedes the bubble outline with the solid line, which is the main interest.

begins to rebound, the wake engulfs the other regions of the bubble's initial impact zone, in a "c" shape. The late stages of this process may be visualised in Figure 6.19 (b).

In Figure 6.22 (i), the secondary peak in period *b* at 35 *ms*, with a marginally higher convective flux, occurs when the bubble impacts the surface for the second time, as depicted in Figure 6.21 (d). At this moment, the bubble is at the outer edge of the initial impact zone, with point (2) being outside the direct impact zone. The slight dip in heat flux at an approximate time of 45 *ms* is primarily due to this secondary impact process drawing both cool and warm fluid towards the surface, as the bubble prepares to bounce away a second time. The localised peak in convective heat flux between 45 – 60 *ms* occurs as the bubble rebounds from the surface, drawing in cool fluid. The dip at 65 *ms* coincides with the final impact of the bubble; in this case the bubble has shifted its position, as previously mentioned. The final peak at an approximate time of 75 *ms* is thought to be due to the bubble's oscillation, in which the bubble bounces, but not away from the surface, drawing in fluid. This final peak is followed by a reduction in convective heat flux as the bubble has moved away from the impact zone and is oscillating very slowly, with the only convection

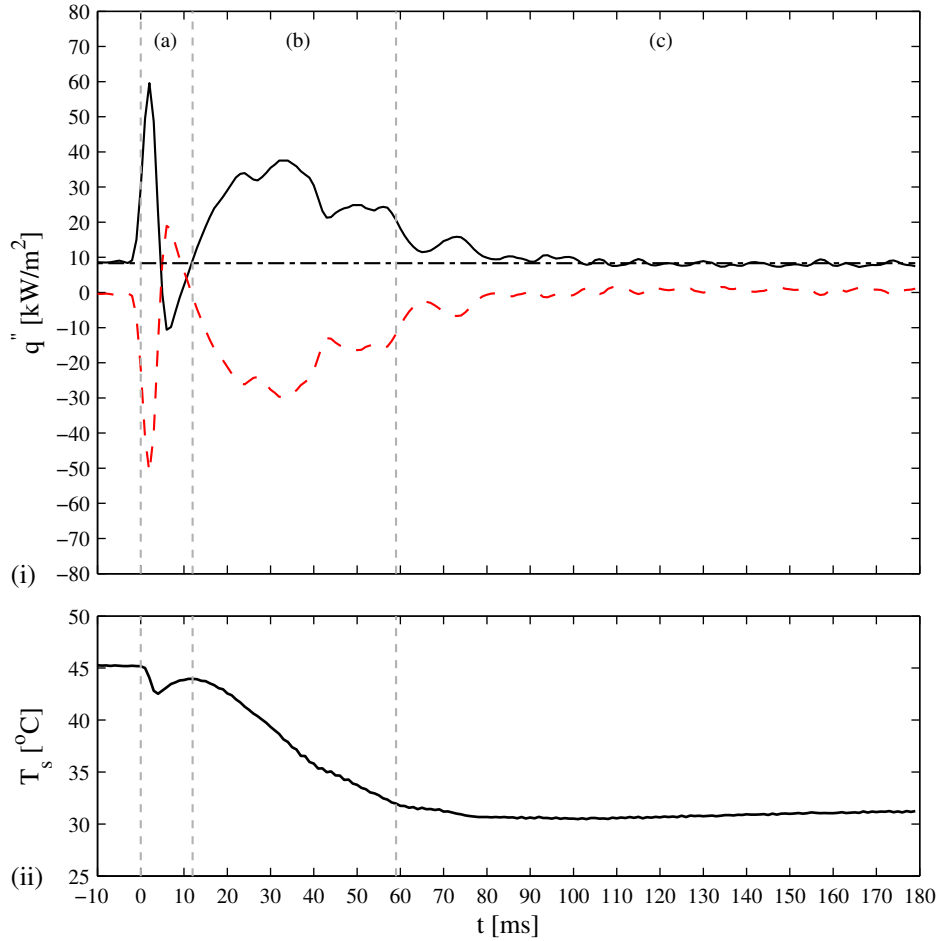

Figure 6.22: Time trace of (i) heat flux and (ii) temperature at point (2), shown in Figure 6.19. The time begins from when the bubble impacts the surface. The upper graph illustrates the change in surface heat flux, with the lower graph illustrating the change in surface temperature. The — solid line represents the convected heat flux, with the – – dashed line being the stored flux. *a*, *b* and *c* represent distinct bubble motion periods, with *a* corresponding to the impact, up until the bubble leaves the surface. Period *b*, extends from when the bubble leaves the surface up until the bubble no longer bounces away from the surface, with *c* corresponding to the time the bubble is no longer moving away from the surface, while still oscillating.

being liquid natural convection.

Convective heat flux and surface temperature for the third point of interest, point (3), are illustrated in Figure 6.23. The initial location of point (3) is at the edge of the bubble's initial impact zone at a position of (-0.5, -1) *mm*. It is clear from Figure 6.23 that only two distinct peaks are observable at this location. The first initial peak, with a modest heat flux value of 40 kW/m^2, is a result of the initial impact of the bubble, as illustrated in Figure 6.21 (a).

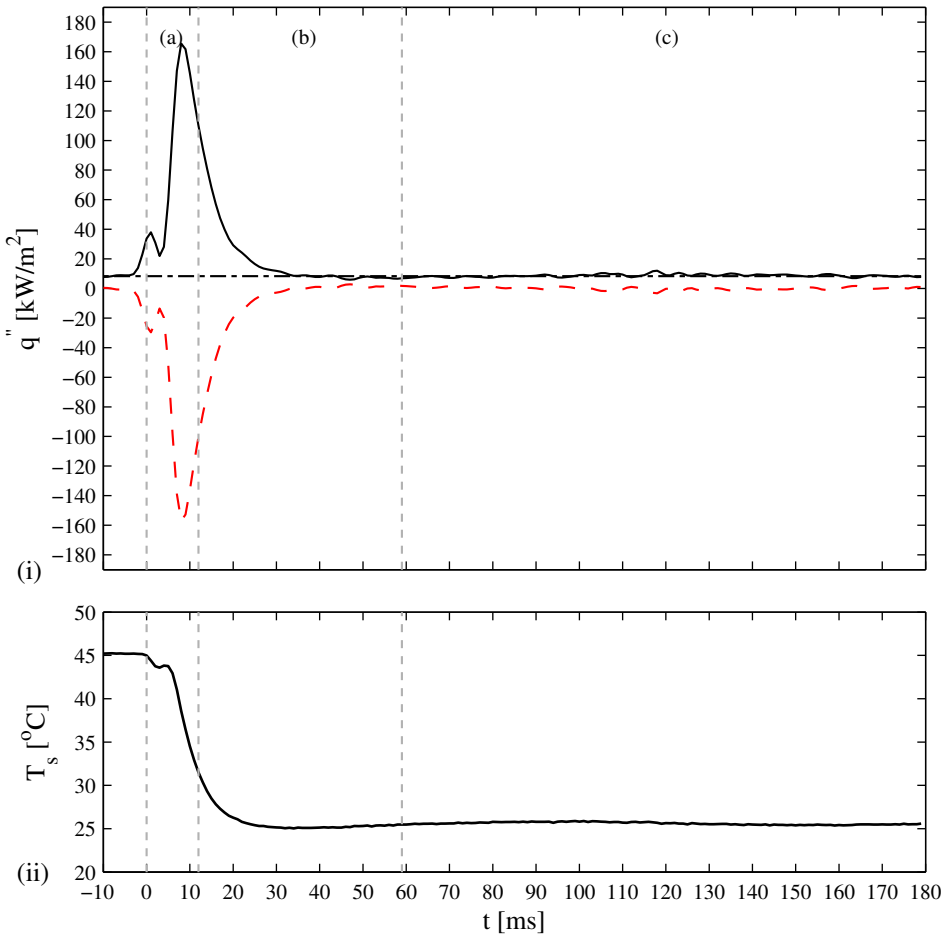

Figure 6.23: Time trace of (i) heat flux and (ii) temperature at point (3), shown in Figure 6.19. The time begins from when the bubble impacts the surface. The upper graph illustrates the change in surface heat flux, with the lower graph illustrating the change in surface temperature. The — solid line represents the convected heat flux, with the – – dashed line being the stored flux. *a*, *b* and *c* represent distinct bubble motion periods, with *a* corresponding to the impact, up until the bubble leaves the surface. Period *b*, extends from when the bubble leaves the surface up until the bubble no longer bounces away from the surface, with *c* corresponding to the time the bubble is no longer moving away from the surface, while still oscillating.

Point (3) is approximately located at the left hand side of Figure 6.21 (a). This point is not the initial point of contact of the bubble against the surface but rather the continuation of the impact process, as the bubble impacts from left to right[4]. After the initial impact a more significant increase in convective heat flux is observable; this is contrary to the other edge locations at which a significant decrease in convective flux occurred. This peak has

[4]The impact is along a 45 degree angle to the S_x direction.

a maximum value of approximately 170 kW/m^2 at point (3), and is a result of the impact of the bubble's rising wake, which impacts on the left of the contact zone as the bubble moves right. After a time of 40 *ms* the convective heat flux returns to that of liquid natural convection. After 40 *ms*, point (3) is no longer affected by the rolling wake vortex, which spreads outwards along the surface, no longer affecting point (3), with this being evident in Figure 6.20 (b) as point (3) is inside the rolling vortex.

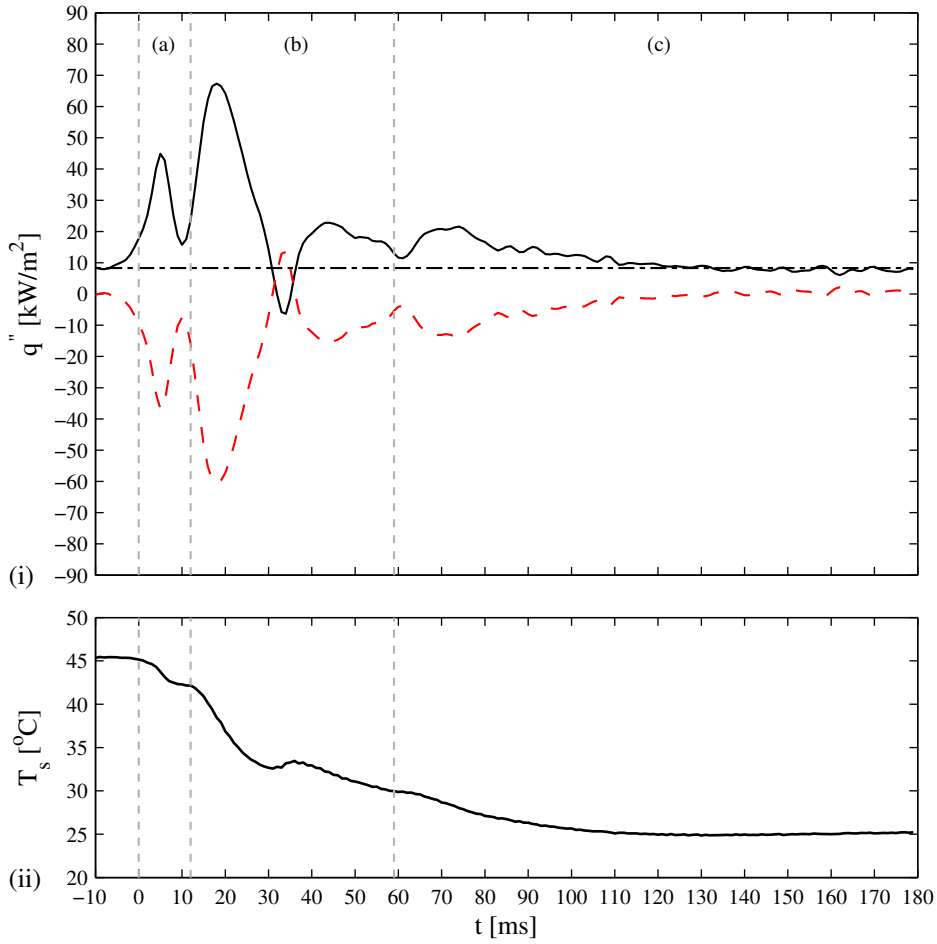

Figure 6.24: Time trace of (i) heat flux and (ii) temperature at point (4), shown in Figure 6.19. The time begins from when the bubble impacts the surface. The upper graph illustrates the change in surface heat flux, with the lower graph illustrating the change in surface temperature. The — solid line represents the convected heat flux, with the – – dashed line being the stored flux. *a*, *b* and *c* represent distinct bubble motion periods, with *a* corresponding to the impact, up until the bubble leaves the surface. Period *b*, extends from when the bubble leaves the surface up until the bubble no longer bounces away from the surface, with *c* corresponding to the time the bubble is no longer moving away from the surface, while still oscillating.

The final point of interest, point (4), is located slightly left of centre during the initial impact, at a position of (0.2, 0) *mm*. The bubble's direct impact with the surface occurs at a time of 0 *ms*, while a slight increase in convective heat flux is observable 5 *ms* prior to impact, demonstrating that the bubble pushes fluid ahead of itself, during its rise. In Figure 6.24 (i), the initial spike in heat flux within time period *a*, is a result of the initial impact. It is notable that the time to reach this maximum is longer than that for a similar spike in Figure 6.22, with this being a result of point (4) being positioned slightly inside the impact rim. As the bubble begins to rebound from the surface, a drop in convective cooling is observed. However, no negative heat flux is observed, which is due to the sudden impact of the bubble's wake. This wake is directed by the bubble's rebound towards point (4), resulting in the second increase in convective heat flux. The negative dip at 35 *ms* was found to be a result of the bubble's second impact. Thus, point (4) is outside the second impact zone and therefore not subject to significant enhancement due to the second impact. Instead a reduction in heat flux occurs, as warm fluid is pushed into the region where the initial wake impacted. This region was subject previously to high levels of heat flux, which caused a drop in local surface temperature, so subsequent heating by warm boundary layer fluid is plausible. This marginal increase in temperature may be noticed at a time of 35 *ms* in Figure 6.24 (ii).

The convective heat flux peak at around 45 *ms* occurs as the bubble begins to bounce away from the surface for a second time; again the direction of the bouncing is away from point (4). This movement away causes an enhancement followed by a slight reduction, at the end of time period *b*, which is the re-impact time. Finally, as in the case of Figure 6.22, the broad peak in heat flux in time period *c* is due to the bubble oscillating on the surface. After 120 *ms* the local convective heat flux settles to that of liquid natural convection.

6.4.2 Case 2: 3.3 *mm* Bubble

Figure 6.25 illustrates the convective heat flux for a 3.3 *mm* bubble released from a height of 25 *mm* at two distinct times, with the first being 6 *ms* after the initial impact of the bubble (Figure 6.19 (a)), and the second being the last moment that the bubble is not in contact with the surface (106 *ms*); after this time the bubble is either resting or oscillating on the surface

(Figure 6.25 (b)).

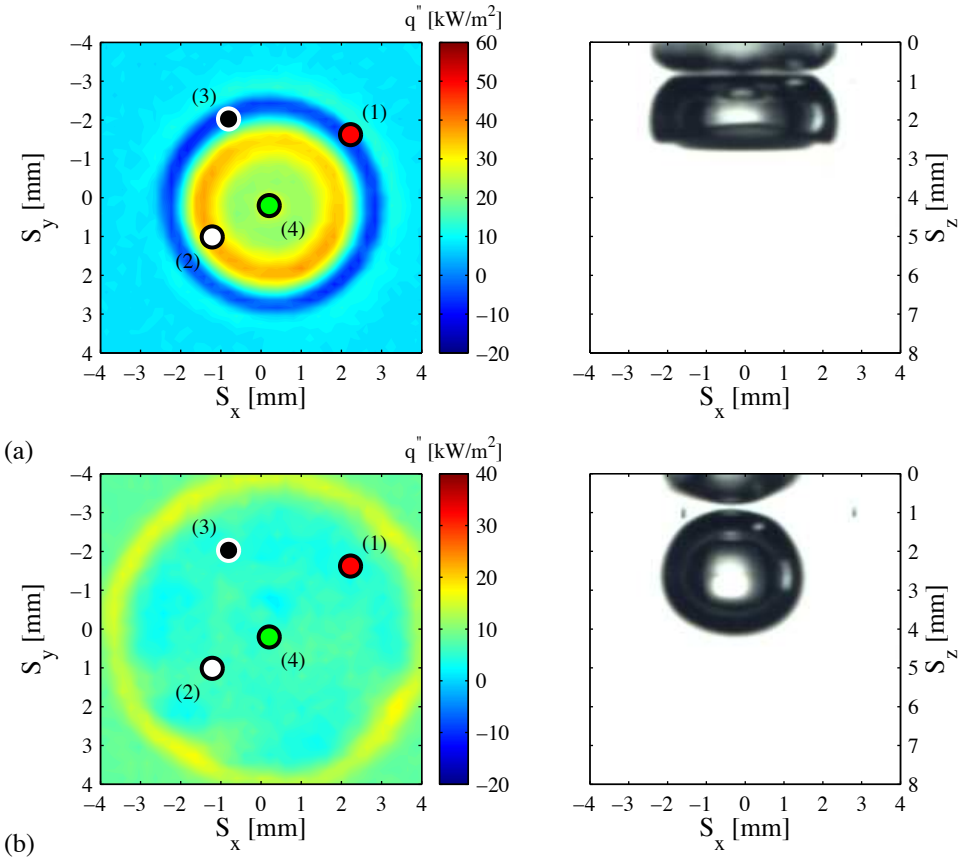

Figure 6.25: Image pair depicting both convective heat flux and bubble location on the surface and the points of interest (1, 2, 3 and 4). (a) corresponds to a time of 6 *ms* after impact and (b) corresponds to the bubble approaching the surface for the final time after completing a number of bounces, which in this case is 106 *ms*. The convective heat flux scale varies between the two cases, illustrating the enhancement reduction with time. In this case the release height is 25 *mm*, with a bubble diameter of 3.3 *mm*.

Figure 6.26 illustrates the time varying heat flux and surface temperature at the first point of interest, marked as point (1) in Figure 6.25 at an approximately position of (2.2, -1.6) *mm*. Point (1) is at the outer edge of the bubble during the initial impact, and just outside the final location of the bubble. As in the previous example, the black solid line represents the time varying convective heat flux, the red dashed line represents the change in the stored flux, with the horizontal line representing the generated heat flux. Figure 6.26 (ii) corresponds to the surface temperature at that location.

During the time period *a*, two distinct peaks are present. The first peak, with a maximum amplitude of 40 kW/m^2, is again the result of the bubble's direct impact on the surface. The

shape of the bubble's impact is sketched in Figure 6.27 (a), from which it is clear that more significant shape changes occur when the 3.3 *mm* bubble is compared to the smaller 2.8 *mm* bubble. Firstly, the bubble's path in this example is vertically orientated, which results in a symmetrical heat transfer pattern; this may be inferred from Figure 6.25 (a). The increased bubble volume has an effect on the bubble's impact shape, causing more spreading, in essence increasing the impact area. This increased impact area also affects the volume of trapped fluid at the centre of the bubble, illustrated in Figure 6.27 (a), with the depth of the trapped fluid being greater.

The large spike in convective flux at around 15 *ms* is perhaps due to the bubble's wake, which is continually rising as the bubble impacts and rebounds. This wake is unable to impact the surface initially due to the size of the bubble, which spreads outwards on impact. However, as the bubble retracts, this allows the wake access to the surface. During the retraction process (Figure 6.27 (b)) the wake hugs the bubble's edge, slipping in between the boundary layer fluid and the bubble. With this retraction a reduction in convection would be expected; instead a substantial increase in convective heat flux occurs, reaching a value of 120 kW/m^2. A significant drop in surface temperature is also evident in Figure 6.26 (ii).

As the bubble continues to recover its shape a secondary dimple is formed, as illustrated by the dashed bubble cross section in Figure 6.27 (b). The two dimples are visible due to the transparent nature of the bubble, and at their closest are 0.3 *mm* away from each other. The sudden change in the bubble's shape propels the cool fluid onto the surface, causing an annular enhancement region. This region does not extend beyond the extremities of the bubble depicted in Figure 6.27 (b) (solid line), which is also evident in Figure 6.13. As the bubble retracts in time period *b*, the spike in convective flux steadily reduces to very low values, which is caused by the repeated bouncing of the bubble in the same region, not allowing cooling fluid access to the surface. Instead, the local fluid is recycled, while being continuously heated by the surface.

Figure 6.28 illustrates the convective heat flux and surface temperature for the second point of interest, marked as point (2) in Figure 6.25 at an approximately position of (-1.2, 1) *mm*. The initial location of point (2) is inside the annular ring where the highest convective heat flux occurs at impact. At this point an immediate increase in convective heat flux does not occur. Instead, a gradual increase is observed, which may be seen in time period *a*.

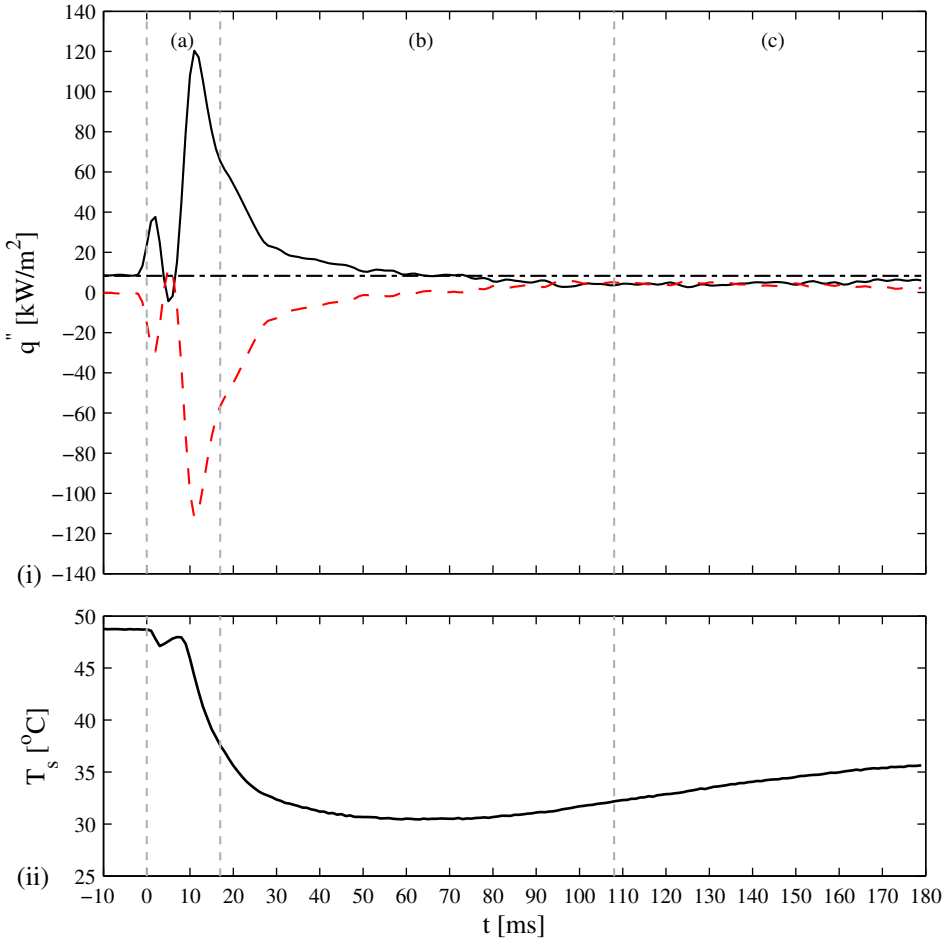

Figure 6.26: Time trace of (i) heat flux and (ii) temperature at point (1), shown in Figure 6.25. The time begins from when the bubble impacts the surface. The upper graph illustrates the change in surface heat flux, with the lower graph illustrating the change in surface temperature. The — solid line represents the convected heat flux, with the – – dashed line being the stored flux. *a*, *b* and *c* represent distinct bubble motion periods, with *a* corresponding to the impact, up until the bubble leaves the surface. Period *b*, extends from when the bubble leaves the surface up until the bubble no longer bounces away from the surface, with *c* corresponding to the time the bubble is no longer moving away from the surface, while still oscillating.

This altered trend results from the dimple created during the impact process. As the bubble begins its retraction from the surface, the edges of the bubble are drawn across the surface, which is consistent with the steady increase in convective flux. The dip in convective flux that follows is again due to the continuation of the rebound process.

The large spike in heat transfer at the beginning of time period *b*, is related again to the rising wake being propelled against the surface as the bubble rapidly changes shape. The

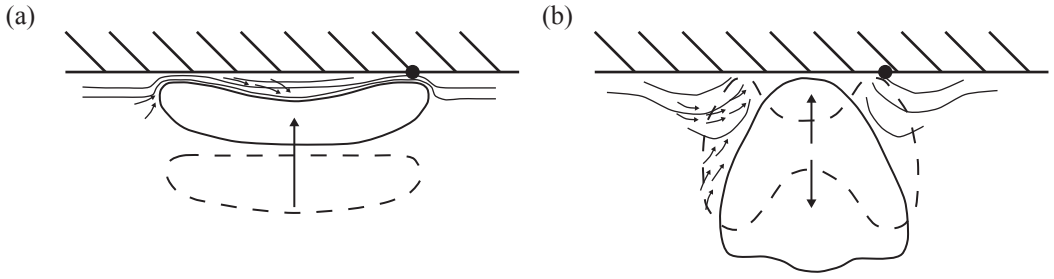

Figure 6.27: Sketches showing (a) the bubble approach (-4 – 0 *ms* prior to impact), (b) bubble initial rebound from the surface (8 – 16 *ms*). The dashed bubble is the bubble's shape and position prior to the solid solid outline. The black circle indicates the approximate location of point (1).

large dip in convective flux, at a time of 50 *ms*, coincides with the bubble's second impact. A sharp rise in the surface temperature is observable in Figure 6.28 (ii), at the same time. Point (2) is at the outer edge of the bubble during its second impact, with the reduction in heat flux thought to be caused by warm fluid, entrained during the initial rebound, now being propelled back to the surface. This is consistent with the increase in surface temperature at point (2) at around 50 *ms*. The entrainment of fluid in this way has been observed by Beer [117] and Lucic *et al.* [118].

At a time of 55 *ms* an increase in the convective heat flux is observable, which is thought to be due to the new dimple, created on the second impact, inverting. This may propel cool fluid against the surface, extending steadily outwards. This spike in heat flux falls off as the bubble bounces for the second time, re-impacting at a time of 80 *ms*. This time coincides with the reduced convective heat flux, approximately half that of liquid natural convection. The small peak at a time of 95 *ms* is again a result of the bubble's rebound from the surface. What is notable in this case is the extent of time period *b*, being almost double that for the smaller 2.8 *mm* bubble. The very small peaks at 125 and 160 *ms* are a result of the bubble oscillating on the surface, with the peaks coinciding with the bubble's rebound. This is similar to the previous case at 95 *ms*, although the bubble does not leave the surface in these cases.

Figure 6.29 depicts the convective heat flux and surface temperature at the third point of interest, initially located at (-0.8, -2) *mm*. Point (3) is located within the annular region where the maximum enhancement occurs upon impact, while also being at the edge of the formed dimple. This results in a heat transfer pattern similar to that of point (1), with the

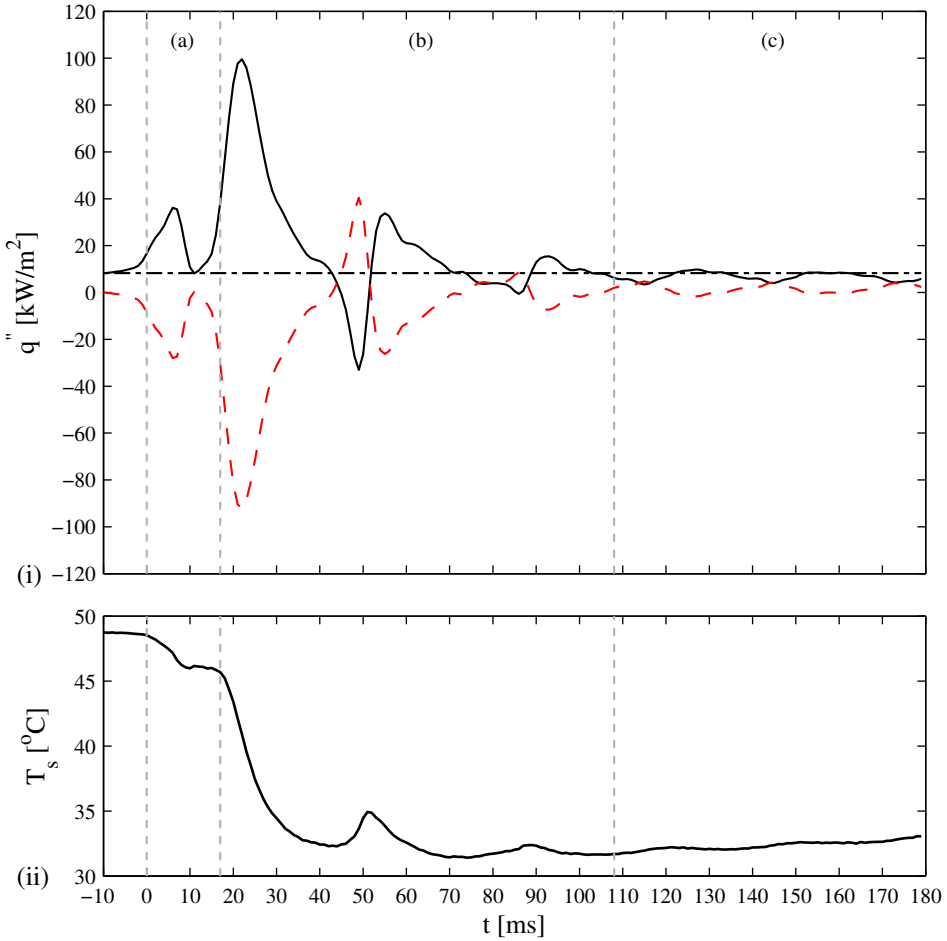

Figure 6.28: Time trace of (i) heat flux and (ii) temperature at point (2), shown in Figure 6.25. The time begins from when the bubble impacts the surface. The upper graph illustrates the change in surface heat flux, with the lower graph illustrating the change in surface temperature. The — solid line represents the convected heat flux, with the – – dashed line being the stored flux. *a*, *b* and *c* represent distinct bubble motion periods, with *a* corresponding to the impact, up until the bubble leaves the surface. Period *b*, extends from when the bubble leaves the surface up until the bubble no longer bounces away from the surface, with *c* corresponding to the time the bubble is no longer moving away from the surface, while still oscillating.

only discernible difference occurring at a time of 95 *ms*, where a slight peak in heat flux occurs. This peak is related again to the bubble bouncing away from the surface. These undulations were not observed in Figure 6.26 as point (1) is slightly further away from the centre of the bubble.

Point (4), data for which are shown in Figure 6.30, is located at the approximate centre of the impact zone, as shown in Figure 6.25. This point is always beneath the bubble, as

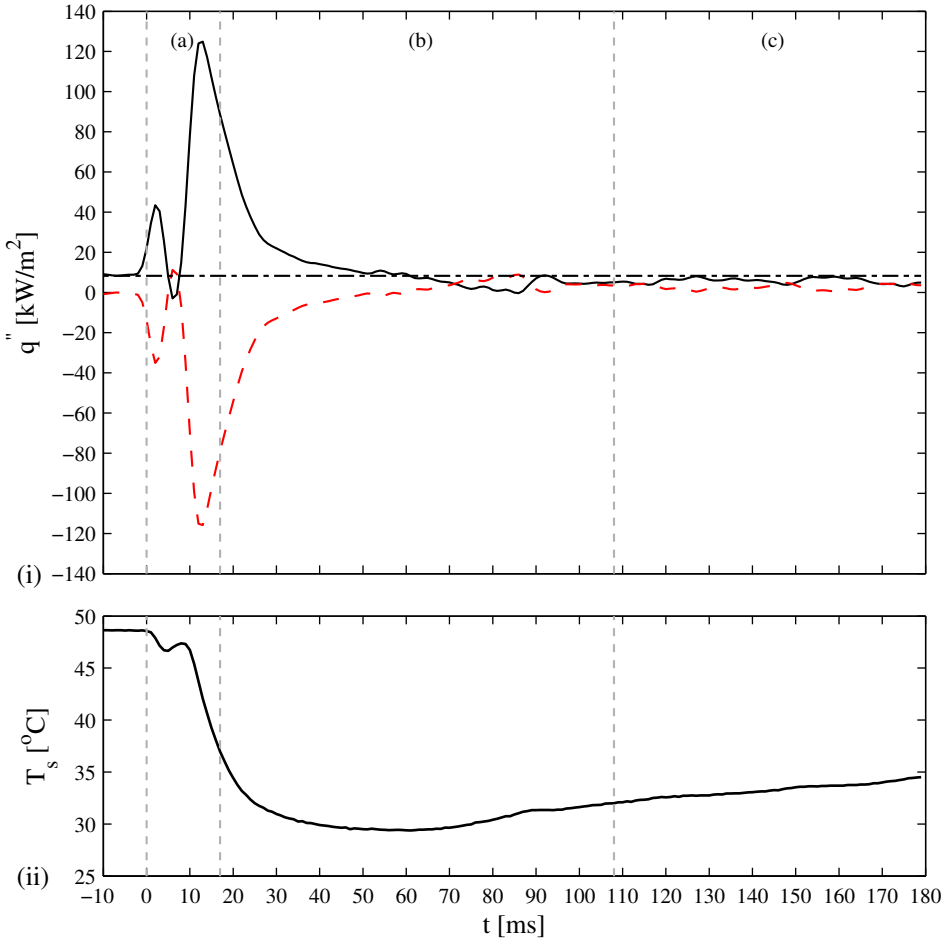

Figure 6.29: Time trace of (i) heat flux and (ii) temperature at point (3), shown in Figure 6.25. The time begins from when the bubble impacts the surface. The upper graph illustrates the change in surface heat flux, with the lower graph illustrating the change in surface temperature. The — solid line represents the convected heat flux, with the – – dashed line being the stored flux. *a*, *b* and *c* represent distinct bubble motion periods, with *a* corresponding to the impact, up until the bubble leaves the surface. Period *b*, extends from when the bubble leaves the surface up until the bubble no longer bounces away from the surface, with *c* corresponding to the time the bubble is no longer moving away from the surface, while still oscillating.

the bubble does not drift significantly in any direction. During the initial impact, point (4) is located at the centre of the dimple. The exact fluid temperature within the dimple is not known, although it is believed to contain a mixture of warm trapped boundary fluid along with cool fluid collected prior to impact.

The first initial spike in heat flux, during time period *a*, is linked to the dimple. It has already been shown that the direct impact of the bubble significantly enhances heat transfer.

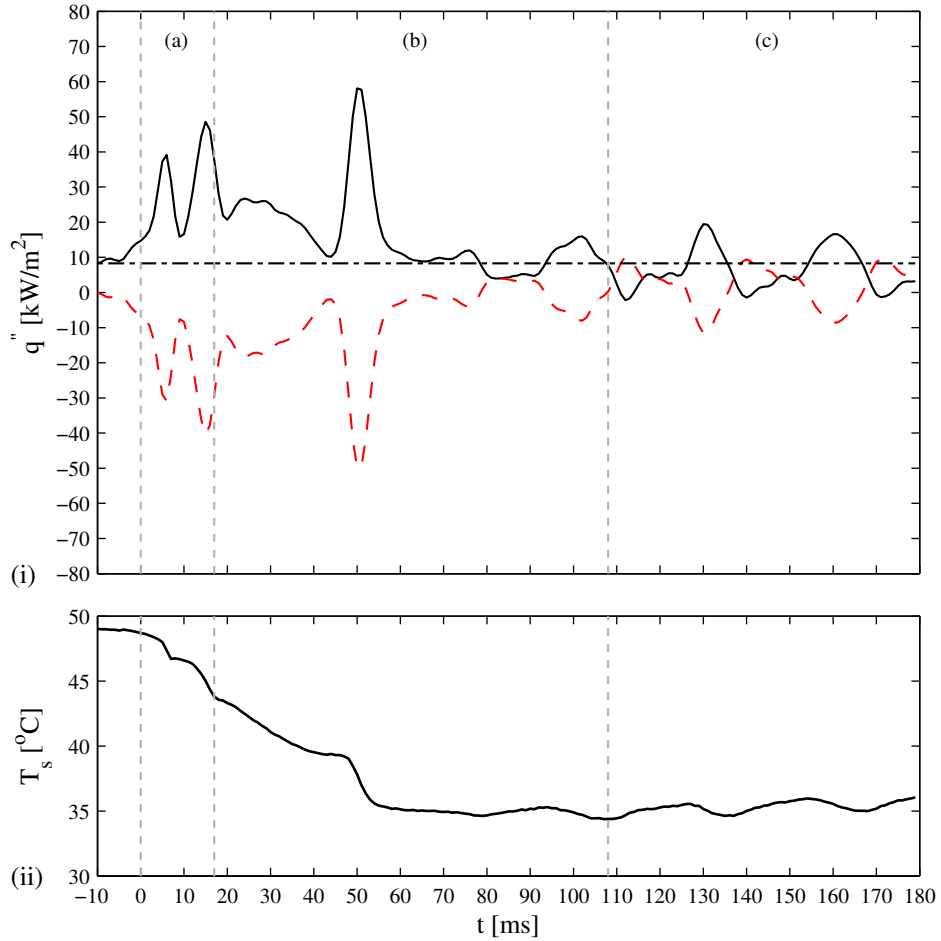

Figure 6.30: Time trace of (i) heat flux and (ii) temperature at point (4), shown in Figure 6.25. The time begins from when the bubble impacts the surface. The upper graph illustrates the change in surface heat flux, with the lower graph illustrating the change in surface temperature. The — solid line represents the convected heat flux, with the – – dashed line being the stored flux. *a*, *b* and *c* represent distinct bubble motion periods, with *a* corresponding to the impact, up until the bubble leaves the surface. Period *b*, extends from when the bubble leaves the surface up until the bubble no longer bounces away from the surface, with *c* corresponding to the time the bubble is no longer moving away from the surface, while still oscillating.

In this case, the surface is mostly separated from the bubble by the dimple, but the centre of the dimple does tip the surface i.e. partial inversion, observable for a few milliseconds. This partial inversion is cut short by the rebound process and the hemispherical dimple returns as depicted by the dashed line in Figure 6.27 (b). This point then experiences a quick reduction in convective heat flux as the centre of the dimple is no longer in contact with the surface; the edges of the bubble are drawn inwards, mixing the fluid within the dimple and causing

the reduction observed. The second spike is also due to the dimple; in this case, the dimple fully inverts as depicted in Figure 6.27 (b), pushing the trapped fluid towards the surface.

The broad time period of raised heat flux, between the times of 20 – 40 *ms*, occurs as the bubble is bouncing on the surface, with its re-impact corresponding to a the dip at 45 *ms*. The large spike in heat flux at a time of 50 *ms* is a result of the direct impact of the bubble. Again, due to the bubble's size a small dimple is formed upon re-impact. After a time of 60 *ms*, the undulations are similar to those of Figure 6.28 and are due to the bubble bouncing and oscillating on the surface. As point (4) is directly beneath the bubble more significant undulations occur than at the peripheral locations.

6.4.3 Case 3: 4.1 *mm* Bubble

Figure 6.31 illustrates the convective heat flux for a 4.1 *mm* bubble released from a height of 25 *mm* at two distinct times, with the first being 6 *ms* after the initial impact of the bubble (Figure 6.31 (a)), and the second being the last moment that the bubble is not in contact with the surface (50 *ms*); after this time the bubble is either resting or oscillating on the surface (Figure 6.31 (b)). This larger bubble is broadly similar to the 3.3 *mm* bubble, however the bubble impact is at a slight angle, while the centre of the bubble does not impact at the centre of the test section. This results in an asymmetric bouncing event which is evident in Figure 6.31.

Figure 6.32 shows the convective heat flux and surface temperature at the first point of interest, marked as point (1) in Figure 6.31 at an approximately position of (-0.4, 2.6) *mm*; this is just at the edge of the bubble during the initial impact. Notable, the initial impact process (time period *a*) has a longer duration when compared to those of the smaller bubbles. This longer duration also changes the profile of the initial spike in heat transfer, producing a feature of longer duration but with similar amplitude. Similarly, the reduction in convective heat flux occurs for a longer time period. At the beginning of time period *b*, a significant increase in convective heat transfer occurs. This significant increase in convective heat flux is due to the bubble's wake as will be shown and discussed in Section 7.2.3. As sketched for the smaller bubbles, during the retraction process the continually rising wake is propelled towards the surface as the bubble retracts and rebounds from the surface. In the present

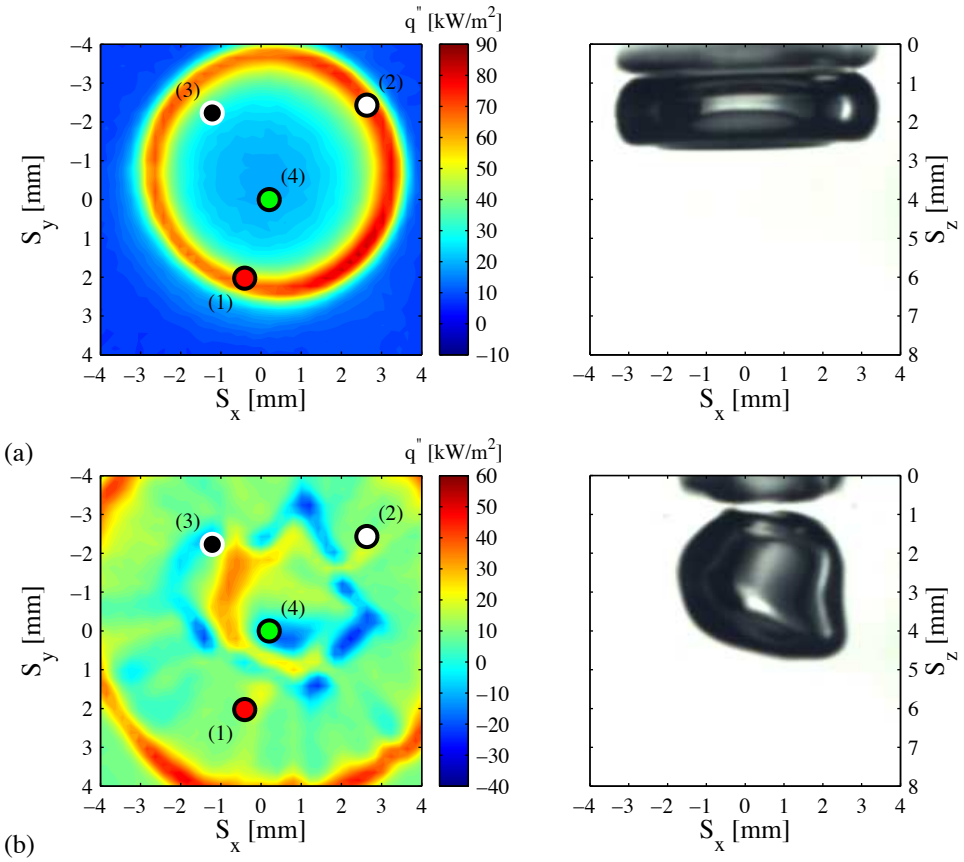

Figure 6.31: Image pair depicting both convective heat flux and bubble location on the surface and the points of interest (1, 2, 3 and 4). (a) corresponds to a time of 6 *ms* after impact and (b) corresponds to the bubble approaching the surface for the final time after completing a number of bounces, which in this case is 50 *ms*. The convective heat flux scale varies between the two cases, illustrating the enhancement reduction with time. In this case the release height is 25 *mm*, with a bubble diameter of 4.1 *mm*.

case the wake initially impacts at a time of 15 *ms*, in the annular region outside the impact zone; with the bubble's continued retraction the wake is pulled further inwards atop point (1). This enhancement process steadily reduces as the bubble continues to bounce, up until the re-impact at 52 *ms*. The effect of re-impact is not evident until 55 *ms*, due to the spatial distance between the point of first impact and the location of point (1).

In Figure 6.32, the slight peak in convective heat transfer at a time of 70 *ms* is due to the bubble beginning to bounce away from the surface. In this case, the second bounce of the bubble lasts for only 2 – 3 *ms*, with the bubble only marginally leaving the surface. After a time of 90 *ms*, very little variation in heat transfer is observed, with just a small reduction in liquid natural convection. At this time the bubble has moved to the right away from point

(1), with the only convection being slowly drifting fluid.

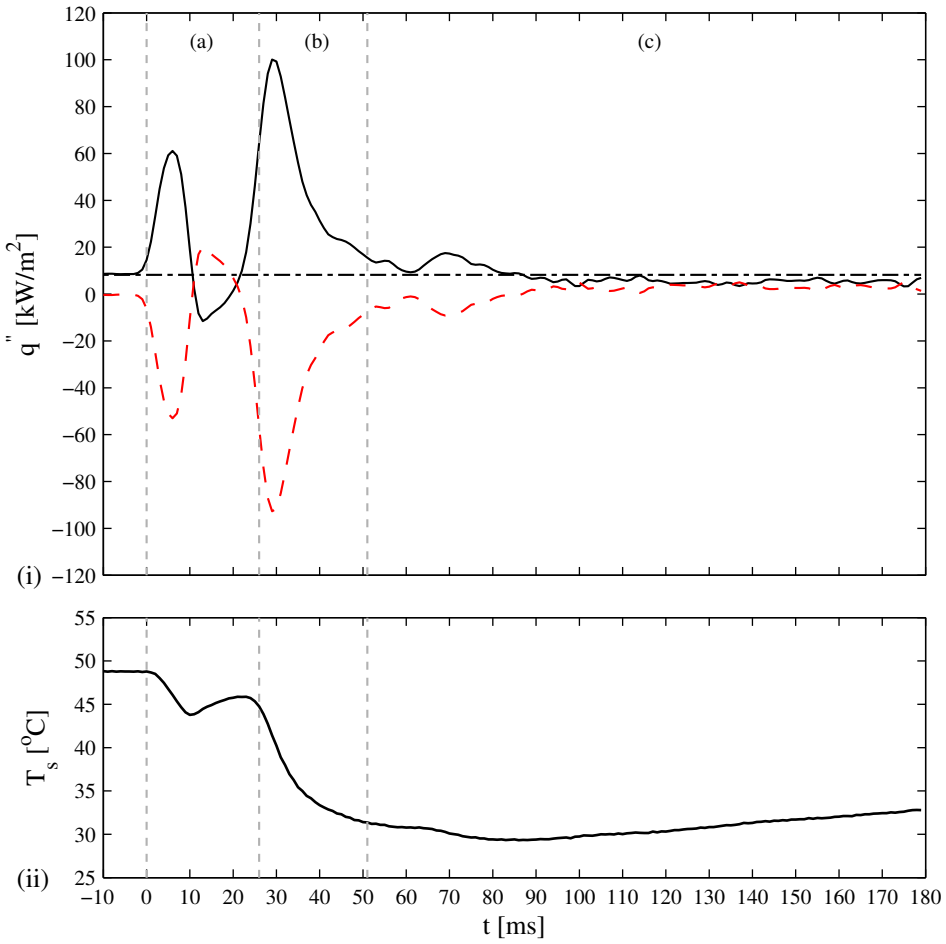

Figure 6.32: Time trace of (i) heat flux and (ii) temperature at point (1), shown in Figure 6.31. The time begins from when the bubble impacts the surface. The upper graph illustrates the change in surface heat flux, with the lower graph illustrating the change in surface temperature. The — solid line represents the convected heat flux, with the – – dashed line being the stored flux. *a*, *b* and *c* represent distinct bubble motion periods, with *a* corresponding to the impact, up until the bubble leaves the surface. Period *b*, extends from when the bubble leaves the surface up until the bubble no longer bounces away from the surface, with *c* corresponding to the time the bubble is no longer moving away from the surface, while still oscillating.

Convective heat flux and surface temperature for point (2) are shown in Figure 6.33, with this position again being at the edge of the bubble's impact zone at (2.6, -2.4) *mm*. Even though points (1) and (2) are both in the contact zone, as seen from Figure 6.31, point (2) on the right hand side of this zone experiences convective heat fluxes that are some 25% higher than at point (1) on the left during the initial impact. This was found to be due to the

irregular impact process. Similarly, a higher negative heat flux occurred on the right hand side. The second peak is remarkably similar to that of Figure 6.32 for point (1), having a steep incline and a somewhat gradual decline; this enhancement was attributed to the bubble wake.

At a time of approximately 65 *ms*, a significant reduction in convective heat flux occurs. At this time the bubble has re-impacted the surface, while having shifted its position slightly to the right in the direction of point (2). This shifting causes a "c" shaped region of high heat flux on the left hand side of the bubble and a "c" shaped region of low heat flux on the right hand side, which is consistent with the dip observed in Figure 6.33 at point (2), on the right. This region of very low convective heat flux must be a result of warm fluid being drafted onto the surface as a sudden increase in the surface temperature is observable at 65 *ms*.

At times of 100 and 140 *ms*, similar patterns in heat transfer occur. The enhancement process is the same in each case, but with a variation in the amplitude of the bubble motion. As the bubble oscillates in the positive S_x direction, warm fluid is collected and then pushed towards the surface. This reduction in heat transfer coincides with the bubble returning to surface. At each instant a visible jump in surface temperature occurs. At a time of 170 *ms*, the bubble begins to attach to the surface, with the apparent rupture of the thin layer of fluid separating the bubble from the surface, accompanied by the bubble spreading across the surface. This event does not appear in the short time frame shown for the smaller bubbles which is 180 *ms*.

Point (3), data for which are shown in Figure 6.34, is located at (-1.2, -2.2) *mm*, which is inside the initial impact bubble ring. As this point is inside the initial annular region of high heat transfer, the first spike in heat flux has two stages, with levels of 30 kW/m^2 and 50 kW/m^2, respectively. The first stage corresponds to the direct bubble impact, while the latter stage is due to the bubble's retraction, moving across point (3), as it begins its rebound from the surface. The secondary spike at 35 *ms* is again due to the impact of the bubble's wake. The reduction in heat transfer at the end of time period *b* occurs due to the re-impact of the bubble against the surface. Due to the larger size of the bubble, the time for the entire bubble to settle before rebounding again is longer than 11 *ms*; this settling results in the undulation in the convective heat flux between the times of 60 – 70 *ms*. At a time of 90 *ms*,

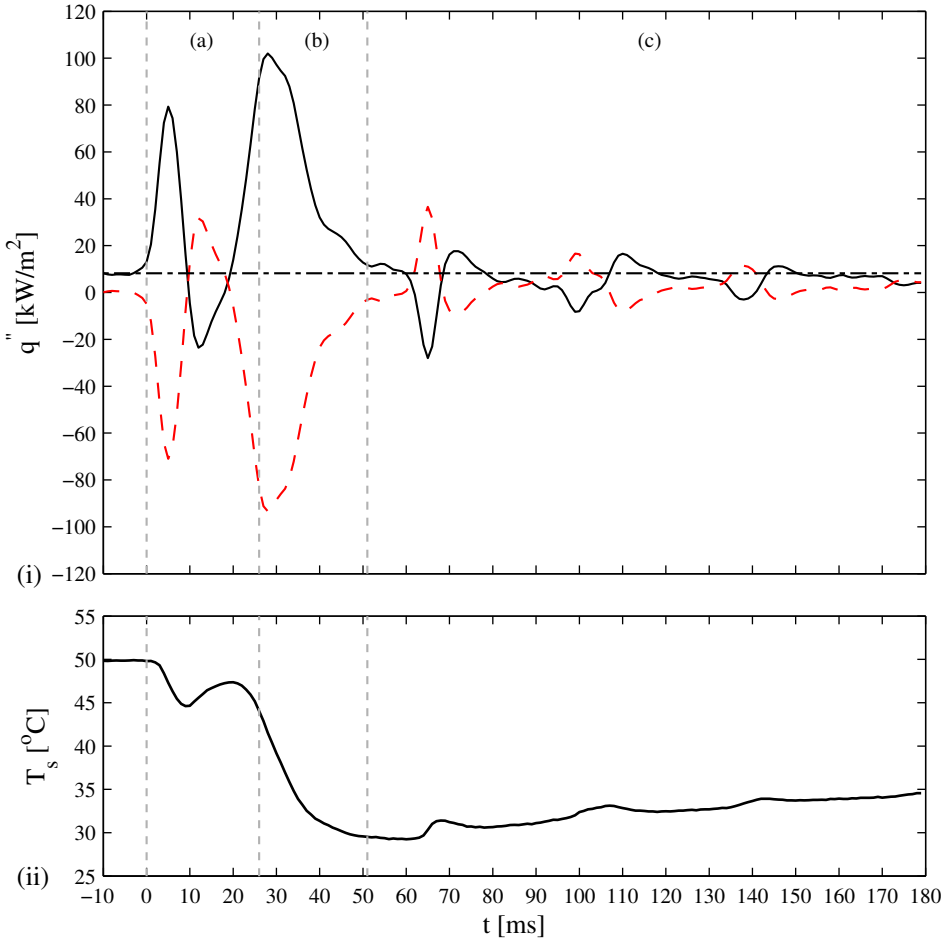

Figure 6.33: Time trace of (i) heat flux and (ii) temperature at point (2), shown in Figure 6.31. The time begins from when the bubble impacts the surface. The upper graph illustrates the change in surface heat flux, with the lower graph illustrating the change in surface temperature. The — solid line represents the convected heat flux, with the – – dashed line being the stored flux. *a*, *b* and *c* represent distinct bubble motion periods, with *a* corresponding to the impact, up until the bubble leaves the surface. Period *b*, extends from when the bubble leaves the surface up until the bubble no longer bounces away from the surface, with *c* corresponding to the time the bubble is no longer moving away from the surface, while still oscillating.

a peak in heat transfer occurs, followed by a steady reduction before stabilising to liquid natural convection levels. This peak and gradual reduction is due to the bubble's motion from left to right in the S_x plane, creating a wake at the rear of the bubble; a similar feature was seen in Figure 6.20 at point (1) for the 2.8 *mm* bubble.

Figure 6.35 shows the heat flux and surface temperature at point (4), which is located at the centre of the test surface, almost at the centre of the bubble impact zone. The convective

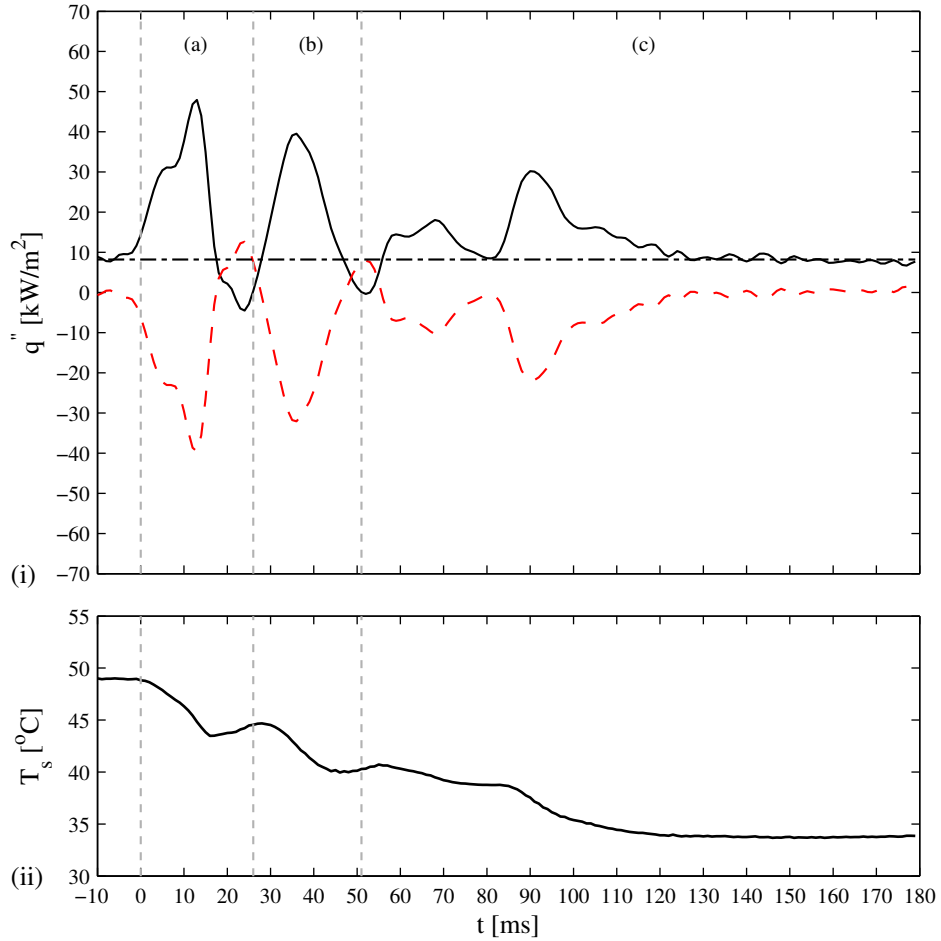

Figure 6.34: Time trace of (i) heat flux and (ii) temperature at point (3), shown in Figure 6.31. The time begins from when the bubble impacts the surface. The upper graph illustrates the change in surface heat flux, with the lower graph illustrating the change in surface temperature. The — solid line represents the convected heat flux, with the – – dashed line being the stored flux. *a*, *b* and *c* represent distinct bubble motion periods, with *a* corresponding to the impact, up until the bubble leaves the surface. Period *b*, extends from when the bubble leaves the surface up until the bubble no longer bounces away from the surface, with *c* corresponding to the time the bubble is no longer moving away from the surface, while still oscillating.

heat flux in time period *a* is significantly different from that of points (1) – (3), with two peaks of positive convective heat flux, and no negative peak within time period *a*. The initial peak, with an approximate value of 20 kW/m^2, is linked to direct bubble impact but for a point within the dimple. Due to the size of the bubble, 10 *ms* passes before this peak heat flux is reached. At 25 *ms*, the large increase in convective cooling is related to the inversion of the bubble's dimple. This inversion process pushes a mixture of warm boundary layer

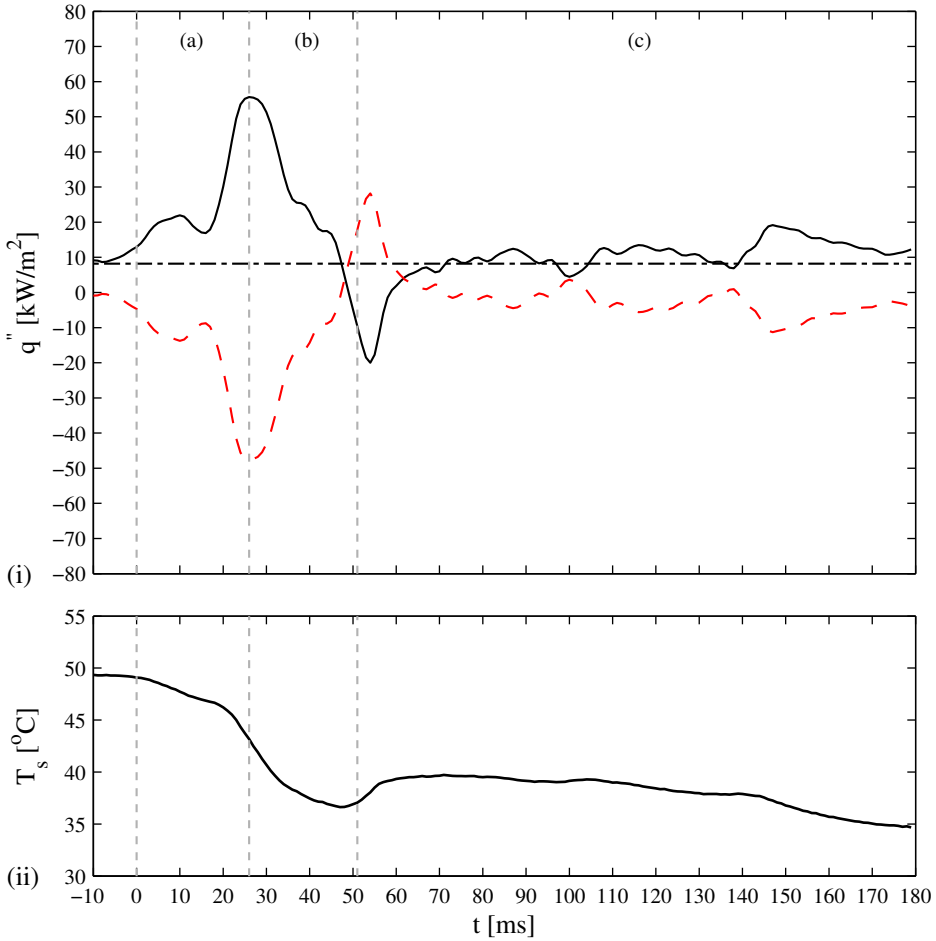

Figure 6.35: Time trace of (i) heat flux and (ii) temperature at point (4), shown in Figure 6.31. The time begins from when the bubble impacts the surface. The upper graph illustrates the change in surface heat flux, with the lower graph illustrating the change in surface temperature. The — solid line represents the convected heat flux, with the – – dashed line being the stored flux. *a*, *b* and *c* represent distinct bubble motion periods, with *a* corresponding to the impact, up until the bubble leaves the surface. Period *b*, extends from when the bubble leaves the surface up until the bubble no longer bounces away from the surface, with *c* corresponding to the time the bubble is no longer moving away from the surface, while still oscillating.

fluid and cooler wake fluid against the surface, locally increasing heat transfer.

At approximately 55 *ms*, a significant reduction in convective cooling occurs; this coincides with the second impact of the bubble. Warm boundary layer fluid, captured during the rebound process, is thought to be convected by the bubble, which results in a local surface temperature rise. Two similar peaks in convective cooling occur at 85 and 120 *ms*, and are though to be the result of the oscillation process; in each case, the centre of the peak coin-

cides with the bubble's centroid being the furthest away from the surface. As the bubble has moved from left to right, point (4) is no longer directly beneath the bubble, but instead to the rear of the bubble; this results in different convective cooling, when compared to point (2) at the leading edge of the bubble in Figure 6.28. The final peak at 145 *ms*, is a result of a similar process, to that observable at an earlier time of 90 *ms* in Figure 6.29. This enhancement is due to the motion of the bubble from left to right, causing a slow moving wake to form, which steadily reduces as the bubble settles on the surface. This type of wake is similar to wakes observed for sliding bubbles under low inclination angles. However, in this case the velocity of the bubble is extremely low, making any comparison to available literature difficult.

6.5 Maximum Convective Heat Flux

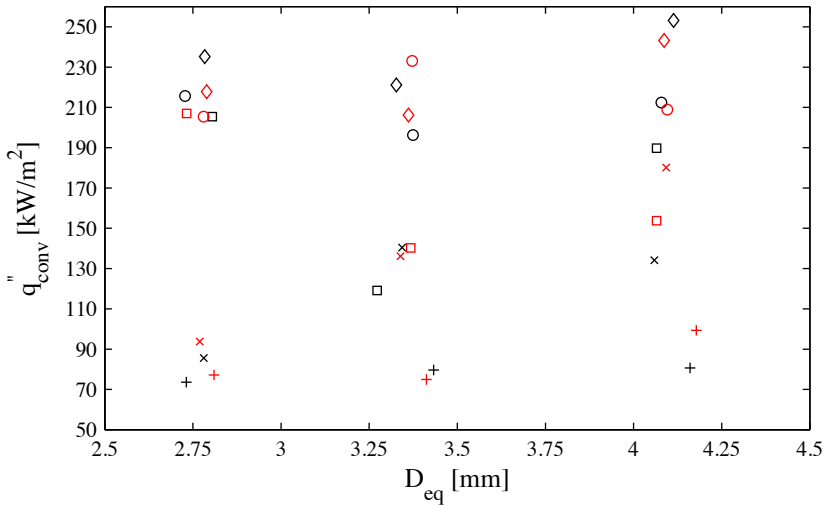

Figure 6.36: Maximum convective heat flux, for all three bubble sizes and heights. The symbols represent the different release heights, while the black and red represent tests one and two: $+$ is 10 *mm*, $\times$ is 20 *mm*, $\square$ is 25 *mm*, $\bigcirc$ is 30 *mm* and $\diamond$ is 35 *mm*. The corresponding occurrence times are tabulated in Table 6.2.

Figure 6.36 illustrates the maximum convective heat flux achieved in all testing, versus the bubble diameter and release height. Figure 6.36 contains results of two tests under identical conditions. The corresponding occurrence times are tabulated in Table 6.2. For the

Table 6.2: Time since initial bubble impact for the maximum convective heat flux, plotted in Figure 6.36 to occur.

D_{eq}	+ 10 *mm*	× 20 *mm*	□ 25 *mm*	○ 30 *mm*	◇ 35 *mm*
2.8 *mm*	5 *ms*	15 *ms*	7 *ms*	6 *ms*	7 *ms*
2.8 *mm*	4 *ms*	12 *ms*	8 *ms*	5 *ms*	13 *ms*
3.3 *mm*	4 *ms*	19 *ms*	21 *ms*	14 *ms*	10 *ms*
3.3 *mm*	4 *ms*	19 *ms*	19 *ms*	10 *ms*	8 *ms*
4.1 *mm*	6 *ms*	19 *ms*	24 *ms*	12 *ms*	14 *ms*
4.1 *mm*	6 *ms*	14 *ms*	25 *ms*	11 *ms*	9 *ms*

small 2.8 *mm* bubble, two distinct groups of data form. The first grouping is for the lower release heights of 10 and 20 *mm*, which achieve maximum heat fluxes of around 70 – 90 kW/m^2. The remaining release heights reach heat fluxes above 200 kW/m^2. As previously shown, the maximum enhancement occurs either due to the direct impact or the impact of the bubble's wake. For the release height of 10 *mm*, the maximum heat flux generally corresponds to direct impact of the bubble. For release heights greater than 20 *mm* the impact of the bubble's wake results in the maximum convective heat flux. If the bubble tilts upon impact the wake enhancement will occur earlier. However, at a height of 20 *mm* in this case, the wake enhancement occurs later; this is because the bubble partially blocks the wake access to the surface, which is dependent on the impact angle and bounce trajectory of the bubble. This is evident in Table 6.2, when comparing occurrence times for the 2.8 *mm* bubble.

In the case of the 3.3 *mm* bubble, three closely defined groups again appear. The lowest enhancement is for the 10 *mm* release height, which occurs at a time of 4 *ms*; this is associated with the direct bubble impact against the surface, disturbing the thermal boundary layers. The second group includes the 20 and 25 *mm* release heights, with a maximum heat flux occurrence time of 19 *ms*; this is related to the wake impacting annularly around the bubble. The final group results in the highest convective heat flux and occurs at intermediate times; this is due to the increased bubble angle of tilt which leads to the wake reaching the surface faster. For the largest bubble, 4.1 *mm*, a clear separation in the data occurs, with the only grouping occurring for nominally identical tests. Again, the convective heat flux for the 10 *mm* release height is related to the direct impact of the bubble, with the remaining values being directly related to the bubble's wake, impacting around the bubble. All three bub-

ble sizes have comparable maximum convective heat flux, with the main difference being both the duration of enhancement and the enhancement affected area. A significant scatter is present in Figure 6.36, although this is to be expected considering the different enhancement mechanisms which are responsible for the maximum heat flux and the variability in bubble motion observed.

6.6 Closing Remarks

This chapter has examined the enhancement in convective heat transfer from a metal horizontal surface during the impact and bouncing process for three different sized bubbles released from four different release heights in uncontaminated fluid. Firstly, liquid natural convection from the surface has been explored, as this provides a baseline for this study. This is followed by an investigation into the change in dimensionless surface temperature, from the moment the bubble leaves the growth orifice up until the end of the recording. The next section provides detailed description of the local variation in convective heat flux, during the impact process, with the final section detailing the temporal variation in convective heat flux at specific locations during the initial impact period.

It was found that the bouncing bubble process could be split into three different regimes by viewing the variation in the surface temperature and relating it to the bubble's motion. The first regime is liquid natural convection and begins once the bubble is released from the growth orifice and extends up until the bubble impacts the surface. The second regime relates to the direct bouncing of the bubble upon the surface and extends from the moment of impact up until the bubble attaches itself to the surface. The final regime is related to the bubble's wake, which extends from the moment of attachment up until the end of the experiment. In most cases, the bubble's wake was observed to disrupt the boundary layer prior to the bubble being attached to the surface.

In the next section, examples of the convective enhancement were presented for the different bubble sizes and four different release heights of 10, 20, 25 and 30 *mm*. It was clear from the images that substantial variation in convective heat flux occurs, with both high and low heat flux levels being observed. These variations were found to be due to rapid movements of the bubble, during the impact and rebound processes. If the rise path of the

bubble was not vertical, the bubble's wake was found to be always displaced in the opposite direction to the bubble's motion. In the case where the bubble rise was in a vertical path, the bubble's wake interacts with the bubble bouncing motion, enhancing heat transfer further.

The next section reported on the temporal variation in both the surface temperature and the convective heat flux. Distinct locations were chosen for analysis, with each location having a different profile. Sketches depicting the bubble's motion and local fluid movement were presented, showing key moments in the bouncing process. The final section of this chapter looked at the minimum and maximum heat flux and the times at which these heat flux levels occurred, relating these levels to different enhancement mechanisms. The maximum observed convective heat flux was 253 kW/m^2, for a 4.1 *mm* bubble, released from a height of 35 *mm*.

Once the bubble has impacted the surface a substantial variation in convective heat transfer occurred. This variation was found to be either spatially symmetric or confined to annular regions, both within the confines of the bubble and the ensuing wake. Within an area close to the bubble, substantial and rapid fluctuations in convective heat flux were observed, being linked to the direct motion of the bubble. On some occasions negative heat flux was observed, indicating that warm liquid was momentarily in contact with the previously cooled surface. This occurred most notably upon the initial rebound of the bubble from the surface. However, it was found to occur also during the re-impact and bouncing process, although the affected area was found to be lower in these cases.

Due the bubble's size, a fluid dimple formed when the bubble was in the vicinity of the surface. This fluid dimple was found to initially retard enhancement in the bubble's centre, although during the bubble's rebound from the surface, the captured fluid was propelled towards the surface due to the inversion of the bubble back to a spherical shape, further enhancing convective heat transfer. Overall the bubble motion was found to enhance convective heat transfer quite significantly. However, it was found that the ensuing wake was found to have the greatest convective enhancement, both spatially and temporarily. Two distinct modes of wake enhancement were found to occur, both being related to the tilt angle of the bubble upon impact. If the bubble's impact was parallel with the surface then its wake created an annular region of cooling around the bubble, whereas if the bubble impact was at an angle then the wake was displaced to one side of the bubble, creating a "c" shaped

cooling region. Chapter 7 will focus on the bubble's wake, as a link to the local fluid motion is key to the understanding of the enhancement levels encountered in this chapter.

Chapter 7

Fluid Flow Field Around Bouncing Bubble

This chapter presents the general features of the wake created by a rising air bubble. The local fluid velocity and direction will be investigated and presented in the form of instantaneous streamlines, velocity vectors and vorticity plots.

Firstly, the fluid motion both ahead of and behind the rising bubble is explored by means of PIV. This is followed by the exploration of different aspects of the ensuing wake and how different bubble paths and shape changes result in different levels of heat transfer enhancement, both spatially and temporally. The final section will explore the flow responsible for secondary enhancement after the bubble has attached to the surface.

This chapter serves as an introduction into the complex fluid flow field around a bouncing bubble.

7.1 Bubble Rise & Impact

In this section instantaneous fluid velocity, velocity streamlines and vorticity data will be presented for all three bubble sizes of 2.8, 3.3 and 4.1 *mm* for a release height of 30 *mm*. As observed by some authors, the wake structure of a bubble may be split into two regions: the

primary and secondary wakes [18]. The primary wake is the region of the wake which may be considered to be still attached to the rear of the bubble, while the secondary wake consists of fluid structures which are shed from the primary wake and may not follow the bubble's direction directly. Secondary wake structures consist either of a standing eddy structure or, more commonly, fluid structures which are shed from the path of the bubble as presented by Veldhuis [28].

This section presents the results of Particle Image Velocimetry (PIV) measurements of the fluid direction and velocity in the x-z plane; the main focus is on the primary wake, immediately at the rear of the bubble. All tests were performed with simultaneous heat transfer measurements. As the laser light sheet is shone from left to right in the x-z plane, the bubble blocks and reduces the laser light intensity on the right hand side of the plane i.e where S_x is positive. This causes spurious vectors and structures, which are not part of the localised fluid motion, to appear. As shown in previous chapters, the bubble undergoes significant shape changes during its rise and, in particular, upon impact and rebound. As the bubble shape becomes more spherical, while still being illuminated by the light sheet, the bubble itself acts as a large seeding particle; this spherical shape induces Mie scattering, resulting in a "flash" of light, which consumes an area much larger than the bubble itself. This again causes spurious vectors and artificial flow structures. With the present set-up, these anomalies are unavoidable and are an inherent problem with two phase flow PIV. Where possible, images with Mie scattering due to the bubble are not presented, instead a similar image at a later time is presented.

The approximate location and maximum extremities of the bubble have been inferred from the raw PIV images and will be depicted by means of an ellipse; this is not the exact outline of the bubble. The interior of this ellipse contains velocity vectors, which, in fact, represent the bubble's velocity. This is due to the fact that the glass tracer particles stick to the bubble and are, in turn, illuminated, allowing the bubble's velocity to be inferred. The following sections will explore the wake generated by the three different bubble sizes.

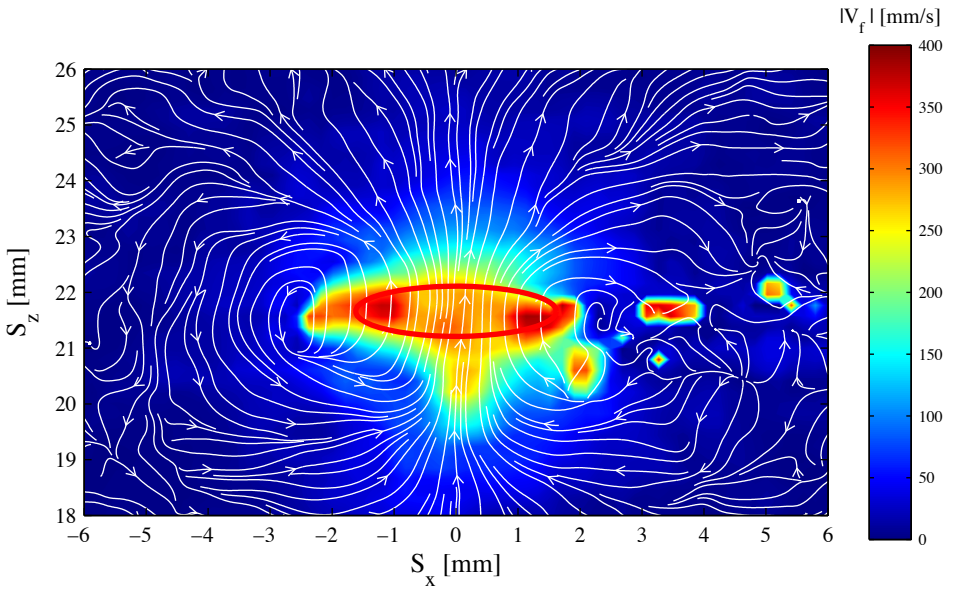

Figure 7.1: Instantaneous streamlines around a 2.8 *mm* bubble, released from a height of 30 *mm*, at a time of 24 *ms* prior to impact. The approximate outline of the bubble is illustrated by means of a red ellipse. The surface is at S_z =30 *mm*.

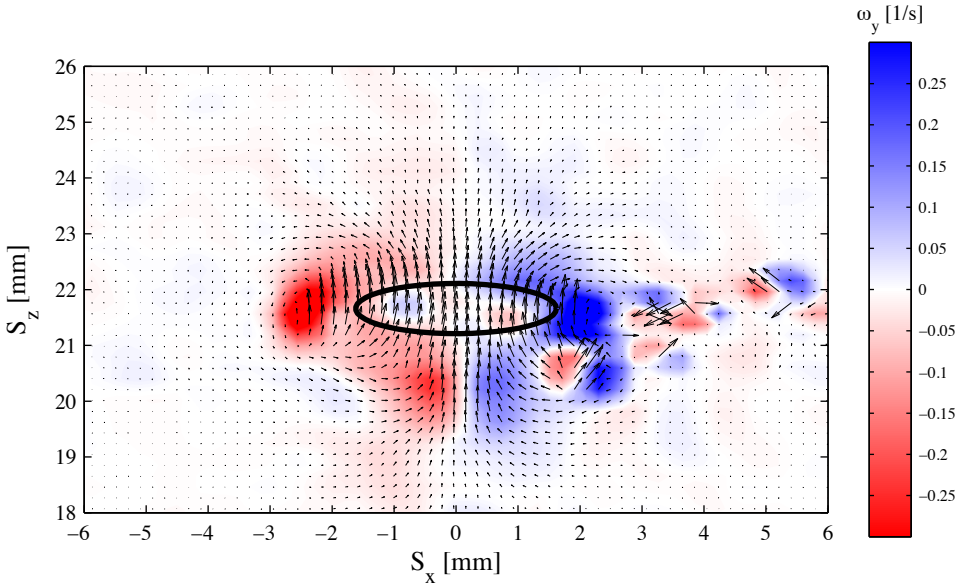

Figure 7.2: Instantaneous velocity vectors and vorticity (ω_y) around a 2.8 *mm* bubble, released from a height of 30 *mm*, at a time of 24 *ms* prior to impact. The approximate outline of the bubble is illustrated by means of a black ellipse. Clockwise vorticity is coloured blue, anti-clockwise is coloured red. The spurious vectors are evident on the bubble's right hand side.

7.1.1 Case 1: 2.8 *mm* Bubble

This section presents the instantaneous velocity streamlines and vorticity data for the flow around a 2.8 *mm* bubble at different times during the bubble's rise. For all cases shown the

surface is at 30 *mm*. Figure 7.1 illustrates the velocity magnitude, $|V_f|$, of the fluid, with the instantaneous streamlines superimposed, at a time of 24 *ms* prior to impact against the heated solid surface. The bubble is 8 *mm* from the surface at this instant. As the major axis is parallel with the surface at this particular instant, there is a symmetry in the streamline and velocity data[1]. Figure 7.2 illustrates the same 2.8 *mm* bubble at the same time, with vorticity (ω_y) and velocity vectors being depicted.

In these figures, it is clear that high levels of velocity and vorticity are present both ahead and behind the bubble, with an area extending to 1 *mm* ahead of the bubble having a significant forward fluid motion. The fluid at the rear of the bubble, extending over a 1 – 2 *mm* region, is significantly affected by the bubble's presence. In Figure 7.1, the streamlines ahead of the bubble indicate that the far field fluid is affected by the presence of the bubble, as it is constrained between the surface and the rising bubble. Fluid at the side of the bubble flows around the edge and collects at the rear of the bubble. This creates a region of fluid circulation, which is highlighted by the streamlines and high counter clockwise vorticity at the bubble's left hand edge. This shear flow combines with the rest of the bubble's wake at the rear of the bubble.

Figures 7.3 and 7.4 illustrate the same 2.8 *mm* bubble but at 12 *ms* prior to impact on the surface, with the bubble's centroid being at S_z = 25.5 *mm*. The bubble's major axis in this case has begun to tilt, by approximately 2°. This shift results in slightly higher fluid velocity on the left hand side of the bubble. The streamlines in Figure 7.3 indicate, that the fluid is still flowing around the bubble, although the rear primary wake is no longer symmetric, as can be inferred from Figure 7.4. In this case, a kink in the primary wake occurs, with the more dominant structure occurring on the left hand side of the bubble. This instability initially occurs at a time of 18 *ms* prior to impact, which corresponds to a height (S_z) of approximately 22.5 *mm*. In Figure 7.4 it can be seen that the line of no vorticity is centred to the left of the central axis (S_x) at 22.5 *mm*, but that this region of zero vorticity at a height of 24 *mm* is centred in the positive S_x direction. It is thought that this shift at the rear of the bubble causes the bubble to turn.

Figures 7.5 and 7.6 illustrate the flow field around the 2.8 *mm* bubble, 6 *ms* prior to

[1]The fluid motion on the right hand side of the bubble can not be completely determined due to the laser light being blocked by the bubble itself.

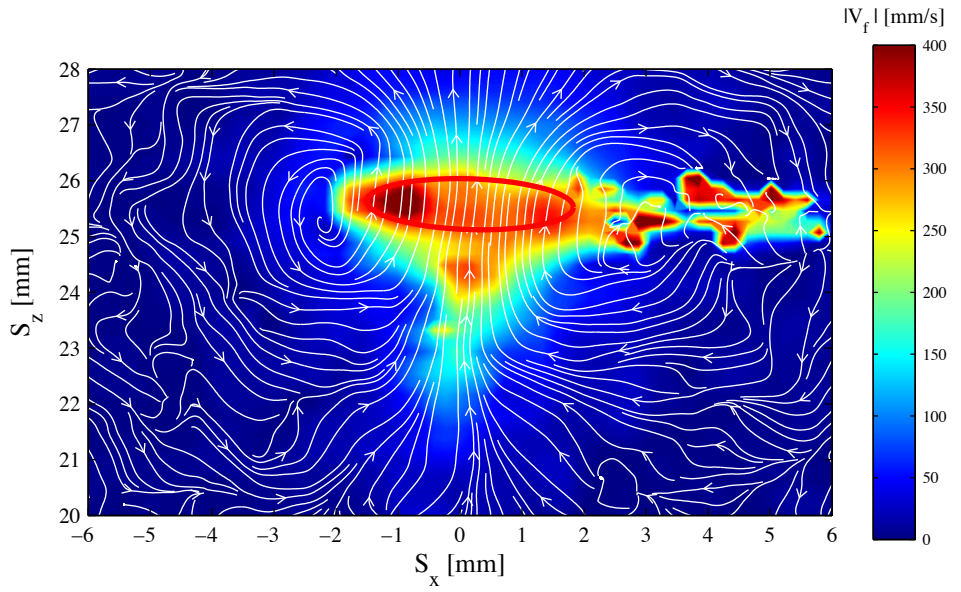

Figure 7.3: Instantaneous streamlines around a 2.8 *mm* bubble, released from a height of 30 *mm*, at a time of 12 *ms* prior to impact. The approximate outline of the bubble is illustrated by means of an red ellipse.

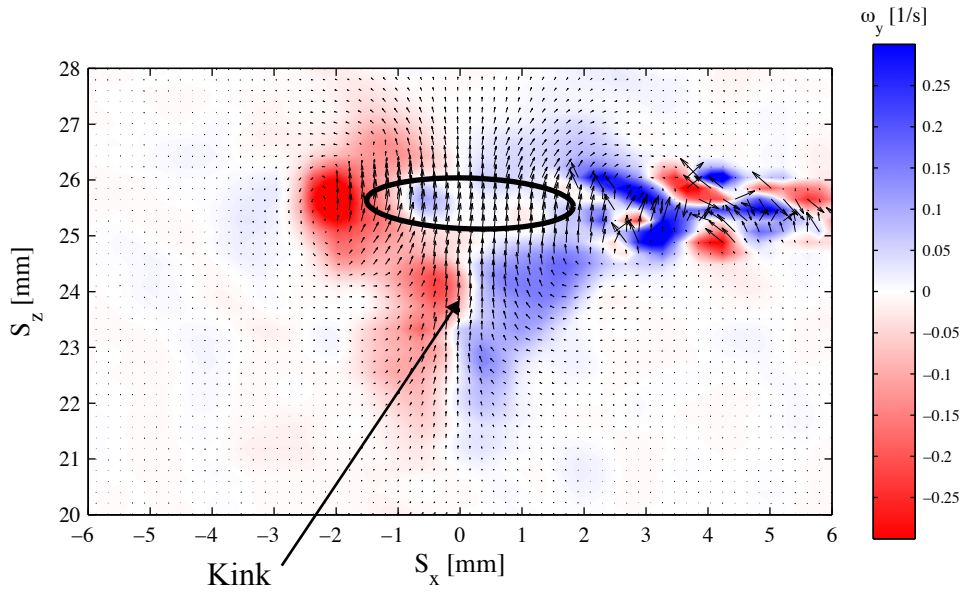

Figure 7.4: Instantaneous velocity vectors and vorticity (ω_y) around a 2.8 *mm* bubble, released from a height of 30 *mm*, at a time of 12 *ms* prior to impact. The approximate outline of the bubble is illustrated by means of an black ellipse. Clockwise vorticity is coloured blue, anti-clockwise is coloured red.

impact. In this case the surface can be inferred at a height of 30 *mm*, 2 – 3 *mm* above the bubble position. The bubble's major axis was found to be at an angle of approximately 10° from the horizontal, with the bubble's centroid moving away from the centre of the test

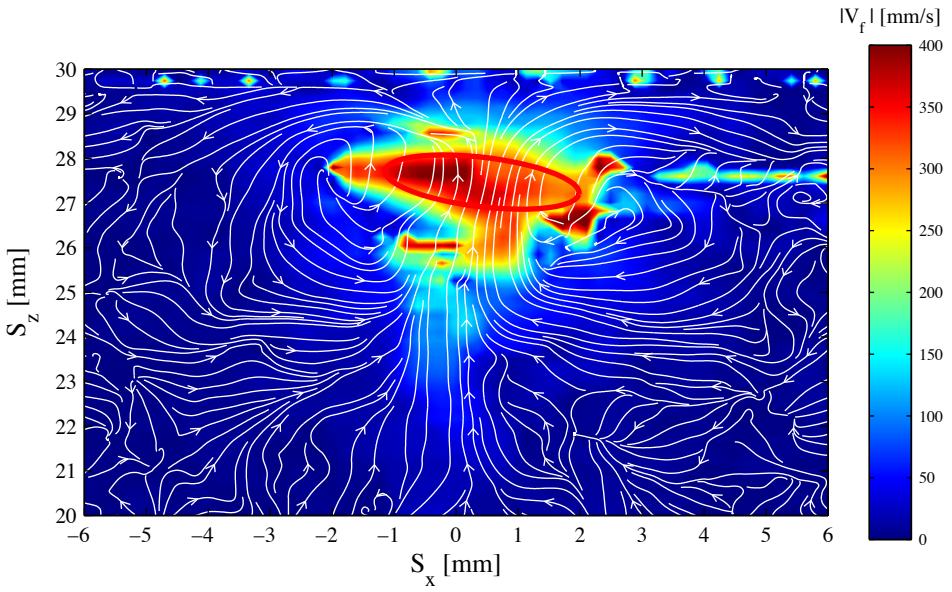

Figure 7.5: Instantaneous streamlines around a 2.8 *mm* bubble, released from a height of 30 *mm*, at a time of 6 *ms* prior to impact. The approximate outline of the bubble is illustrated by means of an red ellipse.

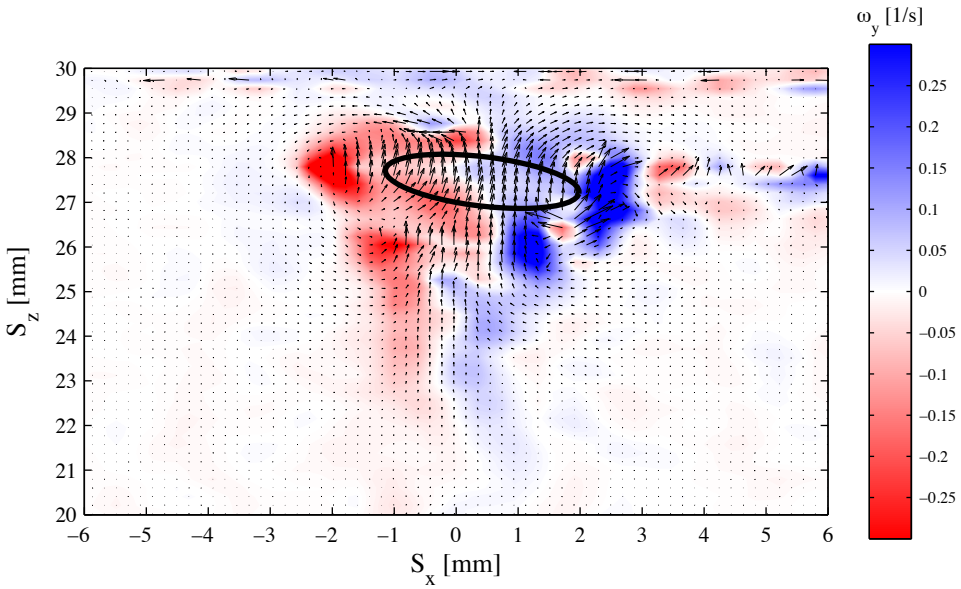

Figure 7.6: Instantaneous velocity vectors and vorticity (ω_y) around a 2.8 *mm* bubble, released from a height of 30 *mm*, at a time of 6 *ms* prior to impact. The approximate outline of the bubble is illustrated by means of an black ellipse. Clockwise vorticity is coloured blue, anti-clockwise is coloured red.

section. The direction of motion in the *y*-*z* plane is unknown as only a single camera is utilised in the current PIV set-up. In the region ahead of the bubble, the fluid no longer has a vertical escape route, therefore fluid must move either to the left or right of the bubble, to regions of lower pressure. In Figure 7.5, it can be seen that the fluid divides in this way

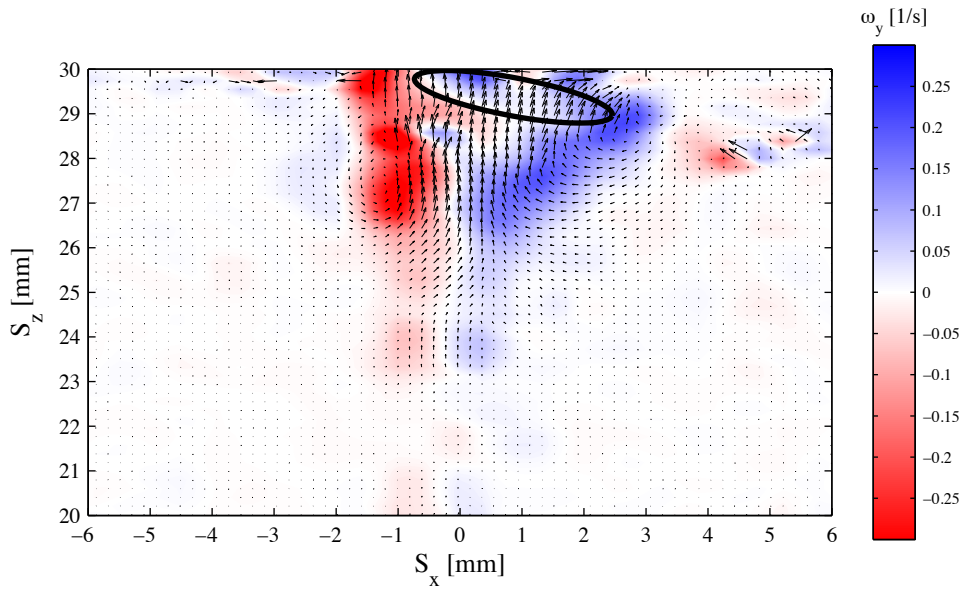

Figure 7.7: Instantaneous velocity vectors and vorticity (ω_y) around a 2.8 *mm* bubble, released from a height of 30 *mm*, as the bubble impacts the surface. The approximate outline of the bubble is illustrated by means of an black ellipse. Clockwise vorticity is coloured blue, anti-clockwise is coloured red.

at a position of (-0.5, 29) *mm*, even though two thirds of the bubble is to the right of this position.

Figure 7.7 shows the vorticity and velocity vectors as the left hand edge of the bubble impacts the surface. At this point in time it is clear that much of the bubble is to the right of the centre line, while a significant portion of the wake has a direct path to the surface. The direction of this rising wake is still along a vertical path. What is notable in Figure 7.7 is the extent of the wake, which is still rising as the bubble impacts the surface. As shown in Chapter 5 the bubble achieves its maximum rise velocity approximately 50 *ms* into its rise (Figure 5.16), with the majority of the wake being created after this time; this wake is what is visible for $20 \leq S_z \leq 28$ *mm* in Figure 7.7. Interestingly, in Figure 7.7 the trailing wake exhibits separated regions of higher vorticity.

Figure 7.8 illustrates the same time frame as Figure 7.7, although in this case the instantaneous convective heat flux along the line coincident with the laser light sheet is shown, in conjunction with the velocity magnitude and velocity streamlines. Again the approximate outline of the bubble is shown in red. In this case the bubble has only tilted in the *x*-*z* plane. This was inferred from the IR images. One noticeable feature is the spike in convective flux

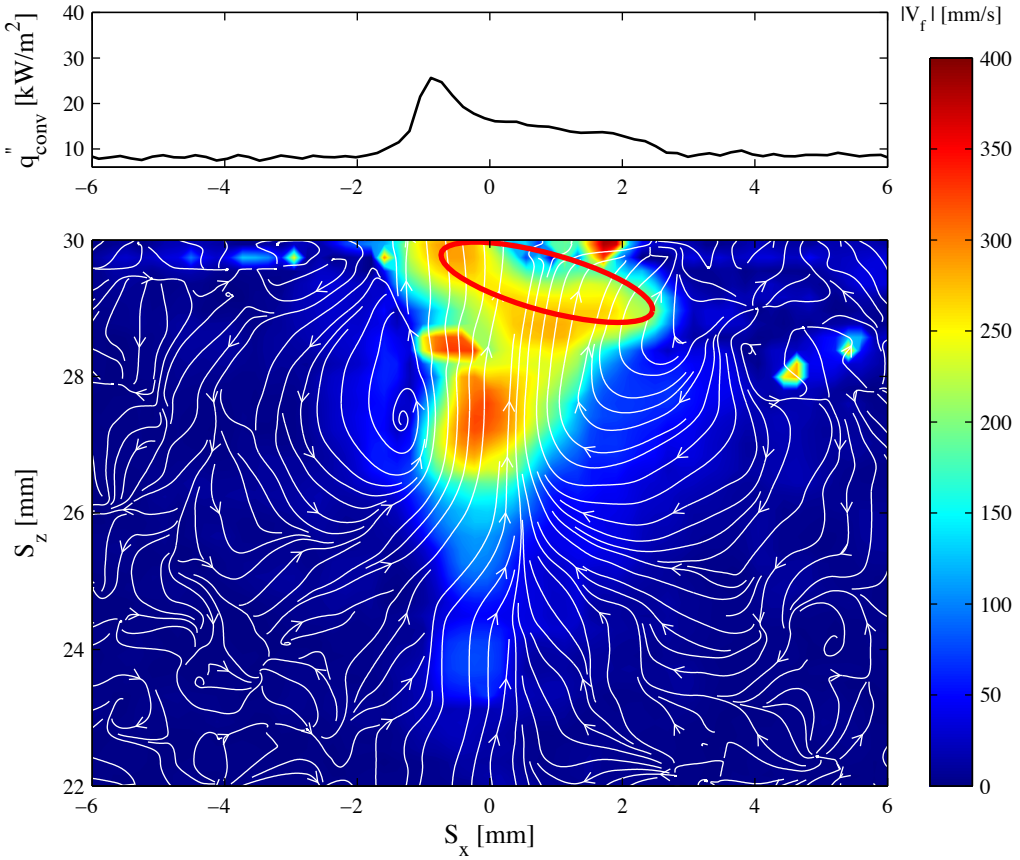

Figure 7.8: Instantaneous streamlines around a 2.8 *mm* bubble, released from a height of 30 *mm*, as the bubble impacts the surface. The upper graph is the instantaneous convective heat flux along a line coincident with the laser light sheet. The approximate outline of the bubble is illustrated by means of a red ellipse.

where the first edge of the bubble impacts the surface. This spike is thought to be initiated by the bubble impact and further enhanced by the bubble's wake. The wake is evident in Figure 7.8, as the region of high velocity at the rear of the bubble. As the bubble impacts at an angle, its impact position is to the right of the ensuing wake and is thought to displaced the majority of the thermal boundary layer, reducing its thickness. This is believed to allow the cool wake fluid access to the surface, thereby facilitating strong convective cooling.

Figure 7.9 illustrates the continued impact of the bubble on the surface, 1 *ms* after the first edge of the bubble impacted the surface. In this case the bubble has shifted slightly to the right, expelling warm boundary layer fluid to the right of the bubble. What is notable at this time is that, adjacent to the surface at (-1, 29.5) *mm*, velocity vectors indicate that fluid is pulled towards rather than pushed away from the bubble. A rapid decrease in convective

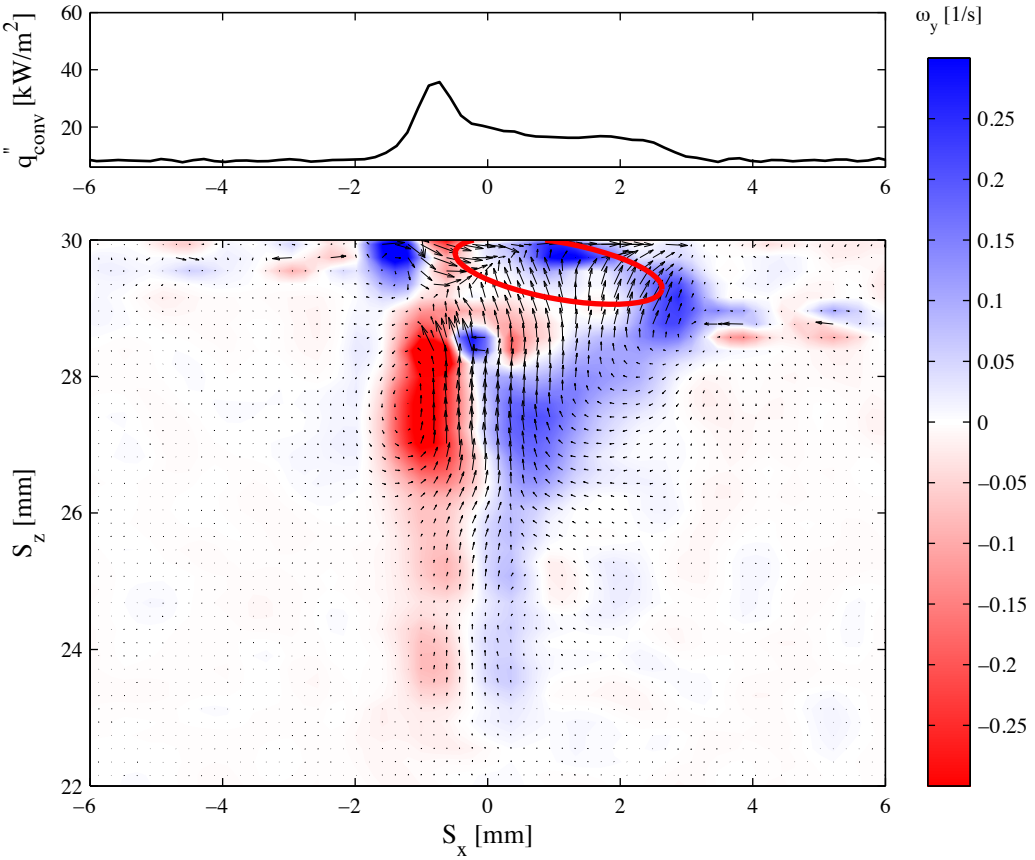

Figure 7.9: Instantaneous velocity vectors and vorticity (ω_y) for flow around a 2.8 *mm* bubble, released from a height of 30 *mm*, 1 *ms* after the initial impact of the bubble. The upper graph is the instantaneous convective heat flux along a line coincident with the laser light sheet. The approximate outline of the bubble is illustrated by means of a red ellipse.

flux is expected to result from warm boundary layer fluid being pulled across a previously cooled region of the surface. However, in this case the boundary layer fluids to the left of the bubble has been replaced by cool wake fluid due to the impact angle of the bubble. Hence, the lateral fluid moment shown in Figure 7.9 is, in fact, cool fluid being drawn along the surface, thereby increasing convective heat flux.

Figure 7.10 illustrates the continued impact of the bubble on the surface, 3 *ms* after the first edge of the bubble was impacted. Firstly, the main difference in terms of convective heat flux is an increase in the peak heat flux amplitude, when comparing Figures 7.9 and 7.10. The left hand spike in Figure 7.10 is thought to be from the initial impact being re-convected by the bubble's rebound motion, while the second, lower peak may result from the continued impact of the bubble. In this case, the infrared images pointed towards the

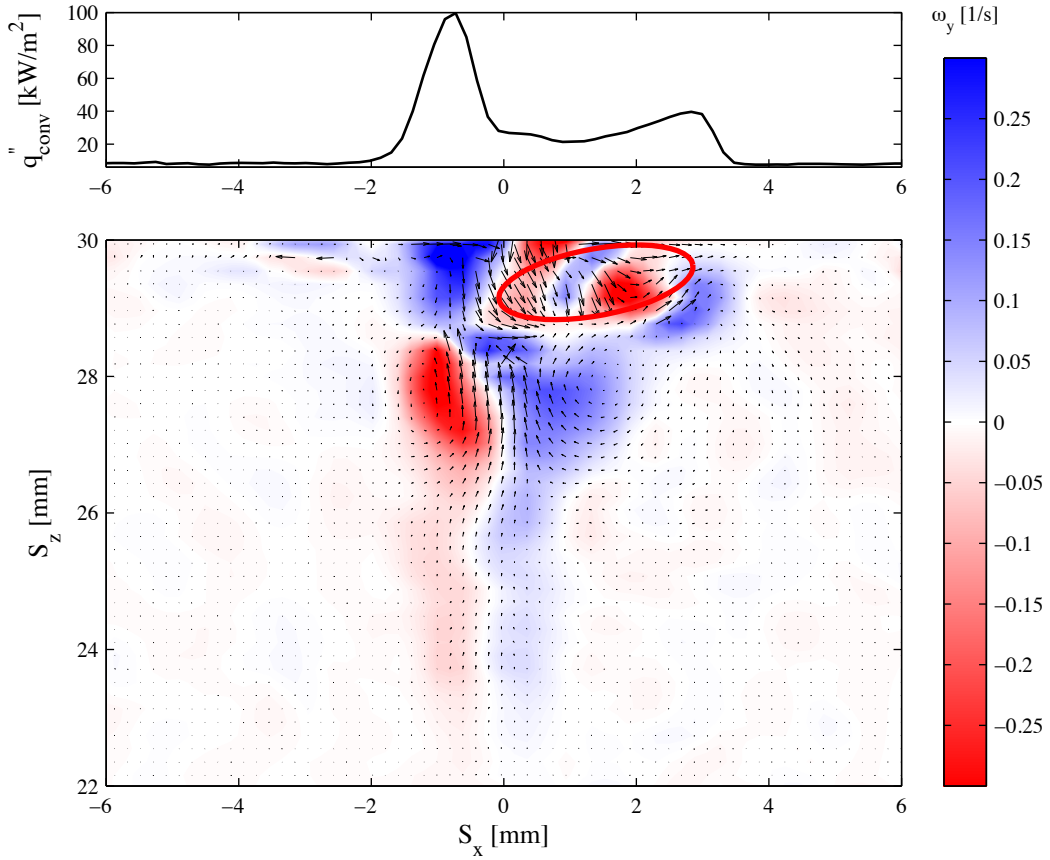

Figure 7.10: Instantaneous velocity vectors and vorticity (ω_y) for flow around a 2.8 *mm* bubble, released from a height of 30 *mm*, 3 *ms* after the initial impact of the bubble. The upper graph is the instantaneous convective heat flux along a line coincident with the laser light sheet. The approximate outline of the bubble is illustrated by means of a red ellipse.

presence of an impact dimple; this can be inferred from Figure 7.10 as the PIV plane passes though the centre of the bubble's impact zone. At the rear of the bubble, it appears that perhaps a toroidal vortex is still present at an approximate height of 28 *mm*. The main portion of the wake has shifted a little closer to the surface, while the portion of the wake which impacted first is disrupted by the rebound of the bubble into the wake; this, in turn, stops the convective enhancement for a few milliseconds.

7.1.2 Case 2: 3.3 *mm* Bubble

Figures 7.11 and 7.12 illustrate the velocity magnitude, streamlines and vorticity for the flow field around a 3.3 *mm* bubble released from a height of 30 *mm*. The time in this case is 24 *ms* prior to impact and the bubble is at approximately 8.5 *mm* below the test surface.

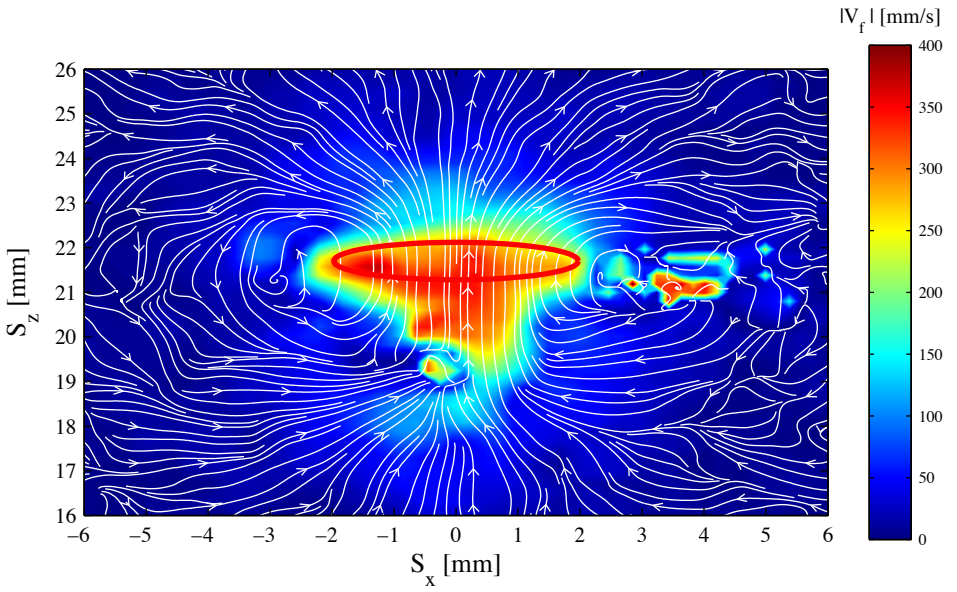

Figure 7.11: Instantaneous streamlines from a 3.3 *mm* bubble, released around a height of 30 *mm*, at a time of 24 *ms* prior to impact. The approximate outline of the bubble is illustrated by means of a red ellipse.

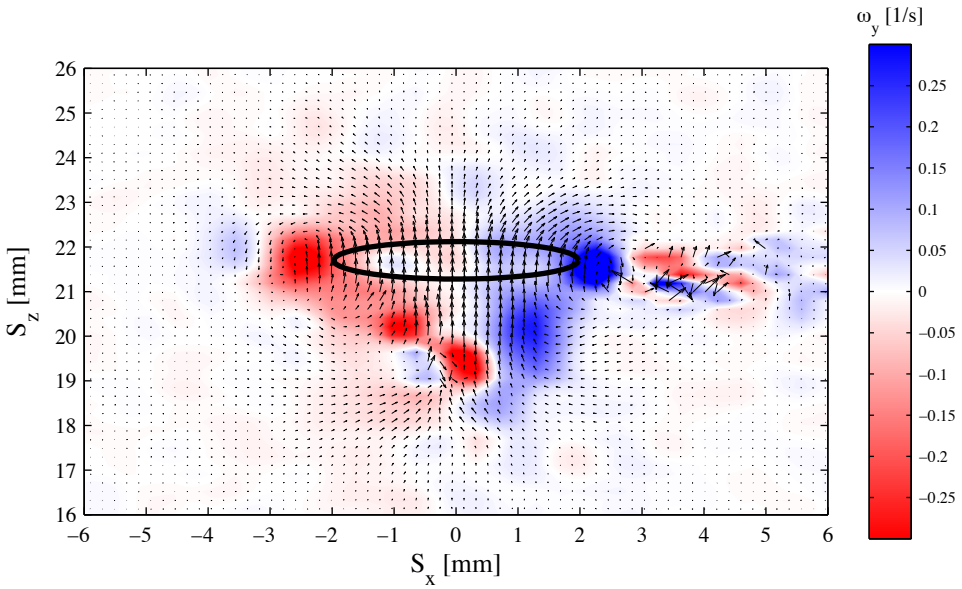

Figure 7.12: Instantaneous velocity vectors and vorticity (ω_y) around a 3.3 *mm* bubble, released from a height of 30 *mm*, at a time of 24 *ms* prior to impact. The approximate outline of the bubble is illustrated by means of a black ellipse. Clockwise vorticity is coloured blue, anti-clockwise is coloured red.

When comparing this 3.3 *mm* bubble to the 2.8 *mm* bubble at the same time prior to impact (Figures 7.1 and 7.2), the larger bubble is noticeably wider, while being similar in height. The fluid velocity at the rear of the 3.3 *mm* bubble is significantly higher, with maximum

values of around 350 *mm/s*, compared with 270 *mm/s* behind the 2.8 *mm* bubble. The extent of the 3.3 *mm* bubble's wake is also marginally (1 *mm*) longer[2]. The streamline patterns are remarkably similar for the two cases, with the main variation being the density of streamlines at particular locations.

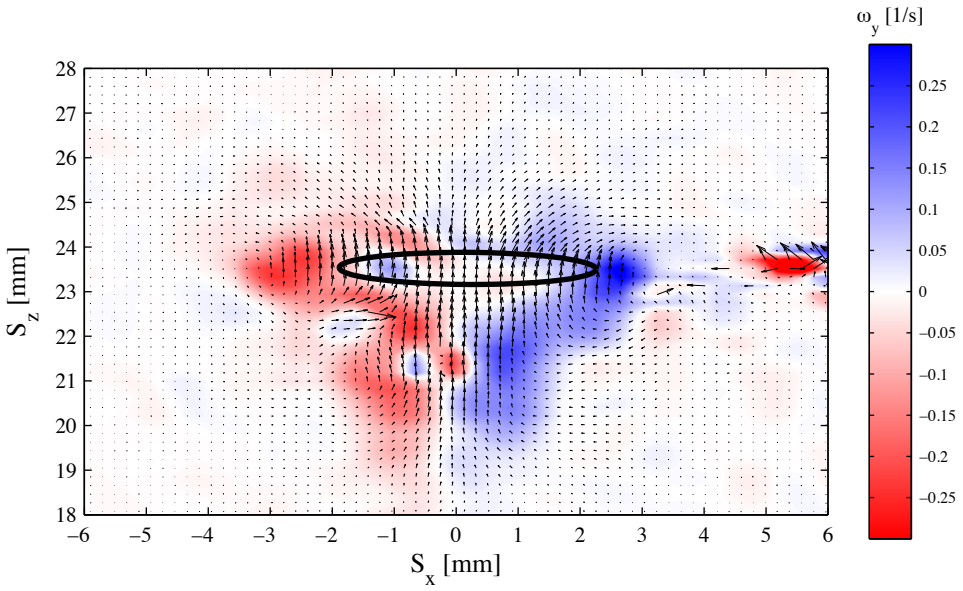

Figure 7.13: Instantaneous velocity vectors and vorticity (ω_y) around a 3.3 *mm* bubble, released from a height of 30 *mm*, at a time of 18 *ms* prior to impact. The approximate outline of the bubble is illustrated by means of a black ellipse. Clockwise vorticity is coloured blue, anti-clockwise is coloured red.

For the 3.3 *mm* bubble featured in Figure 7.11, the wake structure is asymmetric at a time of 24 *ms* prior to impact, while at a time of 26 *ms* (not shown here) a symmetric wake structure was apparent. As noted in Chapter 5, during the bubble rise the bubble's shape continually oscillates. Also, the lateral extremities of the bubble shift from being above the centroid to being below the centroid, which suggests that the edges of the bubble move almost separate to the centroidal movement. This causes regions of higher vorticity to roll off the bubble's edge, which become entangled in the wake. As can be seen in Figure 7.12 at a position of (0, 19.5) *mm*, small counter rotating vortices appear. As these are against the direction of the main flow, they are forced to reverse and follow the ensuing wake within 1 *ms*; this partial flow separation occurred periodically during the bubble's rise.

Figure 7.13 illustrates the vorticity and velocity vectors for the 3.3 *mm* bubble 6 *ms* later

[2]The length of the wake is defined as a zone with a velocity of greater than 150 *mm/s*.

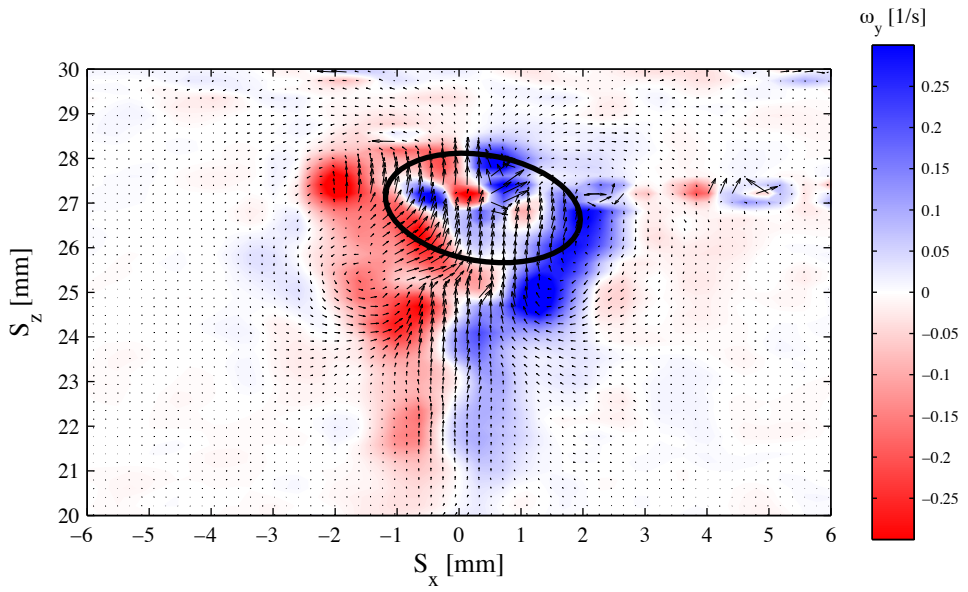

Figure 7.14: Instantaneous velocity vectors and vorticity (ω_y) around a 3.3 *mm* bubble, released from a height of 30 *mm*, at a time of 12 *ms* prior to impact. The approximate outline of the bubble is illustrated by means of a black ellipse. Clockwise vorticity is coloured blue, anti-clockwise is coloured red.

in its rise. Again similarities arise with Figure 7.12, with the same small counter rotation vortices being engulfed by the larger toroidal vortex. This vortex pair is at a height of $S_z = 21.5$ *mm*, while in Figure 7.12, this joining event occurs at a height of $S_z = 19.5$ *mm*. These structures are continually generated as the bubble's shape varies; this is consistent with the variation in the bubble's aspect ratio (χ) shown in Figure 5.15 for contaminated fluid.

In Figure 7.14, 6 *ms* later, the bubble changes shape and direction. As previously discussed in Section 5.1, if the bubble becomes increasingly elongated during its rise, it will suddenly almost stop and revert to a more spherical shape. A very approximate bubble shape is illustrated in Figure 7.14. In this case the bubble moves out of the laser plane slightly, all the while shifting to the right.

7.1.3 Case 3: 4.1 *mm* Bubble

Figures 7.15 and 7.16 illustrate the velocity magnitude, streamlines and vorticity for flow around a 4.1 *mm* bubble released from a height of 30 *mm*. The time shown is 42 *ms* prior to impact, which is early in the bubble's rise. Notably, the affected area due to the rising bubble

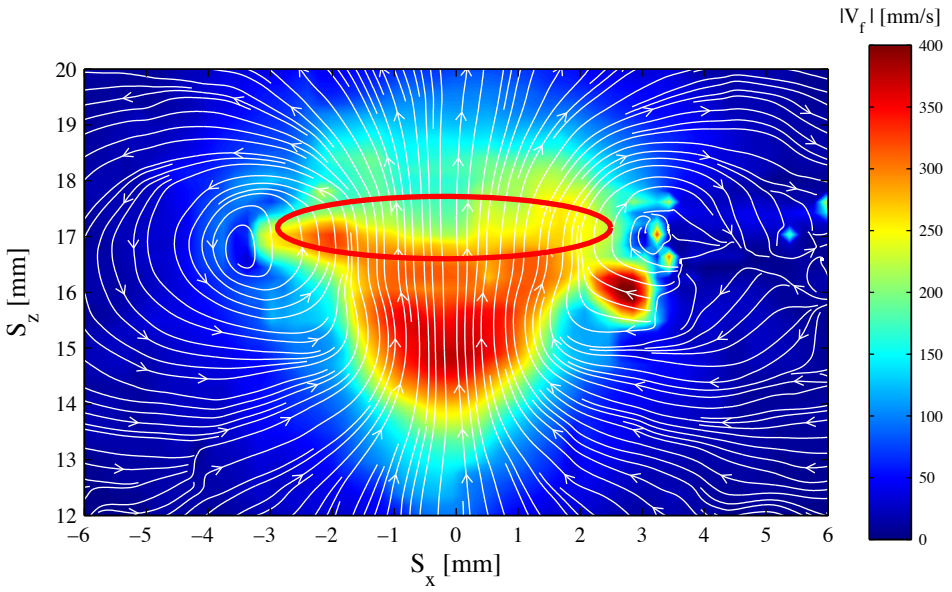

Figure 7.15: Instantaneous streamlines in the flow field around a 4.1 *mm* bubble, released from a height of 30 *mm*, at a time of 42 *ms* prior to impact. The approximate outline of the bubble is illustrated by means of a red ellipse.

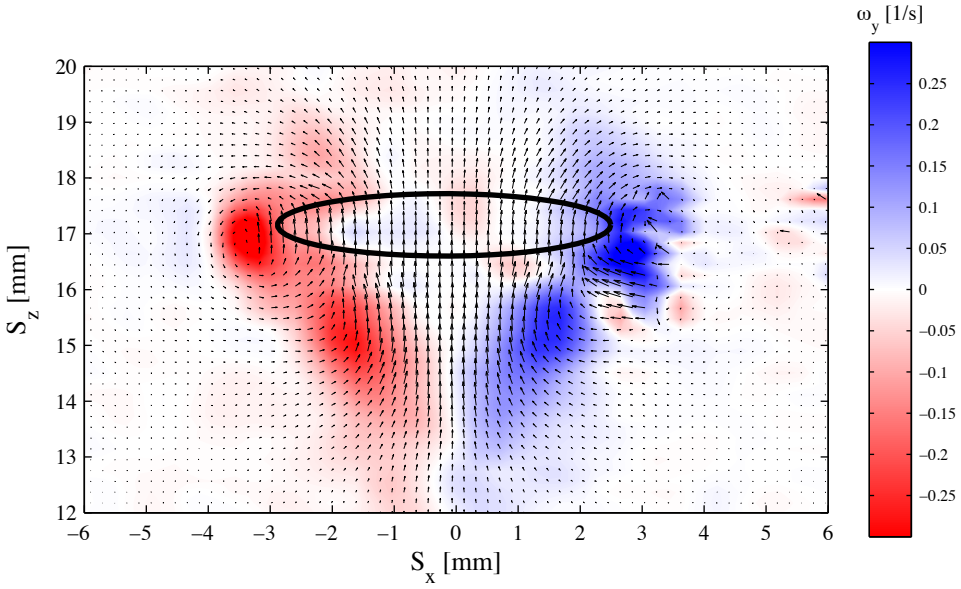

Figure 7.16: Instantaneous velocity vectors and vorticity (ω_y) from a 4.1 *mm* bubble, released from a height of 4.1 *mm*, at a time of 42 *ms* prior to impact. The approximate outline of the bubble is illustrated by means of a black ellipse. Clockwise vorticity is coloured blue, anti-clockwise is coloured red.

is significantly larger, when compared to the smaller bubbles. This is evident in comparing the streamline patterns in Figure 7.15 with those for the previous two bubbles in Figures 7.1 and 7.11 (at a different time). The streamlines in Figure 7.15 extend to ± 6 *mm*, well beyond

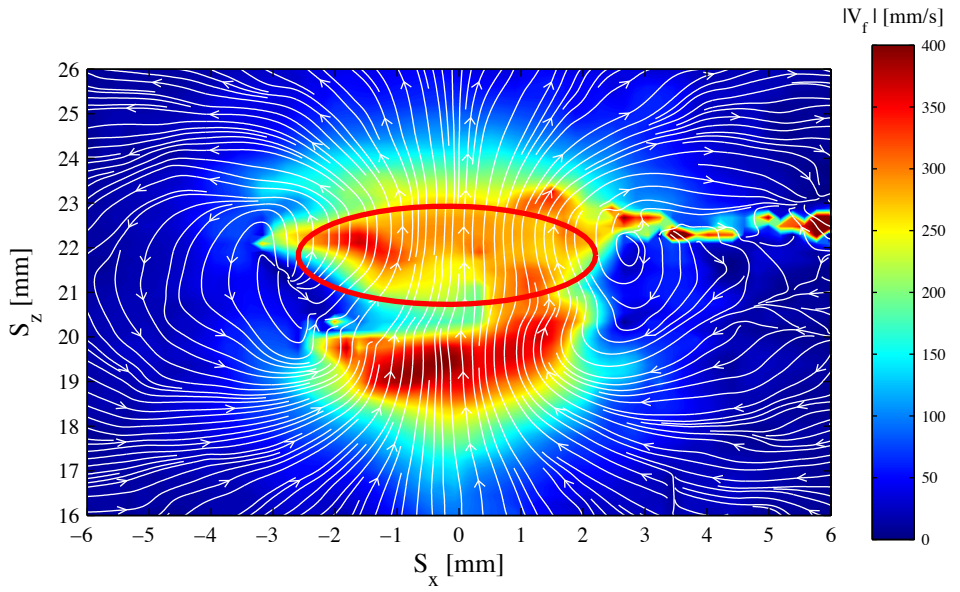

Figure 7.17: Instantaneous streamlines around a 4.1 *mm* bubble, released from a height of 30 *mm*, at a time of 24 *ms* prior to impact. The approximate outline of the bubble is illustrated by means of a red ellipse.

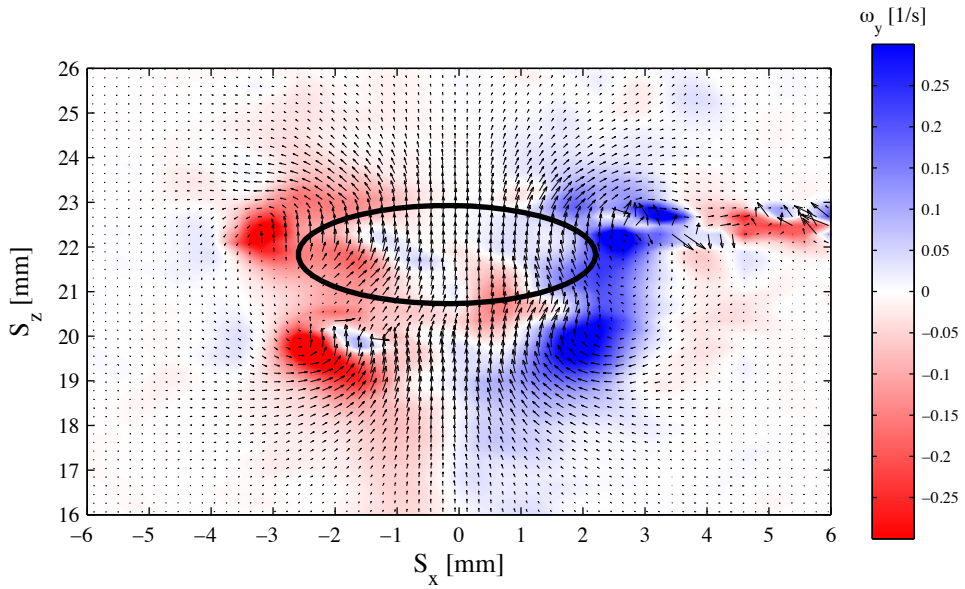

Figure 7.18: Instantaneous velocity vectors and vorticity (ω_y) around a 4.1 *mm* bubble, released from a height of 30 *mm*, at a time of 24 *ms* prior to impact. The approximate outline of the bubble is illustrated by means of a black ellipse. Clockwise vorticity is coloured blue, anti-clockwise is coloured red.

the zone affected for the smaller bubbles. At this particular time period, the wake at the rear of the bubble appears steady and symmetrical, extending a significant distance behind the bubble.

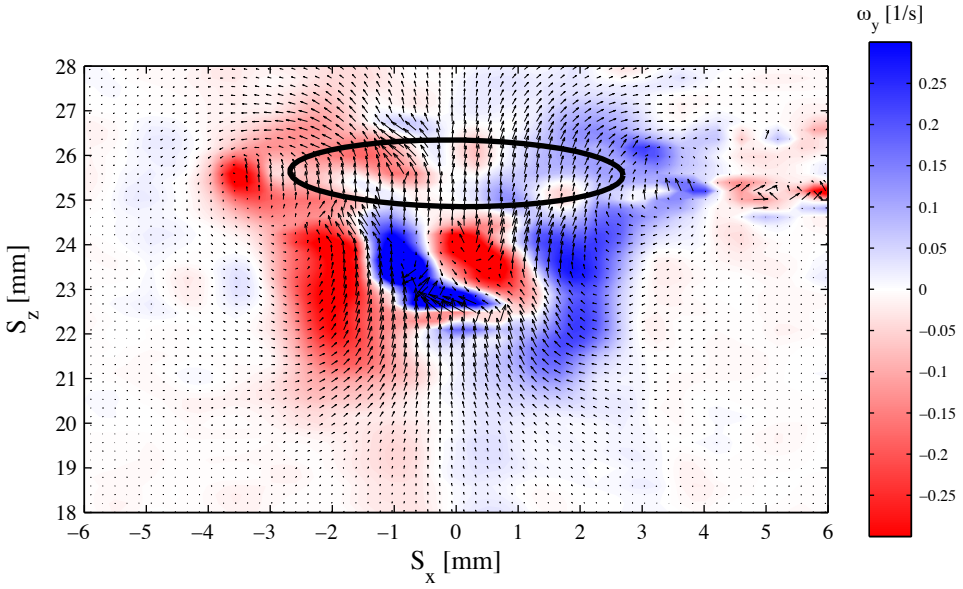

Figure 7.19: Instantaneous velocity vectors and vorticity (ω_y) for flow around a 4.1 *mm* bubble, released from a height of 30 *mm*, at a time of 12 *ms* prior to impact. The approximate outline of the bubble is illustrated by means of a black ellipse. Clockwise vorticity is coloured blue, anti-clockwise is coloured red.

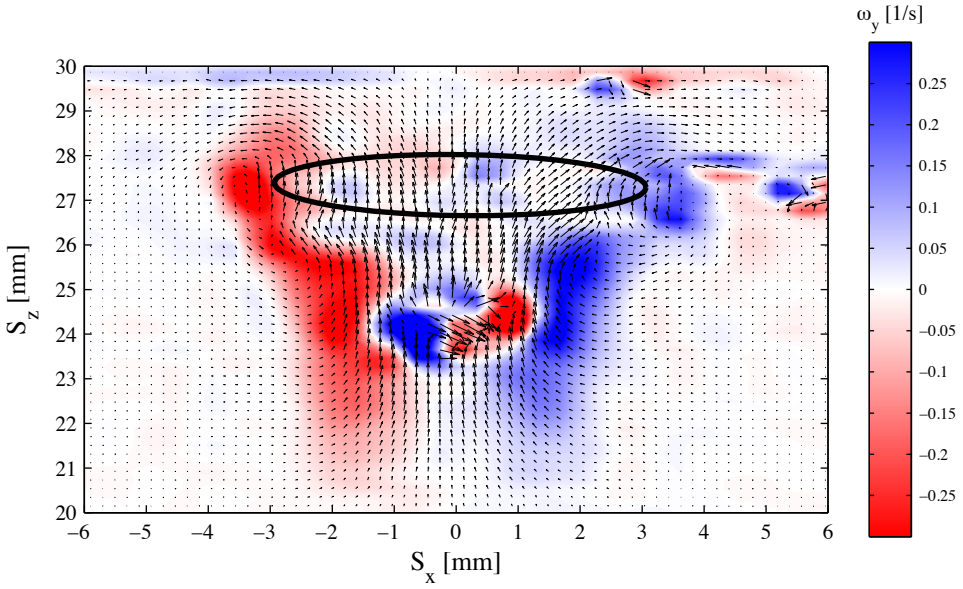

Figure 7.20: Instantaneous velocity vectors and vorticity (ω_y) for flow around a 4.1 *mm* bubble, released from a height of 30 *mm*, at a time of 6 *ms* prior to impact. The approximate outline of the bubble is illustrated by means of a black ellipse. Clockwise vorticity is coloured blue, anti-clockwise is coloured red.

In contrast, Figures 7.17 and 7.18, for a time of 24 *ms* prior to impact, illustrate a far more turbulent wake, with regions of high turbulence. What is notable is the change to a

less elongated bubble shape, with the high velocity region of the wake being separated from the bubble. Again, as shown in Chapter 5 the oscillation frequency for this larger bubble is significantly lower than that for the smaller bubbles (Figure 5.21).

Figure 7.19 illustrates the vorticity at a time of 12 *ms* prior to impact. It is clear that counter rotating vortices are interacting with one another at the rear of the bubble. Thus, at a position of (0, 23.5) *mm* in Figure 7.19, two small vortices, which appear to be opposing the main flow direction in this zone, are surrounded by the main circulation toroidal vortex. Again it is evident that the bubble is less elongated than at the earlier times shown in Figures 7.15 and 7.16.[3]

Figure 7.20 illustrates the vorticity at a time of 6 *ms* prior to impact and 6 *ms* after that shown in Figure 7.19. In this case the region of opposing vorticity discussed in relation to Figure 7.19 has shifted slightly to a position of (0, 24.5) *mm*. The exact source of these vortices is thought to be the periodic and rapid change in the bubble's shape as it rises through the fluid.

As the bubbles in this study are quite large, while also having high initial rise velocities, a significant amount of fluid is entrained at the rear of the bubble. This region, in which vortices are formed and subsequently shed, is known as the primary wake [18], as shown in Figure 2.8. These shed vortices form the far wake and continue to rise and mix with the surrounding fluid as the bubble rises. The primary wake was found to have the highest fluid velocity, with a fall-off in velocity with distance from the bubble's rear.

7.2 Wake Development

In this section the wake ensuing from the bubble will be explored, both from a fluid flow and convective heat transfer perspective. The development of the bubble's wake has been shown to be dictated by the size of the bubble and the oscillation of the bubble's shape as it rises through the test section, with its impact angle/major axis angle being of most importance. It is this angle which will determine the wake's direction relative to the surface and the level and affected area of enhancement. This section will mainly focus on the wake produced

[3]The illustrated ellipse is not the true bubble shape, it is merely an indicator of the centroid and extent of the bubble's edges. The actual outer tips of the bubble may be above or below the bubble's centroid.

by a bubble which impacts at an angle, with the final section exploring the enhancement due to bubbles which impact the surface with a major axis parallel to the surface. The convective enhancement will be presented for a slice of the surface along the direction of motion of the bubble, and will show the local temporal variation in the convective heat flux and dimensionless surface temperature. In some cases the slice, S_{sl}, might be aligned with the S_x direction, although this will not always occur. This temporal variation in convective heat flux and temperature will be used in conjunction with instantaneous 2D surface maps, and with fluid velocity and streamline data at appropriate points in time.

The convective heat flux and surface temperature are shown at a specific instant in time, however in order to get a sufficient *pixel* shift in the post processing of the corresponding PIV data, Δt was varied depending on the *pixel* shift observed.

7.2.1 Case 1: 2.8 *mm* Bubble

Figure 7.21 illustrates the instantaneous convective heat flux and dimensionless surface temperature (Equation 6.6) along a line on the surface for a 2.8 *mm* bubble with a bubble release height of 30 *mm*. Data are plotted at 2 *ms* intervals for a period from 0 – 20 *ms* after the initial impact. The line, one *pixel* in width, along which the data are plotted is marked in Figure 7.22, which shows the instantaneous convective heat flux and dimensionless surface temperature at 10 *ms* after impact.

It is apparent in Figure 7.21 that a significant variation, both spatial and temporal, in convective heat flux occurs. Within this time frame, 0 – 20 *ms*, the bubble's impact and rebound process is captured. The left hand side of the bubble was found to impact first at S_{sl} = -0.5 *mm*, before the right hand side of the bubble impacts. The impact zone extends as far as 3 *mm*, with the impact wash extending to 4 *mm*. In this particular example, the featured slice along the surface happens to be through the central region of the bubble, where the impact dimple is present, as the bubble motion was found to be confined in the S_x plane. This results in a limited convective enhancement within the central region, which is also highlighted by the local peak in surface temperature at a distance of around 1 – 2 *mm*. The direct enhancement due to the bubble is evident up until a time of 6 – 8 *ms*. At 8 *ms*, the bubble has fully departed the surface, with an approximate centroidal position of (1.6,

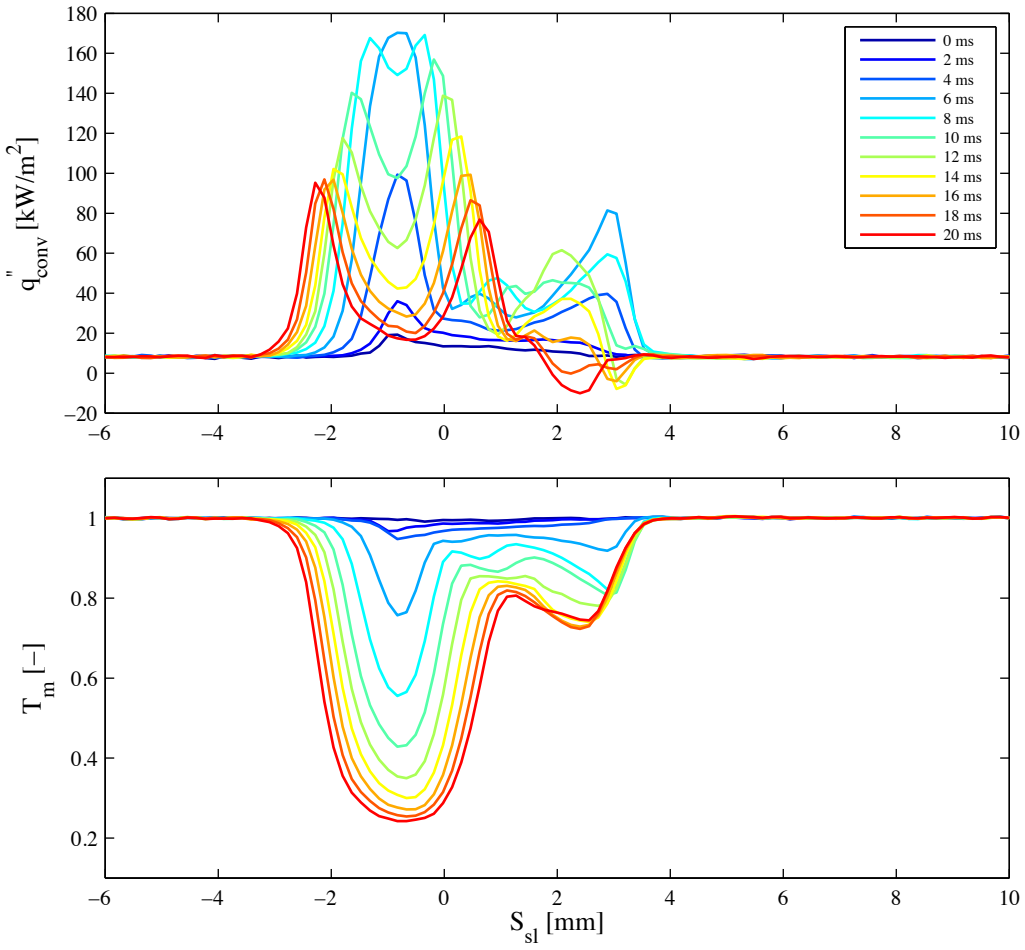

Figure 7.21: Convective heat flux and dimensionless surface temperature along a defined slice of the surface, with data shown at 2 *ms* intervals, during a time period of 0 – 20 *ms*, where 0 *ms* correspond to the impact of the bubble on the surface. Bubble diameter = 2.8 *mm* with a release height of 30 *mm*.

28.7) *mm* in the *x*-*z* plane. At this particular time the convective heat flux begins to reduce at a position of S_{sl} = -0.5 *mm* in Figure 7.21, while the surface temperature continues to drop. However, the temperature drop per millisecond is reduced, which can be inferred due to the closer temperature lines.

Figure 7.22 illustrates the instantaneous convective heat flux and dimensionless surface temperature at a time of 10 *ms* after the initial impact, with the black line indicating the location and direction of the surface slice featured in Figure 7.21. It is immediately evident that the left hand zone has significantly higher convective heat flux spatial variations, with the right hand side exhibiting low negative heat flux values. As previously discussed, the

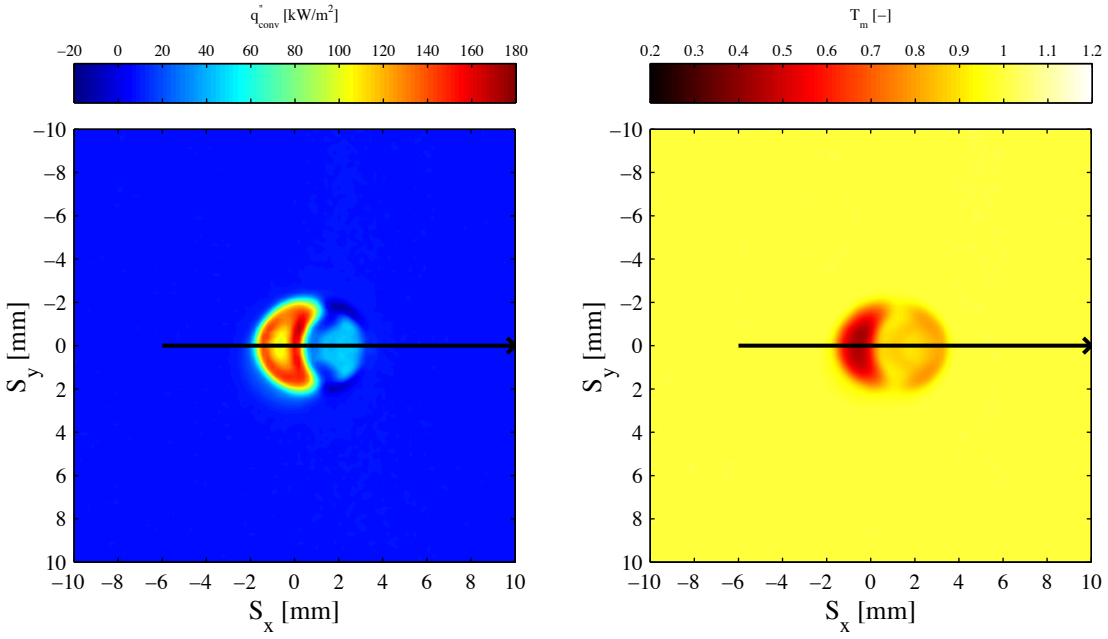

(a) (b)

Figure 7.22: (a) Convective heat flux and (b) dimensionless surface temperature for a 2.8 *mm* bubble, at a time of 10 *ms* after the initial impact. The black line indicates the surface slice shown in Figure 7.21. Bubble diameter = 2.8 *mm* with a release height of 30 *mm*.

maximum convective enhancement due to the direct impact of the bubble was found to be 100 kW/m^2; this indicates that in Figure 7.22 the very high enhancement observed on the left hand side is wake related rather than a result of direct bubble enhancement. In order to explore further the effect of the wake, the instantaneous streamlines and fluid velocity at a time of 8 *ms* are presented[4] in Figure 7.23.

In Figure 7.23 the main region of relevance for heat transfer enhancement is the negative S_x direction. This is because the region between 0 – 4 *mm* contains the bubble, and beyond 4 *mm* in the positive x direction any apparent fluid motion is in fact a loss of correlation between images, due to the bubble blocking the laser light sheet. The majority of the fluid within the plot is undisturbed, but the main wake created during the bubble rise can be inferred at a position of 0 *mm*. In the zone where the bubble is present, centred on $S_x = 2$ *mm*, the rebound of the bubble pushes fluid back into the bulk fluid. This fluid motion is evident due to the streamline direction at an approximate position of (3, 26) *mm* in the x-z plane.

[4]At a time of 10 *ms* the bubble's shape is spherical, causing a flash of laser light which affects the PIV correlation resulting in a significant amount of spurious vectors. Therefore a time of 8 *ms* is presented instead.

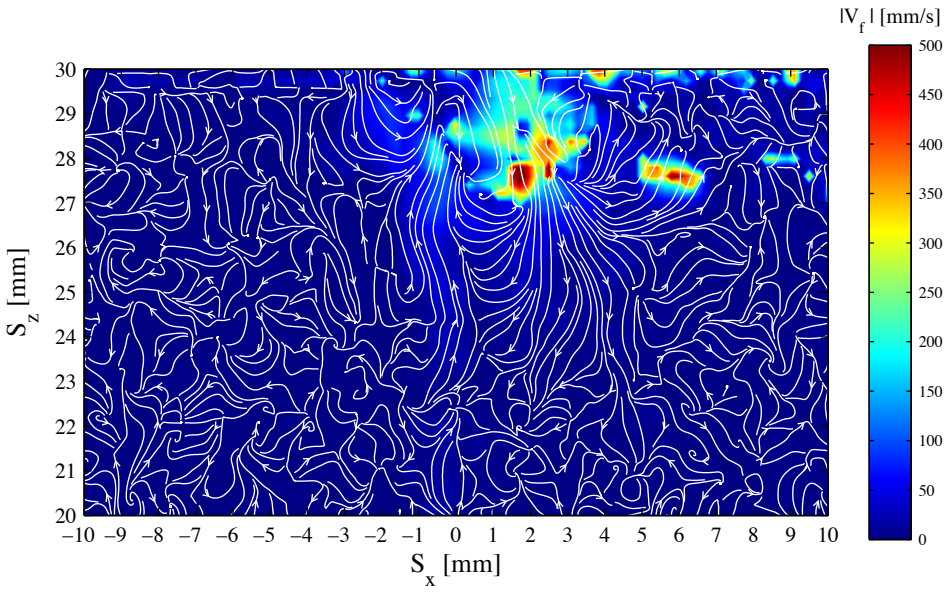

Figure 7.23: Instantaneous streamlines for a 2.8 *mm* bubble, released from a height of 30 *mm*, at a time of 8 *ms* after impact.

The portion of the wake which is of interest for enhancement is that positioned at the surface, around $S_x = 0$ *mm*. This portion of the wake impacts extremely quickly, as the bubble has shifted its rise position as the bubble direction changes, which is to be expected as a bubble of this size would have a final spiral path. Once the wake impacts the surface, any boundary layer fluid within the impact zone is thought to be expelled from the region. In the next phase the bubble begins to rebound from the surface, which, in turn, causes a portion of the impacted wake to be drawn away from the surface. This results in a re-circulation zone at a position of (-2, 29) *mm* in Figure 7.23. This zone recombines with the wake which is continuing to rise, further reducing the surface temperature. This is consistent with the surface temperature plot shown in Figure 7.21, with the recirculating fluid and fresh cool wake impacting the surface in both the positive and negative S_{sl} direction. In terms of enhancement levels, the maximum convective heat flux occurs at a time of 6 *ms*, with a value of approximately 170 kW/m^2.

Figure 7.24 illustrates the instantaneous variation in the convective heat flux and dimensionless surface temperature along the same line on the surface between the times of 20 – 60 *ms*. In this case the time interval between frames is increased to 4 *ms*, to account for the reduced fluid velocity. The bubble diameter is 2.8 *mm* and the release height is 30 *mm*, as before. At a time of 20 *ms*, the bubble was found to be at a position of (2.4, 27.5) *mm* in

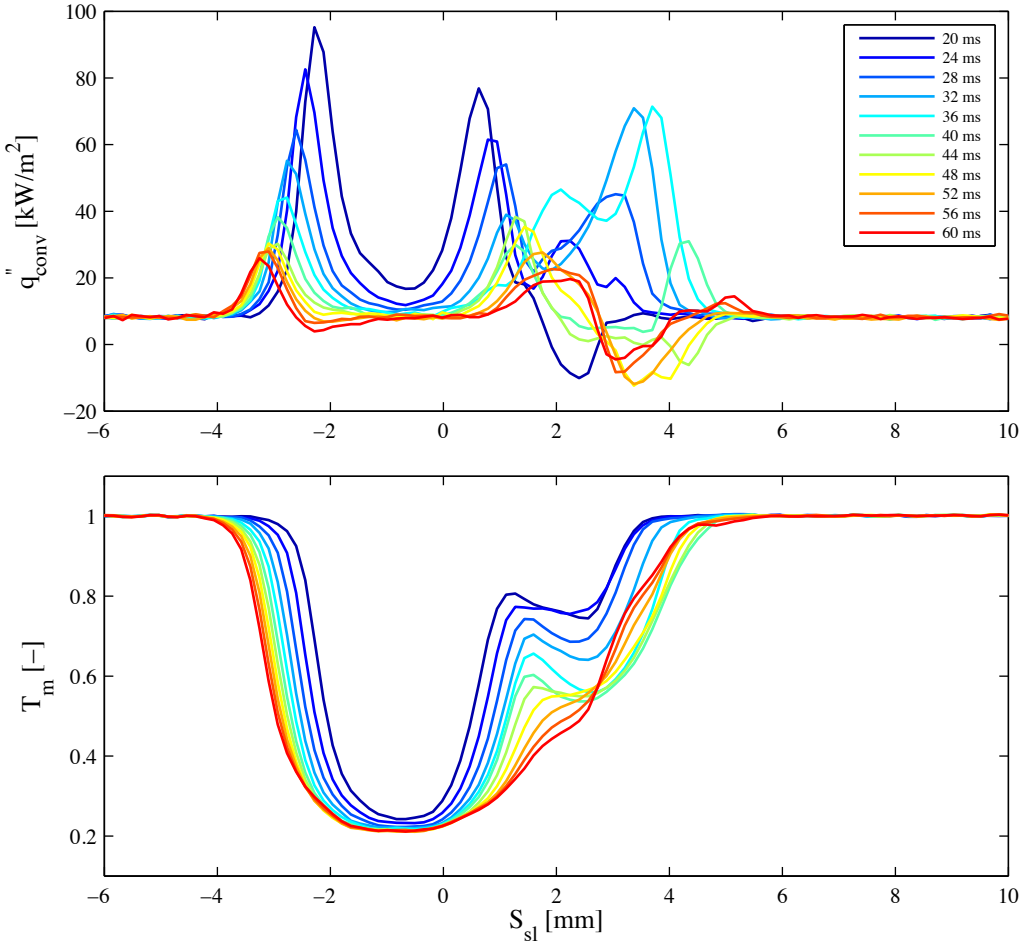

Figure 7.24: Convective heat flux and dimensionless surface temperature along a defined slice of the surface, during a time period of 20 – 60 *ms*. The convective flux scale is lower in this case. Data shown at a 4 *ms* interval, for a 2.8 *mm* bubble and a release height of 30 *mm*.

the *x*-*z* plane, before re-impacting at a time of 34 *ms*. At a time of 45 *ms*, the bubble begins its second bounce, with its re-impact occurring at a time of 59 *ms* at a new position of (3.7, 28.6) *mm*, in the *x*-*z* plane. The bouncing event dictates the variation in convective heat flux, in the zone between 2 *mm* and 6 *mm*. Notably, both negative and positive convective heat flux occur in the time period shown, with the negative convective heat flux thought to be due to warm boundary layer fluid being convected towards the surface, due to the bubble motion.

As observed in Figure 7.21, the convective enhancement was found to be moving in two directions along the featured line, both towards and away from the bubble. This enhance-

ment structure continues in Figure 7.24, although as time continues the enhancement levels reduce steadily from 100 kW/m^2 at 20 *ms* to 30 kW/m^2 at a time of 60 *ms*, at the left hand side of the wake ($S_{sl} < 0$ *mm*).

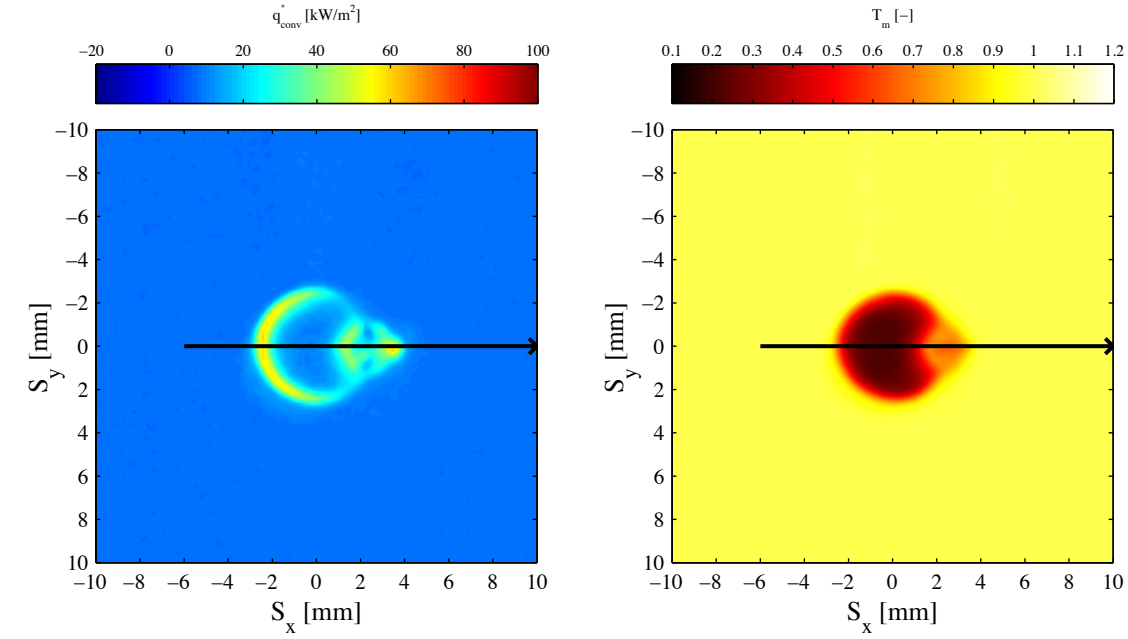

Figure 7.25: (a) Convective heat flux and (b) dimensionless surface temperature for a 2.8 *mm* bubble, at a time of 30 *ms* after the initial impact. Bubble release height is 30 *mm*.

As the bubble in this particular case has shifted to the right, away from its initial impact zone, this exposes the surface to the continually rising wake. This sideways motion was found to drag the continually rising wake to this newly exposed zone, resulting in a rapid reduction in temperature. This rapid reduction in surface temperature is apparent between the limits of $S_{sl} = 0 - 3$ *mm* in Figure 7.24. This region was the initial impact zone, which was within the bubble's impact dimple and therefore did not experience a significant drop in temperature until this moment.

Figure 7.25 illustrates the convective heat flux and dimensionless temperature map for the entire surface at a time of 30 *ms*. In Figure 7.25 (a), it is clear that the wake has spread symmetrically either side of the chosen line. Two zones have significant convective heat flux, these being the bouncing bubble region ($S_x \approx 3$ *mm*) and the zone affected by the wake ($S_x \approx$ -2 *mm*). Figure 7.26 illustrates the streamlines and velocity magnitude at the same time of 30 *ms*. An increased time step of 2 *ms* was used for the PIV testing in this case,

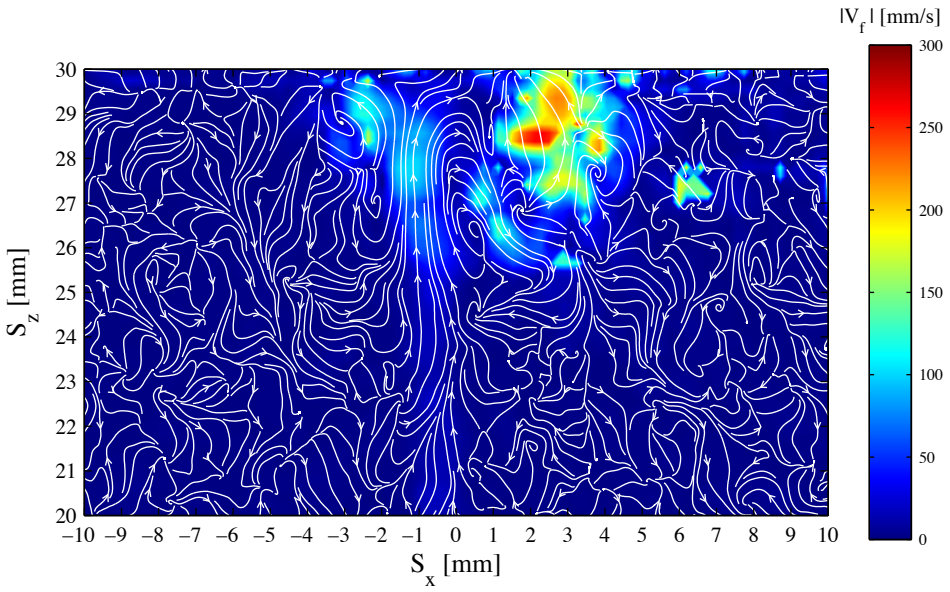

Figure 7.26: Instantaneous streamlines of a 2.8 *mm* bubble, released from a height of 30 *mm*, at a time of 30 *ms* after impact.

allowing the continually rising wake to be more defined. In Figure 7.26 the splitting of the wake is evident, with regions of circulation at S_x = -2 *mm* and S_x = 1 *mm*, respectively.

Figure 7.27 illustrates the convective heat flux and surface temperature for the same surface slice, but in this case the time period runs from 60 to 140 *ms*; with an increased time step of 8 *ms* for clarity. During this time period the bubble was found to be oscillating on the surface, moving from $S_{sl} = 3.7$ *mm* to $S_{sl} = 6.3$ *mm*. This lateral motion results in an enhancement akin to a bubble sliding beneath an inclined surface, although in this case the motion is slow and the bubble's shape is oscillatory. At a position of $S_{sl} > 3$ *mm* in Figure 7.27, a significant dip in convection occurs at a time of 60 *ms*, in a zone between the edge of the bubble and its centroid; this results from warm fluid being forced onto the surface due to the bubble's motion. This drop in convection is immediately followed by a spike in enhancement, which steadily reduces and shifts from a maximum at $S_{sl} = 3$ *mm* towards a lower peak at $S_{sl} = 5$ *mm*. This convective cooling results from the primary wake generated by the sliding, oscillating bubble, that draws cool fluid from the continually rising wake, along the surface. It is difficult to observe the fluid motion ahead of the bubble. However, as the bubble slides it continually oscillates; this is thought to pull and push the undisturbed boundary layer fluid slightly ahead of the bubble.

Notably at a time of approximately 100 *ms* the surface temperature increases slightly, just

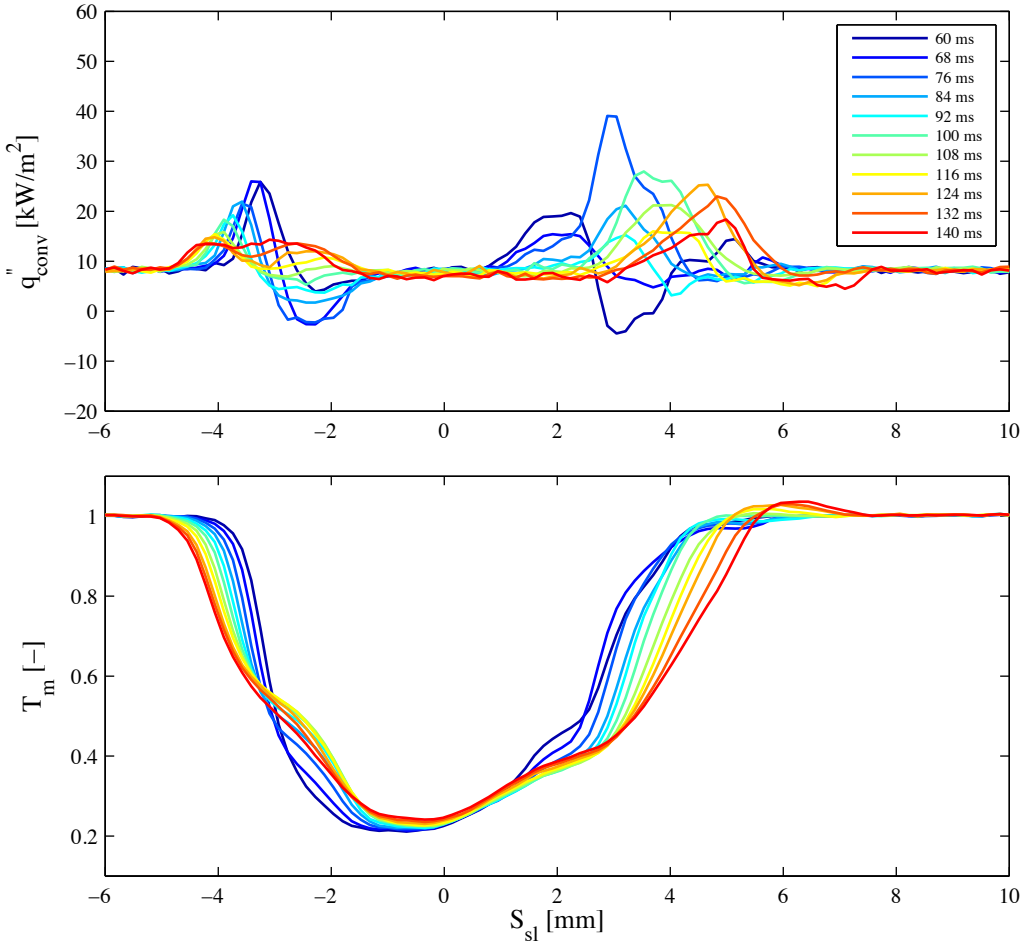

Figure 7.27: Convective heat flux and dimensionless surface temperature along a define slice in the surface, during a time period of 60 – 140 *ms*. The convective flux scale is lower in this case. Data shown at a 8 *ms* interval, for a 2.8 *mm* bubble and a release height of 30 *mm*.

observable at $S_{sl} = 4$ *mm*, followed by a steady and more pronounced increase as its position shifts to $S_{sl} = 6$ *mm*. The maximum expected dimensionless surface temperature of $T_m = 1$ is determined by liquid natural convection. However, in this particular case, it is the air within the bubble, which is in contact with the surface, which causes the observed increase in temperature. This temperature increase coincides with a reduction in the convective heat flux, which can be inferred at a time of 140 *ms*, in the region defined by $S_{sl} = 6 - 8$ *mm*. The shift in position is simply due to the motion of the bubble. In this case it is thought that the liquid film which separates the bubble from the surface is still intact, as the bubble slides along the surface.

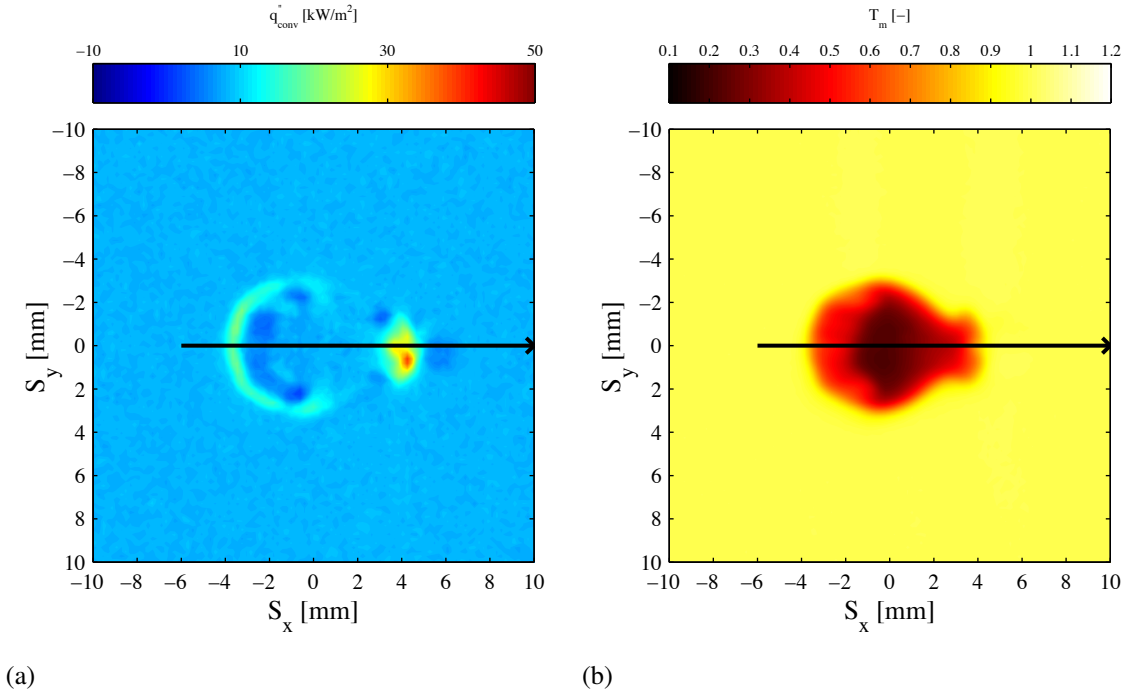

(a) (b)

Figure 7.28: (a) Convective heat flux and (b) dimensionless surface temperature for a 2.8 *mm* bubble, at a time of 100 *ms* after the initial impact.

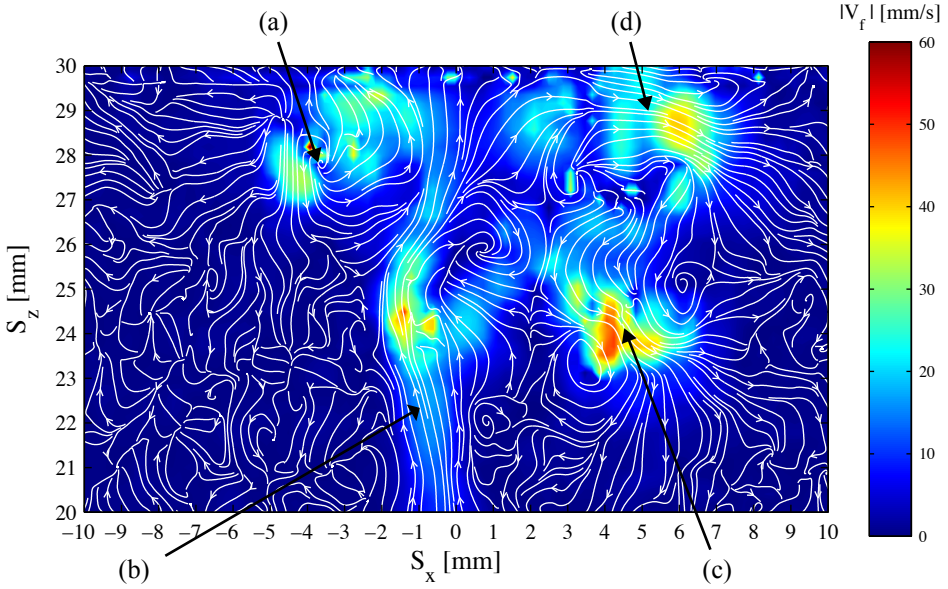

Figure 7.29: Instantaneous streamlines for flow around a 2.8 *mm* bubble, released from a height of 30 *mm*, at a time of 100 *ms* after impact. (a) left region of recirculation, (b) main rising wake, (c) mixing region and (d) fluid motion linked to sliding/bouncing bubble motion.

Figure 7.28 illustrates the convective heat flux and dimensionless temperature at a time of 100 *ms*. At a position of (4, 0) *mm* in Figure 7.28 (a), a small region of locally high

convective heat flux occurs. This is thought to be due to the sliding motion of the bubble in the positive S_x direction. Although difficult to see in this map, a small region of low convective heat flux occurs at a position of (6, 0) *mm*, corresponding to the current location of the bubble. The fluid motion at 100 *ms* is illustrated in Figure 7.29, with a correlation separation time Δt of 8 *ms*. In Figure 7.29 four distinct regions of fluid flow are present: the main rising wake, the left region of circulation in the negative S_x direction, the fluid motion parallel with the surface in the direction of the bubble's motion in the positive S_x direction, and a mixing zone located at (5, 24) *mm* in the *x*-*z* plane.

The left most region identified as point (a) in Figure 7.29 is mostly comprised of re-circulating fluid, with a portion of the fluid being expelled to the bulk fluid. The right most wake, which is indicated by streamlines parallel to the surface, point (d), is again thought to be a result of the sliding motion of the bubble, drawing the rising wake along the surface. The final flow region identified, point (c), consists of two counter rotating vortices at (5, 24) *mm*, and was created during the initial bubble rebound from the surface; this highlights the high velocity during the bubble's rebound from the surface. The direction of this vortex pair is though to be dictated by the bubble rebound process and by the rising wake, which causes some deflection. The local fluid temperature in this mixing zone is not known; however, visual observations indicate that density variations are present, indicating that a portion of this wake contains some boundary layer fluid.

Figure 7.30 illustrates the convective enhancement and dimensionless surface temperature between times of 140 – 260 *ms* in the same test, with a time step of 12 *ms*. From Figure 7.30 three zones of convective cooling are evident, these being the left hand wake, the central region and a region of enhancement at around (4 – 8) *mm* in the positive S_{sl} direction. The region centred on $S_{sl} =$ -4 *mm* represents wake continually spreading along the surface, albeit significantly more slowly than in the previous time frames. The convective enhancement is only twice that of liquid natural convection, with a value of less than 20 kW/m^2. In the central region, -2 $\leq S_{sl} \leq$ 4 *mm*, the convective heat flux is at the level of liquid natural convection. This is not sufficient to match the heat generation, resulting in a steady increase in T_m, as seen in Figure 7.30. In this case the initial surface temperature prior to impact is approximately $53^{\circ}C$.

The convective heat flux beneath the bubble is approximately half that of liquid natural

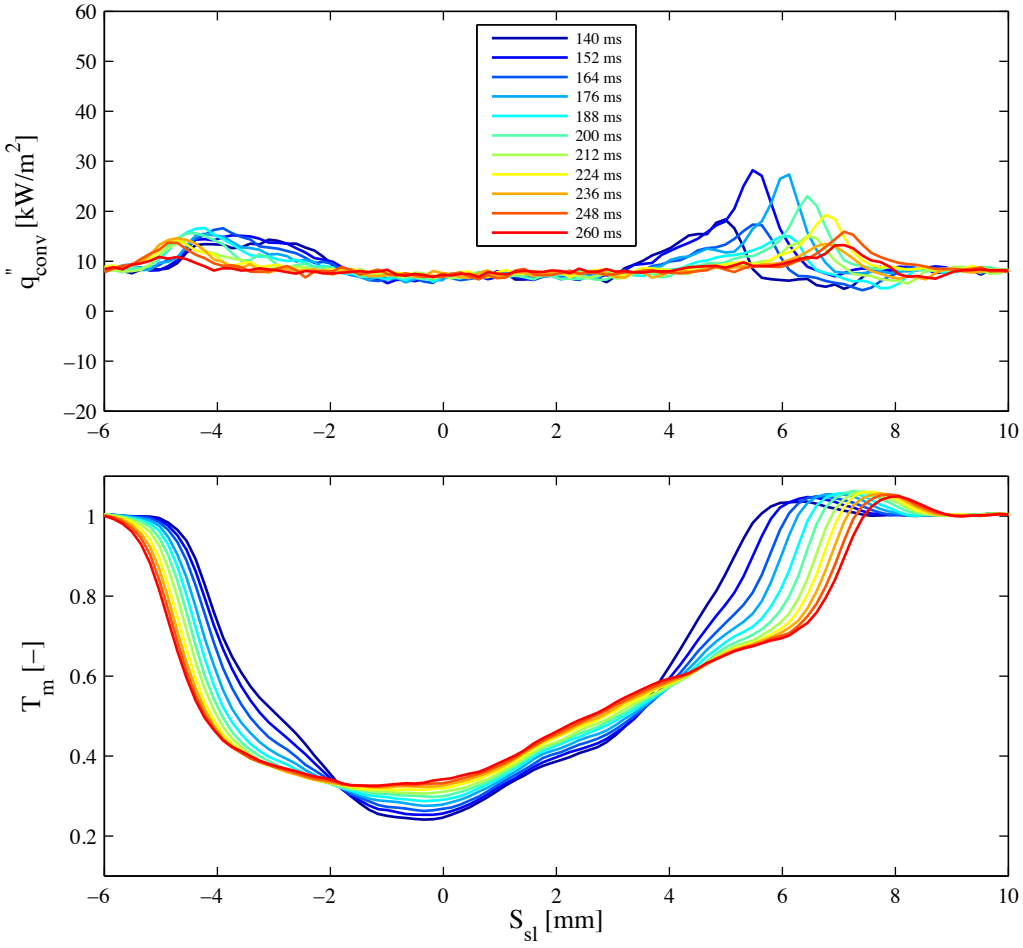

Figure 7.30: Convective heat flux and dimensionless surface temperature along a defines slice in the surface, during a time period of 140 – 260 *ms*. The convective flux scale is lower in this case. Data shown at a 12 *ms* interval, for a 2.8 *mm* bubble and a release height of 30 *mm*.

convection. At a time of 140 *ms*, the bubble is positioned at $S_{sl} = 6.2$ *mm*, before moving to the position $S_{sl} = 7.7$ *mm* at a time of 260 *ms*, leading to an increase in surface temperature of around 3°C. As the bubble is continually moving, the increase in surface temperature is reduced by the bubble's wake, which steadily reduces in strength as the bubble's velocity decreases. This wake is again evident in Figure 7.31 (a) at a position of $S_x = 6$ *mm*, at a time of 150 *ms*. Again the reduced convective heat flux beneath the bubble can be just detected ahead of the ensuing wake in Figure 7.31 (a).

Figure 7.32 illustrates the streamlines and fluid velocity at a time of 150 *ms*, with a time step of 12 *ms*. In this case, five regions of fluid circulation are observable. The first four

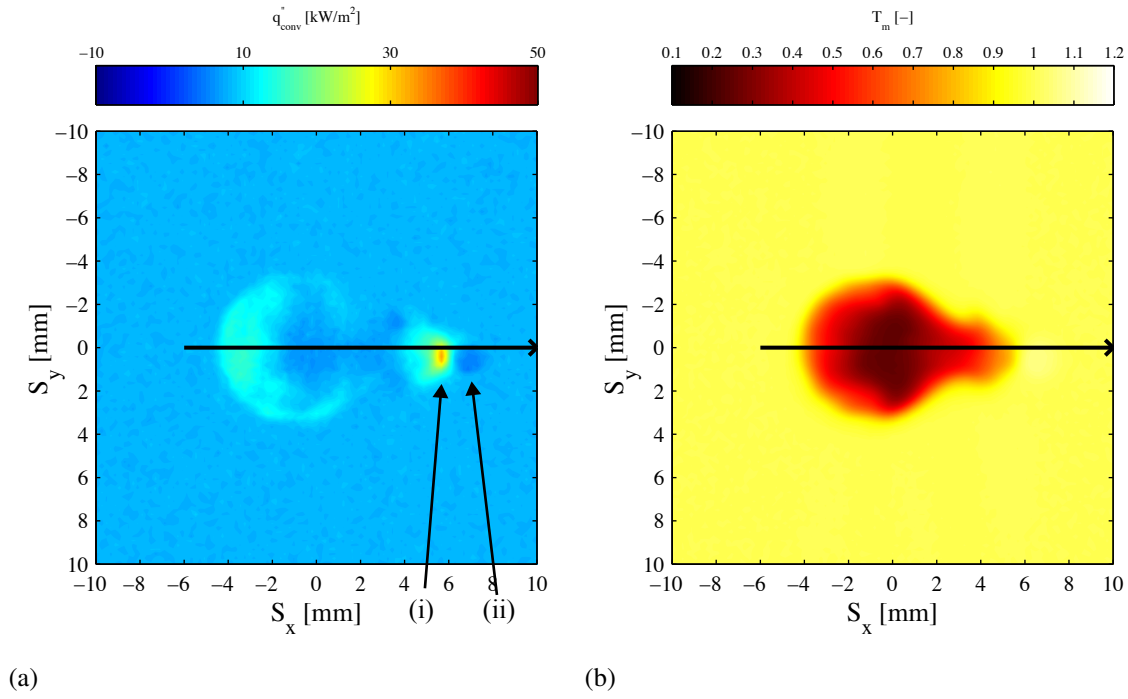

Figure 7.31: (a) Convective heat flux and (b) dimensionless surface temperature for a 2.8 *mm* bubble, at a time of 150 *ms* after the initial impact. (i) is the wake enhancement and (ii) is the bubble location.

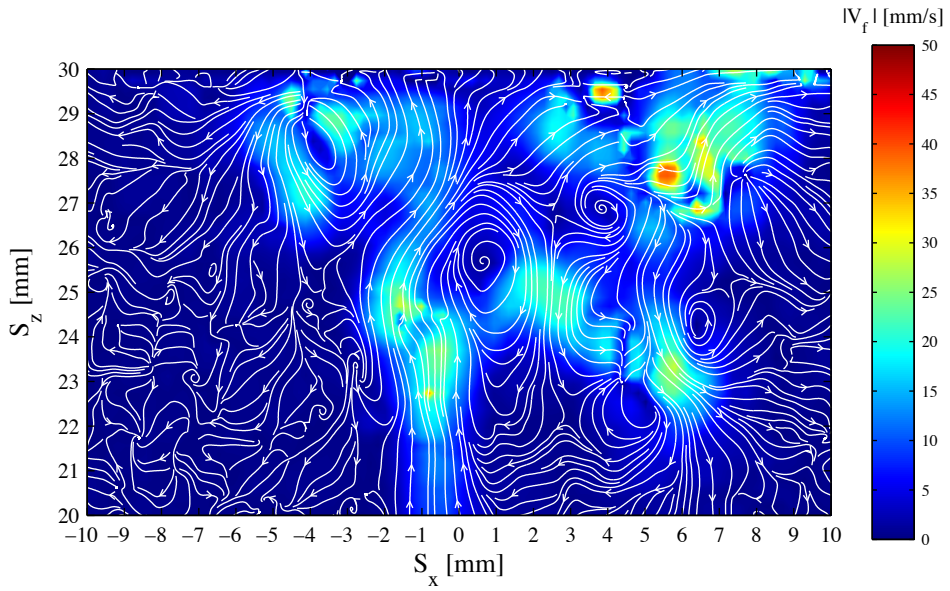

Figure 7.32: Instantaneous streamlines around a 2.8 *mm* bubble, released from a height of 30 *mm*, at a time of 150 *ms* after impact.

are similar in origin to those observed in Figure 7.29 and described above. The two counter rotating vortices originally at (5, 24) *mm*, have now shifted to (6, 23) *mm*. The additional region of high velocity occurs at a position of (1, 24) *mm*, with a clockwise rotating vortex to

the left. This region of fluid moving away from the surface is thought again to be produced by the rebounding bubble; as it is directly opposing the rising wake a significantly sized vortex is created, which deflects the rising wake.

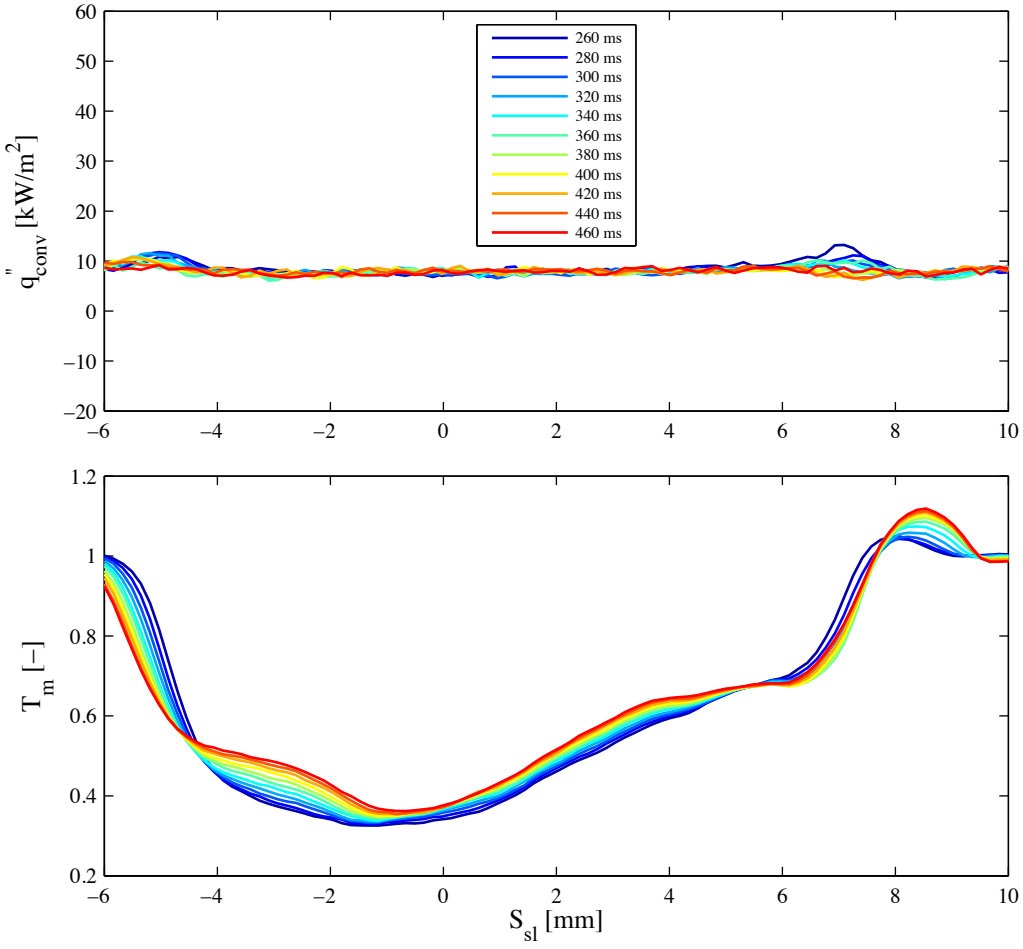

Figure 7.33: Convective heat flux and dimensionless surface temperature along a define slice in the surface, during a time period of 260 – 460 *ms*. The convective flux scale is lower in this case. Data shown at a 20 *ms* interval, for a 2.8 *mm* bubble and a release height of 30 *mm*.

Figure 7.33 illustrates the convective heat flux variation between 260 and 460 *ms*. During this time period the bubble only moves 0.3 *mm*, with its final position being at approximately 8 *mm*. The film separating the bubble directly from the surface is thought to rupture at a time of 340 *ms*. This rupture results in an increase in the surface temperature beneath the bubble, which is evident in Figure 7.33 from a time of 340 *ms* onwards. Notably, the convection at S_{sl} = -6 *mm*, although at heat flux levels just above liquid natural convection, is responsible

for a reduction in surface temperature. The central zone can be seen to begins its recovery towards the original surface temperature, the beginning of which is seen in Figure 7.34.

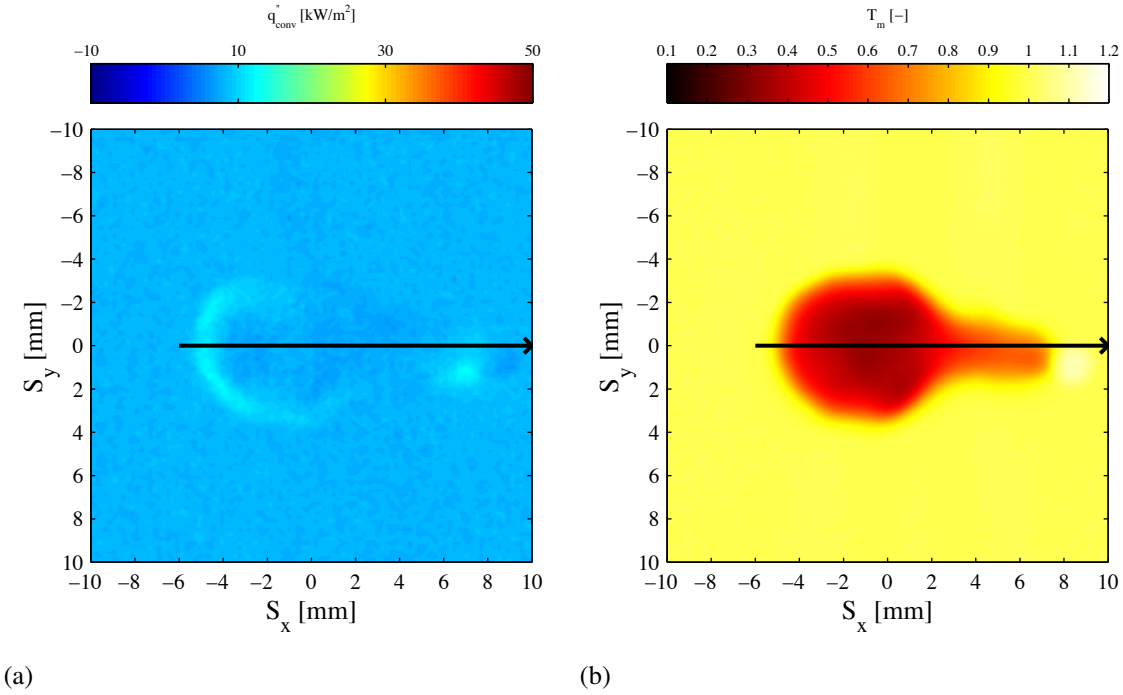

(a) (b)

Figure 7.34: (a) Convective heat flux and (b) dimensionless surface temperature for a 2.8 *mm* bubble, at a time of 300 *ms* after the initial impact.

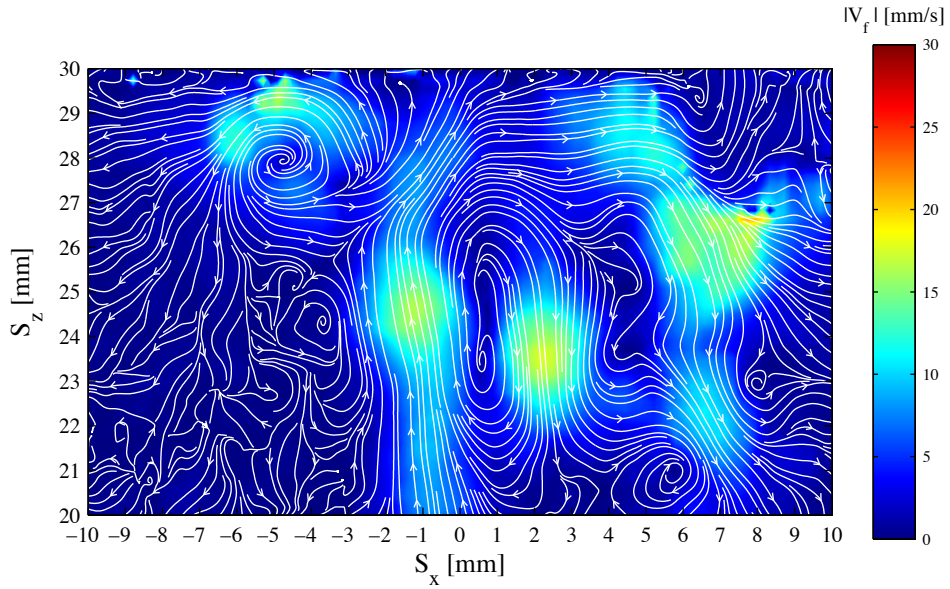

Figure 7.35: Instantaneous streamlines of a 2.8 *mm* bubble, released from a height of 30 *mm*, at a time of 300 *ms* after impact.

In order to understand this recovery in temperature the temporal response of the sys-

tem is assessed, based on the water thermal diffusivity, α, and the thermal boundary layer thickness, δ. Thus, the response time for the boundary layer to redevelop ($\tau_{water} = \alpha/\delta^2$) is of the order of $\tau_{water} = 38$ *ms*, indicating that the surface should recover more rapidly than observed here. The reason for slow recovery in surface temperature may be due to the continually shifting wake, shown in Figure 7.35, where significant fluid motion is still taking place, disrupting the outer thermal boundary layers.

This example of the wake is for the 2.8 *mm* bubble at a release height of 30 mm; similar processes occur as the release height is increased. Also, larger bubbles which impact at an angle produce similar convective heat transfer patterns to those shown in this example, although with an increased affected area. In the next section an example will be presented whereby the separate regions of vorticity in the wake impact the surface separately, with this type of convection being evident in Figure 6.10 for a 2.8 *mm* bubble.

7.2.2 Case 2: 3.3 *mm* Bubble

As the bubble size is increased, the extent of the wake or impact zone is much larger, with the wake having a slightly greater enhancement effect. This may be inferred from the area of disturbed fluid as the bubble rises through the test section, which increases with increasing bubble volume. Although the area affected increases, the way in which this occurs is the same as described in the previous section for the 2.8 *mm* bubble. In this section the wake of a 3.3 *mm* bubble, released from a height of 35 *mm*, will be presented. This was found to be an unusual case, where the wake appears to partially separate from the upon impact. This situation was not observed during PIV experiments for the lower release height of 30 *mm*, so the following section will only show the bubble's position by means of the camera images.

Figure 7.36 illustrates the time varying convective heat flux and dimensionless surface temperature for a 3.3 *mm* bubble, released from a height of 35 *mm*. The direction along the surface investigated by the slice line is marked on Figure 7.37 and is in the bubble's wake impact and travel direction. During the bubble's rise, above a height of 25 *mm*, the bubble's major axis tilts, as the bubble moves in the negative S_x and positive S_y direction. Furthermore, at a height approaching 30 *mm*, the bubble veers further in the negative S_x

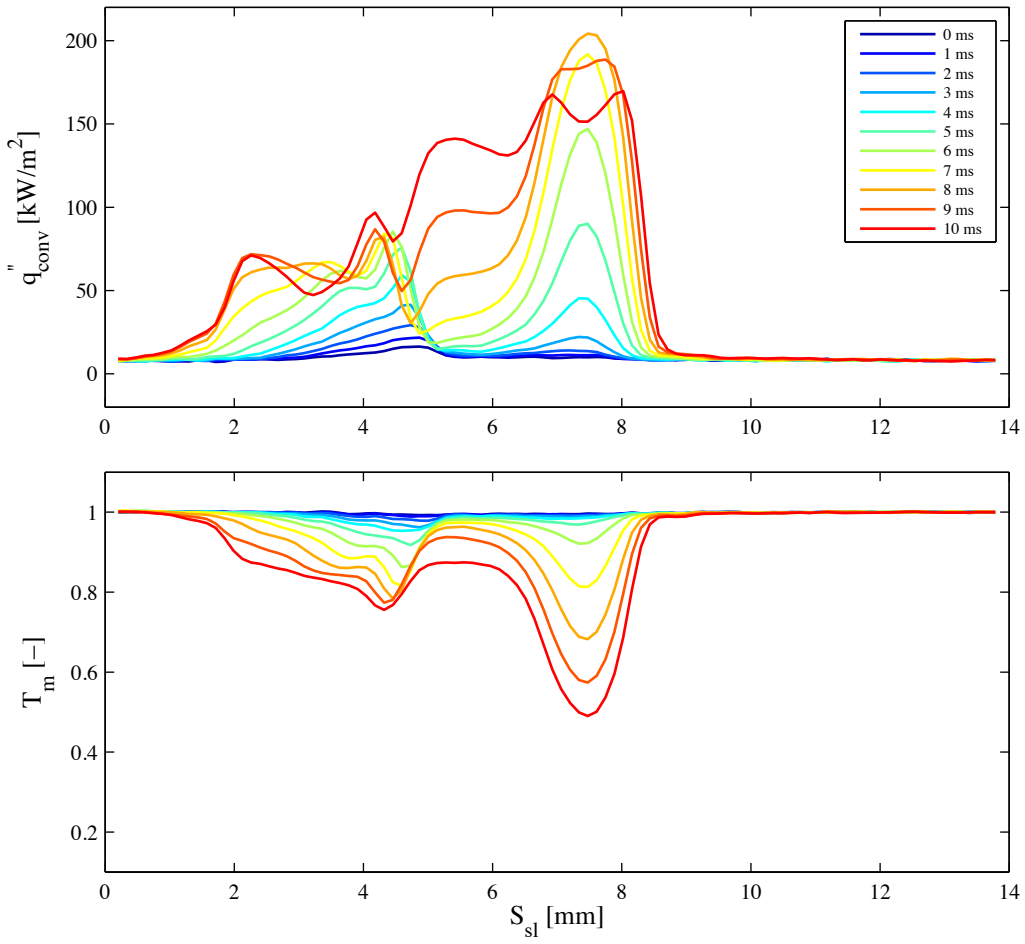

Figure 7.36: Convective heat flux and dimensionless surface temperature along a defined slice in the surface, with a time separation of 1 *ms*, during a time period of 0 – 10 *ms*, 3.3 *mm* bubble, rise height of 35 *mm*.

direction, although not displayed here. The rapid change of direction is perhaps due to the increase in pressure ahead of the bubble and the fact that the bubble's shape was found to be very elongated. This rapid change in direction is followed by a rapid change in the bubble's shape. The shape and location of the bubble at impact is shown in Figure 7.38 (a). Notably, the bubble's centroid is at approximately S_x = -4 *mm*.

In Figure 7.36, two main zones of cooling occur, one being due to direct impact of the bubble ($S_{sl} = 2-5$ *mm*), with the second being around ($S_{sl} = 6-9$ *mm*), during the first 7 *ms* after the initial impact. These two cooling zones can be inferred from Figure 7.37 at a time of 8 *ms*; with the bubble's impact being the left most zone. At a time of 8 *ms*, the separation

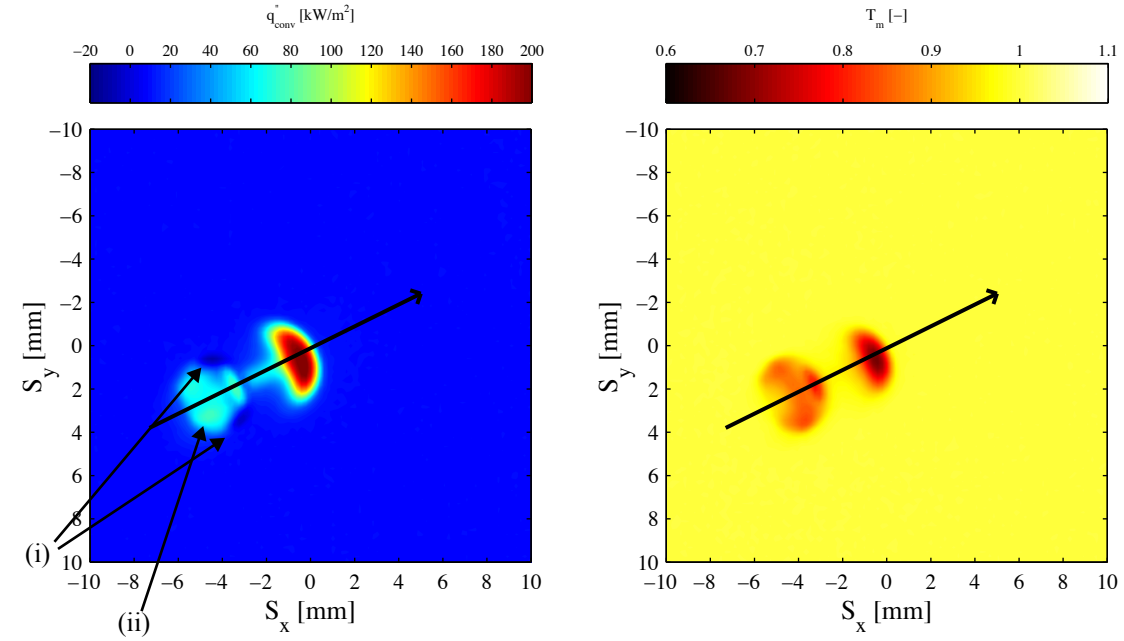

(a) (b)

Figure 7.37: (a) Convective heat flux and (b) dimensionless surface temperature for a 3.3 *mm* bubble, at a time of 8 *ms* after the initial impact. The black line indicates the slice shown in Figure 7.36. (i) points to the symmetric zones of low convective flux and (ii) is the approximate location of the bubble.

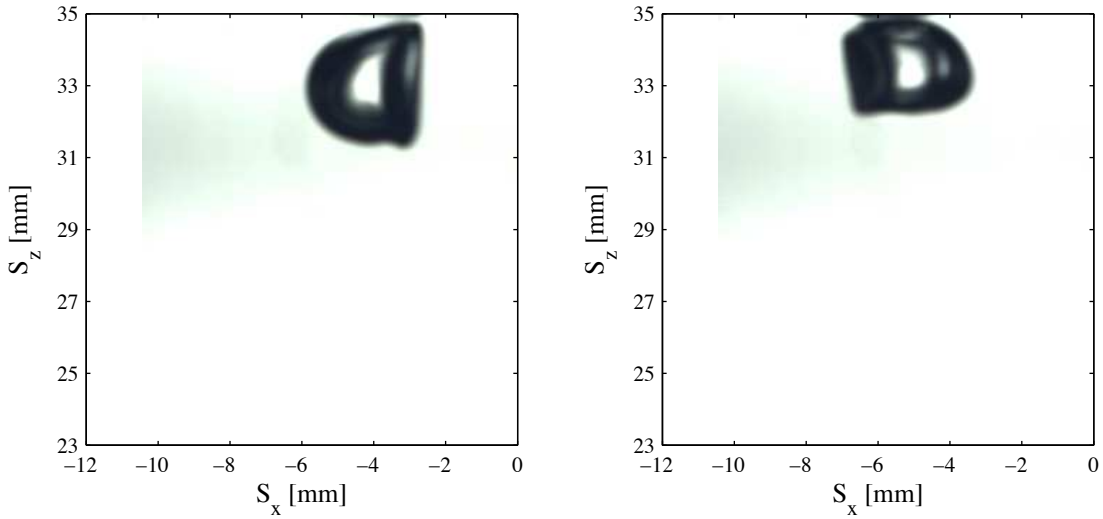

(a) (b)

Figure 7.38: Bubble images at (a) Impact and (b) 8 *ms* after impact for a 3.3 *mm* bubble, released from a height of 35 *mm*.

region between the two zones begins also to experience an increase in convective cooling. The bubble's position at 8 *ms* is shown in Figure 7.38 (b), with the bubble having shifted its position by 1 *mm* in the negative S_x direction. The bubble's shape also undergoes a rapid change, with the "vertical" right hand edge, rolling to the left hand side (Figure 7.38 (a)–(b)). This causes an increase in the convective cooling, although two symmetrical regions of low convective flux are observable in Figure 7.37, either side of the line, at the initial impact zone.

In Figure 7.36 the highest convective heat flux occurs at a time of 8 *ms*. The peak heat flux falls off steadily after this, while the zone of enhancement increases as the wake continues to impact the surface. The separation of the main wake from the bubble is thought to be entirely due to the rapid movement of the bubble prior to impact. The bubble's impact zone and the wake impact zone do not stay separate for a long period as the wake is drawn towards the bubble's location; also, between the time period of 7 – 10 *ms*, the bubble moves slightly to the left (negative S_x). The entrainment effect of the bubble was captured in the previous example. In this particular case the bubble does not bounce away from the surface, but rather slides, while irregular waves travel on the bubble's surface.

Figure 7.39 illustrates the instantaneous distribution of convective heat flux and dimensionless surface temperature, between time of 10 – 30 *ms*. During this time period significant variations in the convective heat flux occur, with the central zone between the initial bubble impact and wake impact zone undergoing the biggest change in surface temperature. At a time of 16 – 18 *ms*, at a position of $S_{sl} = 2$ *mm*, a reduction in convective heat flux occurs; this is thought to be due to bubble induced re-circulation of warm boundary layer fluid, along with bubble shape changes. Figure 7.40 illustrates the convective heat flux and surface temperature at a time of 22 *ms* after the initial impact, with the corresponding bubble location being presented in Figure 7.41 (a).

Interestingly, the impacted wake is split into three regions, illustrated in Figure 7.40 (a). The first of those zones (i) is centred at around (-2, 2) *mm* in the S_x and S_y directions, mirrored either side of the line. The second wake region (ii) is the initial impact zone centred at (1, 0) *mm*, while the final zone (iii) lies just ahead of this. This last zone is again centred on the featured line but with a low level of enhancement along the line itself. This zone impacts the surface separately from the initial wake, before eventually combining

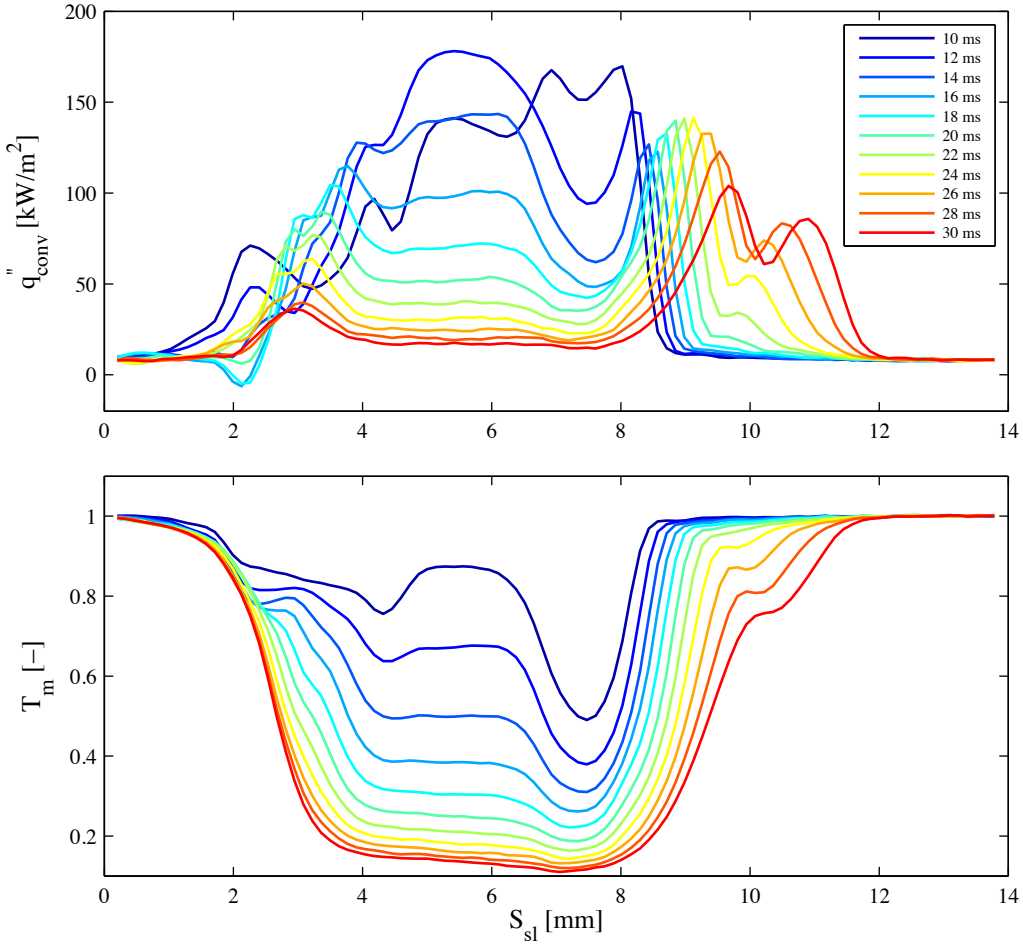

Figure 7.39: Convective heat flux and dimensionless surface temperature along a define slice in the surface, with a $\Delta t = 2$ *ms*, during a time period of 10 – 30 *ms*.

with the initial impact wake. This event can be inferred from Figure 7.39 at $S_{sl} = 10$ *mm*, although the central zone along the slice is not as prominent a feature as the side zones. This separation feature is more evident at a time of 25 *ms*, as illustrated by Figure 7.42, with the new zone being slightly separated from the initial impact wake, as seen in both the heat flux and temperature maps.

Figure 7.43 illustrates the instantaneous variation in convective heat flux and dimensionless surface temperature between times of 30 – 70 *ms*. At a time of 42 *ms*, at a position of $S_{sl} > 8$ *mm*, the two separate wakes are seen to merge into a single wake, which continues to spread along the surface. In this case the bubble does not continually slide along the surface, which is known to cause a trailing wake. Instead, the bubble moves very little, edging

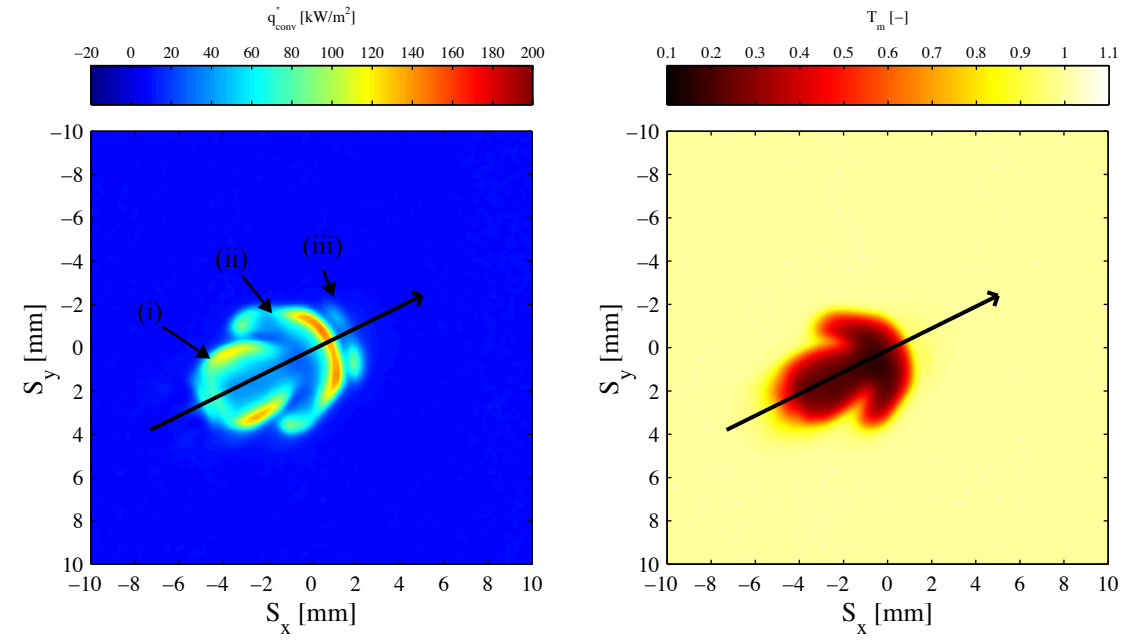

(a) (b)

Figure 7.40: (a) Convective heat flux and (b) dimensionless surface temperature for a 3.3 *mm* bubble, at a time of 22 *ms* after the initial impact. The three separate zones are depicted in (a).

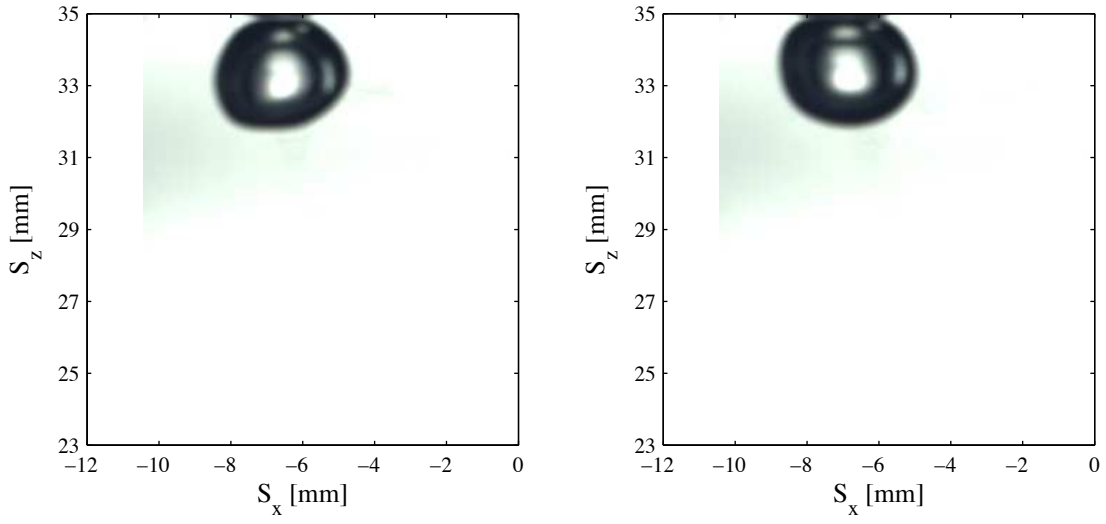

(a) (b)

Figure 7.41: Bubble images at (a) 22 *ms* and (b) 30 *ms* after impact for a 3.3 *mm* bubble, released from a height of 35 *mm*.

towards $S_{sl} = 0$ *mm*. The high levels of convective flux at approximately $S_{sl} = 2$ *mm*, are thought to be due to the spreading wake impacting the bubble's edge, with the bubble being

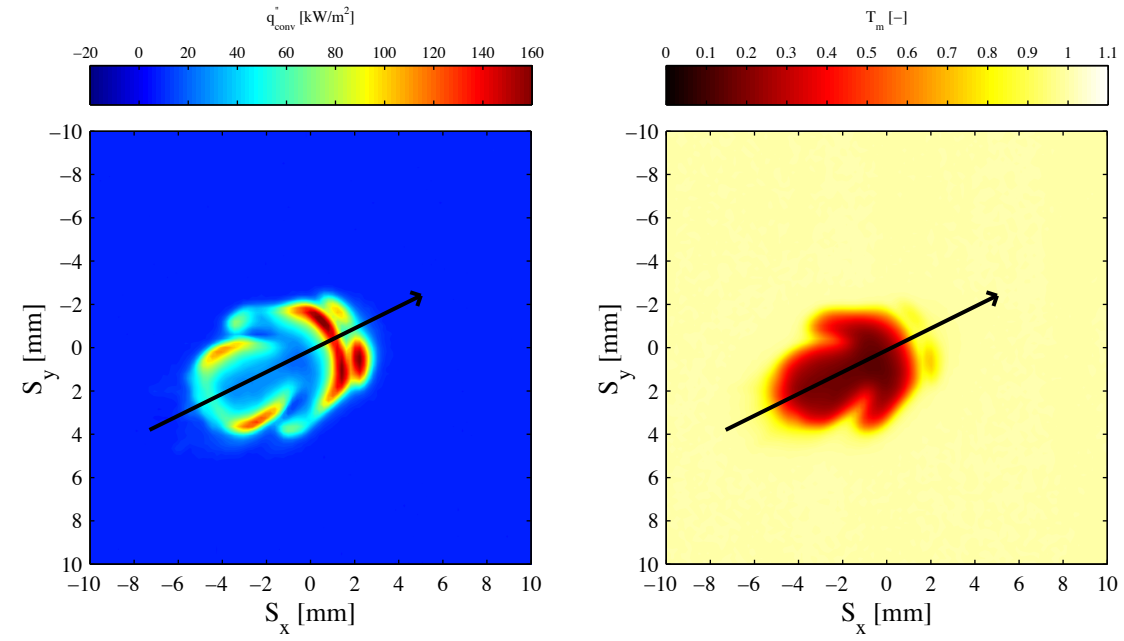

(a) (b)

Figure 7.42: (a) Convective heat flux and (b) dimensionless surface temperature for a 3.3 *mm* bubble, at a time of 25 *ms* after the initial impact. The black line indicates the slice shown in Figure 7.39.

attached to the surface during this particular time period.

Once the wake impacts the bubble in this manner, it continues to flow around the bubble before dissipating. This flow can be inferred from Figures 7.44 and 7.45, where the surface slice only cuts through the edge of the bubble's final resting position. As the starting position of this line is inside the edge of the bubble, the increase in surface temperature at a time of 70 *ms* is observable. This increase in surface temperature coincides with a decrease in the convective heat flux, within the bubble's footprint, which is evident in Figure 7.45 (a) at a time of 200 *ms*.

Figure 7.45 illustrates the convective heat flux and dimensionless surface temperature at a time of 200 *ms* after the initial impact. At this stage the bubble has attached itself to the surface, as evident from Figure 7.45 (b), where the dimensionless surface temperature is greater than one. In this case, the wake is observed to spread latterly, initiated by two zones of high convective heat flux ($\approx$25 kW/m^2) that can be seen in Figure 7.45 (a). This portion of the wake spreads latterly, finally stopping 1.2 *s* later.

During the spreading of the wake, the convective heat flux levels in the central region correspond to liquid natural convection, as seen in Figure 7.46. The peak heat flux at the

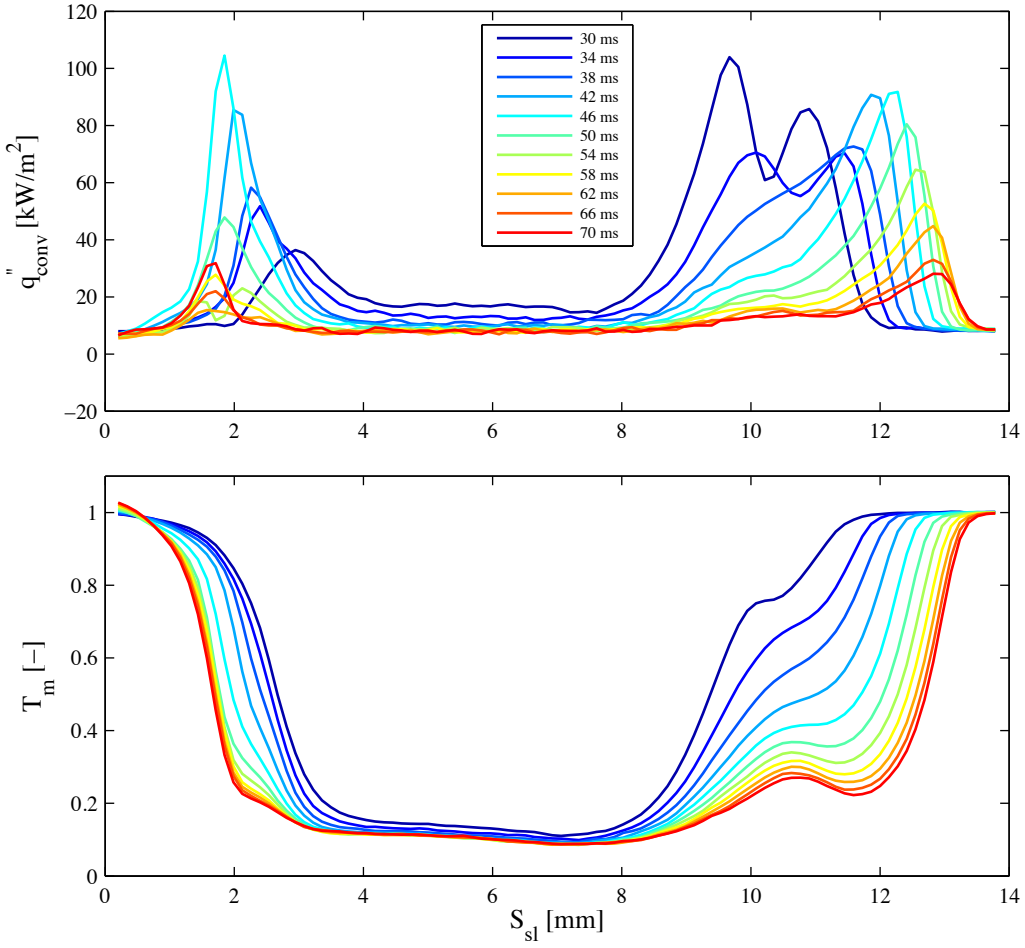

Figure 7.43: Convective heat flux and dimensionless surface temperature along a defined slice in the surface, with a $\Delta t = 4$ *ms*, during a time period of 30 – 70 *ms*.

left hand side of Figure 7.46 coincides with the wake pushing against the side of the bubble whereas on the right hand side a region of negative heat flux, coinciding with an increase in the surface temperature, occurs at approximately $S_{sl} = 12$ *mm*. In order to examine further this reduction in convective heat flux, a second surface slice, during the same time period 70 – 170 *ms*, is taken at approximately 90° from the initial slice line. This new slice line is illustrated in Figure 7.47 at a time of 110 *ms*.

From Figure 7.47, the reduction in convective heat flux is found to be confined to three small locations, directly behind a region of high heat flux. One such zone is at the leading edge of the wake, point (i), along the original slice line, illustrated in previous figures, whereas the other two zones are at positions of (0, -3) *mm* and (2, 2) *mm*, point (ii). Con-

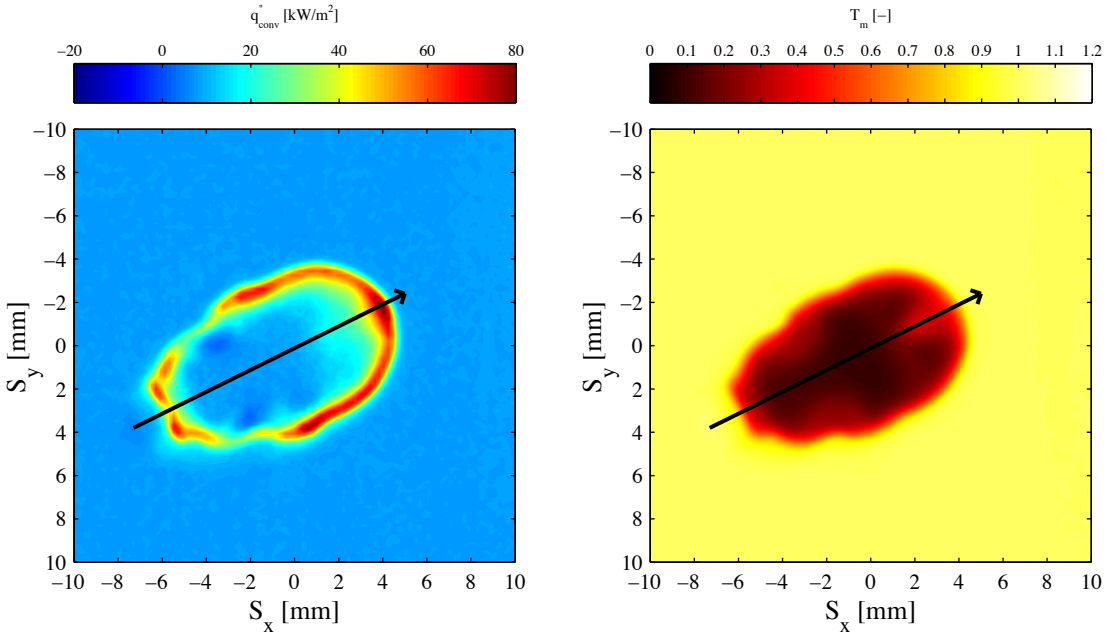

(a) (b)

Figure 7.44: (a) Convective heat flux and (b) dimensionless surface temperature for a 3.3 *mm* bubble, at a time of 50 *ms* after the initial impact.

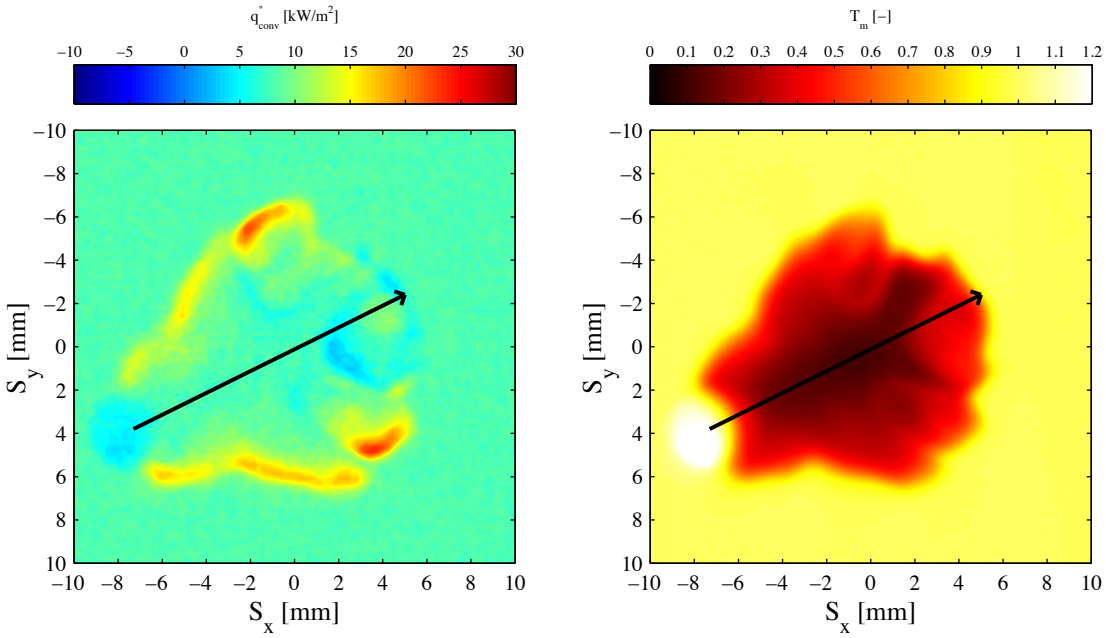

(a) (b)

Figure 7.45: (a) Convective heat flux and (b) dimensionless surface temperature for a 3.3 *mm* bubble, at a time of 200 *ms* after the initial impact.

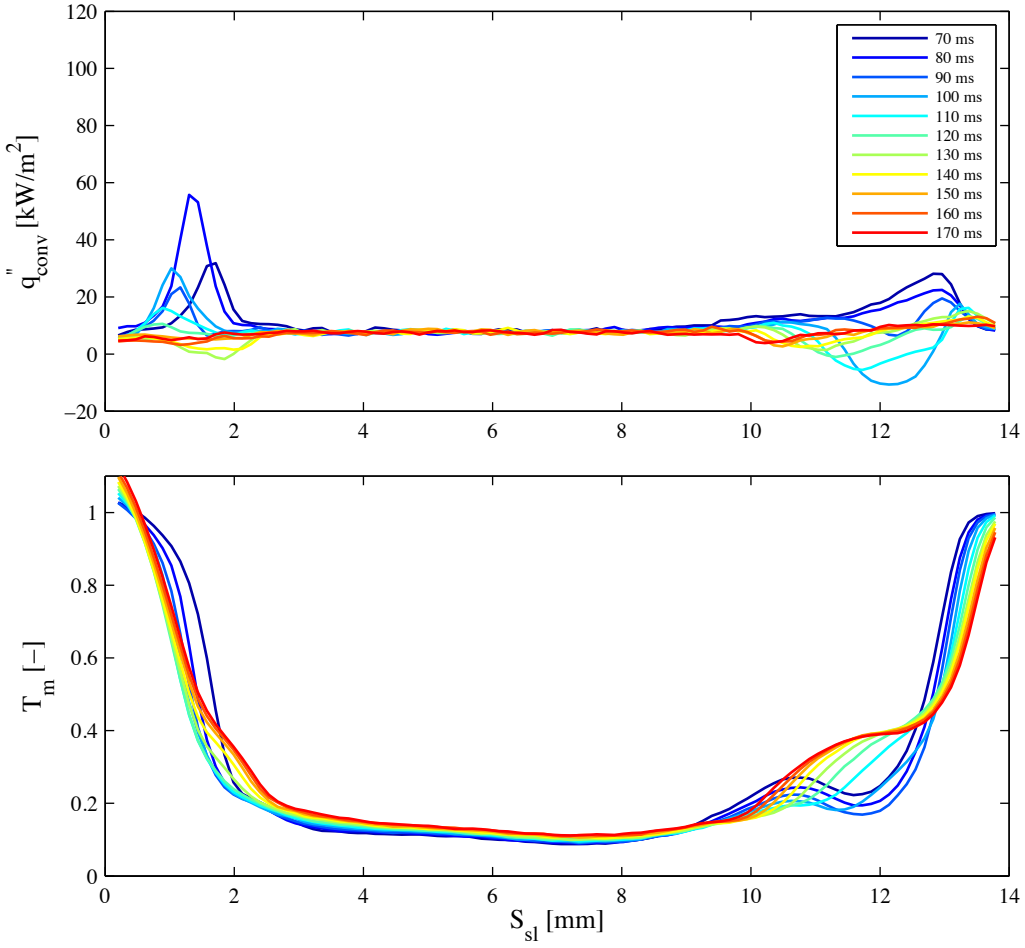

Figure 7.46: Convective heat flux and dimensionless surface temperature along a defined slice in the surface, with a $\Delta t = 10$ *ms*, during a time period of 70 – 170 *ms*.

vective heat flux and surface temperature along the new slice are illustrated in Figure 7.48. Regions of increased surface temperature and reduced convective heat flux are evident, particularly between $S_{sl} = 6 - 8$ *mm*, where the main wake, appears to roll over the slice line. The impact of the wake is symmetric along the original slice line, although the right hand side of the wake along the original slice line is slightly stronger, with this being possibly due to disturbances during the original rise of the bubble.

The explanation for the regions in which the surface temperature increases is thought to be circulation of boundary layer fluid. As the wake spreads out along the surface, a rolling vortex is created. This vortex rotates in such a way as to lift boundary layer fluid ahead of it. This fluid motion has been observed with a reduced light intensity which permitted the

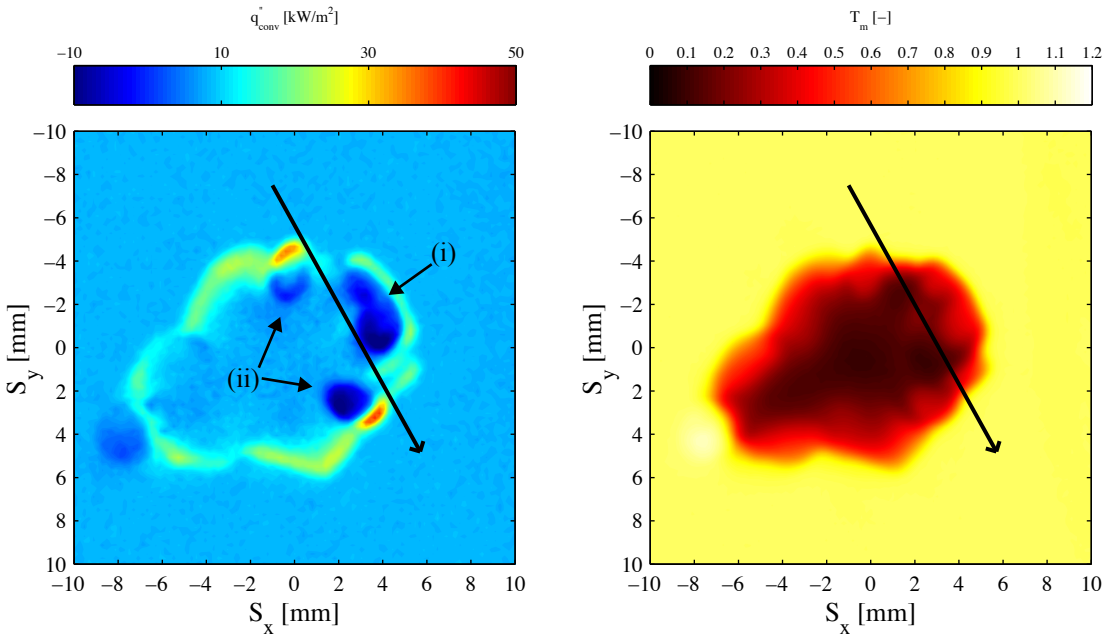

(a) (b)

Figure 7.47: (a) Convective heat flux and (b) dimensionless surface temperature for a 3.3 *mm* bubble, at a time of 110 *ms* after the initial impact. The black line indicates the slice shown in Figure 7.46. The zones of negative heat flux are shown in (a).

different fluid temperatures to be visualised[5]. The diameter of the rolling vortex, was found to measure approximately 1 – 2 *mm*.

Figure 7.49 (a) illustrates the main impact wake and the vortex rollup at an approximate time of 10 – 20 *ms* after the initial impact. In this case, the rollup vortex can be inferred to be separated from the surface; this may be due to the continually rising main wake, which slides underneath the rolling vortex, as highlighted by the black circle. The vortex at this point is still pulling the boundary layer fluid away from the surface, but is unable to re-impact the surface due to the main rising wake.

As the wake continues, two changes occur: firstly, the rising wake velocity reduces, as inferred from PIV data, and secondly the rollup vortex moves further away from the main rising wake, which was visually observed from fluid density gradients. This is depicted in Figure 7.49 (b), with the rollup vortex being slightly further away from the main wake. At the point of interest, the black circle, it is clear that the main rising wake is no longer separating the rollup vortex from the surface. Instead, the warm boundary layer fluid is transported

[5]This reduced light resulted from the delamination of one of the nine LED lights from the circuit board, resulting in a slightly reduced light intensity at the impact surface.

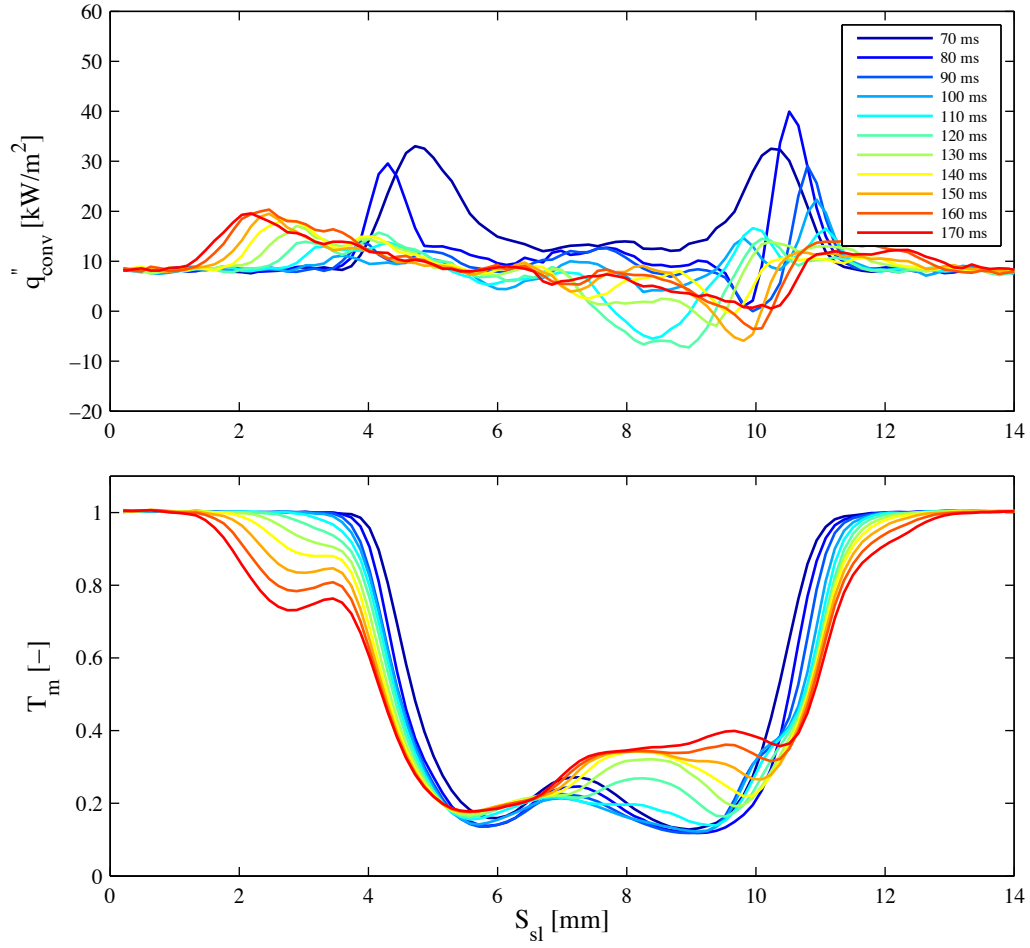

Figure 7.48: Convective heat flux and dimensionless surface temperature along a defined slice on the surface, with a $\Delta t = 10$ *ms*, during a time period of 70 – 170 *ms*. This example is in a different direction to that shown in Figure 7.46.

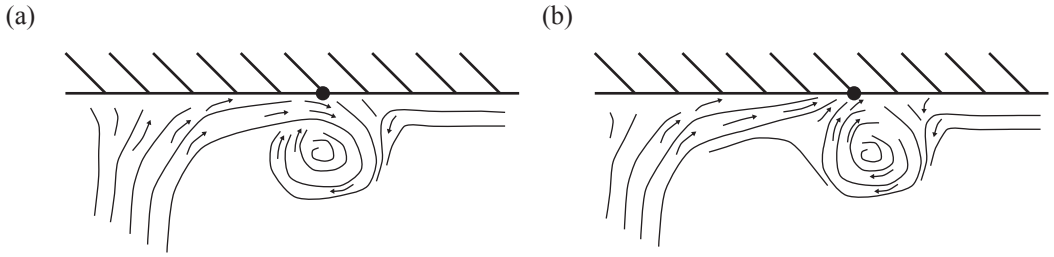

Figure 7.49: (a) initial rising wake impact and rollup (b) rising wake and rollup at a time period after the initial impact. The distance from the wake to vortex centre is slightly greater in case (b).

from the front of the vortex to its rear, which now impacts the surface. The further the vortex travels, the more boundary layer fluid will be pulled on top of the previously cooled surface,

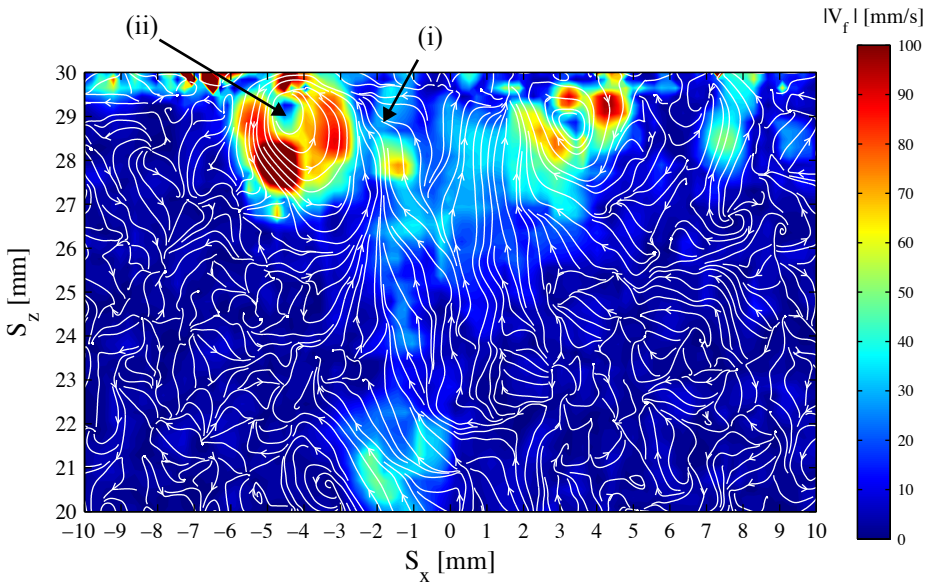

Figure 7.50: Instantaneous streamlines of a 3.3 *mm* bubble, released from a height of 30 *mm*, at a time of 50 *ms* after impact. (i) rising wake, (ii) rolling vortex.

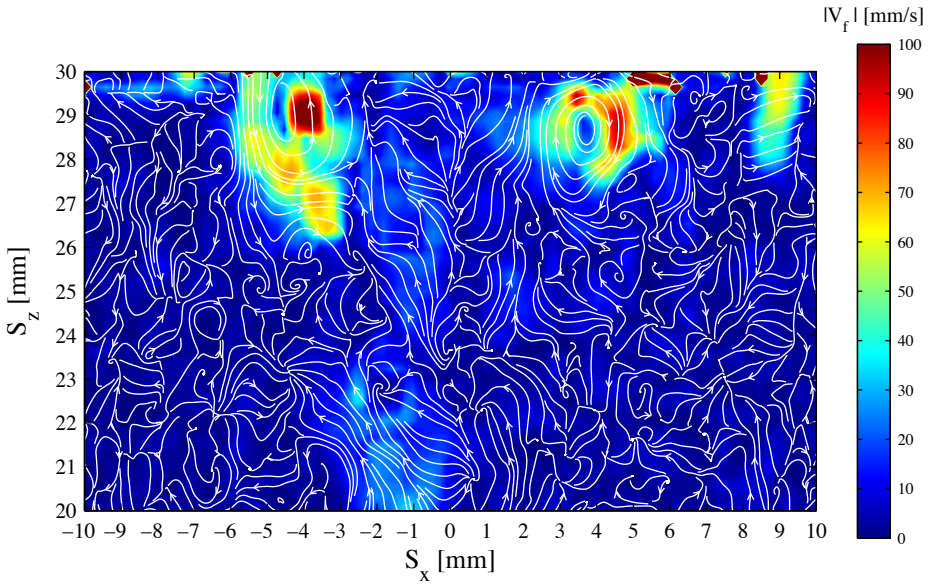

Figure 7.51: Instantaneous streamlines of a 2.8 *mm* bubble, released from a height of 30 *mm*, at a time of 80 *ms* after impact.

as the distance from the main rising wake increases. Again, three of these rolling vortices are labeled in Figure 7.47.

Figures 7.50 and 7.51 illustrate the streamlines for a 3.3 *mm* bubble released from a height of 30 *mm* at two instances. In Figure 7.50 the left most vortex is similar to that observed in Figure 7.44, with the main portion of the wake at $S_x = 0$ *mm* continuing to

feed into the left vortex. In this case the bubble has shifted to the right. After 30 *ms* in Figure 7.51, there is a noticeable change in the vortex structure, with the fluid at $S_x = -5$ *mm* being convected to the right, to an approximate position of $S_x = -3$ *mm*. This type of fluid motion is thought to cause the reduction in convective heat flux which was observed in Figure 7.47.

7.2.3 Case 3: 4.1 *mm* Bubble

In this section, the wake from a 4.1 *mm* bubble will be investigated. As previously reported for the 2.8 *mm* bubble, if the bubble impacts at an angle, the ensuing wake impacts and develops in the direction away from the bubble. This holds true for all bubble sizes tested if the impact is at a significant angle, which causes path deviation. The amount of path deviation and the variation in bubble size will dictate the area affected by the bubble and its ensuing wake.

In cases where a bubble rose vertically, with the bubble's major axis being approximately parallel to the heated surface, then the enhancement due to the ensuing wake was found to be approximately annular. This type of convective enhancement pattern was found to occur more for larger bubbles whose rise path was less susceptible to deviation. In order to interpret this form of wake motion, both PIV data and favourable Schlieren effects will be utilised, to visually interpret the combined bubble and wake motion.

Figures 7.52 to 7.58 illustrate the initial rebound of a 4.1 *mm* bubble, released from a height of 20 *mm*, between the times of 0 – 13 *ms*. These images are of interest due to the observable temperature gradients, as a result of reduced lighting, and allow a partial insight into the fluid motion during the initial impact and rebound event. The impact wake and bubble were found to be symmetric and approximately central in the test section. The variation in the fluid density, which is coupled to the wake impact, is evident at either side of the bubble in Figures 7.52 to 7.58.

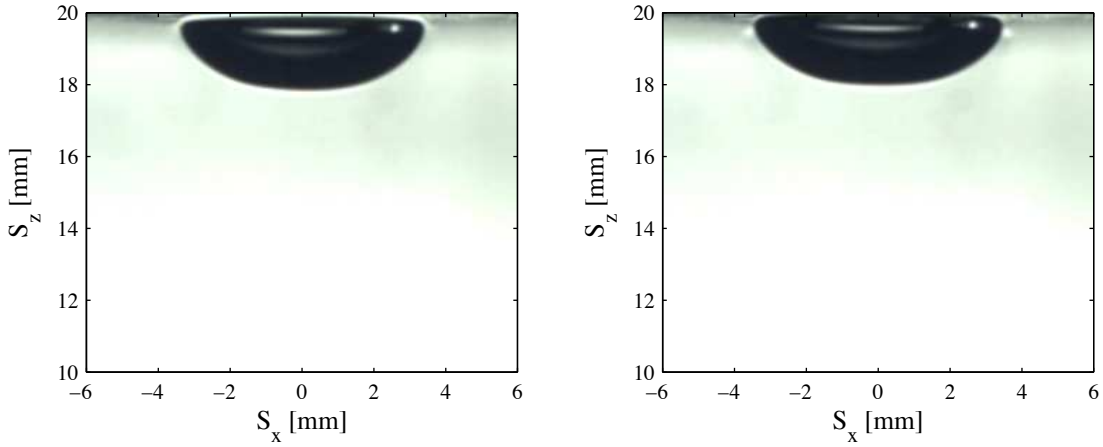

(a) (b)

Figure 7.52: Impact of a 4.1 *mm* bubble released from a height of 20 *mm*, (a) at a time of 0 *ms* and (b) 1 *ms*.

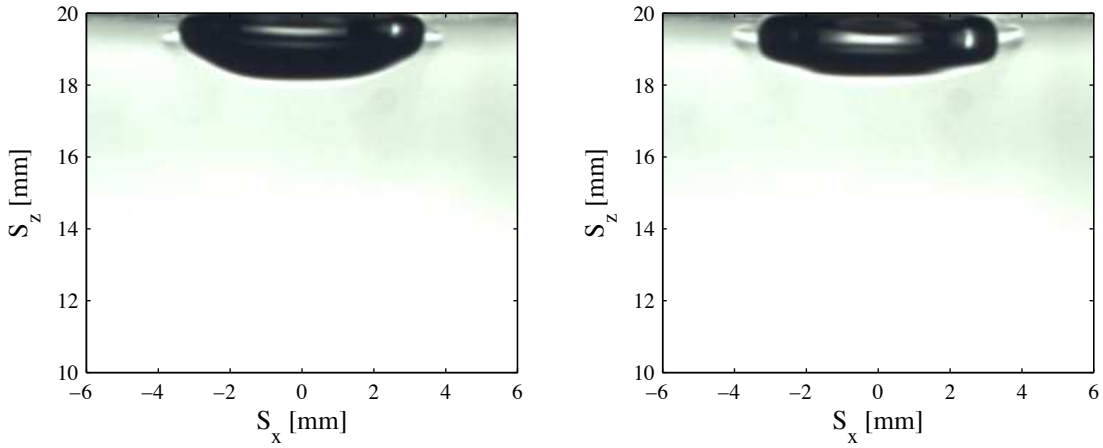

(a) (b)

Figure 7.53: Impact of a 4.1 *mm* bubble released from a height of 20 *mm*, (a) at a time of 2 *ms* and (b) 3 *ms*.

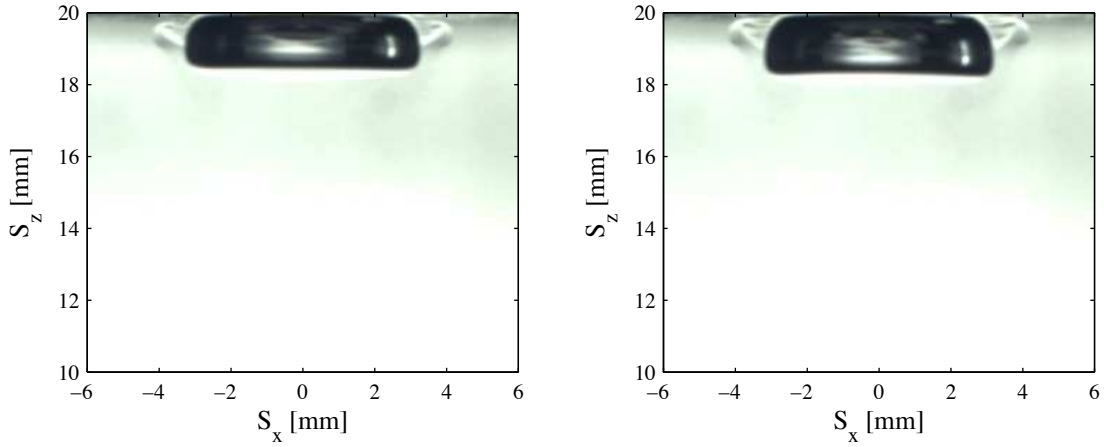

(a) (b)

Figure 7.54: Impact of a 4.1 *mm* bubble released from a height of 20 *mm*, (a) at a time of 4 *ms* and (b) 5 *ms*.

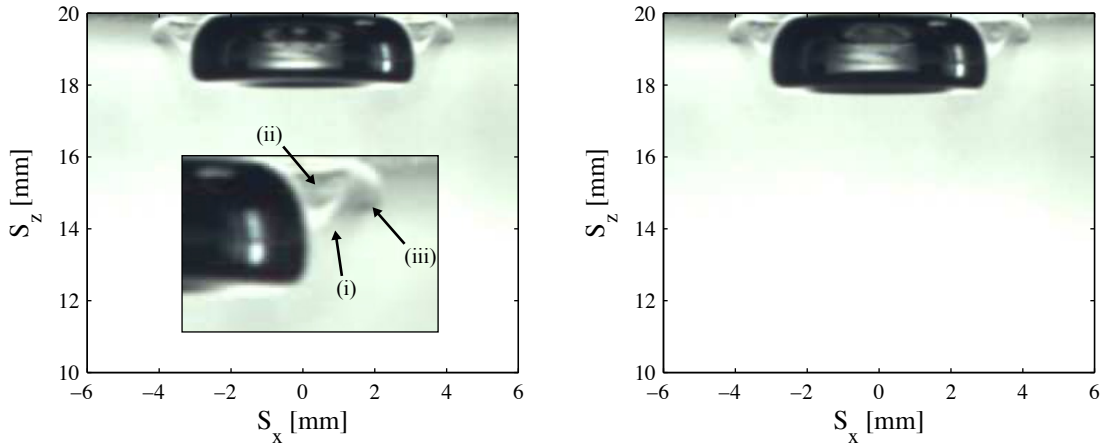

(a) (b)

Figure 7.55: Impact of a 4.1 *mm* bubble released from a height of 20 *mm*, (a) at a time of 6 *ms* and (b) 7 *ms*. (i) dark fluid, (ii) inner vortex and (iii) outer vortex.

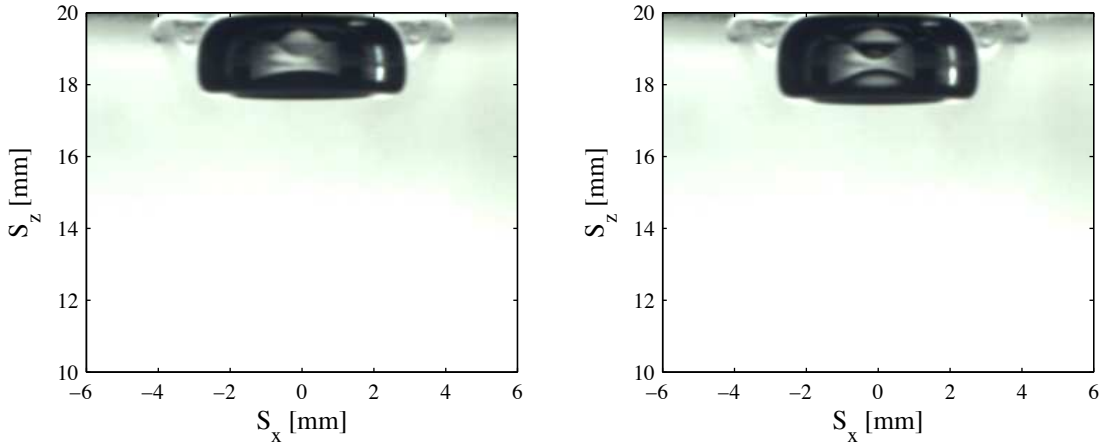

(a) (b)

Figure 7.56: Impact of a 4.1 *mm* bubble released from a height of 20 *mm*, (a) at a time of 8 *ms* and (b) 9 *ms*.

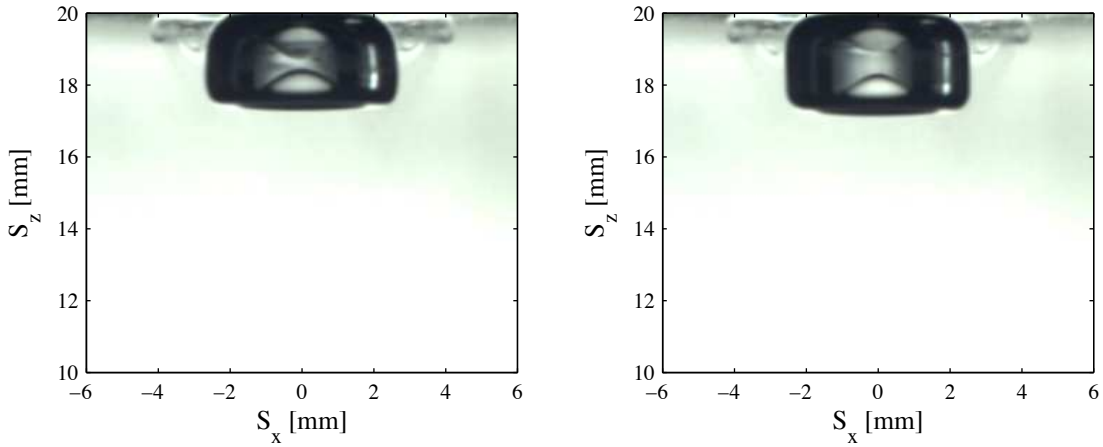

(a) (b)

Figure 7.57: Impact of a 4.1 *mm* bubble released from a height of 20 *mm*, (a) at a time of 10 *ms* and (b) 11 *ms*.

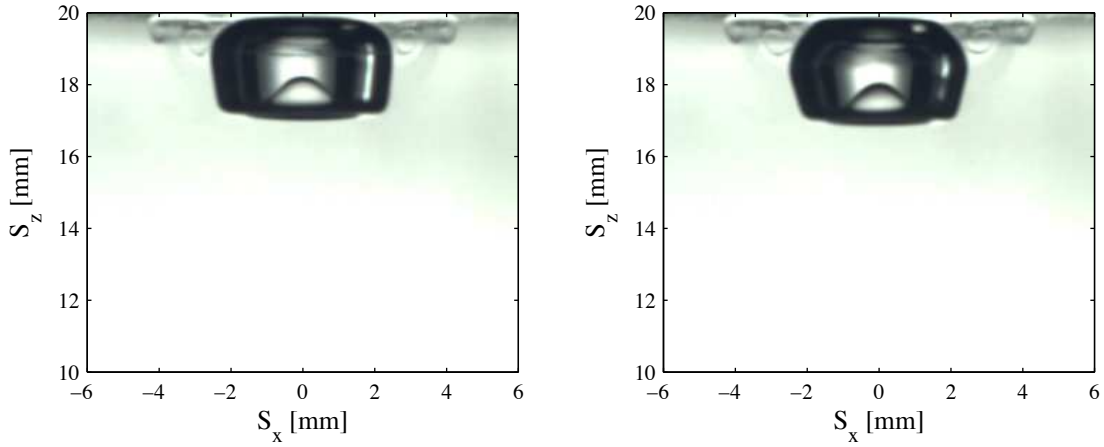

Figure 7.58: Impact of a 4.1 *mm* bubble released from a height of 20 *mm*, (a) at a time of 12 *ms* and (b) 13 *ms*.

In Figure 7.52 at a time of 1 *ms*, a region of counter clockwise fluid motion occurs on the right hand side of the bubble at a position of $S_x = 4$ *mm*, with the opposite occurring on the left hand side. This rotation of fluid was found to be linked to the bubble's rebound. Between times of 2 – 3 *ms* (Figure 7.53) this vortex grows slightly extending beyond $S_x = 4$ *mm* as the bubble pulls inwards. Figure 7.54 illustrates the bubble motion at 4 and 5 *ms*; in this case a secondary vortex appears due to the continued retraction of the bubble. This vortex is located between the bubble and the original vortex, although difficult to observe. The original vortex on the bubble's right hand side was found to be rotating in a counter clockwise direction. The direction of the new inner vortex is again counter clockwise on the bubble's right hand side, with the outer vortex being pushed towards the surface. This, in turn, changes the rotation direction of the outer vortex to that of a clockwise rotating vortex. The inner vortex was found to grow in size between times of 4 – 13 *ms*, which may be inferred from Figures 7.54 to 7.58. At times of 10 – 13 *ms*, just visible in Figures 7.57 to 7.58, at a position of $S_x = 3$ *mm*, a region of "dark" fluid visually appears at the edge of bubble, ending between the inner and outer vortex, which is depicted in Figure 7.55 (a). This stream of fluid actually begins earlier, but is difficult to identify. It was found to initiate at the outer corner of the bubble, the point furthest from the surface, and is thought to be the

stream of fluid which reverses the direction of the original outer vortex.

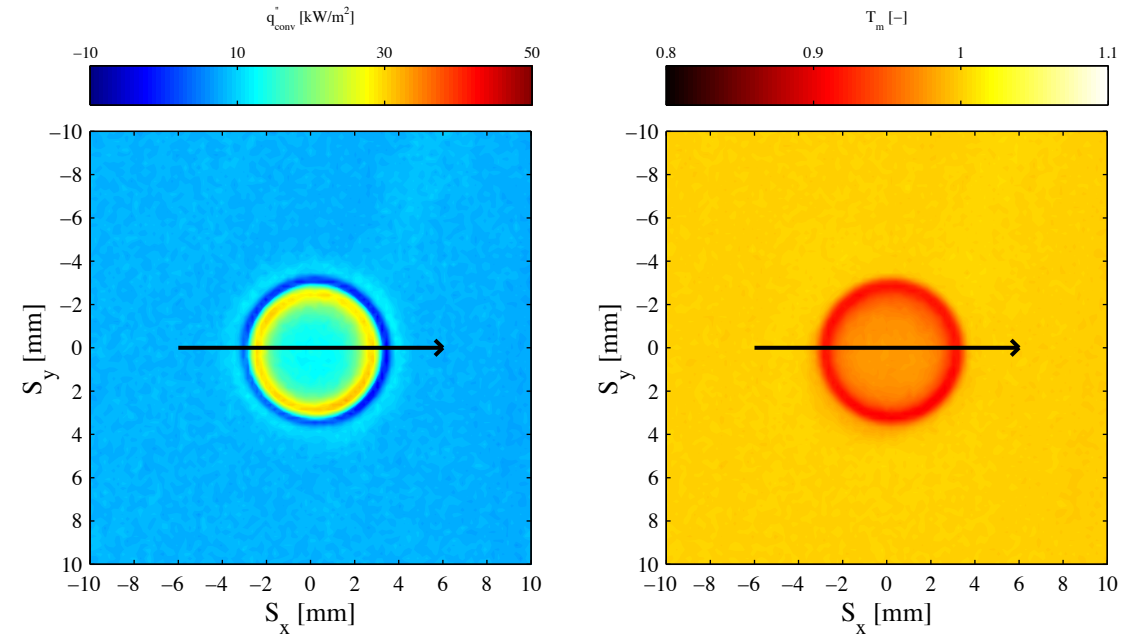

Figure 7.59: (a) Convective heat flux and (b) dimensionless surface temperature for a 4.1 *mm* bubble, at a time of 10 *ms* after the initial impact. The black line indicates the slice shown in Figure 7.60.

Figure 7.59 illustrates the convective heat flux and dimensionless surface temperature at a time of 10 *ms* for the 4.4 *mm* bubble impacting from a height of 20 *mm*. The direction and location of the following surface slice is shown, which cuts through the centre of the impact zone. Figure 7.60 illustrates the convective heat flux and dimensionless surface temperature between the time of 0 – 20 *ms*. Once more the symmetry of the cross section is noteworthy. In Figure 7.60, two different enhancement zones are present; the first is due to the bubble's impact, with the second being assumed to be a result of the wake. As the bubble impact and developing wake is symmetric, one side will be commented on. The effect of the bubble impact and the beginning of its rebound is evident between the limits of $S_{sl} = 1.5 - 3$ *mm*. The initial impact edge of the bubble is at $S_{sl} = 3$ *mm*; as the release height is low the enhancement is insignificant until a time of 4 – 6 *ms*. The initial impact convective heat flux has a maximum of approximately 40 kW/m^2 at 6 *ms*. As the edges of the bubble pull inwards this ring of convective enhancement shifts inwards, being at a position of $S_{sl} = 1.5$ *mm* at a time of 20 *ms*. Notably, as the edges of the bubble move inwards, the region where the initial impact occurred experiences a reduction in convective heat flux as the surface

temperature rises slightly. This region of low convective heat flux is thought to be related to the counter clockwise inner vortex, visible in Figure 7.57. From Figure 7.59, the outer ring of negative convective heat flux at a time of 10 *ms* is evident, as the bubble begins to recover its shape.

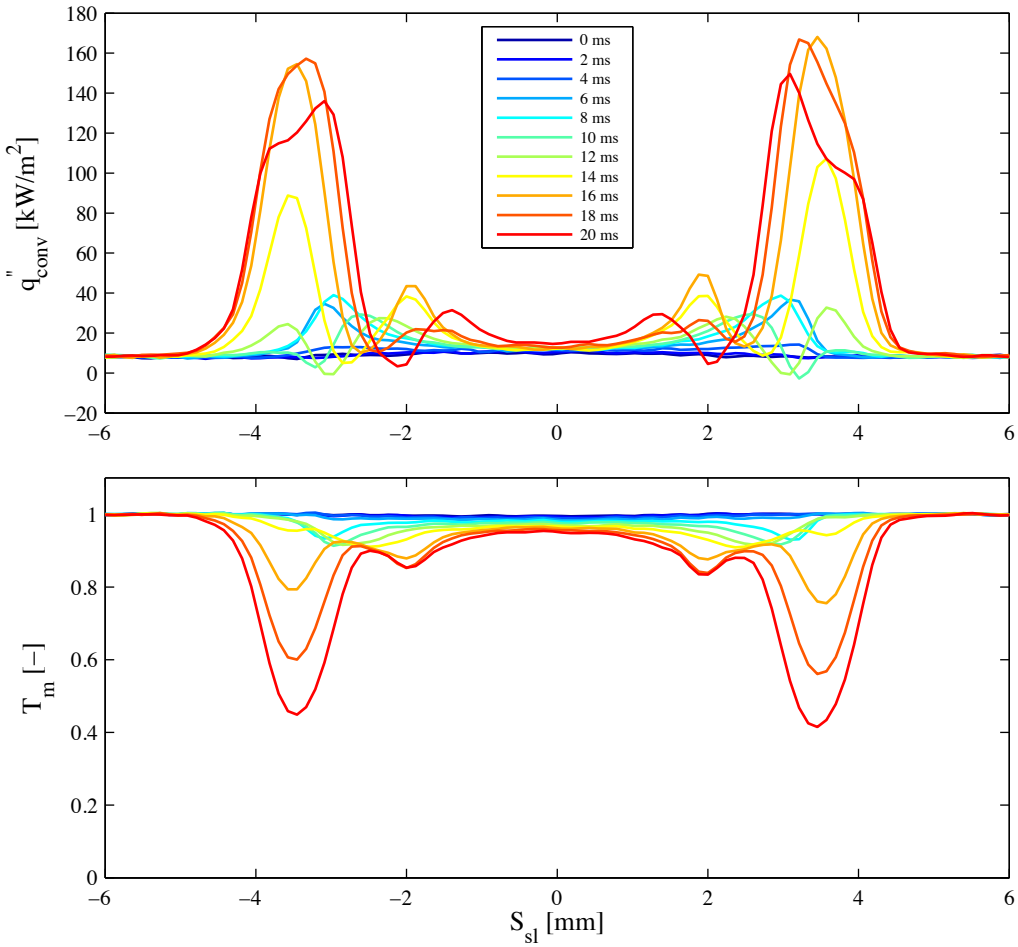

Figure 7.60: Convective heat flux and dimensionless surface temperature along a defined slice on the surface, with a $\Delta t = 2$ *ms*, during a time period of 0 – 20 *ms*.

At the outer regions (3 – 4.5 *mm*) of enhancement in Figure 7.60, the impact of the wake can be inferred to begin at a time of 12 *ms*. This is related to the flow field shown in Figure 7.58, whereby the "dark" cool fluid forces itself between the inner and outer vortices. The outer initial vortex appears not to enhance or reduce heat transfer during the initial impact and rebound, as it is thought that this vortex is slightly separated from the surface. Once the ensuing wake (dark fluid) impacts the surface, the convective heat flux increases signifi-

cantly, to levels just above 150 kW/m^2, in a short time period. The peak in enhancement in Figure 7.60 occurs between the times of 16 – 18 *ms*, while at a time of 20 *ms*, the peak is depressed slightly.

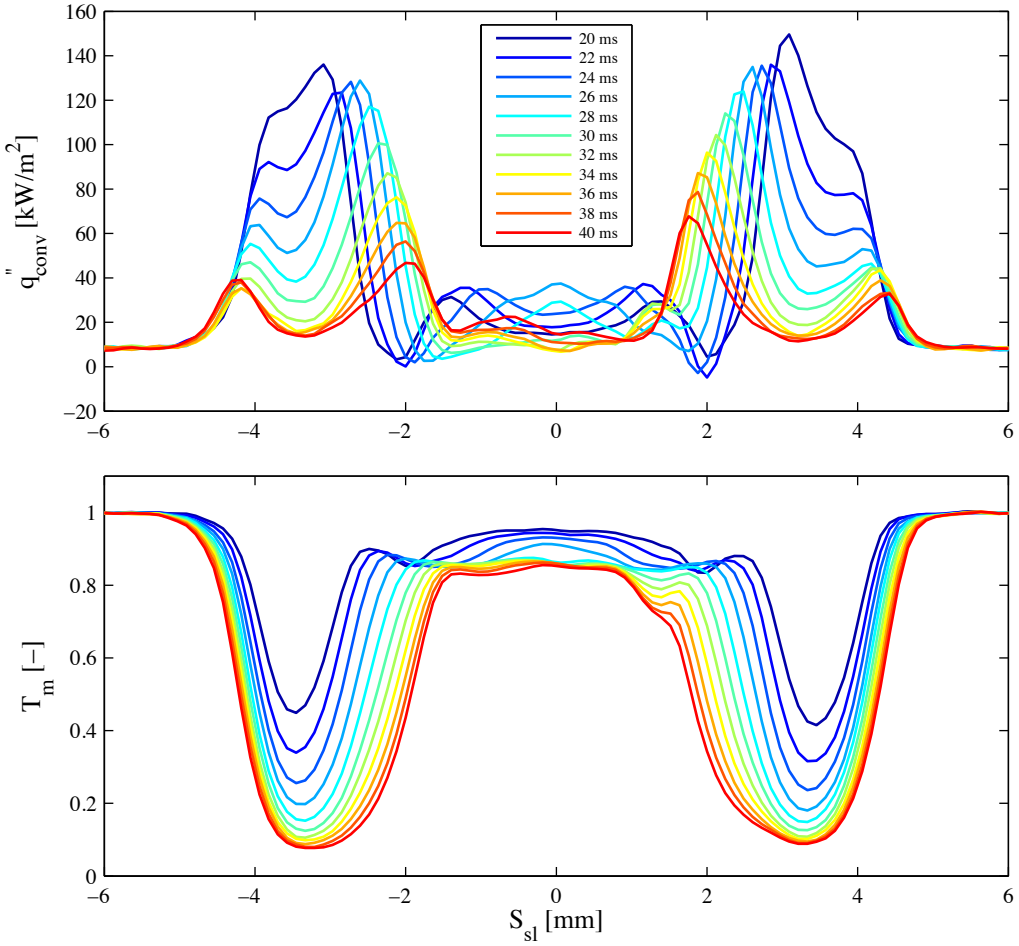

Figure 7.61: Convective heat flux and dimensionless surface temperature along a define slice in the surface, with a $\Delta t = 2$ *ms*, during a time period of 20 – 40 *ms*.

Figure 7.61 illustrates the convective heat flux and dimensionless surface temperature between times of 20 – 40 *ms*. The bubble was found to completely rebound from the surface at a time of 23 *ms* as illustrated in Figure 7.62; again the bubble's rebound process was found to be symmetric. During the time period shown in Figure 7.61, after 23 *ms* the bubble is away from the surface. In this case, the impacted wake was found to spread only slightly beyond ± 4 *mm*; instead, it appears that the wake actually shifts inwards, as far as ± 2 *mm*. This rapid shift inwards is thought to be due to the bubble's shape change. Thus,

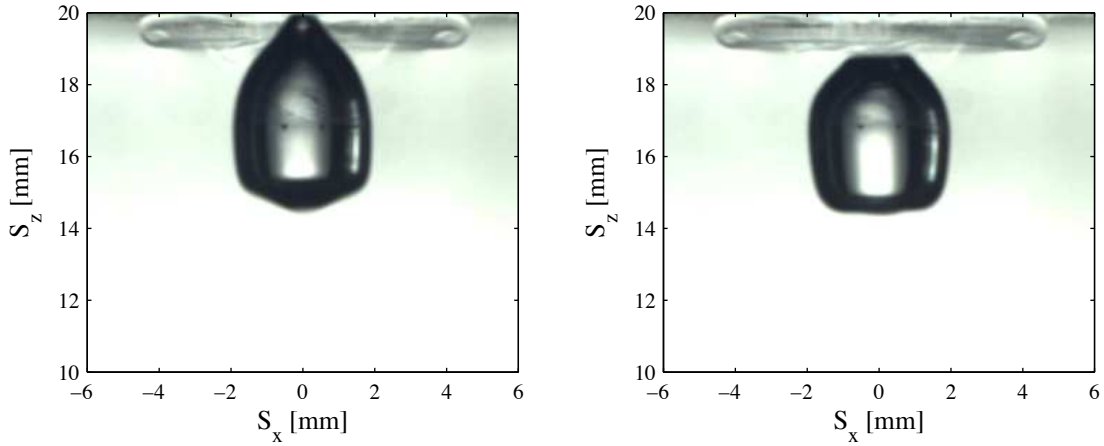

Figure 7.62: Impact of a 4.1 *mm* bubble released from a height of 20 *mm*, (a) at a time of 21 *ms* and (b) 23 *ms*.

the bubble originally extended as far as ± 3.5 *mm* (Figure 7.52), which is reduced to ± 2 *mm* (Figure 7.62). Notably, the enhancement zone did not extend inside the extremities of the bubble, which in this case is ± 2 *mm*.

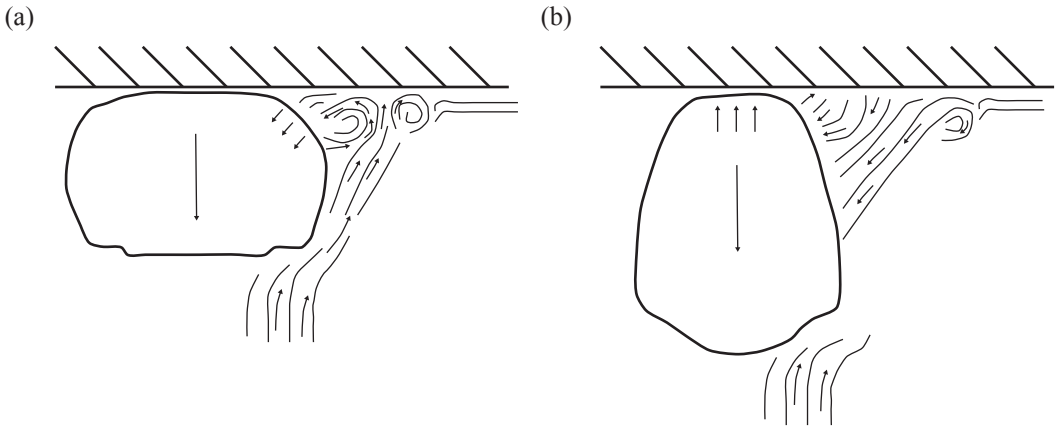

Figure 7.63: Bubble outline and approximate fluid motion at a time of (a) 14 *ms* and (b) 19 *ms*.

This wake motion is thought to result from the actual shape of the bubble prior to leaving the surface, together with the influence of the fluid which is trapped within the impact dimple. The outline of the bubble at two time periods of 14 and 19 *ms* is sketched in Figure 7.63. In Figure 7.63 (a), both the inner and outer vortex are present, as inferred from

the temperature gradients. As the bubble has retracted from its impact shape, the lower edges pull inwards, in turn, this drags the inner vortex inwards. In this case the rising wake continues its rise path around the bubble as depicted.

Figure 7.63 (b) illustrates the bubble at a time of 19 *ms*. At this instance the bubble has a vertical height of 5 *mm*, with an approximate width of 4 *mm* at its widest. As the bubble has pulled inwards, this results in the rising wake (dark fluid), which was impacting in-between the two vortices, being pushed away from the surface. Thus, during the impact process, two dimples form on the bubble's surface: one between the bubble and the surface, the second at the bubble's lower edge. Both dimples can be clearly seen at a time of 9 *ms* in Figure 7.56 (b). As the bubble continues its retraction, this lower dimple inverts, expelling captured wake fluid, back against the continually rising wake. This reversal of fluid is furthered by the bubble rebounding into the rising wake, which disconnects the ensuing wake from the enhancement zone as illustrated in Figure 7.63 (b).

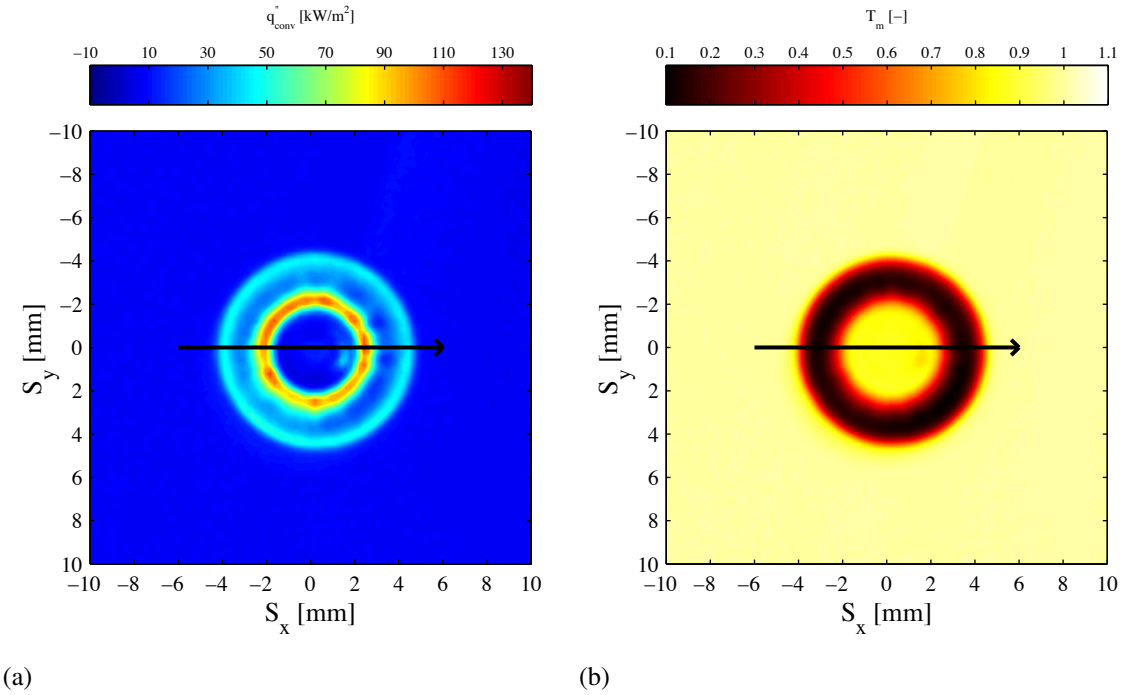

(a) (b)

Figure 7.64: (a) Convective heat flux and (b) dimensionless surface temperature for a 4.1 *mm* bubble, at a time of 30 *ms* after the initial impact.

Once the bubble has left the surface at a time of 22 *ms*, the zone extending beyond ± 3 *mm* experiences a continued temperature reduction, as illustrated in Figure 7.61. This peak steadily shifts inwards to ± 2 *mm* at a time of 40 *ms*, all the while steadily reducing. The

source of this enhancement has been inferred from a single PIV test in which the bubble bounced in a similar fashion to that shown here. Between the time period of 20 – 40 *ms*, the outer vortex on the right hand side rotates in a clockwise direction; this rotation moves fluid towards the void left by the bubble's shape recovery. In Figure 7.62 (b), the vortex is located at approximately (4, 19) *mm*, while the "void" is at (2.5, 18) *mm*. This vortex motion (clockwise) combines with the motion of the bubble to cool the surface, by circulating fluid into the void. The fluid which is pulled inwards is the bulk fluid which is adjacent to the boundary layer; this is likely to be a mixture of both warm and cool fluid. The extent of the wake may be perceived from Figure 7.64 at a time of 30 *ms*.

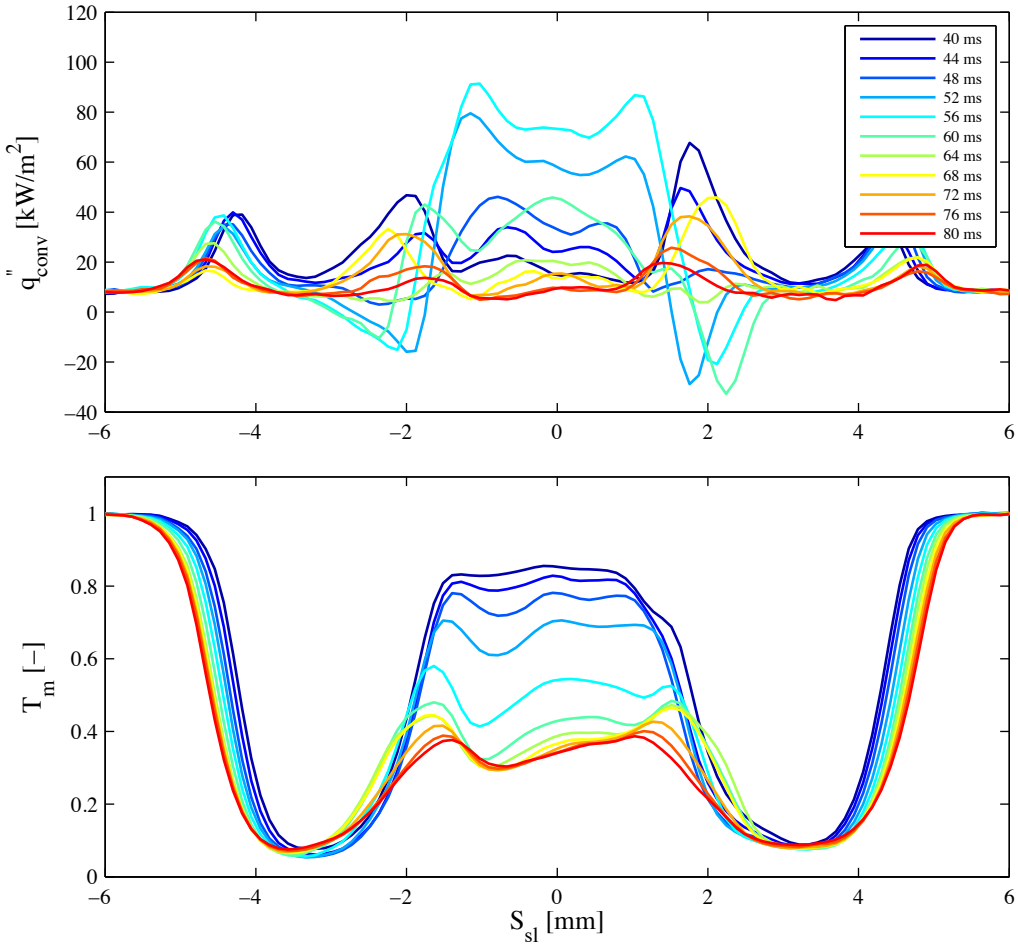

Figure 7.65: Convective heat flux and dimensionless surface temperature along a defined slice on the surface, with a $\Delta t = 4$ *ms*, during a time period of 40 – 80 *ms*.

The bubble's dimple was found to be fully inverted at a time of 21 *ms*, resulting in both

increases and decreases in convective heat flux which are observable within the limits of ± 2 *mm* in Figure 7.61, while the main portion of the wake does not encroach inside this limit. This limit again was found to be the minimum width of the bubble upon rebound from the surface.

At a time of 40 *ms* as seen from Figure 7.61, the convection has reduced significantly. As inferred from PIV images, this is due to the vortex shifting further outwards, reducing in strength, and due to the fact that the bubble is no longer pulling inwards. This lower enhancement may also be linked to the inversion of the bubble's impact dimple, which is thought to contain both warm boundary layer fluid and cool bulk fluid.

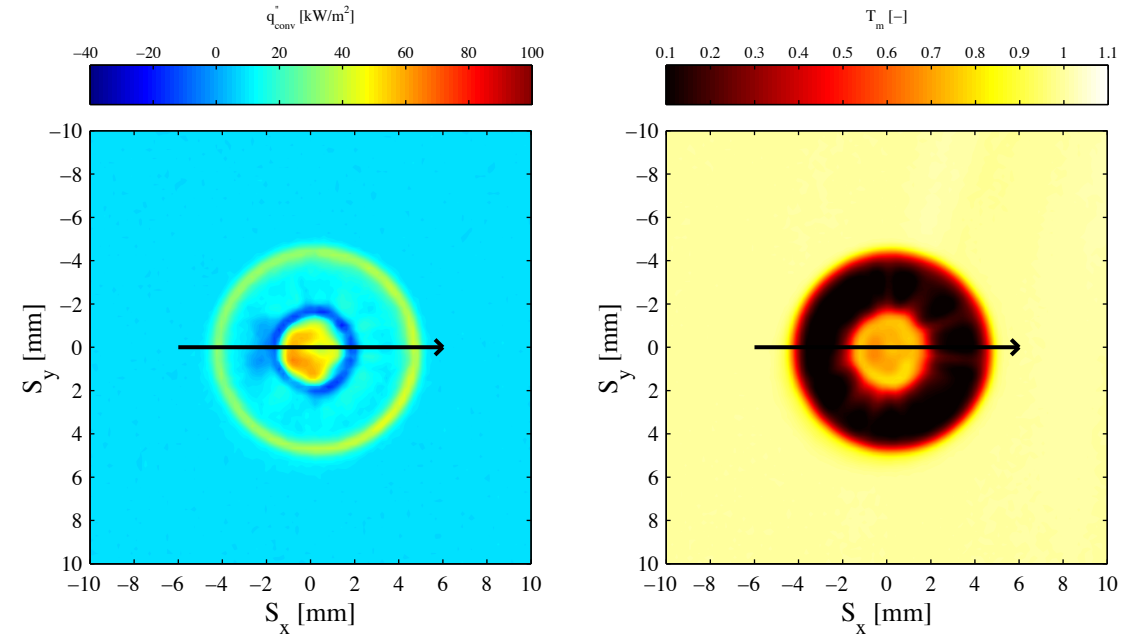

(a) (b)

Figure 7.66: (a) Convective heat flux and (b) dimensionless surface temperature for a 4.1 *mm* bubble, at a time of 50 *ms* after the initial impact.

Figure 7.65 illustrates the variation in the convective heat flux and dimensionless surface temperature between the times of 40 – 80 *ms* for the 4.1 *mm* bubble and a 20 *mm* release height. During this time period the bubble re-impacts the surface at a time of 48 *ms* before rebounding from the surface again at a time of 70 *ms*. The initial re-impact at 48 *ms* causes an increase in the convective heat flux in the central region, while at the bubble's edge negative heat flux occurs. This ring of negative heat flux is evident in Figure 7.66 (a) at a time of 50 *ms*. This re-impact causes both enhancement and reduction of heat transfer,

particularly at a position of ± 2 *mm*. At this position, there is initially positive enhancement of approximately 40 kW/m^2; as the bubble re-impacts the surface, the edges of the bubble impact this region with a greater velocity than the main portion of the bubble. This causes the rapid decrease in convective heat flux at this point, as warm fluid is forced against the surface, to an approximate value of -35 kW/m^2. As the bubble rebounds from the surface, this region experiences positive enhancement of approximately 30 kW/m^2, which steadily reduces over time. The bubble re-impacted the surface once more at a time of 94 *ms* (not shown), which was again found to affect the convective enhancement. During this time period the outer vortex, $S_{sl} > 4$ *mm*, cools the surface slowly, with the height of the vortex increasing in size to a diameter of 2.5 *mm*. Eames & Dalziel [119] investigated the flow around a rigid sphere impacting a solid surface. It was found that when the sphere made contact with the wall, a wake vortex, initially located at the rear of the sphere, was able to shroud the sphere and to impact on the wall. This generated a secondary vortex ring which, together with the initial wake, was found to push liquid radially outwards. Images captured by Eames & Dalziel [119] were found to be consistent with the results observed in this study.

7.3 Secondary Enhancement

Once the bubble had settled on the surface, a region surrounding the bubble experienced a drop in temperature. This drop in temperature was found to develop slowly, in contrast with the enhancement due to the bubble's impact and ensuing wake. This late enhancement process was found to be related to the bubble size and the final shape which the bubble took upon attachment to the surface. For study of this phenomenon a release height of 30 *mm* will be presented, for which the ensuing wake significantly affects the surface convective heat transfer. When the bubble was released from a height of 10 *mm*, the enhancement due to the wake was found to be limited, while the secondary enhancement was found to be similar to the example that follows.

Figure 7.67 illustrates the surface temperature at times of 0.197 *s* and 0.332 *s* after the initial impact of the 2.8 *mm* bubble, with a release height of 30 *mm*. The location of the bubble can be inferred from the increase in the surface temperature beneath the bubble (white zone). The green and blue circles indicate the point locations for which the temporal

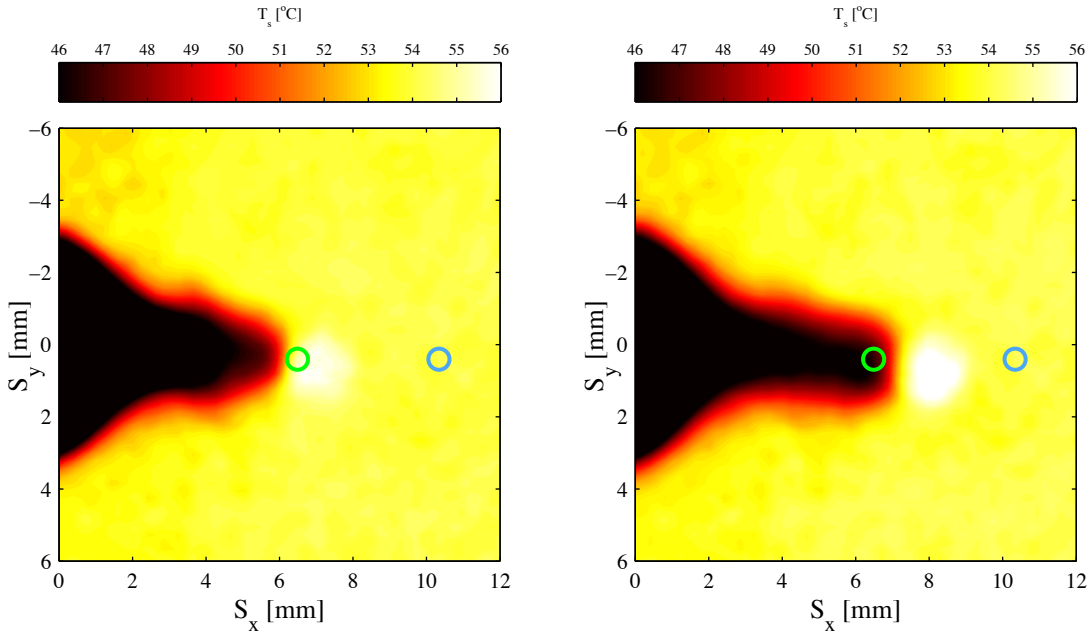

Figure 7.67: Surface temperature at a time of (a) 0.197 *s* and (b) 0.332 *s* for a 2.8 *mm* bubble, with a release height of 30 *mm*. The green circle (left) corresponds to the black line in Figure 7.68, while the blue circle (right) corresponds to the red line in Figure 7.68. The location of the bubble may be inferred from the increase in surface temperature (white zone).

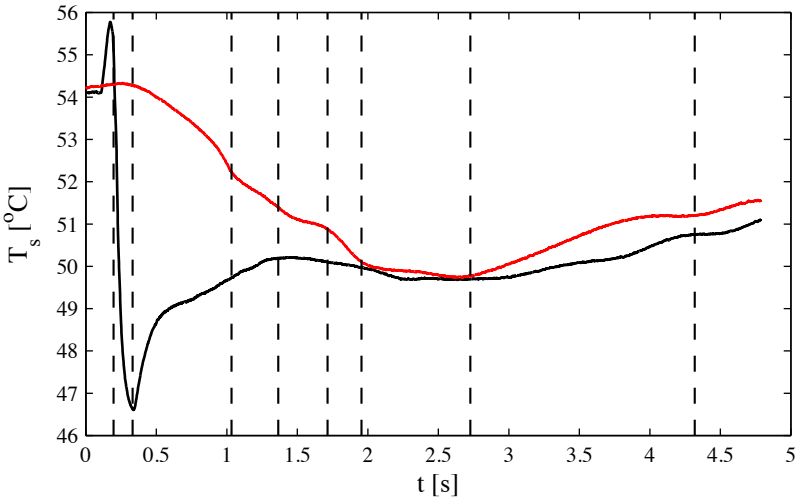

Figure 7.68: Temporal variation in surface temperature at two particular positions marked in Figure 7.67. The black line corresponds to the green point on the left of the bubble while the red line correspond to the blue position on the bubble's right. The vertical lines correspond to specific times illustrated in the following figures.

variation in surface temperature is shown in Figure 7.68; the black line corresponds to the green point on the left of the bubble while the red line corresponds to the blue position to the bubble's right. The vertical lines correspond to the surface temperature maps that follow. In conjunction with discrete temperature maps, the velocity magnitude and streamlines are also presented. As the fluid velocity is very low at this stage, the Δt between PIV correlation images changes with time. Figure 7.69 illustrates the velocity magnitude and streamlines at a time of around 0.197 *s*. The red circle indicates the approximate location of the bubble, while the vertical lines indicate the locations where the temperature is plotted in Figure 7.68. Note that as the Δt between correlations is 10 *ms* in Figure 7.69, the bubble has shifted 0.13 *mm* to the right[6] during the period over which the PIV data are collected, as indicated by the direction of the streamlines and the velocity.

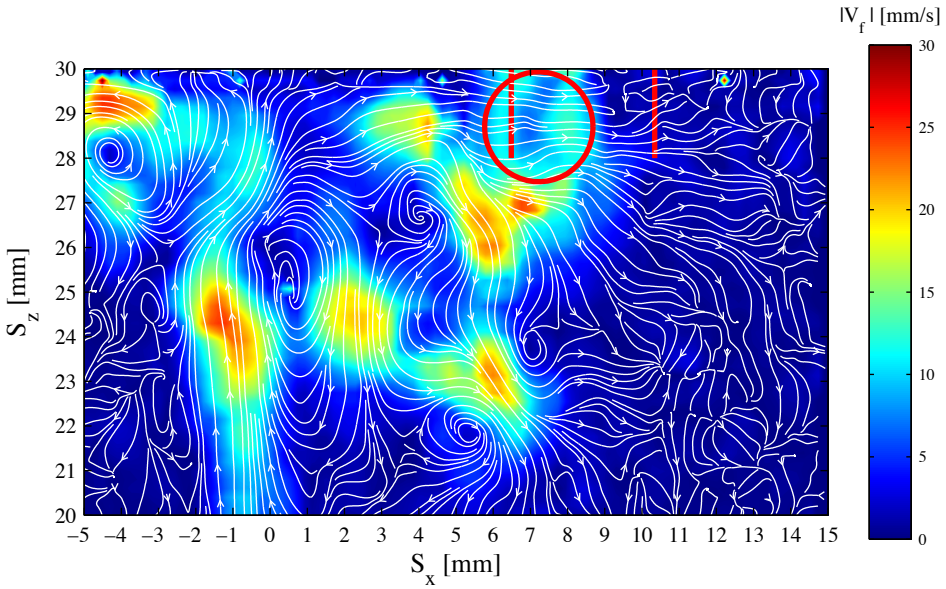

Figure 7.69: Instantaneous streamlines of a 2.8 *mm* bubble, released from a height of 30 *mm*, at a time of 0.197 *s* after impact.

In Figure 7.68 two different temperature reduction processes are evident. On the left hand side of the bubble (black line), an initial spike in temperature occurs, with this being due to the bubble sliding over this position. This temperature increase is followed by a rapid reduction in temperature, due to the ensuing wake enveloping the left hand portion of the bubble. This behaviour can be inferred from Figure 7.67, which corresponds to the first two

[6]During the PIV measurement period, the location of the bubble in red, has shifted 0.13 *mm* to the right of the image shown, as the second correlation image is at a time of 0.207 *s*.

vertical lines in Figure 7.68. During this early period, the temperature change on the right hand side of the bubble is quite small. This is due to the location of the bubble; as indicated by the red vertical lines in Figures 7.69 and 7.70, the bubble has only begun to affect the second point of interest at a time of 0.322 *s* (second vertical dashed line in Figure 7.68).

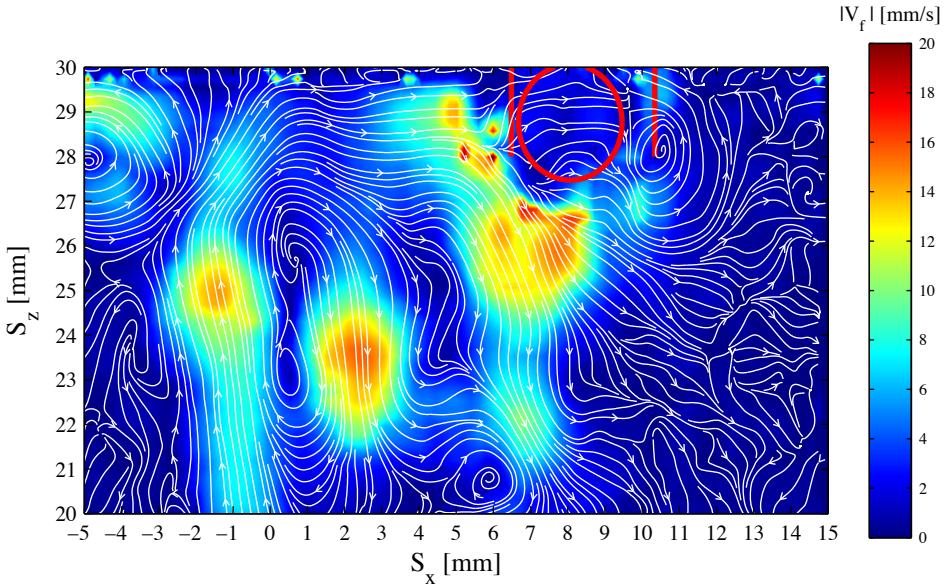

Figure 7.70: Instantaneous streamlines of a 2.8 *mm* bubble, released from a height of 30 *mm*, at a time of 0.322 *s* after impact.

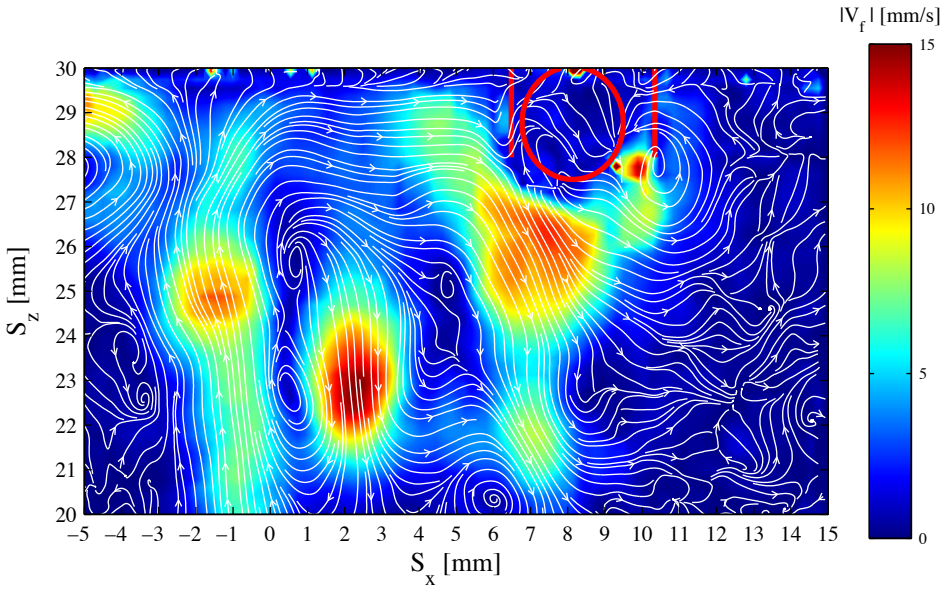

Figure 7.71: Instantaneous streamlines of a 2.8 *mm* bubble, released from a height of 30 *mm*, at a time of 0.397 *s* after impact.

After 0.322 *s*, the surface temperature on the right hand side of the bubble begins to drop, up until a time of approximately 1 *s*. This drop in temperature was found to result from a counter rotating vortex at the right hand side of the bubble. This vortex is evident in Figures 7.70 and 7.71 at times of around 0.322 *s* and 0.397 *s*, respectively. The vortex appears to be rotating about a point at (10.5, 28) *mm* in Figure 7.70; in fact, this vortex extends much closer to the surface than observed here. As the bubble blocks the laser sheet in this region, the cross correlation is quite low; thus, the actual extent of the counter clockwise vortex is inferred from raw images. This vortex is thought to draw in cool fluid while expelling warm boundary layer fluid. On the left hand side of the bubble in Figures 7.70 and 7.71, the ensuing wake is clearly evident, being partially deflected by the bubble into the bulk fluid.

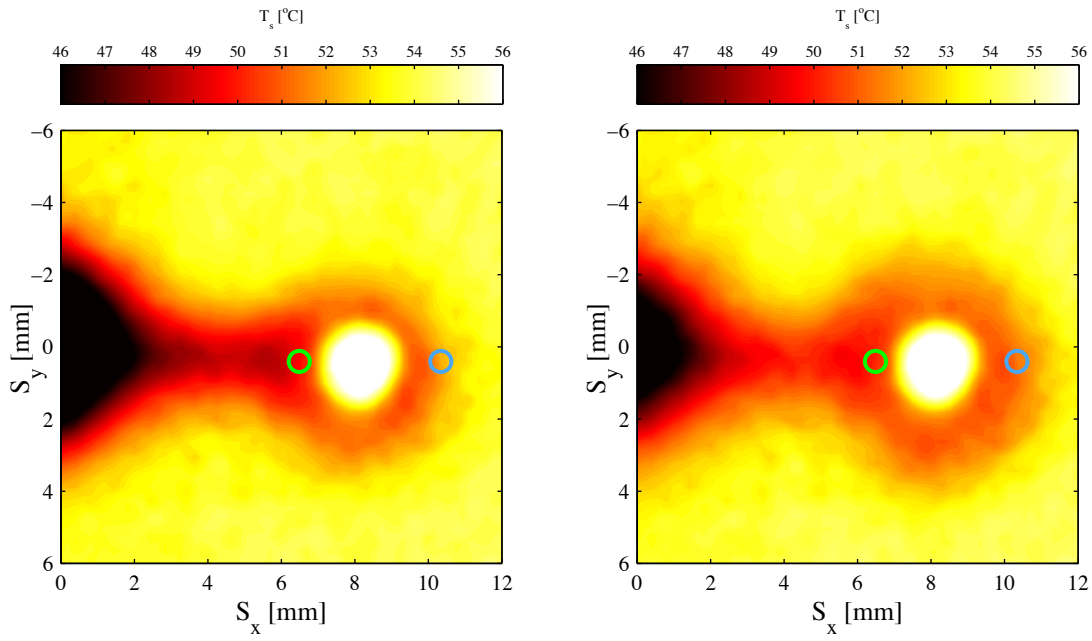

(a) (b)

Figure 7.72: Surface temperature at times of 1.034 *s* and 1.365 *s*. The green circle (left) corresponds to the black line in Figure 7.68, while the blue circle (right) corresponds to the red line in Figure 7.68. The location of the bubble may be inferred from the increase in surface temperature (white zone).

Figure 7.72 illustrates the surface temperature map at times of 1.034 *s* and 1.365 *s*, which are the next two times marked on Figure 7.68. Figures 7.73 and 7.74 respectively illustrate the velocity magnitude and streamlines at each of these times. In Figure 7.72 the cooling associated with the wake is not "separated" from the bubble zone, while within a zone surrounding the bubble a ring of lower temperature is evident at both times featured.

In Figure 7.73 the counter rotating vortex that was located to the right of the bubble is no longer present. This change occurs in conjunction with a change in fluid direction within the bulk fluid region below the bubble; this is now moving towards the surface. This fluid moves mostly to the right hand side of the bubble first, causing the continued drop in surface temperature that is evident there from Figure 7.68 (red line). The surface temperature on the left hand side of the bubble (black line, Figure 7.68), reaches a local peak at 1.365 *s* (fourth vertical line in Figure 7.68); this coincides with the creation of a counter clockwise vortex on the left hand side of the bubble, evident in Figure 7.74.

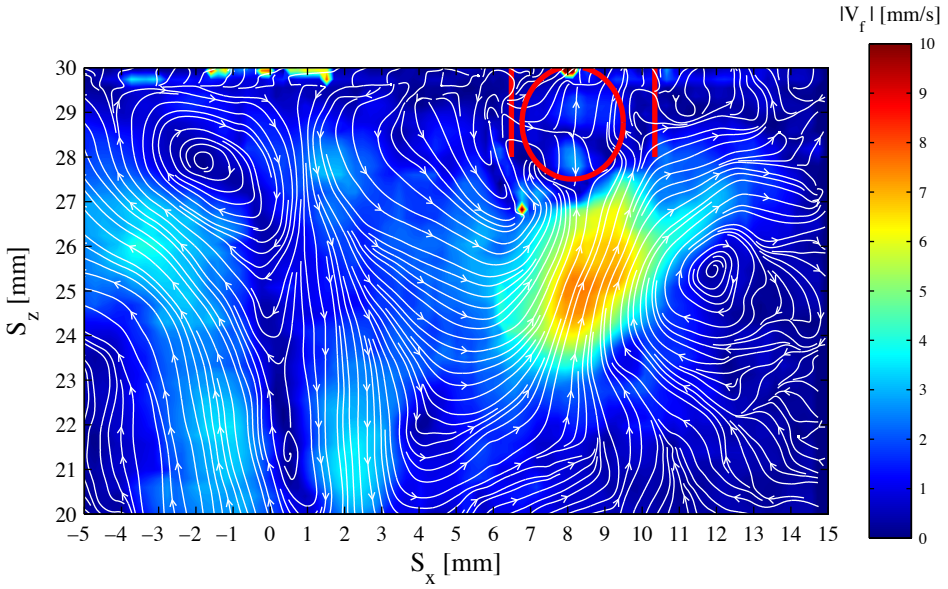

Figure 7.73: Instantaneous streamlines of a 2.8 *mm* bubble, released from a height of 30 *mm*, at a time of 1.034 *s* after impact.

Figure 7.75 illustrates the surface temperature map at times of 1.714 *s* and 1.955 *s*, corresponding to the next two times marked on Figure 7.68. During this time period, the surface temperature continually drops, with both the left and right hand side of the bubble having the same temperature at 1.955 *s*. The velocity streamlines at these times of 1.714 *s* and 1.955 *s*, are illustrated in Figures 7.76 and 7.77, respectively. The vortex on the left hand side of the bubble has grown significantly in size, although its effect on reducing the surface temperature is minimal. The fluid motion on the bubble's right hand side also has a minimal effect on the surface temperature after 1.955 *s*. This fluid velocity of 4 – 5 *mm/s* is thought to be too low to penetrate the thermal boundary layer, which is continually recovering. In Figure 7.77, at a time of 1.955 *s*, the thermal boundary layer is evident, to a

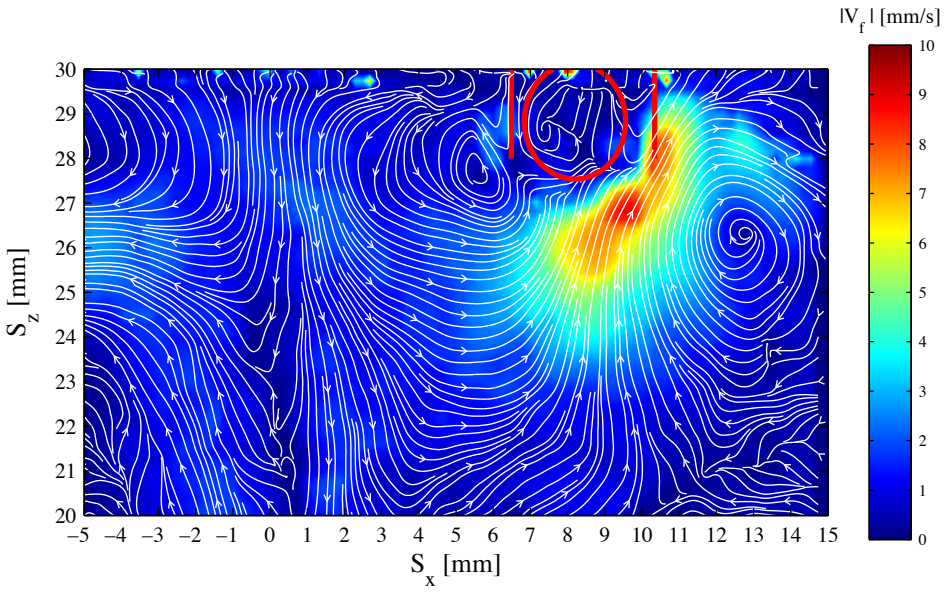

Figure 7.74: Instantaneous streamlines of a 2.8 *mm* bubble, released from a height of 30 *mm*, at a time of 1.365 *s* after impact.

depth of approximately 1 *mm*.

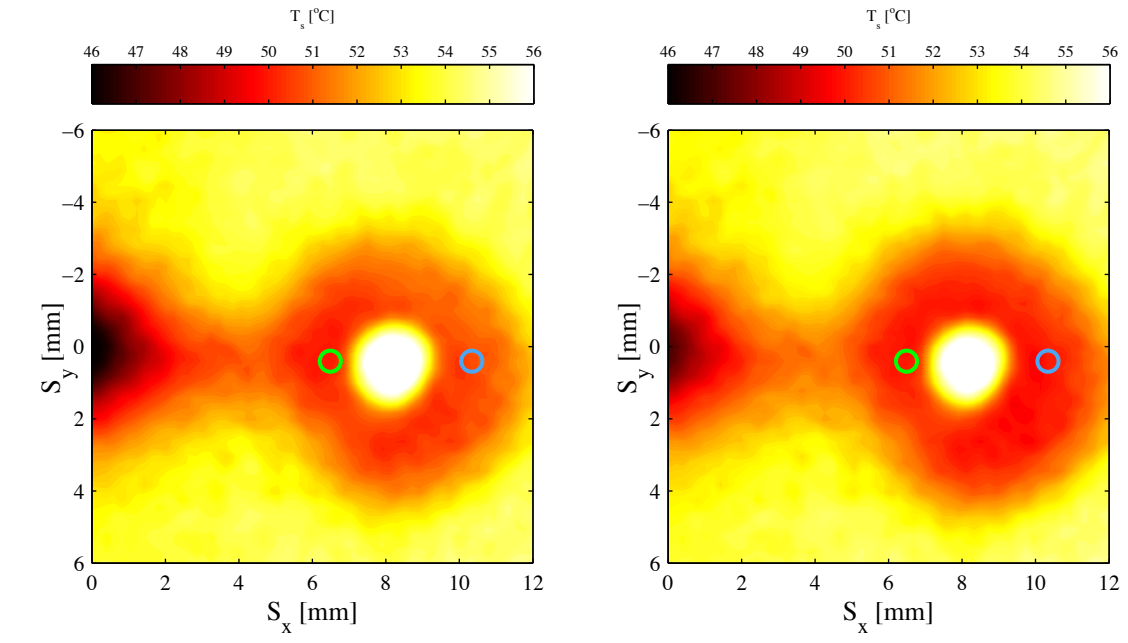

Figure 7.75: Surface temperature at times of (a) 1.714 *s* and (b) 1.955 *s*. The green circle (left) corresponds to the black line in Figure 7.68, while the blue circle (right) corresponds to the red line in Figure 7.68. The location of the bubble may be inferred from the increase in surface temperature (white zone).

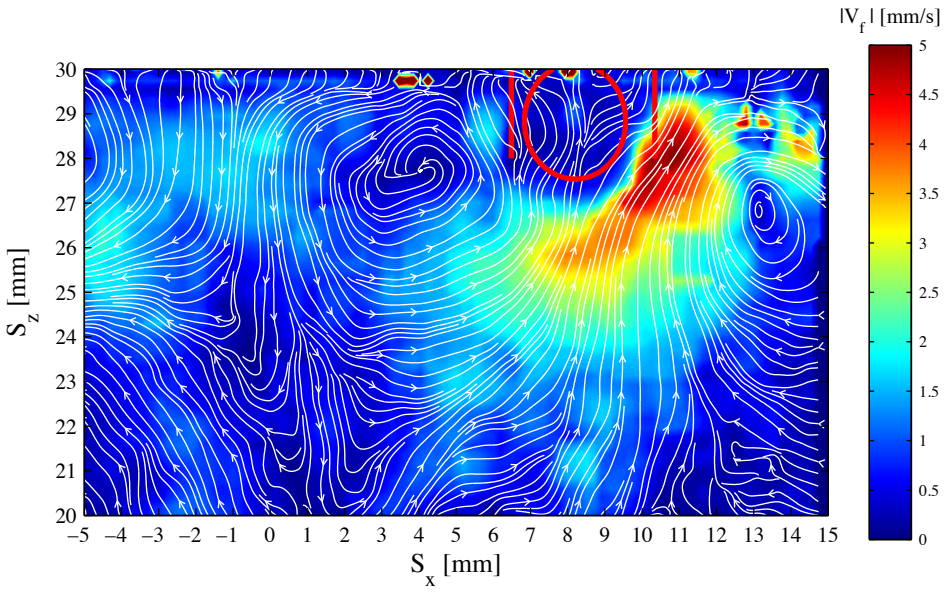

Figure 7.76: Instantaneous streamlines of a 2.8 *mm* bubble, released from a height of 30 *mm*, at a time of 1.714 *s* after impact.

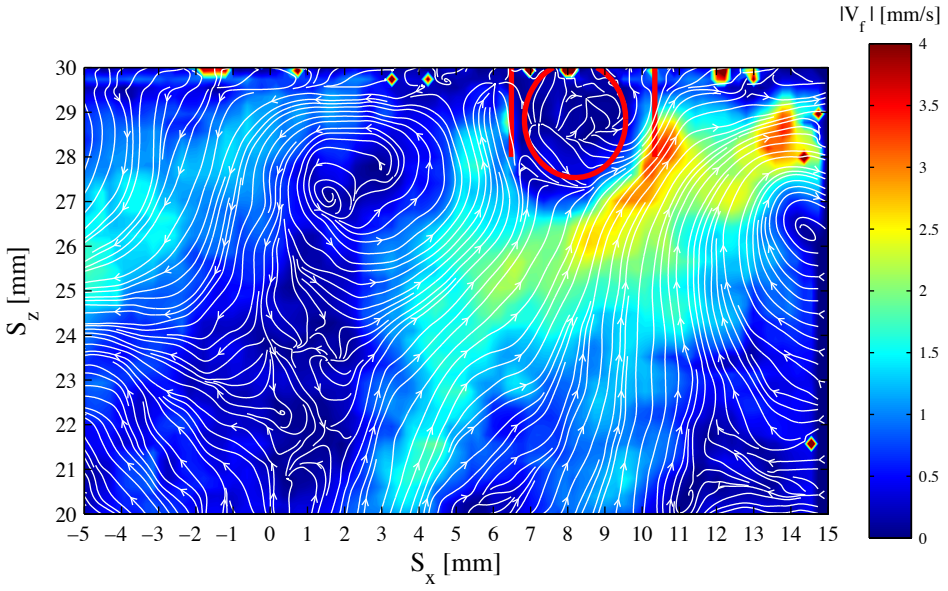

Figure 7.77: Instantaneous streamlines of a 2.8 *mm* bubble, released from a height of 30 *mm*, at a time of 1.955 *s* after impact.

Figure 7.78 illustrates the surface temperature at times of 2.727 *s* and 4.318 *s*, which are the final two times marked in Figure 7.68. From 2.727 *s* onwards the surface temperature continually rises, while the affected area reduces in size. The surface temperature within the attached zone was found to change from 58°C to 60°C. The corresponding streamline and velocity maps are shown in Figures 7.79 and 7.80. Both of these figures show limited fluid

motion within the region of the bubble, except for liquid natural convection.

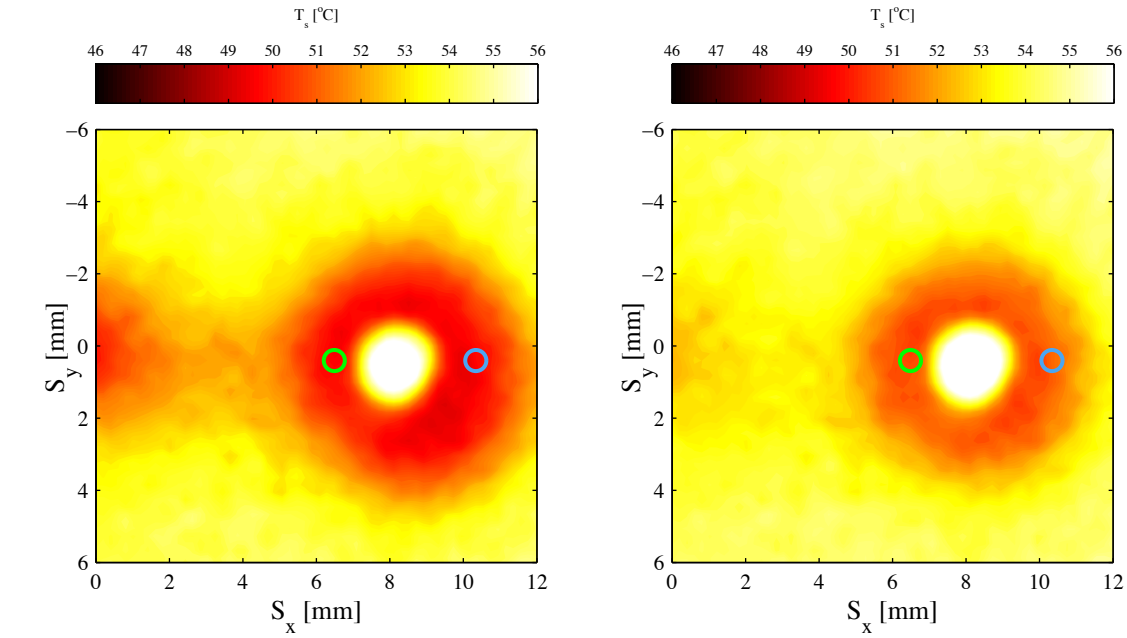

Figure 7.78: Surface temperature at times of (a) 2.727 *s* and (b) 4.318 *s*. The green circle (left) corresponds to the black line in Figure 7.68, while the blue circle (right) corresponds to the red line in Figure 7.68. The location of the bubble may be inferred from the increase in surface temperature (white zone).

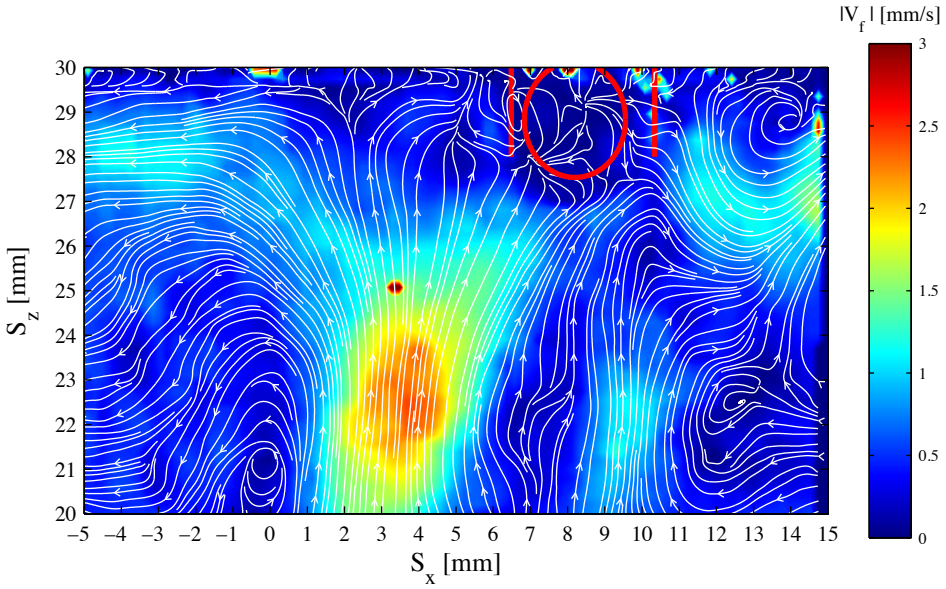

Figure 7.79: Instantaneous streamlines of a 2.8 *mm* bubble, released from a height of 30 *mm*, at a time of 2.717 *s* after impact.

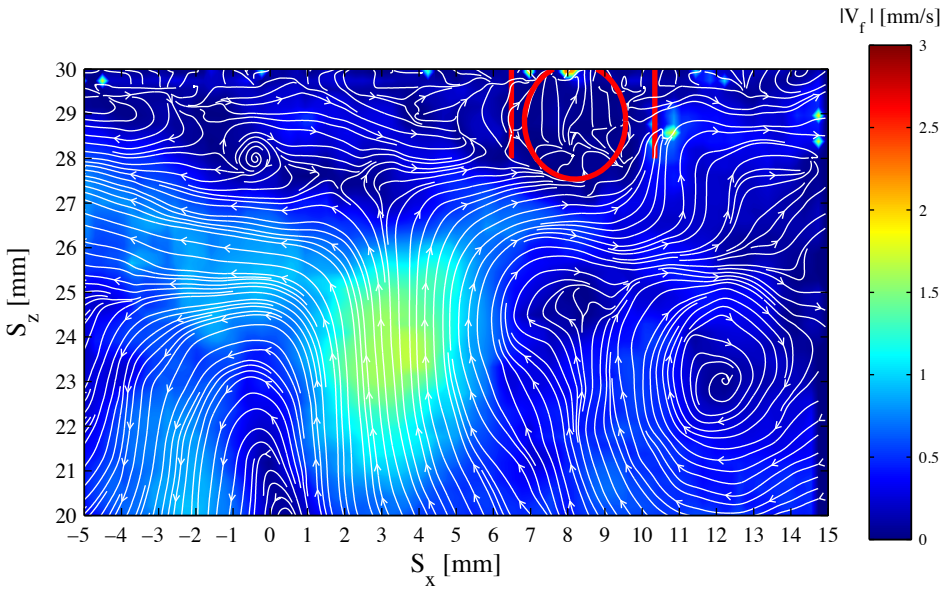

Figure 7.80: Instantaneous streamlines of a 2.8 *mm* bubble, released from a height of 30 *mm*, at a time of 4.318 *s* after impact.

In order to quantify the significance of this secondary heat transfer, the maximum temperature drop at the rear of the bubble, away from the effect of the ensuring wake, was examined for every experiment conducted. The is reported in Table 7.1, together with the attached bubble diameter and the outer diameter of the cooled zone. The results reported in Table 7.1 include the mean and standard error for each bubble diameter.

Table 7.1: Secondary heat transfer: temperature change (ΔT), outer diameter cooling extent (D_o), internal diameter of the bubble's contact zone (D_i) and the affected area (A_{aff}).

D_{eq}	[-]	ΔT [°C]	D_o [mm]	D_i [mm]	A_{aff} [mm^2]
2.8 *mm*	μ	6.51	7.68	1.80	43.77
	$S_{\bar{x}}$	0.17	0.18	0.22	2.22
3.3 *mm*	μ	7.10	8.59	3.12	50.41
	$S_{\bar{x}}$	0.32	0.31	0.26	3.95
4.1 *mm*	μ	6.63	9.51	5.19	48.79
	$S_{\bar{x}}$	0.37	0.44	0.57	9.55

The maximum temperature difference (ΔT) between the minimum at the rear of the bubble and the undisturbed surface temperature has a mean value for all experiments of 6.75 ± 0.37°C, with all three bubbles experiencing a similar temperature drop. The outer diameter, D_o, is the diameter of the maximum region affected by the secondary heat transfer

and D_i, is the diameter of the contact patch, when the bubble is fully attached to the surface, i.e. where the surface is in contact with the air within the bubble.

The affected area, A_{aff}, as described in Equation 7.1, is the total area affected by the secondary heat transfer. From Table 7.1, it can be seen that the mean values of affected area are quite similar, for all three bubble sizes investigated.

$$A_{aff} = \frac{\pi \left(D_o^2 - D_i^2\right)}{4} \tag{7.1}$$

Considering the significant variation in the bubble sizes and contact zones, the similarity in area affected suggests that another parameter must affect the generation of the vortex at the rear of the bubble. It is thought that the parameter of influence here may be the contact angle, which is the angle between the bubble and the surface, measured on the water side. The contact angles were found to be approximately 30°, 40° and 55° respectively, for the bubbles of diameters 2.8 *mm*, 3.3 *mm* and 4.1 *mm*. The role of the contact angle requires further investigation; however, in a case where the contact angle was found to be 90°, no secondary heat transfer occurred. This secondary enhancement associated with the attached bubble was found to last for 8 – 12 *s*. If a bubble for which secondary enhancement occurred was left attached to the surface and the surface was subsequently let cool and then heated again, no secondary convection occurred.

Although speculative, an argument can be put forward for the role of the bubble contact angle following attachment. Thus, the vortex which is created at the rear of the bubble is thought to be a result of the bubble's contact angle, as the wake impacts the left hand side of the bubble. For contact angles of less than 90°, a vortex with a clockwise rotation wants to begin but instead the wake continually forces fluid into that region. As the wake continually pushes the left hand side of the bubble, fluid moves around the bubble, which can be observed from the measured drop in surface temperature. Once the vortex is at the rear of the bubble, it is now a counter clockwise rotating vortex in the *x*-*z* plane, which is what is captured by the PIV set-up.

7.4 Closing Remarks

This chapter has examined the flow field and bubble behaviour associated with convective heat transfer enhancement for three different sized bubbles released from various heights. In the first section, the wake at the rear of the rising bubble is explored by means of PIV. This is followed by a detailed analysis of the wake ensuing from a 2.8 *mm* bubble, by linking PIV measurements to temporal variation in convective heat flux. The next section examines the situation in which the ensuing wake impacts the surface separate from the bubble impact zone. This is followed by the examination of the symmetric wake from a 4.1 *mm* bubble. The final section explores secondary heat transfer, which occurs after the bubble has impacted the surface.

During the bubble's rise significant wake structures were found to develop at the rear of the bubble, instigated by the change in the bubble's aspect ratio. Variations in aspect ratio and bubble velocity have been linked to the bubble's departure conditions, as shown by Tomiyama *et al.* [41] and Wu & Gharib [45]. As the bubble's volume is increased the size of these structures and the length of the wake increased. It is clear that the wake impact results in the highest convective heat transfer; the main portion of the wake is deflected away from the bubble, while a small portion of the wake follows in the direction of bubble. Notably, a significant amount of high velocity fluid is directed into the bulk fluid, mainly due to the rebound of the bubble from the surface.

In cases where large bubble deformations occur, the wake can become partially separated from the bubble, impacting in separate zones. Similarly, the previously observed wake structure at the rear of the rising bubble may, in some cases, result in separate cooling zones on the surface. In cases where the wake spreads significantly along the surface, a situation can arise in which a rolling vortex which initially cooled the surface becomes counter productive, convecting warm boundary layer fluid on top of the previously cooled surface. If a bubble impacts the surface evenly, the cooling pattern is symmetric, while being split into two regions. The inner region is a result of the bubble impact, while the outer region was found to be due to the ensuing wake, moving around the bubble.

Once the bubble is attached to the surface, a region surrounding the bubble experiences a slight level of cooling; this may be related to the bubble contact angle, which might be

responsible for a vortex structure surrounding the bubble. The affected area was found to be very similar for all the bubble sizes investigated, while all had approximately the same level of cooling.

Chapter 8

Discussion

The convective enhancement effects of a single bouncing air bubble are extremely complex and require a deep understanding of the bubble's shape, as well as of the flow structures created in the bubble's wake, both prior to and during the impact process. Chapter 5 has outlined the bubble's motion, projected shape, shape oscillations, centroidal velocity, and forces experienced by the bubble during its rise. The key bubble and fluid parameters for the present study are presented in Table 8.1.

Table 8.1: Bubble and fluid parameters for the current set-up.

Equivalent diameter	D_{eq} $[mm]$	2.8	3.3	4.1
Bubble volume	$[\mu l]$	11.5	18.8	36.1
Max velocity	$\|V\|$ $[mm/s]$	350	360	340
Reynolds number	Re [-]	1143	1385	1625
Morton number	Mo [-]	1.43×10^{-11}	1.43×10^{-11}	1.43×10^{-11}
Eötvös number	Eo [-]	1.069	1.485	2.293
Weber number	We [-]	4.8	5.9	6.6
Oscillation frequency	f_{V_z} $[Hz]$	69	54	37

The majority of researchers have explored the motion and velocity of bubbles which are far from their point of introduction to the flow [28, 41, 44]. In these cases, the bubble is in a steady state regime, with no further changes in its oscillation path or terminal velocity being observed. In the present case the maximum height a bubble can achieve before impacting the solid surface is 35 *mm*; this indicates that the bubble is in a transient state, as established by the work of Tomiyama *et al.* [41]. Although conditions are more variable, the

study of bubbles in restricted situations is important as heat exchangers and other practical applications often involve spatial constraints.

As the bubble motion is in a transitional phase in the present study, its rise velocity is significantly higher (20 – 30%) than that reported in the literature [19, 28]. This higher velocity does, however, match the work of Tomiyama *et al.* [41], for large initial shape fluctuations. This was found to be the case for the bubbles in the present study, as the increased velocity coincided with a decrease in the bubble's aspect ratio. During the bubble's short rise, it was found to accelerate and decelerate a number of times; this was linked to the drag force experienced by the bubble, instigated by shape changes. This rapid change in acceleration induces shape oscillations from pole to pole, which are known as $f_{2,0}$ oscillations, with the frequency of oscillation in the bubble's rise velocity (V_z) being found to match the prediction of Lunde & Perkins [47] and the experimental data of Veldhuis [28]. This $f_{2,0}$ frequency was found to predict regions of separate vorticity at the bubble's rear [28, 49], which are most evident when the bubble's rise path is not rectilinear. These regions of separate vorticity were visually observed at the bubble's rear in the present study, by means of PIV. Interestingly, the appearance of separate regions of cooling only occurred when the bubble's path significantly changed from vertical, allowing the regions to stay separate from one another. Other shape oscillations, along the bubble's equator and known as $f_{2,2}$ oscillations, are usually related to bubble secondary motion, which may include a spiral or a zig-zag path. In the current study, this shape oscillation did not appear due to the restricted height, as no secondary motion occurred.

In the next phase of the study the bubble's bouncing sequence was investigated. The majority of studies in the literature investigate bouncing bubbles with either small equivalent diameters (D_{eq}) or in fluids with low Morton numbers [12, 13, 26]. This, in effect, reduces the bubble's surface oscillations, terminal velocity and rebound velocity; this also affects the bubble's rise path, producing linear rise paths. Furthermore, this ensures that the bubble's rebound from the surface is axisymmetric. This reduced shape oscillation upon impact and rebound facilitates investigation of the energy conversion process, from kinetic to surface deformation [12, 13, 21]. When the bouncing process thus described in the literature is compared to that in the present study it is evident that the present bubbles undergo very significant shape changes during the bouncing process; only at low release heights is the

process axisymmetric and stable. Even when the process is axisymmetric, it is still difficult to compare shape oscillations to those reported in the literature, simply due to the bubble's velocity and shape upon impact, as the bubble is in the transitional stage of its rise here.

As the bubbles in the present study are large, they are more susceptible to pressure variations which alter the bubble's shape. The pressure distribution upon approach to the surface is depicted by Tsao & Kock [21], with a high pressure region in the central zone ahead of the bubble. This causes the bubble to "sense" the surface prior to impact, resulting in a significant change in the bubble's shape. This is partially evident as the fluid ahead of the bubble moves to the low pressure regions, either side of the bubble, as observed by means of PIV measurements. This pressure variation results in the formation of a dimple on the top surface of the bubble upon impact [21, 62, 111], with the largest bubble having the largest dimple. Again, as the bubble begins its rebound from the surface a secondary dimple forms, although in this case, on the bubble's lower surface. To the author's knowledge this has not been reported in previous literature. In terms of the total number of bouncing events which occurred following the initial impact, this was found to be related to the initial impact velocity and shape change; the less surface deformation which was experienced, then less of the kinetic energy was found to be dissipated and more bounces occurred.

To the author's knowledge the convective heat transfer associated with direct bouncing of a single bubble on a heated horizontal surface has not been studied. The convective heat flux linked to the direct impact and rebound of a single bubble was detailed in Chapter 6, with spatial and temporal aspects being investigated. The variation in bubble size and release height played a significant role in the convective heat transfer enhancement. A bouncing bubble was found to reduce significantly the surface temperature for approximately 8 – 10 s; however, the surface temperature increases beneath the bubble, once it is attached to the surface, after the bouncing event has occurred.

In terms of convective enhancement due to the bouncing bubble, this was found to be very significant, although small regions of local reduction in heat transfer were also observed. The enhancement was found to be related to the bubble's major axis angle. Thus, if the bubble's impact was direct and approximately axisymmetric, then the rim of the bubble either side of the dimple would have the highest level of convective heat flux as the bubble cuts through the thermal boundary layer, with only the boundary layer within the extremi-

ties of the bubble experiencing an enhancement. In this case, the bubble's rebound would combine with the ensuing wake, creating an annular region of very high convective heat flux enhancement, extending from the bubble's minimum rebound width to a maximum distance that varies with bubble's size.

In the case where the bubble's impact is at an angle, again an annular impact zone appears, although this is usually overshadowed by the impacting wake. This wake impacts at the bubble's edge, creating an initial "moon" shaped enhancement zone. For example, if the bubble tilts to the right, then more often than not the bubble will continue to bounce to the right, with the wake usually impacting on the bubble's left hand side. The extent of the enhancement is partially related to how far the bubble impacts away from the centre of the test surface, which depends on the bubble's major axis angle. From the three different bubble sizes studied, the appearance of the wake was found to be dependent on the bubble's release height. For the lowest release height of 10 *mm*, the bubble's impact was almost always axisymmetric for all three bubble sizes, indicating that the rebound path of the bubble is directly into the path of the rising wake. The wake at this release height is assumed to have a low velocity, which is consistent with there being no firm evidence of the ensuing wake reaching the surface for a release height of 10 *mm*.

As the release height increases, so does the bubble's velocity. Notably, it is the smallest bubble which begins its path deviation first. It is this path deviation which significantly enhances heat transfer. In the case of the largest bubble, 4.1 *mm*, minimal path deviation was observed because of the small rise height. Thus, the same wake patterns were not observed as for the smaller bubbles.

As previously mentioned, transient regions of negative heat transfer (heating, rather than cooling, of the surface) were found to occur during the bubble's impact and rebound. The first occurs immediately after the bubble has impacted the surface, with the second usually occurring during the second impact with the surface. This phenomenon is of particular interest as the process was both visually observed, due to favourable temperature gradients, and identified by means of PIV analysis. As the bubble initially impacts the surface, the bubble deforms, thereby cooling the surface beneath the bubble. As the bubble's retraction begins, its edge was found to draw in warm boundary layer fluid. This event occurs very rapidly (< 2 *ms*), with the warm fluid being drawn atop the previously cooled surface,

resulting in a short term increase in the surface temperature. This usually occurs in an annular region, although if the wake impacts at the bubble's edge then this event will not be observed in that particular region. Notably, in a zone of negative heat flux the lateral conduction was found to be two orders of magnitude lower than the convective component.

The second occurrence of negative heat transfer corresponds to the bubble re-impacting the surface. As the bubble bounces away from the surface, a mixture of both warm and cool fluid is collected between the heated surface and the bubble's upper surface. As the bubble re-impacts the surface, the local convective heat flux in this region may be positive or negative, depending on the instantaneous local fluid to surface temperature difference. As the Biot number for the paint layer was found to be marginally high, rapid changes in surface temperature may, in some cases, be attenuated with their maximum value not being detectable using the current set-up.

Chapter 7 has examined important aspects of the bubble wake and its effect on convective heat transfer. Firstly, at the bubble's rear, regions of separate vorticity were found to occur; these can be linked to the oscillation of the bubble and the previously mentioned vibration modes. These separate zones become more apparent with larger bubbles. In order to fully appreciate the enhancement effect of the bubble's wake, convective heat flux and surface temperature were observed as a function of time, on a line along the surface in the direction of the wake movement. This analysis was combined with instantaneous 2D surface maps and streamline and velocity maps.

The bubble's wake was found to spread significantly in the opposite direction to the bubble's direction of motion, with a smaller portion of the wake being dragged in the direction of the bubble. The fluid streamline data allow for an interesting perspective in terms of bulk fluid motion, with the bouncing motion resulting in significant fluid motion away from the heated surface. During the bubble's rise, the two larger bubbles were found to be very unstable beyond a height of 30 *mm*; this was attributed to the bubble being very elongated or flat. This results in the bubble rapidly changing shape, which reduces its velocity and, in the majority of cases, results in the bubble shifting its position. If this shift in position is significant, the ensuing wake is almost separated from the bubble, although only for a short period of time.

As the wake spreads along the surface, it was found that if the wake spread too far from

the centre of the test section, the rolling vortex could convect warm boundary layer fluid on top of the previously cooled region, thereby briefly reheating the surface. Once the bubble is attached to the surface, a ring of secondary cooling occurs; this may be related to the bubble contact angle with the surface. As the bubble is now attached to the surface, air within the bubble increases in temperature, creating a local "hotspot" on the surface lasting for the duration of the experiment.

Chapter 9

Conclusions

9.1 Conclusions

The characteristic behaviour of a single bubble released from an orifice, which then rises and impacts a solid surface, has been experimentally investigated. The rise motion and bouncing behaviour of the bubble, together with the associated convective heat transfer to the surface form the basis for this study, along with investigation of the developing flow field around the bubble.

In order to interpret the current experimental findings, a comprehensive review of the relevant literature has been performed. This includes an in-depth review of bubble detachment, bubble rise, impact and coalescence and convective heat transfer resulting from bubble motion.

In order to investigate the effect of a single bubble, an experimental apparatus has been designed and built. This apparatus allows for interchangeable growth orifices, variable orifice to surface release heights and alternate surface conditions. The interchangeable orifices of diameter 0.5, 1 and 2 *mm* produce bubbles of equivalent diameter 2.8, 3.3 and 4.1 *mm* respectively. The release heights investigated were 10, 20, 25, 30 and 35 *mm*. In order to analyse the experimental results, application specific computer code was developed. The first stage of this code is used to analyse the data from the high speed images; this results in the detection of the bubble and its motion through the test section. The second part of the code was used to determine the energy flow within the solid surface, with the outcome

being the heat convected to the bulk fluid.

Detailed results for bubble motion after departure have been presented. This motion includes the rise and bouncing of the bubble, on both adiabatic and heated surfaces, in clean and contaminated fluid. The surface temperature has been measured with an IR camera providing a spatial resolution of 203 μm at a frequency of 1 kHz. This was used in conjunction with two high speed cameras, with a spatial resolution of 39 μm, which track the bubble's motion as it leaves the orifice, rises and impacts on the heated surface. Synchronised PIV and heat transfer testing has also been performed for a single release height of 30 mm. Detailed results are presented for cases which best represent the overall data collected. The following section proposes additional work that could be performed to further the current understanding of bouncing air bubbles.

In terms of convective enhancement due to a single bouncing bubble, this was found to be very significant. Increases in both bubble diameter and release height significantly affected local heat transfer, although small regions of local reduction in heat transfer were also observed. The maximum instantaneous heat flux encountered for the direct impact of a bubble was approximately 100 kW/m^2, however, the maximum enhancement due to the bubble's wake approached 250 kW/m^2. The enhancement due to the bubble's wake was found to be linked to the bubble size, release height and impact angle of the bubble. Throughout the bouncing process, isolated zones of transient heating, rather than cooling, of the surface were evident. This phenomenon was believed to result from warm fluid being convected onto a zone which previously experienced convective cooling, causing a local increase in surface temperature. Once the bubble became attached to the surface, a local region surrounding the bubble experienced a small level of cooling, which is thought to be dependent on the bubble contact angle with the surface. This attachment results in a local reduction in instantaneous heat flux beneath the bubble itself, with the air within the bubble being in direct contact with the surface.

9.2 Future Work

Significant work has been performed on a single bouncing bubble. However, compared to studies in the literature even the smallest bubble tested, 2.8 mm, is quite large. This makes it

difficult to relate the current findings to existing literature. The bubbles in the present study also have significant shape oscillations. It would be of interest to assess the enhancement associated with similar sized bubbles, but without shape oscillations as demonstrated by Tomiyama *et al.* [41], in Figure 2.2.

PIV measurements were found to be somewhat hampered by the bubble itself, as a significant amount of scattering of light occurs as the bubble bounces on the surface. This issue could be addressed by utilising Rhodamine B seeding particles rather than hollow glass spheres. Thus, Rhodamine B absorbs light with a wavelength of 540 *nm* and emits light at 625 *nm*. The green spectrum ranges from 495 – 570 *nm*, with the emitted light being in the orange to red spectrum ranging from 570 – 750 *nm*. Therefore, once a band pass filter is applied to the camera the flashes of green light will no longer be present allowing a better representation of the flow field around the bubble.

A rolling vortex was created during the impact event. This vortex was found to both increase and decrease convective cooling in certain situations. As the exact fluid temperatures adjacent to wall are unknown, it would be of interest to examine the rolling vortex using interferometry or another similar technique.

In this study only a single bubble has been studied. It would be of interest to characterise the effect of two bubbles side by side, as well as the effect of two bubbles released one after another. This information would be valuable for practical applications, in which bubble-bubble interactions are commonplace.

Publications

Previous work by the author has yielded publications in both journal and conference proceedings in the following fields: bubbles rising past a heated surface, natural convection flow and bouncing bubble. The following is a list of these publications.

- T. Persoons, I. M. O'Gorman, D. B. Donoghue, G. Byrne and D. B. Murray. Natural convection heat transfer and fluid dynamics for a pair of vertically aligned isothermal horizontal cylinders. *International Journal of Heat and Mass Transfer*, 54(25), 5163–5172, 2011.

- D. B. Donoghue, B. Donnelly and D. B. Murray. The Enhancement Effects of a Plume of Rising Bubbles on Natural Convection from a Heated Vertical Plate. *Journal of Enhanced Heat Transfer*, 19(4), 379–395, 2012.

- D. B. Donoghue, Y. M. C. Delauré, A. J. Robinson and D. B. Murray. Heat Transfer Enhancement from Bouncing Bubble Dynamics. In *6^{th} Baltic Heat Transfer Conference, Tampere University of Technology, August, 2011.*

- D. B. Donoghue, Y. M. C. Delauré, A. Albadawi, A. J. Robinson and D. B. Murray. Bouncing bubble dynamics and associated enhancement of heat transfer. *Journal of Physics: Conference Series* 395(1), 012167, 2012.

- A. Albadawi, Y. M. C. Delauré, D. B. Donoghue, A. J. Robinson and D. B. Murray. Numerical investigation of volume of fluid and level-set interface capturing methods for bubble growth and detachment. *Journal of Physics: Conference Series* 395(1), 012166, 2012.

- A. Albadawi, D. B. Donoghue, A. J. Robinson, D. B. Murray and Y. M. C. Delauré. An Assessment of Volume of Fluid and Level Set Methods for Low Capillary Bubble Growth and Detachment. *Chemical Engineering Science*, 90, 77–91, 2013.

- A. Albadawi, D. B. Donoghue, A. J. Robinson, D. B. Murray and Y. M. C. Delauré. Influence of surface tension implementation in Volume of Fluid and coupled Volume of Fluid with Level Set methods for bubble growth and detachment. *International Journal of Multiphase Flow*, 53, 11–28, 2013.

- D. B. Donoghue, A. Albadawi, Y. M. C. Delauré, A. J. Robinson and D. B. Murray. Wake Effects from a Rising Air Bubble Impacting a Horizontal Heated Surface. In *8^{th} World Conference on Experimental Heat Transfer, Fluid Mechanics and Thermodynamics, Lisbon, Portugal, June, 2013.*

- D. B. Donoghue, A. Albadawi, A. J. Robinson, Y. M. C. Delauré and D. B. Murray. Bubble Impingement and the Mechanisms of Heat Transfer. *International Journal of Heat and Mass Transfer*, 71, 439–450, 2014.

- A. Albadawi, D. B. Donoghue, A. J. Robinson, Y. M. C. Delauré and D. B. Murray. On the assessment of a VOF based “compressive" interface capturing scheme for the analysis of bubble impact on and bounce from a flat horizontal surface. *International Journal of Multiphase Flow*, 65, 82–97, 2014.

Bibliography

[1] D. E. Arvizu. Thermal science: Enabling renewable energy innovation. In *8th World Conference on Experimental Heat Transfer, Fluid Mechanics and Thermodynamics, Lisbon, Portugal, June*, 2013.

[2] M. A. Atmane and D. B. Murray. The effect of the liquid motion induced by air and vapor bubbles on heat transfer around a cylinder. *International Journal of Heat and Mass Transfer*, 48(6):1084–1095, 2005.

[3] B. Donnelly, T. S. O'Donovan, and D. B. Murray. Surface heat transfer due to sliding bubble motion. *Applied Thermal Engineering*, 29(7):1319–1326, 2009.

[4] Y. M. C. Delauré, V. S. S. Chan, and D. B. Murray. A simultaneous PIV and heat transfer study of bubble interaction with free convection flow. *Experimental Thermal and Fluid Science*, 27(8):911–926, 2003.

[5] K. Cornwell. The influence of bubbly flow on boiling from a tube in a bundle. *International Journal of Heat and Mass Transfer*, 33(12):2579–2584, 1990.

[6] S. D. Houston and K. Cornwell. Heat transfer to sliding bubbles on a tube under evaporating and non-evaporating conditions. *International Journal of Heat and Mass Transfer*, 39(1):211–214, 1996.

[7] D. Qiu and V. K. Dhir. Experimental study of flow pattern and heat transfer associated with a bubble sliding on downward facing inclined surfaces. *Experimental Thermal and Fluid Science*, 26(6-7):605–616, 2002.

[8] S. Manickam and V. Dhir. Holographic interferometric study of heat transfer associ-

ated with a single vapor bubble sliding along a downward-facing heater surface. In *ASME Summer Heat Transfer Conference*, 2003.

[9] S. Manickam and V. Dhir. Holographic interferometric study of heat transfer to a sliding vapor bubble. *International Journal of Heat and Mass Transfer*, 55(4):925–940, 2012.

[10] D. B. R. Kenning, O. E. Bustnes, and Y. Yan. Heat transfer to a sliding vapour bubble. *Multiphase Science and Technology*, 14(1), 2002.

[11] M. Fujasová-Zedníková, L. Vobecká, and J. Vejrazka. Effect of solid material and surfactant presence on interactions of bubbles with horizontal solid surface. *The Canadian Journal of Chemical Engineering*, 88(4):473–481, 2010.

[12] R. Zenit and D. Legendre. The coefficient of restitution for air bubbles colliding against solid walls in viscous liquids. *Physics of Fluids*, 21:083306, 2009.

[13] D. Legendre, C. Daniel, and P. Guiraud. Experimental study of a drop bouncing on a wall in a liquid. *Physics of Fluids*, 17:097105, 2005.

[14] A. Albadawi, D. B. Donoghue, A. J. Robinson, D. B. Murray, and Y. M. C. Delauré. On the analysis of bubble growth and detachment at low capillary and Bond numbers using volume of fluid and level set methods. *Chemical Engineering Science*, 90:77–91, 2013.

[15] A. Albadawi, D. B. Donoghue, A. J. Robinson, D. B. Murray, and Y. M. C. Delauré. Influence of surface tension implementation in volume of fluid and coupled volume of fluid with level set methods for bubble growth and detachment. *International Journal of Multiphase Flow*, 53:11–28, 2013.

[16] D. Bhaga and M. E. Weber. Bubbles in viscous liquids: shapes, wakes and velocities. *Journal of Fluid Mechanics*, 105:61–85, 1981.

[17] P. G. Saffman. On the rise of small air bubbles in water. *Journal of Fluid Mechanics*, 1(3):249–275, 1956.

[18] L. S. Fan and K. Tsuchiya. *Bubble wake dynamics in liquids and liquid-solid suspensions*. Butterworth-Heinemann, Boston, Massachusetts, 1990.

[19] R. Clift, J. R. Grace, and M. E. Weber. *Bubbles, drops, and particles*, volume 3. Academic press New York, 1978.

[20] T. Maxworthy, C. Gnann, M. Kürten, and F. Durst. Experiments on the rise of air bubbles in clean viscous liquids. *Journal of Fluid Mechanics*, 321:421–441, 1996.

[21] H. K. Tsao and D. L. Koch. Observations of high Reynolds number bubbles interacting with a rigid wall. *Physics of Fluids*, 9:44, 1997.

[22] A. Perron, L. I. Kiss, and S. Poncsák. An experimental investigation of the motion of single bubbles under a slightly inclined surface. *International Journal of Multiphase Flow*, 32(5):606–622, 2006.

[23] Y. Yan, D. B. R. Kenning, I. A. Grant, and K. Cornwell. Heat transfer to sliding bubbles under plane and curved surfaces. In *Institution of Mechanical Engineers Conference Publications*, volume 2, pages 295–295. Medical Engineering Publications Ltd, 1995.

[24] K. Malysa, M. Krasowska, and M. Krzan. Influence of surface active substances on bubble motion and collision with various interfaces. *Advances in Colloid and Interface Science*, 114:205–225, 2005.

[25] M. Krasowska and K. Malysa. Kinetics of bubble collision and attachment to hydrophobic solids: I. effect of surface roughness. *International Journal of Mineral Processing*, 81(4):205–216, 2007.

[26] M. Fujasová-Zedníková, L. Vobecká, and J. Vejrazka. Effect of solid material and surfactant presence on interactions of bubbles with horizontal solid surface. *The Canadian Journal of Chemical Engineering*, 88(4):473–481, 2010.

[27] A. W. G. De Vries. *Path and Wake of a Rising Bubble*. PhD thesis, University of Twente, Enschede, University of Twente, 2001.

[28] C. H. J. Veldhuis. *Leonardo's paradox: Path and shape instabilities of particles and bubbles*. PhD thesis, University of Twente, Enschede, University of Twente, 2007.

[29] C. Brücker. Structure and dynamics of the wake of bubbles and its relevance for bubble interaction. *Physics of Fluids*, 11:1781–1796, 1999.

[30] R. Ladenburg. Über den einfluß von wänden auf die bewegung einer kugel in einer reibenden flüssigkeit. *Annalen der Physik*, 328(8):447–458, 1907.

[31] W. L. Haberman and R. K. Morton. An experimental investigation of the drag and shape of air bubbles rising in various liquids. Technical report, David Taylor Model Basin, Washington DC, 1953.

[32] A. W. G. De Vries, A. Biesheuvel, and L. Van Wijngaarden. Notes on the path and wake of a gas bubble rising in pure water. *International Journal of Multiphase Flow*, 28(11):1823–1835, 2002.

[33] J. T. Lindt. On the periodic nature of the drag on a rising bubble. *Chemical Engineering Science*, 27(10):1775–1781, 1972.

[34] B. Rosenberg. The drag and shape of air bubbles moving in liquids. Technical report, David Taylor Model Basin, Washington DC, 1950.

[35] O. T. Bryn. Speed of rise of air bubbles in liquids. Technical report, David Taylor Model Basin, Washington DC, 1949.

[36] R. M. Davies and G. Taylor. The mechanics of large bubbles rising through extended liquids and through liquids in tubes. In *Proceedings of the Royal Society of London. Series A, Mathematical and Physical Sciences*, volume 200, pages 375–390, 1949.

[37] A. Frumkin and V. G. Levich. On surfactants and interfacial motion (*in Russian*). *Zh. fiz. khim*, 21:1183–1204, 1947.

[38] N. M. Aybers and A. Tapucu. The motion of gas bubbles rising through stagnant liquid. *Heat and Mass Transfer*, 2(2):118–128, 1969.

[39] N. M. Aybers and A. Tapucu. Studies on the drag and shape of gas bubbles rising through a stagnant liquid. *Heat and Mass Transfer*, 2(3):171–177, 1969.

[40] J. R. Grace, T. Wairegi, and T. H. Nguyen. Shapes and velocities of single drops and bubbles moving freely through immiscible liquids. *Chemical Engineering Research and Design*, 54(a):167–173, 1976.

[41] A. Tomiyama, G. P. Celata, S. Hosokawa, and S. Yoshida. Terminal velocity of single bubbles in surface tension force dominant regime. *International Journal of Multiphase Flow*, 28(9):1497–1519, 2002.

[42] G. P. Celata, M. Cumo, F. D'Annibale, and A. Tomiyama. The wake effect on bubble rising velocity in one-component systems. *International Journal of Multiphase Flow*, 30(7-8):939–961, 2004.

[43] S. S. Alves, S. P. Orvalho, and J. M. T. Vasconcelos. Effect of bubble contamination on rise velocity and mass transfer. *Chemical Engineering Science*, 60(1):1–9, 2005.

[44] K. Ellingsen and F. Risso. On the rise of an ellipsoidal bubble in water: oscillatory paths and liquid-induced velocity. *Journal of Fluid Mechanics*, 440:235–268, 2001.

[45] M. Wu and M. Gharib. Experimental studies on the shape and path of small air bubbles rising in clean water. *Physics of Fluids*, 14(7):L49 – L52, 2002.

[46] P. C. Duineveld. The rise velocity and shape of bubbles in pure water at high reynolds number. *Journal of Fluid Mechanics*, 292:325–332, 1995.

[47] K. Lunde and R. J. Perkins. Shape oscillations of rising bubbles. *Applied Scientific Research*, 58(1):387–408, 1997.

[48] H. Lamb. *Hydrodynamics*. Cambridge University Press, Cambridge, 1932.

[49] T. Sanada, M. Shirota, and M. Watanabe. Bubble wake visualization by using photochromic dye. *Chemical Engineering Science*, 62(24):7264–7273, 2007.

[50] M. Bayareh, S. Dabiri, and A. M. Ardekani. Interaction between a pair of drops ascending in a linearly stratified fluid. In *ASME 2013 Fluids Engineering Division Summer Meeting, Incline Village, Nevada, USA*, 2013.

[51] J. Rodrigo Vélez-Cordero, D. Sámano, and R. Zenit. Study of the properties of bubbly flows in Boger-type fluids. *Journal of Non-Newtonian Fluid Mechanics*, 175:1–9, 2012.

[52] J Rodrigo Vélez-Cordero, D. Sámano, P. Yue, J. J. Feng, and R. Zenit. Hydrodynamic interaction between a pair of bubbles ascending in shear-thinning inelastic fluids. *Journal of Non-Newtonian Fluid Mechanics*, 166(1):118–132, 2011.

[53] D. B. Donoghue, B. Donnelly, and D. B. Murray. The enhancement effects of a plume of rising bubbles on natural convection from a heated vertical plate. *Journal of Enhanced Heat Transfer*, 19(4), 2012.

[54] R. D. Kirkpatrick and M. J. Lockett. The influence of approach velocity on bubble coalescence. *Chemical Engineering Science*, 29(12):2363–2373, 1974.

[55] M. Krzan, K. Lunkenheimer, and K. Malysa. Pulsation and bouncing of a bubble prior to rupture and/or foam film formation. *Langmuir*, 19(17):6586–6589, 2003.

[56] F. Suñol and R. González-Cinca. Rise, bouncing and coalescence of bubbles impacting at a free surface. *Colloids and Surfaces A: Physicochemical and Engineering Aspects*, 365(1-3):36–42, 2010.

[57] A. Sato, M. Shirota, T. Sanada, and M. Watanabe. Modeling of bouncing of a single clean bubble on a free surface. *Physics of Fluids*, 23:013307, 2011.

[58] P. Di Marco. Birth, life and death of gas bubbles rising in a stagnant liquid. *Heat Technol*, 23(2):17–26, 2005.

[59] A. Sheludko. Thin liquid films. *Advances in Colloid and Interface Science*, 1(4):391–464, 1967.

[60] M. Krasowska, M. Krzan, and K. Malysa. Bubble collisions with hydrophobic and hydrophilic surfaces in α-terpineol solutions. *Physicochemical Problems of Mineral Processing*, 37:37–50, 2003.

[61] E. Klaseboer, J. P. Chevaillier, A. Maté, O. Masbernat, and C. Gourdon. Model and experiments of a drop impinging on an immersed wall. *Physics of Fluids*, 13:45, 2001.

[62] M. H. W. Hendrix, R. Manica, E. Klaseboer, D. Y. C. Chan, and C. D. Ohl. Spatiotemporal evolution of thin liquid films during impact of water bubbles on glass on a micrometer to nanometer scale. *Physical Review Letters*, 108(24):247803, 2012.

[63] G. Barthau. Active nucleation site density and pool boiling heat transfer–an experimental study. *International Journal of Heat and Mass Transfer*, 35(2):271–278, 1992.

[64] B. B. Bayazit, D. K. Hollingsworth, and L. C. Witte. Heat transfer enhancement caused by sliding bubbles. *Journal of Heat Transfer*, 125(3):503–510, 2003.

[65] D. B. R. Kenning and Y. Yan. Pool boiling heat transfer on a thin plate: features revealed by liquid crystal thermography. *International Journal of Heat and Mass Transfer*, 39(15):3117–3137, 1996.

[66] Y. Yan, D. B. R. Kenning, and K. Cornwell. Sliding and sticking vapour bubbles under inclined plane and curved surfaces. *International Journal of Refrigeration*, 20(8):583–591, 1997.

[67] D. B. R. Kenning, O. E. Bustnes, and Y. Yan. Heat transfer to a sliding vapor bubble. In *Boiling 2000: Phenomena and Emerging Applications,*, Girdwood, Alaska, 2000.

[68] B. Donnelly, T. S. O'Donovan, and D. B. Murray. Bubble enhanced heat transfer from a vertical heated surface. *Journal of Enhanced Heat Transfer*, 15(2):159–169, 2008.

[69] Crystran Ltd. Crystran: materials. http://www.crystran.co.uk/calcium-fluoride-caf2.htm, 2013. [Online; accessed 17-October-2013].

[70] A. Albadawi, D. B. Donoghue, A. J. Robinson, D. B. Murray, and Y. M. C. Delauré. On the assessment of a VOF based compressive interface capturing scheme for the

analysis of bubble impact on and bounce from a flat horizontal surface. *International Journal of Multiphase Flow*, 65:82–97, 2014.

[71] F. J. Lesage, J. S. Cotton, and A. J. Robinson. Modelling of quasi-static adiabatic bubble formation, growth and detachment for low bond numbers. *Chemical Engineering Science*, 104:742–754, 2013.

[72] F. J. Lesage. *Quasi-static Bubble Shape Analysis in the development of models for adiabatic and diabatic growth and departure*. PhD thesis, McMaster University Library, 2012.

[73] P. Di Marco. Bubble growth and detachment: current status and future prospects. In *5th International Conference on Transport Phenomena In Multiphase Systems, June 30 - July 3, Bialystok, Poland*, 2008.

[74] M. Ochs, A. Schulz, and H. J. Bauer. High dynamic range infrared thermography by pixelwise radiometric self calibration. *Infrared Physics & Technology*, 53(2):112–119, 2010.

[75] A. Schulz. Infrared thermography as applied to film cooling of gas turbine components. *Measurement Science and Technology*, 11:948, 2000.

[76] M. Ochs, T. Horbach, A. Schulz, R. Koch, and H. J. Bauer. A novel calibration method for an infrared thermography system applied to heat transfer experiments. *Measurement Science and Technology*, 20, 2009.

[77] M. Raffel, C. E. Willert, S. T. Wereley, and J. Kompenhans. *Particle Image Velocimetry*. Springer, 2007.

[78] Potters Industries. Potters industries sphericel 110P8 hollow glass spheres. http://www.matweb.com/search/datasheet.aspx?matguid=288b53ebdc414690951488c03bb6c791&ckck=1, 2013.

[79] S. M. O' Shaughnessy. *Bubble-Induced Marangoni Convection*. PhD thesis, Dept. of Mechanical Engineering, University of Dublin, Trinity College, 2011.

[80] D. W. Moore. The velocity of rise of distorted gas bubbles in a liquid of small viscosity. *J. Fluid Mech*, 23(4):749–766, 1965.

[81] C. H. J. Veldhuis, A. Biesheuvel, and D. Lohse. Freely rising light solid spheres. *International Journal of Multiphase Flow*, 35(4):312–322, 2009.

[82] F. P. Incropera, D. P. DeWitt, T. L. Bergman, and A. S. Lavine. *Fundamentals of Heat and Mass Transfer*, volume 6. John Wiley & Sons, Inc, New York, 2007.

[83] K. C. Patel and X. D. Chen. Surface-center temperature differences within milk droplets during convective drying and drying-based Biot number analysis. *AIChE journal*, 54(12):3273–3290, 2008.

[84] G. Maranzana, S. Didierjean, B. Rémy, and D. Maillet. Experimental estimation of the transient free convection heat transfer coefficient on a vertical flat plate in air. *International Journal of Heat and Mass Transfer*, 45(16):3413–3427, 2002.

[85] I. Golobic, J. Petkovsek, M. Baselj, A. Papez, and D. B. R. Kenning. Experimental determination of transient wall temperature distributions close to growing vapor bubbles. *Heat and mass transfer*, 45(7):857–866, 2009.

[86] I. Golobic, J. Petkovsek, and D. B. R. Kenning. Bubble growth and horizontal coalescence in saturated pool boiling on a titanium foil, investigated by high-speed IR thermography. *International Journal of Heat and Mass Transfer*, 55(4):1385–1402, 2012.

[87] N. Schweizer. *Multi-scale investigation of nucleate boiling phenomena in microgravity*. PhD thesis, TU Darmstadt, 2010.

[88] B. Sundqvist. Thermal diffusivity and thermal conductivity of chromel, alumel, and constantan in the range 100–450 k. *Journal of Applied Physics*, 72(2):539–545, 1992.

[89] O. Raghu and J. Philip. Thermal properties of paint coatings on different backings using a scanning photo acoustic technique. *Measurement Science and Technology*, 17:2945, 2006.

[90] J. Philip, M. V. Manjusha, and H. Soumya. A travelling photothermal technique employing pyroelectric detection to measure thermal diffusivity of films and coatings. *Review of Scientific Instruments*, 82(10):104901–104901, 2011.

[91] C. A. Decker and T. J. Mackin. Measuring film thickness using infrared imaging. *Thin Solid Films*, 473(2):196–200, 2005.

[92] M. M. Moksin, I. V. Grozescu, Z. A. Wahab, and W. M. M. Yunus. Thermal diffusivity measurement of black and metallic graphite paint coatings. *Measurement Science and Technology*, 10(1):7, 1999.

[93] M. M. Moksin and D. P. Almond. Non-destructive examination of paint coatings using the thermal wave interferometry technique. *Journal of Materials Science*, 30(9):2251–2253, 1995.

[94] A. Renault. Test analysis report no. 21. Technical report, ThermoConcept, 2013.

[95] R. J. Adrian and J. Westerweel. *Particle Image Velocimetry*, volume 30. Cambridge University Press, 2010.

[96] E. Mullins. *Statistics for the quality control chemistry laboratory*. Royal Society of Chemistry, 2003.

[97] H. W. Coleman and W. G. Steele. *Experimentation, validation, and uncertainty analysis for engineers*. Wiley, 2009.

[98] J. H. Kim, T. W. Simon, and R. Viskanta. Journal of heat transfer policy on reporting uncertainties in experimental measurements and results. *Journal of Heat Transfer*, 115:5, 1993.

[99] B. H. Chang A. F. Mills. Error analysis of experimants. Technical report, University of California, Incheon City College, 2004.

[100] J. Stafford, E. Walsh, and V. Egan. Characterizing convective heat transfer using infrared thermography and the heated-thin-foil technique. *Measurement Science and Technology*, 20:105401, 2009.

[101] J. Stafford, E. Walsh, V. Egan, and R. Grimes. Flat plate heat transfer with impinging axial fan flows. *International Journal of Heat and Mass Transfer*, 53(25):5629–5638, 2010.

[102] P. Dunand, G. Castanet, M. Gradeck, D. Maillet, and F. Lemoine. Energy balance of droplets impinging onto a wall heated above the leidenfrost temperature. *International Journal of Heat and Fluid Flow*, 44:170–180, 2013.

[103] T. Persoons. Temporal and spatial covariance functions. Personal communication.

[104] M. Diakides, J. D. Bronzino, and D. R. Peterson. *Medical Infrared Imaging: Principles and Practices*. CRC Press, 2012.

[105] H. Budzier and G. Gerlach. *Thermal Infrared Sensors: Theory, Optimisation and Practice*. Wiley Online Library, 2011.

[106] Santa Barbara Infrared. Sitf signal transfer function. http://www.youtube.com/watch?v=NEFjVGKOIgs, 2012. [Online; accessed 21-November-2013].

[107] Santa Barbara Infrared. Noise equivalent temperature difference (netd). http://www.youtube.com/watch?v=2pVBlqldyj4, 2012. [Online; accessed 21-November-2013].

[108] E. Canot, L. Davoust, M. El Hammoumi, and D. Lachkar. Numerical simulation of the buoyancy-driven bouncing of a 2-d bubble at a horizontal wall. *Theoretical and Computational Fluid Dynamics*, 17(1):51–72, 2003.

[109] F. J. Lesage and F. Marois. Experimental and numerical analysis of quasi-static bubble size and shape characteristics at detachment. *International Journal of Heat and Mass Transfer*, 64:53–69, 2013.

[110] C. Veldhuis, A. Biesheuvel, and L. Van Wijngaarden. Shape oscillations on bubbles rising in clean and in tap water. *Physics of Fluids*, 20:040705, 2008.

[111] Z. Zapryanov and S. Tabakova. *Dynamics of bubbles, drops, and rigid particles*, volume 50. Springer, 1999.

[112] R. Manica, E. Klaseboer, R. Gupta, M. H. W. Hendrix, C-D. Ohl, and D. Y. C. Chan. Modelling film drainage of a bubble hitting and bouncing off a surface. In *Ninth International Conference on CFD in the Minerals and Process Industries, CSIRO, Melbourne, Australia*, volume 100, page 024501, 2012.

[113] T. Fujii and H. Imura. Natural-convection heat transfer from a plate with arbitrary inclination. *International Journal of Heat and Mass Transfer*, 15(4):755–767, 1972.

[114] E. Radziemska and W. M. Lewandowski. Heat transfer by natural convection from an isothermal downward-facing round plate in unlimited space. *Applied energy*, 68(4):347–366, 2001.

[115] A. J. N. Khalifa. Natural convective heat transfer coefficient–a review: I. isolated vertical and horizontal surfaces. *Energy Conversion and Management*, 42(4):491–504, 2001.

[116] G. H. Su, Y. W. Wu, and K. Sugiyama. Natural convection heat transfer of water in a horizontal gap with downward-facing circular heated surface. *Applied Thermal Engineering*, 28(11):1405–1416, 2008.

[117] H. Beer. Das dynamische blasenwachstum beim sieden flüssigkeiten an heizflächen. *Forschung auf dem Gebiete des Ingenieurwesens*, 37:85–90, 1971.

[118] A. Lucic, M. Emans, F. Mayinger, and C. Zenger. Interferometric and numerical study of the temperature field in the boundary layer and heat transfer in subcooled flow boiling. *International Journal of Heat and Fluid Flow*, 25(2):180–195, 2004.

[119] I. Eames and S. B. Dalziel. Dust resuspension by the flow around an impacting sphere. *Journal of Fluid Mechanics*, 403:305–328, 2000.